METALS. SUPERCONDUCTORS

Symmetry breaking in tunnel junctions between partially dielectrized metals with charge or spin density waves

A. I. Voĭtenko and A. M. Gabovich

Institute of Physics, Ukrainian Academy of Sciences, 252650 Kiev, Ukraine
(Submitted July 30, 1997)
Fiz. Tverd. Tela (St. Petersburg) **40**, 385–388 (March 1998)

Tunnel current–voltage characteristics are calculated for symmetric junctions between metals waves of with charge or spin density that have equal absolute values $|\Sigma|$ of the dielectric order parameter. The possibility of different signs for Σ on opposite sides of the junction is considered. As a result, the current–voltage characteristics are highly asymmetric. The predicted effect is a new example of symmetry breaking in many particle systems and makes it possible to explain some experimental data for symmetric URu_2Si_2–URu_2Si_2 microjunctions. © *1998 American Institute of Physics.* [S1063-7834(98)00103-8]

In metals with charge (CDW) or spin (SDW) density waves at temperatures below the transition temperature T_{tr} (the structural transition temperature T_d for CDW or the Neél temperature T_N for SDW), a dielectric gap $|\Sigma|$ develops on nested (congruent) parts of the Fermi surface. In this regard, the properties of metals with completely or partially dielectrized Fermi surfaces and those of superconductors are similar in many ways.[1] This is especially true of the ''semiconducting'' aspects of the Bardeen–Cooper–Schrieffer (BCS) model for superconductors and models of Peierls or exciton dielectrics. The coherence properties of these two types of collective state, however, differ greatly.[2]

It is well known[3] that the BCS theory and its generalizations predict symmetric current–voltage characteristics, for both symmetric and nonsymmetric tunnel junctions involving superconductors. Experiments agree fully with these conclusions. In particular, symmetric current–voltage characteristics are observed for the nonsymmetric superconductor–dielectric–normal metal junction.[3]

In the absence of superconductivity, the tunnel characteristics of CDW and SDW metals are completely identical, and we shall use the abbreviation CSDW (charge–spin density wave). As we have shown previously,[4] the tunnel current–voltage characteristics of nonsymmetric N–I–DM contacts, where DM denotes a partially dielectrized CSDW metal, should be nonsymmetric with respect to the voltage V at the junction for $T<T_{tr}$. The analysis was based on the Bilbro–McMillan model[5–7] for a partially dielectrized superconductor. At the same time, for $T>T_{tr}$ there is no dielectric gap in the electronic spectrum and the corresponding current–voltage characteristic is symmetric with respect to V.

On the other hand, an analysis of CSDWs as reported in Ref. 8 in terms of an anisotropic Hubbard model, including nonideal nesting, leads to a complex realignment of the electronic spectrum below T_{tr} which depends on the relation between the energy parameter $\varepsilon-a$ and $|\Sigma|$. In particular, the gap nature of the spectrum disappears for $\varepsilon_a>|\Sigma|$. However the current–voltage characteristics for N–I–DM junctions remain symmetric in terms of this theory,[8] so that it cannot be used to explain the experimentally observed current–voltage characteristics for nonsymmetric tunnel and point contacts with the CDW metals $NbSe_3$,[9,10] $TiSe_{2-x}S_x$,[11] and $K_{0.3}MoO_3$[12] or the SDW metal URu_2Si_2.[13,14] At the same time, these characteristics agree well with our results.[4]

The situation is even more confused for symmetric DM–I–DM junctions. Measurements for URu_2Si_2–URu_2Si_2 point contacts[13,15] have shown that even in this case the current–voltage characteristics can be nonsymmetric. Here we shall attempt, within the framework of the approach proposed earlier,[4] to give a possible explanation for this surprising fact. As far as we know, there are, as yet, no alternative explanations.

The model Hamiltonian of a system with partial dielectrization of the electronic spectrum has the form

$$H=H_0+H_{\mathrm{MF}}. \tag{1}$$

Here $H-0$ is the free electron Hamiltonian, while the molecular field Hamiltonian H_{MF} is given by

$$H_{\mathrm{MF}}=-\sum_{s=1}^{2}\sum_{\mathbf{p}\alpha}[1+(2\alpha-1)\Psi]\Sigma a^{+}_{s\mathbf{p}\alpha}a_{s,\mathbf{p}+\mathbf{Q},\alpha}+\mathrm{h.c.}, \tag{2}$$

$\Psi=0$ (1) for a CDW (SDW), $a^{+}_{s\mathbf{p}\alpha}$ ($a_{s\mathbf{p}\alpha}$) is the creation (annihilation) operator for a quasiparticle with momentum $\mathbf{p}$ and projected spin α from region s of the Fermi surface. The sum is taken over the nested parts of the Fermi surface ($s=1,2$) where the electronic spectrum is degenerate ($\mathbf{Q}$ is the CSDW vector, $\hbar=1$),

$$\xi_1(\mathbf{p})=-\xi_2(\mathbf{p}+\mathbf{Q}), \tag{3}$$

and the order parameter Σ appears as a consequence of an exciton (Coulomb) or Peierls (electron–phonon) instability of the initial spectrum (3).[1,2,7] In the remainder of the Fermi

 © 1998 American Institute of Physics

surface ($s=3$), the quasiparticle spectrum $\xi_3(\mathbf{p})$ is nondegenerate. We limit ourselves to real values of $|\Sigma|$, since an imaginary value for it corresponds to thus-far unobserved phases with current density or spin current waves.[2]

The tunnel quasiparticle current in junctions with CSDW metals was calculated in a fashion similar to Ref. 4, based on a method developed for superconducting junctions.[16] In our theory it is necessary to include three Green's functions for each electrode:[7]

$$G_{nd}(\mathbf{p};\omega_n)=-[i\omega_n+\xi_3(\mathbf{p})]Z_1^{-1},$$

$$G_d(\mathbf{p};\omega_n)=-[i\omega_n+\xi_1(\mathbf{p})]Z_2^{-1},$$

$$G_{is}(\mathbf{p};\omega_n)=-\Sigma Z_2^{-1}. \tag{4}$$

Here $Z_1=\omega_n^2+\xi_3^2(\mathbf{p})$, $Z_2=\omega_n^2+\xi_1^2(\mathbf{p})+\Sigma^2$, $\omega_n=(2n+1)\pi T$, T is the temperature ($k_B=1$), $n=0,\pm1,\pm2,\ldots$, the subscript nd corresponds to the undielectrized part of the Fermi surface, d to the dielectrized parts 1 and 2, and is to electron-hole coupling. In particular, the function $G_{is}(\mathbf{p};\omega_n)$ is responsible for the large difference between superconductors and exciton (Peierls) dielectrics.

We restrict ourselves to electric fields below threshold, i.e, assume that pinning of the CSDW takes place.[1] All the tunnel matrix elements are assumed to be equal, so that there is a single electrical resistance parameter, R, for the junction.[4]

In our previous work,[4] we have made a detailed analysis of the current–voltage characteristic of a symmetric DM–I–DM junction where the parameters of both electrodes were assumed to be the same. This choice for a symmetric junction is natural, but is not the only one possible. In fact, various thermodynamic properties of dielectrized metals are independent of the sign of Σ.[7] The situation is extremely similar to the degeneracy of the ground state of an Ising magnet as it applies to different directions of magnetization. An arbitrary infinitesimal anisotropy (for example, owing to an external interaction) can make any of these states into a preferred state. We assume that a similar effect can occur for CSDW metals, as well, although it cannot be displayed for a single sample.

The situation changes sharply when two samples are brought into contact. If, for example, the left electrode is characterized by a positive Σ, while that of the right electrode is negative with the same absolute value, then a junction between the two is nonsymmetric, although it is assumed *a priori* to be symmetric. This is the key point of our analysis. As will be shown below, this kind of configuration leads to a nonsymmetric current–voltage characteristic, even though the electrodes have been made of absolutely identical materials. In essence, this represents a new example of a macroscopic manifestation of the breaking of symmetry in a many particle system. Naturally, this effect can only be observed for $T<T_{tr}$.

The calculations yield the following dependence of the quasiparticle current J on the voltage across a junction, $V=V_{\rm right}-V_{\rm left}>0$, for the above choice of signs for the order parameters ($\Sigma_{\rm left}=\Sigma>0$ and $\Sigma_{\rm right}=-\Sigma<0$):

$$J(V)=\sum_{i=1}^{6} J_i(V), \tag{5}$$

where

$$J_1(V)=\varkappa_1(\Sigma,\Sigma),\quad J_2(V)=\Sigma^2\varkappa_2(\Sigma,\Sigma),$$
$$J_3(V)=2\nu\varkappa_1(\Sigma,0),\quad J_4(V)=\nu^2\varkappa_1(0,0),$$
$$J_5(V)=-2\Sigma\varkappa_3(\Sigma,\Sigma),\quad J_6(V)=-2\nu\Sigma\varkappa_3(\Sigma,0). \tag{6}$$

Here

$$\varkappa_1(\Sigma_1,\Sigma_2)=C\int_{-\infty}^{\infty}d\omega f(\omega,eV,T)\times N(\omega,eV,\Sigma_1,\Sigma_2)|\omega||\omega-eV|,$$
$$\varkappa_2(\Sigma_1,\Sigma_2)=C\int_{-\infty}^{\infty}d\omega f(\omega,eV,T)\times N(\omega,eV,\Sigma_1,\Sigma_2)\,\mathrm{sgn}\;\omega\;\mathrm{sgn}(\omega-eV),$$
$$\varkappa_3(\Sigma_1,\Sigma_2)=C\int_{-\infty}^{\infty}d\omega f(\omega,eV,T)\times N(\omega,eV,\Sigma_1,\Sigma_2)|\omega|\mathrm{sgn}(\omega-eV), \tag{7}$$

where

$$f(\omega,eV,T)=\mathrm{th}\,\frac{\omega-eV}{2T}-\mathrm{th}\,\frac{\omega}{2T}, \tag{8}$$

$$N(\omega,eV,\Sigma_1,\Sigma_2)=\frac{\theta(|\omega|-\Sigma_1)}{(\omega^2-\Sigma_1^2)^{1/2}}\,\frac{\theta(|\omega-eV|-\Sigma_2)}{((\omega-eV)^2-\Sigma_2^2)^{1/2}}, \tag{9}$$

$C=-[2eR(1+\nu)^2]^{-1}$, e is the elementary charge, $\theta(x)$ is the Heaviside function, $\nu=N_{nd}(0)/N_d(0)$, and $N_{nd}(0)$ and $N_d(0)$ are the densities of states in the undielectrized and dielectrized parts of the Fermi surface, respectively. In the case studied previously,[4] where there is a symmetry between the positive and negative branches of the current–voltage characteristic, there are no terms $J_{5,6}(V)$. Then the expression for the current when $T=0$ and in the corresponding limit is the same as has been found before.[17]

The components $J_i(V)$ of the currents have different symmetry properties, specifically, $J_{1-4}(-V)=-J_{1-4}(V)$ and $J_{5,6}(-V)=J_{5,6}(V)$. Thus, the total current $J(V)$ considered here has no definite symmetry! If $\Sigma_{\rm left}<0$ and $\Sigma_{\rm right}>0$, the two branches of the current–voltage characteristic simply change places, as for nonsymmetric junctions.[4]

When $T=0$ all the components of the currents are expressed in terms of complete elliptic integrals of the first and second kinds. If, however, $T\neq0$, then only a numerical calculation is possible. Figure 1 shows plots of the calculated dimensionless current through the barrier, $j=JeR/\Sigma_0$ (a), and the corresponding conductivity $g=dj/dx$ (b) as functions of the dimensionless voltage across the junction, $x=eV/\Sigma_0$, where $\Sigma_0=|\Sigma(T=0)|$, for $T/T_{tr}=0.5$. The temperature dependence $\Sigma(T)$ was assumed to be that typical of the BCS theory for superconductors. The parameter values $\nu=0.4$ and 1.5 were chosen in accordance with different published data for URu_2Si_2.[18,19]

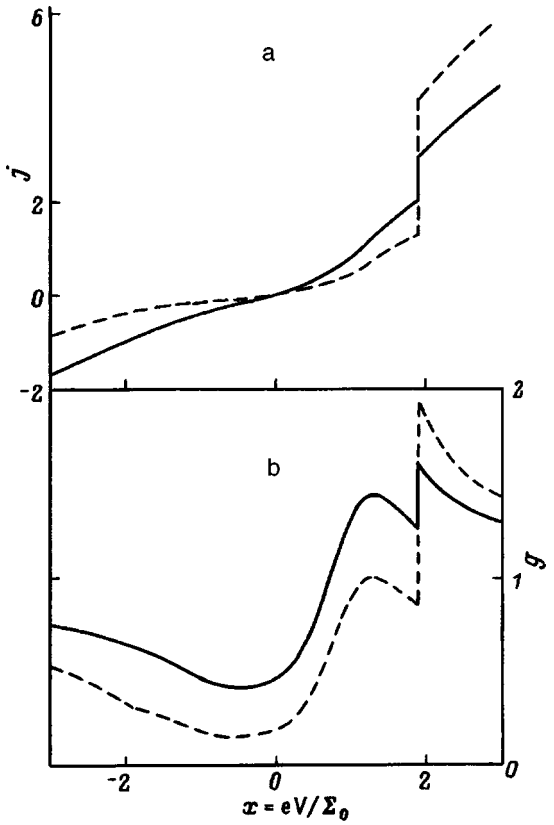

FIG. 1. The dimensionless current $j=JeR/\Sigma_0$ (a) and dimensionless conductivity $g=dj/dx$ (b) as functions of the dimensionless voltage $x=sV/\Sigma_0$ across a URu_2Si_2–URu_2Si_2 tunnel junction with broken symmetry at a temperature $T=0.5T_{tr}$ for different degrees ν of dielectrization of the Fermi surface (where e is the elementary charge, R is the junction resistance, Σ_0 is the absolute value of the dielectric order parameter at zero temperature, and T_{tr} is the dielectric transition temperature). $\nu=0.4$ (dashed curve) and 1.5 (smooth curve).

A comparison of these current–voltage characteristics with the results for symmetric junctions without symmetry breakings[4] shows that in the positive branch the root singularity of the current at $eV=\Sigma$ and the discontinuity in the conductivity at $eV=2\Sigma$ are stronger in the case considered here. In the negative branch of the current–voltage characteristics, on the other hand, the corresponding singularities vanish almost completely owing to destructive interference of the terms J_6 with J_3 and J_5 with J_1+J_2. Thus, the qualitative character of the $j(x)$ and $g(x)$ curves for a symmetric junction with broken symmetry is analogous to the current–voltage characteristic in the nonsymmetric case.[4] It follows from all the above discussion that the symmetry of the DM–I-DM junctions and the corresponding current–voltage characteristics are determined by the complete equivalence of the CSDW in both electrodes (including the signs of Σ). This circumstance was overlooked in the earlier work.[4,20]

The calculated $g(x)$ curves are in qualitative agreement with those measured for URu_2Si_2–URu_2Si_2 microjunctions.[14] Experimenters have observed both symmetric and nonsymmetric current–voltage characteristics in a single series of measurements. This is consistent with our conception, given the thermodynamic equivalence of the CSDWs which differ only in the sign of the order parameter.[7]

In conclusion, we emphasize that in this paper we have predicted a new macroscopic manifestation of a symmetry breaking in a many particle system. It differs fundamentally from the well known effects in bulk media, such as magnetic or ferroelectric materials. In fact, the predicted effect can be observed only when a formally symmetric DM–I–DM junction in inserted in an electrical circuit. Note that here we have neglected correlations of the Josephson type, which are possible in strong electric fields beyond threshold.[1,17]

The authors thank S. N. Artamenko (Institute of Radio Physics and Electronics, Russian Academy of Sciences, Moscow) for valuable information. We also thank R. S. Markiewicz (Boston), J. van Ruitenbeck (Leiden), and I. K. Yanson (Kharkov) for useful discussions.

This work was partially supported by INTAS Grant 94-3862 and the Ukrainian State Foundation for Basic Research (grant 2.4/100).

[1] G. Grüner, Rev. Mod. Phys. **60**, 1129 (1988); **66**, 1 (1994).
[2] B. I. Halperin and T. M. Rice, Solid State Phys. **21**, 115 (1968); Yu. V. Kopaev, Tr. FIAN SSSR **86**, 3 (1975).
[3] E. Burstein and S. Lundqvist, eds., *Tunnelling Phenomena in Solids*, Plenum Press, N.Y. (1969).
[4] A. M. Gabovich and A. I. Voitenko, Phys. Rev. B **52**, 7437 (1995); Phys. Lett. A **223**, 221 (1996).
[5] G. Bilbro and W. L. McMillan, Phys. Rev. B **14**, 1887 (1976).
[6] K. Machida, J. Phys. Soc. Jpn. **50**, 2195 (1981).
[7] A. M. Gabovich and A. S. Shpigel, J. Low Temp. Phys. **51**, 581 (1983); J. Phys. F **14**, 1031 (1984); Phys. Rev. B **38**, 297 (1988).
[8] X.-Z. Huang and K. Maki, Phys. Rev. B **40**, 2575 (1989); **46**, 162 (1992).
[9] T. Ekino and J. Akimitsu, Physica B **194–196**, 1221 (1994).
[10] J. P. Sorbier, H. Trotel, P. Monceau, and F. Levy, Phys. Rev. Lett. **76**, 676 (1996).
[11] Y. Miyahara, H. Bando and H. Ozaki, J. Phys.: Condens. Matter **7**, 2553 (1995); **8**, 7453 (1996).
[12] A. A. Sinchenko, Yu. I. Latyshev, S. G. Zybtsev, I. G. Gorlova, and P. Monso, Pis'ma Zh. Éksp. Teor. Fiz. **64**, 259 (1996) [JETP Lett. **64**, 285 (1996)].
[13] A. Nowack, Yu. G. Naidyuk, P. N. Chubov, I. K. Yanson and A. Menovsky, Z. Phys. B **88**, 295 (1992).
[14] R. Escudero, F. Morales, and P. Lejay, Phys. Rev. B **49**, 15271 (1994).
[15] Yu. G. Naĭdyuk, O. E. Kvitnitskaya, A. Novak, I. K. Yanson, and A. A. Menovskiĭ, Fiz. Nizk. Temp. **21**, 310 (1995) [Fiz. Nizk. Temp. **21**, 236 (1995)].
[16] A. I. Larkin and Yu. N. Ovchinnkov, Zh. Éksp. Teor. Fiz. **51**, 1535 (1966) [Sov. Phys. JETP **23**, 1035 (1966)].
[17] S. N. Artemenko and A. F. Volkov, Zh. Éksp. Teor. Fiz. **87**, 691 (1984) [Sov. Phys. JETP **60**, 395 (1984)].
[18] T. T. M. Palastra, A. A. Menovshy, J. van den Berg, A. S. J. Dirkmaat, P. H. Kes, G. J. Mieuwenhuys, and J. A. Mydosh, Phys. Rev. Lett. **55**, 2727 (1985).
[19] M. B. Maple, J. W. Chen, Y. Dalichaouch, T. Kohara, C. Rossel, M. S. Torikachvili, and N. W. McElfresh, Phys. Rev. Lett. **56**, 185 (1986).
[20] A. M. Ismagilov and Yu. V. Kopaev, Zh. Éksp. Teor. Fiz. **96**, 1492 (1989) [Sov. Phys. JETP **69**, 846 (1989)].

Translated by D. H. McNeill

Near-ordering structural transitions in amorphous metal alloys

V. I. Lavrent'ev

Sumu Institute of Surface Modification, 244030 Sumu, Ukraine
(Submitted June 16, 1997; resubmitted October 9, 1997)
Fiz. Tverd. Tela (St. Petersburg) **40**, 389–392 (March 1998)

The temperature variations in the modulus of elasticity (Young's modulus) E and internal friction Q^{-1} of the amorphous metal alloys $Ti_{50}Cu_{50-x}Ni_x$ ($5 \leqslant x \leqslant 20$) are studied at temperatures of 300–800 K. There is an anomalous increase in $E(T)$ at temperatures above T_x (which varies from 440 to 525 K, depending on the composition). When the amount of nickel in the alloy is high ($x > 12$ at. %), a small peak shows up in $Q^{-1}(T)$. These effects are related to structural transitions in near-ordering regions (clusters). A model for structural relaxation of near ordering in amorphous alloys is proposed on the basis of these experiments. © *1998 American Institute of Physics.* [S1063-7834(98)00203-2]

Structural relaxation processes in amorphous metal alloys lead to observable changes in many physical properties, in particular the elastic and inelastic parameters.[1–5] These properties are highly sensitive to structural changes,[6] and this determines their effectiveness in studies of relaxation processes in amorphous metal alloys. Thus, work on internal friction has made it possible to develop some ideas about structural defects in amorphous metal alloys.[4,5,7,8] The data in these papers have been analyzed in terms of the concept of the free volume, which is phenomenological in nature, and attempts to use it to specify more clearly the atomic realignments responsible for various inelastic effects in amorphous metal alloys have encountered entirely understandable difficulties associated with the indeterminacy of an amorphous structure.[9] These difficulties can apparently by overcome by examining other fundamental concepts associated with near ordering.[10–12] The purpose of this paper is to study elastic and inelastic properties of Ti–Cu–Ni amorphous metal alloy systems, whose thermodynamic equilibrium plots contain many interesting phases and critical points[13] and for which the probability of different phase transitions with changing temperature is large, and also to develop the concept of near ordering based on our experimental results.

1. EXPERIMENTAL TECHNIQUE

A spin melt technique was used to obtain 30–40μ thick strips of amorphous metal alloy. The melt was cooled at a rate of 3×10^6 K/s. The amorphism of the original samples was monitored using a DRON-3 x-ray diffractometer (Cu K_α radiation). The internal friction and modulus of elasticity were determined on a device in which bending vibrations are excited electrostatically[14] in a vacuum of 10^{-4} Pa as the original amorphous metal alloy samples are heated. The samples were heated at a rate of 10 K/min at temperatures of 300–800 K. The relative deformation of the samples during the measurements was less than 10^{-6}. The frequency f of the free vibrations of the amorphous metal alloy samples was in the range 300–600 Hz. The error in determining f was less than 0.5%.

2. EXPERIMENTAL RESULTS

The internal friction Q^{-1} and dynamic modulus of elasticity (Young's modulus) E ($E \propto f^2$)[14] of the amorphous metal alloys were measured at various temperatures by heating the samples at a constant rate. Some of the resulting $Q^{-1}(T)$ curves are shown in Fig. 1. Figure 2 shows some plots of the normalized modulus of elasticity E/E_0 as a function of temperature. (E_0 is the modulus of elasticity of the initial amorphous metal alloy sample at room temperature.) In these curves, several effects show up, some of which are obvious in nature. Thus, the strong peak in the internal friction at temperatures of 670–730 K is related to crystallization (Fig. 1) and the temperature at which it occurs and its shape are consistent with the crystallization process in these amorphous alloys.[3,15] The sharp drop in the modulus of elasticity of the amorphous metal alloys at temperatures above 590–660 K is caused by vitrification processes and the temperature at which the drop sets in is the vitrification temperature T_g.[16] The other effects are not so predictable, although, they apparently should show up in many amorphous metal alloys. Thus, depending on the composition of the alloy, at

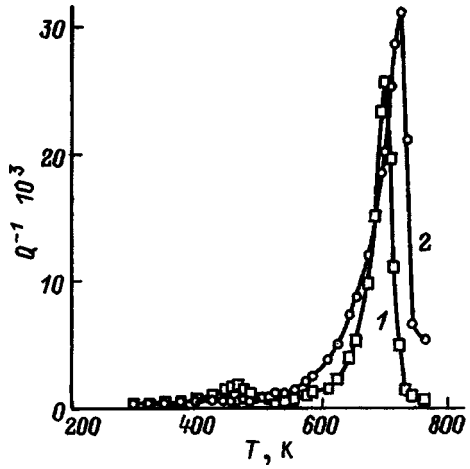

FIG. 1. Internal friction of $Ti_{50}Cu_{50-x}Ni_x$ amorphous metal alloys as a function of temperature for $x=5$ (*1*) and 20 (*2*). The rate of heating is 10 K/min.

 © 1998 American Institute of Physics

temperatures of 440–525 K the drop in the modulus of elasticity as the sample is heated is replaced by a rise (Fig. 2). The temperature T_x at which E begins to rise varies nonmonotonically with composition (Fig. 3). The alloy with composition $Ti_{50}Cu_{38}Ni_{12}$ has the highest value of T_x. The maximum in the modulus of elasticity, E_{max}, owing to its increase during heating also varies nonmonotonically. The largest rise in E is observed for the amorphous metal alloys $Ti_{50}Cu_{32}Ni_{18}$ and $Ti_{50}Cu_{34}Ni_{16}$ (Fig. 2). In the amorphous alloys $Ti_{50}Cu_{50-x}Ni_x$ with greater than 12 at. % nickel, the change from a drop in the modulus of elasticity to a rise is accompanied by the appearance of a small nonrelaxation peak in $Q^{-1}(T)$ (Fig. 1).

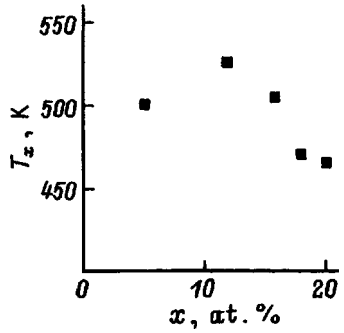

FIG. 3. The temperature T_x at which the elastic modulus of $Ti_{50}Cu_{50-x}Ni_x$ amorphous metal alloys begins to rise as a function of the Ni concentration in the alloy.

3. DISCUSSION OF RESULTS

Effects similar to those we have observed (a peak in the internal friction around 450–500 K and an anomalous increase in the modulus of elasticity at these temperatures) have been observed in studies of the elastic and inelastic properties of the amorphous metal alloys $Fe_{40}Ni_{38}Mo_4B_{18}$ and $Fe_{67}Co_{18}B_{14}Si_1$ in a saturation magnetic field after various sorts of annealing and deformation.[17] The nonrelaxation character of the peak in the internal friction was noted and the observed effects were related to structural transitions in the amorphous phase which affect the degree of near ordering. An analysis of scanning differential calorimetry data indicates that these structural transitions may be a type of order-disorder transition.[10] The papers cited here show that regions with near ordering (clusters) are of enormous importance in forming the structure and properties of amorphous metal alloys, and also suggest that the anomalous effects observed in the present paper are caused by cluster phase formation.

It is assumed that the structure of the clusters corresponds to the structure of crystalline phases formed by heating above the crystallization temperature T_c.[18] This assumption is imprecise, since during high-speed quenching from the liquid state, the multicomponent system may pass through temperature intervals where different phases coexist. Thus, the structure of the clusters is metastable, having inherited elements of the structure of one of the high-temperature crystalline phases; this is indicated, in particular, by the phase diagrams of rapidly quenched alloys.[19] As an amorphous alloy is heated within the confines of the volume of a cluster with dimensions of several nanometers,[1] nuclei of a new (more stable) phase will be formed. When the degree of metastability is high, the critical nuclei of the new phase r_c can be very small and may form a sphere with a volume of a few atoms.[20] Growth of nuclei with radius $r > r_c$ leads to a phase transition within the cluster volume. The possibility of such a transition is also indicated by data on phase formation in amorphous metal alloys by *in situ* electron microscopy,[18] and the data imply that these transitions can be reversible. Phase transitions within the volume of clusters cause a reduction of the free energy of amorphous metal alloys, so that they can be referred to as ''structural relaxation of the near ordering.'' If the modulus of elasticity of the new phase is greater than that of the old phase, then, because of these cluster phase transitions, the effective modulus of elasticity of the amorphous metal alloy sample will be higher.

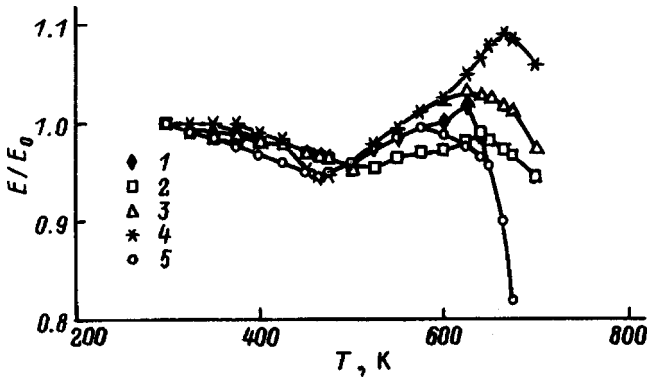

FIG. 2. The normalized elastic modulus of $Ti_{50}Cu_{50-x}Ni_x$ amorphous metal alloys as a function of temperature for $x=5$ (*1*), 12 (*2*), 16 (*3*), 18 (*4*), and 20 (*5*). The heating rate is 10 K/min.

These arguments make it possible to understand the anomalous effects in the elastic and inelastic properties of amorphous metal alloys observed during heating. In rapidly quenched $Ti_{50}Cu_{50-x}Ni_x$ amorphous alloys, the structure of the ordered clusters at room temperature corresponds to a metastable solid solution of the β-phase stabilized by copper and nickel.[21] Raising the temperature increases the atomic vibrations within the cluster volumes and this initially causes the observed reduction in the elastic modulus (Fig. 2). Near the temperature T_x the energies of the thermal fluctuations are high enough for formation of nuclei of a new phase with critical size r_c. Further growth of nuclei with $r > r_c$ determines a phase transition within the confines of the clusters with the formation of higher molecular weight phases of TiCu, Ti_2Cu, and Ti_2Ni:[21] structural relaxation of the near ordering takes place. Here the phase transitions in the amorphous metal alloys $Ti_{50}Cu_{50-x}Ni_x$ with different compositions have their distinct features and this is responsible for the quantitative differences in T_x and E_{max}, the atypical effects observed in the experiment. Thus, raising the nickel content of the alloy from 5 to 12 at. % facilitates a reorganization of the near ordering in accordance with the transitions $\beta \rightarrow$ TiCu and $\beta \rightarrow Ti_2Cu$, with the fraction of the structure of the latter compound predominating at elevated concentrations of Ni.[22] At the same time, the structure of the amor-

phous alloy is stabilized and this causes the onset temperature of the transition to increase (Fig. 3). Further elevation of the nickel content favors the formation of clusters of the Ti_2Ni phase[19,22] with its enhanced elastic properties. This leads to an increase in E_{max} for the amorphous metal alloys with compositions $Ti_{50}Cu_{34}Ni_{16}$ and $Ti_{50}Cu_{32}Ni_{18}$ (Fig. 2). Binding nickel in the Ti_2Ni and TiNi phases during nucleation facilitates the $\beta \rightarrow \alpha$ transition, which becomes more frequent as the Ni content of the alloy is raised. This is reflected in a lower transition onset temperature T_x (Fig. 3) and in a lower peak of the modulus, E_{max} (Fig. 2). Part of the $\beta \rightarrow \alpha$ transition proceeds via a martensite mechanism,[15,22] which is distinguished by the appearance of a nonrelaxation peak in the internal friction at temperatures near T_x (Fig. 1). When the nickel content of the amorphous metal alloys is low ($x<10$ at. %), this kind of transition is suppressed by Cu and Ni atoms, which are good stabilizers of the β-phase.[23]

The extensive temperature range within which the elastic modulus increases as an amorphous metal alloy is heated above T_x indicates that in clusters the TiCu, Ti_2Cu, and Ti_2Ni phases are formed by a diffusion mechanism. Martensite clusters, on the other hand, develop within a very short time interval. The martensite transition takes place in first order, since it is prepared by suitable atomic realignments within the confines of the clusters owing to thermal fluctuations during formation of critical nuclei of the new phases.

The proposed model for structural relaxation of the near ordering based on our experimental data can be used to make several quantitative estimates. Thus, we assume that the work of formation for a critical nucleus of the new phase, R_{max}, is given by[20]

$$R_{max}=\frac{4\pi\alpha}{r}\,r_c^2, \tag{1}$$

where α is the specific surface energy. Assuming that this work is equal to the energy of the harmonic oscillators in the volume of a critical nucleus at temperature T_x, we can write

$$nkT_x=\frac{4\pi\alpha}{3}\,r_c^2, \tag{2}$$

where n is the number of atoms forming the critical nucleus and k is the Boltzmann constant. In Eq. (2) the energy of a critical nucleus at T_x is determined by the classical formula through a sum of noninteracting oscillators. This estimate is justified by the rather high values of T_x in this case. ($T_x > \Theta$, where Θ is the Debye temperature.) For many metals this definition of the energy is satisfactory even at room temperature.[20,24] In terms of the present model, this estimate for the energy is even more justified by the fact that, at temperatures near T_x, the crystalline lattice of a metastable phase in the volume of a critical nucleus is extremely unstable, while the influence of correlations in the interatomic interactions, which determine the quantum mechanical effects, is minimal and unimportant.

For cubic (bcc) packing of the atoms in the nucleus, geometric considerations yield an estimate for the relation between r_c and n in the neighborhood of the first coordination spheres of

$$r_c \approx \frac{a}{2}\left(\frac{n}{2}\right)^{1/3}, \tag{3}$$

where a has the significance of a lattice parameter of the nucleus. Given Eqs. (2) and (3), the size of a critical nucleus in the new phase can be estimated in terms of the thermodynamic parameters as

$$r_c \approx \frac{\pi\alpha a^3}{12kT_x}. \tag{4}$$

From the experiment we have $T_x=5\times10^2$ K and, taking $\alpha\sim1$ J/m^2,[25] we obtain $r_c\sim10^{-9}$ m for $a\sim3\times10^{-10}$ m. This estimate of r_c is consistent with the assumptions of our model for near-order structural relaxation and also indicates a high degree of metastability of the phases that form the initial structure of the clusters.

In this paper we have proposed a model for phase transitions in the interior of clusters which may offer good prospects for developing a theory of the amorphous state of metal alloys. This model is based on the standard assumptions of equilibrium thermodynamics and kinetic theory and, with the aid of these, it can be used to study the nature of the amorphous state through the prism of microscopic volumes with an ordered structure. From the standpoint of this model it is clear that such quantities as the cluster size and degree of metastability of the phase within a cluster have definite limited intervals within which phase transitions in a cluster will be reversible, and this controls the reversible variation of the macroscopic properties.[2,3] The irreversible growth of clusters owing to diffusion processes at the cluster-amorphous shell interface, however, forces an ever larger number of clusters to go outside these intervals; this lowers the degree of reversibility of these properties and inevitably leads to crystallization of the amorphous metal alloys.

[1] K. Suzuki, H. Fujimore, and K. Hashimoto, *Amorphous metals* [Russian translation], Metallurgiya, Moscow (1987), 328 pp.
[2] I. V. Zolotukhin and Yu. E. Kalinin, Usp. Fiz. Nauk **160**(9), 75 (1990) [Sov. Phys. Uspekhi **33**, 720 (1990)].
[3] V. I. Lavrent'ev and V. A. Khonik, Metallofizika **10**(6), 95 (1988).
[4] H. S. Chen and N. Morito, J. Non-Cryst. Solids **72**, 287 (1987).
[5] N. Morito and T. Egami, Acta Metall. **32**, 603 (1984).
[6] A. S. Noeick and B. S. Berry, *Anelastic Relaxation in Crystalline Solids*, Academic Press, N.Y. (1972), 472 pp.
[7] F. Spaepen, Acta Metall. **25**, 497 (1977).
[8] K. Bothe, N. Hausmann, and H. Neuhauser, Scr. Metall. **19**, 1513 (1985).
[9] I. V. Zolotukhin, Yu. V. Barmin, and A. V. Sitnikov, Fiz. Tverd. Tela **25**, 3456 (1983) [Sov. Phys. Solid State **25**, 1988 (1983)].
[10] P. T. Vianco and J. C. M. Li, J. Mater. Res. **2**, 461 (1987).
[11] E. Bonetti, Philos. Mag. B **56**, 185 (1987).
[12] P. Allia, E. Bonetti, E. Evangelista, L. Turroni, and F. Vinai, Phys. Status Solidi A **88**, 521 (1985).
[13] S. P. Alisova and P. B. Vudberg, Izv. RAN. Metally **4**, 218 (1992).
[14] V. S. Postnikov, *Internal Friction in Metals and Alloys Consultants Bureau, New York* (1967); [in Russian], Metallurgiya, Moscow (1974), pp. 352.
[15] N. V. Matveeva and O. V. Kostyanaya, in *Physical Chemistry of Amorphous (Glassy) Metallic Materials* [in Russian], Yu. K. Kovneristyĭ (Ed.), Nauka, Moscow (1987), p. 117.

[16] V. A. Zelenskiĭ, V. A. Khonik, N. M. Matveeva, and A. V. Kryukov, Fizika Khimiya Obrab. Materialov **2**, 119 (1986).
[17] E. Bonetty, Philos. Mag. B **61**, 751 (1990).
[18] G. E. Abrosimova and A. S. Aronin, Fiz. Tverd. Tela **32**, 1742 (1990) [Sov. Phys. Solid State **32**, 1014 (1990)].
[19] S. P. Alisova, P. B. Vudberg, T. I. Barmina, and N. V. Lutskaya, Izv. RAN. Metally **2**, 205 (1993).
[20] L. D. Landau and E. M. Lifshitz, *Statistical Physics*, Part I, Pergamon, Oxford, (1980); Nauka, Moscow (1976), 584 pp.
[21] V. N. Eremenko, *Titanium and its Alloys* [in Russian], Izd-vo. AN UkrSSR, Kiev (1960), pp. 500.
[22] É. V. Kozlov, V. B. Koshirin, N. M. Matveeva, and L. L. Maĭsner, in *Physical Chemistry of Amorphous (Glassy) Metallic Materials* [in Russian], Yu. K. Kovneristyĭ (Ed.), Nauka, Moscow (1987), p. 51.
[23] M. K. Macwillen, *Phase Transitions in Titanium and its Alloys* [Russian translation], Metallurgiya, Moscow (1967), 76 pp.
[24] Ya. I. Frenkel', *Introduction the Theory of Metals* [in Russian], Nauka, Leningrad (1972), 424 pp.
[25] J. Hirth and G. Pound, *Condensation and Evaporation: Nucleation and Growth Kinetics*, Pergamon, Oxford (1963); Metallurgiya, Moscow (1966).

Translated by D. H. McNeill

Critical current of an inhomogeneous Josephson junction at an intergrain boundary with a random distribution of dislocations

E. Z. Meĭlikhov and R. M. Farzetdinova

Russian Scientific Center ''Kurchatov Institute,'' 123182 Moscow, Russia
(Submitted September 16, 1997)
Fiz. Tverd. Tela (St. Petersburg) **40**, 393–402 (March 1998)

The critical current $J_c(\theta)$ of an intergrain boundary is calculated as a function of the contact misorientation angle θ of the granules. It is assumed that the ordering parameter is suppressed in regions near boundaries with an enhanced mechanical stress induced by randomly distributed surface dislocations. The stress distribution function is determined using a probabilistic approach. Assuming that the weak coupling at the boundary is Josephson coupling, an analytic expression is found for the angular dependence $J_c(\theta)$ (for tilt and twist boundaries). The magnitude of the residual critical current of a boundary in a strong magnetic field is estimated. © *1998 American Institute of Physics.* [S1063-7834(98)00303-7]

The low value of the critical current in high-temperature superconducting ceramics is known to be determined by a set of weak intergrain bonds at the boundaries between neighboring superconducting granules. These weak bonds are caused by the reduction in the superconduction ordering parameter near boundaries of this type. The reasons for this may be different; however, at pure boundaries, with no impurities or structural defects, the reduction in the ordering parameter is most often attributed to the field of mechanical stresses σ_{ik} $(i,k=x,y,z)$ generated by the dislocations which develop at grain boundaries.[1–3]

Without examining the specific mechanism for suppression of the superconductivity ordering parameter in those regions subject to strong mechanical stresses, we note that it is related to the appearance of an electrical potential during deformation of the lattice, the so called deformation potential $\varphi \propto \Xi\varepsilon$, where $\Xi \sim 10$ eV is a constant of the deformation potential and $\varepsilon \sim \sigma/\sigma_0$ is the lattice deformation. When the displacement of the electronic energy levels, $\sim \varepsilon\varphi$, becomes comparable to the Fermi energy $\varepsilon_F \sim 0.1$ eV (for HTSC), the electronic spectrum undergoes a radical realignment which leads to suppression of the superconducting state. Thus, we can regard a stress $\sigma_c \sim (\varepsilon_F/\Xi)\sigma_0 \sim 0.01\sigma_0$, in which the relative lattice deformation is $\sim 1\%$, as ''severe.''

At the same time, experiments show that the spatial distribution of the oxygen concentration in $YBa_2Cu_3O_{7-\delta}$ films has a minimum near an intergrain boundary.[4] Far from a boundary it satisfies $\delta \approx 0.05$ and at a boundary, $\delta \sim 0.3$ and $\sim 0.5–0.6$ for $\theta = 7$ and 31°, respectively.[1)] The oxygen concentration recovers its bulk value over a distance of only ~ 20 nm from a boundary. Thus, the width of the oxygen-depleted layer is close (see below) to the width of the boundary region that has been distorted by dislocations. Thus, it is entirely probable that this sort of reduction in the oxygen concentration is related to dislocation stresses concentrated near an intergrain boundary.

The stress field at the boundary is completely determined by the system of boundary dislocations. In the theory of dislocations, intergrain boundaries are usually associated with a periodic system of edge (for tilt boundaries) or screw (for twist boundaries) dislocations,[6] whose density is higher when the misorientation angle θ of the neighboring grains is larger. The dislocation density is customarily characterized by the distance D between them, which is related to the angle θ by the simple formula $D = b/[2\sin(\theta/2)]$, where b is the magnitude of the Burgers vector, which does not differ greatly from the crystalline lattice constant a in the direction of this vector. (In the simplest cases b is simply the same as a.)[2)]

As the dislocations converge (i.e., as the misorientation angle between neighboring grains increases), the stresses they create cancel one another and the width of the severe stress boundary region is reduced.[3] According to this model, the intergrain coupling should then become ever weaker, while the intergrain critical current increases. This completely contradicts the numerous experiments which reveal a rapid drop in the intergrain critical current with increasing misorientation angle θ for all types of boundaries (tilt, twist, and mixed) in high temperature superconducting films[7,8] and crystals.[9]

We assume that this disagreement between theory and experiment is not related to a failure of the model, but to an incorrect assumption of periodicity in the system of boundary dislocations. In fact, there are various reasons for the breakdown of this periodicity. It is sufficient to recall thermal fluctuations, which displace the dislocations over a distance on the order of the lattice constant, as well as the generally unavoidable incommensurability of the period D of the dislocation structure with the lattice constant. Thus, it is physically more correct to regard a system of different dislocations as random, assuming that each of them may be displaced in a random manner from its regular position by a distance on the order of a. Consequently, the problem substantially reduces to calculating the stress field of a system of random dislocations near an intergrain boundary. Numerical calculations of this type, which have been reported

 © 1998 American Institute of Physics

elsewhere,[3] demonstrate qualitative agreement with experiment and confirm the fruitfulness of this kind of random model. In this paper we develop an analytical method for solving this problem. Since, as already noted, the exact stress dependence of the superconductivity ordering parameter is unknown, in calculating the intergrain critical current we have used a simple approximation, according to which the ordering parameter goes to zero in those regions where $\sigma_{ik} \geqslant \sigma_c$ and is constant where $\sigma_{ik} < \sigma_c$.

1. PROBABILISTIC MODEL FOR A RANDOM STRESS FIELD AT A BOUNDARY

In the following we begin with the standard expressions[6] for the components of the stress tensor created by a single edge dislocation located at the origin of the coordinate system and characterized by a Burgers vector b directed along the x axis (since this kind of dislocation corresponds to an extra half plane parallel to the y axis, we shall call it a Y-dislocation):

$$\sigma_{xx}^{Y} = -b\sigma_0 \frac{y(3x^2+y^2)}{(x^2+y^2)^2}, \quad \sigma_{yy}^{Y} = +b\sigma_0 \frac{y(x^2-y^2)}{(x^2+y^2)},$$

$$\sigma_{xy}^{Y} = +b\sigma_0 \frac{x(x^2+y^2)}{(x^2+y^2)^2}, \tag{1}$$

where $\sigma_0 = G/[2\pi(1-\mu)]$, G is the shear modulus, and μ is the Poisson coefficient.

This is the so-called Volterra equation for a continuous medium. It neglects the atomic structure of the crystal and, in particular, the details of the structure of the dislocation kernel. The latter could be taken into account using the physically more correct Peierls equation,[6] but the resulting corrections to the stress are important only at distances on the order of the lattice constant a. They have no noticeable effect on the superconducting properties of the boundary region, since the width of the latter is determined by the coherence length ξ_n of the electrons in a normal metal, which greatly exceeds a. We note also that we have $b \approx a$ in Eqs. (1).

A simple (symmetric) tilt intergrain boundary coincident with the yz plane can be represented as a set of Y-dislocations lying at equal distances $D_y = a/[2\sin(\theta/2)]$ from one another, where θ is the misorientation angle of the crystallites (grains). The total stresses created by a line of such dislocations can be calculated using the standard formulas[6]

$$\sigma_{xx}/\sigma_0 = -\left(\frac{\pi b}{D_y}\right) \times \frac{\sin 2\pi Y(\cosh 2\pi X - \cos 2\pi Y + 2\pi X \sinh 2\pi X)}{(\cosh 2\pi X - \cos 2\pi Y)^2},$$

$$\sigma_{yy}/\sigma_0 = -\left(\frac{\pi b}{D_y}\right) \times \frac{\sin 2\pi Y(\cosh 2\pi X - \cos 2\pi Y - 2\pi X \sinh 2\pi X)}{(\cosh 2\pi X - \cos 2\pi Y)^2},$$

$$\sigma_{xy}/\sigma_0 = +\left(\frac{\pi b}{D_y}\right) \frac{2\pi X(\cosh 2\pi X \cos 2\pi Y - 1)}{(\cosh 2\pi X - \cos 2\pi Y)^2} \tag{2}$$

in which $X = x/D_y$ and $Y = y/D_y$.

Let us consider a straight line (we shall refer to it a an x-line) parallel to the boundary and located a distance x from it. The stress σ_{ik} varies along the x-line and can be described by a distribution function $f_x(\sigma_{ik})$, where the subscript means that this function applies to an x-line. At some points of the x-line, $|\sigma_{ik}| > \sigma_c$, while at others $|\sigma_{ik}| < \sigma_c$. The probability w_x that an arbitrary point of the x-line is ''good'' (i.e., $|\sigma_{ik}| < \sigma_c$ at this point) is determined by the relative fraction of good parts in the line and equals

$$w_x = \int_{-\sigma_c}^{\sigma_c} f_x(\sigma_{ik})\, d\sigma_{ik}, \tag{3}$$

while the probability that a point on the x-line is ''bad'' (i.e., $|\sigma_{ik}| > \sigma_c$ at this point) is, naturally, equal to $(1-w_x)$.

Let us now consider an x-strip, a region bounded by an intergrain boundary and an x-line. The probability that some part of this strip is bad and the corresponding region outside it is good is proportional to the product of two probabilities: the probability that even the interior points of this part of the x-strip farthest from the boundary are still bad and the probability that all points adjacent to this part of the x-strip on the outside are already good. It is clear that these two probabilities coincide with w_x and $(1-w_x)$, respectively. Thus, the probability $p(x)$ that the width of the bad layer in this part of the boundary is equal to x is given by the simple equation

$$p(x) = p_0 w_x (1-w_x), \tag{4}$$

where p_0 is a normalizing factor defined by the condition $\int_0^\infty p(x)dx = 1$. Essentially, $p(x)$ is the probability that the width of a bad strip, as measured along a randomly chosen normal to the boundary, is equal to x.

Now we can easily find the average (averaged over a boundary with a nonuniform stress σ_{ik}) value of any physical quantity that depends on the width of the bad strip. In particular, the most probable width of such a strip is given by $\langle x \rangle = \int_0^\infty x p(x) dx$.

The problem of determining the critical current for an intergrain boundary considered as a Josephson junction, in which boundary dislocations cause its properties to be uniform, therefore, reduces to finding the above distribution function $p(x)$ for one or another distribution of dislocations along the boundary.

First we consider a periodic system of dislocations in which the stress $\sigma_{ik}(x,y)$ is a periodic function of the coordinate y with period D_y. It is clear that for a low density of dislocations, whose stress fields are essentially nonoverlapping (this corresponds to large values of D_y and small misorientation angles $\theta \propto 1/D_y$), the ''bad'' fraction of the boundary is proportional to the dislocation density, i.e., to $1/D_y$. This leads to a drop in the critical current of the boundary that is linear in the misorientation angle, i.e., $(i_0 - i_c) \propto (1/D_y) \propto \theta$. This simple result, which is contained in Ref. 1, was extended there (incorrectly, as is shown below) to the case of large angles θ ($\sim 10°$).

For a periodic system of dislocations, the distribution function $f_x(\sigma_{ik})$ is expressed simply in terms of the coordinate dependence of the stress,

$$f_x(\sigma_{ik})=\left(\frac{2}{D_y}\right)\left|\frac{\partial y(\sigma_{ik},x)}{\partial\sigma_{ik}}\right|. \tag{5}$$

The function $y(\sigma_{ik},x)$ in Eq. (5) is the inverse of $\sigma_{ik}(x,y)$, which determines the spatial distribution of the stress in the dislocation system [see Eq. (2)].

For concreteness, in the following we shall consider the diagonal component of the stress, σ_{xx}, which, as was shown before, is the most important for our problem.[3] As a simple approximation that yields an explicit inversion of $\sigma_{ik}(x,y)$, let us consider the situation in which the width of the bad strip is still rather large, specifically, such that $2\pi X\gtrsim 1$. Then Eq. (2) for σ_{xx} and the inverse function $y(\sigma_{xx},x)$ can be written approximately in the form

$$\sigma_{xx}(x,y)=-\sigma_{\max}\sin\left(\frac{2\pi y}{D_y}\right),$$

$$y=-\left(\frac{D_y}{2\pi}\right)\arcsin\left(\frac{\sigma_{xx}}{\sigma_{\max}}\right), \tag{6}$$

where $\sigma_{\max}=\sigma_{\max}(x)=\pi\sigma_0(b/D_y)[(2\pi x/D_y)\sinh(2\pi x/D_y)+\cosh(2\pi x/D_y)]/\cosh^2(2\pi x/D_y)$. According to Eq. (5), the distribution function in this case is determined by

$$f_x(\sigma_{xx})=\begin{cases}\dfrac{1}{\pi\sqrt{\sigma_{\max}^2-\sigma_{xx}^2}}, & |\sigma_{xx}|<\sigma_{\max},\\ 0, & |\sigma_{xx}|>\sigma_{\max},\end{cases} \tag{7}$$

which, upon substitution in Eq. (3), gives[3)]

$$p(x)=\begin{cases}p_0\arcsin\left(\dfrac{\sigma_c}{\sigma_{\max}}\right)\left[1-\dfrac{2}{\pi}\arcsin\left(\dfrac{\sigma_c}{\sigma_{\max}}\right)\right], & |\sigma_c|<\sigma_{\max},\\ 0, & |\sigma_c|>\sigma_{\max}.\end{cases} \tag{8}$$

Since the xx-component of the stress of an isolated y-dislocation positioned at the coordinate origin is an odd function of y [see Eq. (1)], as the density of dislocations increases (above some value) their overlapping stress fields begin to compensate one another, leading to a reduction in the effective width of the bad strip. Accordingly, the average width $\langle x\rangle=\int_0^\infty xp(x)dx$ of the bad boundary layer should decrease as the dislocation density increases (i.e., as D_y decreases). Thus, the critical current of an intergrain contact with a periodic system of dislocations should vary nonmonotonically: as the period D_y decreases, the critical current initially falls and then rises. Although this conclusion clearly conflicts with conventional ideas,[1] it is confirmed by direct calculation (see below).

The critical current of a Josephson junction at a uniform boundary can be written in the form

$$i_c=i_0\exp\left(-\frac{d}{\xi_N}\right), \tag{9}$$

where i_0 is the critical current in the volume, d is the thickness of the bad (not superconducting but, for example, a normal metal) layer at the boundary, and ξ_N is the electron correlation length in the normal metal. The generalization of this expression to the nonuniform case has the form

$$\langle i_c\rangle=i_0\int_0^\infty\exp(-2x/\xi_N)p(x)dx, \tag{10}$$

where $p(x)$ is assumed normalized to unity and the factor 2 accounts for the presence of a bad strip on both sides of the boundary.

Figure 1 shows distribution functions $p(x)$ calculated using Eq. (8) for the case in which the critical stress σ_c is 1% of σ_0 (i.e., $\sigma_c/\sigma_0=0.01$). It is clear that as the period D_y of the dislocation structure is reduced (when the misorientation angle θ increases), the maximum probability $p(x)$ shifts toward smaller x. In accordance with this, Fig. 2 illustrates the reduction in the average width $\langle x\rangle$ of the bad strip and Fig. 3, the rise in the intergrain critical current [calculated using Eq. (10)] as the misorientation angle θ is increased.

This result, as might be expected, completely contradicts Ref. 1. More importantly, it absolutely disagrees with experiments[7–9] indicating a rise in the critical current as the misorientation angle is increased. In light of the above remarks, it is clear that the defect in the naive model examined here lies in the traditional assumption of a periodic dislocation structure near the intergrain boundary. A more realistic model should, as already noted, take into account the loss of strict periodicity in the location of the dislocations at the intergrain boundary owing to their slight (over a distance on the order of the crystal lattice constant) random displacement along the boundary.

In this case, the total stress created at an arbitrary point in the crystal is given by a sum of random quantities (the

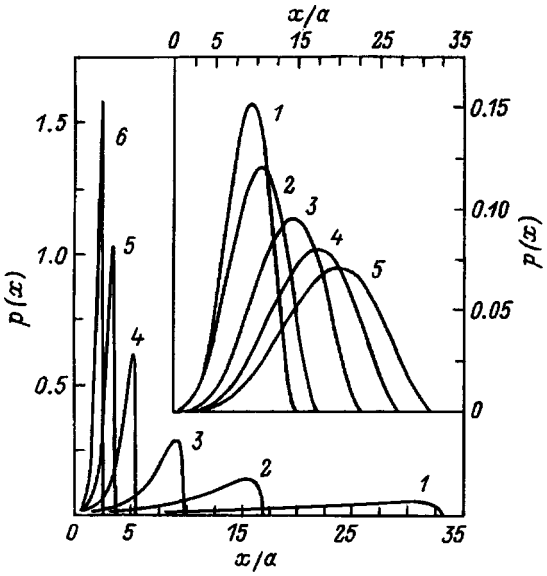

FIG. 1. The probability $p(x)$ that the width of the bad layer near an intergrain boundary equals x. The curves are plotted only where the condition for applicability of the computational formulas ($2\pi X\geqslant 1$) is not violated. The periodic system of dislocations has a separation D_y (in units of b) between dislocations (misorientation angle θ, deg): *1*—50 (1.1); *2*—20 (3); *3*—10 (5.7); *4*—5 (11.7); *5*—3 (19); *6*—2 (29). The inset shows a system of random dislocations with $\Delta/a=1$ and misorientation angle θ (deg): *1*—3; *2*—6; *3*—12; *4*—20; *5*—30.

stress from the individual dislocations) and is also a random quantity. Obviously, this stress cannot be calculated using an equation such as Eq. (1) and the natural way of describing the stresses in the crystal becomes the distribution function $f_x(\sigma_{xx})$ introduced above. If this function were known, then the method described above could be used to calculate the intergrain critical current for a random system of dislocations, as well.

In principle there is a method which can be used to find the distribution of the sum of random quantities distributed in a known fashion: the Markov method.[10] However, in this case it does not yield a sufficiently simple analytic expression for this distribution function. Thus, we have chosen another, simpler, approach based on using an approximate form of the distribution function $f_x(\sigma_{xx})$.

It is known that a distribution function is completely determined by the complete set of its moments $M_n = \int(\sigma_{xx})^n f_x(\sigma_{xx})d\sigma_{xx}$.[11] Functions, all of whose moments coincide, are identical, while functions for which only a finite number of the earliest moments coincide are similar to one another, with their degree of similarity being greater for a larger number of coincident moments. For approximate calculations, it is sufficient to restrict ourselves to coincidence of the first two or three moments.[4)]

Of course, the first two or three moments are still not enough to write down an expression for the distribution function. Thus, in order to get an idea of its shape, we use a numerical calculation of the stresses for some example of a random dislocation distribution (see Ref. 3). Figure 4 shows the stress distribution functions $f_x(\sigma_{xx})$ at a distance $x=5a$ from a boundary with a misorientation angle $\theta=10°$ for different values of the parameter Δ, which serves as a measure of the randomness in the position of the dislocations. (Δ is the same as the root mean square deviation of the dislocations from their regular positions.)[5)] Similar results have been obtained for other values of $\theta \gtrsim 1°$, $x \gtrsim a$, and $\Delta \gtrsim 0.02$. Clearly, the ratio $f_x(\sigma_{xx})/\sigma_2$ is linear in the stress

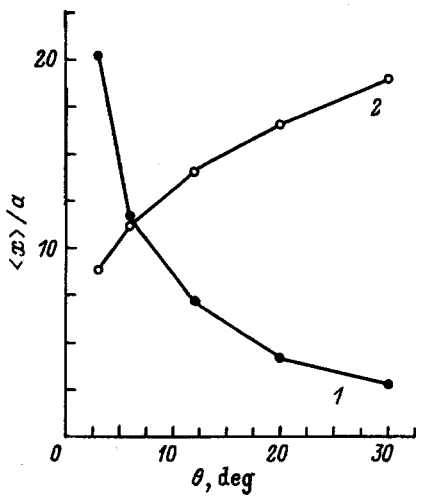

FIG. 2. The average width of the bad strip near an intergrain boundary as a function of the misorientation angle θ. (*1*) Periodic system of dislocations, (*2*) system of random dislocations ($\Delta/a=1$).

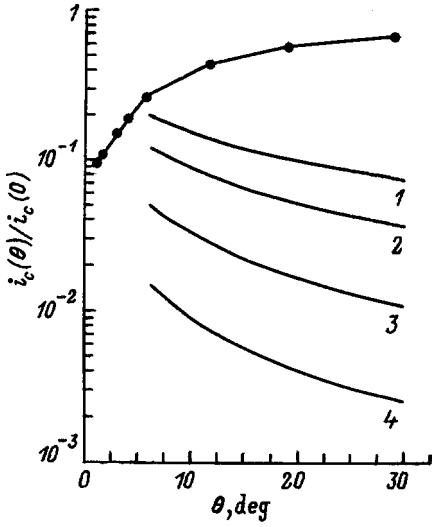

FIG. 3. The Josephson critical current i_c for an intergrain boundary as a function of the misorientation angle θ. The upper curve is for a periodic system of dislocations. The average width $\langle x\rangle$ of the bad layer near the boundary satisfies the condition $2\pi\langle x\rangle/D_y \geqslant 1$; for the opposite inequality ($\theta \to 0$) the critical current increases with decreasing θ and $i_c/i_0 \to 1$. The lower curves (*1–4*) are for a system of random dislocations. The parameter μ_0: *1*—8; *2*—10; *3*—16; *4*—24.

to good accuracy. This means that the distribution function can be written in the form

$$f_x(\sigma_{xx}) \propto |\sigma_{xx}[\sigma_1(x,\Delta,\theta)-\sigma_{xx}]|, \tag{11}$$

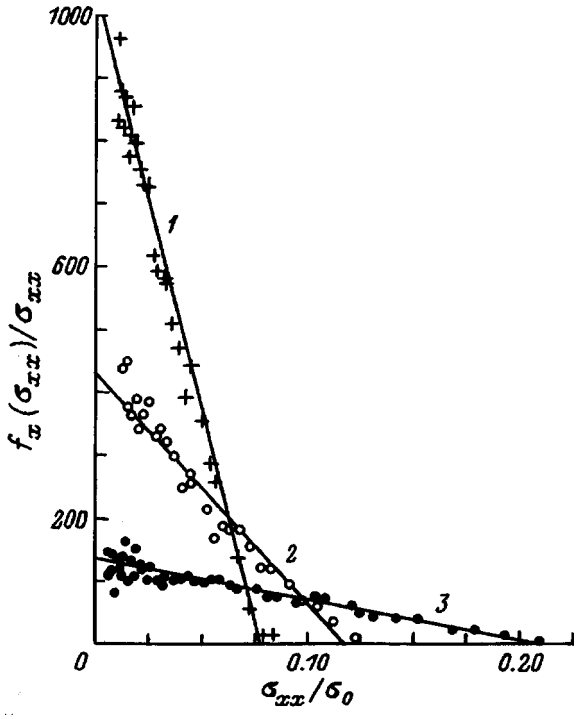

FIG. 4. Numerically calculated stress distribution functions $f_x(\sigma_{xx})$ at a distance $x=5a$ from an intergrain boundary with a misorientation angle $\theta=10°$ for different values of Δ: *1*—2; *2*—1; *3*—0.05. The coordinates have been chosen so as to reveal the form of the functional dependence $f_x(\sigma_{xx})$. The straight lines are the corresponding linear approximations.

where $\sigma_1(x,\Delta,\theta)$ is the only parameter of the distribution, which determines all its properties and, in particular, the dispersion $D(x,\Delta,\theta)$. It is easy to show that for a parabolic distribution of the form (11) we have $D=(3/10)\sigma_1^2$. Thus, it is sufficient to know the dispersion for a complete description of the distribution $f_x(\sigma_{xx})$.

In order to determine the dispersion of the stress near a boundary owing to the combination of stresses from individual, randomly positioned dislocations, we shall use a well known theorem according to which the dispersion of a sum of random quantities (under extremely general assumptions) is equal to the sum of their dispersions.[11] In our case the dispersion D_n of the stress $\sigma_{xx}^{(n)}$ created by an individual (nth) dislocation is determined by the distribution function $f_n(y_n)$ of the random coordinate y_n of this dislocation with a regular position $y_n^0=y+nD_y$. The dispersion can be found using Eq. (1) with the substitution $y\to y_n=y_n^0+n\Delta_n$, where Δ_n is the random displacement of the n-th dislocation and

$$D_n=\int (\sigma_{xx}^{(n)}-\langle\sigma_{xx}^{(n)}\rangle)^2 f_n(y_n)dy_n, \tag{12}$$

where

$$\langle\sigma_{xx}^{(n)}\rangle=\int \sigma_{xx}^{(n)}(y_n)f_n(y_n)dy_n. \tag{13}$$

For simplicity, we make the (not at all fundamental) assumption that the random coordinates y_n of the dislocations are uniformly distributed over equal intervals $y_n^0-\Delta<y_n<y_n^0+\Delta$ of width 2Δ. Then it is possible to use the approximations[6)]

$$\langle\sigma_{xx}^{(n)}\rangle=\frac{1}{2\Delta}\int_{y_n^0-\Delta}^{y_n^0+\Delta}\sigma_{xx}^{(n)}dy_n\approx\sigma_{xx}^{(n)}(y_n^0)+\frac{\Delta^2}{6}(\partial^2\sigma_{xx}^{(n)}/\partial y_n^2)\Big|_{y_n=y_n^0}+\ldots, \tag{14}$$

and

$$\langle(\sigma_{xx}^{(n)})\rangle=\frac{1}{2\Delta}\int_{y_n^0-\Delta}^{y_n^0+\Delta}(\sigma_{xx}^{(n)})^2dy_n\approx[\sigma_{xx}^{(n)}(y_n^0)]^2+\frac{\Delta^2}{6}(\partial^2[\sigma_{xx}^{(n)}]^2/\partial y_n^2)\Big|_{y_n=y_n^0}+\ldots, \tag{15}$$

which imply that

$$D_n=\langle(\sigma_{xx}^{(n)})^2\rangle-(\langle\sigma_{xx}^{(n)}\rangle)^2\approx\frac{\Delta^2}{3}(\partial\sigma_{xx}^{(n)}/\partial_n)^2\Big|_{y_n=y_n^0}. \tag{16}$$

According to Eq. (1), the derivative in Eq. (16) equals

$$\partial\sigma_{xx}^{(n)}/\partial y_n|_{y_n=y_n^0}=b\sigma_0\left[\frac{4(y+nD_y)^2[3x^2+(y+nD_y)^2]}{[x^2+(y+nD_y)^2]^3}-\frac{3}{x^2+(y+nD_y)^2}\right]. \tag{17}$$

Finally, the dispersion of the total stress σ_{xx} is found as the sum of the dispersions D_n of the stresses of the individual dislocations,

$$D=\sum_{n=-\infty}^{\infty}D_n\approx\frac{\sigma_0^2b^2\Delta^2}{3D_y^4}\times\sum_{n=-\infty}^{\infty}\left[\frac{4(n+Y)^2[3X^2+(n+Y)^2]}{[X^2+(n+Y)^2]^3}-\frac{3}{X^2+(n+Y)^2}\right]^2, \tag{18}$$

where $X=x/D_y$ and $Y=y/D_y$.

By use of some algebraic identities, Eq. (18) can be written in the form

$$D\approx\frac{\sigma_0^2b^2\Delta^2}{3D_y^4}(\Sigma_2+8X^2\Sigma_3-64X^6\Sigma_5+64X^8\Sigma_6), \tag{19}$$

where $\Sigma_k=\Sigma_{n=-\infty}^{\infty}[x^2+(n+Y)^2]^{-k}$.

The sums Σ_k in Eq. (19) are easily calculated using the recurrence relation $\Sigma_{k+1}=-(1/2kX)[\partial\Sigma_k/\partial X]$ and the standard formula[6]

$$\Sigma_1=\sum_{n=-\infty}^{\infty}\frac{1}{X^2+(n+Y)^2}=\left(\frac{\pi}{X}\right)\frac{\sinh 2\pi X}{\cosh 2\pi X-\cos 2\pi Y}. \tag{20}$$

In the following, we restrict ourselves to the case $2\pi X\gtrsim 1$. Then $\Sigma_1\approx\pi/X$ and, accordingly,

$$\Sigma_2=\frac{\pi}{2X^3},\quad \Sigma_3=\frac{3\pi}{8X^5},\quad \Sigma_4=\frac{5\pi}{16X^7},$$
$$\Sigma_5=\frac{35\pi}{128X^9},\quad \Sigma_6=\frac{63\pi}{256X^{11}}. \tag{21}$$

Finally, we obtain

$$D\approx\frac{7\pi}{12}\sigma_0^2\left(\frac{b^2\Delta^2}{x^3D_y}\right). \tag{22}$$

By comparing this expression for D with the dispersion in Eq. (11), we can find the parameter σ_1, which determines all the properties of this distribution,

$$\sigma_1=\sigma_1(x,\Delta,\theta)=\left(\frac{35\pi}{18}\right)^{1/2}\left(\frac{b\Delta}{x^{3/2}D_y^{1/2}}\right)\sigma_0\approx 3.5\sigma_0\sqrt{\sin\frac{\theta}{2}}\left(\frac{a^{1/2}\Delta}{x^{3/2}}\right), \tag{23}$$

where the rightmost expression has been obtained under the assumption $b=a$ and we have used the relationship between the misorientation angle θ and the period D_y of a system of edge dislocations, $D_y=a/[2\sin(\theta/2)]$.

Now, finally, we can write down an explicit expression for the distribution function $f_x(\sigma_{xx})$ of the stresses near a boundary and (in accordance with the scheme described above), use it to calculate the critical current of an intergrain Josephson junction. The normalized (on the segment $-\sigma_1<\sigma<\sigma_1$) distribution function has the form[7)]

$$f_x(\sigma)=\frac{3}{\sigma_1^3}\sigma(\sigma_1-\sigma), \tag{24}$$

which makes it possible to write down the probability $p(x)$, introduced above, as follows:

$$p(x)=p_0\int_{-\sigma_c}^{\sigma_c} f_x(\sigma)d\sigma\left[1-\int_{-\sigma_c}^{\sigma_c} f_x(\sigma)d\sigma\right]$$
$$=3p_0\left(\frac{\sigma_c}{\sigma_1}\right)^2\left(1-\frac{\sigma_c}{\sigma_1}\right)^2\left[1+\frac{4}{3}\left(\frac{\sigma_c}{\sigma_1}\right)\left(1-\frac{\sigma_c}{\sigma_1}\right)\right]. \quad (25)$$

According to Eq. (25), the width of the bad strip cannot exceed some value x_1 determined by the condition $\sigma_1=\sigma_c$: $x_1\approx 2.3a(\sigma_0/\sigma_c)^{2/3}(\Delta/a)^{2/3}[\sin(\theta/2)]^{1/3}$. (Thus, for $\Delta=a$, $\sigma_c=0.1\sigma_0$, and $\theta=5°$, we have $x_1\approx 40a$.) The normalizing factor p_0 can be found from the normalization condition for the probability, $\int_0^{x_1}p(x)dx=1$, and is given by

$$p_0\approx(3.9/a)(\sigma_c/\sigma_0)^{2/3}(\Delta/a)^{-2/3}[\sin(\theta/2)]^{-1/3}.$$

Figure 1 (inset) shows plots of distribution functions $p(x)$ calculated using Eq. (24) for the case in which the critical stress σ_c is 1% of σ_0 (i.e., $\sigma_c/\sigma_0=0.01$). As opposed to the situation with a periodic system of dislocations (Fig. 1), an increase in the misorientation angle θ shifts the maximum of the probability $p(x)$ toward larger x, which corresponds to an increase in the most probable width $\langle x\rangle$ of the bad strip.

2. CRITICAL CURRENT OF A BOUNDARY WITH A RANDOM SYSTEM OF DISLOCATIONS

The critical current of a nonuniform Josephson junction is given by Eq. (10). Substituting the above distribution $p(x)$ in it, we finally find the intergrain critical current at a boundary with a random system of edge dislocations,

$$\langle i_c\rangle/i_0=27\left[\tilde{\gamma}(4,\mu)-\frac{2}{3}\tilde{\gamma}(11/2,\mu)-3\tilde{\gamma}(7,\mu)\right.$$
$$\left.+4\tilde{\gamma}(17/2,\mu)-\frac{4}{3}\tilde{\gamma}(10,\mu)\right], \quad (26)$$

where

$$\tilde{\gamma}(\nu,\mu)=\int_0^1 s^{\nu-1}e^{-\mu x}dx, \quad \mu=\mu_0[\sin(\theta/2)]^{1/3},$$
$$\mu_0=\frac{4.6}{(\xi_N/a)}\left[\frac{\Delta/a}{\sigma_c/\sigma_0}\right]^{2/3}.$$

For $\theta\gtrsim 5°$ and a reasonable choice of the parameter μ_0 (see below) we have $\mu\geqslant 10$. Then the main contribution to the sum (26) is from the first term $\tilde{\gamma}(4,\mu)\approx 6/\mu^4$. This makes it possible to write Eq. (26) in the following, although approximate, simple form:

$$\langle i_c\rangle/i_0\approx\frac{160}{\mu^4}=\frac{160.\mu_0^4}{[\sin(\theta/2)]^{4/3}}. \quad (27)$$

Equation (26) gives the average critical current of the Josephson junction. The local critical current density, however, varies randomly along the junction and is characterized by the distribution function

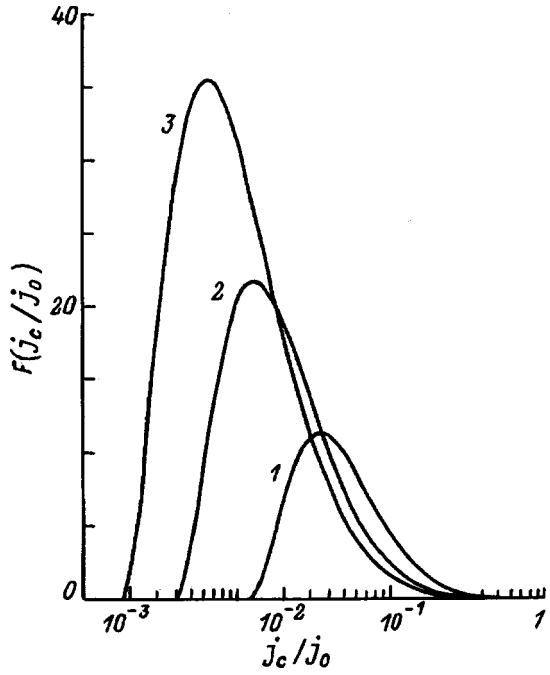

FIG. 5. The distribution function of the local critical current density at an intergrain boundary with a random system of dislocations ($\Delta/a=2$; $\xi_N/a=10$). Misorientation angle θ (deg): *1*–10; *2*–20; *3*–30.

$$F(j_c)=p[x(j_c)]\left|\frac{dx}{dj_c}\right|, \quad x(j_c)=-\frac{\xi_N}{2}\ln\left(\frac{j_c}{j_0}\right), \quad (28)$$

where j_0 is the volume critical current density.

As can be seen from Fig. 5, as the misorientation angle θ increases, this distribution function shifts substantially toward small values of the local critical current density; this causes a drop in the average critical current $\langle i_c\rangle$ (Fig. 3). The magnitude of the latter is determined solely by the parameter μ_0 (of course, neglecting the angle θ). (See Eq. (26).) Taking $\sigma_c/\sigma_0=0.01$, $\xi_N/a=10$, and $\Delta/a=1$ (arguments in favor of this choice are given in Ref. 3), we obtain $\mu_0\approx 10$. At the same time, Fig. 3 implies that the magnitude of the average critical current of the junction depends rather strongly on μ_0: when μ_0 is increased by a factor of 3, $\langle i_c\rangle$ falls by a factor of 10–20. This may explain the rather large scatter of the data observed in many experiments. In fact, the degree of randomness of the system of dislocations at the boundary, which is characterized by the parameter Δ, may be determined to some extent by its structural features, which are related to the techniques used to form it, the purity of the initial materials, the substrate properties (for film structures), etc.

The level of agreement between the proposed model and experiment can be judged from Fig. 6, which shows experimental data for Josephson junctions in YBa_2Cu_3O films on bicrystalline substrates,[8)] as well as the calculated angular variation in the critical current of an intergrain Josephson junction. It is clear that for misorientation angles $\theta\lesssim 25°$, the widely scattered experimental data fall within a strip bounded by the theoretical curves corresponding to reasonable values of μ_0. For angles $\theta\gtrsim 45°$, on the other hand, the experimental data sink well below and evidently can no

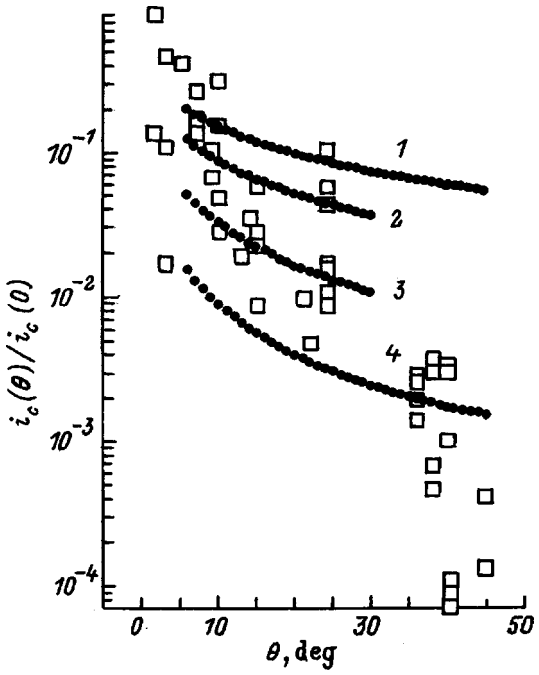

FIG. 6. A comparison of the theoretical angular dependences of the critical current of an intergrain Josephson junction (circles) with experimental data (squares) for junctions in YBa_2Cu_3O-films on bicrystalline substrates.[8] μ_0: *1*—8; *2*—10; *3*—16; *4*—24.

longer be described in terms of our model. For these angles, the interaction between nearby dislocations[8] probably becomes so strong that it leads, on one hand, to a realignment of the dislocation kernels (and, therefore, in the stress fields created by them) and, on the other, to the appearance of a certain correlation in their positions (which, of course, was not taken into account above since the random positions of the dislocations were assumed to be mutually noninteracting).

In conclusion, we note that the above procedure for calculating the random stresses is suitable for analyzing the system of edge dislocations at a twist boundary, as well as at a tilt boundary. The former is usually represented as a grid (lying in the yz plane of the boundary) of screw dislocations consisting of two periodic (with period D) systems of dislocations: in one of them the dislocations are parallel to the z axis and in the other, to the y axis. Using the standard expressions[6] for the stresses created by individual screw dislocations and the computational technique developed above, one can find the dispersion of the distribution of stresses for a random system of screw dislocations at a twist boundary,

$$D(\sigma_{zy}) \approx \frac{\pi}{6}(1-\mu)^2\sigma_0^2\left\langle\frac{b^2\Delta^2}{x^3D}\right\rangle,$$

$$D(\sigma_{xy}) = D(\sigma_{zx}) \approx \frac{\pi}{12}(1-\mu)^2\sigma_0^2\left\langle\frac{b^2\Delta^2}{x^3D}\right\rangle. \tag{29}$$

It is clear (for other conditions the same) that the stresses near the twist boundary do not differ greatly from those at a tilt boundary [see Eq. (22)], so there is every reason to expect the current carrying characteristics of these boundaries to be similar. This conclusion is confirmed by experiment.[8]

3. RESIDUAL CRITICAL CURRENT OF A NONUNIFORM JOSEPHSON JUNCTION IN A HIGH MAGNETIC FIELD

For calculating many physical properties of boundaries with a random system of dislocations, it is necessary to know both the stress distribution function $f_x(\sigma_{xx})$ and the stress correlation function. In order to find it, we break up the function $\sigma_n(y)=\sigma_{ik}(y+nD+\Delta_n)$ into two parts: a regular part, $\sigma_n^0(y)=\sigma_{ik}(y+nD)$ corresponding to $\Delta_n=0$, and a random part, $\sigma_n^*(y)=\sigma_n(y)-\sigma_n^0(y)$ which can be written in the form

$$\sigma_n^*(y) \approx \Delta_n \left.\frac{\partial\sigma_{ik}(y)}{\partial y}\right|_{y=y+nD}$$

The total stress is equal to $\sigma_{ik}(y)=\Sigma_n\sigma_n(y)$ and its correlation function is

$$\psi(\delta)=\langle\langle\sigma_{ik}(y)\sigma_{ik}(y+\delta)\rangle\rangle, \tag{30}$$

where the double averaging symbol denotes averaging both over y (for the regular and random parts) and over Δ_n (for the random part).

Then,

$$\begin{aligned}
\psi(\delta) &= \left\langle\left\langle \sum_n \sigma_n(y)\cdot\sum_m \sigma_m(y+\delta)\right\rangle\right\rangle \\
&= \left\langle\left\langle \sum_n [\sigma_n^0(y)+\sigma_n^*(y)]\cdot\sum_m [\sigma_m^0(y+\delta)\right.\right. \\
&\quad \left.\left. +\sigma_m^*(y+\delta)]\right\rangle\right\rangle \\
&= \left\langle \sum_n \sigma_n^0(y)\cdot\sum_m \sigma_m^0(y+\delta)\right\rangle \\
&\quad + \left\langle\left\langle \sum_n \sigma_n^0(y)\cdot\sum_m \sigma_m^*(y+\delta)\right\rangle\right\rangle \\
&\quad + \left\langle\left\langle \sum_n \sigma_n^0(y+\delta)\cdot\sum_m \sigma_m^*(y)\right\rangle\right\rangle \\
&\quad + \left\langle\left\langle \sum_n \sigma_n^*(y)\cdot\sum_m \sigma_m^*(y+\delta)\right\rangle\right\rangle.
\end{aligned}$$

The second and third terms of this last expression for $\psi(\delta)$ are zero and the last is

$$\begin{aligned}
&\left\langle\left\langle \sum_n \sigma_n^*(y)\cdot\sum_m \sigma_m^*(y+\delta)\right\rangle\right\rangle \\
&\quad = \left\langle\left\langle \sum_n \sigma_n^{8*}(y)\sigma_n^*(y+\delta)\right\rangle\right\rangle \\
&\qquad + \left\langle\left\langle \sum_{m\neq n} \sigma_m^*(y)\sigma_n^*(y+\delta)\right\rangle\right\rangle,
\end{aligned}$$

where the second term equals zero.

Therefore, we have

$$\psi(\delta)=\left\langle \sum_n \sigma_n^0(y)\sum_m \sigma_m^0(y+\delta)\right\rangle$$

$$+\left\langle\left\langle \sum_n \sigma_n^*(y)\sigma_n^*(y+\delta)\right\rangle\right\rangle. \qquad (31)$$

For screw dislocations,

$$\sigma_n^0(y)=\frac{\alpha y}{x^2+y^2},$$

$$\Delta_n \left.\frac{\partial\sigma(y)}{\partial y}\right|_{y=y+nD}=\left(\frac{\alpha\Delta_n}{D^2}\right)\frac{X^2-(Y+n)^2}{[X^2+(Y+n)^2]^2},$$

where $\alpha=b\sigma_0(1-\mu)$, and

$$\sum_n \sigma_n(y)=\left(\frac{\pi\alpha}{D}\right)\frac{\sin 2\pi Y}{\cosh 2\pi X-\cos 2\pi Y},$$

where $X=x/D$ and $Y=y/D$.

Thus, the first term of Eq. (31) for $\psi(\delta)$ is given by

$$\left\langle \sum_n \sigma_n^0\cdot\sum_m \sigma_m^0(y+\Delta)\right\rangle=\left(\frac{\pi\alpha}{D}\right)^2\left\langle\frac{\sin 2\pi Y\,\sin[2\pi(Y+t)]}{[\cosh 2\pi X-\cos 2\pi Y][\cosh 2\pi X-\cos(2\pi(Y+t))]}\right\rangle$$

$$\approx\left(\frac{\pi\alpha}{D}\right)^2\frac{\cos 2\pi t}{2\cosh^2 2\pi X}\approx\left(\frac{\pi\alpha}{D}\right)^2\exp(-4\pi X)\cos 2\pi t,$$

where $t=\delta/D$.

Then, we have

$$\left\langle\left\langle \sum_n \sigma_n^*(y)\sigma_n^*(y+\delta)\right\rangle\right\rangle=(\alpha/D^2)^2\left\langle\left\langle \sum_n \frac{[X^2-(Y+n)^2][X^2-(Y+n+t)^2]}{[X^2+(Y+n)^2]^2[X^2+(Y+n+t)^2]^2}\Delta_n^2\right\rangle\right\rangle.$$

For a random distribution Δ_n uniform over the interval $\Delta<\Delta_n$, averaging over Δ_n gives

$$\left\langle\left\langle \sum_n \sigma_n^*(y)\sigma_n^*(y+\delta)\right\rangle\right\rangle=\frac{1}{3}(\alpha\Delta/D^2)^2\left\langle\sum_n \frac{[X^2-(Y+n)^2][X^2-(Y+n+t)^2]}{[X^2+(Y+n)^2]^2[X^2+(Y+n+t)^2]^2}\right\rangle,$$

where the average over Y still has to be taken. To do this, it is necessary to calculate (and average over y) the corresponding sum.

This sum must be found in the way described above. For $2\pi X\gg 1$ it equals

$$\left\langle\left\langle \sum_n \sigma_n^*(y)\sigma_n^*(y+\delta)\right\rangle\right\rangle\sim 2\pi(\alpha\Delta/D^2)^2\frac{X(4X^2-t^2)}{(4X^2+t^2)^3}$$

$$\sim\sigma_0^2\left(\frac{b^2\Delta^2}{x^3D}\right)\frac{4-(\delta/x)^2}{[4+(\delta/x)^2]^3},$$

in agreement with the above expressions (22) and (29) for the dispersion of the random part of the stress, $\sigma^*=\Sigma_n\sigma_n^*(y)$.

Thus, for $2\pi X\gg 1$, we have

$$\psi(\delta)\approx\sigma_0^2\left(\frac{\pi b}{D}\right)^2\left[\exp(-4\pi X)\cos 2\pi t+\text{const}\left(\frac{\Delta}{D}\right)^2\frac{X(4X^2-t^2)}{(4X^2+t^2)^3}\right], \qquad (32)$$

where const$\sim$1. On setting $b,\Delta\sim a$ and assuming that the characteristic value of x is determined by the width of the bad strip $\langle x\rangle\sim 10a$, it is easy to show that the first term in the expression for $\psi(\delta)$ (corresponding to a system of periodic dislocations) can be neglected for $\theta\geqslant 5°$.

The width $\langle x\rangle$ of the bad boundary strip is, itself, a random function of the coordinate y along the boundary. The existence of a direct coupling between the local perturbations in the stress and $\langle x\rangle$ means that the correlation properties of $\langle x\rangle$ can also be described roughly by the correlation function $\psi(\delta)$.

We may assume that the correlation function for $\langle x\rangle$ is close to that for the stress at $x=\langle x\rangle$ and falls off relatively slowly for $\delta\geqslant\langle x\rangle$. This means that the correlation function of the local critical current density $j_c\propto\exp(-\langle x\rangle/\xi_n)$ (which depends exponentially on $\langle x\rangle$) can be written in the form

$$\langle j_c(y)j_c(y+\delta)\rangle\propto e^{-\delta/\langle x\rangle}. \qquad (33)$$

Thus, the width of the bad strip, $\langle x\rangle$, serves as a correlation length for the local critical current density, which in the Yanson model[12] determines the so-called residual critical current $i_{c,\text{res}}$. The latter is the critical current of an infinite Josephson junction in a strong magnetic field (provided the statistical properties of the local critical current density are described by an exponential correlation function of the form (31)). For a nonuniform junction of finite length, the residual current determines the relative height of the plateau in the magnetic field dependence of its total critical current $i_c(H)$,[12]

$$\frac{i_{c,\text{res}}}{i_c(H=0)}\sim\left(D_j\frac{\langle x\rangle}{L}\right)^{1/2}, \qquad (34)$$

where L is the length of the boundary, $D_j=\langle(j_c-\langle j_c\rangle)^2\rangle/\langle j_c\rangle^2$ is the dispersion of the local critical current density distribution function for $H=0$, and $\langle j_c\rangle\propto i_c(H=0)/L$ is the average value of j_c for $H=0$.

The residual critical current of Josephson junctions of length $L\sim 20$ μm in $YBa_2Cu_3O_7$ films on bicrystalline substrates with misorientation angles $\theta=10-30°$ has been measured.[13] The magnitude of the residual critical current was $i_{c,\mathrm{res}}/i_c(H=0)=0.01-0.1$. In order to understand whether these values correspond to those predicted by Eq. (34) we use the data presented in Figs. 2 and 5. This implies that $i_{c,\mathrm{res}}/i_c(H=0)\sim 10(a/L)^{1/2}$. Taking $a\approx 4\times 10^{-8}$ cm and $L=20$ μm, we obtain $J_{c,\mathrm{res}}/J_c(H=0)\sim 0.1$, which agrees quite well with the experimental data.[13]

[1)]Recall that the superconducting transition temperature in $YBa_2Cu_3O_{7-\delta}$ depends strongly on δ: $T_c\approx 92$ K for $\delta=0.05$, $T_c\approx 60$ K for $\delta=0.4$, and $T_c=0$ for $\delta\geqslant 0.6$.[5]

[2)]In the case of a tilt boundary, this formula is valid only for a boundary which is symmetric with respect to the corresponding crystallographic planes of the grains in contact (a so-called symmetric tilt boundary). The general relation for an asymmetric boundary is given elsewhere.[6]

[3)]Equation (8) for $p(x)$ could also be obtained without calculating the distribution function $f_x(\sigma_{xx})$. In fact, Eqs. (3) and (5) imply that $w_x=(2/D_y)[y(\sigma_c)-y(-\sigma_c)]$, which, with the second of Eqs. (6), immediately leads to Eq. (8). A more ''embroidered'' approach is used in the text only in order to illustrate the sequence of steps for the case in which the inverse function $y(\sigma_{xx})$ is unknown, but the form of the distribution function $f_x(\sigma_x)$ is known (or assumed). This is the situation that will be examined below in this paper.

[4)]The first three moments have a simple ''geometric'' significance. The average value of the stress, $\langle\sigma_{xx}\rangle$ and its dispersion D determine, respectively, the center of gravity of the distribution and its effective width. Specifying the first two moments of the distribution, M_1 and M_2, is equivalent to specifying the average stress $\langle\sigma_{xx}\rangle$ and its dispersion D. Thus, $\langle\sigma_{xx}(x)\rangle=\int\sigma_{xx}f_x(\sigma_{xx})d\sigma_{xx}=m_1$, while the dispersion is given in terms of M_1 and M_2 by $D=\langle(\sigma_{xx})^2\rangle-(\langle\sigma_{xx}\rangle)^2=M_2-M_1^2$. The third moment M_3 is related to the degree to which the shape of the distribution function deviates from symmetric (relative to the mean value). This asymmetry is usually characterized by the parameter $\gamma=\langle(\sigma_{xx}-\langle\sigma_{xx}\rangle)^3\rangle/D^{3/2}=(M_3-4M_1^3+3M-1M_2)/D^{3/2}$.

[5)]The distribution function is even in σ_{xx}. The figure only shows the part corresponding to $\sigma_{xx}>0$.

[6)]Similar equations are also obtained for a gaussian distribution of y_n with dispersion Δ^2.

[7)]It can be shown that the distribution function (24) obeys a simple scaling relation. Let us introduce the notation $\sigma_{11}=\sigma(x=\Delta=D_y=a)$. Then for $x/a=\Delta/a=D_y/a=1$, the normalized distribution function (11) can be written in the form $f_{11}(\sigma)=(3/\sigma_{11}^3)\sigma(\sigma_{11}-\sigma)$. Now it is easy to see that the normalized distribution function for arbitrary x, Δ, and D_y is given in terms of f_{11} by $f(\sigma)=kf_{11}(k\sigma)$. Here k is a scaling parameter, which is given by $k=(x^3D_y)^{1/2}/(b\Delta)$ according to Eq. (22).

[8)]For a misorientation angle $\theta=40°$ the distance between dislocations calculated formally according to the formula $d_y=a/[2\sin(\theta/2)]$ is $1.3a$, which is comparable to the size of the dislocation kernels. Of course, it is no longer appropriate to speak of using a dislocation model under these conditions.

[1] M. F Chisholm and S. J. Pennycook, Nature (London) **351**, 47 (1991).
[2] S. E. Babcock and J. L. Vargas, Annu. Rev. Mater. Sci. **25**, 193 (1995).
[3] E. Z. Meĭlikhov, Zh. Éksp. Teor. Fiz. **110**, 1453 (1996) [JETP **83**, 803 (1996)].
[4] Yimei Zhu, J. M. Zuo, A. R. Moodenbaught, and M. Suenaga, Philos. Mag. A **70**, 969 (1994).
[5] R. G. Munro and H. Chen, J. Am. Ceram. Soc. **79**, 603 (1996).
[6] J. P. Hirth and J. Lothe, *Theory of Dislocations*, McGraw-Hill, N.Y. (1968).
[7] D. Dimos, P. Chaudhari, J. Mannhart, and F. K. LeGoues, Phys. Rev. Lett. **61**, 1653 (1988).
[8] R. Gross, in *Proceedings International Conference on Polycryst. Semicond.*, Saint Malo (1993).
[9] M. St. Louis-Weber, V. P. Dravid, V. R. Todt, X. F. Zhang, D. J. Miller, and U. Balachandran, Phys. Rev. B **54**, 16238 (1996).
[10] S. Chandrasekhar, Rev. Mod. Phys. **15**, 1 (1943).
[11] W. Feller, *An Introduction to Probability Theory and its Applications*, Wiley, N.Y. (1970).
[12] I. Yanson, Zh. Éksp. Teor. Fiz. **58**, 1497 (1970) [Sov. Phys. JETP **31**, 800 (1970)].
[13] E. Sarnelli, P. Chaudhary, and J. Lacey, Appl. Phys. Lett. **62**, 777 (1993).

Translated by D. H. McNeill

Raman scattering in $YBa_2Cu_3O_7$ single crystals: anisotropy in normal and superconductivity states

M. F. Limonov,* A. I. Rykov, and S. Tajima

Superconductivity Research Laboratory, International Superconductivity Technology Center, 10-13, Shinonome 1-Chome, Koto-ku, Tokyo 135 Japan

A. Yamanaka

Research Institute for Electronic Science, Hokkaido University, Sapporo 060, Japan
(Submitted April 29, 1997; resubmitted October 2, 1997)
Fiz. Tverd. Tela (St. Petersburg) **40**, 403–412 (March 1998)

Precise temperature and polarization dependences of Raman spectra have been investigated for fully oxygenated twin-free $YBa_2Cu_3O_7$ single crystals. We have found a striking superconductivity-induced $x-y$ anisotropy in the temperature behavior of the 340 cm^{-1} line: the magnitudes of the softening and broadening are quite different in the xx- and yy-polarizations. This anisotropy suggests a contribution of the CuO-chain superconductivity with a pairing symmetry different from that for the CuO_2 plane, or indicates that the superconducting gap amplitudes are different in the k_x and k_y directions. The $d+s$ gap symmetry is the only realistic symmetry in the case of $\Delta_x \neq \Delta_y$. © *1998 American Institute of Physics.* [S1063-7834(98)00403-1]

1. INTRODUCTION: TEN YEARS LATER

Raman scattering spectra (RSS) provide important information on the phononic and electronic excitations in high-T_c superconductors and serves as a tool for testing the properties of the superconducting gap. Over the past ten years, a wealth of data was obtained on superconductivity-induced effects in the phonon behavior in $YBa_2Cu_3O_7$ (YBCO) crystals. Let us summarize the main results obtained in studies of the phononic RSS in high-T_c materials. The most important one is related to the softening of the 340 cm^{-1} mode below T_c found by Macfarlaine, Rosen and Seky on polycrystalline samples in 1987, indicating a strong EPI.[1] The softening of the 340 cm^{-1} mode was confirmed by many groups which measured different states of YBCO including ceramics, thin films and single crystals.[2–4]

However, the linewidth anomaly depended critically on sample. Friedel *et al.* reported that the half-width at the half maximum (HWHM) of the 340 cm^{-1} line increased monotonically with decreasing temperature in the superconducting state.[5] Other work[4,6] showed that the temperature dependence of the HWHM exhibited a maximum at intermediate temperatures $0<T^*<T_c$. This maximum was believed to originate from a resonance of the phonon energy $h\nu$ with the superconducting gap energy $2\Delta(T)$ at $T=T^*$.[7] Accordingly, this result indicates that the gap energy at $T\rightarrow 0$ is larger than the phonon energy of 340 cm^{-1}: $2\Delta(0)>340$ cm^{-1}.

Later, it was found that the 430 and 500 cm^{-1} A_g modes also show similar anomalies, namely, additional hardening at $T<T_c$.[8–10]

In 1988, Zeyher and Zwicknagl (ZZ) have calculated theoretically the superconductivity-induced effects on the phonon self-energy at $q=0$, by assuming an isotropic s-wave gap and strong coupling for EPI.[11,12] According to the ZZ-model, the renormalization of the phonon self-energy results in softening for the phonons with frequencies $h\nu<2\Delta(T)$ without a significant change in the HWHM, whereas for phonons with frequencies $h\nu>2\Delta(T)$ hardening accompanying additional broadening of the linewidth is predicted. Friedl, Thomsen and Cardona have investigated the broadening of the B_{1g}-like modes in various $RBa_2Cu_3O_{7-\delta}$ compounds with different rare earth elements R.[5] Using the ZZ-model, they calculated the value of the gap $2\Delta(0)$ to be 316 cm^{-1} $(2\Delta/kT_c\sim 5)$, however, being smaller than the phonon energy 340 cm^{-1}.

A number of experimental studies were devoted in the ensuing period to accurate determination of the temperature-dependent behavior of the 340 cm^{-1} mode and gap value $2\Delta(0)$, but the results are surprisingly different from each other. Altendorf *et al.* found that the 340 cm^{-1} mode exhibited no anomalous broadening below T_c, indicating $2\Delta(0)/kT_c=5.9$.[9] McCarty *et al.* reported the narrowing of the 340 cm^{-1} mode below T_c and, therefore, deduced a much larger value of the gap: $6.8kT_c<2\Delta(0)<7.7kT_c$.[10] The attempts to reconcile the widely varying results were limited by the influence of impurities, defects and oxygen deficiencies. Thomsen *et al.* have shown that the temperature behavior of the 340 cm^{-1} line depends dramatically on the amount of defects in the samples.[13] Altendorf *et al.*[6] examined the superconductivity-induced change in the linewidths as a function of the oxygen content. Nevertheless on the basis of the ZZ-model, it is difficult to explain by the above factors all the differences of the RSS published in the literature.

Recently, Nicol, Jiang and Carbotte (NJC) have calculated the phonon-self-energy effect for d-wave pairing.[14] In contrast to the isotropic s-wave ZZ-model, NJC found that a phonon with $h\nu<2\Delta(T)$ softens and broadens. The broadening takes place just below T_c and shows a maximum at $T=T^*$; $h\nu=2\Delta(T^*)$. The frequency ν exhibits a discon-

 © 1998 American Institute of Physics

tinuous change from hardening to softening at the same temperature T^*.

Another missing ingredient of the majority RSS analysis is the overlooked importance of the orthorhombicity of the YBCO structure. The tetragonal approach for describing both superconducting gap and RSS was implied or discussed explicitly in the large number of papers. However, McCarty *et al.*[15] have found that the 120, 150, 340 and 500 cm^{-1} A_g phonon lines exhibit significant anisotropy at room temperature, e.g., their lineshapes and peak frequencies are quite different in the xx-, yy- and zz-polarizations. This fact demonstrates both in-plane and out-of-plane anisotropy of the EPI. Thus, we expect that some of the complicated phenomena observed in the RSS below T_c originate from the anisotropic properties of the superconducting order parameter.

We should note that, in spite of the large number of the experimental and theoretical works published during the ten years since the first RSS studies were done on YBCO, several major issues still remain unsolved. The most important and unsettled problems are summarized as follows.

1) No RSS study concerning the temperature dependencies of the out-of-plane and in-of-plane anisotropies have been reported.

2) Although the in-plane anisotropy in the RSS at room temperature has already demonstrated[15] the limitation of the tetragonal approach, the validity and limitation of this approach to the superconducting induced phenomena have not been examined sufficiently.

3) No significant superconducting-induced effect has been observed in the 120 and 150 cm^{-1} modes, although the condition $h\nu < 2\Delta(0)$ should obviously hold for these modes.

4) The temperature-dependent behavior of the 340 cm^{-1} mode is still controversial.

5) No RSS analysis was applied to examine the possible constraints imposed by the Raman experiment on the choice of the actual gap symmetry among pure isotropic s, anisotropic s, mixed $s+id$ and $s+d$ symmetries. This leads to the question about the possibilities of the phononic RSS in resolving the problem of pairing state symmetry and the mechanism of superconductivity in high-T_c copper-oxides.

These issues, which may be enlightening for the mechanism of the high-T_c superconductivity, are addressed in the present study.

2. EXPERIMENTAL

1) *Single crystal preparation and properties.* The single crystal pulling technique developed in ISTEC-SRL (Tokyo). called the SRL-CP method,[16] allows one to prepare for the measurements a large number of crystals with different characteristics of twinning, oxygen content and impurity level. In order to avoid any influence of surface defects on RSS,[17] the crystals were studied immediately after annealing or freshly cleaved just before the measurements. Another problem which has to be solved before collecting reliable spectroscopic data is how to reduce the impurity concentration down to the p.p.m level. Because almost all cationic impurities in YBCO exert a large detrimental effect on T_c, the measurements of T_c were crucial for crystal selection. A large number of crystals were examined after detwinning process[18] annealing at 490 °C in an oxygen flow. For detwinning, a uniaxial pressure of typically 10 MPa was applied during cooling from 700° to 490 °C over a week and, as a result, large untwinned orthorhombic crystals (typical volume 10 cm^3) with oxygen content close to ''$O_{6.8}$'' were obtained. The annealing temperature of 490 °C results in optimal doping of the single crystals, whereas a lower annealing temperature leads to an overdoped state. Since the stoichiomatric YBCO is overdoped[19–21] we avoid obtaining the overdoped state at the first state of oxygen loading, which is needed to select the purest crystals. The first step of sample preparation leads to optimal doping and allowed us to select for the study crystals with a maximum T_c of 93.6 K (Fig. 1).

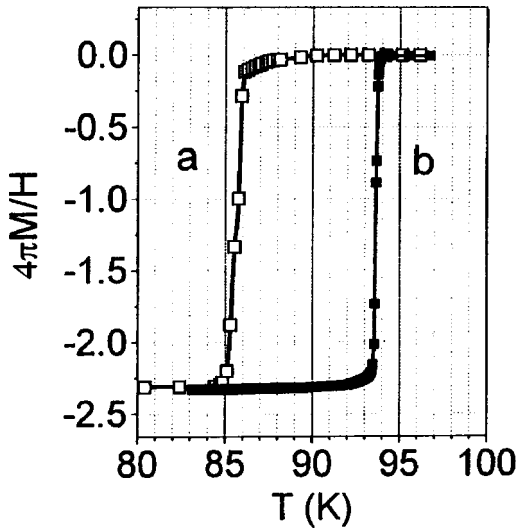

FIG. 1. Superconducting transitions in overdoped ($T_c = 86$ K) (a) and optimally doped ($T_c = 93.6$ K) (b) twin-free YBCO single crystals measured in zero-field cooled samples at the applies field of 10 Oe. The estimated diamagnetization factor $D = 2.3$ correspond to $\chi = -1/4\pi$, in agreement with a 100% shielding effect.

The most important finding in the second step of sample preparation is that the apparent degree of overdoping could be much larger in the high-purity single crystals than, for instance, in ceramics or powder. This was again reflected in the T_c values, which indicate that the detrimental effect from oxygen overdoped into a single crystal is the most pronounced in high-quality single crystals. The latter effect could be understood from the simple idea that the lateral surface layer parallel to ab or ac plane in a small powder particle or single crystallite of granular material could be intrinsically oxygen-depleted or highly defects of surface.[17] Therefore, the powder or ceramic materials may show higher value of T_c when the measurement of T_c is done using the surface-sensitive resistive method, or the low-field magnetic measurements, in which a screening current is induced in the surface layer of a small crystallite. With increasing yield, the current capacity of such a thin surface layer becomes insufficient and the superconductive transition broadens for the granular material. Such a broadening occurs when the powder or ceramic sample is overdoped in the bulk, but shows optimal T_c relative to the surface. On the contrary, we ob-

serve in single crystals, which have a sharp transition, a small uniform shift of T_c with increasing field instead of the broadening of the superconductive transition. Since the surface contribution is negligible in the large crystals, the transition reflects the bulk oxygen content. These considerations are inconsistent with the fact that the preparation process for the apparently optimally doped granular materials requires much lower temperature of annealing in oxygen or in air[20] than that for genuinely optimally doped single crystals.[21]

The importance of preparation of the overdoped crystals involves two reasons. One is that the close-to-ideal stoichiometric defect-free structure would exhibit the narrowest lines in the spectra. The other is that the anisotropic properties of YBCO are very different in the optimally doped and overdoped states.[22] In particular, at 320 °C the overdoped sample shows apparently half as much out-of-plane anisotropy $\gamma = (m_c/m_{ab})^{1/2}$, where m_c and m_{ab} are the effective carrier mass in the out-of-plane and in-plane directions, respectively. This could be roughly estimated from the slopes of the irreversibility lines and fishtail lines.[22] The large difference in the in-plane anisotropies $\gamma = (m_a/m_b)^{1/2}$ between optimally doped and overdoped at 320 °C was found in the normal state magnetic susceptibilities. The large in-plane anisotropy in the untwinned overdoped crystals is of particular interest in the present study. Thus, the best crystals were selected in the first stage of oxygen loading and then were annealed again at 320 °C. As a result, high-quality samples with $T_c = 86$ K and transition width ΔT_c of 0.4 K (Fig. 1) were obtained.

2) *Raman scattering technique.* The RSS were studied with using a triple-stage T64000 Jobin–Ivon spectrometer equipped with a liquid-nitrogen cooled CCD detector. The typical spectral resolution was 3 cm^{-1}, and several spectra were measured with the resolution of 1 cm^{-1}. To accurately study the temperature dependence of RSS and eliminate the systematic error in the determination of frequence shifts, RSS was observed in the spectrographic mode, i.e., the spectral regime was fixed without scanning the diffraction gratings. The pseudo-backscattering configuration was adopted. The xx- and yy-polarized RSS were obtained from the same partions on the mirrorlike regions of crystals. As for the zz-polarization, the RSS taken from the ac and bc-surfaces, which were the native and cleft ones, were essentially the same. The 514.5 nm line of the Ar-ion laser was employed as an excitation light source. The power density was adjusted to be 0.2–1 W/cm^2 on the sample surface, and, as result, the overheating was suppressed to 3 K in all the experiments. To measure the temperature dependence of the RSS, the close-cycle UHV cryostat was used with temperature stabilization to better than 1 K. The spectra were corrected for the spectral response of the optical system and normalized for laser power.

3. RESULTS AND DISCUSSION

The RSS in the overdoped and optimally doped YBCO crystals at 290 K are shown in Fig. 2. Let us specify for the sake of clarity three spectral regions, comprising the lines at 120 and 150 cm^{-1} (low-frequency region), 340 cm^{-1} (mid-frequency region) and 430 and 500 cm^{-1} (high-frequency region). The rest of this paper is organized as follows: In Section 3.2 the temperature behavior of the 120 and 150 cm^{-1} modes (Fig. 3) is described; the RSS in the mid-frequency region and their analysis is presented in Section 3.3 (Figs. 4–6); in Section 3.4, the phonons in the high-frequence region is discussed; from these experimental results we analyzed superconducting gap symmetry in Section 3.5. Our discussion of the RSS is based on the results of the dynamical calculations,[23] which showed quite satisfactory agreement between the experimental data and the calculations (see, for example, review in Ref. 24).

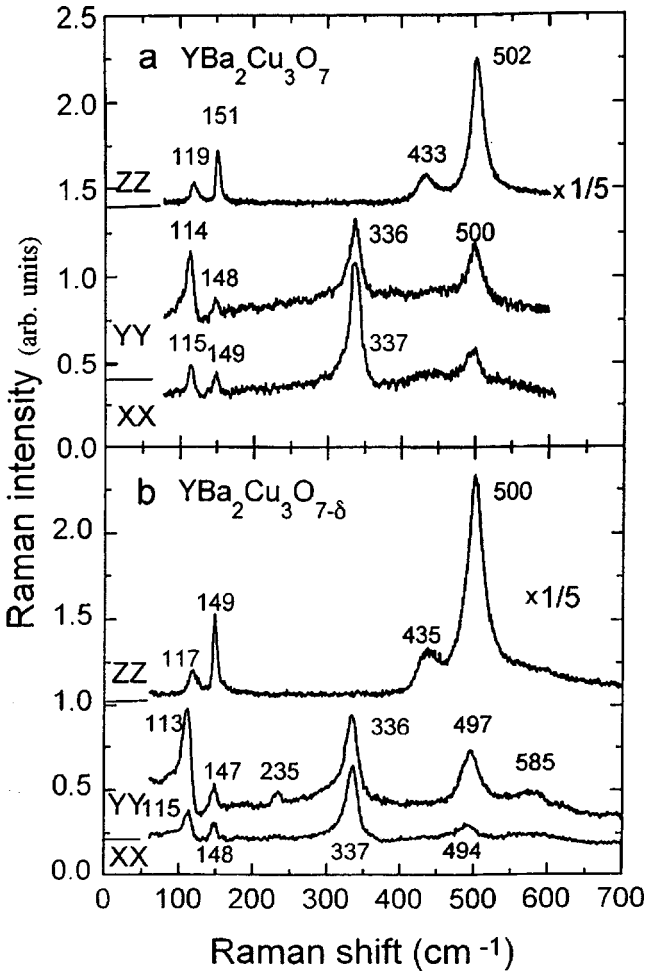

FIG. 2. Raman spectra of the overdoped ($T_c = 86$ K) (a) and optimally doped ($T_c = 94$ K) (b) twin-free YBCO single crystals in the xx-, yy- and zz-polarizations at $T = 290$ K.

1) *Raman scattering in optimally doped and overdoped* YBCO *crystals at room temperature.* In Fig. 2, we can see a number of effects of varying the oxygen content of RSS. First, the frequencies of all the modes shift slightly. Second, the 234 and 583 cm^{-1} modes, which are observed in the yy-polarization in the optimally doped YBCO, vanish in the overdoped crystals. The appearance of these modes is related to the oxygen disorder at the Cu(1)−O(4)-chains. According to the dynamical calculations,[23] in the fully stoichiometric YBCO the IR-active vibration of Cu(1) along the chains is at 153 cm^{-1}, and the corresponding chain oxygen mode is at

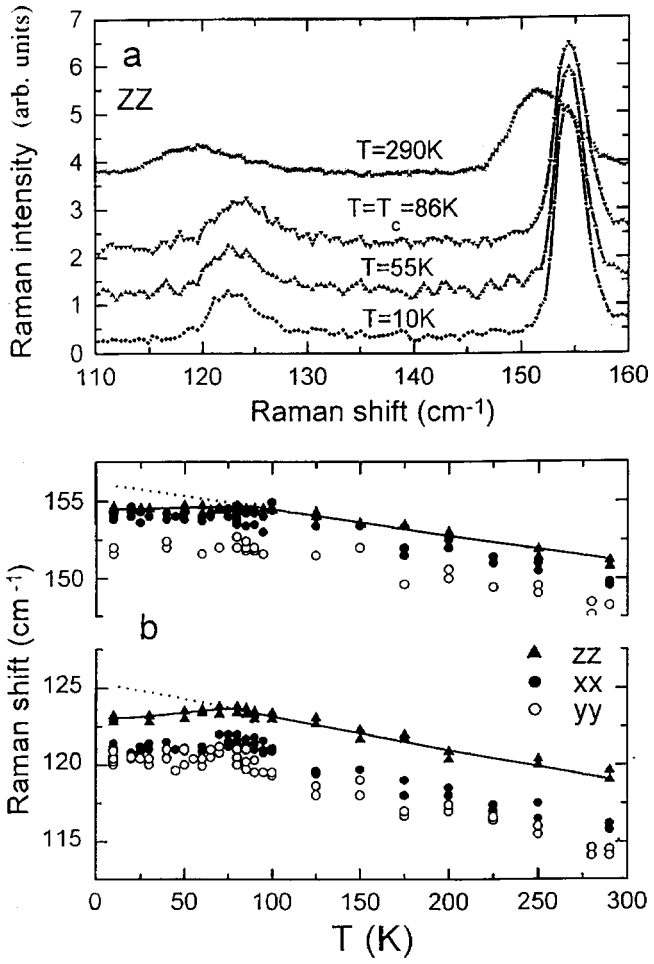

FIG. 3. (a) Low-frequency region of RSS of the overdoped twin-free YBCO single crystals in *zz*-polarization at different temperatures above and below T_c. Shown in (b) are the temperature dependences of the 120 and 150 cm^{-1} modes in *xx*-, *yy*- and *zz*-polarizations. All curves are guides to the eye.

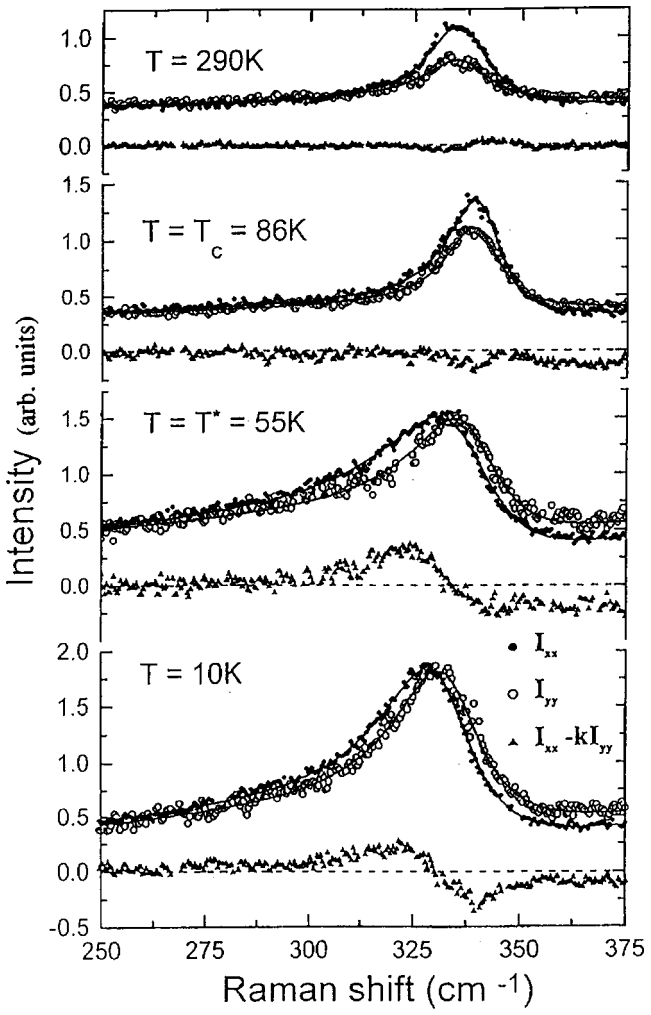

FIG. 4. Raman spectra in the region of the 340 cm^{-1} mode at different temperatures in the *xx*-(filled circles) and *yy*-polarizations (open circles). The spectra are normalized to the intensity at 250 cm^{-1}. The filled triangles show the differential $I_x - kI_y$ spectra with the normalizing factor $k = I_x(\nu_x)/I_y(\nu_y)$.

593 cm^{-1}. In the oxygen-deficient crystal these vibrations become Raman-active and appear in the *yy*-polarization the (*y* axis is along the chains).

The distinctive features of the RSS in the overdoped crystals are a well articulated polarization dependence and the absence of any additional line which is usually activated from oxygen disorder or impurity atoms, as mentioned above. The RSS shows only the five well known vibrations of the A_g symmetry. Note that all the results presented below are relevant to the overdoped ''O_7'' crystals.

2) *The* 120 *and* 150 $cm^{-1}A_g$*-modes.* The 120 and 150 $cm^{-1}A_g$ vibrations are formed mainly by *z*-displacements of Ba and planar Cu, respectively. According to Ref. 23, the atomic displacements at the Γ-point in the Brillouin zone at $T = 290$ K are as follows:

$$120\ cm^{-1}:\quad 6Ba+1Cu+1\ O(2)+1\ O(3), \tag{1}$$

$$150\ cm^{-1}:\quad 9Cu+3\ O(1)+1\ O(2)+1\ O(3), \tag{2}$$

where the coefficients preceding the atoms denote corresponding normalized *z*-displacements; O(1) is the apical oxygen, O(2) and O(3) are the oxygen from the CuO_2 plane. Thus, admixture of *z*-displacements of other atoms is expected to be small.

As for the 120 cm^{-1} mode, we successfully observe the effect of the out-of-plane anisotropy of the electron–phonon interaction (EPI) in the full temperature range between 10 K and 300 K (Fig. 3b). This effect manifests itself in the significant difference of the peak frequencies between the out-of-plane *zz*-polarization and the planar *xx*- and *yy*-polarization. The anisotropic EPI is more clearly seen in the shape of the 120 cm^{-1} mode (Fig. 2a). In the *yy*-polarization, the line shape is strikingly asymmetric, resulting from the coupling to the intense electronic background (Fano-type interference). On the other hand, in the *zz*-polarization, in which the electronic scattering at low frequencies is negligibly weak, the lineshape is symmetric and described well by a Lorentzian profile. As can be seen in Figs. 2a and 3b, the out-of-plane anisotropy is also apparent in the 150 cm^{-1} mode (although not so conspicuously as for the 120 cm^{-1} mode).

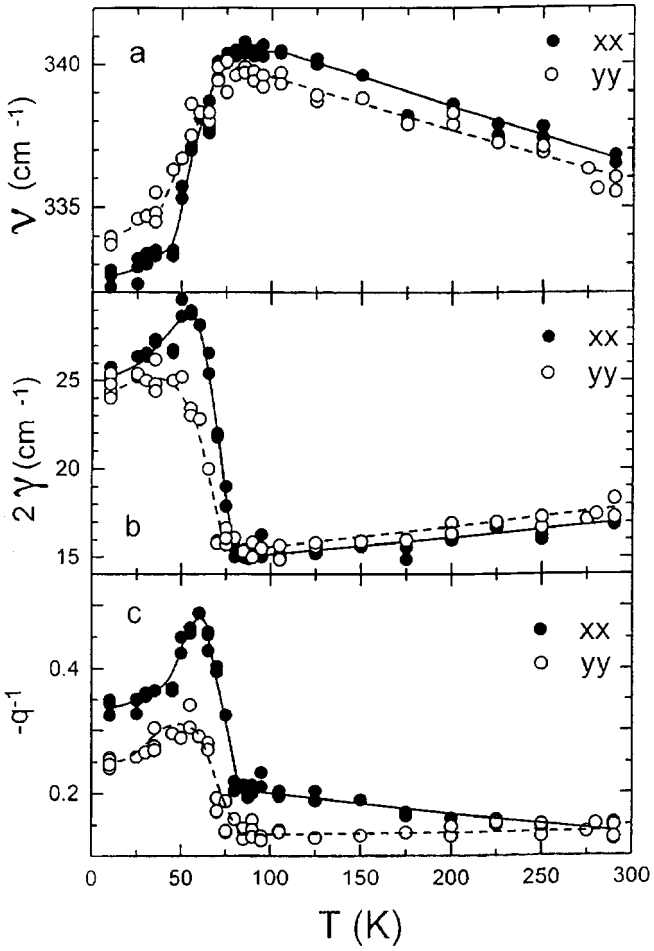

FIG. 5. Temperature dependences of the frequency ν_α (a), the linewidth γ_α (b) and inverse asymmetry parameter $1/q_\alpha$ (c) for the 340 cm^{-1} line in the xx- and yy-polarizations. All curves are guides to the eye.

One of the significant findings is the superconductivity-induced behavior of the 120 and 150 cm^{-1} modes in xx, yy and zz-polarizations (Fig. 3b). The 120 cm^{-1} mode frequence exhibits the usual broadening as the temperature decreases from 290 K to T_c. However, below T_c this frequence slightly decreases. Therefore, superconductivity-induced softening of the 120 cm^{-1} mode takes place. As for the 150 cm^{-1} mode, it is almost temperature-independent below T_c. Softening of these modes lying below T_c entirely within the gap $h\nu < 2\Delta(0)$ was predicted by several theories.[5,8] Note that the successful observation of this effect is due to the narrow Raman lines in our high-quality samples. For example, the HWHM for the line at 150 cm^{-1} in zz-polarization is only 1.5 cm^{-1} at 10 K.

3) *The* 340 cm^{-1} B_{1g}*-like mode.* In the majority of studies of the superconductivity effects on the RSS in YBCO, the 340 cm^{-1} mode is the main target. In a crude tetragonal assessment, this vibration has B_{1g} symmetry and corresponds to the out-of-phase displacements with equal amplitudes of the O(2) and O(3) oxygens in the direction of the z-axis. In the genuine orthorhombic structure of the oxygen-undepleted YBCO, the symmetry of the 340 cm^{-1} mode turns into the totally symmetric A_g one, and the z-displacements of the O(2) and O(3) atoms are unequal:[23]

$$340\ cm^{-1}:\quad 13\ O(2) - 12\ O(3). \tag{3}$$

The deviation of the ideal B_{1g}-vibrational configuration is small (below 10%). Hence this mode still has a B_{1g} character even in the orthorhombic YBCO, which is consistent with the polarization dependence reported in the literature.

Our key discovery deals with the character of softening of this mode. Because the relative magnitude for the 340 cm^{-1} line is the largest one, it is possible to accurately measure the difference in the temperature behavior of the xx and yy polarizations. The results refer to the magnitude of

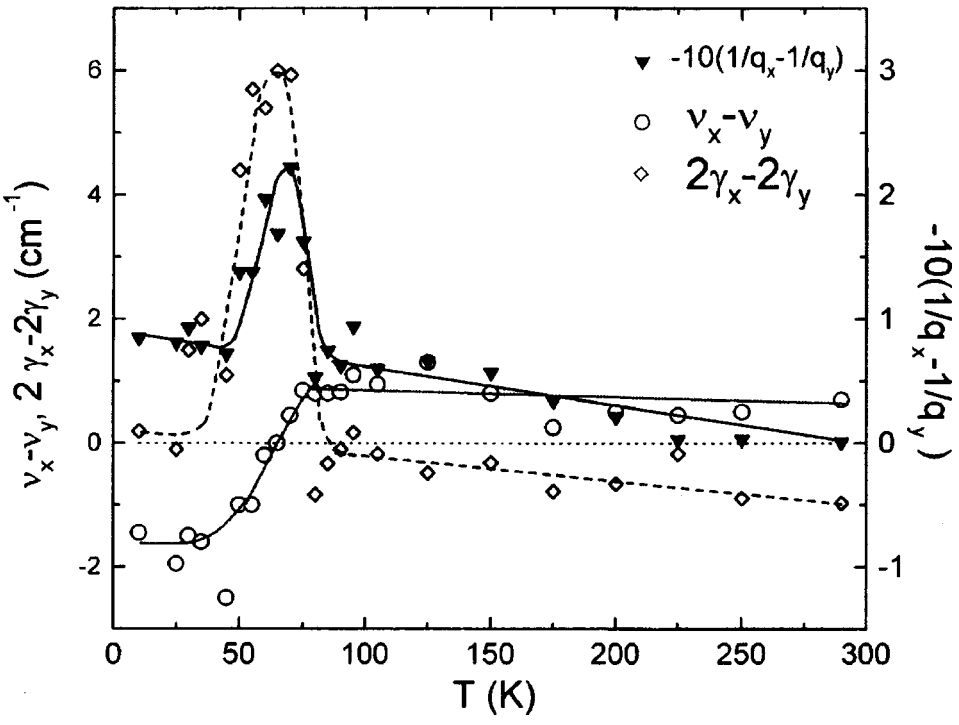

FIG. 6. Temperature dependences of the $x-y$ differences of ν_α, γ_α, and $1/q_\alpha$ for the 340 cm^{-1} mode. All curves are guides for the eye.

softening and the character of broadening are illustrated in Figs. 4–6. We performed a least-squares fits to the RSS in the spectral region around the 340 cm^{-1} mode (175 $cm^{-1} < \nu < 400\ cm^{-1}$) in terms of a standard expression

$$I = A + B\nu + C\nu^2 + I_0(\varepsilon + q)^2/(1+\varepsilon^2), \tag{4}$$

where the term $A + B\nu + C\nu^2$ describes the background continuum arising from the electronic Raman scattering. The last term describes the Fano profile of the 340 cm^{-1} line where $\varepsilon = (\nu - \nu_\alpha)/\gamma_\alpha$ and q_α is the asymmetry parameter ($\alpha = x,y$). Here the frequency ν_α and linewidth γ are renormalized by the real and imaginary parts of the electronic response $\chi(\omega) = -R(\omega) + i\pi\rho(\omega)$ as $\nu_\alpha = \Omega + V^2 R$ and $\gamma_\alpha = \Gamma + V^2\pi\rho$, respectively, where Ω and Γ are the uncoupled frequency and damping ($\Omega_x \equiv \Omega_y$, $\Gamma_x \equiv \Gamma_y$ for nondegenerate A_g-modes), and V is the coupling constant. It should be noted that the thermal Bose factor does not affect significantly the numerical fitting in the relevant frequency region.

In Fig. 4, the 340 cm^{-1} line is shown in the xx- and yy-polarizations together with the normalized differential spectra $I_x - kI_y$, which demonstrate clearly the in-plane anisotropy. In the normal state, the frequency of the 340 cm^{-1} line in the xx-polarization (ν_x) is slightly higher that in the yy-polarization (ν_y) (Fig. 5a). The difference $\nu_x - \nu_y$ is roughly temperature-independent (Fig. 6) while the differences of the parameters γ and $1/q$ increase with decreasing temperature (Figs. 5b and 5c). Noticeably, we can see in Fig. 4 that the line shapes are almost symmetric in both polarizations at $T = 290$ K, while at $T = T_c$ this line in the xx-polarization already shows a slight asymmetry.

At temperatures just below T_c, the frequency of the 340 cm^{-1} line deviates slightly from the T-linear dependence of the normal state one. As the temperature decreases further, this mode exhibits a steep softening. As for the xx-polarization, the frequency decreases by about 7 cm^{-1} in temperature range $40 < T < 70$ K, whereas the decrease is only 1 cm^{-1} below 40 K. In the yy-polarization, the total softening of this mode is about 5.5 cm^{-1}, less than that in the xx-polarization. Significantly, at the midpoint of the main softening temperature range at $T_x^* = 55$–60 K the maximum broadening of this line occurs in the xx-polarization, whereas in the yy-polarization, there is an uncertain maximum in the linewidth dependence at the temperature T_y^* about 45–50 K (Fig. 5b). The in-plane anisotropy of both the inverse line asymmetry $1/q$ and linewidth γ is quite large in the region $40\ \text{K} < T < T_c$ while the anisotropy is small again at low temperatures. As can be seen from Fig. 3, the differential spectrum $I_x - kI_y$ is inverted when passing through T^*, demonstrating the changeover from $\nu_x > \nu_y$ above T^* to $\nu_y > \nu_x$ below T^*.

4) *The* 430 *and* 500 cm^{-1} A_g*-modes.* The 430 cm^{-1} vibration is mainly due to in-phase z-displacements of the O(2) and O(3) oxygens. While the displacements of O(2) and O(3) are equal in oxygen-depleted tetragonal YBCO, in the orthorhombic structure this mode accompanies the z-displacements of Cu(2) and O(1) as follows

$$430\ cm^{-1}: \quad 12\ \text{O(2)} + 13\ \text{O(3)} - 1\text{Cu(2)} - 1\ \text{O(1)}. \tag{5}$$

From Eqs. (3) and (5), it follows that the orthorhombic distortion mixes the tetragonal B_{1g} (O(2)−O(3)) and A_{1g} (O(2)+O(3)) modes belonging to the same A_g symmetry in the D_{2h} structure. Note that the distortion is very small for the 430 cm^{-1} A_g-vibration, as in the case of the B_{1g}-like mode. As for the 500 cm^{-1} vibration, it is preferentially associated with the apical oxygen displacements along the z-axis:

$$500\ cm^{-1}: \quad 17\ \text{O(1)} - 1\text{Cu(2)}. \tag{6}$$

The temperature behavior of the 430 and 500 cm^{-1} lines (Fig. 7) is similar to that reported previously.[8–10] The additional hardening of these lines takes place between $T_c = 86$ and 40 K. The hardening of these modes indicates that the magnitude of the superconducting gap is less than 430 cm^{-1}.

5) *The symmetry of the superconducting gap in* $YBa_2Cu_3O_7$. In this Section, we first discuss the general features of the effects of superconductivity on RSS. Next, we explore a possible origin of the in-plane anisotropy of the 340 cm^{-1} line and discuss the gap symmetry on the basis of the experimental data.

The main features of the self-energy effects agree basically with those expected in a d-wave state.[14] Namely, the theory predicts that the step-like softening and maximum of the line broadening should be at the same temperature $T^* < T_c$ (Fig. 5a and 5b). Actually, the temperature region of softening is broadened up to the appreciable width of 30 K (Fig. 5a). This could be related to the significant width of the 340 cm^{-1} line, so that the 2Δ-peak of the density of states crosses this line in the finite temperature interval. On the other hand, the broadening of the 340 cm^{-1} line starts in both xx- and yy-polarizations immediately at the superconducting transition, again in accordance with the theoretical analysis.[4]

Here we shall discuss the possible origin of the observed in-plane anisotropy in the RSS. According to the results of the numerical calculations for the s-wave and d-wave states, the magnitude of the softening is directly linked to the difference between the phonon and gap energies, that is $2\Delta(t) - h\nu$. If the xx- and yy-polarized phonons probe predominantly the values of Δ_x and Δ_y, respectively, the $x-y$ anisotropy in the superconductivity-induced effects should result from the difference in the gap values: $\Delta_x \neq \Delta_y$. Note that $\Delta_x = \Delta_y$ holds in all the cases of s^0, s^+, d, $s+id$ and $d+is$ symmetries with gaps of the forms

$$\Delta^{s(0)} = \text{const}, \tag{7a}$$

$$\Delta^{s(+)} = \Delta^s(\cos k_x - \cos k_y), \tag{7b}$$

$$\Delta^d + \Delta^d(\cos k_x - \cos k_y), \tag{7c}$$

$$\Delta^{s+id} = \Delta^s(\cos k_x + \cos k_y) + i\Delta^d(\cos k_x - \cos k_y), \tag{7d}$$

$$\Delta^{d+is} = \Delta^d(\cos k_x - \cos k_y) + i\Delta^s(\cos k_x + \cos k_y). \tag{7e}$$

To be specific, the functions (7b) and (7c) for the case of spherical Fermi surface with a radius of 0.7π (i.e., $k_x = 0.7\pi\cos\varphi$, $k_y = 0.7\pi\sin\varphi$, $0 \leqslant \varphi \leqslant 2\pi$) are depicted in Fig. 8. Clearly, no $x-y$ anisotropy is seen in the figure for either of these functions. In this respect, it is pertinent to

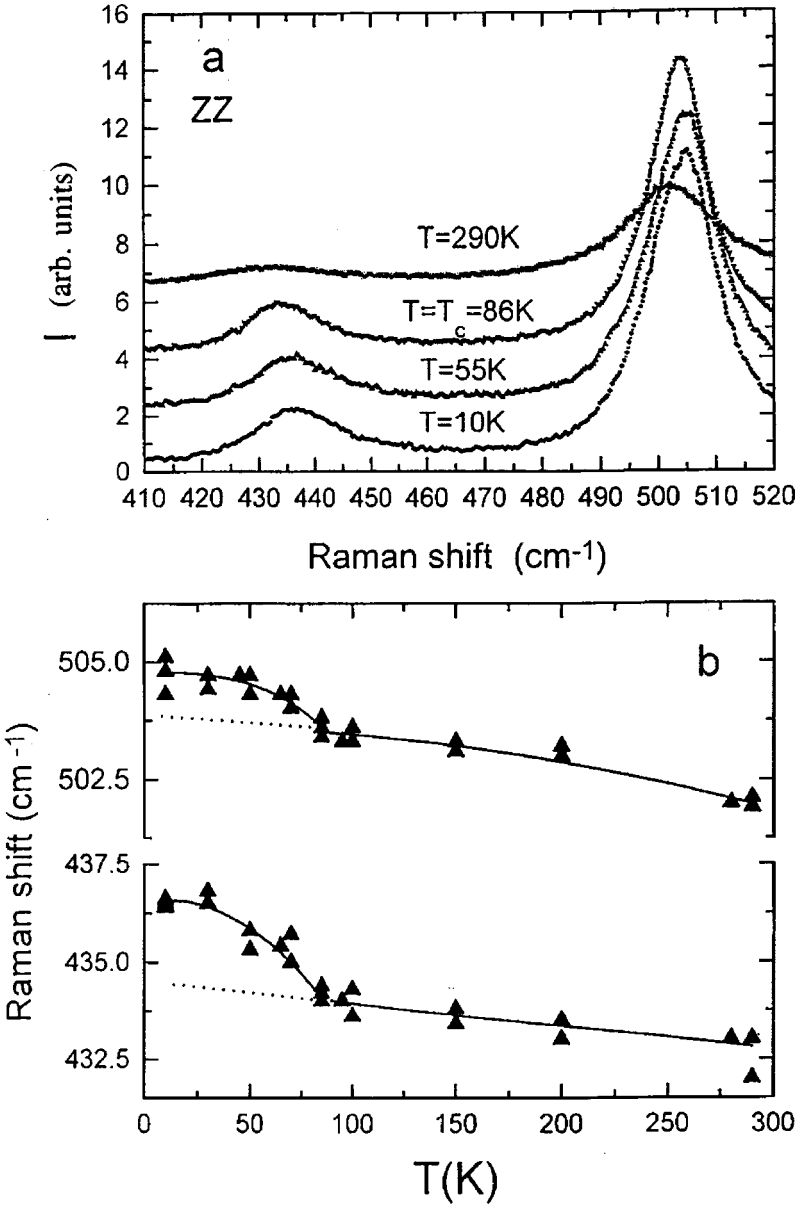

FIG. 7. Temperature dependence of the RSS in high-frequency region (a) and the frequencies of 430 and 500 cm^{-1} lines (b) in the *zz*-polarizations. All curves in panel (b) are only guides for the eye.

recall here the evolution of continuing debates on this gap symmetry problem. Three main periods in the chronology of events can be identified: 1) quick discarding of the model of the isotropic *s*-gap; 2) attempts to choose between the anisotropic *s*-gap and the *d*-gap; 3) extension of the number of proposed models due to the mixed $s+d$, $s+id$ and $d+is$[25] symmetries and even due to coexistence of two types of condensate with different order parameters of *s* and *d* symmetry.[26]

A large number of the experimental techniques have been used for determining the symmetry. Up until now, definite progress has been made in agreeing that the *d*-wave component could be predominant in the gap wave function. It has been revealed, however, that the Ginzburg–Landau solution for the orthorhombic symmetry leads directly to the $d+s$ symmetry (or $s+d$ if the dominant component is taken to be placed first).[27–30] Experimental confirmation of the mixed symmetry is still lacking. A possible exception could be related to a rationalization of the tunnel experiments by Dynes and co-workers,[31] in which a current from Pb (*s*-wave superconductors) to YBCO was observed, although no such current is expected in the pure *d*-wave state. Thus, the possibility of an admixture of the *s*-wave component owing to orthorhombicity might be suggested by this observation.[23,33]

In the discussion of our experiments, it should be emphasized that the $d+s$ symmetry is the only realistic symmetry which applies to the case $\Delta_x \neq \Delta_y$. The $s+d$ state has a gap function of

$$\Delta^{d+s} = \Delta^d(\cos k_x - \cos k_y) + \Delta^s(\cos k_x + \cos k_y). \quad (8)$$

Figure 8 shows the angular dependence of the magnitude of the gap at a cylindrical Fermi surface with $k_x = 0.7\pi \cos\varphi$ and $k_y = 0.7\pi \sin\varphi$ for various ratios between the *d* and *s* component amplitudes. Because the main features of the RSS can be described in accordance with the *d*-wave model,[14] the *s*-component is expected to be weaker than the *d*-component. The observation of the maximum $\gamma_x(T)$ near $T_x^* = 55$ K implies $2\Delta_x(55\text{ K}) \cong \Omega$. In order to estimate the

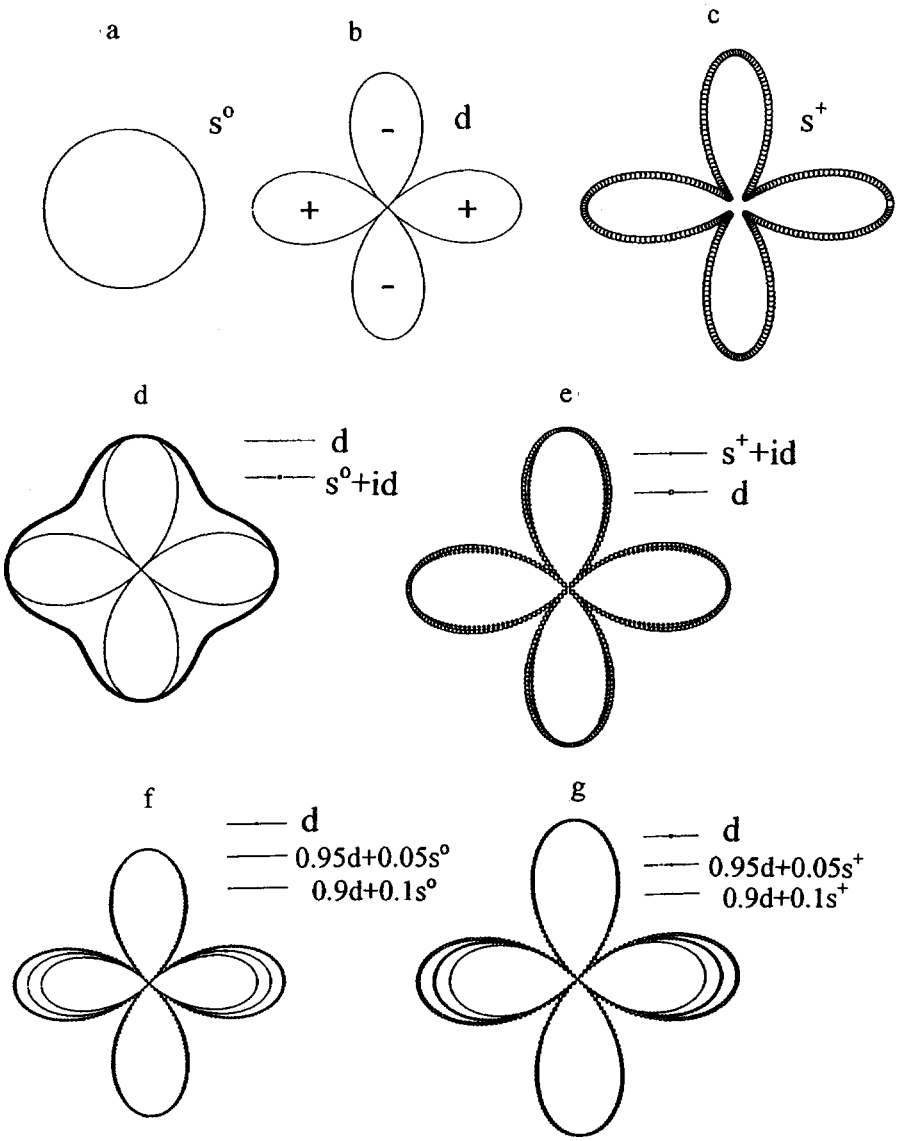

FIG. 8. The gap functions for various ratios between the d- and s-component amplitudes. (a)—isotropic s^0, (b)—d, (c)—anisotropic s^+, (d)—d and mixed s^0+id, (e)—d and mixed s^++id, (f)—d and mixed $0.95d+0.05s^0$, $0.9d+0.1s^0$, (g)—d and mixed $0.95d+0.05s^+$, $0.9d+0.1s^+$.

value of the uncoupled frequency Ω, one must analyze the observed spectrum in terms of a more complicated Green's function, taking into account the ν-dependence of the electron–electron scattering rate $\tau(\nu)$ and mass $m(\nu)$. According to this analysis, $\Omega \cong 350\ \mathrm{cm}^{-1}$ is larger than ν_α by about $10\ \mathrm{cm}^{-1}$ in the normal state. Assuming a BCS-like T-dependence of $\Delta(T)$, we obtain $2\Delta_x(0)=400\ \mathrm{cm}^{-1}=6.7kT_c$ (Fig. 9). For the yy-spectrum, the maximum $\gamma_y(T)$ is observed around 45 K, $2\Delta_y(0)=370\ \mathrm{cm}^{-1}=6.2kT_c$. Therefore we have $2\Delta_x(0)/2\Delta_y(0)\cong 1.1$, which leads to a small admixture of $\Delta_s \cong 0.05\Delta_d$ (Fig. 8).

Because of the substantial linewidth of the $340\ \mathrm{cm}^{-1}$ mode, which is $30\ \mathrm{cm}^{-1}$ at $T^*=55$ K, we can ignore broadening of the softening temperature range and estimate the width of this region. By assuming the BCS dependence for $\Delta(T)$, we find (Fig. 9) that the width of the softening region is $\Delta T=15$ K, which is quite comparable with the experimental value of 30 K (Fig. 5a) broadened additionally due to the finite width of the 2Δ-peak of the electronic state density.

Now we shall discuss other possible explanations for the observed $x-y$ anisotropy in superconductivity-induced effects. It could be due to the CuO chain contribution. The coupling of the $340\ \mathrm{cm}^{-1}$ phonon with the chain electronic excitation is not expected to be strong, because this phonon mode does not involve vibrations of the atoms in the chain (see Eq. 3). However, the coupling could be enhanced by a resonance of this phonon energy and the interband excitation energy between the CuO chain and the CuO_2 plane bands. In this case, the $340\ \mathrm{cm}^{-1}$ phonon must be affected by the gap opening in the chain. If the chain superconductivity is induced mainly by the attractive interaction within the one-dimensional chain, the gap function cannot be a d-wave but should be a s-wave. Thus, the Raman response should be quite different from that for d-symmetry in the plane superconductivity. Consequently, the phonon self-energy effect is observed to be different in the yy-spectrum from that in the xx-spectrum, which reflects only the d-gap in the plane.

4. CONCLUSIONS

The effect of the out-of-plane and the in-plane anisotropies, the softening below T_c of the 120, 150 and $340\ \mathrm{cm}^{-1}$

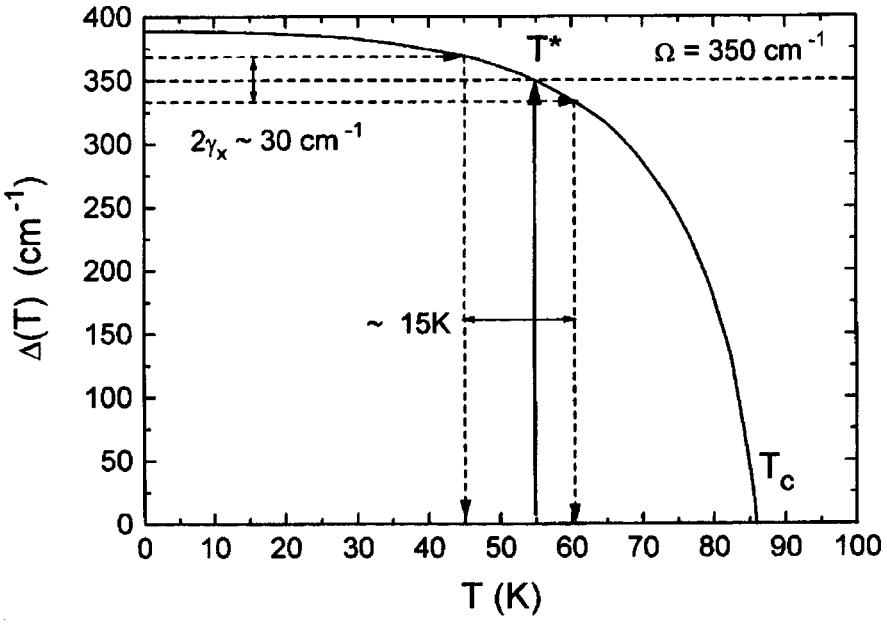

FIG. 9. The BCS dependence of $\Delta(T)$ for $T_c = 86$ K and $\Delta(55\text{ K}) = 350\text{ cm}^{-1}$.

modes with frequencies $h\nu \leqslant 2\Delta(0)$ along with the well-known hardening of the 430 and 500 cm^{-1} modes with frequencies $h\nu > 2\Delta(0)$, and the discovery that bounded region of softening for the 340 cm^{-1} mode coincides in temperature with the maximum broadening of this line constitute the entire picture of the phonon behavior in the superconducting phase of YBCO.

It is remarkable than until now, when a variety of the experimental techniques were used for determining the symmetry, the main goal was the search for the nodes of the gap functions and the investigation of the behavior of the phase of the order parameter in a 90° rotation around z-axis. From the results of Raman experiment we have succeeded in examining the symmetry of the gap in a quite different manner. We compared the magnitudes of the gap along the x and y crystal axes, in which not minima but maxima of the $\Delta(k)$ gap function are expected, i.e., we compared the amplitudes of the order parameter for a 90° rotation around z-axis. Neither the ZZ pure s-model[11,12] mor the NJC pure d-model[14] cannot consistently explain the presented results, which should provide impetus for further development of the theory.

One of the plausible candidates for the origin of the observed $x-y$ anisotropy in both broadening and softening for the 340 cm^{-1} mode is the $d+s$ gap symmetry. We have deduced the gap value $2\Delta_x(0) = 6.7kT_c$ along the x-axis and $2\Delta_y = 6.2kT_c$ along the y-axis. The value of the $x-y$ anisotropy of the gap value is significant $(2\Delta_x(0) - 2\Delta_y(0) = 0.5kT_c)$, so that the admixture of the s-component is about 5%.

Another possibility for explaining the $x-y$ anisotropy is an independent superconducting channel in the CuO chain with a different pairing symmetry from that of the CuO_2 plane superconductivity. In this case, the anisotropy could be attributed to the contribution of the chain superconductivity to the yy-spectrum.

Finally, it should be emphasized that the issue of gap symmetry may be intimately related to the physical origin of pairing interactions. It is well known that the s-wave is likely linked with long-range interactions and implies a phononic mechanism. On the other hand, the d-wave pairing arises from the spin-fluctuation mechanism[34]. It might then be speculated that the mechanism of the superconductivity in $YBa_2Cu_3O_{7-x}$ crystals originates from the mixed interactions.

The authors thank A. G. Panfilov, R. Eder, Yu. E. Kitaev and V. P. Smirnov for their helpful discussions.

This work was supported by NEDO for the R&D of the Industrial Science and Technology Frontier Program.

*Permanent address: A. F. Ioffe Physicotechnical Institute, 194021 St. Petersburg, Russia.

[1] M. Macfarlane, H. J. Rosen, H. Seki, Solid State Commun. **63**, 831 (1987).
[2] A. Wittlin, R. Liu, M. Cardona, L. Genzel, W. Konig, W. Bauhofer, Hj. Mattausch, A. Simon, Solid State Commun. **64**, 477 (1987).
[3] R. Feile, U. Schmitt, P. Leiderer, J. Schubert, U. Poppe, Z. Phys. B **72**, 161 (1988).
[4] S. L. Copper, F. Slakey, M. V. Klein, J. P. Rice, E. D. Bukowski, D. M. Ginsberg, Phys. Rev. B **38**, 11934 (1988).
[5] B. Friedl, C. Thomsen, M. Cardona, Phys. Rev. Lett. **65**, 915 (1990).
[6] E. Altendorf, X. K. Chen, J. C. Irwin, R. Liang, W. N. Hardy, Phys. Rev. B **47**, 8140 (1993).
[7] S. L. Copper, F. Slakey, M. V. Klein, J. P. Rice, E. D. Bukowski, D. M. Ginsberg, J. Opt. Soc. Am. B **6**, 436 (1989).
[8] C. Thomsen, M. Cardona, B. Friedl, C. O. Rodriguez, I. I. Mazin, O. K. Andrsen, Solid State Commun. **75**, 219 (1990).
[9] E. Altendorf, J. Chrzanowski, J. C. Irwin, A. O'Reilly, W. N. Hardy, Physica C **175**, 47 (1991).
[10] K. F. McCarty, H. B. Radousky, J. Z. Liu, R. N. Shelton, Phys. Rev. B **43**, 13 751 (1991).
[11] R. Zeyher, G. Zwicknagl, Solid State Commun. **66**, 617 (1988).
[12] R. Zeyher, G. Zwicknagl, Z. Phys. B **78**, 175 (1990).
[13] C. Thomsen, B. Friedl, M. Cieplak, M. Cardona, Solid State Commun. **78**, 727 (1991).
[14] E. J. Nicol, C. Jiang, J. P. Carbotte, Phys. Rev. B **47**, 8131 (1993).

[15] K. F. McCarty, J. Z. Liu, R. N. Shelton, H. B. Radousky, Phys. Rev. B **41**, 8792 (1990).
[16] Y. Yamada, S. Shiohara, Physica C **217**, 182 (1993).
[17] A. I. Rykov, M. F. Limonov, S. Tajima., in Advances in Superconductivity IX/Ed., S. Nakajima and M. Murakami. Springer, Verlag, Tokyo (1997). P. 391.
[18] A. I. Rykov, W. J. Jang, H. Unoki, S. Tajima., in Advances in Superconductivity VIII/Ed., H. Hayakawa and Y. Enomoto. Springer-Verlag, Tokyo (1996). p. 341.
[19] J. Tallon, N. E. Flower, Physica C **204**, 237 (1993).
[20] A. N. Lavrov, Physica C **216**, 36 (1993).
[21] S. Miyamoto, Y. High, J. Schutzmann, H. Kutami, S. Tajima, Y. Shiohara, in Advances in Superconductivity VII/Ed., K. Yamafuji and T. Morishita. Springer Verlag, Tokyo (1995). p. 129.
[22] A. I. Rykov, S. Tajima, in *Critical Currents in Superconductors* (Ed.), T. Matsushitaand, K. Yamafuji. World Scientific, Singapore (1996). p. 369.
[23] Yu. E. Kitaev, M. F. Limonov, A. G. Panfilov, R. A. Evarestov, A. P. Mirgorodsky, Phys. Rev. B **49**, 9933 (1994).
[24] Yu. E. Kitaev, M. F. Limonov, A. P. Mirgorodsky, A. G. Panfilov, R. A. Evarestov, Phys. Solid State **36**, 475 (1994).
[25] G. Kootliar, Phys. Rev. B **37**, 3664 (1988).
[26] K. A. Muller, Nature (London) **377**, 133 (1995).
[27] Q. P. Li, B. E. Koltenbah, and R. Joynt, Phys. Rev. B **48**, 437 (1993).
[28] C. O'Donovan, J. P. Carbotte, Phys. Rev. B **52**, 16 208 (1995).
[29] C. O'Donovan, J. P. Carbotte, J. Low Temp. Phys. **105**, 495 (1996).
[30] K. Maki, M. T. Beal-Monod, Phys. Lett. A **208**, 365 (1995).
[31] A. G. Sun, D. A. Gajevski, M. B. Maple, R. C. Dynes, Phys. Rev. Lett. **72**, 2267 (1994).
[32] M. Sigrist, T. M. Rice, Rev. Mod. Phys. **67**, 503 (1995).
[33] D. J. van Harlingen, Rev. Mod. Phys. **67**, 515 (1995).
[34] D. Pines, Physica C **185**, 120 (1991).

Published in English in the original Russian journal. Reproduced here with stylistic changes by the Translation Editor.

Temperature dependence of the electronic specific heat of superconductors with quantum defects

A. P. Zhernov

Russian Scientific Center ''Kurchatov Institute,'' 123182 Moscow, Russia
(Submitted October 9, 1997)
Fiz. Tverd. Tela (St. Petersburg) **40**, 413–418 (March 1998)

The electronic specific heat of metals with quantum defects in the superconducting state is examined. The role of the electron–polaron effect, as well as that of the level population factor of two-level states, is analyzed in an adiabatic approach. The cases of intermediate and strong coupling are discussed. © *1998 American Institute of Physics.* [S1063-7834(98)00503-6]

The tunnelling of particles in an electron fluid is known to be accompanied by a strong electron–polaron effect. This problem has recently been analyzed rigorously in an adiabatic approach by Kagan and Prokof'ev.[1] Based on this approach, we have examined[2,3] a number of parameters of superconductors with quantum defects. In particular, we have studied[2] some specific features of the behavior of the superconducting transition critical temperature T_c owing to the electron–polaron effect. Here we note that the effect of two-level states on T_c has been discussed in a number of papers. For the case of tunnelling states with a symmetric potential, we mention Ref. 1. A more realistic situation has been examined, for example, by Kozub.[5] In addition, the behavior of the isotropic shift factor and the order parameter Δ_0, as well as of the magnetic field H_{c2}, have also been studied.[2,3] Experiments on amorphous systems and dilute metal hydrides have been discussed in terms of this theory.

This paper is a continuation of Refs. 2 and 3. We study the effect of quantum defects on the electronic specific heat of metals in the superconducting state in terms of the adiabatic theory. It is assumed that these defects can be described by sets of two-level states.

Note that systems with two-level states differ from a standard superconductor. In them, besides a phonon mechanism for coupling of electrons through a two-level state, a nonphonon mechanism is possible. Here, because of a spatial delocalization of the tunnelling particles, the coupling constant λ_{TS} may be large, and strong coupling may be realized. The characteristic frequencies $\Omega_{\rm TS}$ in the interaction spectrum $S_{\rm TS}(\omega)$ of the electrons with the two-level state may be lower than or on the order of the critical temperature T_c. Both of these parameters depend on the temperature (see below) because of the electron–polaron effect, as well as because of the level population factors.

Recall, also, that when there is a strong electron–polaron effect in the well, the energy difference between the symmetric and antisymmetric two-level states is substantially lower. The renormalization scale depends on the relation between the seed tunnel amplitude and the effective phonon frequency, a parameter which characterizes the interaction between the electron–hole pairs and the tunnelling atoms, and the critical temperature T_c (or superconducting gap). (See Ref. 1, for example.) Here there is an intrinsic width that may be comparable to the level splitting in the well. Given these remarks, we intend to show, using a rigorous adiabatic approach, that for subbarrier motion of the defect, the electron–polaron effect causes a significant renormalization of the electron specific heat in superconductors.

The behavior of the electron specific heat at temperatures from zero to T_c is analyzed using the Bardeen–Stephen representation for the jump in the free energy[6] and a system of Eliashberg integral equations for the order parameters and for the renormalization of the electron mass. The kernel of the system was expressed in terms of the delta-function spectral function $S_{\rm TS}(\omega)$ which we have found earlier.[2,3] The quantity $\delta C(T)=\Delta C(T)/\Delta C(T_c)$, where $\Delta C(T)$ is the difference in the specific heats of the superconducting and normal states, was examined directly. The cases of intermediate coupling with the standard attraction spectrum and strong coupling with the nonstandard spectrum $S_{\rm ST}(\omega)$ are discussed.

In Section 1 basic equations and algebraic relations for determining the factor δC in various special cases are given. In Section 2 a model spectrum $S_{\rm TS}(\omega)$ is determined for the interaction of electrons with a two-level state. In the last section this spectrum and the representations of δC introduced in Section 1 are used to analyze the effect of a strong electron–polaron effect, and of the level population factor, on the specific heat.

1. GENERAL EQUATIONS FOR THE ELECTRONIC SPECIFIC HEAT OF SUPERCONDUCTORS

A general expression for the jump in the free energy as the system goes from the normal (N) to the superconducting (S) state,

$$\Delta F=F_S(T)-F_N(T)$$

has been obtained by Wada.[7] Bardeen and Stephen[6] used an analytical relation between the Green's functions of the quasiparticles to greatly simplify the expression for ΔF. They found that in the Matsubara representation

$$\frac{\Delta F}{N(\varepsilon_F)}=-\pi T\sum_n\ [\sqrt{\omega_n^2+\Delta^2(i\omega_n)}-|\omega_n|]$$

 © 1998 American Institute of Physics

$$\left[Z_S(i\omega_n) - Z_N(i\omega_n) \frac{\omega_n}{[\omega_m^2 + \Delta^2(i\omega_m)]^{1/2}} \right],$$

$$\omega_n = \pi T(2n+1), \quad n = 0,1,2,\ldots . \tag{1}$$

Here $\Delta(i\omega_n)$ and $Z(i\omega_n)$ are, respectively, the gap function and renormalization factor for the electron mass. $N(\varepsilon_F)$ denotes the band density of electron states at the Fermi level.

$\Delta(i\omega_n)$ and $Z(i\omega_n)$ satisfy a system of standard nonlinear integral equations of the Eliashberg form

$$\Delta(i\omega_n)Z(i\omega_n) = \pi\lambda T \sum_{m=-\infty}^{\infty} I(i\omega_n - i\omega_m) \times \frac{\Delta(i\omega_m)}{[\omega_m^2 + \Delta^2(i\omega_m)]^{1/2}}, \tag{2a}$$

and

$$Z(i\omega_n) = 1 + \frac{\pi\lambda T}{\omega_n} \sum_{m=-\infty}^{\infty} I(i\omega_n - i\omega) \times \frac{\Delta(i\omega_m)}{[\omega_m^2 + \Delta^2(i\omega_m)]^{1/2}}. \tag{2b}$$

The kernel of these equations, $I(i\omega_n - i\omega_m)$ is expressed in terms of the spectral function of the attractive interelectronic interaction, $S(\omega)$, by

$$I(i\omega_n - i\omega_m) = \frac{1}{\lambda} \int_0^\infty d\omega^2 \frac{S(\omega)}{\omega^2} \frac{\omega^2}{\omega^2 - (i\omega_n - i\omega_m)^2}. \tag{3}$$

For simplicity, in Eq. (2) the coupling constant λ is assumed to be much greater in magnitude than the Coulomb pseudopotential.

By definition

$$\Delta C = C_S(T) - C_N(T) = -T \frac{\partial \Delta C}{\partial T^2}.$$

The temperature behavior of the factor ΔC has been analyzed many times in terms of an electron–phonon mechanism. The cases of intermediate and strong coupling have been examined, with standard and nonstandard S-spectra of a general form (in the first case $\pi T_c < \omega_{ln}$, where ω_{ln} is a characteristic frequency of the spectrum and in the second, $\pi T_c \leqslant \omega_{ln}$). Pioneering work was done by Geĭlikman and Kresin. This is summarized in the book by Geĭlikman.[8] The results of later work have been summarized in a review by Carbotte.[9]

In the case of intermediate coupling and a standard S-spectrum, for temperatures near T_c experimental data have been fitted[10] to yield an analytic representation of the form

$$\delta C = \Delta C(T \leqslant T_c) = \frac{\Delta C(T \leqslant T_c)}{\frac{2}{3}\pi^2(1+\lambda)N(\varepsilon_F)T_c} = 1.43\left[1 + c_1\left(\frac{T_c}{\omega_{ln}}\right)^2 \ln\frac{\omega_{ln}}{d_1 T_c}\right] - 3.77\left[1 + c_2\left(\frac{T_c}{\omega_{ln}}\right)^2 \ln\frac{\omega_{ln}}{d_2 T_c}\right] t,$$

$$t = 1 - \frac{T}{T_c},$$

$$c_1 = 53, \quad c_2 = 117, \quad d_1 = 3, \quad d_2 = 2.9. \tag{4}$$

An analytic expression has been found[11] for δC that is applicable over a wider range than Eq. (4), specifically,

$$\delta C = \frac{3}{2}\frac{a_c^2}{2\pi^2} Y_c(1-t)\left(1 + \left(\frac{\pi T_c}{\omega_{ln}}\right)^2\right) - 6\frac{a_c^6}{\pi^2 b_c^4} t Y_c^3 \left(\frac{3}{4}\frac{b_c^4}{a_c^4}\left[1 + 6a_c^2\left(\widetilde{L}\left(\frac{T_c}{\omega_{ln}}\right) - \frac{2}{3}\left(\frac{T_c}{\omega_{ln}}\right)^2 - \frac{\pi^2}{3a_c^2}\left(\frac{T_c}{\omega_{ln}}\right)^2\right)\right] - \frac{1}{2}\right). \tag{5}$$

For brevity, we introduce the notation

$$a_c = \pi\sqrt{\frac{8}{7\xi(3)}}, \quad b_c = \pi\left[\frac{128}{93\xi(5)}\right]^{1/4},$$

$$Y_c^{-1} = 1 - 3a_c^2\left(\widetilde{L}\left(\frac{T}{\omega_{ln}}\right) + \frac{1}{3}\left(\frac{T}{\omega_{ln}}\right)^2\right),$$

$$\widetilde{L} = \left(\frac{T_c}{\omega_{ln}}\right)^2 \ln\frac{1.13\omega_{ln}}{eT}.$$

In the limit $T \to T_c$, Eq. (5) has the same form as Eq. (4), but

$$c_1 = 3a_c^2, \quad c_2 = 122, \quad d_1 = 1, \quad d_2 = e.$$

The results of using Eqs. (4) and (5) were close.

An approximate analytic representation for δC can also be obtained in the strong-coupling limit; it is valid for an arbitrary relationship between the characteristic frequency of the tunnelling mode and T_c. Using the expression for the jump in the free energy given in Ref. 9, we have

$$\delta C = \frac{12}{\lambda}(1 - 4t). \tag{6}$$

We now go to the limit of low temperatures. Let the coupling be intermediate. Then the factor δC is given roughly by the formula[11]

$$\delta\Delta = t - \sqrt{8\pi\frac{\Delta_0^5}{T^3 T_c^2}}\, e^{-\Delta_0/T} \times \left(1 + \frac{\Delta_0}{T} L\left(\frac{\Delta_0}{\omega_{ln}}\right) - 2\frac{2\Delta_0^2}{\omega_{ln}^2}\right), \tag{7}$$

where

$$L\left(\frac{\Delta_0}{\omega_{ln}}\right) = \frac{\Delta^2}{\omega_{ln}^2} \ln\frac{2\omega_{ln}}{eT}.$$

Note that the parameters T_c and Δ_0 obey

$$\frac{2\Delta_0}{T_c} = 3.53 g\left(\frac{T_c}{\omega_{ln}}\right),$$

where the factor g describes the deviation from the BCS theory. It can be written in the form

$$g=1+\alpha\left(\frac{T_c}{\omega_{ln}}\right)^2 \ln\frac{1.13\omega_{ln}}{\beta T_c}.$$

Fitting to a large number of experiments[12] yields $\alpha=12.3$, $\beta=2$. (An analytic calculation[13] gave $\alpha=\pi^2$, $\beta=e$.)

Because of the relation between the order parameter and T_c, δC $(T\to T_c)$ in Eq. (7) actually depends on two parameters, ω_{ln}/T_c and T/T_c.

For the case of strong coupling, in this paper we have analyzed the behavior of δC $(T\to T_c)$ by comparing the results obtained by solving Eqs. (2) iteratively for different values of the parameters which determine the interaction spectrum and kernel (3).

We conclude this section by noting an important point. Let the interaction spectrum have the Einstein form, i.e.,

$$S(\omega)=A\,\delta(\omega-\omega_{ln}),\quad A=\frac{\lambda\omega_{ln}}{2}. \tag{8}$$

Then, by substituting Eq. (8) in Eqs. (1) and (2) we can confirm that over the entire temperature range from zero to T_c, δC is a function of two parameters (for details, see elsewhere[9,14]), specifically,

$$\delta C=f(\omega_{ln}/T_c, T/T_c). \tag{9}$$

Here the effective Sommerfeld factor $\varkappa$ (used to describe the nontrivial temperature dependence of the specific heat C_N) in Eq. (9) is given by

$$\varkappa=\frac{m_0 k_F}{3}\,[1+2\lambda Z(T/\omega_{ln})],$$

where m_0 is the free electron mass and k_F is the Fermi momentum. The factor $Z(x)$ is a universal function for which an algebraic approximation exists.[15]

2. SPECTRAL FUNCTION FOR THE INTERACTION OF ELECTRONS WITH A TWO-LEVEL STATE

The spectral function $S_{\rm TS}(\omega)$ has been determined[4,16] for the interaction of electrons with a two-level state which lies in a double potential well with equivalent minima when the electron–polaron effect is neglected. When the electron-polaron effect is taken into account, it is redefined.[2,17] We have

$$S_{TS}(\omega)=N(\varepsilon_F)\sum_l \langle\langle(\gamma_{\rm TS}^{(l)}(q)V_l(q))^2\rangle\rangle \times\tanh\frac{\Omega_{\rm TS}^{(l)}}{2T}\,\frac{\Gamma_l}{(\omega-\Omega_{\rm TS}^{(l)})^2+\Gamma_l^2}. \tag{10}$$

Here $\gamma_{\rm TS}^{(l)}(q)$ and $V_l(q)$ are, respectively, the pseudospin form factor and the pseudopotential of the l-th defect, with

$$\gamma_{\rm TS}^{(l)}(\mathbf{q})\approx i\,\sin\frac{\mathbf{q}\cdot\mathbf{R}_d}{2} \tag{11}$$

(R_d is the distance between the minima of the potential well), and $\Omega_{\rm TS}^{(l)}$ and Γ_l are the characteristic energies and broadening of the l-th level (owing to the interaction with the electrons). The symbol $\langle\langle ...\rangle\rangle$ is interpreted as follows:

$$\langle\langle f(\mathbf{q})\rangle\rangle=\int_{S_F}\int_{S_F}\frac{dS_k}{\nu_F(k)}\,\frac{dS_{k'}}{\nu_F(k')}\,f(\mathbf{k}-\mathbf{k}')\Big/\left(\int_{S_F}\frac{dS_k}{\nu_F(k)}\right)^2.$$

The integration is taken over the Fermi surface, an element of which is denoted by dS_k, ν_F is the electron group velocity, and $\mathbf{q}=\mathbf{k}-\mathbf{k}'$.

As already noted, in metals electronic shielding of a tunnelling particle plays an important role. Then,[1] ''fast'' virtual electron-hole pairs with energies $\omega_0<E<\varepsilon_b$ (ω_0 is a characteristic energy of the particle motion on the order of the Debye frequency and ε_b is on the order of the Fermi energy or band gap) follow a particle adiabatically, both when it moves in the well and during subbarrier transitions. The electron–polaron effect arises only because of the interaction of a particle with ''slow'' virtual excitations that have energies below ω_0. It is important that the energy of this sort of electron–hole pair is also bounded below. The reciprocal of the particle lifetime in the well, τ^{-1}, appears as a corresponding quantity for normal metals. For a superconductor, the cutoff occurs at a frequency on the scale of the energy gap parameter $\Delta_0(T)$, rather than at τ^{-1}.

According to the theory of Ref. 1, the narrowing of the level (of which the seed quantity is $\Delta_{\rm TS}^{(l)}$, which equals the energy difference between the symmetric and antisymmetric states in the well) is described by a factor P_l, with

$$\Omega_{\rm TS}^{(l)}=P_l\Delta_{\rm TS}^{(l)}, \tag{12}$$

and

$$P_l=\begin{cases}(\Delta_{\rm TS}^{(l)}/\omega_0)^{b_l/(1-b_l)}, & \Delta_{\rm TS}^{(l)}>\pi T(2\Delta_0(T)),\\ (\pi T 2\Delta_0(T)/\omega_0)^{b_l}, & \pi T(2\Delta_0(T))>\Delta_{\rm TS}^{(l)}.\end{cases} \tag{13}$$

As for the intrinsic width Γ_l of the level, it is given by

$$\Gamma_l\approx\pi b_l T/[1+\exp(\Delta_0(T)/T)]^{-1} \tag{14}$$

(assuming $T\approx\Omega_{TS}$). This expression for Γ is valid both above and below the superconducting transition temperature T_c.

Let us comment on Eqs. (12) and (14). First, if in a normal metal the renormalized frequency $\Omega_{\rm TS}$ satisfies a condition of the form $\Omega_{\rm TS}>2\Delta_0(0)$, then below T_c its magnitude actually does not change. If, on the other hand, $\Omega_{\rm TS}<2\Delta_0(0)$, then for $T\leqslant T_c$ this frequency is greater than its value in the normal metal by a factor of $(e\Delta_0/2\Delta_{\rm TS})^b$ (owing to a change in the rate of relaxation of the tunnel state). Second, in both cases, for $T\leqslant T_c$ the level width Γ falls off exponentially with decreasing temperature owing to a weakening of the interaction of the particle with the electron medium.

The distribution function of possible values of the effective tunnelling amplitudes appear implicitly in Eq. (10) for $S(\omega)$. Keeping in mind the qualitative aspect of the phenomenon, we assume further that the distribution function has a Lorentzian form in the neighborhood of some typical value of $\Omega_{\rm TS}$; here the superscript l is omitted.

We now determine the coupling constant using Eq. (10) for the interaction spectrum. We have

$$\lambda_{\rm TS}=2\int_0^\infty \frac{d\omega}{\omega}\,S_{\rm TS}(\omega)\approx c_{\rm TS}\,\frac{\eta}{\Omega_{\rm TS}}\tanh\frac{\Omega_{\rm TS}}{2T_c},$$

$$\eta=N^2(\varepsilon_F)\langle\langle\gamma^e_{\rm TS}(q)V^2(g)\rangle\rangle, \qquad (15)$$

where $c_{\rm TS}$ is the effective concentration of light tunnelling atoms and η is customarily called the Hopfield factor.

Let us comment on Eq. (15). For quantum defects such as hydrogen (localized at interstitial sites), as a rule $\Omega_{\rm TS}\leqslant 1$ K and the factor $\eta/\Omega_{\rm TS}\approx 10^4$.[2,3] It is customarily assumed that the number of tunnelling states within the energy interval from 0 to 1 K is on the order of 10^{-5}, while in the interval 1–10 K, $c_{\rm TS}\approx 10^{-4}$. In highly nonequilibrium systems, such as freshly prepared amorphous materials, the concentrations of two-level states may greatly exceed the standard values. Thus, in principle, the parameter λ_{TS} may be much greater than unity.

Note the according to the definition (15), the coupling constant of electrons with a two-level state is proportional to the population factor, with

$$\lambda_{\rm TS}\sim\tanh\frac{\Omega_{\rm TS}}{2T}/\omega_{\rm TS}.$$

A situation is possible in which the characteristic frequency $\Omega_{\rm TS}$ is less (and on the order of) the critical temperature T_c. Then, owing to the population factor the constant $\lambda_{\rm TS}$ may increase substantially as $T\to 0$.

We summarize the above remarks. If the condition

$$\Delta_{\rm TS}>\Delta_0,\ T_c$$

is satisfied, then over the entire temperature range $(0-T_c)$ the following relations hold:

$$\Omega_{\rm TS}=\Delta_{\rm TS}(\Delta_{{\rm TS}/\omega_0})^b, \quad \lambda_{\rm TS}=\overline{\eta}/\Omega_{\rm TS}. \qquad (16)$$

Here for brevity we have set $\overline{\eta}=c_{TS}\eta$.

In the strong coupling case, where

$$\Omega_{\rm TS}<\Delta_0,\ T_c,$$

the effective amplitude is given by

$$\Omega_{\rm TS}\begin{cases}\Delta_{\rm TS}\left(\dfrac{T_c}{\omega_0}\right)^b, & T=T_c,\\ \Delta_{\rm TS}\left(\dfrac{\Delta_0}{\omega_0}\right)^b, & T=0.\end{cases} \qquad (17)$$

The approximate temperature $T_*^{(1)}$ at which $\Omega_{\rm TS}$ changes is found from the equation

$$\Delta_0(T_*^{(1)})\approx T_c.$$

At the same time, when the explicit form of the population factor is taken into account, the coupling constant λ_{TS} is given by the equations

$$\lambda_{\rm TS}=\begin{cases}\overline{\eta}/2T_c, & T=T_c,\\ \overline{\eta}/2\Omega_{\rm TS}, & T=0\end{cases} \qquad (18)$$

(the corresponding crossover temperature is $T_*^{(2)}\approx\Omega_{\rm TS}$).

To end this section we discuss a question relating to the estimates of the electron–polaron parameters. We have examined this question in detail before.[2] Here we note only that, in principle, this theory applies to metastable systems such as the hydrides of the simple metals, as well as to the ternary palladium–noble-metal–hydrogen compounds. In these systems some part of the hydrogen atoms are apparently localized in T-sites and move in two-well potentials with equivalent minima in neighboring T-sites. In this case the characteristic frequency satisfies $\omega_0\geqslant\Theta_D$, where Θ_D is the Debye frequency, while $\Delta_{TS}\approx 1$ K.

As for the electron–polaron effect parameter b,[11] the interaction potential of a proton with electrons is relatively strong. In addition, the quantity k_FR_d is also not small. As a result,

$$b\approx\left(\frac{1}{3}-\frac{1}{5}\right)\zeta^2, \quad \zeta=N(\varepsilon_F)/N_0(\varepsilon_F),$$

where ζ is the ratio of the band electron density at the Fermi level to the density in the free electron model. Recall that in such metals as Al, Zn, and Sn, we have $\zeta\approx 1$, while for Be and Cd, $\zeta\leqslant 1/2$. In the first case, the role of the electron–polaron effect is substantial, while in the second, it can be neglected. Here the polaron factor is $P\approx 0.5$. Thus, level narrowing is significant, but not catastrophic.

Calculations show that in these MeH_x compounds, Ω_{TS} is less than T_c.[18–20] In addition, the coupling constant satisfies $\lambda>1$. Thus, we are dealing with nonstandard superconductors.

3. THE EFFECT OF THE ELECTRON–POLARON EFFECT ON THE ELECTRONIC SPECIFIC HEAT

As noted above, the temperature behavior of δC is determined by two parameters, T/T_c and $T_C/\Omega_{\rm TS}$. We shall determine them based on the material in Sections 1 and 2.

Consider the case of intermediate coupling (standard spectrum $S_{TS}(\omega)$). Note that T_c can be expressed in terms of the zeroth moment of $S_{\rm TS}(\omega)$,[21] specifically

$$T_c=z_1\Omega_{\rm TS}\lambda_{\rm TS}, \quad z_1=0.072. \qquad (19)$$

Using Eqs. (16) and (19), we immediately obtain

$$\frac{T_c}{\Omega_{\rm TS}}=z_1\overline{\lambda}_{\rm TS}\left(\frac{\omega_0}{\Delta_{\rm TS}}\right)^b, \quad \frac{T}{T_c}=\frac{T}{\overline{\eta}z_1}, \qquad (20)$$

where for brevity we set

$$\overline{\lambda}_{\rm TS}=\lambda_{\rm TS}(b=0)=\frac{\overline{\eta}}{\Delta_{\rm TS}}.$$

It turns out that T/T_c is independent of the electron–polaron parameters. As for $T_c/\Omega_{\rm TS}$, it increases as the electron–polaron effect becomes greater.

Let us substitute Eq. (20) in the above equations (4), (5), and (7) for the specific heat. (By definition, $\omega_{ln}=\omega_{\rm TS}$.) It is easy to confirm that as the electron–polaron effect becomes greater (and $T_c/\Omega_{\rm TS}$ increases), for $T\to T_c$ the angular coefficient k increases in the expression for the factor R of the form

$$R=\frac{\Delta C(T)}{\Delta C(T_c)}=(1-kt).$$

For example, for $T_c/\Omega_{TS}=0.1$ and 0.2, respectively, we have $k=3.876$ and 4.291.

We now proceed to the strong coupling case. We use the representation T_c in terms of the first moment of the interaction spectrum,

$$T_c=z_2\Omega_{TS}\lambda_{TS}^{1/2}, \quad z_2=0.183 \tag{21}$$

(see details in Ref. 20). Using Eqs. (17), (18), and (21), for $T\to T_c$ we have

$$\frac{T_c}{\Omega_{TS}}=\frac{z_2}{\sqrt{2}}\,\overline{\lambda}^{1/3}\left(\frac{\omega_0}{T_c}\right)^{b/3}, \tag{22}$$

and

$$\frac{T}{T_c}=\frac{1}{z_2}\frac{1}{\overline{\lambda}^{1/3}}\left(\frac{\omega_0}{\pi T_c}\right)^{2b/3}\frac{T}{\Delta_{TS}}. \tag{22a}$$

In the limit of strong coupling, R depends only on t, with $R=1-kt$ $(k=4)$. Because of Eq. (22), the deviation of R from unity should, in general, decrease as the electron–polaron effect becomes stronger. Note that k is smaller than in the intermediate coupling case for $T_c/\Omega_{TS}=0.2$, but remains substantially larger than in the BCS theory, where $k=2.636$.

It is immediately clear from Eqs. (19) and (22) that the parameter T_c/Ω_{TS} depends strongly on the electron–polaron effect. The above remarks imply that as the electron–polaron effect becomes stronger, for R the angular coefficient initially increases and then begins to decrease.

Let us consider the situation as $T\to 0$. We shall assume that the condition $\Omega_{TS}<2T_c$ is satisfied. Using Eqs. (17) and (18), we have

$$T_c(0)/\Omega_{TS}(0)=K_1\frac{T_c}{\Omega_{TS}(T_c)},$$

$$K_1=\lambda^{1/6}\left(\frac{\pi T_c\omega_0^{1/2}}{\Delta_0^{3/2}}\right), \tag{23}$$

and

$$\frac{T}{T_c(0)}=K_2\frac{T}{T_c},$$

$$K_2=\frac{2}{\lambda^{1/6}}\left(\frac{\pi T_c}{\Delta_0}\right)^{2b/3}\left(\frac{\Delta_0}{\omega_0}\right)^{b/6}. \tag{23a}$$

Here $T_c(0)$ and $\Omega_{TS}(0)$ denote the parameters determined by Eqs. (20) and (17) for $T\to 0$. The change in these parameters owing to the temperature dependence of the level population factor and of the polaron factor P are taken into explicit account through K_1 and K_2.

We note the approximate relation[2] between Δ_0 and T_c of the form

$$2\Delta_0/T_c\approx 9^{1+2/3}\overline{\lambda}^{1+4b/6}(\omega_0/\Delta_0)^{b(1+4b)/6}.$$

Then, given $B<1/2$, for the quantities K_1 and K_2 in Eqs. (23) and (23a) we have

$$K_1\approx\lambda^{1/6}\left(\frac{\omega_0}{\Delta_0}\right)^{b/6}, \quad K_2\approx\frac{2}{\lambda^{(1+b)/6}}\left(\frac{\Delta_0}{\omega_0}\right)^{b/6}. \tag{24}$$

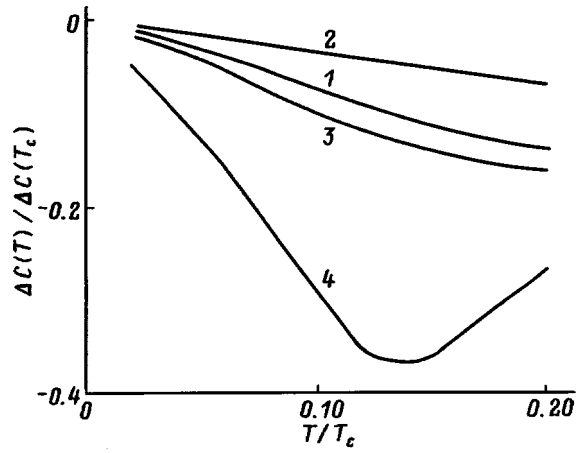

FIG. 1. The factor $\Delta C(T)/\Delta C(T_c)$ as a function of T/T_c. (*1*) BCS theory; (*2–4*) strong-coupling theory with the parameter T/ω_{ln} equal, respectively, to 0.2, 0.6, and 1.2.

According to Eq. (24), $K_1>1$ and $K_2\leqslant 1$. For example, for $\lambda\approx 20$, we have $K_1\approx 2$ and $K_2\approx 1$.

As an illustration of the possible role of the renormalization of the factor K_1, numerical calculations were done using the general form of Eqs. (1)–(3) and specifying the kernel of the Eliashberg equations in the form (8). The results are shown in Fig. 1, where the factor $\Delta C(T)/\Delta C(T_c)$ is plotted as a function of T/T_c for $T/T_c\ll 1$. It was assumed that $\omega_{ln}/T_c=0.2$, 0.6, and 1.2. The curve for the BCS theory is shown in the figure for comparison.

It is immediately evident from the figure that, for strong coupling with $\lambda\geqslant 20$, when $\omega_{ln}/T_c\approx 1$, $\Delta C(T)/\Delta C(T_c)$ can increase substantially owing to the temperature dependence (over the interval $0-T_c$) of the level population factor and the polaron factor P (cf. curves *3* and *4*). Here it is also necessary to take the renormalization of the Sommerfeld parameter into account. Since $\varkappa\propto\sqrt{\lambda}T_c$ holds, the corresponding quantity equals $(\Delta_0/T_c)^{b/2}$. Note also that in the case of intermediate coupling, as we have noted, the dependence of the factor $R(T\to 0)$ on t becomes weaker (cf. curves *1* and *2*).

In this paper we have examined the effect of quantum defects on the electronic specific heat of metals in the superconducting state. The electron–polaron effect has been taken into account in the framework of the adiabatic theory.[1] It has been shown that for light defects such as hydrogen, the tunnelling parameters are significant. The intermediate and strong coupling cases have been discussed. For a delta-function spectrum of the interelectronic interaction, it has been known that the temperature behavior of δC is determined by two parameters, Ω_{TS}/T_c and T/T_c. In this paper we have investigated the dependence of these parameters and $\Delta C(T)$ on the electron–polaron effect, taking the temperature variation of the level populations into account. We note that if the electron attraction spectrum parameter Ω_{TS}/T_c at $T=T_c$ without the electron–polaron effect is equal to a few tenths, then when the electron–polaron effect is strong the type of coupling may change. As a result, the character of the temperature dependence of $R=\Delta C(T)/\Delta C(T_c)$ changes significantly compared to the case of intermediate coupling; in

particular, for $\lambda_{TS} \gg 1$ at temperatures near T_c, the dependence of R on T becomes weaker (rather than stronger) and as $T \to 0$, on the other hand, it becomes stronger (rather than weaker).

The above theory can be applied, in principle, to systems such as the hydrides of the sp-metals, as well as to palladium, including ternary systems. The theory requires further development for application to systems with a sharp peak in the density of electronic states (for example, weak hydrides such as niobium–gaseous impurity–hydrogen).

Note that in this paper we have examined two-level states corresponding to a symmetric potential. Here the splitting of the levels was related to tunnelling. Actually, because of elastic stress fields and mesoscopic fluctuations in the electron density, the degeneracy should also be removed for symmetric configurations.[22,23] A more realistic case will be examined in another paper.

Another interesting question which merits special examination involves defects with an internal degree of freedom.[24]

The author thanks the reviewer for valuable comments.

[1] Yu. M. Kagan and N. V. Prokof'ev, Zh. Éksp. Teor. Fiz. **90**, 2176 (1986) [Sov. Phys. JETP **63**, 1276 (1986)]; *ibid.* **97**, 1698 (1990).
[2] A. P. Zhernov, Supercond. Phys. Chem. Technol. **8**, 1 (1995).
[3] A. P. Zhernov, Fiz. Nizk. Temp. **22**, 556 (1996) [Low Temp. Phys. **22**, 428 (1996)].
[4] G. M. Vijicic, V. L. Aksenov, N. M. Plakida, and S. J. Stamenkovic, Phys. C **14**, 2344 (1981).
[5] V. I. Kozub, Phys. Rev. B **49**, 6895 (1994).
[6] J. Bardeen and M. Stephen, Phys. Rev. **136**, A1485 (1964).
[7] Y. Wada, Phys. Rev. **135**, A1481 (1964).
[8] B. T. Geĭlikman, *Studies in Low Temperature Physics* [in Russian], Atomizdat, Moscow (1979).
[9] J. P. Carbotte, Rev. Mod. Phys. **62**, 1027 (1990).
[10] F. Marsiglio and J. P. Carbotte, Phys. Rev. B **33**, 6114 (1986).
[11] A. P. Zhernov and E. P. Chulkin, Supercond. Phys. Chem. Technol. **6**, 1 (1993).
[12] D. Mitrovic, H. G. Zarate, and J. P. Carbotte, Phys. Rev. B **29**, 184 (1984).
[13] A. P. Zhernov and E. P. Chulkin, Supercond. Phys. Chem. Technol. **5**, 236 (1992).
[14] F. Blesius and J. P. Carbotte, J. Low Temp. Phys. **73**, 255 (1988).
[15] E. O. Zaĭtsev and V. Z. Kresin, Zh. Éksp. Teor. Fiz. **74**, 1886 (1978) [Sov. Phys. JETP **47**, 983 (1978)].
[16] G. M. Vujičič and N. M. Plakida, Fiz. Niz. Temp. 9, 278 (1982) [Sov. Low Temp. Phys. **9**, 134 (1983)].
[17] J. Kondo, Phys. B **123**, 175 (1984).
[18] B. Stritzker and F. Ochmann, Nucl. Instrum. Methods **209/210**, 831 (1983).
[19] B. I. Belevtsev and V. I. Odnokozov, Fiz. Nizk. Temp. **11**, 459 (1985) [Sov. J. Low Temp. Phys. **11**, 249 (1985)].
[20] L. R. Zherikhina and V. B. Ginodman, Fiz. Nizk. Temp. **13**, 452 (1987) [Sov. J. Low Temp. Phys. **13**, 255 (1987)].
[21] C. R. Leavens, J. Phys. C **7**, 1911 (1977).
[22] B. L. Al'thshuler and B. Z. Spivak, JETP Lett. **49**, 772 (1989).
[23] V. I. Kozub, Solid State Commun. **95**, 415 (1995).
[24] V. G. Karpov and D. I. Parshin, JETP Lett. **51**, 596 (1990).

Translated by D. H. McNeill

SEMICONDUCTORS AND INSULATORS

Polar-center phase nuclei in He^+-irradiated CuO single crystals

N. N. Loshkareva, Yu. P. Sukhorukov, B. A. Gizhevskiĭ, S. V. Naumov, and A. A. Samokhvalov

Institute of Metal Physics, Ural Branch of the Academy of Sciences, 620219 Ekaterinburg, Russia

A. S. Moskvin

Ural State University, 620083 Ekaterinburg, Russia

T. A. Belykh

Ural State Technical University, 620002 Ekaterinburg, Russia

(Submitted June 13, 1997)
Fiz. Tverd. Tela (St. Petersburg) **40**, 419–424 (March 1998)

Irradiation of various single-crystal CuO faces $[ac,bc,(110)]$ with 4.6-MeV He^+ ions has been found to result in reduction of CuO to Cu_2O and Cu on the irradiated and unirradiated sides, lifting of forbiddenness from optical transitions in the $[CuO_4]^{7-}$ electron center in the 0.7–0.95-eV energy range, a change in dichroism near the bands corresponding to transitions in the hole centers, $[CuO_4]^{5-}$, and electron centers, $[CuO_4]^{7-}$, as well as in a resonant increase of absorption at 0.95–1.30 eV with an unusual polarization dependence. The results of He^+ irradiation of CuO single crystals are discussed in terms of a model of the nucleation of the phase of polar (electron and hole) centers in copper–oxygen systems. © *1998 American Institute of Physics.* [S1063-7834(98)00603-0]

The antiferromagnetic semiconductor CuO is a model object for copper-oxide-based high-T_c semiconducting phases. The properties of CuO are similar in many respects to those of lightly-doped copper-oxide high-T_c systems with charge inhomogeneities and can be explained using the model[1] of nucleation of the phase of polar (hole, $[CuO_4]^{5-}$, and electron, $[CuO_4]^{7-}$) Jahn–Teller centers in the host matrix $[CuO_4]^{6-}$. The narrow region of homogeneity of the CuO crystals does not permit one to produce in them a significant concentration of defects by doping and annealing which would act as nucleation centers. Defects in high concentrations can be created by irradiation. This work is a continuation of a series of publications dealing with the influence of radiation-induced defects as nucleation centers on the optical and electrical properties of single-crystal CuO. Irradiation of CuO single crystals with 5-MeV electrons was found[2] to increase the resistivity by two orders of magnitude and change the concentration of the Jahn–Teller hole centers, which manifest themselves as absorption bands in the medium IR range at 0.2 and 0.1 eV (MIR bands). Implantation of 6.65-MeV oxygen ions at fluences of up to 3×10^{17} cm^{-2} was shown[3] not to affect noticeably the electrical and optical properties of single-crystal CuO. Copper oxide belongs to the oxides which release oxygen easily under ion bombardment.[4] It is known[4] that irradiation of polycrystalline CuO with 1.5-keV Ar^+ ions reduces the irradiated surface to metallic copper. Reduction of CuO to Cu_2O was also observed to occur in polycrystalline CuO irradiated by He^{2+} ions in the 5–32-MeV energy range.[5] It is natural to expect that the reduction reaction would increase the number of $[CuO_4]^{7-}$ electronic centers in the $[CuO_4]^{6-}$ matrix. This work studies the effect of irradiation of CuO single crystals by He^+ ions on optical absorption spectra in the IR range, where the transitions involving hole and electronic Jahn–Teller centers become manifest.

1. SAMPLES AND EXPERIMENTAL RESULTS

CuO single crystals were irradiated with 4.6-MeV He^+ ions on the U-120 cyclotron at USTU-UPI. The sample temperature under irradiation did not exceed 100 °C, and vacuum was 10^{-6} Torr.

The absorption spectra were taken on an improved, computer-controlled IKS-21 spectrometer in the photon energy range 0.12–1.5 eV and on a KSVU-12 spectrometer in the 1.0–1.7-eV range, at room temperature and 80 K, in unpolarized and linearly polarized light. As polarizers served teflon- and polyethylene-based grating polarizers, as well as a Glan prism. Absorption index calculations took into account the reflection coefficient of the crystal.[6]

Three crystals were chosen for optical studies, namely, sample N1 cut in the *ac* plane, N2 cut in the *bc* plane, and N3, cut in the (110) plane, which is the natural face of a growing CuO single crystal with monoclinic structure. The samples measured typically $2\times3\times0.3$ mm.

Attention was focused primarily on sample N1, because the changes observed in earlier studies[2] of CuO irradiation by electrons were largest in the *ac* plane. In this work, the

 © 1998 American Institute of Physics

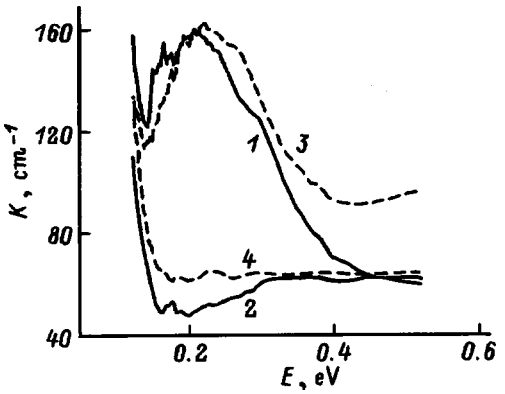

FIG. 1. Absorption spectra of CuO(ac) (*1,2*) before irradiation and (*3,4*) after first irradiation for two polarizations: *1, 3*—$\mathbf{E}\|[\bar{1}01]$, and *2, 4*—$\mathbf{E}\perp[\bar{1}01]$.

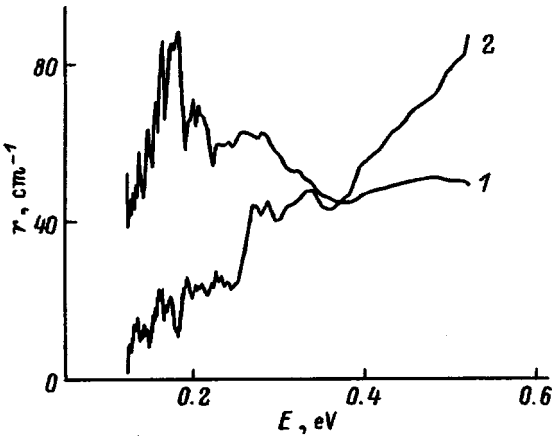

FIG. 2. Difference between the CuO(ac) absorption spectra obtained after (*1*) the second and first irradiations and (*2*) third and second irradiations for $\mathbf{E}\|[\bar{1}01]$.

sample was subjected to five consecutive He^+ irradiations with fluences of 10^{17} cm^{-2} each. Samples N2 and N3 were irradiated twice with fluences of 10^{17} cm^{-2} each.

Each irradiation was followed by x-ray diffraction and electrical resistance measurements. Structural changes in the samples were observed to begin at a fluence of 2×10^{17} cm^{-2}. The total intensity of the (110) and (020) reflections increases, and Cu_2O and Cu phases appear on the irradiated face and (to a larger degree) on the side opposite it. The projected depth of He^+ ion penetration in our case is 10.4 μm. Segregation of copper to an irradiated CuO surface has been reported by a number of authors.[4,5] Observation of Cu_2O and copper on unirradiated crystal faces was unexpected.[7] A copper film was visually observed to appear on sample N1 after the second irradiation, with more copper segregated to the unirradiated side.

In contrast to electron irradiation which resulted in an increase of electrical resistance of CuO single crystals,[2] the resistance of the samples subjected to He^+ ions decreased only slightly (by 15–20%) before the second phase appeared. Segregation of copper brought about a stronger decrease in resistance.

Absorption spectra of sample N1 were studied in two polarizations, namely, with the light-wave electric vector parallel and perpendicular to the $[\bar{1}01]$ direction. The anisotropy in the optical and electrical properties is largest in the $[\bar{1}01]$ direction in the ac plane of the CuO crystal,[1] and it is in this direction that the antiferromagnetically coupled Cu–O–Cu chains are aligned. We will show the successive action of irradiation fluences on optical spectra.

1. A fluence of 10^{17} cm^{-2} changes insignificantly the spectra of sample N1 in the region of the absorption band connected with $[CuO_4]^{5-}$ hole centers. As seen from Fig. 1, He^+ irradiation results in a slight shift of the 0.2-eV absorption band toward higher energies, which is the opposite of the case of electron irradiation.[2] After irradiation, the weak absorption band at 0.16 ± 0.01 eV disappears, and absorption in the high-energy domain increases. The 0.16-eV band behaves irregularly under further irradiation, appearing and disappearing. It was reliably resolved in the spectra of CuO samples bombarded by electrons.[2]

2. After the second irradiation, copper was seen to appear on the face opposite the irradiated one. The absorption spectra exhibit a general rise in both polarizations. The difference between the spectra obtained after the second and first irradiations in the $\mathbf{E}\|[\bar{1}01]$ polarization (Fig. 2) shows a weakly wavelength-dependent absorption (following a certain rise near the 0.16-eV band) associated with the contribution to absorption due to the copper film. The film was ground off with diamond paste (grain size 0.1 μm), after which the spectrum of the sample approached that measured after the first irradiation.

3. The third irradiation resulted in a strong increase of absorption in the high-energy region. The difference between the spectra measured after the third and second irradiations (after the sample grinding) shown in Fig. 2 grows monotonically with increasing energy. This growth in absorption is due to the appearance in the near IR range of absorption bands absent in the unirradiated crystal. Figure 3 presents new broad absorption bands of complex shape for two polarizations. The band obtained with $\mathbf{E}\|[\bar{1}01]$ peaks at 0.72

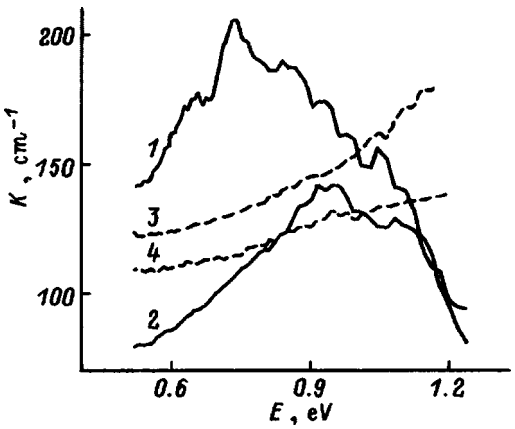

FIG. 3. CuO(ac) absorption spectra in the near IR range obtained (*1,2*) after the third and after (*3,4*) the fourth irradiations for two polarizations: *1,3*—$\mathbf{E}\|[\bar{1}01]$, and *2,4*—$\mathbf{E}\perp[\bar{1}01]$.

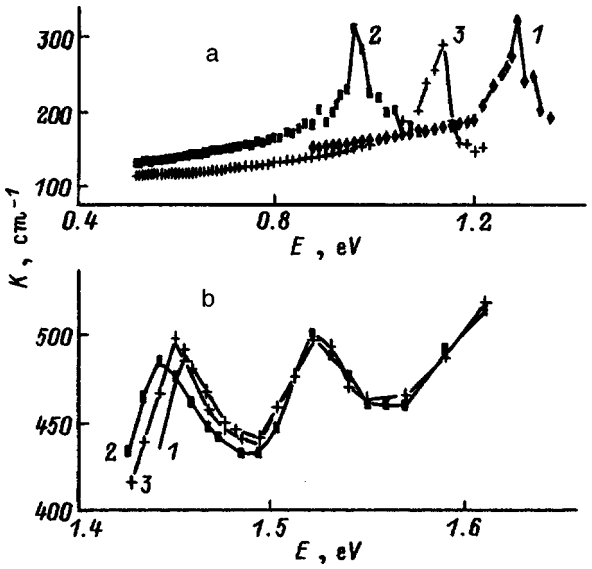

FIG. 4. CuO(ac) absorption spectra obtained with (a) IKS-21 and (b) MDR-12 monochromators, for different light polarizations: *1*—natural light, *2*—$\mathbf{E}\|[\bar{1}01]$, *3*—$\mathbf{E}\perp[\bar{1}01]$.

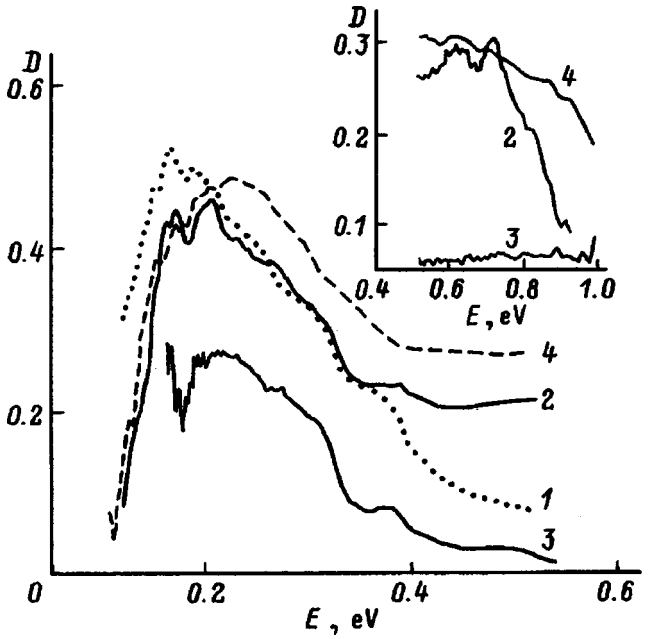

FIG. 5. Dichroism of CuO(ac) with respect to the $[\bar{1}01]$ axis (*1*) before irradiation, (*2*) after the third irradiation, (*3*) after the fourth irradiation, and (*4*) after the fifth irradiation and removal of 80 μm from each side of the sample. Inset: dichroism in the near IR.

± 0.03 eV and has a shoulder at 1.10 ± 0.03 eV. In the first three irradiations only one of the crystal faces was exposed.

4. In the fourth irradiation, the face opposite the one bombarded earlier was exposed. The spectra exhibit the following changes: in the medium IR range, the $\mathbf{E}\|[\bar{1}01]$ spectrum in the region of the 0.2-eV band did not change, whereas in the $\mathbf{E}\perp[\bar{1}01]$ polarization the spectrum as a whole rose by approximately 30–40 cm^{-1}, which evidences a change in absorption anisotropy. In the near IR (Fig. 3), the broad bands at 0.7–1.1 eV found after the third irradiation disappeared leaving a rise in absorption, monotonic for both polarizations, toward the absorption edge, with only a slight difference between the values for $\mathbf{E}\|[\bar{1}01]$ and $\mathbf{E}\perp[\bar{1}01]$ (a small dichroism).

5. The surface exposed to the fifth irradiation was the same as in the fourth one. X-ray diffraction data did not reveal any substantial change in the amount of Cu and Cu_2O on the surfaces. In the region of the 0.2-eV band, the spectrum underwent changes opposite those observed after the fourth one, namely, the absorption coefficient increased in $\mathbf{E}\|[\bar{1}01]$ polarization while changing only insignificantly for $\mathbf{E}\perp[\bar{1}01]$. A narrow resonance feature is observed near the fundamental absorption edge (Fig. 4a). The polarization characteristics of this feature are unusual for bands originating from optical transitions between two levels, in that the highest energy of this feature is observed in unpolarized light, 1.28 ± 0.12 eV, and its position changes from 0.97 ± 0.12 to 1.13 ± 0.12 eV with the polarization changed in direction from $\mathbf{E}\|[\bar{1}01]$ to $\mathbf{E}\perp[\bar{1}01]$. We observed such an absorption band at 1.34 ± 0.12 eV in spectra of electron-irradiated CuO, with the absorption coefficient at its maximum reaching as high as 1000 cm^{-1}. The results shown in Fig. 4a were obtained on an IKS-21 prism spectrometer in a large number of measurements made in single-channel accumulation mode. Therefore while the error in determination of the energy position of the bands is large (the spectral width is large), the relative position of the bands measured in different polarizations can be considered correct. This is supported by absorption measurements in the region of the above band made with an MDR-12 grating monochromator with a slit spectral width smaller than 0.01 eV (Fig. 4b). The low-energy band peaking at 1.458 ± 0.005 eV in unpolarized light, and at 1.441 ± 0.005 and 1.450 ± 0.005 eV in the $\mathbf{E}\|[\bar{1}01]$ and $\mathbf{E}\perp[\bar{1}01]$ polarizations, respectively, has the same nature as the feature presented in Fig. 4a. The high-energy, polarization-independent band at 1.522 ± 0.005 eV is an exciton-like feature associated with the transition from the b_{1g} ground state to the strongly correlated e_u' state of the Jahn-Teller doublet in the $[CuO_4]^{6-}$ doublet.[8] This band was observed after the sample had been successively ground off on both sides and disappeared when the thickness of the removed layer reached ~ 80 μm on each side. After the last grinding the absorption spectra observed both in the fundamental absorption region and in the medium IR range were found to be close to those of the unirradiated sample.[8] Note that in contrast to the measurements carried out with the MDR-12 monochromator under normal incidence of monochromatic radiation on the sample, in the IKS-21 spectrometer the nonmonochromatic light was incident at 6° to the normal.

Figure 5 shows the fluence dependence of the dichroism, i.e., of the ratio of the difference and sum of the absorption coefficients for the $\mathbf{E}\|[\bar{1}01]$ and $\mathbf{E}\perp[\bar{1}01]$ polarizations in the region of the band associated with the ${}^1A_{1g}-{}^1E_u$ transition in the $[CuO_4]^{5-}$ hole cluster. We see that the dichroism decreases, particularly when the irradiated surface is changed (the fourth irradiation). After the fifth irradiation, the dichroism is close to that seen after the fourth one. In the high-

energy region, above 0.4 eV, the dichroism is comparatively small, both before the irradiation and at fluences which do not give rise to bands within 0.7–0.95 eV (for instance, the fourth irradiation; see inset to Fig. 5). When these bands appear after the third irradiation, the dichroism remains large (up to 30%) down to the absorption edge. After the last, fifth irradiation, the dichroism was as large, but only in the central part of the sample obtained after about ~ 80 μm were ground off on both sides of the crystal, although no bands within 0.7–0.95 eV were directly observed in the absorption spectrum of this part of the sample before this procedure.

Irradiation of the *bc* face of the single-crystal sample N2 also results in reduction of CuO to Cu_2O and Cu, as revealed by x-ray diffraction, but no copper film was seen visually. The main change in absorption spectra observed to occur in the region of transitions in the $[CuO_4]^{5-}$ hole center consists of a decrease in absorption after the irradiation near the 0.1-eV band,[1] which also belongs to the hole center (Fig. 5). Similar to the case with the *ac* plane, broad bands appear in the near IR range at 0.89 ± 0.03 and 1.02 ± 0.03 eV (see inset to Fig. 5). The long-wavelength side of the measurement range was limited by 1.1 eV because of the smallness of the sample. After the second irradiation the absorption coefficient increased throughout the range studied by more than 60 cm^{-1} and obscured the details of the spectrum. The dichroism relative to the *b* axis near the 0.2-eV band was practically unaffected by irradiation, but in the near IR range (above 0.4 eV) it increased to 20%.

Irradiation of the (110) plane of sample N3 also resulted in a rise of the absorption spectrum, which was particularly pronounced in the near IR. No broad bands were observed in this region. The narrow band like the one detected from the *ac* plane, has an energy 1.28 ± 0.12 eV.

2. DISCUSSION OF RESULTS

The main findings obtained in irradiation of CuO single crystals with 4.6-MeV He^+ ions can be summed up as follows: (1) Reduction of CuO to Cu_2O and Cu, which is particularly pronounced on the side opposite to the irradiated one; (2) Appearance in the near IR of broad bands having a complex structure within 0.7–0.95 eV; (3) Appearance in the energy range 0.95–1.30 eV of an absorption feature with an unusual polarization dependence; and (iv) A decrease of dichroism in the region of the absorption band associated with the hole center (at 0.2 eV) with increasing fluence for an *ac*-cut CuO crystal, and an increase of dichroism in the region of the 0.7–0.95-eV bands.

Like the high-T_c cuprate superconductors, the physical properties of the magnetic semiconductor CuO are described in terms of a model considering nucleation of a polar phase of Jahn–Teller centers.[1,9] The existence of nuclei of a mixed-valence phase, whose shape and size depend on the concentration of hole and electron polar Jahn–Teller centers, suggests that these compounds are materials with charge inhomogeneity. Optical spectra of CuO and of weakly doped high-T_c cuprates are similar both at the absorption edge, where they originate from charge-transfer transitions in the main $[CuO_4]^{6-}$ cluster, and in the medium IR range, where they are due to transitions in the hole cluster $[CuO_4]^{5-}$. In contrast to high-T_c superconductors, in CuO optical transitions in the electron center $[CuO_4]^{7-}$ are forbidden because of the electron center in CuO having a triplet ground state. These transitions are observed, however, in microcontact spectra of CuO above 0.7 eV.[10] The radiation-induced defects which are produced in CuO single crystals irradiated by He^+ ions become nucleation centers and change the concentrations of the hole and electron centers.

Reduction of CuO to Cu_2O and Cu on the unirradiated side in the sample of thickness 280 μm with a projected He^+ penetration depth of only 10.4 μm, implies that He^+ bombardment affects the properties of CuO to distances considerably in excess of the ion mean free path (the so-called long-range effect). Various mechanisms are proposed to explain the long-range effects in semiconductor irradiation. These include, for instance, anomalous diffusion which may be enhanced by the Jahn–Teller effect,[11] or anomalous radiation-stimulated diffusion caused by quantum diffusion, with the potential barrier undergoing periodic inversion due to charge exchange of diffusing atoms.[12] The latter mechanism can be favored in CuO by the low threshold of the disproportionation reaction[1] involving formation of polar Jahn–Teller centers and by charge density waves, whose existence in copper oxides was experimentally established.[13] The effect of elastic waves excited by the ion beam on the native-defect system has recently been widely discussed.[14,15] It has been shown recently that shear strain produces in CuO results similar to those observed under He^+ irradiation, namely, reduction to Cu_2O and Cu, and a change in the (020) x-ray reflection corresponding to the parameter *b*. This makes the elastic-wave mechanism of phase transformations and of the long-range effect under He^+ irradiation of CuO highly probable.[7,16] The elastic waves generated in atomic collisions in a sample bombarded by energetic particles, or subjected to strong shear strains under pressure result in excitation of atoms, which entails chemical bond rupture and formation of additional polar centers. Copper segregation to the *ac* face indicates anisotropy in the long-range effect, with the preferred direction along the twofold axis *b* in the monoclinic crystal CuO.

The effect of He^+ irradiation on the MIR absorption bands at 0.2 and 0.1 eV, which are due, respectively, to the $^1A_{1g} - {}^1E_{u'}$ and $^1A_{1g} - {}^1E_{u''}$ transitions in the $[CuO_4]^{5-}$ hole cluster (medium IR range), differs substantially from that of irradiation by electrons. Electron irradiation produced a red shift of the 0.2-eV band, its intensity increased, and an additional band at 0.165 eV appeared against its background.[2] This was assigned to an increase in hole center concentration and a decrease in the activation energy and binding energy of polarons. At the same time the large (two orders of magnitude) increase in the resistivity of *p*CuO observed to occur under electron irradiation is apparently related to the more substantial increase in the electron center concentration. Electron centers are not seen in absorption spectra because optical transitions in them are forbidden. The copper layer forming on optical *ac* surfaces under He^+ irradiation introduces additional constant absorption, which does not permit an unambiguous conclusion on the character of the change in

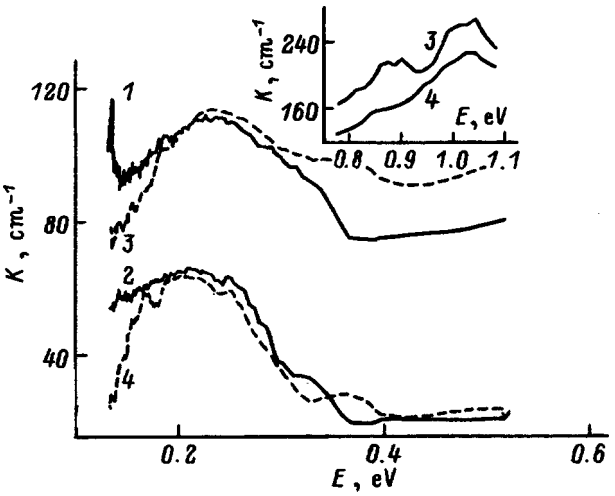

FIG. 6. CuO(bc) absorption spectra obtained (*1,2*) before irradiation and (*3,4*) after irradiation for two polarizations: *1,3*—$\mathbf{E}\|b$, and *2,4*—$\mathbf{E}\perp b\|c$. Spectra 2,4 are shifted by 40 cm^{-1}. Inset: near-IR spectra of irradiated sample.

the 0.2-eV band intensity and, hence, on the change in hole center concentration. The strong change of the dichroism (by a factor two) in the region of this band (Fig. 6) indicates considerable atomic displacements under irradiation and a change in anisotropy, which is particularly substantial when the irradiated surface is replaced (the fourth and fifth irradiations). Bombardment by He^+ particles of the bc face does not affect the dichroism in the region of the 0.1–0.2-eV bands, although the intensity of the 0.1-eV band ($^1A_{1g}-{}^1E_{u''}$ transition) drops significantly (Fig. 6).

The 0.7–0.9-eV absorption bands in near IR, in our opinion, arise because transitions in electron Jahn–Teller centers, which are present in inhomogeneous-phase nuclei formed at radiation defects, become allowed. The anisotropy near these bands, which exhibits preferential absorption along the $[\bar{1}01]$ axis of the crystal, persists like that of the hole center. The dichroism with respect to the $[\bar{1}01]$ axis reaches as high as 30%. A change in the radiation-defect distribution gradient results in disappearance of the bands and in a decrease of the dichroism. Thus optical transitions in a triplet electronic Jahn–Teller center require for their existence strong local distortions near radiation-induced defects in the CuO crystal, like those generated under ionic bombardment. In the case of electron irradiation the character of local distortions is probably not so important, and the transition forbiddenness is not lifted.

It would be natural to associate the narrow ''absorption'' feature appearing near the fundamental edge at energies above 0.97 eV (Fig. 4) with point defects like Frenkel defects; indeed, this band is not seen before irradiation and appears in samples irradiated with either electrons or He^+ ions. The unusual pattern of the polarization dependence of this band, namely, a monotonic shift of the position of the maximum with polarization between the values corresponding to $\mathbf{E}\|[\bar{1}01]$ and $\mathbf{E}\perp[\bar{1}01]$, and a change in the relative position of the band in natural and polarized light argue, however, against its being due to optical transitions between two levels. Note also the higher intensity of the absorption peak in the electron-irradiated sample (1000 cm^{-1}) compared to that of the 300-cm^{-1} peak for the He^+-bombarded crystal. This feature is not connected with interference effects in a thin boundary layer. It exists at depths of up to 80 μm from the surface. This anomalous band is possibly due to light scattering from a radiation-textured system of nuclei of the polar-center phase with a refractive index different from that of the matrix. The scattering takes place in connection with strong dispersion of the refractive index of the matrix near the absorption edge. The differences in the band position and halfwidth obtained with two instruments should be attributed to different slopes of the refractive-index dispersion associated with the different spectral width of the instruments. The deviation from normal incidence and the nonmonochromaticity of the radiation also contribute to the scattering pattern. Incidentally, a strong increase of the refractive index of the matrix under ion irradiation, which is the result of radiation-stimulated escape of oxygen and formation of colloidal particles with metallic conduction, was observed to occur, for instance, in zirconium.[17]

The long-range effect indicates the volume character of the changes induced by He^+ irradiation of CuO. The disappearance of the scattering feature after removal of material from both sides of the sample and the associated restoration of the absorption spectrum in unpolarized light to that seen before the irradiation suggests that the most significant changes occur near the surface, at depths below 80 μm. At the same time the large dichroism (up to 30%) near transitions in the electronic center in the central part of the sample implies reduction (formation of electron centers) in this part of the sample too.

Absorption spectra measured in the region of antiferromagnetic ordering in CuO at 80 K did not reveal any new features in addition to those seen in unirradiated and electron-irradiated samples.[1,2]

Thus a study of the effect of He^+ bombardment provided optical evidence in support of light scattering from nuclei of the phase of polar centers forming near radiation-induced defects, permitted determination of optical transitions in electronic Jahn–Teller canters, and revealed a long-range effect consisting in reduction of CuO to Cu_2O and copper on the side opposite the irradiated face.

The support of the Russian Fund for Fundamental Research (Grant 96-02-16063a) is gratefully acknowledged.

[1] A. S. Moskvin, N. N. Loshkareva, Yu. P. Sukhorukov, M. A. Sidorov, and A. A. Samokhvalov, Zh. Éksp. Teor. Fiz. **105**, 967 (1994) [JETP **78**, 518 (1994)].
[2] N. N. Loshkareva, Yu. P. Sukhorukov, B. A. Gizhevskiĭ, V. L. Arbuzov, S. V. Naumov, and A. A. Samokhvalov, Fiz. Tverd. Tela (St. Petersburg) **37**, 376 (1995) [Phys. Solid State **37**, 203 (1995)].
[3] B. A. Gizhevskiĭ, T. A. Belykh, T. M. Pyatkova, S. V. Naumov, N. A. Viglin, N. N. Loshkareva, A. A. Puzanov, and A. A. Samokhvalov, Pis'ma Zh. Tekh. Fiz. **22**, No. 21, 30 (1996) [Tech. Phys. Lett. **22**, 877 (1996)].
[4] *Sputtering by Particle Bombardment*, edited by R. Behrish (Springer, Berlin, 1981; Mir, Moscow, 1986).
[5] K. Sekar, P. V. Satyam, D. P. Mahapatra, B. N. Dev, N. C. Mishra, B. S. Acharya, and P. Sen, Nucl. Instrum. Methods B **83**, 140 (1993).
[6] A. A. Samokhvalov, N. N. Loshkareva, Yu. P. Sukhorukov, V. A.

Gruverman, B. A. Gizhevskiĭ, and N. M. Chebotaev, JETP Lett. **49**, 523 (1989).
[7] B. A. Gizhevskiĭ, T. A. Belykh, S. V. Naumov, N. N. Loshkareva, N. A. Viglin, A. A. Samokhvalov, A. A. Puzanov, and G. N. Tatarinova, *Abstracts of Russian-Japanese Symposium on Interaction of Fast Particles with Solids*, Belgorod, 1996, p. 26.
[8] Yu. P. Sukhorukov, N. N. Loshkareva, A. S. Moskvin, and A. A. Samokhvalov, Zh. Eksp. Teor. Fiz. **108**, 1821 (1995) [JETP **81**, 998 (1995)].
[9] A. S. Moskvin, *The Origin of the Unusual Physical Behavior of Copper Oxides* [in Russian], Ekaterinburg, 1995.
[10] A. A. Samokhvalov, N. A. Viglin, B. A. Gizhevskiĭ, N. N. Loshkareva, V. V. Osipov, N. I. Solin, and Yu. P. Sukhorukov, Zh. Eksp. Teor. Fiz. **103**, 951 (1993) [JETP **76**, 463 (1993)].
[11] V. S. Vavilov, A. E. Kiv, and O. R. Niyazova, *Mechanisms of Defect Formation and Migration in Semiconductors* [in Russian], Nauka, Moscow, 1981.
[12] B. L. Oksengendler, JETP Lett. **24**, 9 (1976).
[13] H. L. Edwards, D. J. Derro, A. L. Barr, J. T. Markert, and A. L. de Lozanne, Phys. Rev. Lett. **75**, 1387 (1995).
[14] D. I. Tetel'baum, V. P. Sorvina, and M. G. Belyanina, High-Purity Substances No. 2, 47 (1995).
[15] V. V. Ovchinnikov, *Abstracts of IV All-Russian Conference on Modification of the Properties of Construction Materials by Charged-Particle Beams* (Tomsk, 1996), p. 133.
[16] B. A. Gizhevskiĭ, T. A. Belykh, V. A. Teplov, S. V. Naumov, N. N. Loshkareva, Yu. P. Sukhorukov, and N. M. Chebotaev, in: *Detection of Ionizing Radiations* [in Russian], Intercollege Collection of Papers, Ekaterinburg, 1996, p. 3.
[17] O. N. Gorshkov, T. A. Gracheva, A. P. Kasatkin, N. D. Malygin, V. A. Novikov, and A. F. Shchurov, High-Purity Substances No. 2, 85 (1995).

Translated by G. Skrebtsov

HgSe:Fe—a mixed-valency system and the problem of the ground state

I. G. Kuleev

Institute of Metal Physics, Ural Branch of the Russian Academy of Sciences, 620219 Ekaterinburg, Russia
(Submitted August 11, 1997)
Fiz. Tverd. Tela (St. Petersburg) **40**, 425–432 (March 1998)

The dependence of the electron mobility on the iron impurity content N_{Fe} and temperature is studied for three variants of the ordering of Fe^{3+} ions in crystalline HgSe:Fe, a weakly correlated gas, states with near ordering like that in a strongly correlated Coulomb liquid, and long-range ordering. The electron mobilities owing to scattering on the correlated system of Fe^{3+} ions are determined. The temperature dependence of the mobility is analyzed for electron scattering on fluctuations in the charge density in a system of Fe^{2+}–Fe^{3+} iron ions with mixed valency, and the correlation length is determined. It is shown that the ordering region for the Fe^{3+} ions encompasses only the first coordination sphere, i.e., near ordering in the position of the Fe^{3+} ions is established, as in a liquid. The coupling between the ordering of the Fe^{3+} ions and the formation of a correlation gap in the density of impurity *d*-states and its effect on the low-temperature behavior of the electron mobility in HgSe:Fe crystals are examined.
© *1998 American Institute of Physics.* [S1063-7834(98)00703-5]

Studies of spatial ordering in mixed-valency systems and the determination of the type of ground state in these systems are important for interpreting the physical properties of crystalline HgSe:Fe and other mixed valency systems.[1] Experimental studies[2] have shown that the anomalous dependences of such physical properties of these compounds as their conductivity,[3,4] thermal emf, longitudinal and transverse Nernst–Ettingshausen effects,[5–8] etc., on the iron impurity concentration N_{Fe} and temperature T are determined by some features of electron scattering resulting from the spatial ordering of trivalent iron ions.

A state with mixed valency of the Fe^{3+}–Fe^{2+} ions in HgSe:Fe occurs for concentrations $N_{Fe} > N^* = 4.5 \times 10^{18}$ cm^{-3}, when the Fermi level reaches the donor level of iron ($\varepsilon_d = 0.21$ eV).[2] A further rise in the iron content only raises the concentration of neutrals in the lattice of Fe^{2+} ions ($N_0 = N_{Fe} - N^*$), while the Fermi level is fixed at the *d*-level of iron. For $N_{Fe} > N^*$ in Fe^{3+}-Fe^{2+} mixed- valency systems with the same energies, positive charges on iron ions (*d*-holes) can be redistributed over the lattice sites occupied by Fe^{2+} ions. Coulomb repulsion of the *d*-holes leads to spatial correlations in their positions: the larger the iron content, the more free sites there are for redistribution of the *d*-holes and the higher the degree of ordering in the correlated system of Fe^{3+} ions. The Fe^{3+} ions are the principal scattering centers in HgSe:Fe at low temperatures, so as they become ordered, scattering is reduced and the electron mobility increases.[3,4]

Crystalline HgSe:Fe is a convenient object for studying the role of interimpurity Coulomb correlations in mixed-valency systems. First, when they displace Hg^{2+} in the crystal lattice sites, the Fe^{2+} ions do not disrupt the spectrum of the band current carriers but only cause alloy scattering of the electrons owing to the potential difference $\Delta V = V_{Fe} - V_{Hg^{2+}}$. This potential is localized in a unit cell and its contribution to electron scattering can easily be isolated.[4] Thus, in crystals with different impurity iron contents, the contribution to the electron mobility from scattering on the correlated Fe^{3+} ion system can be distinguished. Second, because of the low concentration of Fe^{3+} ions, their effect on the conduction electron spectrum is negligible, in both the ordered and disordered states. Third, studies of the contribution of electron scattering on correlated Fe^{3+} ion systems to the mobility (or to other kinetic characteristics[5–8]) can be used to determine the degree of ordering as a function of the iron concentration and to track the dynamics of the changes in the ordering of Fe^{3+} ions with temperature.

Coulomb correlations in the Fe^{2+}–Fe^{3+} ion system in crystalline HgSe:Fe (as in other mixed-valency systems[1]) at high iron contents and low temperatures lead to one of three types of ordering: (1) a weakly correlated gas of Fe^{3+} ions; (2) a state with near ordering like that found in a highly correlated liquid of Fe^{3+} ions; and (3) long-range ordering in a system of charged centers, i.e., the formation of a Wigner crystal of Fe^{3+} ions.

To explain the anomalous rise in the mobility of conduction electrons in HgSe:Fe for $N_{Fe} > N^*$ the hypothesis has been advanced[9] that a Wigner crystal of Fe^{3+} ions is formed. Later, others proposed[10,11] a model of short-range correlations (MKKI) in which it was assumed that ordering occurs in the immediate neighborhood of a given Fe^{3+} ion. It has been shown[4] that this variant of the MKKI model,[10,11] which is based on approximating the pairwise correlation function by a step function, is restricted to weak interimpurity correlations. This approximation corresponds to ordering in the correlated system of Fe^{3+} ions of the weakly correlated gas type.[4] The variant of the MKKI model proposed in Ref. 4 is valid for arbitrary magnitudes of the Coulomb correlations in an Fe^{3+} ion system. It has made it possible to calculate $\mu(N_{Fe})$ qualitatively over a wide range of iron contents. It was shown that for $N_{Fe} \gg N^*$ in HgSe:Fe crystals, Coulomb correlations lead to the formation of a ground state of the

 © 1998 American Institute of Physics

correlated Fe^{3+} ion system of the correlated Coulomb liquid type. However, this conclusion about the type of ordering,[4] which is based only on an analysis of the dependence $\mu(N_{Fe})$, is limited. First, the two other orderings of Fe ions (weakly correlated gas and Wigner crystal) were not analyzed and, in this regard, the question of the adequacy of these data remained open. Second, this conclusion is limited to an approximation of the correlated Fe^{3+} ion system by a model system of hard spheres. Thus, the variations in the mobility $\mu(N_{Fe})$ for the three ways of ordering the Fe^{3+} ions when $N_{Fe} \gg N^*$ have been analyzed further. In this paper it is shown that for $N_{Fe} \gg N^*$ the dominant contribution to the relaxation of the electron momentum is from alloy scattering and that it is rather difficult to reach an unambiguous conclusion in favor of one of the ordering variants based solely on data about $\mu(N_{Fe})$. In this regard, we have examined the temperature dependence of the mobility for electron scattering on fluctuations in the density of charged centers resulting from thermally activated transitions of d-holes between Fe^{2+} and Fe^{3+} ions and determined the correlation length $\xi_c(T)$. We have also shown that the ordering region of the correlated Fe^{3+} ion system encompasses only the first coordination sphere (as in a liquid). This makes it possible to determine the type of ground state in the Fe^{3+} ion system of HgSe:Fe for low temperatures and $N_{Fe} \gg N^*$ without using the hard-sphere model approximation for the correlated Fe^{3+} ion system.

A second important problem involving mixed valency systems is to study the effect of the ordered correlated Fe^{3+} ion system on the structure of the impurity d-band. It is known[12,13] that in gapless compensated semiconductors such as HgCdTe the interaction of oppositely charged donors and acceptors leads to the formation of Coulomb pseudopotentials at the Fermi level, a minimum in the density of impurity states with $g(\varepsilon_F) > g_e(\varepsilon_F)$.[12] An analysis[11,14] of EPR data on Fe^{3+} ions based on the MKKI model, which is valid in the case of weak Coulomb correlations, showed that there is a minimum in the density of d-states, but could not establish whether a gap or a pseudogap is formed at the Fermi level. A Coulomb gap in the density of impurity d-states was necessary for them to reduce the effect of resonance electron scattering on d-states of the impurity iron, inclusion of which had led to catastrophically low values for the electron mobility in HgSe:Fe.[2] It is shown in Section 4 that in the weak Coulomb correlation region, the ordering of the correlated ion system in HgSe:Fe leads to the appearance of a correlation gap in the density of impurity d-states, i.e., to the formation of a finite energy gap between the filled (Fe^{2+}) and empty (Fe^{3+}) states, where $g_d(\varepsilon) = 0$, and to complete suppression of resonance electron scattering.

1. ELECTRON MOBILITY IN HgSe:Fe WITH SCATTERING ON THE CORRELATED Fe^{3+} ION SYSTEM FOR THE THREE TYPES OF ORDERING

In accordance with the model proposed in Ref. 4, we shall treat the scattering of conduction electrons in HgSe:Fe as in a binary alloy consisting of charged Fe^{3+} and neutral in-the-lattice Fe^{2+} centers. We write the electron mobility in the form

$$\mu(N_{Fe}) = \left(\frac{1}{\mu_c} + \frac{1}{\mu_{a1}} \right)^{-1}, \tag{1}$$

where μ_c and μ_{al} are the contributions to the mobility for scattering of electrons on the correlated Fe^{3+} ion system and on the alloy potential. Scattering on the alloy potential causes a monotonic reduction in the mobility as the iron content is raised,

$$\mu_{al} = \mu_{BH} \left\{ \frac{\Lambda}{\Phi_{BH}} \left[2 \left(\frac{N_0}{N_+} \right)^{1/2} \Phi_{+0} + \frac{\Lambda}{2} \frac{N_0}{N_+} \right] \right\}^{-1}. \tag{2}$$

Here N_0 and N_+ are the concentrations of Fe^{2+} and Fe^{3+} ions, respectively, and μ_{BH} is the electron mobility for scattering on a disordered aggregation of ions. According to the Brooks-Herring theory, $\Phi_{BH} = \ln(1+b_s) - 1/(1+b_s^{-1})$, where $b_s = (2k_F r_s)^2$, r_s is the Thomas-Fermi screening radius, $\Phi_{+0} = 1 - b_s^{-1} \ln(1+b_s)$, and Λ is the ratio of the interaction constants for the electrons with the neutral and charged centers, estimated[4] as $\Lambda = 0.1$. For scattering on the correlated Fe^{3+} ion system, the expression for the mobility has the form

$$\mu_c(N_{Fe}) = \mu_{BH} \frac{\Phi_{BH}}{\Phi_c},$$

$$\Phi_c(k_F) = 2 \int_0^1 \frac{x^3 S(2k_F x)}{(x^2 + b_s^{-1})^2}\, dx, \tag{3}$$

where $S(q)$ is a structure factor characterizing the degree of ordering of the donor system determined in Ref. 4. For a disordered system $S(q) = 1$ and $\Phi_c(k_F) = \Phi_{BH}$.

Equations (1) and (2) make it possible to isolate from the experimentally measured mobility $\mu^{exp}(N_{Fe})$ the contribution $\mu_c^{exp}(N_{Fe})$ owing to scattering on the correlated Fe^{3+} ion system,

$$\mu_c^{exp} = (\mu_{exp}^{-1} - \mu_{al}^{-1})^{-1}. \tag{4}$$

An analysis of experimental data using Eq. (4) showed that for $T = 4.2$ K and $N_{Fe} > 3 \times 10^{19}$ cm^{-3}, scattering on the correlated Fe^{3+} ion system is roughly 8 times less likely than that on randomly distributed Fe^{3+} ions.[4] Thus, in HgSe:Fe, interimpurity Coulomb correlations are strong and cause a substantial spatial redistribution of the Fe^{3+} ions.

In calculating the structure factor $S(q)$ in the strong Coulomb correlation region[4–8] we have used the Perkus-Yevick approximation[15] for the hard sphere model system. Here the integral equation for the direct correlation function can be solved exactly, and $S(q)$ is found without using perturbation theory in a small parameter.[15] The physical reason which permits the correlated Fe^{3+} ion system to be approximated by a hard sphere model system is the following: an analysis of the gain in free energy for ordering of the correlated Fe^{3+} ion system has shown[16] that Coulomb repulsion of d-holes redistributes them in a way such that a correlation sphere of radius r_c without any other d-holes in it develops around each Fe^{3+} ion. This makes it possible to approximate the correlated Fe^{3+} ion system by a system of hard spheres

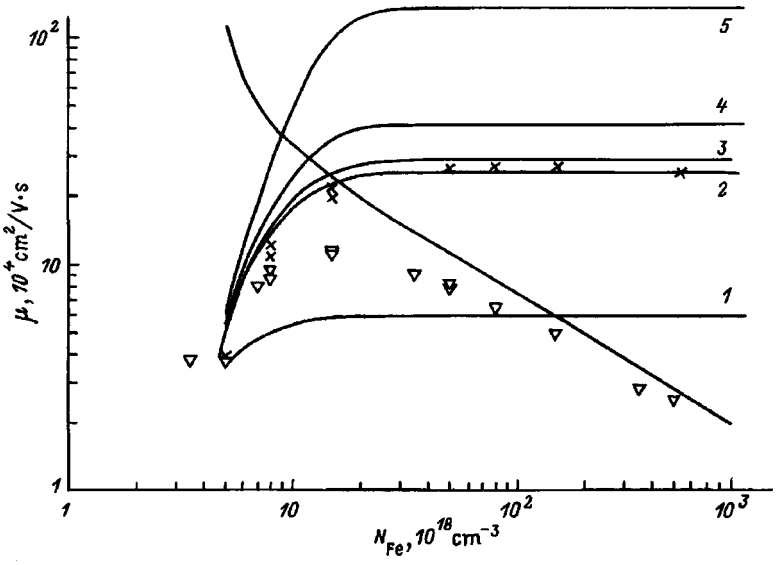

FIG. 1. The contribution to the mobility from scattering on the correlated Fe^{3+} ion system as a function of the amount of iron impurity for the three types of ordering, (*1*) weakly correlated gas ($\eta_\infty=0.125$), (*2*) and (*3*) strongly correlated Coulomb liquid ($\eta_\infty=0.45$ and 0.47), (*4*) and (*5*) Wigner crystal ($\eta_\infty=0.52$ and 0.64), and (*6*) the contribution $\mu_{al}(N_{Fe})$ to the mobility owing to alloy scattering. The triangles denote experimental values of $\mu^{exp}(N_{Fe})$ taken from Ref. 3 and the crosses, values of $\mu_c^{exp}(N_{Fe})$.

of diameter $d=r_c$ in which the degree of ordering is determined by the packing parameter $\eta=\pi d^3 N_+/6$, equal to the ratio of the volume occupied by the hard spheres to the total volume of the system. As the concentration N_{Fe} is raised, the number of free sites for redistribution of d-holes increases, so that r_c and, therefore, the degree of ordering become larger.[16] This approach has been fruitful for describing thermogalvanomagnetic effects in crystalline HgSe:Fe.[4–8]

As $\eta\to 0$, the aggregation of scattering centers is entirely disordered ($S(q)=1$). The range $\eta<0.125$ corresponds to a weakly correlated gas.[4] For the correlated Coulomb liquid, $\eta=0.45-0.47$. These values of the packing parameter are obtained for all liquid metals.[15,17] The degree of spatial ordering in a hard sphere model system increases discontinuously as the packing parameter is raised, and for $\eta=0.74$ ideal hexagonal close packing is realized. According to the statistical theory of Bernal,[15] for defective hexagonal close packing, $\eta\approx 0.64$. The calculated values of η for dense-packed cubic and body-centered cubic lattices are 0.52 and 0.68, respectively. Nevertheless, this does not mean that one of the above lattice types will be realized in a hard sphere system. Since for $\eta>0.52$ the peak in the pairwise correlation function of the distribution corresponding to the third correlation sphere is fairly distinct, we can take this value as an arbitrary boundary between near and far ordering. As we shall see below, the final result will be insensitive to this assumption.

It is evident that the spatial correlations in the Fe^{3+} ion system are stronger, the higher the concentration of neutral Fe^{2+} centers. For $N_{Fe}\gg N^*$, one of the three types of ordering is established in the correlated Fe^{3+} ion system. An equation for the packing parameter as a function of N_{Fe}, which is valid for the three types of ordering in the correlated Fe^{3+} ion system, can be obtained in a way similar to that employed in Ref. 4,

$$\eta=\eta_\infty\left[1-\exp\left(-\frac{\eta}{\eta_\infty}\frac{N_{Fe}}{N_+}\right)\right], \tag{5}$$

where η_∞ determines the limiting value of the packing parameter when $N_{Fe}\gg N^*$ for the different kinds of ground state: for the weakly correlated gas $\eta_\infty=0.125$, for the strongly correlated Coulomb liquid $\eta_\infty=0.45-0.47$, and for the Wigner crystal $\eta_\infty=0.52-0.64$.

Plots of $\mu_c(N_{Fe})$ calculated using Eqs. (3) and (5) for all the types of ordering of the Fe^{3+} ions in HgSe:Fe at low temperatures are shown in Fig. 1. This figure implies that the weakly correlated gas model can be used only for concentrations $N_{Fe}<6\times 10^{18}$ cm^{-3}. The values of the mobility $\mu_c(N_{Fe})$ for $N_{Fe}>3\times 10^{19}$ cm^{-3} lie in a region corresponding to a strongly correlated Coulomb liquid. Mobilities $\mu_c(N_{Fe})$ for long-range ordering like that in Wigner crystals lie somewhat higher. Thus, an analysis of the ordering of the correlated Fe^{3+} ion system in HgSe:Fe at low temperatures would suggest that the ground state of the system of Fe^{3+} ions in the hard-sphere approximation is a strongly correlated Coulomb liquid. Actually, however, data on the mobility $\mu_c(N_{Fe})$ alone are not sufficient for such an unambiguous conclusion. In fact, for $N_{Fe}\gg N^*$ the dominant contribution to the relaxation of the electron momentum is from alloy scattering (curve *6* of Fig. 1) and the total mobility becomes insensitive to variations in η_∞ from 0.45 to 0.52. Figure 2 shows calculated $\mu_c(N_{Fe})$ curves for different values of the parameters η and Λ. It is clear from this figure that the $\mu_c(N_{Fe})$ curves *2–4* are close to the experimental ones, although the values of μ_c for $N_{Fe}\gg N^*$ differ greatly. Therefore, in the following we shall consider another method for determining the type of ordering of the Fe^{3+} ions in HgSe:Fe at low temperatures.

2. THE TEMPERATURE DEPENDENCE OF THE MOBILITY FOR SCATTERING ON DENSITY FLUCTUATIONS IN THE CORRELATED Fe^{3+} ION SYSTEM AND THE CORRELATION LENGTH

The temperature dependence of the electron mobility $\mu(T)$ in crystalline HgSe:Fe has been examined elsewhere.[18–20] Beginning with a model of Wigner crystal

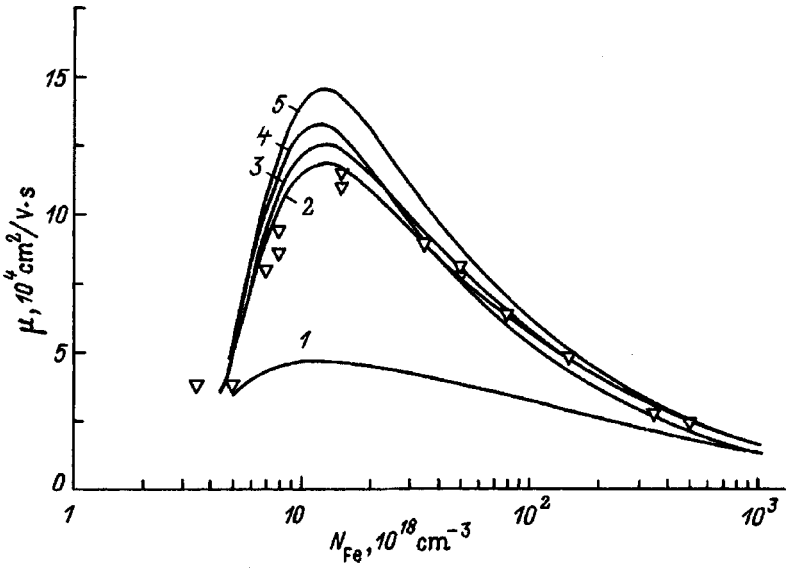

FIG. 2. A comparison of the calculated $\mu(N_{\mathrm{Fe}})$ curves with experimental data[3] for different values of the parameters $\eta_\infty = 0.125$ (*1*), 0.45 (*2*), 0.47 (*3*), and 0.52 (*4,5*) and $\Lambda = 0.1$ (*1–3,5*) and 0.12 (*4*).

Fe^{3+} ions, an analysis was made[18] of the effect of the nonidealness and vibrations of the Wigner lattice of the Fe^{3+} ions on the mobility $\mu(T)$. This approach has been criticized in Ref. 2. The results of a calculation of $\mu_c(T)$ have been compared[19] with the total mobility $\mu^{\exp}(T)$. In fact, it was necessary to isolate the contribution owing to scattering on the correlated Fe^{3+} ion system from the experimental data according to Eq. (4) and to compare the theoretically calculated $\mu_c(T)$ with this contribution, as we have done here. In Ref. 20, the total mobility $\mu(T)$ and $\mu_c(T)$ were calculated for crystalline HgSe:Fe using a temperature-dependent hard-sphere model, and qualitative agreement was obtained with experimental data. In the following, another method is proposed for describing the temperature dependence of the mobility. It has the advantage that it can be used to determine the type of ordering in the correlated Fe^{3+} ion system.

Let us consider the temperature dependence of the contribution to the mobility $\mu_c(T)$ from electron scattering on the Fe^{3+} ion system for $N_{\mathrm{Fe}} \gg N^*$. As the temperature is raised, the migration of *d*-holes between Fe^{2+} and Fe^{3+} ions is enhanced, and this leads to disruption of the order in the correlated Fe^{3+} ion system and hence to increased scattering of electrons by the charged centers. Transitions of *d*-holes between iron ions can be regarded as thermally activated fluctuations in the density of charged Fe^{3+} centers in a binary Fe^{3+}–Fe^{2+} alloy. It has been shown[15] that the spectrum of long-wavelength fluctuations in these systems is well described by the Ornstein–Zernike theory,[21] which makes it possible to estimate the scale of ordering in alloys and similar systems. The degree of ordering of the system of particles in this case may be determined by a correlation function of the form[15]

$$\Gamma(r) \approx \frac{1}{r} \exp\left(-\frac{r}{\xi_c}\right), \tag{6}$$

where ξ_c is the correlation length characterizing the size of the ordering region. The temperature dependence of ξ_c describes the change in the scale length of the ordering of the system. At high temperatures the system is disordered and $\xi_c \to 0$. With ordering, ξ_c increases and in the limit $\xi_c \to \infty$ long range ordering is established. The temperature T_c at which this happens is the critical temperature for the order–disorder (strongly correlated Coulomb liquid–Wigner crystal) phase transition.

Calculations of Wigner crystallization of electron plasmas[22,23] have shown that the nonidealness parameter of the plasma at the phase transition point is

$$\Gamma_c = \sqrt[3]{4\pi N_+/3}\,\frac{e^2}{\chi k_{\mathrm{B}} T_c} \cong 155 \pm 10, \tag{7}$$

where χ is the dielectric permittivity. This gives an order–disorder transition temperature for the *d*-holes in an Fe^{3+}–Fe^{2+} system (for $\chi = 20$) of $T_c \cong 1$ K. During the onset of near ordering in the correlated Fe^{3+} ion system, ξ_c should be on the order of the interimpurity distance $R_+ = N_+^{1/3}$. We shall examine scattering on long-wavelength fluctuations in the Fe^{3+} ion density and show that, in fact, for $T = 5-10$ K, $\xi_c = (1-2)R_+$. In this case the expression for the mobility $\mu_c(T)$ has the form[19]

$$\mu_c(T) = \frac{3\pi h}{4\varepsilon_{\mathrm{B}} F_c} = \frac{\mu_{BH} F_{BH}}{F_c(T)},$$

$$F_c(T) = \frac{t b_0}{(b_c - b_s)}\left[\frac{b_c}{(b_c - b_s)} \ln \frac{b_c(1+b_s)}{b_s(1+b_c)} - \frac{1}{1+b_s}\right]. \tag{8}$$

Here ε_B is the Bohr energy, $t = T/T_c$, $\xi_c = A r_0^2 \times |t-1|^{-1}$, A is an adjustable parameter of the theory, $b_0 = (1/2k_F r_0)^2$, $b_s = (1/2k_F r_s)^2$, $b_c = b_A(t-1)$, and $b_A = b_c/A$. As can be seen from Eq. (8), the expression for $\mu_c(T)$ contains three parameters: r_0, T_c, and A. We can eliminate r_0 from Eq. (8) by taking the ratio $\mu_c(T)/\mu_c(T_0)$, where we have taken T_0 to be 10 K. By varying the parameters T_c and b_A, we attempt to describe the experimental $\mu_c^{\exp}(T)$ curves for different concentrations of iron in HgSe:Fe. The values of the main parameters $m(\varepsilon_F)$, k_F, r_s, etc., have been chosen to be the same as in the analysis of the concentration dependence of the mobility.

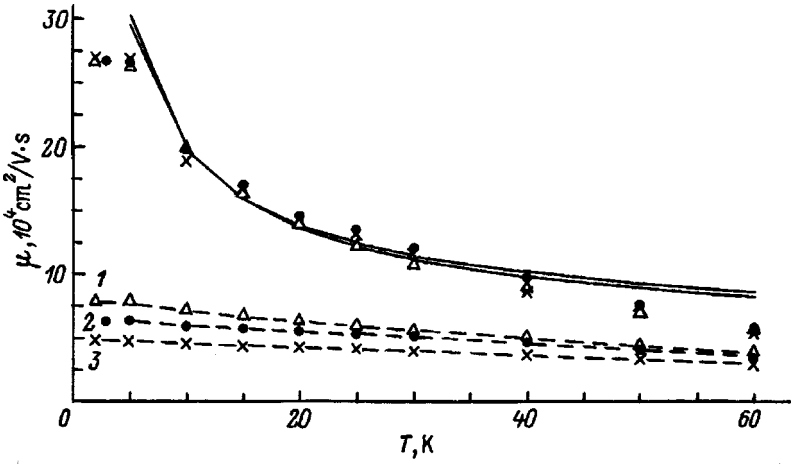

FIG. 3. Electron mobility as a function of temperature. The calculated $\mu_c(T)$ are shown as solid curves ($T_c = 1-2$ K, $b_A = 0.005-0.01$). The points joined by dashed curves and labelled *1–3* correspond to experimental values[3] of $\mu^{\exp}(T)$ for samples of HgSe:Fe with iron concentrations $N_{\mathrm{Fe}} = 5,8,15\times10^{18}$ cm^{-3}. The upper points correspond to $\mu_c^{\exp}(T)$ for the same concentrations N_{Fe}.

Figure 3 shows the calculated $\mu_c(T)$ curves and experimental data $\mu^{\exp}(T)$ for HgSe:Fe samples with large iron impurity contents. Note that the values of $\mu_c^{\exp}(T)$ for HgSe:Fe samples with $N_{\mathrm{Fe}} > 3\times10^{19}$ cm^{-3} are essentially the same over a wide range of temperatures. This confirms our model for ordering of the Fe^{3+} ions; a ground state has formed in the correlated Fe^{3+} ion system, so that the temperature variation in the degree of ordering of the Fe^{3+} ions no longer depends on the iron content. It is clear from the figure that over temperatures of 5–40 K, the computational results are in fair agreement with the experimental data.[3] At higher temperatures the calculated $\mu_c(T)$ exceed the measured values. This difference occurs because we have neglected electron-phonon scattering, which makes a significant contribution to the mobility for $T > 40$ K.[24] The values of the variable parameters are $T_c = 1-2$ K and $b_A = 0.005-0.01$, while $r_0 = (1-2)\times10^{-6}$ cm^{-3}. Thus, the value of T_c obtained by fitting the $\mu(T)$ curve is consistent with the value found for Wigner crystallization of an electron plasma.[22,23]

The correlation length determined from $\mu_c(T)$ is $\xi_c = (1-1.6)R_+$ for $T = 5$ K. Thus, an analysis of the temperature dependence of the mobility during scattering on fluctuations in the density of charged centers has shown that, in fact, the ordering of the correlated Fe^{3+} ion system in HgSe:Fe for low temperatures and $N_{\mathrm{Fe}} \gg N^*$ encompasses only the first coordination sphere, i.e., near ordering develops in the positions of the Fe^{3+} ions, as in a liquid (hence the term strongly correlated Coulomb liquid). For $T < 5$ K, the experimental mobility data cease to depend on the temperature,[25] while the theory of scattering on critical fluctuations predicts a sharp increase in the mobility owing to the further development of ordering in the correlated Fe^{3+} ion system as $T \to T_c$. As we shall see below, the observed mobility behavior as $T \to 0$ is caused by the presence of a correlation gap in the density of impurity *d*-states.

3. THE CORRELATION POTENTIAL AND THE GAP IN THE DENSITY OF IMPURITY *d*-STATES

In the absence of ordering effects, the random fields of the Fe^{3+} ions cause spreading of the energies of the *d*-states and the formation of an impurity gap with a width on the order of 10 meV. The Fermi level separates the empty Fe^{3+} *d*-states from the filled states (Fe^{2+}). With ordering, each Fe^{3+} ion at point R_i lies in the field of a correlation potential $U_s(R_i)$ determined by the self-consistent effect of the potentials of the other Fe^{3+} ions surrounding the given ion,[16]

$$U_s(R_i) = \sum_{j\neq i} V(R_{ij})(g(R_{ij}) - 1). \tag{9}$$

Here $V(R_{ij})$ is the potential created by the *j*-th Fe^{3+} ion at the point R_i. For a screened Coulomb interaction of the ions, we have

$$U_s(R_i) = \frac{e^2}{\chi\pi}\int_0^\infty \frac{q^2 dq}{q^2 + r_s^{-2}}\,(S(q)-1)\,\frac{\sin(qR_i)}{qR_i}. \tag{10}$$

The potential $U_s(r)$ tends to redistribute the *d*-holes in the system of Fe^{2+}–Fe^{3+} ions when $N_{\mathrm{Fe}} > N^*$ so as to ensure a minimum in the potential energy at those places where there are Fe^{3+} ions. Equations (9) and (10) make it possible to analyze the gain in the Coulomb energy per center, ΔE_{k1}, for an ordered ion distribution compared to a disordered one,[16,17]

$$\Delta E_{k1} = \frac{\Delta E_k}{N_{\mathrm{Fe}}^{3+}} = \frac{1}{2}\,U(0) = \frac{e^2}{2\chi\pi}\int_0^\infty \frac{q^2 dq}{q^2 + r_s^{-2}}\,(S(q)-1). \tag{11}$$

Figure 4 shows plots of ΔE_{k1} as a function of N_{Fe} for the three types of ordering of the charged centers. It is clear from this figure that the gain in energy for the weakly correlated gas differs greatly from the ΔE_{k1} obtained for a strongly correlated Coulomb liquid. On the other hand, the energies ΔE_{k1} for a strongly correlated Coulomb liquid and a system with long-range ordering differ little (by 0.3–0.4 meV); this confirms that the system of Fe^{3+} ions is close to a strongly correlated Coulomb liquid–Wigner crystal phase transition. The sharp rise in ΔE_{k1} for $N^* < N_{\mathrm{Fe}} < 1\times10^{19}$ cm^{-3} takes place because it is primarily the closest *d*-holes which move away from one another during ordering. This yields a maximum gain in the Coulomb energy and leads to the formation of correlation spheres around each Fe^{3+} ion.[16] It is this cir-

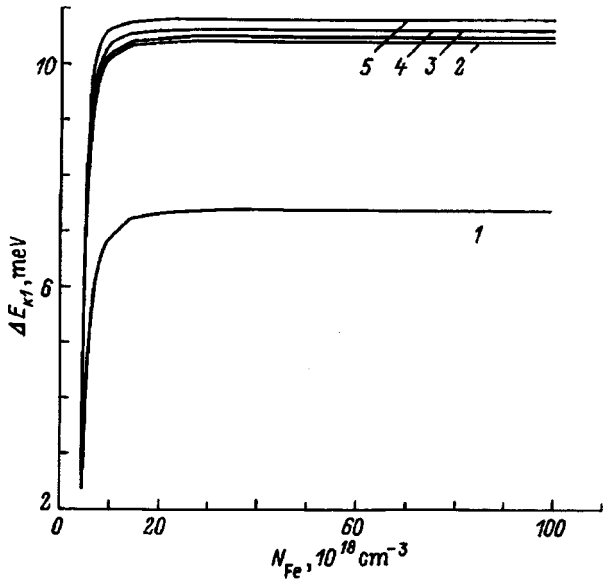

FIG. 4. ΔE_{k1} as a function of N_{Fe} for the three types of ordering of the charged centers: (*1*) weakly correlated gas ($\eta_\infty = 0.125$), (*2*) and (*3*) strongly correlated Coulomb liquid ($\eta_\infty = 0.45$ and 0.47), (*4*) and (5) Wigner crystal ($\eta_\infty = 0.52$ and 0.64).

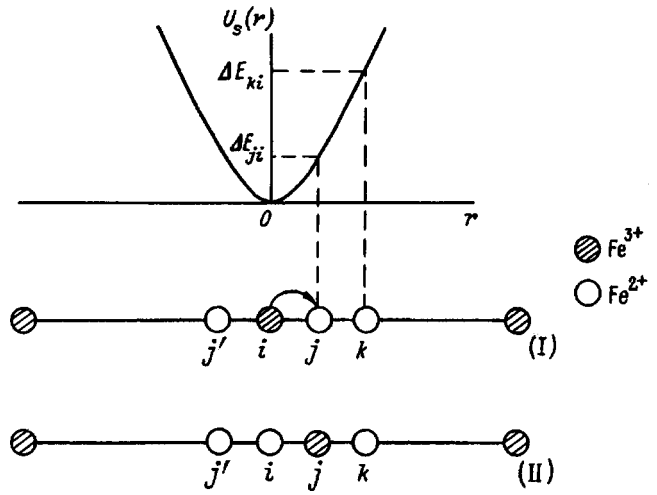

FIG. 5. The form of the potential $U_s(r)$ and the energy scheme for inelastic transitions in a one-dimensional near-ordering cluster of Fe^{3+} and Fe^{2+} ions. ΔE_{ji} is the energy of an inelastic transition of a d-hole from point R_i to R_j, equal to the difference in the energies of the two configurations (I) and (II) of the near-ordering cluster.

cumstance which allows us to approximate the spatial-correlation system of the Fe^{3+} ions by a system of hard spheres.

In discussing the impurity d-states of iron ions in HgSe:Fe crystals, two competing effects must be taken into account: $s-d$-hybridization, which facilitates the delocalization of d-holes, and Coulomb correlations of d-holes, which tend to preserve the local character of the impurity states. Since the width of a d-level owing to $s-d$-hybridization is less than 0.1 meV,[10,11] while the energy of the Coulomb correlations of the d-holes is two orders of magnitude greater, the local character of the d-states is maintained in crystalline HgSe:Fe. It should be noted that, although the $s-d$-hybridization interaction is weak, it can play an important role in the inelastic scattering of conduction electrons and lead to charge exchange of iron ions.[7] The potential $U_s(R_j)$ inhibits jumping by d-holes from Fe^{3+} to Fe^{2+} ions, thereby contributing to their localization on charged centers. Because of the random distribution of the Fe^{2+} ions over the crystal lattice sites (and, therefore, in near-ordering clusters), the probability of many-particle transitions by d-holes is small, and their contribution can be neglected at low temperatures. Here we restrict ourselves to examining single-particle transitions: we shall assume that a transition of a d-hole in a near-ordering cluster from an Fe^{3+} ion located at the point R_i to an Fe^{2+} ion at the point R_j takes place in the static field of the remaining Fe^{3+} ions (Fig. 5). The inelastic energy ΔE_{ji} of this kind of transition is equal to the difference in the energies of the two configurations (Fig. 5),

$$\Delta E_{ji} = U(R_j) - U(R_i). \tag{12}$$

Since iron ions displace Hg^{2+} ions at lattice sites, there is a minimum jump length for a d-hole, $\Delta R_{ij} \geqslant \Delta R_{\min}$. Given the Coulomb interimpurity correlations at the sample preparation temperature ($T \sim 10^3$ K), it turns out that $R_{\min} \sim (1-2)a_0$ (a_0 is the lattice constant). Thus, $\Delta E_{ji} > \Delta E_{\min} = \Delta$. Equations (10) and (12) then imply

$$\Delta \approx \frac{e^2(\Delta R_{\min})^2}{6\pi\chi} \int_0^\infty \frac{q^4 dq}{q^2 + r_s^{-2}} (S(q)-1). \tag{13}$$

For $\Delta R_{\min} = 10^{-7}$ cm, Eq. (13) gives $\Delta \sim 5$ K when $N_{\mathrm{Fe}} > 3 \times 10^{19}$ cm^{-3}. Roughly the same estimate of Δ has been obtained[23] for a linear chain model of Fe^{3+} ions. The existence of a minimum energy for the d-electron transitions means that the band of filled Fe^{2+} d-states is separated from the band of empty d-states by a finite energy Δ, where Δ is substantially greater than T_c, the temperature of the strongly correlated Coulomb liquid–Wigner crystal phase transition.

Thus, ordering of the correlated Fe^{3+} ion system in mixed valency systems leads to the formation of a correlation gap between the filled and empty d-states and not to an Éfros–Shklovskiĭ pseudogap,[12,13] as has been assumed elsewhere.[10,11] The role of resonance scattering of conduction electrons on d-states in HgSe:Fe compounds at low temperatures has been discussed actively in the literature.[2,10,11] Based on the above analysis, we can say definitively that interimpurity Coulomb correlations completely suppress resonance scattering: the density of d-states at the Fermi level, $g_d(\varepsilon_F) = 0$, and $\Delta \gg \Gamma_d$ (Γ_d is the width of the d-level owing to $s-d$-hybridization; according to Refs. 10 and 11, $\Gamma_d < 0.1$ meV). As can be seen from Fig. 4, for $N_{\mathrm{Fe}} \gg N^*$ resonant capture of a conduction electron at the d-level of the Fe^{3+} ion requires a large activation energy $U_s(0) \sim 20$ meV, unlike scattering processes with charge exchange of d-centers.[7] The mobility behavior of HgSe:Fe for $N_{\mathrm{Fe}} \gg N^*$ and $T \to 0$ also becomes understandable (Fig. 3). At temperatures $T < 5$ K, d-hole jumps are frozen out, the correlated Fe^{3+} ion system loses its capacity for long-range ordering, and the electron mobility, as observed in experiments,[25] ceases to depend on temperature. The near

ordering of the correlated Fe^{3+} ion system ''freezes'' and in a certain sense we can speak of a transition of the Fe^{3+} ion system into a metallic glass state[26,27] (taking this term to mean a frozen strongly correlated Coulomb liquid). Thus, long-range ordering of the Fe^{3+} ions in HgSe:Fe is impossible for low temperatures and $N_{Fe} \gg N^*$, not because of screening of the electrons by the potentials of the Fe^{3+} ions, as assumed in Ref. 2, but because of the discreteness of the distribution of impurity iron over the lattice sites and the resulting formation of a correlation gap in the density of impurity d-states.

In sum, the three types of ordering of the correlated Fe^{3+} ion system in crystalline HgSe:Fe have been investigated for low temperatures and $N_{Fe} \gg N^*$. It has been shown that the ordering of Fe^{3+} ions in the mixed valency Fe^{2+}–Fe^{3+} system at low temperatures corresponds to a ground state like that found in a strongly correlated Coulomb liquid. A correlation gap Δ develops in the density of d-states which separates the filled d-states from the empty ones. At temperatures $T < \Delta$, the system of Fe^{3+} ions loses its capacity for further ordering and enters a state similar to a metallic glass. Thus, the low temperature electron anomaly in HgSe:Fe can be regarded as the consequence of a continuous phase transition from a weakly correlated gas to a strongly correlated Coulomb liquid to a metallic glass, which takes place in the mixed valency Fe^{3+}–Fe^{2+} system as the temperature is reduced.

By generalizing the results obtained in this paper it is possible to formulate some rules which may be useful for examining ordering in mixed valency systems. If a Coulomb pseudogap develops in the density of impurity states at the Fermi level during ordering of charged centers in a mixed valency system, then long-range ordering (a Wigner crystal) may develop in the correlated ion system as the temperature is reduced. If a correlation gap Δ develops in the density of impurity states, while the transition temperature T_c for the long-range ordering transition exceeds Δ, then the correlated ion system may transform into a Wigner crystal state. For $T_c < \Delta$ (as happens in HgSe:Fe), long-range ordering cannot occur.

The author thanks A. P. Tankevich, G. I. Kharus, and V. V. Kondrat'ev for discussing the present results and Yu. G. Cherepanov for help with the numerical calculations.

This work was supported by the INTAS program (Grant No. 93-3657 EXT).

[1] D. I. Khomskiĭ, Usp. Fiz. Nauk **129**, 443 (1979) [Sov. Phys. Usp. **22**, 379 (1979)].
[2] I. M. Tsidil'kovskiĭ, Usp. Fiz. Nauk **162**, 63 (1992) [Sov. Phys. Uspekhi **35**, 85 (1992)].
[3] F. S. Pool, J. Kossut, U. Debska, and R. Reifenberger, Phys. Rev. B **35**, 3900 (1987).
[4] I. G. Kuleev, I. I. Lyapilin, A. T. Lonchakov, and I. M. Tsidil'kovskiĭ, Zh. Éksp. Teor. Fiz. **102**, 63 (1992) [Sov. Phys. JETP **75**, 893 (1992)].
[5] I. G. Kuleev, I. I. Lyapilin, A. T. Lonchakov, and I. M. Tsidil'kovskiĭ, Zh. Éksp. Teor. Fiz. **103**, 1447 (1993) [JETP **76**, 707 (1993)].
[6] I. G. Kuleev, I. I. Lyapilin, A. T. Lonchakov, and I. M. Tsidil'kovskiĭ, Fiz. Tekhn. Poluprovodn. **28**, 937 (1994) [Semiconductors **28**, 544 (1994)].
[7] I. G. Kuleev, I. I. Lyapilin, A. T. Lonchakov, and I. M. Tsidil'kovskiĭ, Zh. Éksp. Teor. Fiz. **106**, 1205 (1994) [JETP **79**, 653 (1994)].
[8] I. G. Kuleyev, I. I. Lyapilin, A. T. Lonchakov, and I. M. Tsidilkovskiĭ, Semiconductors **10**, 314 (1995).
[9] J. Mycielski, Solid State Commun. **60**, 165 (1986).
[10] Z. Wilamowski, K. Swaitek, T. Dietl, and J. Kossut, Solid State Commun. **74**, 833 (1990).
[11] Z. Wilamowski, Acta Phys. Polon. A **77**, 133 (1990).
[12] Z. Wilamowski, A. Micelski, W. Jantsch, and G. Hendorfer, Acta Phys. Polon. A **77**, 133 (1990).
[13] B. I. Shklovskiĭ and A. L. Éfros, *Electronic Properties of Doped Semiconductors*, Springer, N.Y. (1984).
[14] V. L. Nguen, M. É. Raĭkh, and A. L. Éfros, Fiz. Tverd. Tela **28**, 2019 (1986) [Sov. Phys. Solid State **28**, 1129 (1986)].
[15] J. Ziman, *Models of Disorder*, Cambridge Univ. Press (1979).
[16] I. G. Kuleev, Fiz. Tverd. Tela **39**, 250 (1997) [Phys. Solid State **39**, 219 (1997)].
[17] E. I. Khar'kov, V. I. Lysov, and V. E. Fedorov, *The Physics of Fluid Materials* [in Russian], Vishcha Shk., Kiev (1979).
[18] N. N. Ablyazov and A. L. Éfros, Zh. Éksp. Teor. Fiz. **95**, 1450 (1989) [Sov. Phys. JETP **68**, 837 (1989)].
[19] I. M. Tsidil'kovskiĭ, I. G. Kuleev, and I. I. Lyapilin, Zh. Éksp. Teor. Fiz. **102**, 26 (1992) [JETP **75**, 14 (1992)].
[20] I. G. Kuleev, I. I. Lyapilin, and I. M. Tsidil'kovskiĭ, Fiz. Tverd. Tela **37**, 2360 (1995) [Phys. Solid State **37**, 1291 (1995)].
[21] L. S. Ornsetin and F. Zernicke, Proc. Acad. Sci. Amsterdam **17**, 793 (1914).
[22] E. L. Pollock and J. P. Hansen, Phys. Rev. A **8**, 3110 (1973).
[23] W. Ebeling, W. Kraeft, and D. Kremp, *Theory of Bound States and Ionization Equilibrium in Plasmas and Solids*, Akademie Verlag, Berlin (1976).
[24] T. Dietl and W. Szymanska, J. Phys. Chem. Solids **39**, 1041 (1978).
[25] I. G. Kuleev, N. K. Lerinman, I. I. Lyapilin, L. D. Sabrizyanova, and I. M. Tsidil'kovskiĭ, Fiz. Tekhn. Poluprovodn. **27**, 519 (1993) [Semiconductors **27**, 292 (1993)].
[26] *Amorphous Metal Alloys* [in Russian], Metallurgiya, Moscow (1987).
[27] N. H. March, R. A. Street, and M. Tosi, Eds., *Amorphous Solids and the Liquid State*, Plenum, N.Y. (1985).

Translated by D. H. McNeill

Mott transitions in heavily doped magnetic semiconductors

É. L. Nagaev

Institute of High Pressure Physics, Russian Academy of Sciences, 142092 Troitsk, Moscow Region, Russia
(Submitted January 4, 1997; resubmitted September 11, 1997)
Fiz. Tverd. Tela (St. Petersburg) **40**, 433–437 (March 1998)

A generalization applicable to magnetic semiconductors is proposed for the Mott criterion for transitions of heavily doped semiconductors from an insulating into a highly conducting state. Based on this generalization, a study is made of insulator–metal transitions in a ferromagnetic semiconductor associated with temperature variations and of insulator–metal transitions in an antiferromagnetic semiconductor acted on by a magnetic field. These results are of independent interest for nondegenerate semiconductors as well, since they yield the temperature and field dependence for the impurity state radii and for the energies and magnetizations of unionized donors or acceptors. © *1998 American Institute of Physics.* [S1063-7834(98)00803-X]

Many heavily doped magnetic semiconductors undergo a transition from a highly conducting to an insulating state when the type of magnetic ordering is changed or when the ordering is destroyed. For example, within a certain range of donor impurities as the temperature is raised the ferromagnetic semiconductor EuO experiences a transition from a highly conducting state into an insulating state in which the jump in resistance is a record 19 orders of magnitude.[1] As the temperature is raised further, samples with a high impurity content pass through a peak resistance in the neighborhood of the Curie point T_C and return to a highly conducting state, while samples with a lower impurity content remain in an insulating state up to the highest temperatures. Similar, although less marked resistive singularities occur in the manganites ($La_{1-x}Ca_xMnO_3$, etc.). (See the review by Nagaev.[2])

In some manganites magnetic fields are found to induce a transition from an insulating to a highly conducting state. It occurs simultaneously with a discontinuous transition from the antiferromagnetic into the ferromagnetic state, e.g., in $Pr_{1-x}Ca_xMnO_3$ with $0.3 \leqslant x \leqslant 0.5$.[2]

The nature of the insulator–metal transitions which occur as the temperature is changed is the following:[3] the radius of the electron orbit at a donor in a ferromagnetic semiconductor is smaller for finite temperatures than for $T=0$ because of enhanced magnetization in the neighborhood of the donor owing to indirect exchange between d-spins through the donor electron. The difference between the magnetization averaged over the crystal and the local magnetization in the neighborhood of the donor is greatest for temperatures close to T_C. Thus, if the Mott criterion (1) is satisfied at $T=0$, it may cease to be valid in the neighborhood of T_C, and as the temperature increases a transition from the metallic to the insulating state should take place.

It might be supposed that a reverse transition should occur at very high temperatures, since a correlation between spins is absent everywhere, including the neighborhood of donors or acceptors. It will be shown below, however, that the low-temperature radius actually exceeds the high-temperature one, so that the system may remain in an insulating state up to very high temperatures.

The simplest theory of insulator–metal transitions induced by a magnetic field is the following: As first shown by Irkhin,[4] a gap appears in the conduction band for antiferromagnetic ordering. When the band is half filled, the lower subband is completely filled and is separated by a gap from the upper subband, i.e., the system is in an insulating state. When a ferromagnetic ordering is established, the gap vanishes and the crystal becomes highly conducting. This simple theory, however, is clearly inadequate for systems in which the conduction band is much less than half full.

In this paper a theoretical interpretation of these transitions is given under conditions such that the conduction band is far less than half filled. A mechanism is proposed for these transitions based on the development of a local magnetization in the neighborhood of a defect and the smoothing out of the magnetization over the crystal in an external magnetic field. This mechanism is related to that described above and operates when the impurity concentration is close to the critical value at which a Mott transition takes place. It can explain Mott transitions which occur during temperature changes, as well as in a magnetic field.

The emergence of magnetization in the neighborhood of a donor and the associated reduction in the orbital radius were first noticed in a study of an antiferromagnetic semiconductor,[5] and shortly thereafter it was pointed out[6] that the local magnetization increases near a donor in a ferromagnetic semiconductor at finite temperatures. The question of the orbital radius was not discussed there.

1. INDIRECT EXCHANGE THROUGH A LOCALIZED ELECTRON

As opposed to an Anderson transition, a Mott transition is associated only with electron correlations, and not with disorder in the positioning of impurity atoms. It is well known that, even in a periodic system of atoms far removed from one another, if the distance between them is sufficiently

 © 1998 American Institute of Physics

large, the electrons will remain localized, each at its own atom. They become delocalized when the distances $n^{-1/3}$ between atoms becomes comparable to their atomic radius a_A. As a criterion for the delocalization in nonmagnetic superconductors, Mott proposed the inequality[7]

$$n^{1/3}a_A > 0.25, \tag{1}$$

where a_A is the same as the Bohr radius $a_B = \varepsilon_0/me^2$ ($\hbar = 1$). The Mott criterion follows from the condition for the existence of a discrete level in the screened Coulomb potential of a degenerate semiconductor, i.e., from the condition of absolute instability of the metallic state. This approach, however, can hardly be viewed as rigorous, since the number of potential wells in a crystal coincides with the number of atoms and the appearance of a discrete level in an individual well by no means excludes the formation of an energy band from these levels. The Mott criterion agrees so well with experiment, that it makes sense to regard it more as empirical.

The question arises of how to extend this relationship to magnetic semiconductors, whose electrical properties affect their magnetic properties and *vice versa*. This can be attempted, taking the initial state to be either the metallic or the insulating state. The first approach,[8] like that of Mott himself, is based on the condition for appearance of a discrete level in the total potential, including the screened Coulomb and exchange potentials. As a result, in the atomic radius of Eq. (1) the actual permittivity ε_0 is replaced by an effective permittivity for a degenerate semiconductor which includes the exchange interaction between the conduction electrons and the magnetization.

Besides the fact, already mentioned above, that the appearance of an isolated discrete level is not equivalent to an insulator–metal transition, this approach has the further shortcoming that the effective permittivity has always been calculated for a highly degenerate semiconductor, i.e., assuming that the wave functions of the conduction electrons correspond to plane waves, which is hardly true near a transition boundary. Otherwise, a specific examination of an insulator–metal transition based on this generalization of the Mott criterion has not been made.

In this paper we analyze an insulator–metal transition with the insulating state as the basis. In this case, the atomic radius a_A in Eq. (1) is chosen to be the actual radius in a nondegenerate semiconductor and it, specifically, is compared with the average distance between impurities. This analysis is more physical. Besides information on the insulator–metal transition, it provides information on the properties of nondegenerate magnetic semiconductors, a topic of independent value.

The basis of this discussion is the one-electron hamiltonian in an $s-d$ model with an additional energy from the Coulomb interaction between the electron and a donor. In the coordinate representation it has the form

$$H = H_e + H_{sd} + H_{dd}, \quad H_e = -\frac{\Delta}{2m} - \frac{e^2}{\varepsilon_0 r}, \quad (\hbar = 1),$$

$$H_{sd} = -A\sum_g (\mathbf{S_g}\cdot\mathbf{s})D(\mathbf{r}-\mathbf{g}),$$

$$H_{dd} = -\frac{1}{2}\sum (\mathbf{S_g}\cdot\mathbf{S_{g+\Delta}}) - \sum (\mathbf{S_g}\cdot\mathbf{H}), \tag{2}$$

where $D(\mathbf{r}-\mathbf{g})$ equals 1 inside the unit cell $\mathbf{g}$ and zero outside it, and $\mathbf{S_g}$ and $\mathbf{s}$ are the spins of the atom ($\mathbf{g}$) and conduction electron, respectively. The interaction of the s-electron with the external magnetic field need not be written down, since it is constant for $A>0$ and a given field.

In the following we shall assume that the inequality $AS \ll W \sim 1/ma^2$ is satisfied, where a is the lattice constant and S is the spin of the magnetic atom. This condition is clearly satisfied in the europium chalcogenides.[2] In addition, it may also be satisfied in materials such as the manganites which are currently of great interest because of their enormous magnetic resistance. Although for a long time it was assumed that the holes in them move over the Mn ions, so that double exchange ($W \ll AS$) occurs in them, recent experimental data[9] indicate that they, in fact, move along the oxygen ions, which corresponds to the opposite inequality.

We begin the discussion with the long-range paramagnetic region. in order to find the ground state of an electron at a donor, we shall use a variational procedure.

Since a system of d-spins can be regarded as slow compared to the s-electron subsystem, it is natural to use an adiabatic approximation, assuming that the state of the magnetic subsystem depends on its averaged characteristics. The conditions for this are the inequalities $AS/W \ll 1$ and $IS/A \ll 1$. A test wave function is, therefore, sought in the form

$$\Psi(\mathbf{r}, S^z) = \psi(\mathbf{r})\Phi\{S^z\}, \tag{3}$$

where Φ is the normalized magnetic wave function, which will be made more specific below as a functional of the electron wave function ψ. After constructing a wave equation with the hamiltonian (2) and wave function (3), by multiplying it by ψ on the left and integrating with respect to the coordinates we obtain the wave equation for the magnetic subsystem:

$$H_\psi\Phi = (E - E_e)\Phi, \quad E_e = \int \psi^* H_e \psi d\mathbf{r},$$

$$H_\psi = -A\sum w(\mathbf{g})(\mathbf{S_g}\cdot\mathbf{s}), \quad w(g) = |\psi(\mathbf{g})|^2 a^3. \tag{4}$$

We seek a magnetic wave function of the form

$$\Phi\{S^z\} = \varphi\{S^z\}\delta(\sigma, 1/2) + \chi\{S^z\}\delta(\sigma, -1/2); \tag{5}$$

where $\delta(\sigma, \pm 1/2)$ is the s-electron spin wave function, (φ,χ) is the two component wave function of the d-spins, and $\{S^z\}$ is the set of its variables. Using Eqs. (4) and (5), we have

$$\frac{AL^+}{2}\varphi + \left(E - \frac{AL^z}{2}\right)\chi = 0,$$

$$\left(E + \frac{AL^z}{2}\right)\varphi + \frac{AL^-}{2}\chi = 0,$$

$$\mathbf{L}=\sum_{\mathbf{g}} w(\mathbf{g})\mathbf{S}_{\mathbf{g}}, \tag{6}$$

where $L^{\pm}=L^x\pm iL^y$.

Solving the system of Eqs. (6) with an accuracy of $1/(2SN_A)$, where N_A is the number of magnetic atoms over which an electron is spread at a local level, yields the following expression for the effective magnetic hamiltonian H_{me}, which has the same eigenvalues as the hamiltonian H_{ψ}, but only acts on the φ component of the wave function Φ:

$$H_{me}=\pm\frac{A}{2}\left\{\sum_{\mathbf{g},\mathbf{f}} w(\mathbf{g})w(\mathbf{f})\mathbf{S}_{\mathbf{g}}\cdot\mathbf{S}_{\mathbf{f}}\right\}^{1/2}. \tag{7}$$

The double sign in Eq. (7) corresponds to the two permitted values of the total angular momentum of the system, $L+1/2$ and $L-1/2$, obtained by adding the total momentum L of the system in this region and the electron spin. The upper and lower signs correspond to the first and second of these two values of the angular momentum, respectively. In order to confirm this directly, it is sufficient to write the indirect exchange hamiltonian H_{me} for the case of $w(\mathbf{g})=1/N_A$, retaining terms $\sim 1/N_A$,

$$H_{me}=\frac{A}{2N_A}\left[\frac{1}{2}\mp\sqrt{L^2+\frac{1}{4}}\right], \tag{8}$$

for which the exact eigenvalues are $-AL/2$ and $A(L+1)/2$. In deriving Eqs. (7) and (8) we have used the following equations, which are valid for any function of S^z:

$$S^-f(S^z)=f(S^z+1)S^-, \quad L^-L^+=L^2-L^z(L^z+1). \tag{9}$$

They follow from the definition of the operator S^- and the spin operator commutation rules.

Evidently, the hamiltonians (7) and (8) are isotropic, as they should be. Unlike the Heisenberg hamiltonian, they describe many-spin exchange, involving up to $N_A(N_A-1)$ d-spins, rather than bilinear exchange. The intensity of indirect exchange between spins depends on the distance between each spin and the center, rather than on the distance between spins. Thus, despite its apparently simple structure, the hamiltonians (7) and (8) are quite complicated. (The eigenvalues of the latter are known, but determining the eigenfunctions is an extremely complicated problem.)

The hamiltonians (7) and (8) give perfectly correct values of the $s-d$-exchange energy for ferromagnetic ordering. But, even for $T\to\infty$, when there is no correlation between d-spins, this energy is still nonzero. As Eq. (8) implies, then it is given by

$$E_{em}(\infty)=\mp\frac{A\sqrt{S(S+1)}}{\sqrt{N_A}}. \tag{10}$$

The physical significance of Eq. (10) becomes clear if we recall that, in accordance with mathematical statistics, a system of N noninteracting spins must have a total angular momentum on the order of $(N)^{-1/2}$ times their maximum momentum. The direction of this total angular momentum is not fixed, and fluctuates freely in space, so that its average value is zero. The spin of an s-electron, however, is always oriented parallel or antiparallel to the direction of the angular momentum and fluctuates along with it. This ensures a maximum gain in the $s-d$-exchange energy for the energetically favorable direction of the s-spin relative to the angular momentum of the localization region.

2. TEMPERATURE-INDUCED MOTT TRANSITIONS

At high temperatures, when correlations between the d-spins are weak, the magnetic hamiltonian (7) can be represented in the Heisenberg form

$$H_M=-\frac{A}{2}\sqrt{P}+H_H, \quad H_H=-\frac{1}{2}\sum_{\mathbf{f}\neq\mathbf{g}} I(\mathbf{g},\mathbf{f})\mathbf{S}_{\mathbf{g}}\cdot\mathbf{S}_{\mathbf{f}},$$

$$I(\mathbf{g},\mathbf{f})=\frac{A}{2\sqrt{P}}w_{\mathbf{g}}w_{\mathbf{f}}+I_d(\mathbf{g}-\mathbf{f}),$$

$$P=S(S+1)\sum w_{\mathbf{g}}^2, \tag{11}$$

where direct $d-d$-exchange has been taken into account. Then the free energy of the system is given by

$$F=E_e-\frac{A}{2}\sqrt{P}-T\ \ln\ \mathrm{Tr}\ \exp\left(-\frac{H_H}{T}\right). \tag{12}$$

Using the high-temperature expansions, for the first order in $1/T$ we find

$$F\approx E_e-\frac{A}{2}\sqrt{P}-NT\ \ln(2S+1)$$
$$-\frac{S^2(S+1)^2}{12T}\sum J^2(\mathbf{g},\mathbf{f}). \tag{13}$$

Equation (13) will be minimized with respect to the electron wave function ψ.

As Eq. (10) implies, $s-d$-exchange tends to reduce the size of the localization region for the s-electron, since then the $s-d$-exchange energy is lowered. According to this principle, it is appropriate to choose the orbital radius as a variational parameter in the condition for minimizing the free energy. Assuming that the electrostatic energy is much greater than the $s-d$-exchange energy for $T\to\infty$ given by Eq. (10), we seek a test electron wave function in the form

$$\psi(\mathbf{r})=C\ \exp\left(-\frac{xr}{a_B}\right), \quad C=\sqrt{\frac{x^3}{\pi a_B^3}}. \tag{14}$$

After substituting Eq. (14) in Eq. (13), using Eqs. (4) and (11), and replacing the sum over $\mathbf{g}$ in the expression for P by integration with respect to $\mathbf{r}$, we obtain

$$F\cong(x^2/2-x)\ \frac{e^2}{\varepsilon_0 a_B}-Lx^{3/2}-\frac{1}{T}$$
$$\times\left\{Mx^3+S(S+1)I_dLx^{3/2}+\frac{NI_d^2S^2(S+1)^2}{2}\right\},$$

$$L=\frac{A}{2}\sqrt{\frac{S(S+1)}{8\pi}}\left(\frac{a}{a_B}\right)^{3/2},$$

$$M=\frac{A^2S(S+1)}{384\pi}\left(\frac{a}{a_B}\right). \tag{15}$$

In writing down Eq. (15) we have used the nearest-neighbor approximation for the d-spins, along with the inequality $a_B \gg a$. For $T\to\infty$, minimizing Eq. (15) with respect to x yields

$$x_\infty=\left\{\frac{R}{2}+\sqrt{1+\frac{R^2}{4}}\right\}^2, \quad R=\frac{3\varepsilon_0 L a_B}{2e^2}. \tag{16}$$

Equation (15) can also be used to find a correction to x for finite temperatures,

$$\delta x=\frac{3Mx_\infty^2+3S(S+1)I_dLx_\infty^{3/2}/2}{N(e^2/\varepsilon_0 a_B-3L/2x_\infty^{1/2})}. \tag{17}$$

Under the above assumption that the electrostatic energy exceeds the energy of $s-d$-exchange, the denominator in Eq. (17) is positive. The sign of the numerator depends on the sign and magnitude of the direct exchange integral I_d. If it is positive or negative, but small in absolute value, then the orbital radius decreases as the temperature is lowered.

The above analysis must be supplemented by an analysis of the insulator–metal transition in the spin-wave region. If we follow the ideology of Ref. 8, then it would be sufficient for this purpose to use the expression for the effective permittivity of a degenerate ferromagnetic semiconductor given in Ref. 3. In this paper, however, in order to use Eq. (1) we have to find an expression for the donor orbit radius in a nondegenerate semiconductor.

We shall assume that the electron is uniformly distributed over a region of radius a_A. Then indirect exchange renormalizes the magnon frequencies only inside this region. For $T\gg T_C/S$, when only short wavelength magnons are important, we can use an averaged expression for the magnon frequencies,

$$\omega=\frac{A}{2N_A}+J,$$

$$J\sim IS, \quad N_A=N_Bx^3, \quad N_B=\frac{4\pi}{3}\left(\frac{a}{a_B}\right)^3. \tag{18}$$

Using the same computational scheme as in the paramagnetic region and calculating the electron energy (4) with the aid of the wave function (14), we obtain the following expression for the free energy of the system:

$$F=\left(\frac{x^2}{2}-x\right)E_B-\frac{AS}{2}+F_m(x), \quad F_m=TN_A\ln\frac{\omega}{J}. \tag{19}$$

Minimizing Eqs. (18) and (19) with respect to x, we find for low temperatures that

$$x\approx 1+4\pi T\left(\frac{a_B}{a}\right)^3\frac{d}{dN_B}\left\{N_B\ln\left(1+\frac{A}{2N_BJ}\right)\right\}. \tag{20}$$

As can be seen from Eq. (20), in the spin-wave region the orbital radius decreases as the temperature rises. Along with the above conclusion that it decreases in the paramagnetic region as the temperature is lowered, this also implies that the orbital radius should be minimal near T_C. Thus, the probability that the sample goes from a highly conducting to an insulating state is greatest there.

If, however, the sample went from a metallic to an insulating state as the temperature was raised, then it is, by no means necessary that it return to a metallic state as the temperature is raised further. As Eq. (16) implies, when $T\to\infty$ the orbital radius a_Bx is shorter than for complete ferromagnetic ordering with $x=1$. Thus, if the impurity concentration ensures a metallic state for $T=0$ (the inequality (1) is satisfied), it may be insulating for $T\to\infty$ when this inequality is violated.

3. MOTT TRANSITIONS INDUCED BY A MAGNETIC FIELD

In this section we discuss an insulator–metal transition induced by a magnetic field in an antiferromagnetic, doped semiconductor. For $T=0$ we must begin with the minimum energy condition determined by Eqs. (4) and (14) and use the fact that the atomic spin $\mathbf{g}$ forms an angle $\varphi(\mathbf{g})$ with the magnetic field and that all these angles, together with the parameter x in Eq. (14), are the variational parameters,

$$E=\left(\frac{x^2}{2}-x\right)E_B-\sum H_e(\mathbf{g})S\cos\varphi(\mathbf{g})$$
$$-\frac{IS^2}{2}\sum\cos[\varphi(\mathbf{g})+\varphi(\mathbf{g}+\mathbf{\Delta})],$$
$$E_B=\frac{e^2}{\varepsilon_0 a_B}, \quad H_e(\mathbf{g})=H+\frac{A\psi^2(\mathbf{g})a^3}{2}. \tag{21}$$

The energy (21) is minimized with respect to the angles under the assumptions that the Bohr radius a_B is large compared to the lattice constant a and that $x\ll a_B/a$. Then $\varphi(\mathbf{g}+\mathbf{\Delta})$ can be replaced by $\varphi(\mathbf{g})$ in Eq. (21), after which we obtain

$$\cos\varphi(\mathbf{g})=\frac{H_e(\mathbf{g})}{H_F}\Theta\{H_F-H_e(\mathbf{g})\}+\Theta\{H_e(\mathbf{g})-H_F\},$$
$$H_F=-2IS_z, \tag{22}$$

where $\Theta(x)$ is the Heaviside step function and z is the number of nearest neighbors ($I<0$). The cases with $H_F<H_e(0)$ and its opposite must be distinguished. In the first case, there exists a region of full ferromagnetic ordering whose radius h is determined by the condition $H_F=H_e(h)$. At distances greater than h from the donor center, a skewed antiferromagnetic ordering is established instead of a collinear one. Equation (21) implies that

$$h=-\frac{a_B}{2x}\ln\frac{2\pi a_B^3(H_F-H)}{a^3x^3A}. \tag{23}$$

Let us first consider the case in which there is no saturated ferromagnetism. Then, according to Eqs. (21) and (22),

$$E=\left(\frac{x^2}{2}-x\right)E_B-\frac{LE_Bx^3}{3}+\text{const},$$
$$L=\frac{3A^2S^2a^3}{64\pi a_B^3E_BH_F}. \tag{24}$$

Since a minimum of E given by (24) for $x\to\infty$ has no physical significance because of the condition $x\ll a_b/a$ used above, it is sufficient to consider only a minimum in x near unity. On the other hand, if there is no ferromagnetic region, then Eqs. (23) and (24) imply that $L\leqslant 0.01$. Then we obtain an equilibrium value of $x=1+2L$. This result already indicates that the electron orbit radius is less than that with ferromagnetic ordering ($x=1$). It should be noted that here it does not depend on the magnetic field.

The case in which a ferromagnetic region exists around the donor is more interesting. Then the energy is given by

$$E=\left(\frac{x^2}{2}-x\right)E_B-\frac{AS}{2}+\left\{\frac{2\pi h^3}{a^3}+\frac{\pi}{x^3}\right.$$
$$\left.\times\left(\frac{15}{32}+\frac{7xh}{8a_B}+\frac{3x^2h^2}{4a_B^2}\right)\left(\frac{a_B}{a}\right)^3\right\}\frac{2(H_F-H)^2S^2}{H_F}. \tag{25}$$

In place of Eq. (23), we can write, to within logarithmic terms,

$$h\approx\frac{a_Bk}{2x},\quad k=-\ln\frac{2\pi a_B^3(H_F-H)}{a^3A}.$$

Hence, we obtain

$$E=\left(\frac{x^2}{2}-x\right)E_B+\frac{K(H_F-H)^2}{3x^3},$$
$$K=\frac{6\pi S^2a_B^3}{H_Fa^3}\left(\frac{15}{32}+\frac{7k}{16}+\frac{3k^2}{16}+2k^3\right). \tag{26}$$

After minimizing the energy (26) with respect to x, we have

$$x=1+K(H_F-H)^2/E_B,\quad H\to H_F,$$
$$x\approx[K(H_F-H)^2/E_B]^{1/5},\quad x\gg 1. \tag{27}$$

As can be seen from Eq. (27), with ferromagnetic ordering ($x=1$) the donor radius is the same as in the nonmagnetic crystal. But, as H is reduced this radius becomes smaller. Thus, while the Mott condition (1) is not satisfied in the antiferromagnetic state, it may be satisfied in the ferromagnetic state; this implies an insulator–metal transition induced by the magnetic field. Certainly, the field at which the Mott condition begins to be satisfied does depend on the impurity concentration. However, in analyzing experimental data it should be kept in mind that, in general, not all the atoms introduced into a crystal are electrically active. If they form clusters, then they cannot serve as suppliers of free charge carriers. Therefore, the number of impurity atoms which are isolated from others may be several orders of magnitude lower than the total number of impurity atoms.

[1] M. Oliver *et al.*, Phys. Rev. Lett. **24**, 1064 (1970); T. Penny *et al.*, Phys. Rev. B **5**, 3669 (1972); Y. Shapira *et al.*, Phys. Rev. B **8**, 2299 (1973).
[2] É. L. Nagaev, Usp. Fiz. Nauk **166**, 833 (1996).
[3] É. L. Nagaev, *The Physics of Magnetic Semiconductors*, Mir, Moscow (1983); Nauka, Moscow (1979) [in Russian].
[4] Yu. P. Irkhin, Fiz. Met. Metalloved. **6**, 214, 586 (1958).
[5] É. L. Nagaev, Zh. Éksp. Teor. Fiz. **54**, 228 (1968) [Sov. Phys. JETP **27**, 122 (1968)].
[6] A. Janase and T. Kasuya, J. Phys. Soc. Jpn. **25**, 1025 (1968).
[7] N. Mott and E. Davis, *Electronic Processes in Noncrystalline Materials*, Oxford (1971).
[8] É. L. Nagaev, Zh. Éksp. Teor. Fiz. **90**, 652 (1986) [Sov. Phys. JETP **63**, 379 (1986)]; *ibid.* **65**, 322 (1986); *ibid.* **92**, 569 (1987).
[9] T. Saitoh *et al.*, Phys. Rev. B **51**, 13942 (1995).

Translated by D. H. McNeill

Long-range structural interaction effect in gallium arsenide during ion bombardment

N. A. Bert, I. P. Soshnikov, and M. G. Stepanova

A. F. Ioffe Physicotechnical Institute, Russian Academy of Sciences, 194021 St. Petersburg, Russia
(Submitted October 16, 1997)
Fiz. Tverd. Tela (St. Petersburg) **40**, 438–440 (March 1998)

Transmission electron microscopy is used to study changes in the structure of gallium arsenide samples after bombardment by high doses of 5 keV argon ions. A change in the structure of the samples is observed at depths exceeding the average penetration depth of the ions by an order of magnitude. A model is proposed to explain the long-range structural interaction effect in gallium arsenide in terms of a phase transition induced by elastic stresses in the sample.
© *1998 American Institute of Physics.* [S1063-7834(98)00903-4]

A change in the composition of GaAs samples bombarded with high doses of 5 keV argon ions has been observed[1] at depths of 100 nm and more, which is an order of magnitude greater than the average penetration depth of the ions in the target. This effect is not consistent with traditional ideas about the formation of an altered layer during ion bombardment[2,3] and requires deeper study. In this paper transmission electron microscopy is used to study the structure of the altered layer in GaAs samples and a model is developed for its formation.

Sample targets were cut from standard chemically polished AGChT and AgChO gallium arsenide slabs ($n \sim 10^{14} - 10^{16}$ cm^{-3}). Then the samples were subjected to ion bombardment in a special device, described elsewhere,[2] which produces an ion beam with an energy of 5 keV and a current density of 150 μA/cm^2 in a 5 mm diameter spot. A standard method of sample preparation without ion etching was used in the transmission electron microscopic studies. The sample surfaces coincided with the (100) crystallographic plane.

The structures of the irradiated samples were studied on a Philips EM-420 transmission electron microscope. These studies showed that for irradiation doses of up to 10^{18} ion cm^{-2} the altered layer consists of an amorphized region with a thickness of roughly 15 nm. The development of this region is associated with cascade mixing. As the dose is increased over the range $10^{18} - 3.5 \times 10^{19}$ ion/cm^2, yet another region with structural damage is formed under the amorphized layer. Figure 1 shows that the structure of this region differs from that of the amorphized surface layer.

The characteristic feature of the second region is an increase in its thickness with rising irradiation dose. The transmission electron microscope studies showed that for a dose of 0.9×10^{19} ion/cm^2, the lower boundary of the altered layer lies at a depth of about 40 nm, while for a dose of 3.5×10^{19} ion/cm^2 it lies at a depth of 140 nm, substantially deeper than the penetration depth of the ions in the target. The rate at which the altered layer thickens was roughly 0.15 nm/min, in agreement with previous data on changes in the composition of GaAs samples.[1] The long-range structural interaction effect in gallium arsenide was first observed there.

These results cannot be explained in terms of the traditional theory of the formation of an altered layer during ion bombardment.[3,4] The theoretical model developed here explains the formation of a second region in the altered layer of GaAs as a phase transition induced by elastic stresses.

It is known[3,5] that cascade mixing causes formation of a region of higher density in a target. It has been shown[5] that radiation- enhanced diffusion may cause the high-density region to propagate far beyond the confines of the average penetration depth of the ions (Fig. 2). It is assumed that in the high-density region a phase precipitates out with a higher equilibrium density than that of GaAs. This assumption makes it possible to explain the formation of a second damaged region and its anomalous thickness.

In this paper we model numerically the change in the atomic concentrations of Ga and As in crystalline GaAs (the c phase) and in a new precipitate phase (the p phase) under ion bombardment conditions identical to those in the experiment. Thus, the equation for the atomic density of the components of the precipitate, $N_{ic}(x,t)$ (i = Ga, As) has the form

$$\left(\frac{\partial}{\partial t} - V\frac{\partial}{\partial x}\right)N_{ic}(x,t) = K_{cp}N_{ic}(x,t) - \delta(x)JY_{ic}\Omega N_{ic}(x,t) - \frac{\partial}{\partial x}[J^m_{ip}(x,t) + J^d_{ip}(x,t)], \quad (1)$$

where V is the rate of displacement of the sputtered surface, Y_{ic} is the sputtering coefficient of component i, $\delta(x)$ is the delta function, $J^m(x,t)$ is the flux of material associated with cascade mixing, which as calculated in a diffusion approximation,[6] $J^d(x,t)$ is the flux of material associated with radiation enhanced diffusion,[5,6]

$$J^d_{ip}(x,t) = -\frac{D^r_{ip}(x,t)}{kT}N_{ip}(x,t)\Omega_{ip}\frac{\partial}{\partial x}\sigma(x,t) - \frac{\partial}{\partial x}[D^d_{ip}(x,t)N_{ip}(x,t)], \quad (2)$$

where D^r_{ip} and D^d_{ip} are the effective diffusion coefficients, Ω_{ip} is the atomic volume, and σ is the first invariant of the elastic stress tensor. (See the variation in $\sigma(x)$ in Fig. 2.) The

 © 1998 American Institute of Physics

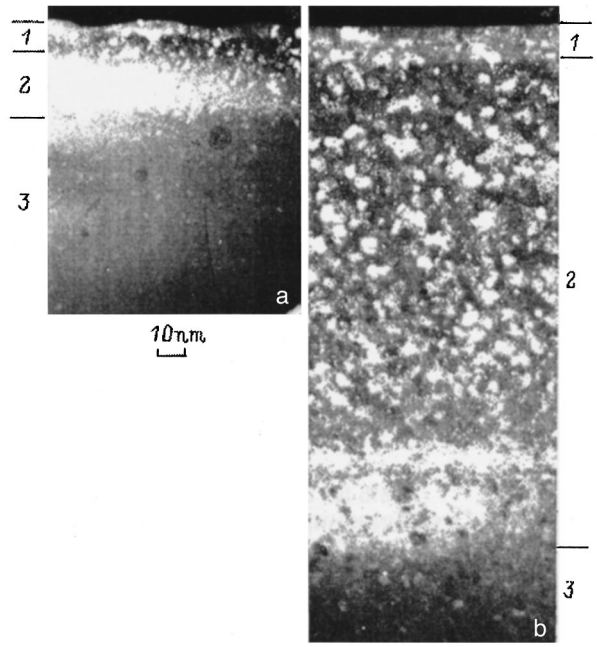

FIG. 1. Dark field images of the transverse cross section of samples irradiated with 5 keV Ar^+ ions to doses of 0.9×10^{19} (a) and 3.5×10^{19} cm^{-3} (b). (*1*) cascade mixing region, (*2*) long-range ''structural'' interaction region, (*3*) crystalline GaAs.

term $K_{cp}N_{ic}(x,t)$ in Eq. (1) describes the $c\rightarrow p$ phase transition (in the region $\sigma>0$ of Fig. 2) and K_{cp} is a phenomenological coefficient.

It has been shown that the model (1) allows two different regimes for the evolution of the concentration profile $C_p(x,t)$ of the precipitate phase $(C_p(x,t)=(N_{Gap}(x,t)+N_{Asp}(x,t))/\Sigma N)$. In the first case, over 10–15 min a steady-state concentration distribution $C_p(x)$ develops. This regime is typical of the formation of an altered layer during ion bombardment.[3,4] The second regime consists of an intense propagation of the $c\rightarrow p$ phase transition which encompasses the entire sample over these minutes. Here the speed of the ''front'' of the $C_p(x,t)$ profile can reach 1 nm/s. A necessary condition for this regime is that the $c\rightarrow p$ phase transition be autocatalytic $(K_{cp}=K_0C_p(x,t))$, and that the diffusion coefficients for the components in phase p be large.

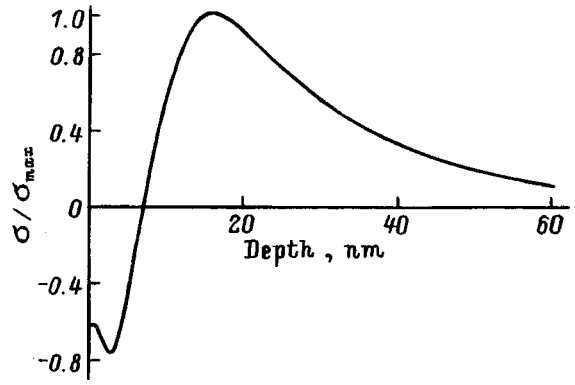

FIG. 2. The stress σ as a function of depth x in GaAs during bombardment by 5 keV, normally incident Ar^+ ions. (Calculation according to the model discussed in Ref. 5.)

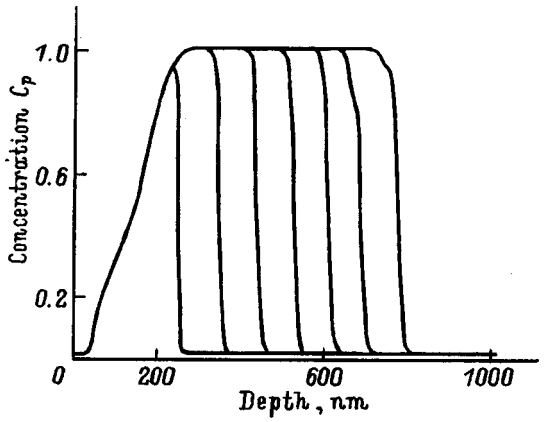

FIG. 3. Profiles of the concentration $C_p(x,t)$ at times $t=1$, 2, 3, 4, 5, and 6 h after the onset of ion bombardment. (Calculation using the model Eqs. (1) and (2)).

As D_{ip}^r and D_{ip}^d increase, there is a sharp transition from the first to the second regime. In models of autocatalytic processes the unbounded propagation of a phase transition (reaction) front is known as a ''Kolomogorov–Petrov–Piskunov wave'' (KPP wave).[7,8]

Since the experimentally observed propagation speed of the second altered region is two orders of magnitude less than the theoretical speed of the phase transition front in the KPP wave regime, the model equation (1) was supplemented by the assumption that the diffusion coefficients D_{ip}^r and D_{ip}^d $(i=\mathrm{Ga},\ \mathrm{As})$ vary across the front. It was assumed that when the concentration C_p exceeds some arbitrary value $C_{\min}$, a structural realignment makes the diffusion coefficients D increase (we omit the labels for simplicity) from their initial values $D_{\min}$ (for which the first regime occurs) to $D_{\max}$ (when a KPP wave develops) according to

$$\tau=\frac{\partial}{\partial x}D(x,t)=D_{\max}-D(x,t) \tag{3}$$

over a characteristic time τ. This made it possible to describe the smooth propagation of the phase decomposition region at a speed which depends on the delay time τ.

Figure 3 illustrates the steady expansion of the concentration profile $C_p(x,t)$ of the precipitate phase over 6 h of ion bombardment with a delay time $\tau=100$ s. The calculations also showed that the propagation speed of the front is inversely proportional to τ.

Thus, the proposed model of an autocatalytic phase decomposition with retarded diffusion provides a qualitative explanation of the experimentally observed long-range structural interaction in gallium arsenide associated with ion bombardment and gives a rate of thickening of the altered layer that is of the same order of magnitude as observed experimentally. This sort of model has not been used before in the theory of the formation of the altered layer.

The possible character of the phase transition has not been discussed in detail so far, since this question is of minor

importance for a qualitative theoretical model. One possibility is that it is the decomposition GaAs→Ga+As, since the atomic density of pure gallium and arsenic are lower than that of GaAs. An experimental test of this proposition is an important topic for further study.

This work was supported by the Russian Fund for Fundamental Research (Grant N 95-03-09617a).

[1] N. A. Bert, K. Yu. Pogrebitskiĭ, I. P. Soshnikov, and Yu. N. Yur'ev, Zh. Tekh. Fiz. **62**(4), 162 (1992) [Tech. Phys. **37**, 449 (1992)].
[2] N. A. Bert and I. P. Soshnikov, Fiz. Tverd. Tela **35**, 2500 (1993) [Phys. Solid State **35**, 1239 (1993)].
[3] P. Sigmund and N. Q. Lam, Mat. Fys. Medd. K. Dan. Vidensk. Selsk. **43**, 255 (1993).
[4] G. Betz and G. Wener, in *Sputtering by Particle Bombardment*, R. Behrisch (Ed.), Plenum, N.Y. (1983), Vol. 2.
[5] M. G. Stepanova, Izv. RAN Ser. Fiz. **56**(6), 53 (1992).
[6] M. G. Stepanova, Nucl. Instrum. Methods **95**, 481 (1995).
[7] A. N. Kolmogorov, I. G. Petrovskiĭ, and N. S. Piskunov, Byul. MGU **1**(6), 1 (1937).
[8] T. S. Akhromeeva, S. P. Kurdyumov, G. G. Malinetskiĭ, and A. A. Samarskiĭ, *Nonstationary Structures and Diffusional Chaos* [in Russian], Nauka, Moscow (1992), p. 22.

Translated by D. H. McNeill

Effect of Ti on the galvanomagnetic properties of single-crystal $Sb_{2-x}Ti_xTe_3$

V. A. Kul'bachinskiĭ, G. V. Zemitan, Ç. Drašar, and P. Lošťák

Moscow State University, 119899 Moscow, Russia

(Submitted June 24, 1997; resubmitted November 13, 1997)
Fiz. Tverd. Tela (St. Petersburg) **40**, 441–444 (March 1998)

A study is reported of the lattice parameters, Hall effect, Shubnikov–de Haas effect, and thermopower of single-crystal $Sb_{2-x}Ti_xTe_3$ as functions of titanium content within the range $0<x<0.04$. An increase in titanium content is shown to decrease the initial hole concentration in a sample without a noticeable change of the energy spectrum. © *1998 American Institute of Physics.* [S1063-7834(98)01003-X]

Tellurides of bismuth, Bi_2Te_3, and of antimony, Sb_2Te_3, and their solid solutions are widely used in thermoelectric devices. The Sb_2Te_3 lattice represents a set of complex quintet layers alternating in the order Te(1)–Sb–Te(2) –Sb–Te(1), where the figures (1) and (2) refer to different Te positions in the lattice. Studies[1–4] of the valence band of Sb_2Te_3 established the existence of two valence bands and the validity of the Drabble–Wolf six-ellipsoid model[5] for the Fermi surface of the upper valence band.[6–10] Characteristic point defects associated with Sb atoms occupying Te positions (antisites) result in *p* conduction of single-crystal Sb_2Te_3 and a high hole concentration, up to 10^{20} cm^{-3}. Doping Sb_2Te_3 with metals permits one to obtain materials with desired physical parameters, such as electrical and heat conductivity, hole mobility, and thermopower, which are essential for development of thermoelectric devices. Incorporation of metal atoms, for instance, of In, into the Sb sublattice increases the polarity of the Sb–Te bond, which reduces the antisite concentration and, hence, the concentration of holes.[6–10] The hole mobility in $In_xSb_{2-x}Te_3$ crystals, however, decreases rapidly with increasing In concentration.

This work studies the effect of titanium on galvanomagnetic properties in the temperature range $4.2<T<300$ K, Shubnikov–de Haas effect, lattice parameters, and thermopower of single-crystal $Sb_{2-x}Ti_xTe_3$ ($0\leqslant x\leqslant 0.04$).

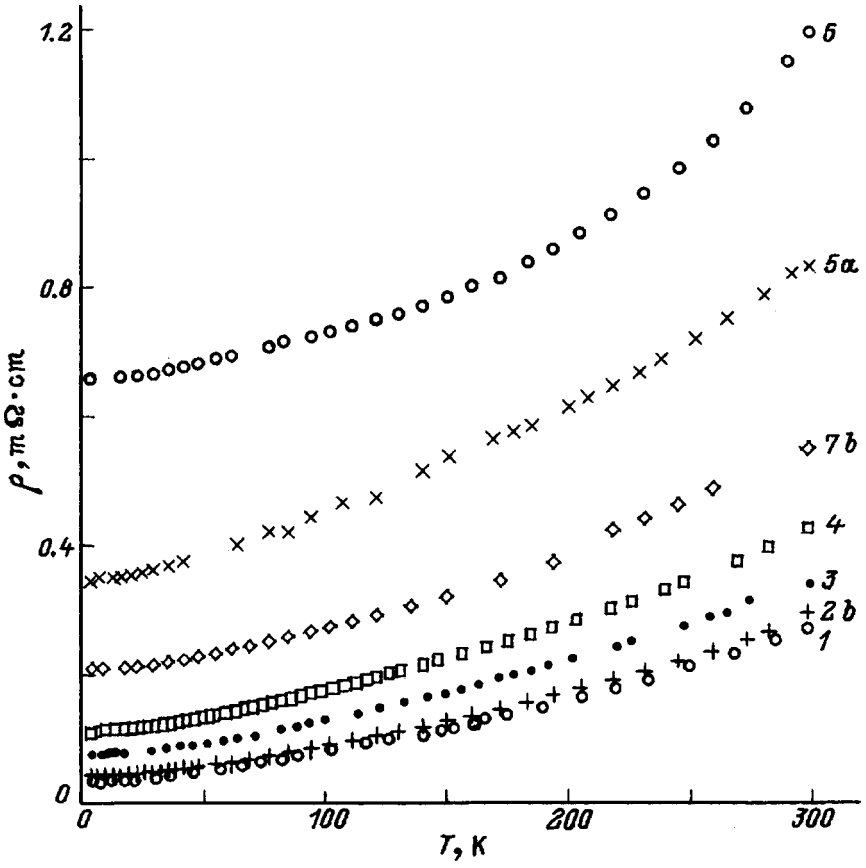

FIG. 1. Temperature dependence of the resistivity of $Sb_{2-x}Ti_xTe_3$ samples. The curves are numbered in accordance with Table II.

 © 1998 American Institute of Physics

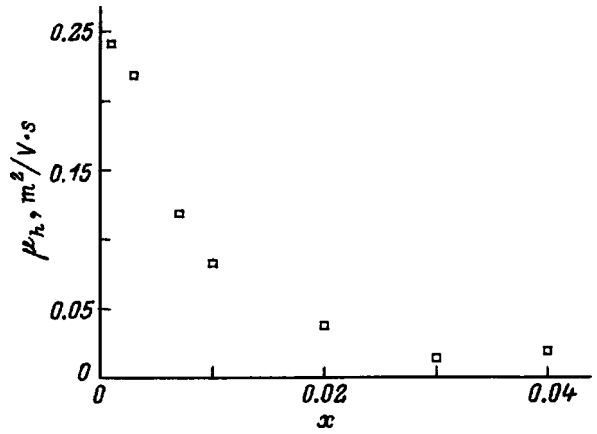

FIG. 2. Hall mobility μ_h of $Sb_{2-x}Ti_xTe_3$ samples vs Ti concentration x at 4.2 K.

1. SAMPLES AND MEASUREMENT TECHNIQUES

$Sb_{2-x}Ti_xTe_3$ single crystals were grown in two stages. First polycrystalline $TiTe_2$ was prepared from 99.999%-pure elemental Te and Ti taken in stoichiometric ratio, by maintaining the mixture at 1100 °C for five days. Analysis showed the $TiTe_2$ synthesized in these conditions to be single phase. Next Sb, Te, and $TiTe_2$ were mixed in the ratio corresponding to the atomic composition (Sb+Ti)/Te=2/3, and the mixture was maintained at 800 °C for two days to produce polycrystalline $Sb_{2-x}Ti_xTe_3$. Single crystals were prepared by directed crystallization by the modified Bridgman method at a temperature gradient of 400 K/cm and with a rate of 0.13 cm/h. The single crystals thus grown were annealed at I=730 °C and removed from the ampoule. The C axis was always perpendicular to the pulling direction. The starting concentration of Ti was determined by the batch composition and refined by microprobe analysis. Samples measuring $0.8\times0.8\times5$ mm were spark cut from the ingots, and six contacts (two current and four potential ones) were soldered to them. The current was passed along the twofold axis, and the magnetic field B was oriented along the trigonal axis. A superconducting coil was used to generate magnetic fields of up to 10 T.

The lattice parameters a and c and the unit cell volume V are presented in Table I as functions of measured Ti concentration in $Sb_{2-x}Ti_xTe_3$. Both parameters and the cell volume are seen to decrease with increasing x. We studied the room-temperature thermopower, temperature behavior of resistivity within the range $4.2<T<300$ K, Hall effect, magnetoresistance and Shubnikov–de Haas effect on $Sb_{2-x}Ti_xTe_3$ samples with seven different compositions within the range $0.001\leqslant x\leqslant0.04$. Some of the parameters of these samples are given in Table II.

TABLE I. Lattice parameters a and c of single-crystal $Sb_{2-x}Ti_xTe_3$ at room temperature.

x	Ti atom concentration 10^{19} cm^{-3}	a, nm	c, nm	V, nm^3
0	0	0.42648(3)	3.0450(1)	0.47964(6)
0.001	0.14	0.42657(4)	3.0443(2)	0.47973(9)
0.007	0.97	0.42649(3)	3.0440(2)	0.47950(7)
0.01	6.2	0.42641(4)	3.0438(2)	0.47930(9)
0.02	10.1	0.42635(3)	3.0441(2)	0.47920(7)
0.04	19.0	0.42633(3)	3.0440(2)	0.47914(8)

2. MEASUREMENT RESULTS AND THEIR DISCUSSION

Figure 1 displays the temperature behavior of the resistivity of the samples. One observes a decrease in resistivity with decreasing temperature, which is characteristic of antimony telluride with a high hole concentration. As the titanium content increases, the sample resistivity grows for all temperatures. This reflects the fact that an increase in titanium content reduces the hole concentration in the crystals. This follows both from the increase in resistivity and from the data on the dependence of the Hall coefficient on Ti content (see Table II). The temperature dependence of the Hall coefficient R_h exhibits an interesting feature, namely, for most samples R_h decreases with temperature decreasing down to $\approx$77 K, after which it practically does not change. If there were only one type of carriers present, this would result in a paradoxical growth of their concentration with decreasing temperature. For holes of two types, light and heavy, whose existence in antimony telluride was established earlier[1,2] and whose parameters were measured,[1,3,4,7,9] such a behavior of $R_h(T)$ allows quantitative explanation. Within this approach, the mobilities of both light and heavy holes

TABLE II. Characteristics of $Sb_{2-x}Ti_x$ samples.

Sample No.	x	$\rho^{300}/\rho^{4.2}$	$R_h^{4.2}$, cm^3/C	R_h^{300}, cm^3/C	$\mu_h^{4.2}$, m^2/V·s	μ_h^{300}, m^2/V·s	Thermopower, μV/K (at 300 K)
1	0.001	7.91	0.082	0.082	0.2412	0.0305	80
2*a*	0.003	6.86	0.035	-	-	-	-
2*b*	0.003	6.70	0.094	0.080	0.2186	0.0277	-
3	0.007	4.46	0.090	0.168	0.1184	0.0496	103
4	0.01	3.87	0.091	0.216	0.0827	0.0507	95
5*a*	0.02	2.41	0.131	0.363	0.0379	0.0436	99
5*b*	0.02	3.29	0.061	-	-	-	-
6	0.03	1.81	0.098	-	0.0144	-	-
7*a*	0.04	2.60	0.034	-	-	-	-
7*b*	0.04	2.44	0.049	0.107	0.0191	0.0170	94

Note: $\rho^{300}/\rho^{4.2}$ is the ratio of resistivities at 300 and 4.2 K. $R_h^{4.2}$ and R_h^{300} are the Hall coefficients, and $\mu_h^{4.2}$ and μ_h^{300}, the Hall mobilities at 4.2 and 300 K, respectively.

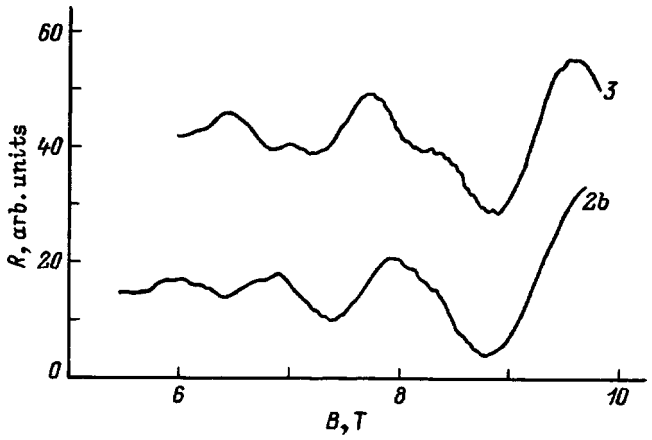

FIG. 3. Shubnikov-de Haas oscillations of the transverse magnetoresistance of $Sb_{2-x}Ti_xTe_3$ samples *2b* and 3 obtained at $T=4.2$ K in a magnetic field oriented parallel to the *C* axis.

are found to grow with decreasing temperature, while their concentrations do not change. The Hall mobilities μ_h in the samples are presented in Fig. 2 as functions of Ti content. Similar to the case of doping with In (Ref. 7–9), μ_h in $Sb_{2-x}Ti_xTe_3$ decreases with increasing x, but not so strongly as it does in $In_xSb_{2-x}Te_3$.

Room-temperature measurements of thermopower showed that it decreases insignificantly with increasing titanium concentration in the samples. These data are listed in Table II.

The energy spectrum of the $Sb_{2-x}Ti_xTe_3$ samples was measured using the Shubnikov–de Haas effect. Figure 3 illustrates oscillations of transverse magnetoresistance in two $Sb_{2-x}Ti_xTe_3$ samples with $x=0.003$ (No. 2) and $x=0.007$, with the magnetic field directed along the *C* axis (i.e. perpendicular to the layers). For this orientation, all six extremal cross-sections *S* of the Fermi surface coincide. Note the spin splitting observed in the oscillations. Figure 4 shows the dependence of the cross-sectional area *S* on titanium content *x*. The cross-sectional area is seen to decrease with increasing *x*. A quantitative comparison of Hall and Shubnikov–de Haas measurements requires the knowledge of the Fermi surface anisotropy. We did not succeed in studying the angular dependence of the extremal cross-sectional areas in $Sb_{2-x}In_xTe_3$ because the magnetic field range covered was too narrow. Qualitative estimates can be made based on Refs. 1, 3. The ellipsoidal nonparabolic model describes satisfactorily the energy spectrum of light holes in Sb_2Te_3. This model gives the following dispersion law:

$$E(k)=\hbar^2/2m(\alpha_{11}k_1^2+\alpha_{22}k_2^2+\alpha_{33}k_3^2+\alpha_{23}k_2k_3), \qquad (1)$$

where the components α_{ij} of the reciprocal effective-mass tensor depend on energy, and k_1,k_2,k_3 are parallel to the twofold, bisector, and trigonal crystal axes, respectively. The tilt angle θ of the ellipsoid can be expressed through α_{ij}

$$\tan(2\theta)=2\alpha_{23}/(\alpha_{33}-\alpha_{22}), \qquad (2)$$

and the period of Shubnikov–de Haas oscillations $\Delta(1/B)$ is related to parameters α_{ij} through

$$\Delta(1/B)=e\hbar/m_0E_F[(\alpha_{22}\alpha_{33}-\alpha_{23}^2)\times\cos^2\alpha+\alpha_{11}\alpha_{33}\cos^2\beta+\alpha_{11}\alpha_{22}\times\cos^2\gamma-2\alpha_{11}\alpha_{23}\cos\beta\cos\gamma]^{1/2}, \qquad (3)$$

where $\cos\alpha$,$\cos\beta$,$\cos\gamma$ are the cosines of the angles between the magnetic field and axes 1, 2, and 3. As follows from our study of the Shubnikov–de Haas effect, in $Sb_{2-x}Ti_xTe_3$ single crystals the Fermi surface of light holes can be described in terms of a six-ellipsoid model. Similar to Sb_2Te_3 (Ref. 3), we take the tilt angle of the ellipsoids to be $\approx 50°$. The hole concentrations in the upper valence band were calculated using Eqs. (1)–(3). Calculations made with the energy spectrum parameters α_{ij} determined in Ref. 3 show that the change in hole concentration can be described in terms of the decrease in Fermi energy in $Sb_{2-x}Ti_xTe_3$ within the rigid-band model, i.e., if one assumes that the anisotropy and the tilt angles of the Fermi surface ellipsoids do not change with hole concentration.

Thus we have established that incorporation of Ti atoms into the Sb sublattice reduces the initial hole concentration in Sb_2Te_3, which means that Ti behaves as a donor. It may be conjectured that titanium, similar to indium, suppresses formation of antisites, and this accounts for its donor action. The carrier mobility in $Sb_{2-x}Ti_xTe_3$ single crystals decreases a few times at the maximum concentration $x=0.04$, whereas in $Sb_{2-x}In_xTe_3$ it drops by two orders of magnitude.[9,10] An increase in Ti concentration reduces the Fermi energy in $Sb_{2-x}Ti_xTe_3$, but the energy spectrum does not change, namely, for the upper valence band (light holes) the Fermi surface retains the six-ellipsoid shape.

Support of the Russian Fund for Fundamental Research (Grant No. 96-15-96500) and of the NATO (Grant HTECH. CRG 960850) is gratefully acknowledged.

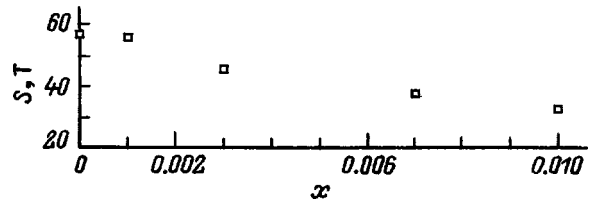

FIG. 4. The areas of the six coinciding extremal Fermi-surface cross-sections *S* for $Sb_{2-x}Ti_xTe_3$ vs Ti content *x*, obtained with magnetic field oriented parallel to the *C* axis.

[1] A. von Middendorff, K. Dietrich, and G. Landwehr, Solid State Commun. **13**, 443 (1973).
[2] M. P. Volotskiĭ, T. S. Gudkin, Z. M. Dashevskiĭ, V. I. Kaĭdanov, and I. V. Zgibnev, Fiz. Tekh. Poluprovodn. **8**, 1044 (1974) [Sov. Phys. Semicond. **8**, 682 (1974)].
[3] H. Köhler and A. Freudenberger, Phys. Status Solidi B **84**, 195 (1977).
[4] M. Stordeur, H. T. Langhammer, H. Sobotta, and V. Riede, Phys. Status Solidi B **104**, 513 (1981).
[5] J. R. Drabble and R. Wolf, Proc. R. Soc. London **69**, 1101 (1956).
[6] P. Lošťák, R. Novotný, J. Kroutil, and Z. Starý, Phys. Status Solidi A **104**, 841 (1987).

[7] P. Lošťák, Z. Starý, J. Horák, and J. Pancíř, Phys. Status Solidi A **115**, 87 (1989).
[8] V. A. Kulbachinskii, M. Inoue, M. Sasaki, H. Negishi, and W. X. Gao, in *Proceedings of the XIV International Conference Thermoelectrics*, St. Petersburg, Russia (1995), p. 151.
[9] V. A. Kul'bachinskiĭ, A. N. Chaĭka, Z. M. Dashevskiĭ, P. Lošťák, and J. Horák, Fiz. Tverd. Tela (St. Petersburg) **37**, 1997 (1995) [Phys. Solid State **37**, 1088 (1995)].
[10] V. A. Kulbachinskii, Z. M. Dashevskii, M. Inoue, M. Sasaki, H. Negishi, W. X. Gao, P. Lostak, J. Horak, and A. de Visser, Phys. Rev. B **52**, 10915 (1995).

Translated by G. Skrebtsov

Influence of structural deformations on the magnetic properties of Jahn–Teller complexes of divalent copper in $Ca_xSr_{1-x}F_2$ mixed crystals

V. A. Ulanov, M. M. Zaripov, V. A. Shustov, and I. I. Fazlizhanov

Kazan Physicotechnical Institute, Russian Academy of Sciences, 420029 Kazan, Russia
(Submitted August 27, 1997)
Fiz. Tverd. Tela (St. Petersburg) **40**, 445–451 (March 1998)

Crystals of variable constituency $Ca_xSr_{1-x}F_2$:Cu ($0 \leqslant x \leqslant 0.05$, $x \cong 0.5$, $1.0 \geqslant x \geqslant 0.95$) are investigated by EPR and x-ray structural analysis. The electron-Zeeman, intrinsic hyperfine, and ligand hyperfine interaction parameters are determined; they characterize the magnetic properties of the copper paramagnetic complexes formed in the crystals. Models of the molecular structures of these complexes are discussed, along with the influence of structural deformations and vibronic interactions on their magnetic properties. © *1998 American Institute of Physics.* [S1063-7834(98)01103-4]

The Cu^{2+} ion in the free state has the ground-state configuration $3d^9$ and the ground-state term ^2D. When it is injected as a substitutional impurity into crystals of the fluorite structural series (CdF_2, CaF_2, SrF_2, and BaF_2), it occupies a lattice cation site, where it exists in a cubic crystal field and is surrounded by eight F^- ions. This field splits the orbital states of the ground-state term of the free state into an excited doublet ^2E_g and a ground-state triplet $^2T_{2g}$. In this orbital ground state the impurity ion can interact efficiently with normal modes of neighboring fluorine nuclei of trigonal (t_{2g}) and tetragonal (e_g) symmetries. The predominant interaction with t_{2g} modes should give rise to complexes in the crystal interior that have trigonally distorted coordination cubes and, accordingly, trigonal symmetry of the low-temperature magnetic properties. If the interaction with the e_g modes dominates, complexes are formed whose magnetic properties have tetragonal symmetry. However, an intermediate case is possible, where an impurity ion in the $^2T_{2g}$ orbital ground state interacts in approximately equal measure with both modes [interaction of the type $^2T_{2g} \times (t_{2g} + e_g)$]. The coordination polyhedron of the impurity ion can undergo orthorhombic distortion in this case, and the low-temperature magnetic properties can acquire orthorhombic symmetry as a result.[1]

Electron paramagnetic resonance (EPR) studies of Jahn–Teller octacoordinated complexes of divalent copper in crystals of the fluorite structural series[2,3] have shown that their molecular structure and the symmetry of their magnetic properties depend largely on the dimensions of the impurity ion-substituted coordination cubes of lattice cations of these crystals. In CdF_2 and CaF_2 crystals, where the sides of the coordination cubes of the Cd^{2+} and Ca^{2+} cations are equal to 2.69 Å and 2.73 Å, respectively, it has been found that their replacement by Cu^{2+} impurity ions[2] leads to the formation of $[CuF_4F_4]^{6-}$ complexes with orthorhombic symmetry of the magnetic properties. The equilibrium positions of the nuclei of the eight nearest-neighbor fluorine ions in this case correspond to the vertices of a coordination polyhedron in the shape of a right rhombic prism, and the equilibrium position of the impurity ion nuclei corresponds to the centroid of this figure (Fig. 1). In these two crystals, therefore, we have a case in which an impurity ion interacts approximately equally with modes of trigonal and tetragonal symmetries.

Paramagnetic complexes of divalent copper with a totally different molecular structure have been observed[3] in SrF_2:Cu and BaF_2:Cu crystals (where the sides of the Sr^{2+} and Ba^{2+} coordination cubes are equal to 2.89 Å and 3.10 Å, respectively). In these complexes the impurity ion is situated in an off-center position, and the symmetry of the resulting complex corresponds to the C_{4v} group (Fig. 2). Consequently, here the CU^{2+} ion interacts with a tetragonal mode, the interaction being superposed on the high polarizability of the complex.

It must be emphasized that in all four of these ionic crystals the impurity ion is surrounded by the very same anions (F^-) which, before the impurity was introduced, occupied equilibrium positions corresponding to the vertices of a cube. Consequently, the main cause of the qualitative changes in the observed low-temperature magnetic properties of the divalent copper complexes formed in the transition from one crystal matrix to another, which are obviously attributable to vibronic interactions, can be interpreted as variations of the size of the coordination cube replaced by the cation impurity. A mere 0.16-Å variation in the size of this cube has produced a change in the symmetry of the molecular structure of the complex and shifted the ion-complexing agent 0.9 Å to an off-center position.

Thus, the principal changes in the molecular structure and magnetic properties of copper impurity complexes in crystals of the fluorite structural series take place in a comparatively narrow range of interionic distances, from values consistent with the CaF_2 crystal to values typical of SrF_2. In this range of interionic distances in matrix crystals the vibronic interactions of an impurity $3d^9$ ion changes from the $^2T_{2g} \times (t_{2g} + e_g)$ to the $^2T_{2g} \times (e_g)$. If this transitional range is not determined by the size of the coordination cube, but by the ratio $\eta = 2(R_{Me} + R_L)/(\sqrt{3}a_c)$ (where a_c is the edge of the coordination cube, R_{Me} is the radius of a paramagnetic

 © 1998 American Institute of Physics

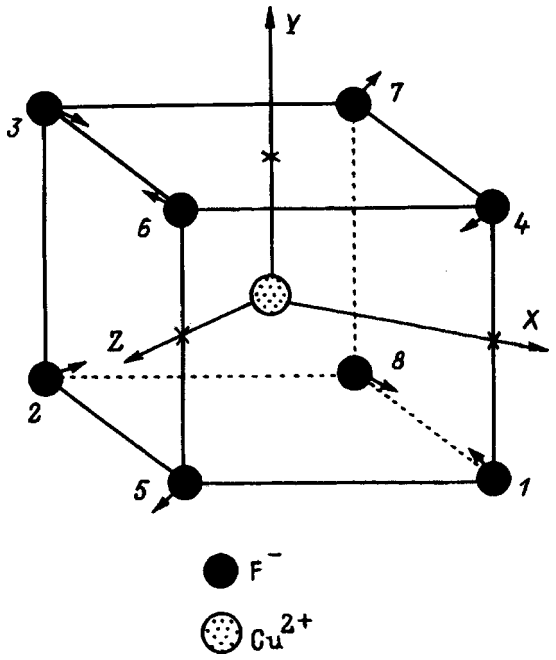

FIG. 1. Molecular structure and orientation of the coordinate axes used to represent the magnetic interaction tensors of copper impurity complexes in CdF_2 and CaF_2 crystals.

impurity ion, and R_L is the ionic radius of its ligands), it is found that a similar dependence of the magnetic properties on the parameter η is also obeyed by divalent copper complexes in $SrCl_2$ crystals[4] and by divalent silver complexes (electron configuration $4d^9$) in CdF_2, CaF_2, SrF_2, BaF_2, and $SrCl_2$ crystals.[5–7]

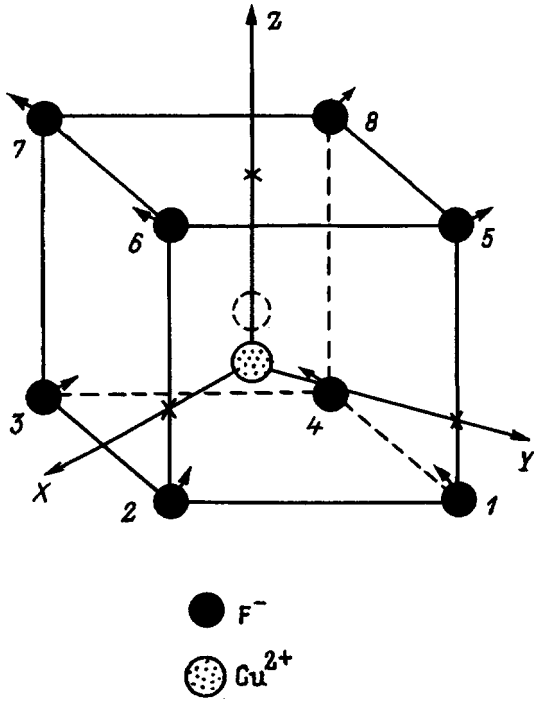

FIG. 2. Molecular structure and orientation of the coordinate axes used to represent the magnetic interaction tensors of copper impurity complexes in SrF_2 and BaF_2 crystals.

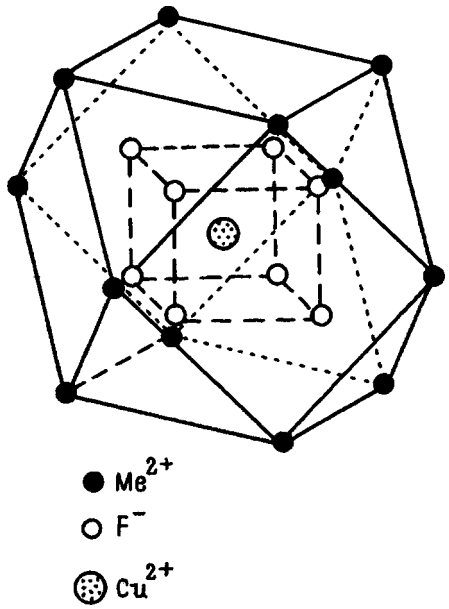

FIG. 3. First nearest-neighbor anionic and cationic spheres of a Cu^{2+} impurity ion in crystals of the fluorite structural series.

These considerations have prompted us to inquire whether it would not be feasible, by inducing deformations of the proper symmetry in a crystal, to intensify vibronic interaction with one of the two effective vibrational modes at the expense of suppressing interaction with the other mode.

To solve this problem experimentally, in the present study we have investigated two possible means of creating anisotropic deformations in the crystal volume: uniaxial mechanical compression of the crystal by an external force; and the isomorphic injection of diamagnetic cations of alkaline-earth metals (AEMs) with different ionic radii as substitutional impurities. In the second case it was expected that for a definite concentration of AEM impurity ions ($\sim$5 mol %) the nearest-neighbor cationic sphere of the majority of copper ions would contain just one AEM impurity cation. It was assumed in this regard that the probability of two such cations appearing simultaneously at the given concentration should be approximately 15–20 times lower. Inasmuch as each of the 12 cations of the first cationic sphere surrounding the copper impurity is situated relative to it in a direction parallel to one of the six $\langle 110 \rangle$ axes of the crystal (Fig. 3), the isomorphic substitution of an AEM impurity ion in place of a primary lattice cation will lead to deformation of the anionic coordination polyhedron of the copper ion in this specific direction.

For example, if a small fraction of Ca^{2+} ions in a CaF_2 crystal is replaced by Sr^{2+} ions, the coordination polyhedron of copper, for which the first nearest-neighbor cationic sphere contains one Sr^{2+} impurity ion, is compressed in one of the crystallographic $\langle 110 \rangle$ directions as a result of the large ionic radius of this cation. In another case, where some of the Sr^{2+} ions in a SrF_2 crystal are replaced by Ca^{2+} ions, the deformation is in the opposite direction. In both cases the symmetries of the deformation field generated by the AEM impurity correspond to the C_{2v} group. Since the displacements of anions of the first coordination sphere of the impu-

rity copper are small in either case ($\leqslant 0.1$ Å), the entire cubic part in the potential of the crystal field of the paramagnetic complex remains predominant, and one expects $^2T_{2g} \times (t_{2g}+e_g)$ vibronic interaction. But if approximately equal numbers of calcium and strontium cations ($x \cong 0.5$) are present in the lattice of a mixed crystal, there is a major increase in the probability that copper complexes occur whose anionic sphere falls under the influence of a low-symmetry deformation field. This phenomenon is attributable to the fact that the nearest-neighbor cationic spheres of the copper ions must, on the average, contain approximately equal numbers of cations of both species in the given situation, but they can have a disordered distribution within the limits of these spheres. However, because the displacement of each anion, taken separately, of the paramagnetic complex in such crystals is the result of the averaged influence of these cations, the entire cubic part in the Hamiltonian of the crystal field in this case as well can be almost as large as for crystals having a fairly low concentration of AEM impurity ions or a disordered distribution of Ca^{2+} and Sr^{2+} cations in crystals with $x=0.5$. Consequently, vibronic interactions can also influence the properties of such impurity centers. However, it is unlikely that the properties of these centers could be predicted without their experimental investigation.

In view of the low success rate of experiments involving the application of uniaxial pressure to a crystal (the crystal samples broke up at comparatively low specific pressures), here we discuss only the results obtained in the investigation of mixed crystals of the type $Ca_xSr_{1-x}F_2$:Cu. The constituency of the investigated crystals was limited to $0 \leqslant x \leqslant 0.05$, $1.0 \geqslant x \geqslant 0.95$, or $x \cong 0.5$. This choice was dictated by the fact that in growth tests high-quality crystals have been obtained only for a comparatively low content of AEM impurity ions ($\leqslant 5\%$) or when two types of AEM ions were present in the melt in approximately equal amounts.

1. EXPERIMENTAL

Crystals of variable composition $Ca_xSr_{1-x}F_2$:Cu were grown by the Czochralski method in a helium atmosphere with small fluorine additives ($\sim 2\%$ of the total gas volume). The main growth parameters were varied in the following ranges: 1) pulling rate of the crystal from the melt from 5 mm/h to 30 mm/h; 2) rate of rotation of the crystal about the vertical axis from 10 min^{-1} to 60 min^{-1}; 3) temperature gradient in the interior of the crystal near the crystallization front from 5 K/mm to 20 K/mm. The growth conditions were chosen so as to ensure the most uniform possible impurity distribution throughout the volume of the growing crystal while maintaining high quality on the part of the latter. The copper impurity was added to the crystal in the form of the predried salt CuF_2.

X-ray structural analysis was used to investigate the structure of the as-grown crystals and to monitor their quality. The x-ray patterns were photographed in the usual $\theta - 2\theta$ geometry on a DRON-3M diffractometer. Figure 4 shows fragments of diffraction patterns for three crystal samples with different contents of calcium and strontium ions. It is evident that the widths of the x-ray reflections

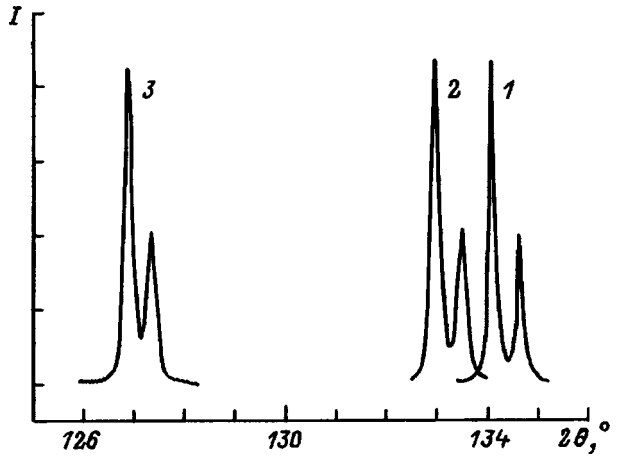

FIG. 4. Fragments of diffraction patterns of $Ca_xSr_{1-x}F_2$:Cu crystals. *1*) $x=1.0$; *2*) 0.95; *3*) 0.5.

(333) for mixed-crystal samples with $x=0.95$ (curve *2*) and 0.5 (curve *3*) are only slightly greater than the width of the corresponding reflection for the impurity-free CaF_2 crystal (curve *1*). On the other hand, the values of the angle 2θ for these three samples differ considerably. The x-ray examinations established that the average size of the unit cell of the mixed crystals increases almost linearly as the composition is varied from $x=1$ to 0. In particular, at $T \approx 300$ K the side of the unit cell is equal to $a_0 = 5.4864 \pm 0.0001$ Å for $x = 0.95$, $a_0 = 5.6239 \pm 0.0001$ Å for $x=0.5$, and $a_0 = 5.7815 \pm 0.0001$ Å for $x=0.05$. The main criteria of quality of the crystals were the size of the regions of coherent scattering of x–rays and the magnitude of the microscopic distortions within the boundaries of these regions. Such information was obtained by harmonic analysis of the profiles of the x-ray interference lines from the (111), (222), and (333) planes of the investigated $Ca_xSr_{1-x}F_2$:Cu single crystals and ''standard'' (impurity-free) CaF_2 single crystals. A comparison of the results of calculations for the mixed crystals and the standard crystal showed that the dimensions of the coherent scattering regions in all the mixed crystals of the indicated composition are greater than 1000 Å, as opposed to the 0.0002 Å scale of the microdistortions. An examination of the cleavage planes of these crystals under a microscope did not reveal any macroscopic defects or evidence of polycrystalline formations. The reported x-ray structural and microscopic examinations therefore attest to the high quality of the crystals.

The structure and magnetic properties of the copper impurity complexes in the mixed $Ca_xSr_{1-x}F_2$:Cu crystals were investigated by the EPR method at frequencies of 9.3 GHz and 37 GHz and at temperatures of (4.2–270) K. The electron-Zeeman, intrinsic hyperfine, and ligand hyperfine interaction parameters, which determine the magnetic properties of the observed complexes, were evaluated from an investigation of crystals of the three most typical compositions ($x=0.05$, 0.5, and 0.95) and are given in Table I. Also shown in the table for comparison are the values of these parameters determined from previous studies of CaF_2:Cu and SrF_2:Cu crystals.[2,3] The orientations of the coordinate axes used to represent the magnetic interaction parameters of

TABLE I. Parameters of the magnetic interaction tensors of divalent copper impurity complexes in $Ca_xSr_{1-x}F_2$ crystals.

Parameters	CaF_2	$Ca_{0.95}Sr_{0.05}F_2$		$Ca_{0.5}Sr_{0.5}F_2$		$Ca_{0.05}Sr_{0.95}F_2$		SrF_2
	1	2	3	4	5	6	7	8
g_x	2.09(9)	2.09(8)	2.10(1)	2.09(8)	2.2(0)		2.49(3)	2.49(3)
g_y	2.14(7)	2.14(5)	2.14(1)	2.13(9)	2.2(0)		2.49(3)	2.49(3)
g_z	2.80(2)	2.79(5)	2.79(2)	2.75(6)	2.3(6)	2.75(1)	2.08(4)	2.08(4)
a_{xx}	97±3	98±10	100±20	70±10			26±5	26±5
a_{yy}	96±3	96±10	100±20	70±10			26±5	26±5
a_{zz}	76±3	71±10	70±20	≈0		≈0	362±5	362±5
Q	−11±3	−10±5	≈−10	−7±5			−8±5	−8±3
A_{xx}	221±5	230±15	230±20	235±15			95±10	99±3
A_{yy}	136±5	130±15	130±20	115±15			380±15	380±8
A_{zz}	58±3	60±10	60±20	70±10		60±20	125±15	127±5
A_{ij}	89±5	80±15	80±20	80±15			85±15	87±5

Note: The parameter groups 1–4 and 6 refer to orthorhombic centers; groups 5, 7, and 8 correspond to tetragonal centers. For both types of centers the ligand hyperfine interaction tensors shown here refer to ligand No. 1 (Figs. 1 and 2). The parameter groups 1 and 2 have been obtained at a temperature of 4.2 K; all the others have been obtained at 77 K. The components of the hyperfine interaction tensor (**a**), the ligand hyperfine interaction tensor (**A**), and the quadrupole interaction tensor (**Q**) are given in MHz.

the complexes are shown in Fig. 1 (for centers whose magnetic properties are characterized by effective orthorhombic symmetry tensors) and in Fig. 2 (for centers whose magnetic properties are close to tetragonal).

The angular variations of the resonance lines and the structure of the EPR spectra observed in $Ca_xSr_{1-x}F_2$:Cu ($x \geqslant 0.95$) crystals were qualitatively similar to those observed in CaF_2:Cu crystals.[2] This means that the composition of the paramagnetic complexes and their molecular structure are identical in these two types of crystals. The differences in the complexes observed in $Ca_xSr_{1-x}F_2$:Cu ($x \geqslant 0.95$) and CaF_2:Cu were as follows: 1) The EPR lines at a temperature of 4.2 K were approximately 3–4 times broader for the first type; 2) the EPR spectra in the first case were observed up to a temperature $T \sim 120$ K, whereas in CaF_2:Cu spectral lines were observed only at a much lower temperature ($T \leqslant 35$ K); 3) the ligand interaction parameters varied insignificantly in the mixed crystals (see Table I), indicating minor variations of the interionic distances in the paramagnetic complexes as a result of deformation of the coordination polyhedron of the ion-complexing agent by an AEM impurity ion. An analysis of the temperature dependence of the total intensity of the EPR spectra of the $Ca_xSr_{1-x}F_2$:Cu ($x \geqslant 0.95$) crystals indicate that at least two types of paramagnetic complexes are encountered here: ''low-temperature'' (EPR spectra observed at $T \leqslant 35$ K) and ''high-temperature'' ($T \leqslant 120$ K). It was also determined that the number of high-temperature complexes increases as the concentration of AEM impurity ions is increased, owing to a decrease in the number of low-temperature complexes.

Paramagnetic complexes of divalent copper with an effective electron-Zeeman interaction tensor of orthorhombic symmetry were also detected in $Ca_xSr_{1-x}F_2$:Cu ($x=0.5$) crystals, but their EPR spectra (Fig. 5) already differed to a substantially greater extent from those observed in CaF_2:Cu crystals. These differences primarily involved the values (see Table I) of the hyperfine interaction parameters and the width of the temperature interval in which these spectra were observed (the interval is much broader here than in crystals with $x=0.95$, $T \leqslant 240$ K). The widths of the spectral lines in $Ca_xSr_{1-x}F_2$:Cu ($x=0.5$) also increased, becoming approximately three times the widths in $Ca_xSr_{1-x}F_2$:Cu ($x=0.95$). One of the components of the hyperfine interaction tensors (A_{zz}) of a copper impurity ion dropped almost to zero.

In addition to the orthorhombic complexes, other complexes described by an electron-Zeeman tensor of axial symmetry were also detected in crystals with $x=0.5$. The direction of the principal axis of this tensor is parallel to one of the crystallographic ⟨001⟩ axes. The EPR spectra were observed at temperatures $T \leqslant 45$ K. The hyperfine and superhyperfine structures of the spectra were not resolved, obviously because of certain differences in the magnetic interaction parameters of different complexes of this kind. The concentration of these complexes (which we call ''tetragonal'') in all the investigated mixed crystals with $x=0.5$ and

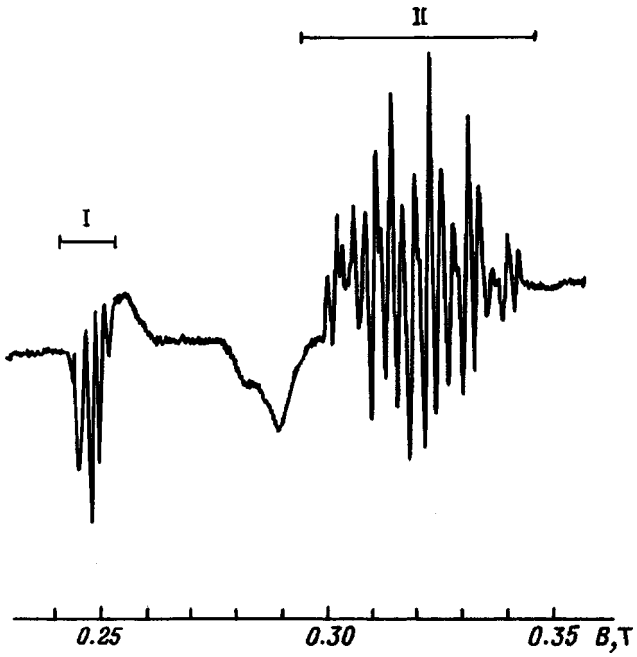

FIG. 5. EPR spectrum of $Ca_{0.5}Sr_{0.5}F_2$ crystal, $\mathbf{B}_0 \| \langle 110 \rangle$, $T=77$ K, $f=9.3$ GHz.

different copper impurity contents was found to be 10–15 times lower than the concentration of orthorhombic complexes. No other paramagnetic centers were detected in crystals with $x=0.5$.

Paramagnetic complexes with electron-Zeeman tensors of orthorhombic and axial symmetry were also observed in $Ca_xSr_{1-x}F_2$:Cu ($x=0.05$) crystals at temperatures $T \leqslant 270$ K. Here, however, the greatest number of complexes had virtually the same electron-Zeeman, hyperfine, and ligand hyperfine interaction parameters as the corresponding tetragonal complexes of copper in SrF_2:Cu (Ref. 3), and only $\sim 2-3\%$ of the paramagnetic complexes detected in the crystals were found to be orthorhombic. In view of the fact that the EPR spectra of both types of complexes were observed in approximately the same temperature interval, the far weaker lines of the orthorhombic complexes were most often masked by the very strong lines of the tetragonal complexes. Consequently, only some of the magnetic interaction parameters were determined for orthorhombic complexes in crystals with $x=0.05$.

It should be emphasized that ligand hyperfine interaction with four equivalent ^{19}F nuclei situated in one of the $\langle 110\rangle$ planes was distinctly observed in the EPR spectra of all types of orthorhombic complexes of divalent copper. Consequently, the constituencies of these complexes in all the investigated crystals with various AEM impurity ion contents is approximately identical. Obviously the only difference in their molecular structure from that of the orthorhombic $[CuF_4F_4]^{6-}$ complexes in CdF_2 and CaF_2 crystals[2] is in the comparatively small displacements of the fluorine and copper nuclei relative to their characteristic sites.

2. DISCUSSION OF THE RESULTS

The method used to induce deformations in the first anionic sphere surrounding a paramagnetic impurity ion by the isomorphic substitution of chemically similar ions for lattice cations has been found to work well. However, it has one idiosyncrasy: The deformation field, which affects the positions of the ions of this nearest-neighbor sphere, is not centrosymmetric. It is evident from the results of the investigations that this asymmetry of the deformation field exerts comparatively little influence on the magnetic interaction parameters in copper complexes in crystals with $0.95 \leqslant x \leqslant 1.0$, its main effect being only to significantly lower the level of the bottom of one of the six adiabatic potential wells of each complex and, naturally, to raise the temperature of observation of the EPR spectra. However, with an increase in the interionic distances in the crystal the properties of the paramagnetic impurity complexes become more sensitive to noncentrosymmetric deformations. In particular, this trend indicates a sharp reduction in the magnitude of the isotropic part of the hyperfine interaction tensor in crystals with $x=0.5$, and such a reduction could account for the intermingling of excited configurations of noncentrosymmetric components of the crystal field potential with the ground-state electron configuration of Cu^{2+} (Ref. 8).

Further evidence of the major influence of noncentrosymmetric deformations on the magnetic properties of copper is the profile of the EPR spectral lines of the $Ca_xSr_{1-x}F_2$:Cu ($x=0.5$) crystal (Fig. 5). Consider the group of lines (group I) introduced into the spectrum by orthorhombic copper complexes with their Z axis oriented parallel to the direction of the external static magnetic field ($\mathbf{B}_0 \parallel Z \parallel \langle 110\rangle$). The lines of this group clearly have an unusual profile. The uncommon asymmetric shape of the lines of the first derivative of the absorption signal is normally encountered in the spectra of powders and is induced by the equiprobable distribution of directions of the crystal axes of the individual single-crystal powder grains. However, data from the x-ray structural examination of these crystals definitely indicate the absence of any kind of disoriented grains in their interior. On the other hand, distortion of the line profiles of the EPR spectrum can also occur in the event of saturation of resonance EPR transitions. However, the form of the EPR spectra remains virtually unchanged at different microwave power levels in the spectrometer cavity in the range from 20 μm to 10 mW. Moreover, the profiles of the lines in group II in Fig. 5, always within the limits of this power range, essentially coincide with the usual profile of the curve representing the first derivative of the absorption signal. In this case, therefore, we can also rule out relaxation mechanisms for the distortion of the EPR signal profile. Consequently, the only explanation we can see for the unusual line profiles in the left group is the hypothesis of small differences in the directions of the principal axes of the corresponding magnetic interaction tensors (magnetic axes) in the ensemble of orthorhombic paramagnetic complexes. In fact, calculations of the profiles of the spectral lines with allowance for the actual angular dependences of the resonance magnetic fields for the left and right groups yield a pattern that essentially coincides with the real spectrum shown in Fig. 5. In the course of these calculations it has been found that the difference in the directions of the magnetic axes of different complexes can be as much as $\pm 5°$. This means that the composition and relative positioning of the calcium and strontium ions in the cationic sphere surrounding the impurity ion are different, so that the anionic coordination polyhedra of the copper impurity ions acquire different shapes from one complex to another. The end result is that the copper impurity ions are subjected to low-symmetry crystal fields characterized by different sets of parameters.

We have performed approximate calculations based on a point model of the crystal field, which show that the low-symmetry components of the potential of this field influence the directions of the principal axes of the effective electron-Zeeman interaction tensor to a greater extent than they affect magnitude of its principal values. However, to explain the emergence of two types of paramagnetic complexes in a crystal, apart from the comparatively small expected displacements of the impurity copper ligands (<0.1 Å), the possibility of displacements of the copper ions themselves must be considered. These displacements can occur in various directions distinct from the principal crystallographic axes. If vibronic interactions are disregarded, the direction of displacement of a given paramagnetic ion in the situation discussed here should roughly coincide with the direction from the centroid of the set of strontium cations situated in

the first cationic sphere of this ion toward the centroid of the same set of calcium cations. In the most probable case, where the centroids of the sets of calcium and strontium cations almost coincide, and the displacements of the copper ion from the site of the cation substituted for it are small, the main components of the crystal field acting on the Cu^{2+} ion will be the components of a cubic field. The impossibility of ignoring vibronic interactions in this case is self-evident; according to the experimental results, they are paramount in determining the magnetic properties of such clusters [$^2T_{2g} \times (t_{2g}+e_g)$ interaction takes place, and complexes with orthorhombic symmetry of the magnetic properties are formed]. Magnetic properties of the same symmetry and approximately the same electron-Zeeman, hyperfine, and ligand hyperfine interaction parameters can also be found in complexes in whose nearest-neighbor cationic sphere the centroids of the sets of Ca^{2+} and Sr^{2+} ions are shifted in opposite directions from the copper impurity ion along directions close to $\langle 111\rangle$ and $\langle 110\rangle$. The problem is that in such crystals components of trigonal and orthorhombic symmetry appear in the potential of the crystal field acting on a paramagnetic copper ion in such complexes as a result of ion displacements. For this reason, impurity copper in lower orbital states (provided that the energy intervals between them do not become too large) can still interact efficiently with nuclear vibrations of trigonal and tetragonal symmetry. In the present situation these complexes probably differ from the first ones primarily in the directions of the magnetic axes and the higher upper limit of the temperature interval in which the EPR spectra are observed.

Tetragonal complexes in crystals with $x=0.5$, on the other hand, can occur in the less probable situation where the centroids of the sets of calcium and strontium ions in the nearest-neighbor cationic sphere of a copper ion are on opposite sides of the central ion in one of the $\langle 001\rangle$ directions. The efficiency of interaction of the impurity copper with vibrations of tetragonal symmetry can increase in this situation. The adiabatic potential surface can acquire several deeper tetragonal minima in addition to the orthorhombic minima. Owing to the complex relief of the adiabatic potential surface, the height of the barriers between the various minima might not be very high, causing the upper limit of the temperature interval of observation of the EPR spectra of the tetragonal complexes to shift toward lower temperatures.

The investigation of $Ca_xSr_{1-x}F_2$:Cu ($x=0.05$) crystals shows that anisotropic deformations have the strongest influence on the magnetic properties of copper complexes in a narrow interval of interionic distances, from values typical of a $Ca_xSr_{1-x}F_2$:Cu ($x=0.5$) crystal to values corresponding to a SrF_2 crystal. The unit cell becomes especially large in these crystals. According to the well-known Goldschmidt crystal-chemical law, a paramagnetic complex is rendered structurally unstable by a drastic reduction of repulsive interaction between the Cu^{2+} ion and its nearest-neighbor F^- ions. Consequently, the occurrence of a single AEM cation with a smaller ionic radius (Ca^{2+}) in the first cationic sphere of a Cu^{2+} ion in the $\langle 110\rangle$ direction produces a qualitative change in the magnetic properties of such complexes, specifically the formation of complexes with an orthorhombic electron-Zeeman interaction tensor. It is obvious that the paramagnetic Cu^{2+} ion in the composition of such complexes is also situated at an off-center site, but the direction of its displacement from the position of the replaced Sr^{2+} cation in this case must be parallel to one of the $\langle 110\rangle$ directions. This conclusion follows primarily from the observation of a characteristic ligand hyperfine interaction with relative line intensities 1:4:6:4:1 in the EPR spectrum in the orientation $\mathbf{B}_0 \| Z \| \langle 110\rangle$.

Consequently, as long as the repulsive interaction between a copper ion and its nearest-neighbor environment of fluorine ions in $Ca_xSr_{1-x}F_2$ ($0.95 \leqslant x \leqslant 1.0$) crystals is sufficiently strong, the low-symmetry deformation field cannot produce any appreciable displacement of the copper ion from the site of the lattice cation replaced by it. This is especially true in that the AEM impurity ion generating the indicated field replaces a principal lattice cation, whose coordination (anionic) polyhedron has already increased in volume on account of Jahn-Teller deformation of the nearest-neighbor (in the $\langle 110\rangle$ direction) anionic cell with the Cu^{2+} ion at the center. Becoming localized in the first cationic sphere of the copper ion in the direction of the X axis (according to Fig. 1), an AEM impurity ion exerts scarcely any additional deforming influence on the anionic sphere surrounding the impurity copper. On the other hand, the average dimensions of the unit cells in crystals of the $Ca_xSr_{1-x}F_2$ ($0.95 \leqslant x \leqslant 1.0$) series differ very little. Naturally, the magnetic interaction parameters of these complexes in the indicated series also differ very little.

As the unit cell increases in size, the electron shells of a Cu^{2+} impurity ion and the surrounding F^- ions soon overlap to a lesser degree, so that the repulsive interaction between the copper ion and the fluorine ions subsides, and the equilibrium position of the impurity copper nucleus, simultaneously with the electrostatic, exchange, and vibronic interactions inside the paramagnetic complex, also begins to be significantly influenced by the deformation field external to this complex. Under these conditions, depending on the symmetry of the deformation field, divalent copper complexes with different symmetries of the magnetic properties are formed in the bulk of the mixed crystal. In the case of the $Ca_{0.5}Sr_{0.5}F2$:Cu crystal we find that the totality of the paramagnetic complexes formed in the process can be divided into two groups, within each of which the magnetic properties differ only slightly. The first group of complexes is characterized by effective electron-Zeeman interaction tensors of orthorhombic symmetry, whose principal axes form small angles with the crystallographic $\langle 110\rangle$ direction. The axes of the electron-Zeeman interaction tensors of the second group approximately coincide with the directions of the $\langle 001\rangle$ axes of the crystal. These special aspects of the magnetic properties of the paramagnetic complexes imply that vibronic interactions still have a significant influence on the evolution of the magnetic properties of the copper impurity complexes in mixed crystals subjected to an array of structural deforma-

tions. For complexes of the first group this influence is mainly from $^2T_{2g}\times(t_{2g}+e_g)$ interactions, and for complexes of the second group the main type is $^2T_{2g}\times e_g$. However, the nature of this influence on the properties of the complexes depends both on the symmetry of the structural deformations and on the relations between the strengths of the Coulomb, exchange, and vibronic interactions within the complex. In particular, the example of $Ca_xSr_{1-x}F_2$:Cu ($0\leqslant x\leqslant 0.05$) crystals shows that whereas the centering influence of repulsive exchange interaction between a copper ion and its ligands weakens, the influence of the deformation field of AEM impurity cations on the magnetic properties of the copper complexes can be especially strong.

[1] M. C. M. O'Brien, Phys. Rev. B **187**, 407 (1969).
[2] M. M. Zaripov and V. A. Ulanov, Fiz. Tverd. Tela (Leningrad) **30**, 1547 (1988) [Sov. Phys. Solid State **30**, 896 (1988)].
[3] M. M. Zaripov and V. A. Ulanov, Fiz. Tverd. Tela (Leningrad) **31**(10), 251 (1989) [Sov. Phys. Solid State **31**, 1796 (1989)].
[4] H. Bill, Phys. Lett. A **44**, 11 (1973).
[5] M. M. Zaripov, V. A. Ulanov, and M. L. Falin, Fiz. Tverd. Tela (Leningrad) **31**(2), 248 (1989) [Sov. Phys. Solid State **31**, 319 (1989)].
[6] M. M. Zaripov, V. A. Ulanov, and M. L. Falin, Fiz. Tverd. Tela (Leningrad) **31**(11), 289 (1989) [Sov. Phys. Solid State **31**, 2004 (1989)].
[7] H. Bill and R. Lacroix, in *Proceedings of the Twelfth Congress Ampere* (1973), p. 233.
[8] C. A. Bates, W. S. Moore, K. J. Standley, and K. W. H. Stevens, Proc. Phys. Soc. London **79**, 73 (1962).

Translated by James S. Wood

Thermooptical investigation of deep levels in doped $Bi_{12}SiO_{20}$ crystals

T. V. Panchenko

Dnepropetrovsk State University, 320625 Dnepropetrovsk, Ukraine
(Submitted August 28, 1997)
Fiz. Tverd. Tela (St. Petersburg) **40**, 452–457 (March 1998)

The temperature dependence of the impurity optical absorption of nominally pure $Bi_{12}SiO_{20}$ (BSO) crystals and BSO crystals doped with Ga, Cr, Mn, and Ag ions is investigated. A method is proposed for determining the thermal activation energy, and certain properties of deep levels are found. © *1998 American Institute of Physics.* [S1063-7834(98)01203-9]

Sillenite $Bi_{12}MO_{20}$ (BMO, M=Si, Ge, Ti) crystals are used as the working medium in holographic interferometry and various types of light-modulating devices. Doping over a wide range of levels alters the characteristics of BMO.[1–5] In particular, Ca ions lower the half-wave voltage, while Al, Ga, and Mn ions increase the diffraction efficiency and modify the write and destructive-readout kinetics of volume phase holograms.[2] Electron-beam-addressable light modulators using Ga- or Ca-doped BMO are characterized by superior resolving power.[3] The photochromic effect is enhanced by Mn, Cr, and Cu ions, which also lengthen (Mn, Fe, Cu) or shorten (Cr) the storage time of written data.[4]

The photorefractive effect, which is the basis of optical data processing, is associated with the presence of shallow and deep levels in the BMO band gap.

Therefore, the key to the successful utilization of doped crystals is a detailed understanding of the structure of the local levels as well as the nature and role of impurity centers. For example, differentiation of the intensity of photoexcitation of the holographic grating and quenching of the diffraction efficiency in BSO:Al and BSO:Mn crystals are linked to deep-level optical charge transfer.[5]

The information on local levels to date is insufficient. It has been shown that doping (with Ga, Al, Ca, Mn, Cr, or Ni) does not produce any new impurity photoresponse bands,[6–11] and a decrease in the photoconductivity is attributed to the occurrence of a fast-recombination center,[11,12] but their parameters have not been determined. The quenching of the optical absorption shoulder of undoped BMO crystals in the interval (2.2–3.0) eV with the introduction of Al, Ga, and Ca ions has been described.[6–9,13–15] It is postulated that Al^{3+} or Ga^{3+} ions acting as acceptors replace Bi^{3+} ions introduced at *M* sites and play the role of color centers,[14,15] or they compensate deep donors of unknown origin responsible for the absorption shoulder.[16–18] Relatively shallow local levels have been detected by thermally stimulated currents, but it does not look as though they can be linked to Al or Ga ions.[6,9,15,19] Deep levels can manifest themselves in the photochromic effect, but in BMO crystals doped with Cr, Mn, Cu, or Fe ions the strong fundamental and photoinduced absorption bands are interpreted merely as in-center transitions.[17–23] On the other hand, these ions can be donors or acceptors, as evinced by the induced photosensitivity,[10] the dark conductivity, and the thermally stimulated currents.[24,25] Consequently, further study of the local levels in doped sillenites is still an important objective.

Useful information about the local centers is obtained by investigating the temperature dependence of the optical absorption. For hydrogenlike centers, where the zone of localization of a bound electron is large, such information can be used to identify shallow-level–conduction-band transitions (lightly doped semiconductors[26]) or to determine the distribution function of the tails of the density of states near the edges of allowed bands (highly doped semiconductors[27]). In the case of deep impurity centers, where an electron is tightly bound to a defect, the photoionization cross section exhibits a unique kind of temperature dependence,[28] which depends on the type of electron–phonon interaction.[28,29]

Here we give the results of an investigation of the temperature dependence of the optical absorption in nominally pure and Ga-, Cr-, Mn-, and Ag-doped $Bi_{12}SiO_{20}$ (BSO) crystals.

1. EXPERIMENTAL

The crystals were grown by the Czochralski method along the crystallographic [001] direction with dopant concentrations of 0.1% (Ga), 0.02% (Cr), and 0.1% (Mn, Ag). The samples were prepared in the form of optically polished wafers of thickness $d=1-5$ mm cut in the (001) plane. The temperature dependence of the optical absorption was investigated through heating–cooling cycles in the temperature range $T=280-700$ K. The optical transmission spectra $t(\lambda)$ were recorded every 5–10 K in the wavelength range $\lambda=0.33-0.91$ μm by means of a Specord M40 dual-beam spectrophotometer. The effective rate of measurement of the temperature was $\sim 0.01\ \mathrm{K\cdot s^{-1}}$. The absorption spectra $\alpha(h\nu)$, where $h\nu$ is the photon energy, were calculated with correction for the reflection spectra $R(\lambda)$ from the relation[26] $t=(1-R)^2\exp(-\alpha d)/[1-R^2\exp(-2\lambda d)]$. Taking into account the strong dependence of the optical and photoelectric properties of BMO on their past history,[30] crystals in a near-equilibrium state (after prolonged storage in the dark at $T\approx 300$ K) were chosen for the investigations.

2. TEMPERATURE DEPENDENCE OF THE ABSORPTION

The temperature dependence of the optical absorption $\alpha(T)$ has been investigated as a function of temperature in the spectral interval $h\nu=1.4-2.0$ eV, where the different

 © 1998 American Institute of Physics

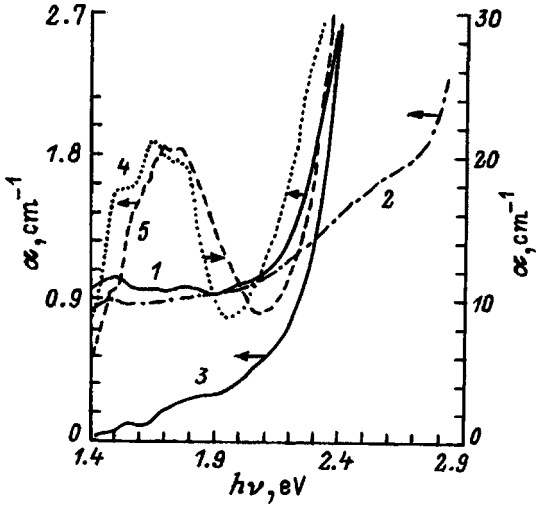

FIG. 1. Spectral plots of the optical absorption of sillenite crystals, $T=297$ K. *1*) BSO; *2*) BSO:Ga; *3*) BSO:Ag; *4*) BSO:Cr; *5*) BSO:Mn.

kinds of influence of impurities are fairly well pronounced (Fig. 1). Here Ga and Ag ions reduce the absorption of nominally pure BSO crystals, whereas Cr and Mn ions produce a strong absorption band, conflictingly described in the literature as a band of in-center transitions in Cr and Mn ions of different valences and localizations.[19–22]

The $\alpha(T)$ curves of the investigated crystals are shown in Figs. 2–4. They all exhibit temperature hysteresis, where the absorption for the heating branch of the $\alpha(T)$ curve exceeds the level in cooling. For BSO, BSO:Ga, BSO:Cr, and BSO:Mn an increase in the temperature causes the absorption to decrease in steps. The height $\Delta\alpha$, width ΔT, slope $\Delta\alpha/\Delta T$, and temperature positions of the descending α steps differ for different dopant ions. However, pairs of similar $\alpha(T)$ curves exist for BSO and BSO:Ga and for BSL:Cr and

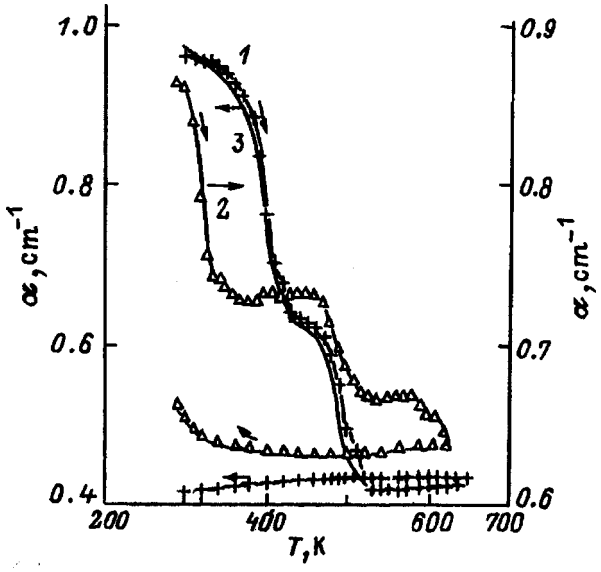

FIG. 2. Optical absorption versus temperature for light with $h\nu=1.65$ eV. *1*) BSO crystal; *2*) BSO:Ga crystal. The arrows pointing toward and away from the temperature axis indicate heating and cooling, respectively. The solid curve *3* represents the calculated temperature dependence of the absorption for BSO crystals.

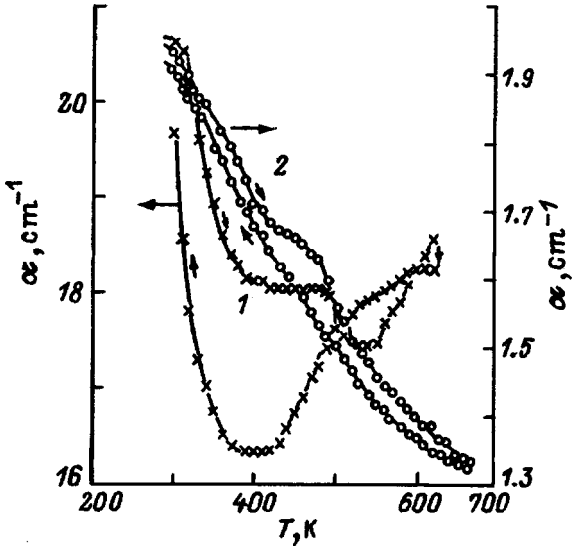

FIG. 3. Optical absorption versus temperature. *1*) For light with $h\nu=1.65$ eV, BSO:Cr crystal; *2*) $h\nu_2=1.68$ eV, BSO:Mn crystal. The arrows pointing toward and away from the temperature axis indicate heating and cooling, respectively.

BSO:Mn. In the first case each curve has two well-defined narrow steps, which are higher for the nominally pure BSO than for BSO:Ga, and the low-temperature steps have different temperature positions (Fig. 2). In the second case the descent of α is slower, the steps are not as distinct, but their temperature positions are all the same, and the increment $\Delta\alpha$ for the Cr-doped crystals is an order of magnitude higher than for BSO:Mn, implying a difference in the absorption intensities in the investigated spectral range (Fig. 3). In the cooling of BSO and BSO:Ga crystals the absorption depends very weakly on the temperature, whereas for the second pair (BSO:Cr and BSO:Mn) we observe a tendency to restore the initial value of α. The direct and reverse branches of the

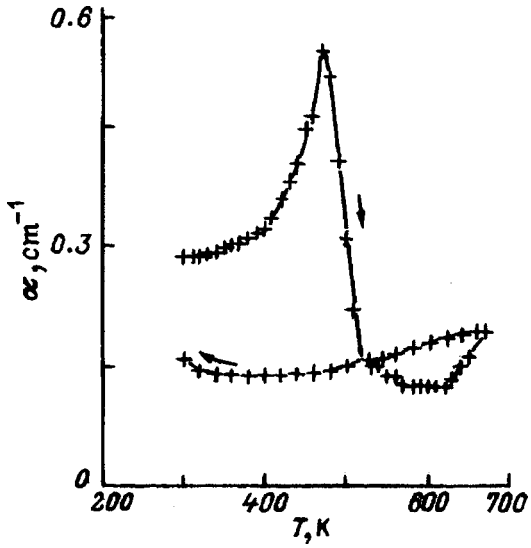

FIG. 4. Optical absorption versus temperature for light with $h\nu=1.65$ eV in BSO:Ag crystals. The arrows pointing toward and away from the temperature axis indicate heating and cooling, respectively.

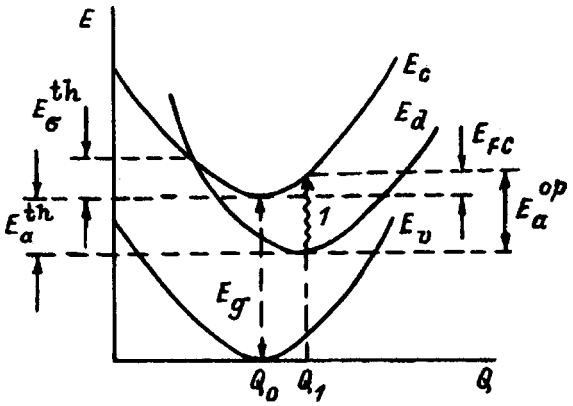

FIG. 5. Total energy E of a crystal with a deep donor level versus configuration coordinate Q, showing the principal energy characteristics. The E_c, E_v, and E_d curves correspond to (respectively) the empty level with an electron in the conduction band, the same with an electron in the valence band, and the electron-occupied level.

$\alpha(T)$ curves in the heating-cooling cycle are the closest together for BSO:Mn.

The heating branches of the $\alpha(T)$ curves for BSO:Ag crystals differ sharply from those described above; here the exponential growth of the absorption [as $\alpha \sim \exp(E_a/kT)$ with $E_a = 0.25$ eV] is superseded by a sudden plunge, followed by a certain increase in α. In the cooling process the absorption in these crystals, as in BSO and BSO:Ga, is practically independent of the temperature (Fig. 5).

The $\alpha(T)$ curves for various values of $h\nu$ in the investigated range for each of the crystals are similar, but the ratio of the heights of the low-temperature and high-temperature steps differs. As $h\nu$ increases, the height of the high-temperature step decreases considerably. This general behavior of these curves tends to change to exponential growth at a point $h\nu < h\nu_c$, where $h\nu_c$ depends on the type of impurity (for example, $h\nu_c \geqslant 2.6$ eV for BSO:Ga crystals).

It is important to note that $\alpha(T)$ curves characterized by decreasing absorption in the range $T = 80-300$ K, similar to those described above, have been obtained[17] for $Bi_{12}GeO_{20}$ (BGO) and BGO:Al crystals in an investigation of the thermal breakdown of photoinduced color centers; several stages of reduction of the photoinduced absorption (thermoregulation) have been observed for BGO:Fe and BSO crystals.[18,31]

The pronounced hysteresis and weak temperature dependence of the absorption in cooling suggest that the various features of the heating parts of the $\alpha(T)$ curves for BSO, BSO:Ga, and BSO:Ag crystals are linked to the thermal detrapping (BSO and BSO:Ga) or charge transfer (BSO:Ag) in local levels of the band gap that participate in the formation of the impurity absorption band. The situation is more complicated in the case of BSO:Cr and BSO:Mn crystals. The $\alpha(T)$ curves obtained in cooling become linear in the coordinates α, $T^{-0.5}$ over the entire temperature range (BSO:Mn) or in the part $T < 500$ K (BSO:Cr). This result indicates in-center transitions involving phonons,[32] but the difference in the behavior of the $\alpha(T)$ curves during heating and cooling and their hysteresis suggest that impurity-level–allowed-band transitions (conduction or valence) contribute to the absorption, and the variation of the absorption during heating, as in the case of BSO and BSO:Ga crystals, is attributable to variation of the populations of these levels.

3. APPROXIMATION OF THE TEMPERATURE DEPENDENCE OF THE OPTICAL ABSORPTION

The optical ionization (activation) energy of the local levels (of the donor type for definiteness) is high ($E_a^{op} = 1.4-2.0$ eV) in the investigated range; consequently, they cannot be treated as hydrogenlike. We therefore use a configuration-coordinate model (Fig. 5) similar to the one described in Refs. 29 and 33. In this model we introduce the effective capture cross section for the thermal trapping of an electron in the conduction band associated with donor ionization:

$$\sigma_s^{th} = a W_\sigma^{th}, \tag{1}$$

where $a = \text{const}$, and W_σ^{th} is the capture probability. According to Ref. 9,

$$W_\sigma^{th} = A_1 (E_{FC} kT)^{-0.5} \exp(-E_\sigma^{th}/kT), \tag{2}$$

where A_1 does not depend on the temperature, E_{FC} is the Franck–Condon shift, k is the Boltzmann constant, and E_σ^{th} is the thermal activation energy of the capture cross section (Fig. 5). Factoring out the temperature dependence, we write

$$\sigma_s^{th} = \sigma_{s0}^{th} (T/T_0)^{-0.5} \exp(-E_\sigma^{th}/kT), \tag{3}$$

where we have assumed that $T_0 = 300$ K.

The flux e_n of thermally activated electrons from donor levels into the conduction band is given by the well-known expression

$$e_n = W_n^{th} \sigma_s^{th} N_c V_T, \tag{4}$$

where $W_n^{th} = \exp(-E_a^{th}/kT)$ is the probability of thermal activation of donors, E_a^{th} is the energy of thermal ionization of a donor level relative to the bottom of the conduction band (Fig. 5), $N_c = N_{c0}(T/T_0)^{1.5}$ is the density of states in the conduction band, where for BSO crystals $N_{c0} = 7.8 \times 10^{19}$ cm^{-3} (according to Ref. 34), and $V_T = V_{T0}(T/T_0)^{0.5}$, $V_{T0} = 6.2$ cm$\cdot$s^{-1}. On the basis of Eq. (3) the preexponential factor is $\sim (T/T_0)^{1.5}$, and we disregard this dependence as weaker than exponential.

We write the kinetic equation for the variation of the density of ionized donors N_d^i in the form

$$dN_d^i/dt = N_d^i e_n. \tag{5}$$

The following simple relation holds between the densities of ionized and neutral donors N_d:

$$N_d^0 = N_d^i + N_d, \tag{6}$$

where N_d^0 is the density of neutral donors at the initial time $T = 0$. To find the temperature dependence $N_d^i(T)$, we make use of the fact that $T = bt$, where b is the rate of change of the temperature. From Eq. (5) we obtain

$$N_d^i = C \exp\left\{ \int_0^T \tau_0^{-1} b^{-1} \exp[-(E_\sigma^{th} + E_a^{th})/k_B T'] \right\} dT'. \tag{7}$$

Here $C=\beta N_d^0$ is determined from the condition that $N_d^i \to \beta N_d^0$ as $T \to T_0$, where the value of β is dictated by the degree of compensation of donor levels by acceptor levels, $\tau_0^{-1}=(\sigma_{s0}^{\text{th}} N_{c0} V_{T0})$, and $E_\sigma^{\text{th}}+E_a^{\text{th}}=E^{\text{th}}$ is the effective thermal activation energy. The integral in Eq. (7) can be replaced by the approximate expression

$$\tau_0^*[(kT^2)/(E^{\text{th}}+1.85kT)]\exp(-E^{\text{th}}/kT), \tag{8}$$

where $\tau_0^*=\tau_0^{-1}b^{-1}$. Consequently,

$$N_d(T)=N_d^0\{1-\beta\ \exp[\tau_0^* kT^2/(E^{\text{th}}+1.85kT)] \times \exp(-E^{\text{th}}/kT)\}. \tag{9}$$

We write the temperature dependence of the optical absorption in the form

$$\alpha(T)=\sigma_a^{\text{op}}(T)N_d(T), \tag{10}$$

where $\sigma_a^{\text{op}}(T)$ is the effective photoionization cross section of the donor level.

According to Ref. 28, in active electron–phonon interaction the cross section σ_a^{op} decreases monotonically as the temperature increases. This functional dependence can be represented by the expression

$$\sigma_a^{\text{op}}(T)=B[\coth(h\omega/2kT)]^{-0.5}, \tag{11}$$

where B is independent of the temperature, and $h\omega$ is the localized-phonon energy.

Expanding $\coth(h\omega/2kT)$ in series form, subject to the conditions $h\omega<2kT$ and $h\omega/2kT<\pi$, we write Eq. (11) as

$$\sigma_a^{\text{op}}(T)=\sigma_a^*(T/T_0)^{-0.5}, \tag{12}$$

where σ_a^* is independent of the temperature.

Thus,

$$\alpha(T)=\sigma_a^*(T/T_0)^{-0.5}N_d(T). \tag{13}$$

The two descending absorption steps can be associated with the vacating of two types of donor levels with thermal activation energies E_1^{th} and E_2^{th}. The temperature dependence of the absorption can now be written in the final form

$$\alpha(T)=(T/T_0)^{-0.5}(\sigma_{a1}^* N_{d1}+\sigma_{a2}^* N_{d2})+\alpha_0, \tag{14}$$

where α_0 is the residual absorption. Equation (14) approximates the experimental observed stepwise decrease of the absorption at certain values of the parameters for each step. In particular, the following values of the parameters apply to a BSO crystal: $\sigma_a^* \approx \sigma_{a2}^* = 10^{-18}$ cm^2, $N_{d1}^0 = 8\times10^{17}$ cm^{-3}, $E_1^{\text{th}}=0.6$ eV, $\tau_{01}^*=3\times10^6$ s, $\beta_1=0.1$, $N_{d2}^0=5\times10^{17}$ cm^{-3}, $E_2^{\text{th}}=0.8$ eV, $\tau_{02}=5\times10^6$ s, $\beta_2=0.05$, $\alpha_0=0.4$ cm^{-1} (Fig. 2).

4. OPTICAL AND THERMAL IONIZATION ENERGIES

We have found that the temperature dependence of the optical absorption is determined mainly by the variation of the density of neutral donors (or acceptors). Consequently, the temperature rate of change of the absorption $d\alpha/dT$ is analogous to the thermally stimulated current intensity, which is determined by the variation of the density of free carriers in the conduction band or the valence band. Differentiating the experimental $\alpha(T)$ curves, we obtain

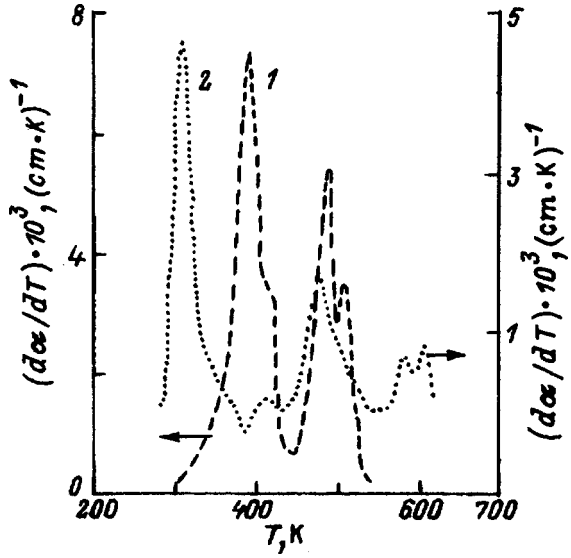

FIG. 6. Differential optical absorption curves for crystals of: *1*) BSO; *2*) BSO:Ga.

$(d\alpha/dT)(T)$ curves, which corroborate this assumption (Figs. 6 and 7). For BSO and BSO:Ga crystals they have peaks whose temperature positions correlate with the analogous positions of the peaks of the thermally stimulated current (TSC) and the thermally stimulated depolarization (TSD) current described in Refs. 35 and 36: For example, in BSO crystals, as opposed to BSO:Ga, the TSD current has no peaks at $T\sim300$ K, or they are not very pronounced. We encounter an analogous situation for the peaks of the $(d\alpha/dT)(T)$ curves. Correlation is also observed for BSO:Cr and BSO:Mn crystals, and it is interesting to note in this case that the $(d\alpha/dT)(T)$ curves reproduce the characteristic behavior of the TSD current, a set of narrow peaks in the interval $E=300-500$ K, and their intensity, like that of the TSD currents, is an order of magnitude higher in BSO:Cr crystal than for BSO:Mn. On the whole, however, the spectra

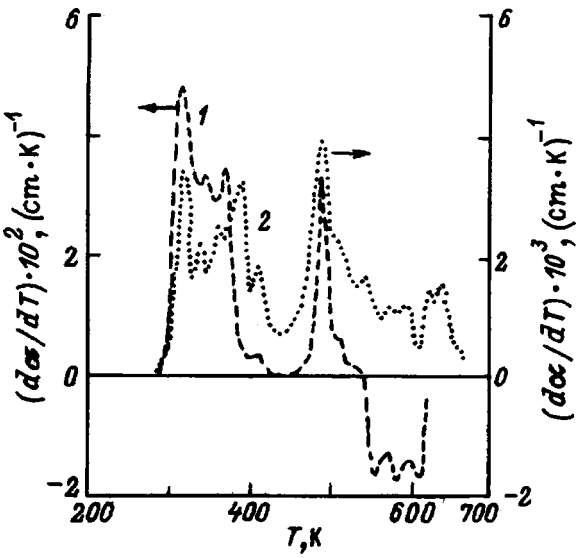

FIG. 7. Differential optical absorption curves for crystals of: *1*) BSO:Cr; *2*) BSO:Mn.

TABLE I. Thermal activation energies of deep levels in BSO, BSO:Ga, BSO:Mn, and BSO:Cr crystals.

Crystal	T_m, K	E^{th}, eV	T_m (K), E^{th} (eV) from TSC data
BSO	393	0.67	370, 0.66–0.72 (Ref. 15)
	488	0.85	
BSO:Ga	305	0.74	300, 0.69 (Ref. 35), 285, 0.71 (Ref. 35)
	480	1.13	
BSO:Mn	410	0.69	460, 0.7 (Ref. 25)
	490	1.15	
BSO:Cr	370	0.59	460, 1.5–1.7 (Ref. 25),
	490	1.56	

of the TSD currents are richer, because they contain the contribution of quasidipole polarization mechanisms. On the other hand, broadening the optical range of the investigations and improving the accuracy of the $\alpha(T)$ measurements can be expected to ''enrich'' the $(d\alpha/dT)(T)$ curves in the sense of achieving better correlation with thermal-activation spectroscopy (TAS) data.

The initial parts of the low-temperature and high-temperature slopes of the distinctly recorded peaks of the $(d\alpha/dT)(T)$ curves become linear in the coordinates $\ln(T^{0.5}d\alpha/dT)$, $1/kT$, and this property can be exploited to determine a number of values of the thermal activation energy E^{th} (see Table I).

The large difference between the optical and thermal ionization energies $E_a^{\text{op}}-E^{\text{th}}=0.5-0.9$ eV, which determines the Franck–Condon shift E_{FC} (Fig. 5), is characteristic of sillenite crystals and indicates a multiphonon mechanism of electron transitions; however, there is a need here to determine E_a^{op} more accurately, for example, by analyzing the heights of the steps characterizing the decrease of the absorption, as a function of the energy of absorbed optical photons. It should also be noted that for peaks with $T_m\sim 500$ K in BSO:Mn crystals the shift E_{FC} decreases, and in BSO:Cr crystals the values of E_a^{op} and E^{th} correlate well with each other; a similar situation has been remarked in an investigation of thermally stimulated currents.[25]

The relation between the values of E_a^{th} and E^{th} in BMO crystals has long been debated in the literature,[6,31,34,37–39] with no consensus among the different authors. For example, it has been postulated[6,34,37,39] that the local states of the band gap with $E_a^{\text{th}}=0.3-1.3$ eV and $E_a^{\text{op}}=1.3-3.0$ eV are identical, whereas other authors[31,38] have concluded that the values of E_a^{op} and E^{th} coincide for the same levels of the band gap. The contradictions stem from the difficulties of comparing these values in the juxtaposition of results obtained by different methods.

The results of the present study lead to the conclusion that the temperature curves of the impurity optical absorption provide additional possibilities for studying this problem, because the investigations have been carried out using a single method and permit the values of E_a^{op} and E^{th} to be tied in with the same deep local levels.

The author is grateful to S. G. Odulov for attention and a valuable discussion regarding the work.

[1] Yu. L. Kopylov, V. B. Kravchenko, and V. V. Kucha, Pis'ma Zh. Tekh. Fiz. **8**, 205 (1982) [Sov. Tech. Phys. Lett. **8**, 88 (1982)].
[2] N. I. Katsavets, E. I. Leonov, V. M. Orlov, and E. B. Shadrin, Pis'ma Zh. Tekh. Fiz. **9**, 424 (1983) [Sov. Tech. Phys. Lett. **9**, 183 (1983)].
[3] A. V. Ivanov, Yu. L. Kopylov, V. V. Kravchenko, V. V. Kucha, and R. Sh. Tukhvatulin, Zh. Tekh. Fiz. **54**, 2416 (1984) [Sov. Tech. Phys. Lett. **29**, 1428 (1984)].
[4] T. V. Panchenko and Yu. G. Osetskiĭ, Pis'ma Zh. Tekh. Fiz. **15**(20), 20 (1989) [Sov. Tech. Phys. Lett. **15**, 795 (1989)].
[5] N. I. Katsavets and E. I. Leonov, Zh. Tekh. Fiz. **56**, 1993 (1986) [Sov. Tech. Phys. Lett. **31**, 1191 (1986)].
[6] S. L. Hou, R. E. Lauer, and J. Aldrich, J. Appl. Phys. **44**, 2652 (1973).
[7] Yu. L. Kopylov, V. B. Kravchenko, and V. V. Kucha, Mikroelektronika **11**, 477 (1982).
[8] T. V. Panchenko, A. Yu. Kudzin, and V. Kh. Kostyuk, Izv. Akad. Nauk SSSR, Neorg. Mater. **19**, 1144 (1983).
[9] V. I. Berezkin, Phys. Status Solidi A **82**, K95 (1984).
[10] M. V. Shilova, V. V. Orlov, E. I. Leonov, E. E. Koslov, and I. A. Karpovich, Izv. Akad. Nauk SSSR, Neorg. Mater. **22**, 103 (1986).
[11] T. V. Panchenko and Z. Z. Yanchuk, Fiz. Tverd. Tela (St. Petersburg) **38**, 3042 (1996) [Phys. Solid State **38**, 1663 (1996)].
[12] I. S. Zakharov, P. A. Petukhov, V. M. Skorikov, M. G. Kisteneva, and Yu. F. Kargin, Izv. Vyssh. Uchebn. Zaved. MV SSO SSSR Fiz. No. 6, 85 (1995).
[13] T. V. Panchenko and N. A. Truseeva, Ukr. Fiz. Zh. **29**, 1186 (1984).
[14] R. Oberschmid, Phys. Status Solidi A **89**, 263 (1986).
[15] B. C. Grabmaier and R. Oberschmid, Phys. Status Solidi A **96**, 199 (1986).
[16] T. V. Panchenko and N. A. Truseeva, Ukr. Fiz. Zh. **34**, 1495 (1989).
[17] I. Foldvari, L. E. Halliburton, G. J. Edvards, and L. Otsi, Solid State Commun. **77**, 181 (1991).
[18] J. J. Martin, I. Foldvari, and G. A. Hunt, J. Appl. Phys. **70**, 7554 (1991).
[19] W. Wardzynski, H. Szymczak, and K. Pataj, J. Phys. Chem. Solids **43**, 767 (1982).
[20] W. Wardzynski, H. Szymczak, and M. P. Borowiec, and K. Pataj, J. Phys. Chem. Solids **46**, 1117 (1985).
[21] A. B. Dubovskiĭ, A. A. Mar'in, G. A. Sidorenko, and A. A. Fotchenkov, Izv. Akad. Nauk SSSR, Neorg. Mater. **22**, 1874 (1986).
[22] T. V. Panchenko and N. A. Truseeva, Ferroelectrics **115**, 73 (1991).
[23] T. V. Panchenko, Yu. G. Osetsky, and N. A. Truseeva, Ferroelectrics **174**, 61 (1995).
[24] V. I. Kalinin, Zh. S. Kuchuk, N. G. Gorashchenko, and A. A. Maĭer, Izv. Akad. Nauk SSSR, Neorg. Mater. **24**, 637 (1988).
[25] A. Yu. Kudzin, T. V. Panchenko, and N. A. Truseeva, Ukr. Fiz. Zh. **29**, 1414 (1984).
[26] Yu. I. Ukhanov, *Optical Properties of Semiconductors* [in Russian] (Nauka, Moscow, 1977).
[27] B. I. Shklovskiĭ and A. L. Éfros, *Electronic Properties of Doped Semiconductors* [Springer-Verlag, Berlin-New York (1984); Nauka, Moscow (1979)].
[28] A. A. Kopylov and A. N. Pikhtin, Fiz. Tverd. Tela (Leningrad) **16**, 1837 (1974) [Sov. Phys. Solid State **16**, 1200 (1974)].
[29] B. K. Ridley, *Quantum Processes in Semiconductors*, 3rd ed., Clarendon Press, Oxford; Oxford Univ. Press, New York (1993) [Russian trans. of 1st ed., Mir, Moscow, 1986].
[30] A. Hamri, M. Secu, V. Topa, and B. Briat, Opt. Mater. **4**, 197 (1995).
[31] V. K. Malinovskiĭ, O. A. Gudaev, V. A. Gusev, and S. I. Demenko, *Photoinduced Processes in Sillenites* [in Russian] (Nauka, Novosibirsk, 1990).
[32] A. F. Lubchenko, *Quantum Transitions in Impurity Centers in Solids* [in Russian] (Naukova Dumka, Kiev, 1976).
[33] D. Bois and A. Chante, Rev. Phys. Appl. **15**, 631 (1980).
[34] R. B. Lauer, J. Appl. Phys. **45**, 1794 (1974).
[35] T. V. Panchenko and G. V. Snezhnoĭ, Fiz. Tverd. Tela (St. Petersburg) **35**, 3248 (1993) [Phys. Solid State **35**, 1598 (1993)].
[36] D. Bloom and S. W. S. McKeever, J. Appl. Phys. **77**, 6521 (1995).
[37] M. G. Ermakov, A. V. Khomich, P. I. Perov, I. A. Gori, and V. V. Kucha, Mikroelektronika **11**, 424 (1982).
[38] V. A. Gusev, V. A. Detinenko, and A. P. Sokolov, Avtometriya, **5**, 34 (1983).
[39] V. I. Berezkin, Fiz. Tverd. Tela (Leningrad) **25**, 490 (1983) [Sov. Phys. Solid State **25**, 276 (1983)].

Translated by James S. Wood

Luminescence spectral properties of Sm- and (Ce, Sm)-containing silica gel glasses

G. E. Malashkevich and I. M. Mel'nichenko

Institute of Molecular and Atomic Physics, Academy of Sciences of Belarus, 220072 Minsk, Belarus

E. N. Poddenezhnyĭ and A. V. Semchenko

F. Skorina Gomel State University, 256699 Gomel, Belarus

(Submitted May 26, 1997; resubmitted September 16, 1997)
Fiz. Tverd. Tela (St. Petersburg) **40**, 458–465 (March 1998)

The spectroscopic behavior of Sm^{3+} ions is investigated in monoactivated and coactivated (with cerium) glasses obtained by the direct sol-gel-glass transition. It is shown that the majority of the Sm^{3+} ions form optical centers of the same type, whose luminescence spectral characteristics depend weakly on the concentration of the activator and the technique used to introduce it. Complex centers, including Sm^{3+} and Ce^{4+} ions bound by bridge oxygen, are also formed in the coactivated glass during the pore nucleation stage. The Sm^{3+} ions in these centers are characterized on the average by higher local symmetry, the efficient enhancement of luminescence by photoreduced $(Ce^{4+})^-$ ions, and its extinction by Ce-containing clusters.
© *1998 American Institute of Physics.* [S1063-7834(98)01303-3]

Glasses containing Sm^{3+} ions are promising materials for quantum electronics. For example, they work well in neodymium laser guns for the absorption of superluminescence radiation propagating perpendicularly to the axis of the active element.[1,2] Moreover, they are characterized by comparatively inefficient quenching cross-relaxation interactions[3] and the absence of the induced absorption from a metastable state commonly associated with the region of fundamental radiative transitions. These attributes well qualify them as active media for visible-range fiber lasers.[4] The preparation of such glasses by the sol-gel technique offers new capabilities for controlling their spectroscopic behavior. In particular, Demskaya and Pivovarov[5] have shown that the luminescence spectra of high-silicon, Sm-containing gel glasses can vary considerably, depending on the heat-treatment temperature and the presence of buffer elements in them. We have recently discovered[6,7] that the role of such buffers can be played by Ce^{4+} ions, which promote the entry of Ce^{3+} and Nd^{3+} ions into silica gel glasses and significantly alter the structure of their luminescence bands. These considerations have stimulated an interest in determining the influence of cerium on the luminescence spectral characteristics and salient features of the injection of Sm^{3+} ions into similar glasses. It is also important to assess this influence from the standpoint of finding luminescence enhancers for these ions, because they are characterized by extremely weak ''working'' absorption bands. The results of such an investigation are presented below.

1. MATERIALS AND EXPERIMENTAL PROCEDURE

The experimental samples were prepared by the direct sol-gel-glass transition using to a standard procedure.[6] Activation was achieved by introducing chlorides of the corresponding lanthanides in the stages of the sol-colloidal system and also by impregnating them with aqueous solutions of xerogels. In chemical purity all the working reagents were classified analytical grade or better. The samples were sintered in air at $T=1250$ °C, followed by cooling. The samples were also annealed at 750° for three hours in hydrogen at a pressure of 1.1 atm. The volume concentration N of activators in the experimental samples was determined by means of an IMS-4F ion microscope with $\pm 15\%$ measurement error limits. The adopted standard was a (Ce, Sm)-containing silica gel glass, in which the mass concentration of the ingredients was determined with a Camebax x-ray microanalyzer[8] and converted into the values of N for the corresponding elements.

The optical extinction spectra were recorded on a Beckman UV5270 spectrophotometer. The luminescence spectra and the luminescence excitation spectra were recorded on an SDL-2 spectrofluorimeter, then were corrected[9] and displayed to show the wavelength dependence of the number of photons (luminescence or excitation) per unit wavelength interval $dn/d\lambda$ or the wavenumber dependence of the number of photons per unit wavenumber interval $dn/d\tilde{\nu}$. Conventional methods[6] were used to reduce excess absorption and extinction of luminescence.

The luminescence kinetics was investigated with a PRA-3000 spectrofluorimeter at various excitation wavelengths λ_{exc} and recording wavelengths λ_{rec}. The average luminescence extinction time was calculated from the equation $\bar{\tau}=\Sigma_i \alpha_i \tau_i / \Sigma_i \alpha_i$, where α_i denotes the coefficients of the decay exponential, which characterize the relative contributions of components with the decay time constants τ_i to the extinction curve. All the luminescence spectral measurements were performed at $T=2988$ K.

2. RESULTS

Traces of extraneous impurity metals such as Al, K, Ca, and Ti are detected in the prepared samples. However, their

 © 1998 American Institute of Physics

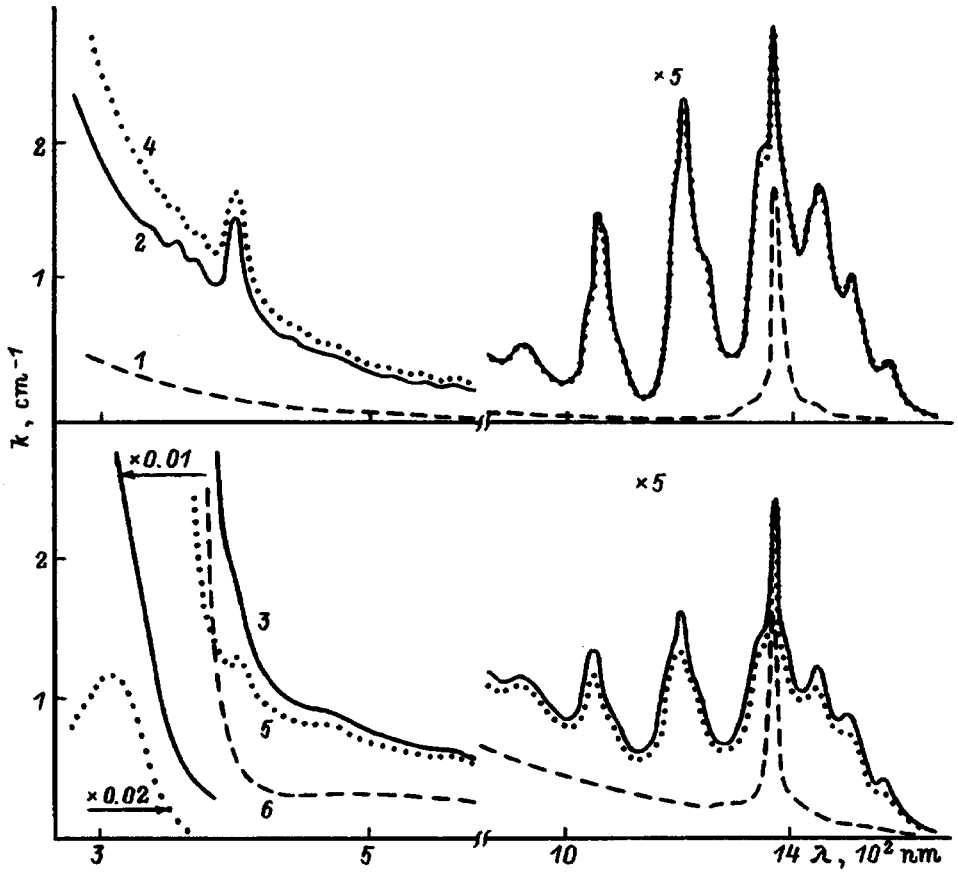

FIG. 1. Optical extinction spectra of nonactivated and Sm-, (Ce, Sm)-, and Ce-containing glasses activated by xerogel impregnation. *1, 6*) $N_{Sm}=0$; *2, 4*) $N_{Sm}=3.0\times10^{19}$ ion/cm^3; *3,5*) $N_{Sm}=3.5\times10^{19}$ ion/cm^3; *1, 2, 4*) $N_{Ce}=0$; *3, 5*) $N_{Ce}=3.5\times10^{19}$ ion/cm^3; *6*) $N_{Ce}=3.7\times10^{19}$ ion/cm^3; *4, 5*) glasses annealed in hydrogen.

concentrations are almost three orders of magnitude lower than those of Ce and Sm. An industrial chlorine impurity is detected only for highly activated samples ($N_{Ln}\approx10^{20}$ ion/cm^3) in concentrations lower than 0.1 times N_{Ln}.

Figure 1 shows the optical extinction spectra of Sm-, (Ce, Sm)-, and Ce-containing glasses. Also shown are the like spectra of the first two glasses after annealing in hydrogen and the spectrum of a nonactivated glass (curve *1*) with the same natural extinction coefficient k at the fundamental wavelength of hydroxyl ions as for the monoactivated glass ($\lambda\approx2720$ nm, Ref. 10). It is evident that activation by samarium in a concentration of 3.0×10^{19} ion/cm^3 is accompanied by a monotonic increase in the attenuation of the glass as λ decreases and by the onset of two groups of weak, narrow bands separated by a long spectral interval (curve *2*). The narrow bands do not exhibit any conspicuous violation of the Bouguer–Lambert–Beer when N_{Sm} is lowered to 8.0×10^{18} ion/cm^3. The introduction of cerium coactivator with $N_{Ce}=3.5\times10^{19}$ ion/cm^3 in the same kind of glass ($N_{Sm}=3.5\times10^{19}$ ion/cm^3 induces strong ultraviolet (UV) absorption and attenuation of the narrow bands (curve *3*). The annealing of Sm-containing glass in hydrogen has scarcely any effect at all on its spectrum (curve *4*). Similar annealing of (Ce, Sm)-containing glass produces a slight reduction in the intensities of the narrow bands and a marked decrease of the attenuation in the UV region (curve *5*). The spectrum of Ce-containing glass ($N_{Ce}=3.7\times10^{19}$ ion/cm^3 takes the form of a strong UV band with a long-wavelength edge and, adjacent to it, a broad, weak band extending into the near infrared (IR) region (curve *6*).

Figure 2 shows the luminescence and luminescence excitation spectra of Sm- and (Ce, Sm)-containing glasses. It is evident that the luminescence of monoactivated glass with $N_{Sm}=9.0\times10^{18}$ ion/cm^3 at $\lambda_{exc}=400$ nm consists of a series of relatively narrow bands having an intricate profile (curve *1*), the strongest band occurring at 15340 cm^{-1} ($\lambda=652$ nm). The spectral half-width $\Delta\lambda_{exc}$ of the strongest component of this band is 90 cm^{-1}. An increase in the activator concentration to 3.8×10^{19} ion/cm^3 and scanning of the short-wavelength group of absorption bands by exciting radiation with $\Delta\lambda_{exc}=4$ nm are not accompanied by any appreciable change in the luminescence spectrum. Nor is it altered by hydrogen annealing. The luminescence excitation spectrum of monoactivated glass (curve *2*) is slightly dependent on λ_{rec} and is similar to the spectrum of its short-wavelength group of absorption bands. The luminescence spectrum of coactivated glass with $N_{Sm}=0.4N_{Ce}=8.0\times10^{18}$ ion/cm^3 at $\lambda_{exc}\geqslant400$ nm is similar to the spectrum of the monoactivated glass. However, a radical change in the narrowband luminescence spectrum is observed when λ_{exc} moves toward the short-wavelength end (curve *3*, $\lambda_{exc}=320$ nm). Appearing simultaneously is a broad, weak luminescence band with a maximum at 23 000 cm^{-1} (not shown on curve *3*). The profile and total intensity of this band are essentially identical for (Ce, Sm)- and Ce-containing glasses of equal thickness and equal N_{Ce}. The excitation spectra of the strongest bands on curve *3* differ slightly and are characterized by the presence of a broad, strong band at 330 nm (curve *4*, $\lambda_{rec}=615$ nm). A similar but much weaker broad band is also observed in the lumi-

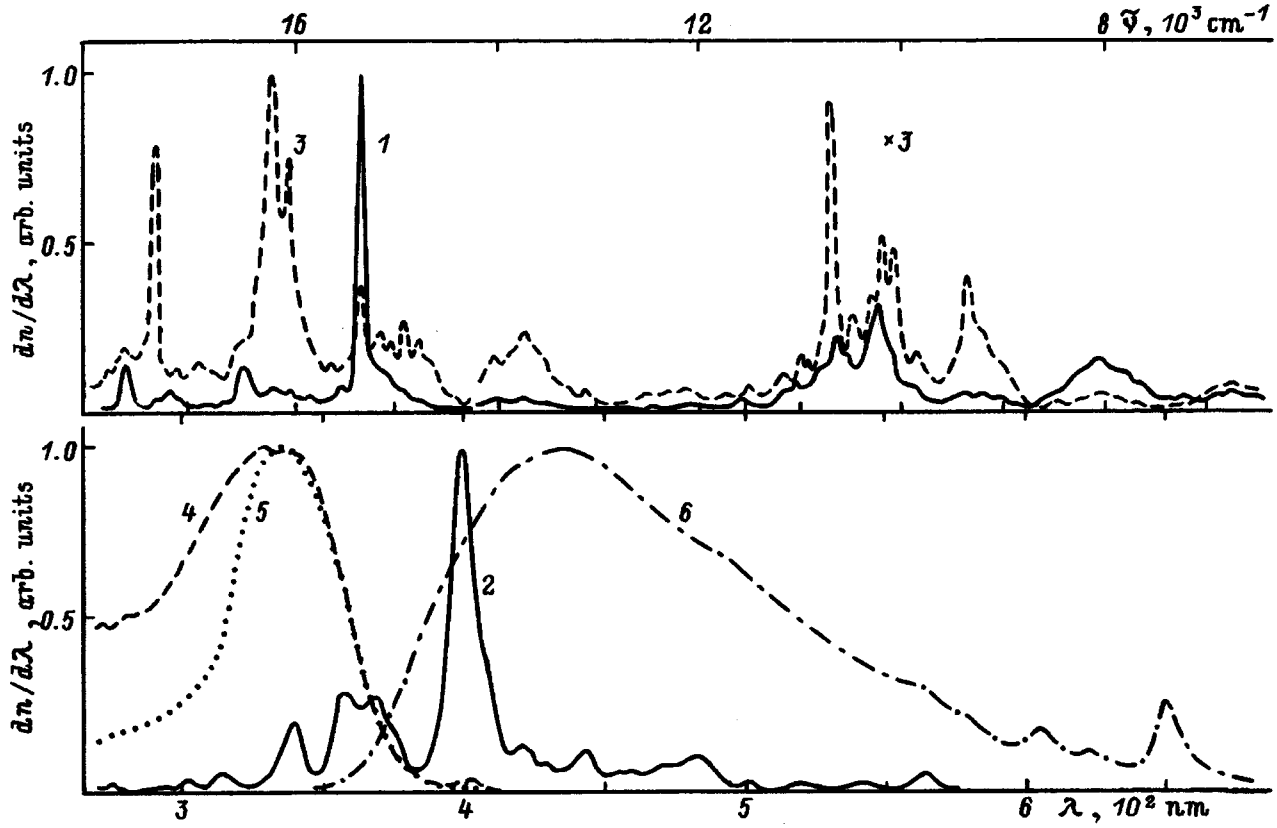

FIG. 2. Normalized and corrected luminescence and luminescence excitation curves of Sm- and (Ce, Sm)-containing glasses activated in the stage of the sol-colloidal system. *1, 3, 6*) Luminescence spectra; *2, 4, 5*) excitation spectra; *3, 6*) $\lambda_{exc}=320$ nm; *1*) 400 nm; *5*) $\lambda_{rec}=430$ nm; *4*) 615 nm; *2*) 650 nm. $\Delta\lambda_{exc}=2\Delta\lambda_{rec}=4$ nm. *3, 4, 6*) $N_{Sm}=8.0\times10^{18}$ ion/cm^3; *1, 2*) $N_{Sm}=9.0\times10^{18}$ ion/cm^3; *1, 2*) $N_{Ce}=0$; *3–6*) $N_{Ce}=2.0\times10^{19}$ ion/cm^3; *6*) glass annealed in hydrogen.

nescence excitation spectrum at 23 000 cm^{-1} (curve *5*, $\lambda_{rec}=430$ nm). As λ_{rec} increases within the limits of this luminescence band, the excitation band broadens considerably toward the long-wavelength end of the spectrum, but there is no perceptible broadening on the short-wavelength side at any wavelength λ_{rec}. The annealing of coactivated glass in hydrogen increases the relative intensity of the broad, short-wavelength band severalfold, but the narrowband luminescence spectrum at $\lambda_{exc}=320$ nm (curve *6*) becomes more like the spectrum of the Sm-containing glass. Also resembling the latter at all values of λ_{exc} are the narrowband luminescence spectra of coactivated xerogels subjected to heat treatment in air at 1000 °C.

Figure 3 shows the luminescence decay kinetics of Sm-, (Ce, Sm)-, and Ce-containing glasses. It is evident that the luminescence decay law of Sm-containing glass over a dynamic intensity range of 10^2 for $N_{Sm}=9.0\times10^{18}$ ion/cm^3, $\lambda_{exc}\geqslant400$ nm, and $\lambda_{rec}=650$ nm is close to a single-exponential curve (curve *2*) with $\bar{\tau}\approx1.6$ ms. As λ_{rec} or λ_{exc} is scanned over the corresponding spectra, the variance of $\bar{\tau}$ does not exceed 15%. An increase in N_{Sm} to 3.8×10^{19} ion/cm^3 is not accompanied by any change in $\bar{\tau}$ or in the nature of the decay process. For coactivated glass with $N_{Sm}=0.4N_{Ce}=8.0\times10^{18}$ ion/cm^3 at $\lambda_{exc}\geqslant400$ nm the narrowband luminescence decay curve (curve *3*) is similar to the corresponding curve for the monoactivated glass. At $\lambda_{exc}=320$ nm, however, it deviates more radically from exponential behavior (curve *4*), and the average time constant $\bar{\tau}$ approaches 0.7 ms. In this case the variation of the decay rate as a function of λ_{exc} and λ_{rec} falls within 20% limits. The attempt to isolate the transient rise of narrowband luminescence was futile: The initial part of the kinetic curve essen-

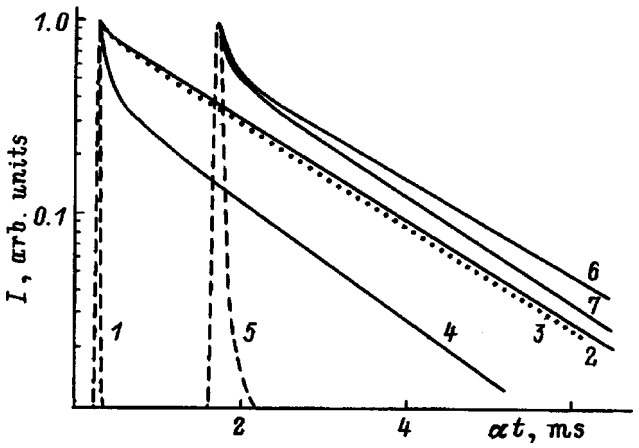

FIG. 3. Luminescence decay kinetics of Sm-, (Ce, Sm)-, and Ce-containing glasses activated in the stage of the sol-colloidal system. *4, 6, 7*) $\lambda_{exc}=320$ nm; *2, 3*) 400 nm; *6, 7*) $\lambda_{rec}=430$ nm; *4*) 615 nm; *2, 3*) 650 nm. $\Delta\lambda_{exc}=\Delta\lambda_{rec}=4$ nm. *6*) $N_{Sm}=0$; *3, 4, 7*) $N_{Sm}=8.0\times10^{18}$ ion/cm^3; *2*) $N_{Sm}=9.0\times10^{18}$ ion/cm^3; *2*) $N_{Ce}=0$; *6*) $N_{Ce}=1.7\times10^{19}$ ion/cm^3; *3, 4, 7*) $N_{Ce}=2.0\times10^{19}$ ion/cm^3; *1, 5*) excitation pulses. *1–4*) $\alpha=1$; *5–7*) $\alpha=2\times10^4$.

tially coincided with the leading edge of the excitation pulse for all values of λ_{exc} and λ_{rec}. The decay of wideband luminescence of Ce-containing glass with $N_{Ce}=9.0\times10^{18}$ ion/cm^3 also departs from an exponential law (curve *6*), but its time constant $\overline{\tau}$ is many orders of magnitude smaller, with a value ≈ 50 ns for $\lambda_{exc}=320$ nm and $\lambda_{rec}=430$ nm. For the coactivated glass under the same excitation and recording conditions the value of $\overline{\tau}$ is shortened to 45 ns, mainly as a result of acceleration of the far decay stage (curve *7*).

These results should be viewed in context with the observation that the indicated luminescence spectral relations of the investigated glasses occur for both of the activation techniques used. However, for glasses coactivated by impregnation with xerogels a radical difference in the luminescence spectra as λ_{exc} is shifted from the region $\geqslant 400$ nm into the UV region occurs at many times lower concentrations N_{Ce}.

TABLE I. Characteristics of the absorption and luminescence bands of Sm^{3+} ions in monoactivated silica gel glass.

Absorption from $^6H_{5/2}$ states		Luminescence from $^4G_{5/2}$ states		
Transition to state	$\lambda/\overline{\nu}$ nm/cm^{-1}	Transition to state	$\lambda/\overline{\nu}$ nm/cm^{-1}	m
$^6F_{1/2}$	1570/6370	$^6F_{11/2}$	1476/6770	6
$^6H_{15/2}$	1520/6580	$^6F_{9/2}$	1240/8060	7
$^6F_{3/2}$	1450/6900	$^6F_{7/2}$	1065/9390	4
$^6F_{5/2}$	1350/7410	$^6F_{5/2}$	976/10250	5
$^6F_{7/2}$	1210/8260	$^6F_{3/2}$	940/10640	4
$^6F_{9/2}$	1060/9430	$^6H_{15/2}$	902/11090	6
$^6F_{11/2}$	940/10640	$^6F_{1/2}$	866/11550	3
$^4G_{5/2}$	565/17700	$^6H_{13/2}$	824/12140	7
?	545/18350	$^6H_{11/2}$	714/14000	6
$^4F_{3/2}$	524/19080	$^6H_{9/2}$	652/15340	7
$^4G_{7/2}$	503/19880	$^6H_{7/2}$	606/16500	6
$^4I_{3/2}+{}^4M_{15/2}$	488/20580	$^6H_{5/2}$	566/17670	4

Note: Here λ and $\overline{\nu}$ are the wavelength and the wavenumber corresponding to the position of the maximum of the given band, and m is the number of Stark splitting components.

3. DISCUSSION OF THE RESULTS

In light of the results of a quantitative analysis we can disregard the presence of impurity metals and industrial chlorine and identify the spectra described above entirely with the presence of the injected activators. Of course, in analyzing the optical extinction spectra associated with these activators (Fig. 1), we need to exclude the band at 1380 nm associated with the first harmonic of the hydroxyl ions.[10] The small differences in the intensity of this band for all the experimental samples indicate an approximately uniform concentration of these ions, whose influence can therefore be ignored in the interpretation of the observed spectral variations.

The narrow extinction bands of Sm- and (Ce, Sm)-containing glasses (Fig. 1) are attributable to absorption transitions within the $4f^5$ shells of the Sm^{3+} ions.[3] The monotonic increase of k in the visible and near-IR regions of the spectrum with decreasing λ for the Sm-containing glass (curve *2*) is logically attributed to light scattering as a result of the material microinhomogeneity induced by the incompatibility of the highly coordinated samarium-oxygen polyhedra with the structural matrix of SiO_2. Cerium activation detracts far less from the optical homogeneity of the glass, but leads to absorption in the visible and near-IR regions (curve *6*) in connection with Ce-containing clusters.[6] When the extrapolated light-scattering spectrum is subtracted from the spectrum described by curve *2*, and when curve *6* is additionally subtracted from curve *3*, it is a simple matter to determine the partial intensities of the narrow IR bands for both glasses. The reduction of the resulting absorption spectra to a single Sm^{3+} ion shows that their total specific intensity I_{Sm} for the coactivated glass is approximately 1.7 times lower than for the monoactivated glass. Two reasons can be cited as capable of producing such a reduction in I_{Sm}. The first is an increase in the degree of covalence of the samarium–ligand bond. Owing to the significantly different degrees of participation of the f and d shells in the chemical bonds (the d shell exhibits greater broadening) decreases the mixing of energy states of opposite parity and intensifies the exclusion of ''stimulated'' electric dipole transitions.[11] The second possible reason is an increase in the symmetry of the optical centers, which also reduces the mixing of these states. As for the strong UV absorption of coactivated glasses, this effect is mainly attributable to the charge-transfer band of Ce(IV) oxo complexes.[6] The absence of explicit manifestations of bands associated with interconfigurational transitions of Ce^{3+} ions[6] and Sm^{2+} ions[12] can be attributed to the fact that sintering of the glasses is not accompanied by the thermal dissociation of silica, a process that imparts reducibility to the matrix.[13]

The very nearly identical values of I_{Sm} for the monoactivated glass before and after hydrogen annealing imply that the reduction of Sm^{3+} ions is not very efficient. Conversely, judging from the abatement of the optical extinction of coactivated glass in the UV region (curve *5*), the reduction of Ce^{4+} ions in the same annealing process is quite efficient. The low annealing temperature in this case suggests that a change in the coordination numbers of rare-earth activators is not very probable. Consequently, the appreciable decrease of I_{Sm} as a result of such annealing favors the entry of Ce^{4+} ions into the first cationic shell of the Sm^{3+} ions. Indeed, the reduction of quadruply charged to triply charged cerium in this case raises the degree of covalence of the bond between the samarium ions and ligands by curtailing the stretching of the latter by cerium ions owing to diminution of the strength of the single cerium–ligand chemical bond from 1.33 to 1.25 arbitrary units.[6]

To achieve a truer interpretation of the results of the luminescence investigations, we have used data on the positions of the energy states of Sm^{3+} ions in aqueous solution and in the crystal lattice[14] to identify the series of absorption bands observed for monoactivated glass; the results are summarized in Table I. The determination of the positions of the weak bands due to transitions to the upper system of multiplets is refined on the basis of the luminescence excitation spectra (curve *2* in Fig. 2). The identification can be regarded as unambiguous except for the extra band at 545 nm, which can be identified with transitions to the upper Stark compo-

nent of the $^4G_{5/2}$ state or to the lower component of the $^4F_{3/2}$ state.

Judging from the insignificant variability of the luminescence spectrum of the Sm-containing glass (curve *1* in Fig. 2) when excitation takes place in different short-wavelength bands, the spectrum must be associated with intraconfigurational transitions of Sm^{3+} ions from a metastable state ($^4G_{5/2}$) to levels of the lower system of multiplets. This conclusion seems natural, since the energy gaps between states of the upper system of multiplets, expressed in cm^{-1} (see Table I), are close to half the wave number corresponding to the fundamental absorption edge of atoms of the silica glass network ($\bar{\nu}\sim 1100$ cm^{-1}, Ref. 10) and are approximately one fifth the wave number of the fundamental valence mode of hydroxyl ions, which have a high concentration in the investigated glasses ($N_{OH}\sim 3\times 10^{20}$ ion/cm^3, Ref. 6). We have used the tabulated data on the positions of the absorption bands of Sm^{3+} ions in such a glass to identify the luminescence bands and to determine the number m of their individual components, which for several transitions is found to be higher than the maximum possible number of Stark splitting components of the corresponding lower states (see Table I). This fact can be attributed to the dissimilar ways in which the activator enters the matrix of the investigated glass or to radiation from thermally populated Stark components of the $^4G_{5/2}$ state. However, considering the low intensity of these extra components and the slight variation of the spectra as λ_{exc} is scanned along the spectrum, we can conclude that the fraction of Sm^{3+} ions that form possible extraneous types of optical centers is minuscule. The high relative intensity of the ultrasensitive electric dipole transition $^4G_{5/2}\rightarrow{}^6H_{9/2}$ (the fraction of photons emitted in the transition is 45%) indicates that the Sm^{3+} ions reside in a low-symmetry local environment in the monoactivated glass.

The similarity of the luminescence spectra recorded for Sm- and (Ce, Sm)-containing glasses at $\lambda_{exc}\geqslant 400$ nm suggests that the optical centers excited in them are of the same type. The radical change of the narrowband luminescence spectrum of the coactivated glass at $\lambda_{exc}=320$ nm (curve *3* in Fig. 2) indicates the excitation of a new type of center. The wide luminescence band observed in such excitation at 23 000 cm^{-1} is attributable to the parity-allowed interconfigurational transitions $4f^05d\rightarrow 4f^1$ of Ce^{3+} ions, the fraction of which remains appreciable when such glasses are sintered in air.[6] The spectroscopic nonappearance of a new type of center as $N_{Ce(IV)}\rightarrow 0$ (see curve *6*) means that they can be ascribed to complex formations, including Ce^{4+} and Sm^{3+} ions linked by bridge oxygen, whose existence is inferred from an analysis of Fig. 1. The major redistribution of the relative luminescence intensity of these Ce–Sm centers in favor of bands corresponding to the resolved magnetic dipole transitions $^4G_{5/2}\rightarrow{}^6H_{5/2},{}^6H_{7/2},{}^6F_{3/2},{}^6F_{7/2}$ justifies the assertion that they are characterized on the average by a far higher local symmetry of the Sm^{3+} ions. We note that the possibility of this type of activator entry into disordered matrices is corroborated by Ref. 15, in which the slightly distorted cubic centers of singly charged copper ions in zirconium fluoride glasses are described. The elevation of the indicated symmetry should be accompanied by the abatement of $f-f$ transitions of Sm^{3+} ions[11] and is very likely the main cause of the above-discussed decrease of I_{Sm} for the coactivated glass without heat treatment in air. The lack of Ce–Sm centers in air-heat-treated activated xerogels fosters the assumption that they are formed only during the consolidation of the matrix in the pore nucleation stage.

The essentially identical intensity of the wideband luminescence of monoactivated and coactivated glasses at equal concentrations N_{Ce} and the difference in the UV luminescence excitation bands of Ce and Ce-Sm centers (curves *5* and *4* in Fig. 2, respectively) attest to the weak participation of Ce^{3+} ions in enhancing the luminescence of Sm^{3+} ions. Consequently, the strong UV band in the luminescence excitation spectrum of Ce–Sm centers is logically attributed to the transfer of Sm^{3+} ions from photoreduced $(Ce^{4+})^-$ ions, whose absorption spectrum is close[16] to the like spectrum of their representatives. The formation of such photocharge-exchanged ions is obviously the result of Ce^{4+} ions capturing electrons from excited sublevels of the charge-transfer complex, which exist in resonance with the corresponding energy states of the $(Ce^{4+})^-$ ions, and is described as follows:

$$Ce^{4+}-O^{2-}-Sm^{3+}+h\nu\rightarrow[(Ce^{4+})^-]^*-(O^{2-})^+-Sm^{3+}.$$

The impossibility of separating the luminescence rise stage of the Sm^{3+} ions leads to the conclusion that excitations are transferred to them in the presence of strong interaction, which is achievable if the Ce^{4+} and Sm^{3+} ions are linked by bridge oxygen with the formation of a nearly collinear configuration.[17] Here the transfer process can probably take place through the transfer of an electron to a Sm^{3+} ion with the formation of an excited photoreduced $[(Sm^{3+})^-]^*$ ion, which is converted into $(Sm^{3+})^*$, giving up an electron to the ligand from its ground state:

$$[(Ce^{4+})^-]^*-(O^{2-})^+-Sm^{3+}\rightarrow Ce^{4+}-(O^{2-})^+-[(Sm^{3+})^-]^*$$
$$\rightarrow Ce^{4+}-O^{2-}-(Sm^{3+})^*.$$

Nor should we rule out the transfer of excitation to a Sm^{3+} ion with the simultaneous return of an electron from the ground state of a $(Ce^{4+})^-$ ion to the ligand, i.e., omitting the middle link in the above photochemical reaction.

The near-exponential luminescence decay kinetics of Sm-containing glass (curve *2* in Fig. 3), the invariance of its characteristics as N_{Sm} is varied in the range $(9-38)\times 10^{18}$ ion/cm^3, and the small variance of $\bar{\tau}$ indicates weak cross-relaxation interaction of the activator ions and a small difference between the probabilities of their radiative transitions. The nearly exact identity of the kinetic curves *2* and *3* confirms the above conclusion that the optical centers excited at $\lambda_{exc}\geqslant 400$ nm in Sm- and (Ce, Sm)-containing glasses are similar. The substantially more pronounced departure from exponential decay of the luminescence of Sm^{3+} ions in coactivated glasses with excitation through the absorption band of the Ce^{3+} ions (curve *4*) is a consequence of the heightened efficiency of deactivation of the $^4G_{5/2}$ state due to the transfer of excitations to a disordered collection of acceptors.[18] The role of the latter in our case can be filled by Sm^{3+} ions and Ce-containing clusters, which absorb in the visible range of the spectrum. An analysis of the kinetic

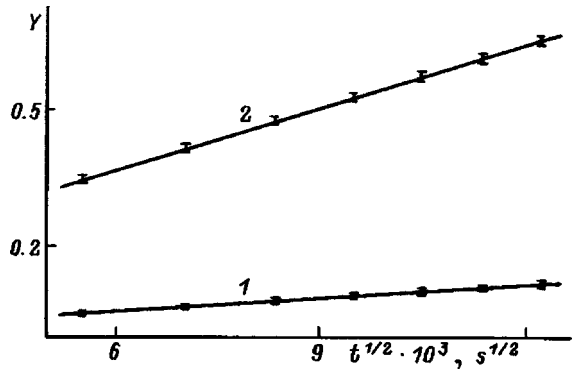

FIG. 4. Plot of the function $Y=\ln I(0)/I(t)-t/\tau_d$ versus $t^{1/2}$ for the luminescence decay kinetics of (Ce, Sm)-containing glass. *2)* $\lambda_{exc}=320$ nm, $\lambda_{rec}=615$ nm; *1)* $\lambda_{exc}=400$ nm, $\lambda_{rec}=650$ nm. $N_{Sm}=0.4N_{Ce}=8.0\times10^{18}$ *ion/cm*^{3}.

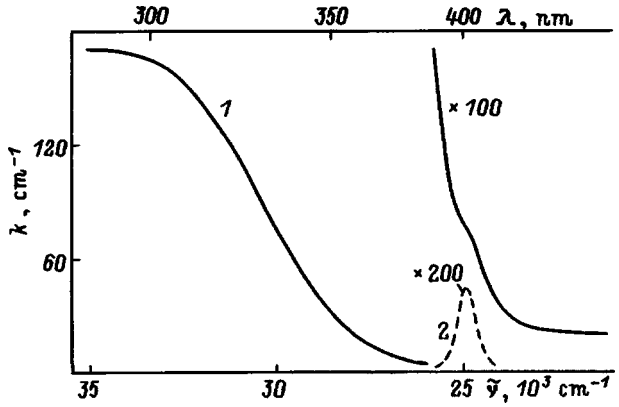

FIG. 5. Absorption spectrum of (Ce, Sm)-containing glass (curve *1*) and its calculated component attributable to Sm^{3+} ions (curve *2*). $N_{Sm}=0.4N_{Ce}=8.0\times10^{18}$ ion/cm^3.

curves *3* and *4* in Fig. 3 has shown that the function characterizing the rate of nonexponential luminescence decay, $Y=\ln I(0)/I(t)-t/\tau_d$, where $I(0)$ and $I(t)$ are the luminescence intensities at the initial (maximum) and final times, τ_d is the time constant of the far exponential, is linear in the coordinates ($t^{1/2}$) in both cases (Fig. 4). This result implies a dipole-dipole donor-acceptor interaction mechanism and means that the Förster decay macroparameters γ can be determined from the slope of the lines 1 ($\lambda_{exc}=400$ nm) and 2 ($\lambda_{exc}=320$ nm) in Fig. 4 relative to the horizontal axis; they are equal to 8 $s^{-1/2}$ and 45 $s^{-1/2}$, respectively.

To ascertain the relationship of the nonexponential behavior to the cross-relaxation interaction of Sm^{3+} ions, we have calculated the overlap integrals[18] normalized to the area of the luminescence spectra ($\lambda_{exc}=320$ nm and 400 nm) and the absorption of these ions in coactivated glass. The integral in question is found to increase only 10% for Ce–Sm centers. This increment is clearly not sufficient for the observed 5.6-fold increase in γ. Such an increase in γ should certainly be impossible in view of the dominant nonresonant interactions in Ln-containing glasses,[19] because the fraction of luminescence photons of Ce–Sm centers within the spectral region corresponding to the long-wavelength group of absorption bands of Sm^{3+} ions is 15% smaller than the analogous fraction of luminescence photons of Sm centers. Consequently, the most probable cause of the nonexponential decay of the narrowband luminescence of Ce–Sm centers is the nonradiative transfer of excitations to Ce-containing clusters, which absorb light in the visible region. It is obvious that the distance between the indicated clusters and Sm^{3+} ions in the Ce–Sm centers is small. Conversely, the weak influence of these clusters on the extinction of luminescence of the Sm centers bears witness to their pronounced spatial confinement. On the other hand, the nonexponential decay of the luminescence of Ce^{3+} ions in monoactivated glass (curve *6*) is attributable to extinction by the indicated clusters and to the nonequivalence of the local environments of these ions.[6] The slight reduction of their constants $\bar{\tau}$ for the coactivated glass (curve *7*) confirms the low efficiency with which the luminescence of Sm^{3+} is enhanced by Ce^{3+} ions.

It should be noted at this point that the close values of τ in the far stage of exponential luminescence decay of Sm^{3+} ions for both the discussed types of optical centers (1.63 ms and 1.47 ms for samples characterized by curves *3* and *4* in Fig. 3, respectively) contradict the conclusion that the $f-f$ transitions of these ions in Ce–Sm centers are highly attenuated. The kinetic curve for narrowband luminescence probably does in fact have a significantly slower exponential segment, but the low intensity of the signal hampers its identification. Not to be overlooked, however, is the possibility that the proximity of these values of τ is associated with the migration of excitations of Sm^{3+} ions from the Ce–Sm centers.

We conclude with an estimate of the concentration of the above-described Ce–Sm centers. It is obviously close to the product of N_{Ce} and the quantum yield of luminescence enhancement of the Sm^{3+} ions (η). This yield can be calculated by comparing the intensities of the cerium and samarium bands at 330 nm and 400 nm in the spectra of absorption and excitation of enhanced luminescence according to the equation $\eta=(\beta_{Sm}k_{Sm}dn_{Ce}/d\lambda)/(k_{Ce}dn_{Sm}/d\lambda)$, where β is the fraction of photons absorbed by Sm^{3+} ions. Determining the parameters in this equation for glass with $N_{Sm}=0.4N_{Ce}=8.0\times10^{18}$ ion/cm^3 from curve *4* in Fig. 2 and from the total (integrated) absorption spectrum (curve *1* in Fig. 5) and, derived from the latter by a standard method,[6,20] the samarium absorption spectrum (curve *2* in Fig. 5), we obtain $\eta\geqslant4\%$. The concentration of Ce–Sm centers then falls at the level of 0.8×10^{18} ion/cm^3, or 10% of N_{Sm}. We note that this value is obtained for glass activated in the stage of the sol–colloidal system. Naturally, for glass activated by xerogel impregnation with $N_{Sm}=N_{Ce}=3.5\times10^{19}$ ion/cm^3 (Fig. 1) the fraction of Ce–Sm centers will be significantly higher, thereby accounting for the observed decrease of I_{Sm}.

We have thus shown that samarium enters into silica gel glasses sintered at 1250 °C in the triply charged state. By far the greater fraction of its ions form optical centers of one type. Such centers are characterized by the weak cross-relaxation interaction of Sm^{3+} ions and a sizable fraction of photons ($\sim45\%$) emitted in the ultrasensitive electric dipole transition $^4G_{5/2}\rightarrow{}^6H_{9/2}$. The coactivation of Sm-containing glasses with cerium results in the formation of a new type of

optical center in the pore nucleation stage, including Sm^{3+} and Ce^{4+} ions bound by bridge oxygen. The Sm^{3+} ions in these complex centers are characterized on the average by higher local symmetry and efficient enhancement of luminescence by photoreduced $(Ce^{4+})^-$ ions. The cross-relaxation interactions of Sm^{3+} ions in the subsystem of these centers are weak, but the extinction of their luminescence is comparatively efficient as a result of the dipole-dipole transfer of excitations to Ce-containing clusters, which absorb light in the visible region of the spectrum. The presence of Ce^{3+} ions in the coactivated glass has a weak influence on the luminescence spectral characteristics of the samarium optical centers.

[1] *Laser Pumping Chambers and Laser Cavity Filters*, (Kigre, Inc., Hilton Head, S.C., 1993).
[2] G. E. Malashkevich, V. I. Aleksandrov, A. L. Blinov, and M. A. Borik, Publication of the Academy of Sciences of the USSR No. 1334624 [in Russian] (Akad. Nauk SSSR, 1987).
[3] I. A. Zhmyreva, V. P. Kolobkov, G. O. Karapetyan, and E. G. Bondarenko, Zh. Prikl. Spektrosk. **8**, 271 (1990).
[4] M. C. Farries, P. R. Morkel, and J. E. Townsend, Proc. SPIE **1171**, 271 (1990).
[5] É. L. Demskaya and S. S. Pivovarov, Fiz. Khim. Stekla **16**, 605 (1990).
[6] G. E. Malashkevich, E. N. Poddenezhny, I. M. Melnichenko, and A. A. Boiko, J. Non-Cryst. Solids **188**, 107 (1995).
[7] G. E. Malashkevich, E. N. Poddenezhny, I. M. Melnichenko, and V. E. Gaishun, in *Proceedings of the 17th International Congress on Glass*, Vol. **4** (Beijing, 1995), p. 320.
[8] G. E. Malashkevich, Inst. Fiz. AN BSSR Preprint No. 397 [in Russian] (B. I. Stepanov Institute of Physics, Academy of Sciences of the Belorussian SSR, Minsk, 1982).
[9] C. A. Parker, *Photoluminescence of Solutions, With Applications to Photochemistry and Analytical Chemistry* [Elsevier, Amsterdam-New York, 1968; Mir, Moscow, 1972, p. 232].
[10] A. R. Silin' and A. N. Trukhin, *Point Defects and Elementary Excitations in Crystalline and Vitreous* SiO2 [in Russian], Zinatne, Riga, 1985.
[11] M. I. Gaĭduk, V. F. Zolin, and L. S. Gaĭgerova, *Luminescence Spectra of Europium* [in Russian], Nauka, Moscow (1974), p. 59.
[12] V. P. Kolobkov, P. I. Kudryashov, G. A. Starostina, and V. I. Shirokov, Fiz. Khim. Stekla **5**, 448 (1979).
[13] V. K. Leko and O. V. Mazurin, *Properties of Quartz Glasses* [in Russian] (Nauka, Leningrad, 1985), p. 21.
[14] W. T. Carnall, P. R. Fields, and K. Rajnak, J. Chem. Phys. **49**, 4424 (1968).
[15] G. E. Malashkevich, A. G. Bazylev, M. A. Borik, and P. A. Gorbunov, Fiz. Tverd. Tela (St. Petersburg) **35**, 2424 (1993) [Phys. Solid State **35**, 1202 (1993)].
[16] V. I. Arbuzov, M. N. Tolstoĭ, M. A. Élerts, and Ya. S. Trokshs, Fiz. Khim. Stekla **13**, 581 (1987).
[17] N. S. Poluéktov, N. P. Efryushina, and S. A. Gava, *Determination of Microscopic Quantities of Lanthanides from the Luminescence of Phosphor Crystals* [in Russian], Naukova Dumka, Kiev (1976), p. 58.
[18] T. Forster, Z. Naturforsch. Teil A **4**, 321 (1949).
[19] A. G. Avanesov, T. T. Basiev, Yu. K. Voron'ko, B. I. Denker, A. Ya. Karasik, G. V. Maksimova, V. V. Osiko, V. F. Pisarenko, and A. M. Prokhorov, Zh. Éksp. Teor. Fiz. **77**, 1771 (1979) [Sov. Phys. JETP **50**, 886 (1979)].
[20] G. E. Malashkevich, E. N. Poddenezhnyĭ, I. J. Mel'nichenko, A. A. Boĭko, and L. G. Brazhnik, Opt. Spektrosk. **78**, 84 (1995) [Opt. Spectrosc. **78**, 74 (1995)].

Translated by James S. Wood

Luminescence-spectrum and strength properties of rhodamine 6G-doped silica gel films

G. E. Malashkevich

Institute of Molecular and Atomic Physics, Academy of Sciences of Belarus, 220072 Minsk, Belarus

E. N. Poddeneznyĭ, I. M. Mel'nichenko, V. B. Prokopenko, and D. V. Dem'yanenko

F. Skorina Gomel State University, 256699 Gomel, Belarus

(Submitted May 26, 1997; resubmitted September 16, 1997)
Fiz. Tverd. Tela (St. Petersburg) **40**, 466–471 (March 1998)

Silica gel films dyed with rhodamine 6G in the sol stage are prepared and investigated. It is shown that the host matrix of the film loosens structurally as a result of intensification of the formation of dye molecular associates, lowering of the luminescence photon yield, and enhancement of the luminescence spectral sensitivity of such films to vapors of highly volatile organic solvents. © *1998 American Institute of Physics.* [S1063-7834(98)01403-8]

Silica gel films stained by organic dyes hold fair prospects as light filters[1] and photochemical sensors.[2,3] Not to be overlooked are their potential applications in quantum electronics and solar power as well.[4] However, reports of comprehensive studies of the luminescence-spectrum and strength properties of such films are unfortunately lacking in the literature, and information of this kind could be used to assess their practical value. Nor have we encountered any published information on their infrared (IR) spectra. In addition, the comparatively recent undertaking of research in this field with vast prospects for varying the chemical technology used to prepare such films makes each new item of information all the more useful.

The objective of the present study is to determine the characteristics of dye fixing in a host silica gel matrix and to assess the possibilities of fabricating glass–organic light filters and sensors with high optical density and a high luminescence-spectrum sensitivity to temperature and organic solvent vapors. Concurrently we have attempted to ascertain the influence of the injected dye concentration on the mechanical strength and water resistance (fastness) of the resulting films.

1. SAMPLES AND EXPERIMENTAL PROCEDURE

The preparation of the films entailed the hydrolysis of tetraethyl orthosilicate in a water–alcohol solution of hydrochloric acid until a sol was obtained [with a molar ratio H_2O:$Si(OC_2H_5)_4$ equal to 10:1]; the sol was then held in storage for one week, at which time the dye was dissolved in it. The dye-containing sol was deposited on a quartz or silicon substrate by centrifugal deposition, and the resulting films where heat-treated at various temperatures (T_{tr}) for 5 min. As soon as the sol film had been formed, immediately after the centrifuging operation, the substrate and film were covered with a matching substrate, and the whole piece was sealed at the edges by a special paste.

The film thickness was monitored on a profilograph–profilometer within $\pm 10\%$ error limits. The fastness of the dye was monitored on the basis of the difference between the total absorption intensities before and after soaking the film in tap water for 4 h, divided by the ''before'' value. The mechanical strength (measured in the number of slip cycles necessary to completely strip the film) was tested with a 0.3-kg load by means of a rubber tip operating through a batiste spacer in alcohol.

The absorption spectra were recorded by means of Beckman UV5270 and UR-2 spectrophotometers. In every case substrates of the same type and identical thickness were placed in a comparison channel. The luminescence spectra were recorded by an SDL-2 spectrofluorimeter, then they were corrected with allowance for the spectral sensitivity of the recording system and were displayed to show the number of luminescence photons per unit wavelength interval as a function of the wavelength, $dn(\lambda)/d\lambda$. The measurements were performed in a frontal excitation and recording geometry.

The quantum luminescence yield η was determined by an established procedure[5] based on comparison of the area under the corrected luminescence spectra of the experimental samples and a standard, with allowance for the refractive indices and the fraction of exciting radiation absorbed by the samples. The adopted standard was a solution of rhodamine 6G in ethanol at a concentration of 10^{-5} mol/liter, which provided a set quantum yield $\eta = 0.94$ (Ref. 6). The samples were excited in transmitted light. The refractive index was determined by a standard spectroscopic procedure.[7]

2. RESULTS

The profilometric monitoring of the prepared gel films shows that their thickness lies between the limits 0.19–0.21 μm. It increases somewhat as the concentration C_{dye} of dye injected into the sol is increased, and it decreases very slightly (no more than 15%) as T_{tr} is raised. The durability is a maximum at $T_{tr} = 300$ °C and at low rhodamine 6G concentrations: For $C_{dye} = 1$ mass % the film withstands 5×10^3 slip cycles, and at the highest concentration $C_{dye} = 12.5$ mass % it survives 250 cycles. The washout of the dye at $C_{dye} = 1$ mass % is less than 5% but increases by mul-

 © 1998 American Institute of Physics

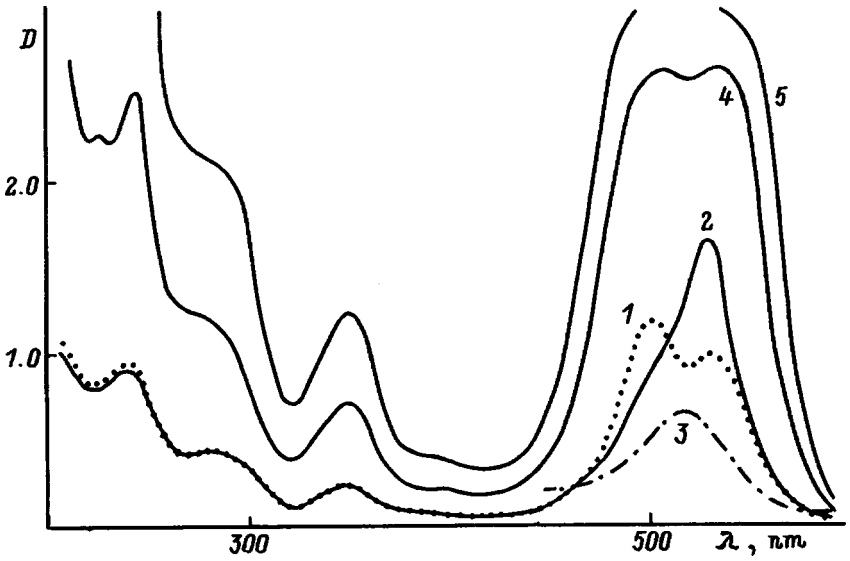

FIG. 1. Infrared absorption spectra of undoped and rhodamine 6G-doped films. *1)* $C_{dye}=0$; *2)* $C_{dye}=3$ mass %; *3)* $C_{dye}=12.5$ mass %. $T_{tr}=300$ °C, $T=22$ °C, film thickness 0.2 μm. The intensities of the spectra are magnified by a factor of two in the interval 2400–4000 cm^{-1}.

tiples as C_{dye} is increased. However, when an undoped silica gel film is deposited on a film with $C_{dye}=12.5$ mass % and is then heat-treated at $T_{tr}=300$ °C, the mechanical strength of such a hybrid film and the fastness of the dye are on a par with the film with $C_{dye}=1$ mass %.

Figure 1 shows IR absorption spectra of undoped and rhodamine 6G-doped gel films with various concentrations C_{dye} and the same $T_{tr}=300$ °C. In the spectrum of the undoped film (curve *1*) we clearly observe a comparatively broad, low intensity band at 3400 cm^{-1}, a strong, double-humped band with a maximum at 1075 cm^{-1}, and a weaker band at 945 cm^{-1}. For a film with $C_{dye}=3$ mass % the maximum of the 3400-cm^{-1} band undergoes a bathochromic shift by approximately 50 cm^{-1} and broadens toward lower frequencies (curve *2*). Simultaneously, an approximately 7-cm^{-1} bathochromic shift of the maximum of the strongest band is observed with appreciable broadening toward the low-frequency end, while the band at 945 cm^{-1} grows stronger and shifts by 15 cm^{-1} toward the high-frequency end; weak, relatively narrow bands also appear in the interval 1075–1700 cm^{-1}. When C_{dye} is increased to 12.5 mass %, the bands in the interval 1075–1700 cm^{-1} become distorted and grow stronger; the intensity of the band at 3350 cm^{-1} increases, and new secondary maxima emerge in its wing; the band at 960 cm^{-1} is amplified and undergoes a further hypsochromic shift; and the spectrum acquires a distinct band at 880 cm^{-1} (curve *3*). Moreover, the doped films exhibit very low-intensity, narrow bands in the interval 3570–3940 cm^{-1}, which become stronger as C_{dye} is raised and the longer the films are kept in a humid atmosphere. As the temperature T_{tr} is lowered, we mainly observe a moderate (up to 30%) increase in the indicated groups of high-frequency bands, the emergence of bands at 3400 cm^{-1} and 945 cm^{-1}, and attenuation of the band at 1075 cm^{-1}.

Figure 2 shows the absorption spectra of rhodamine 6G-doped sol and gel films in the visible and ultraviolet (UV) regions for various values of C_{dye} and T_{tr}. We see that a sol film with $C_{dye}=1$ mass % is characterized by a strong, broad band with a maximum at 500 nm, whose long-wavelength part has a ''shoulder'' at 530 nm, and by a series of overlapping bands in the UV region (curve *1*). Drying of this sol film has the effect of attenuating the short-wavelength component of the absorption band in the visible region at the expense of amplifying its long-wavelength component, which attains maximum intensity at $T_{tr}=300$ °C (curve *2*). At $T_{tr}=360$ °C the dye absorption decreases considerably, and the maximum of the given band shifts in the short-wavelength direction to 515 nm (curve *3*). Halving C_{dye} at fixed $T_{tr}=300$ °C has scarcely any effect on the profiles of the spectral band and is accompanied by a proportionate reduction of the absorption. On the other hand, when C_{dye} is increased above 1 mass %, we observe an increase in the intensity of the short-wavelength component of the absorption band in the visible region but a decrease in its specific intensity

$$I_{dye}=\frac{\int_{\lambda_1}^{\lambda_2}D(\lambda)d\lambda}{C_{dye}},$$

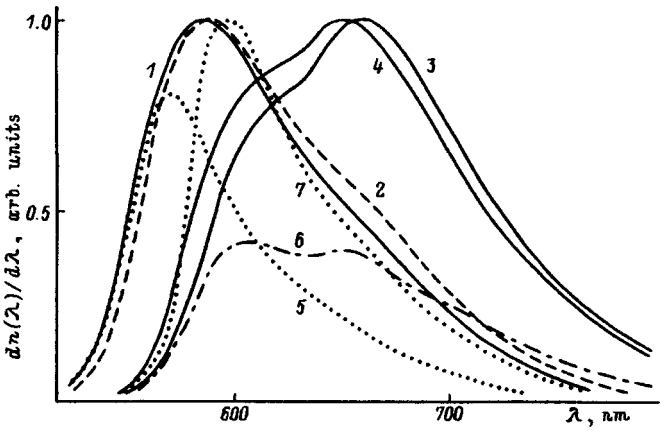

FIG. 2. Absorption spectra of rhodamine 6G-doped films. *1)* Sol film; *2–5)* gel films; *1–3)* $C_{dye}=1$ mass %; *4)* $C_{dye}=12.5$ mass %; *1)* $T_{tr}=22$ °C; *2,4,5)* 300 °C; *3)* 360 °C. $T=22$ °C, thickness of the gel films 0.2 μm. The intensities of spectra 1–3 are magnified by a factor of two.

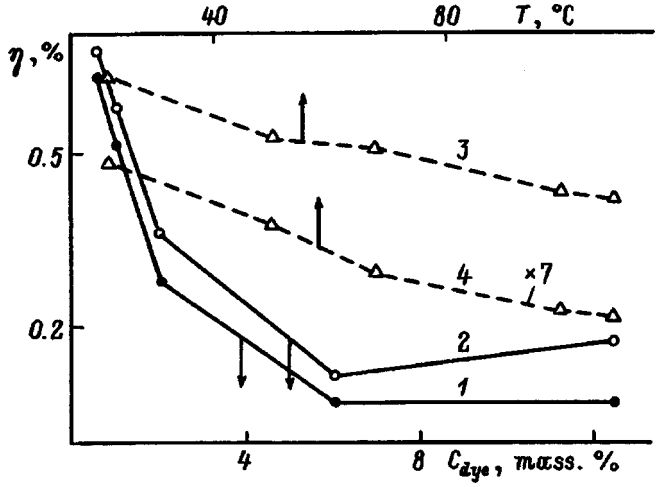

FIG. 3. Luminescence spectra of rhodamine 6G-doped gel films in air (graphs 1–6) and in saturated pyridine vapor (graph 7). *1,5*) $C_{dye}=0.5$ mass %; *2*) $C_{dye}=1$ mass %; *3,4,6,7*) $C_{dye}=12.5$ mass %; *1–3,5–7*) $\lambda_{exc}=350$ nm; *4*) $\lambda_{exc}=520$ nm; *1–4,7*) $T=22$ °C; *5,6*) $T=110$ °C. $T_{tr}=300$ °C. The intensities of spectra 5 and 6 are plotted relative to spectra 1 and 3, respectively.

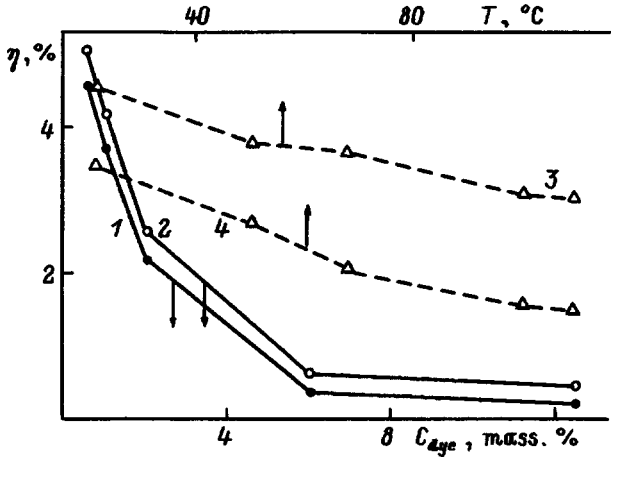

FIG. 4. Luminescence photon yield of rhodamine 6G-doped gel films in air (graphs *1, 3, 4*) and in saturated pyridine vapor (graph *2*). 3) $C_{dye}=0.5$ mass %; 4) $C_{dye}=6$ mass %. $T_{tr}=300$ °C, $T=22$ °C (graphs *1* and *2*).

where $\lambda_1=440$ nm and $\lambda_2=580$ nm. For $C_{dye}=6$ mass % this band broadens considerably (curve *4*), and its intensity I_{dye} drops 20% from the value of the same parameter for curve *2*. For $C_{dye}=12.5$ mass % light is almost totally absorbed in the interval 490–530 nm and at the shorter wavelength of 260 nm, and I_{dye} decreases still further (curve *5*). The prolonged (about one full day) storage of films with $C_{dye}>1$ mass % in a humid atmosphere is accompanied by appreciable amplification of the short-wavelength component and attenuation of the long-wavelength component of the visible absorption band.

Figure 3 shows the luminescence spectra of rhodamine 6G-doped gel films in air and in saturated pyridine vapor at various temperatures. Clearly, for the films exposed to air with $C_{dye}=0.5$ mass % at an excitation wavelength $\lambda_{exc}=350$ nm and $T=22$ °C the given spectrum represents an asymmetric band with a maximum in the vicinity of 585 nm (curve *1*). The scanning of λ_{exc} along the absorption spectrum is not accompanied by any real change in the absorption or the profile of this band. Increasing C_{dye} to 1 mass % produces a small bathochromic shift of the luminescence band and a kink in its long-wavelength component (curve *2*). For a film with $C_{dye}=12.5$ mass % at $\lambda_{exc}=350$ nm there is a significant bathochromic shift of the luminescence band, and it acquires a new maximum at 660 nm (curve *3*). This film also exhibits a shift and distortion of the spectrum when λ_{exc} is varied (cf. curves *3* and *4*). Raising the film temperature to 110 °C decreases the luminescence and simultaneously produces a hypsochromic shift of its spectral band at low C_{dye} (curve *5*) and a redistribution of the intensity in favor of the short-wavelength component at high C_{dye} (curve *6*). The presence of pyridine vapor has a weak influence on the profile of the luminescence band of gel films with $C_{dye}<6$ mass %, but at $C_{dye}=12.5$ mass % an appreciable hypsochromic shift of the luminescence and substantial attenuation of its long-wavelength component are observed (curve *7*). When the saturated vapor temperature of the solvent is raised, a similar variation of the spectrum is observed even for films with $C_{dye}<6$ mass %.

Figure 4 shows the luminescence photon yield of rhodamine 6G-doped gel films in air and in pyridine vapor as a function of C_{dye} and T at $\lambda_{exc}=350$ nm. It is evident that at $C_{dye}=0.5$ mass % and $T=22$ °C the value of η in air is approximately 0.6% and decreases when the doping level is increased to 0.07% at $C_{dye}\geqslant 6$ mass % (curve *1*). The absolute value of η increases somewhat in pyridine vapor, but decreases with increasing concentration C_{dye} in the interval 0.5–6 mass % and increases at $C_{dye}=12.5$ mass % (curve *2*). Heating of the films in air is accompanied by a decrease in η. This decrease is substantially less pronounced for films with $C_{dye}=0.5$ mass % (curve *3*) than for films with $C_{dye}=6$ mass % (curve *4*). We note that heating of the films in saturated pyridine and ethanol vapors is accompanied by a severalfold increase in η and washout of the dye from the film.

3. DISCUSSION OF THE RESULTS

The bands observed in the IR spectrum of the undoped gel film (curve *1* in Fig. 1) at 3400 cm^{-1}, 1075 cm^{-1}, and 940 cm^{-1} are attributable to the fundamental valence oscillations of the OH groups and to the antisymmetric oscillations of the Si–O and $Si–O^-$ bonds, respectively.[8] The bathochromic shift of the band at 3400 cm^{-1} for a film with low C_{dye} (curve *2*) could be evidence of a decrease in the length of the hydrogen bonds,[9] and the analogous shift at 1075 cm^{-1} is logically identified with the stretching and breaking of Si–O bonds.[10] Further evidence of such bond breaking is found in the amplification of the band at 940 cm^{-1}, and the shift of this band toward the high-frequency end suggests the foreshortening of $Si–O^-$ bonds. The significant amplification of the band associated with nonbridge-oxygen centers and the distinct appearance of a spectral band at 800–920 cm^{-1}, corresponding to tricoordinated oxygen,[8] are the results of further disintegration of the

host for a film with the maximum C_{dye} (curve *3*). This conjecture is further indicated by the multiple amplification of the band associated with OH groups, because the breaking of Si–O bonds is accompanied by the formation of free radicals, which interact with atmospheric moisture. In this case one should observe more of a low-frequency shift and attenuation of the band corresponding to oscillations of the Si–O bonds. This band obviously shows up on curve *3* in the form of the shoulder at 1055 cm^{-1}. The band shielding it, like the series of bands in the interval 110–180 cm^{-1} and judging from their similarity to the absorption spectrum of rhodamine 6G in KBr, is associated with dye molecule oscillations. These molecules are probably also responsible for the occurrence of the secondary maximum at 2950 cm^{-1}, which is identified with valence oscillations of C–H bonds.[11] The loosening of the host matrix in connection with the injection of the dye molecules is conducive to amplification of the weak bands in the interval 3570–3940 cm^{-1}, a sizable fraction of which can be referred to the fundamental-mode and combination-mode oscillations of various types of hydroxyl groups on the surface of the film.[11,12] Setting $C_{OH}=0.01k_{OH}$ (mass %) for the investigated films,[13] where k_{OH} is the peak absorption index at 3400 cm^{-1}, we find that C_{OH} is approximately 60% in undoped and lightly doped films. The calculation of this quantity provides a means for estimating the ratio of the volume concentrations of OH groups and silicon atoms from the equation $N_{OH}/N_{Si}=C_{OH}M(SiO_2/C(SiO_2)M_{OH}$, where M denotes the corresponding molecular weights. The resulting estimated ratio $N_{OH}\approx 5N_{Si}$ provides a basis for conceptualizing the structure of such films in the form of a slightly crisscrossed network permeated by pores filled with structurally bound water, residues of organic matter, and injected dye molecules.

The strong band in the visible part of the absorption spectrum of rhodamine 6G-doped gel films (Fig. 2) is attributable to $S_1\leftarrow S_0$ transitions of dye molecules and is the primary functional band when these films are used as light filters. Its spectroscopic behavior as a function of C_{dye} has been well studied, and it has been established that the band is governed by the proportion of monomers, dimers, and more complex associates in the host matrix. For the monomer form of rhodamine 6G, a $S_1\leftarrow S_0$ band with a maximum at 534 nm has been observed in such matrices. Splitting of the band into two components associated with transitions from the ground state to bonding and antibonding orbitals of the excited state is characteristic of the associates.[4] The strongest in the dimer spectrum is the long-wavelength component, which is usually shifted several nanometers into the red relative to the monomer absorption band.[14] The spectrum of complex associates is characterized by the opposite relationship between the intensities of these components and slight changes in the positions of their maxima.[14]

In light of these considerations and the shape of curve *1* we can assume that complex associates of rhodamine 6G molecules are predominant in the sol film. The attenuation of the short-wavelength component of the $S_1\leftarrow S_0$ band in the conversion of the sol film to a gel film indicates a decrease in the concentration of the associates as a result of the formation of silanol (Si–OH) and siloxane (Si–O–Si) groups of ''cages'' in the matrix,[15] which enclose the dye molecules. The further reduction in the concentration of these associates by heat treatment is logically explained by the fact that residual water molecules, which take part in the formation of the associates through hydrogen bonds,[4] are now removed from the film, and also by the shrinking of the cages as hydroxyl ions are replaced by bridge oxygen according to the reaction $\equiv Si-OH+HO-Si\equiv \rightarrow \equiv Si-O-Si\equiv +H_2O\uparrow$. However, the possibilities for raising T_{tr} are limited, because even at approximately 360 °C thermal degradation of the dye sets in, manifested by a drastic decrease in the absorption (cf. curves *2* and *3*). The essentially constant value of I_{dye} when D_{dye} is reduced below 1 mass % indicates the low degree of association of rhodamine 6G molecules in such films. Conversely, the increase in the relative intensity of the short-wavelength component of the $S_1\leftarrow S_0$ band when C_{dye} is raised above this value (cf. curves *2* and *4*) bears witness to the fact that the cages are no longer strong enough to prevent the formation of associates of rhodamine 6G molecules. The similar phenomenon observed when the gel films are kept in a humid atmosphere is indicative of their fairly high capacity for absorption relative to water molecules.

The strong dependence of the luminescence spectrum of rhodamine 6G-doped gel films on C_{dye} (Fig. 3) is consistent with the above-described concentration variation of the degree of association of the dye molecules. For example, the luminescence band of a gel film with $C_{dye}=0.5$ mass % (curve *1*) must be ascribed to $S_1\leftarrow S_0$ transitions of its monomers. The invariance of the position and profile of this band as λ_{exc} is a sign of its uniform broadening. The presence of a small kink in the long-wavelength part of the band at $C_{dye}=1$ mass % (curve *2*) and the substantial increase in the relative intensity of its corresponding component with a further increase in C_{dye} (curve *3*) are attributable to luminescence from complex associates.[14] The bathochromic shift of the monomer component of the luminescence band with an increase in C_{dye} indicates the inhibition of reorientation of structural elements of the cage around a dye molecule during the lifetime of the excited state of the latter. A consequence of such inhibition is the onset of nonuniform broadening of the luminescence band of highly doped films, as evinced by the shift of this band when λ_{exc} is varied (cf. curves *3* and *4*). The intensity redistribution of this band in favor of the short-wavelength component during heating of the film (curve *6*) indicates disintegration of the dye-molecule associates. The analogous phenomenon observed when the film is placed in pyridine vapor (curve *7*) can be attributed to the absorption of dye molecules by the film, which then form solvate shells around the rhodamine 6G molecules, and the effect of these shells in preventing association of the dye molecules. On the other hand, the narrowing of the $S_1\rightarrow S_0$ band of a lightly doped film as the temperature is raised indicates a decrease in the distortions of the rhodamine 6G molecules under the influence of the host matrix. This effect can be identified with thermal expansion of the matrix and an increase in the mobility of its structural elements, which encourages dye molecules to occupy sites having a less nonuniform environment.

The most probable cause of the low value of η for the

investigated rhodamine 6G-doped gel films (Fig. 4) is the migration of energy of excitation of monomers to nonluminescing dimers[14] and weakly luminescing complex associates. Thus, assuming that the cross section of the $S_2 \leftarrow S_0$ ($\lambda_{max} \approx 350$ nm) varies negligibly in the transition from solution ($\sigma \approx 3.8 \times 10^{-17}$ cm^2, Ref. 16) to gel film, we readily determine that the volume concentration of rhodamine 6G in a film with $C_{dye} = 0.5$ mass % is close to 3.2×10^{20} molecules/cm^3. In this case, assuming that the dye molecules are spherical and form a statistically uniform volume distribution, we obtain for the distance between their centers $R = (4\pi N_{dye}/3)^{-1/3} \approx 9.1$ Å. This distance is smaller than the diameter of the rhodamine 6G monomer molecules (~ 10 Å, Ref. 15), leading to the assumption that dimers exist even in such a faintly colored film and are effective as a sink for the excitation energy. The conclusion that dimers are formed in the film is further confirmed by the presence of troughs in its luminescence excitation spectrum at 505 nm and 535 nm. The low pH of the matrix[17] because of the acid sol used in the work can also lower η. In view of the poor thermal stability of rhodamine 6G associates,[18] it was logical to expect η to increase as the temperature increased. The experimentally observed opposite temperature behavior of η (see curves *3* and *4*) can be attributed to the formation of nonluminescing excimers, which are produced during collisions as a result of temperature oscillations of excited and unexcited monomer molecules.[19] The appreciable increase in η (cf. curves *1* and *2*) for highly doped films placed in pyridine vapor confirms that the pronounced loosening of the matrix as C_{dye} is increased and that the solvent molecules form solvate shells around the rhodamine 6G molecules.

To summarize, as a result of the study we have demonstrated the feasibility of fabricating thin-film, glass–organic light filters having a high optical density and acceptable service parameters. We have established that the injection of dye molecules into the investigated silica gel films is accompanied by loosening of the film structure through the stretching and breaking of Si–O bonds due to the formation of dimers and more complex associates of the dye molecules. The strong hygroscopicity and weak cross-linking of the structural network of highly doped films of the films sets the stage for molecules of vapors from highly volatile solvents to form solvate shells around the dye molecules. This effect tends to increase the luminescence photon yield of the structures while simultaneously producing a hypsochromic shift of the luminescence spectrum and making these films serviceable as luminescence sensors. Raising the heat-treatment temperature inhibits structural loosening of the host matrix and reduces the fraction of dye associates, but at high rhodamine 6G concentrations their negative influence cannot be overcome.

[1] I. J. M. Snijkers-Hendriks and J. van de Ven, in *Proceedings of the 16th International Congress on Glass*, Vol. 4 (Beijing, 1995), p. 9.
[2] V. Chernyak, R. Reisfeld, R. Gvishi, and D. Venezky, Sens. Mater. **2**, 177 (1990).
[3] V. Chernyak and R. Reisfeld, Sens. Mater. **4**, 195 (1993).
[4] R. Reisfeld, R. Zusman, Y. Cohen, and M. Eyal, Chem. Phys. Lett. **147**, 142 (1988).
[5] C. A. Parker, *Photoluminescence of Solutions, With Applications to Photochemistry and Analytical Chemistry* [Elsevier, Amsterdam-New York, 1968; Mir, Moscow, 1972].
[6] A. V. Butenin, B. Ya. Kogan, and N. V. Gundobin, Opt. Spektrosk. **47**, 1022 (1979) [Opt. Spectrosc. **47**, 568 (1979)].
[7] G. E. Malashkevich, N. V. Ovcharenko, T. V. Smirnova, A. G. Bazylev, L. A. Meleshchenko, A. S. Gigevich, A. V. Mazovko, and V. V. Panteleev, Fiz. Khim. Stekla **17**, 52 (1991).
[8] A. R. Silin' and A. N. Trukhan, *Point Defects and Elementary Excitations in Crystalline and Vitreous* SiO2 [in Russian], Zinatne, Riga (1985), p. 159.
[9] V. L. Mamoshin, V. G. Arkhipov, P. I. Buler, and L. V. Ivanova, Fiz. Khim. Stekla **13**, 510 (1987).
[10] I. I. Novak, K. N. Kuksenko, and V. P. Pukh, Fiz. Khim. Stekla **1**, 529 (1975).
[11] L. H. Little, *Infrared Spectra of Adsorbed Species* [Academic Press, New York-London, 1966; Mir, Moscow, 1969].
[12] A. V. Kiselev and V. I. Lygin, *Infrared Spectra of Surface Compounds and Adsorbed Substances* [in Russian], Nauka, Moscow (1972).
[13] V. K. Leko and O. V. Mazurin, *Properties of Quartz Glasses* [in Russian], Nauka, Leningrad (1985).
[14] A. K. Chibisov, G. A. Ketsle, L. V. Levshin, and T. D. Slavnova, Opt. Spektrosk. **38**, 83 (1975) [Opt. Spectrosc. **38**, 45 (1975)].
[15] D. Amir, D. Levy, and R. Reisfeld, J. Phys. Chem. **88**, 5956 (1984).
[16] K. H. Drexhage, T. W. Hansch, E. P. Ippen, F. P. Schafer, C. V. Shank, and B. B. Snavely, in *Dye Lasers*, edited by F. P. Schafer [Springer-Verlag, Berlin-New York, 1974; Mir, Moscow, 1976].
[17] M. M. Snegov, I. I. Reznikova, and A. S. Cherkasov, Opt. Spektrosk. **36**, 96 (1974) [Opt. Spectrosc. **36**, 55 (1974)].
[18] L. V. Levshin, E. Yu. Bekhli, T. D. Slavnova, and V. I. Yuzhakov, Opt. Spektrosk. **36**, 503 (1974) [Opt. Spectrosc. **36**, 290 (1974)].
[19] B. M. Krasovitskiĭ and B. M. Bolotin, *Organic Luminescent Materials*, (Weinheim, New York, 1988; Khimiya, Moscow, 1984).

Translated by James S. Wood

Electrically active defects in BiSiO crystals undoped and doped with Cr and Mn ions

T. V. Panchenko and L. M. Karpova

Dnepropetrovsk State University, 320625 Dnepropetrovsk, Ukraine
(Submitted May 14, 1997; resubmitted October 14, 1997)
Fiz. Tverd. Tela (St. Petersburg) **40**, 472–474 (March 1998)

The influence of doping of $Bi_{12}SiO_{20}$ (BSO) with chromium and manganese ions on the thermal depolarization currents (TDCs) is investigated. Measurements are performed in the temperature interval 300–800 K as the preliminary polarization temperature is varied in the range $T_p = 300-523$ K. It is shown that doping significantly alters the structure of the TDC spectra. The Cr and Mn ions produce a set of new peaks over the entire investigated temperature range. The thermal activation energies are 0.85–1.98 eV (BSO:Cr) and 0.58–1.72 eV (BSO:Mn). Another consequence of doping is an increase in the amplitudes of the peaks and the charge accumulated during preliminary polarization. © *1998 American Institute of Physics.* [S1063-7834(98)01503-2]

A comprehensive series of investigations of material properties sensitive to point defects has been reported to date for crystals of the sillenites $Bi_{12}SiO_{20}$ (BSO) and $Bi_{12}GeO_{20}$ (BGO). A variety of methods has been used: optical absorption spectroscopy (OAS), photoelectric absorption analysis (PAA), thermally stimulated current (TSC) spectroscopy, thermoluminescence spectroscopy (TLS), and photoluminescence spectroscopy (PLS) (Refs. 1 and 2). Thermoregulation (TR) processes[2] and alternating-current conductivity (ACC) (Ref. 3) have been investigated. A diagram of local states of the bandgap has been proposed,[2] tying in with the absorption and photoconductivity ''shoulders'' (Ref. 2), thermoelectric and photoelectric states,[4] the photochromic effect,[5] space-charge stratification[6] etc. Doping offers the possibility of exercising direct control of these properties of sillenites by transforming the spectrum of local states. Transition-metal ions of the iron group are of special interest in this scenario. As a multiply charged impurity, these ions by virtue of the splitting of *d* terms in the ligand field produce levels that have been well-studied, for example, in such wide-gap semiconductors as GaAs and GaP (Ref. 7).

Information on local levels in sillenites doped with transition metals is not very plentiful.[1,3,8,9] Only in-center transitions are analyzed in studies of optical absorption and the photochromic effect.[10–12] Levels at 1.5 eV, 1.6–1.7 eV, and 2.27 eV have been found in BSO:Cr and BSO:Mn crystals.[1]

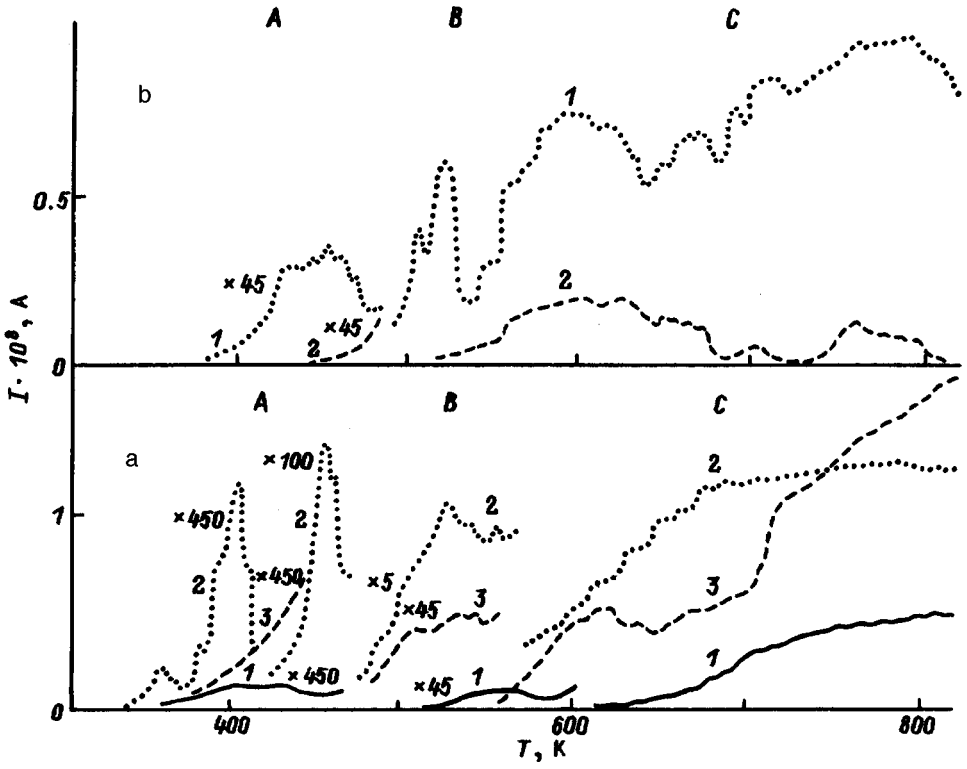

FIG. 1. a) Spectra of thermally stimulated depolarization currents: *1*) BSO; *2*) BSO:Cr; *3*) BSO:Mn. b) Calculated spectra: *1*) $\Delta I(T) = I(T)_{\mathrm{BSO:Cr}} - I(T)_{\mathrm{BSO}}$; *2*) $\Delta I(T) = I(T)_{\mathrm{BSO:Mn}} - I(T)_{\mathrm{BSO}}$. Polarization temperature: a) $T_p = 373$ K; b) 323 K. Polarization voltage $U_p = 139$ eV.

 © 1998 American Institute of Physics

TABLE I. Parameters of electrically active defects in BSO, BSO:Cr, and BSO:Mn crystals.

Crystal	T_m, K	E_a, eV	Q_i, C	Activation energies (eV) from published data, method [Refs.]
BSO	417	0.67	1.51×10^{-9}	0.62–0.68, TLS, TSC, PAA, TR
	554	0.74	7×10^{-9}	0.72–0.78, TLS, TSC, PAA, TR
	599	0.9	4.8×10^{-9}	0.9, TSD [14]
	618	0.91	6×10^{-8}	
	749	1.07*	1.86×10^{-7}	1.04, OAS [9]
	783	1.12*	2.37×10^{-7}	1.12, TSD [14]
	800	1.15*	4.18×10^{-7}	1.15, TLS, PAA, PLS, TR
BSO:Mn	431	0.58	1.82×10^{-9}	
	476	0.83	8.34×10^{-8}	
	536	0.91*	2×10^{-7}	
	587	1.14	5.42×10^{-7}	
	647	1.25	1.19×10^{-6}	1.5–1.7, OAS [9, 15], TSC [1]]
	701	1.54	8.24×10^{-7}	
	749	1.65*	2.74×10^{-6}	
	780	1.72*	2.08×10^{-6}	
BSO:Cr	363	0.85*	4.1×10^{-10}	0.85, OAS [9], ACC [3], (BGO:Cr)
	406	0.95	2.54×10^{-9}	
	460	1.15	1.13×10^{-8}	1.18, OAS [9]
	531	1.27	7.68×10^{-7}	
	637	1.5*	5.3×10^{-7}	1.5–1.7, OAS [9, 15], TSC [1]
	696	1.65*	1.1×10^{-6}	
	764	1.8*	1.19×10^{-6}	
	800	1.89*	7.74×10^{-7}	

However, the TSC method used in this work has a low sensitivity. Here we give the results of further investigation of the local levels in BSO:Cr and BSO:Mn crystals using the more sensitive thermally stimulated depolarization (TSD) method.[13]

The concentrations of Mn and Cr in the BSO crystals were 0.1 mass % and 0.05 mass %, respectively. The thermal depolarization of thermoelectric states created beforehand in BSO, BSO:Cr, and BSO:Mn crystals was investigated. The polarization temperature was varied in the interval $T_p = 300-523$ K. The polarizing voltage was $U_p = 190$ V, and the polarization time was held constant (30 min) in every case. The TSD currents $I(T)$ were measured during linear heating of the samples at a rate of 0.16 $\mathrm{K\cdot s^{-1}}$ in the temperature interval 300–800 K. The sample preparation and measurement procedure is described in Ref. 14. The activation energy was calculated by the initial-rise method (E_a) and by utilizing the temperature position of the maximum, with $E_a^* = \alpha k T_m$ (Ref. 13). We estimated α on the basis of the equality of E_a and E_a^* for the same discrete peaks of the TSD spectra.

The spectra $I(T)$ obtained here are shown in Fig. 1a. Assuming that the contributions from different centers to the resultant spectra are additive, we have also calculated the differential spectra $\Delta I(T) = I(T)_{\mathrm{BSO:Cr(Mn)}} - I(T)_{\mathrm{BSO}}$ (see Fig. 1b). This procedure permits sharper discrimination of the dopant contribution at a concentration $\sim 10^{16}$ $\mathrm{cm^{-3}}$, because the densities of native point defects are much higher in nominally pure BSO crystals ($\sim 10^{18}$ $\mathrm{cm^{-3}}$). It is evident that doping with Cr and Mn ions significantly transforms the structure of the spectra $I(T)$. Three groups of peaks A, B, C) are discernible in the corresponding temperature intervals 300–480 (A), 480–581 (B), 581–823 (C) (see Fig. 1).

Groups A and B are represented by a set of quasidiscrete peaks. For group C the $I(T)$ thermograms have the appearance of structured curves. Heterocharge relaxation is observed for all the investigated crystals, irrespective of the polarization conditions. Total depolarization occurs at $T < 823$ K. A characteristic trait of doping with Cr ions, as opposed to Mn ions, is the appearance of a set of narrow peaks in group A (the temperature spreading of the maxima $\Delta T < 30$ K) having an essentially symmetric profile. In both cases (BSO:Cr and BSO:Mn) the peaks of group B are characterized by large ΔT ($\Delta T > 100$ K).

The spectra of TSD currents for the investigated crystals are found to be sensitive to variation of the polarization conditions. An increase in T_p lowers the intensities of the peaks and the charge Q_i released at the TSD current peaks for group C in the case of doped crystals, thereby improving the resolution of details of the spectrum. The variation of T_p discloses a series of peaks, whose parameters are shown in Table I. For the doped crystals correlation is observed in the interval 1.5–1.7 eV (BSO:Mn) and 0.85–1.7 eV (BSO:Cr). The TSD method has enabled us to distinguish, in addition to these data, several new levels in the lower-energy range for BSO:Mn and over the entire range for BSO:Cr. BSO crystals are more sensitive to Cr doping than to Mn doping (see Fig. 1).

A consequence of doping is an increase (relative to undoped BSO) in the intensities of the peaks and the total charge Q released in depolarization; we define this quantity as

$$Q=\int_{t_1}^{t_2} I(t)dt,$$

where t_1 and t_2 are fixed times in the conversion from the temperature scale to the time scale. On the whole, the influence of doping on Q is indicative of an increase in the concentrations of all local levels both in BSO:Cr and in BSO:Mn. Especially noteworthy is the increase in the concentration of levels with activation energies in the interval 0.7–0.9 eV, which have been identified[2] with the photochromism of nominally pure BSO crystals. Consequently, the enhancement of the photochromic effect in BSO:Cr(Mn) crystals, manifested in additional absorption in the near-infrared wavelength range,[10–12] can be ascribed to an increase in the concentration of these levels.

[1] A. Yu. Kudzin, T. V. Panchenko, and N. A. Truseeva, Ukr. Fiz. Zh. **29**, 1414 (1983).
[2] V. K. Malinovskiĭ, O. A. Gudaev, V. A. Gusev, and S. I. Demenko, *Photoinduced Effects in Sillenites* [in Russian] (Nauka, Novosibirsk, 1990).
[3] V. I. Kalinin, Zh. S. Kuchuk, N. G. Gorashchenko, and A. A. Maĭer, Izv. Akad. Nauk SSSR, Neorg. Mater. **24**, 637 (1988).
[4] T. V. Panchenko and G. V. Snezhnoĭ, Fiz. Tverd. Tela (St. Petersburg) **33**, 3546 (1991) [Phys. Solid State **33**, 1992 (1991)].
[5] T. V. Panchenko, N. A. Truseyeva, and Yu. G. Ostesky, Ferroelectrics **129**, 113 (1992).
[6] V. N. Astratov, A. V. Ilinsky, and A. S. Furman, Phys. Status Solidi A **150**, 611 (1988).
[7] V. F. Masterov and B. E. Samorukov, Fiz. Tekh. Poluprovodn. **12**, 625 (1978) [Sov. Phys. Semicond. **12**, 363 (1978)].
[8] B. C. Grabmaier and R. Oberschmid, Phys. Status Solidi A **96**, 199 (1986).
[9] M. V. Shilova, L. V. Chertkova, V. M. Orlov, and E. E. Kolosov, Izv. Akad. Nauk SSSR, Neorg. Mater. **20**, 541 (1984).
[10] T. V. Panchenko and N. A. Truseyeva, Ferroelectrics **115**, 73 (1991).
[11] W. Wardzynski, H. Szymczak, M. T. Borowiec, K. Pataj, T. Lukasiewicz, and J. Zmija, J. Phys. Chem. Solids **46**, 1117 (1985).
[12] W. Wardzynski, H. Szymczak, K. Pataj, T. Lukasiewicz, and J. Zmija, J. Phys. Chem. Solids **43**, 767 (1982).
[13] Yu. A. Gorokhovatskiĭ, *Fundamentals of Thermal Depolarization Analysis* [in Russian] (Moscow, 1981).
[14] T. V. Panchenko and G. V. Snezhnoĭ, Fiz. Tverd. Tela (St. Petersburg) **35**, 2945 (1993) [Phys. Solid State **35**, 1446 (1993)].
[15] T. V. Panchenko and N. A. Truseeva, Ukr. Fiz. Zh. **34**, 1186 (1984).

Translated by James S. Wood

DEFECTS. DISLOCATIONS. PHYSICS OF STRENGTH

Metastable states and physical characteristics of a subsystem of interstitial impurities

A. A. Berzin, A. I. Morozov, and A. S. Sigov

M. V. Lomonosov Moscow State Institute of Radio Engineering, Electronics, and Automation, 117454 Moscow, Russia

(Submitted September 24, 1997)
Fiz. Tverd. Tela (St. Petersburg) **40**, 475–480 (March 1998)

The behavior of mobile interstitial impurities in a crystal matrix has been simulated numerically. The contribution of the impurity subsystem to the heat capacity, and the effect of clusterization on the temperature dependence of the impurity diffusion coefficient have been studied. © *1998 American Institute of Physics.* [S1063-7834(98)01603-7]

Due to their quantum properties, light interstitial impurities remain mobile at low temperatures. A prominent example of such impurities is hydrogen isotopes in the matrix of a transition metal.

Although at high temperatures transitions of an impurity from one equivalent interstice to another occur primarily via activated over-barrier processes, tunneling between adjacent equivalent interstitial sites becomes increasingly dominant as the temperature decreases. Since the probability of coherent tunneling increases with decreasing temperature, one would expect the diffusion coefficient D to have a temperature dependence like that shown in Fig. 1.

Experiments on hydrogen diffusion in metals do not, however, reveal anything of the kind.[1] The reason for this lies in the impurity clusterization phenomenon.

It is known that in an insulator the long-range part of the interaction between point defects is elastic, i.e., it is an indirect interaction via acoustic phonons. In a metal, one should add to this the indirect interaction via Friedel oscillations in electron density. Since both these interactions have an alternating character, for any pair of defects in a metal matrix and a pair of neutral defects in an insulator a set of bound states develops, irrespective of the actual form of the short-range part of the interaction.[2,3] As the temperature is lowered, this leads inevitably either to capture of a mobile defect by a fixed one, or to clusterization of mobile defects. We shall limit ourselves here to a consideration of the latter case.

If cooling were performed in quasistatic conditions, clusterization would result in a large-scale separation of the system into phases, which would contain impurities in a high (b) and a low (a) concentration, with the equilibrium impurity concentration in the a phase tending to zero with decreasing temperature. The time required for the impurity subsystem to reach equilibrium at low temperatures, however, as a rule, is considerably longer than the duration of the experiment.

This is why in a crystal with a low concentration of interstitial impurities, $x \leqslant 10^{-2}-10^{-1}$ (x is the dimensionless concentration per unit cell), small clusters, containing only a few impurity atoms each, appear in place of large-scale phase separation. These metastable states are long-lived, because clusterization reduces strongly the mobility of impurities. Metastable states differ from one another in the relative position and number of particles in a cluster, their location and concentration.

These metastable states are separated in phase space from one another and from the equilibrium state by high barriers, whose heights differ by many orders of magnitude. During an experiment, the impurity system undergoes averaging not over the whole phase space but only in the vicinity of the deep minimum which the system reached under cooling. In other words, the behavior of the impurity system is not ergodic. In this sense its behavior is similar to that of spin glasses; only the potential barriers between metastable states in our system remain finite.

This work was aimed at studying the properties of the above metastable states by numerical simulation, because analytical treatment would involve very considerable difficulties.

The first part of the work describes the model used. The second part presents the results of calculation of the heat capacity of the impurity subsystem, and the third, those for the impurity diffusion coefficient. In the end, the main conclusions are summed up.

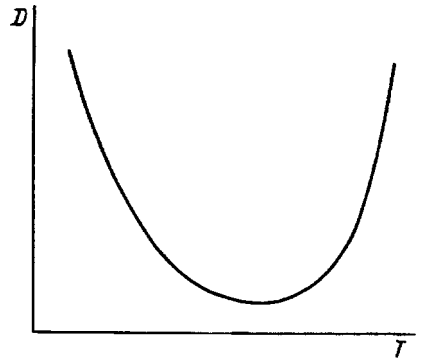

FIG. 1. Temperature dependence of the impurity diffusion coefficient in the absence of clusterization processes.

 © 1998 American Institute of Physics

1. DESCRIPTION OF THE MODEL

A. Interaction potential

Besides interaction with one another, impurities interact with the crystal matrix, and the potential of this interaction has sharp minima at interstices. We shall assume that the interaction of the impurities with the matrix is the strongest, and neglect the change in equilibrium positions of the impurities at interstitial sites caused by their interaction with one another. We take a cubic lattice of interstices with an edge a, which corresponds to tetrahedral pores in an fcc lattice. Interstitial impurities are distributed over the positions of the interstitial lattice. We shall assume the short-range part of the interaction among impurities to be repulsive and oppose the transition of an impurity to a site already occupied by another impurity.

The elastic interaction between impurities in a weakly anisotropic cubic crystal can be presented in the form[4]

$$W_{\rm elas}=\alpha\left(\frac{a}{r}\right)^3\left[\frac{3}{5}-\left(\frac{X}{r}\right)^4-\left(\frac{Y}{r}\right)^4-\left(\frac{Z}{r}\right)^4\right], \tag{1}$$

where $\mathbf{r}=(X,Y,Z)$ is the distance between impurities in the coordinate frame whose axes coincide with the crystallographic axes of the cubic crystal, and the constant α has the same sign as the combination of the elastic constants $2c_{44}+c_{12}-c_{11}$. In the given interstice lattice, the dimensionless vector $\rho=\mathbf{r}/a$ has integer coordinates, $\rho=(\tilde{X},\tilde{Y},\tilde{Z})$.

The interaction via Friedel oscillations in electron density will be prescribed in a simple form corresponding to a spherical Fermi surface:

$$W_{el}=\beta\left(\frac{a}{r}\right)^3\cos(2k_Fr), \tag{2}$$

where k_F is the Fermi wave vector of the conduction electrons, and $\beta>0$. The constants α and β are of the same order of magnitude. For hydrogen in a metal, $\alpha\sim\beta\sim10^{-2}$ eV.

After making all energy quantities dimensionless by dividing them by the constant $\alpha+\beta$, we finally arrive at the interaction potential acting on impurities at interstitial sites i and j:

$$\tilde{W}_{ij}=\frac{b[3/5-(\tilde{X}/\rho)^4-(\tilde{Y}/\rho)^4-(\tilde{Z}/\rho)^4]+(1-b)\cos(\gamma\rho)}{\rho^3}, \tag{3}$$

where $\gamma=2k_Fa$, and $b=\alpha(\alpha+\beta)$.

The value $b=1$ corresponds to the case of an insulator ($\beta=0$).

B. Transition probability

The simulation was performed for a cube of $30\times30\times30$ interstices, which was extended periodically to eliminate boundary effects. The number of impurity atoms was set equal to 30 and 100, which corresponds to concentrations $x=3.6\times10^{-4}$ and 1.1×10^{-3} per site (or to concentrations twice as large per matrix atom).

The behavior of the impurity system was studied using the Metropolis algorithm for the Monte Carlo method,[5] by which the impurity and the adjacent site j to which it could transfer from site i were generated randomly. Next the quantity ξ_{ij}, the change in potential energy of the chosen impurity in the field of the other impurities, was calculated

$$\xi_{ij}=\sum_{m\neq i}(\tilde{W}_{jm}-\tilde{W}_{im}), \tag{4}$$

where the summation runs over all impurities with the exception of the one chosen in the beginning.

Let J_0 be the tunneling matrix element for impurity transition between adjacent equivalent interstices in the absence of disorder, i.e., for $\xi_{ij}=0$.

In the case $|\xi_{ij}|\gg J_0$, the transition of an impurity from one interstitial site to another is caused by either its interaction with conduction electrons (in a metal) or one-phonon processes. The transition probability determined by interaction with electrons is, in order of magnitude,[6]

$$w_{\rm el}\sim J_0^0/\hbar\,\xi_{ij}[\exp(\xi_{ij}/T)-1], \tag{5}$$

where T is the temperature.

The transition probability due to phonon emission or absorption can be written[7]

$$w_{\rm ph}\sim J_0^2\tilde{E}\xi_{ij}/\hbar\,\theta^3[\exp(\xi_{ij}/T)-1], \tag{6}$$

where $\tilde{E}$ is atomic-scale energy, and θ is the Debye temperature.

The total transition probability is the sum of $w_{\rm el}$ and $w_{\rm ph}$. For $\xi_{ij}<0$, it depends weakly on ξ_{ij}, while for $\xi_{ij}>0$ it falls off exponentially with increasing ξ_{ij}. Therefore the total transition probability can be represented to a good approximation in the form

$$w_{ij}=\begin{cases}1 & \text{for } \xi_{ij}\leqslant0,\\ \exp(-\xi_{ij}/T) & \text{for } \xi_{ij}>0\end{cases}. \tag{7}$$

With this choice of the jump probability, the jump time in the absence of interaction between impurities, i.e., for $\xi_{ij}=0$, turns out to be dimensionless for the duration of the jump. This does not affect in any way the static characteristics of the system. When simulating the diffusion process, however, we obtain in place of the diffusion coefficient D the ratio D/D_0, where D_0 is the diffusion coefficient for noninteracting impurities.

C. Calculation of the heat capacity of the impurity system

We performed simulated annealing from the high-temperature region where the distribution of interstitial impurities over interstices is a random function. The initial impurity distribution was chosen in a random way. The temperature of the system was varied linearly

$$T=T_0-ct, \tag{8}$$

where T_0 is the initial temperature of the system, c is the cooling rate, and t is the time (i.e., the number of steps).

The energy of the impurity system E was determined as the sum of their pair interaction energies. Different cooling

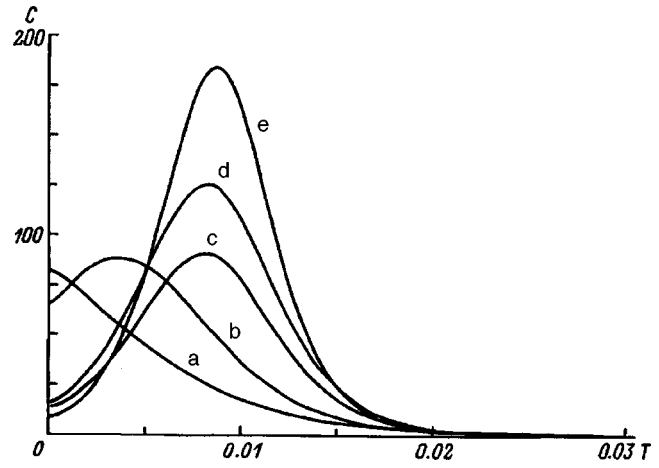

FIG. 2. Heat capacity of the impurity subsystem for $x=3.6\times10^{-4}$, $b=0.5$, $\nu=$: (a) 100, (b) 500, (c) 1000, (d) 2000, and (e) 5000.

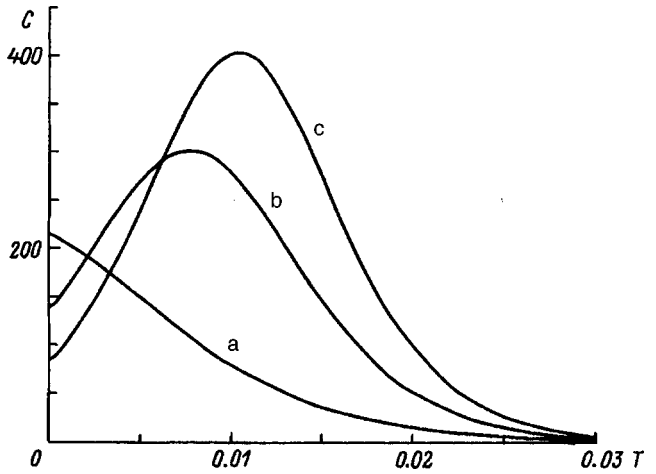

FIG. 3. Heat capacity of the impurity subsystem for $x=1.1\times10^{-3}$, $b=0.5$, $\nu=$ (a) 100, (b) 500, and (c) 1000.

rates were chosen, so as to generate from 100 to 5000 impurity jumps in each step in temperature ($\nu=100-5000$).

The $E(t)$ relation [or, after the corresponding transformation, $E(T)$] for a given initial realization of impurities was found to be an oscillating function because of the breakup and formation of clusters, which results from the boundedness of the system under study. Therefore we performed averaging over a large number of realizations, thus smoothing the oscillations. The heat capacity of the impurity system at constant volume was found by differentiating the relation thus obtained with respect to temperature.

D. Diffusion coefficient

To determine the diffusion coefficient, we used the Einstein relation connecting the diffusion coefficient with the mobility μ:

$$D=T\mu, \tag{9}$$

where the quantity μ was defined as the coefficient of proportionality between the velocity of directed impurity motion and the applied force.

After creation of a weak potential gradient along one of the crystallographic axes, the initial impurity coordinates were generated. Next annealing was simulated from the high-temperature region to the final level T_f according to

$$T=T_f+(T_0-T_f)\exp(-ct). \tag{10}$$

This resulted in relaxation of the impurity subsystem to the steady state. Indeed, in the low-temperature domain the distribution of impurities is not random because of their interaction with one another (clusters appear). The time at which the steady state was reached was determined by monitoring the total energy of the impurity system.

After the steady state was reached, the impurity flux produced by the applied constant force F was determined. The ratio of the particle flux to F yielded the mobility. The force was chosen so as to meet the condition $Fa\ll T$. This is needed in order to be able to take into account the potential energy gradient only in the first nonvanishing approximation.

In this way the temperature dependence of the quantity D/D_0 was found.

2. HEAT CAPACITY

Figures 2 and 3 display the temperature dependence of the heat capacity C for different cooling rates obtained for 30 and 100 impurity atoms. The fact that the impurity system did not reach equilibrium is evidenced by the hysteresis in the $E(T)$ relation observed under temperature cycling (Fig. 4). Note also that at equilibrium $C(T)\to0$ for $T\to0$.

For high cooling rates (small ν) the heat capacity grows with $T=0$ is reached. The reason for this is that at such cooling rates particles do not have time enough to form clusters (Fig. 5a), although the nuclei of clusters are seen clearly. Some impurity atoms freeze out.

As the cooling rate decreases (ν increases), the heat capacity passes through a maximum at $T_{\max}\neq0$. It shifts with increasing ν toward higher temperatures finally freezing at the true clusterization temperature $T_{\rm cl}$. It can be estimated as[2,3]

$$T_{\rm cl}=w_0/|\ln x|, \tag{11}$$

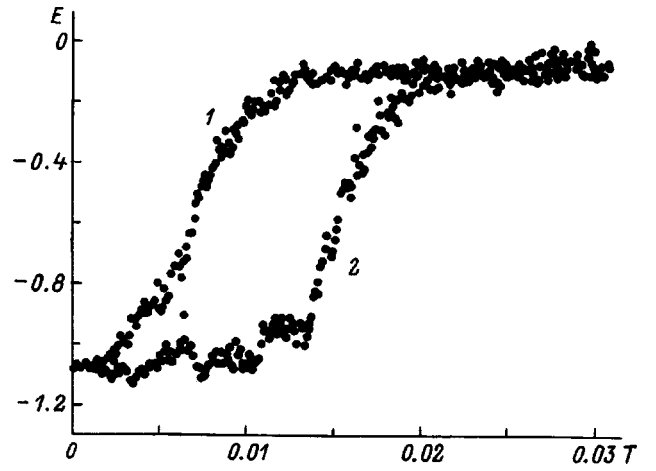

FIG. 4. Energy of the impurity subsystem vs temperature under (1) cooling and (2) heating for $x=3.6\times10^{-4}$, $b=0.5$, $\nu=1000$.

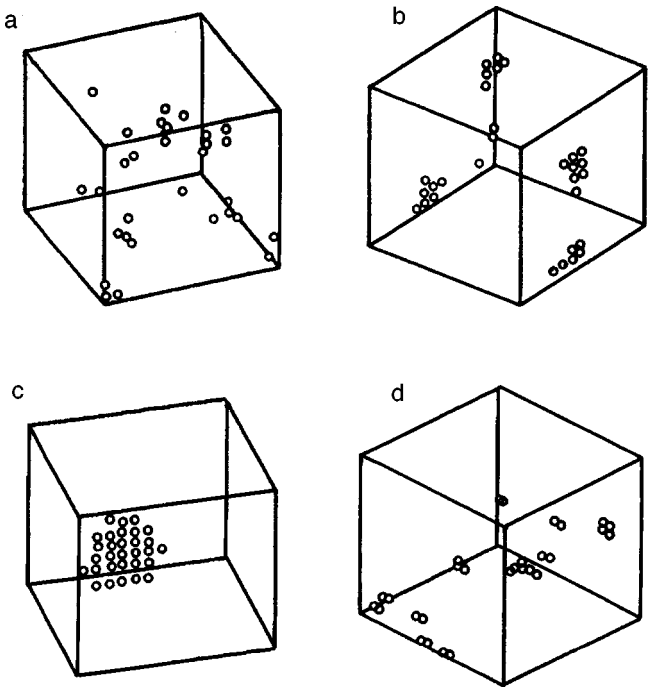

FIG. 5. Impurity distribution produced by cooling for $x=3.6\times10^{-4}$, $b=0.5$, $\nu=$ (a) 100, (b) 500, (c) 2000, and (d) $b=0.8$, $\nu=1000$.

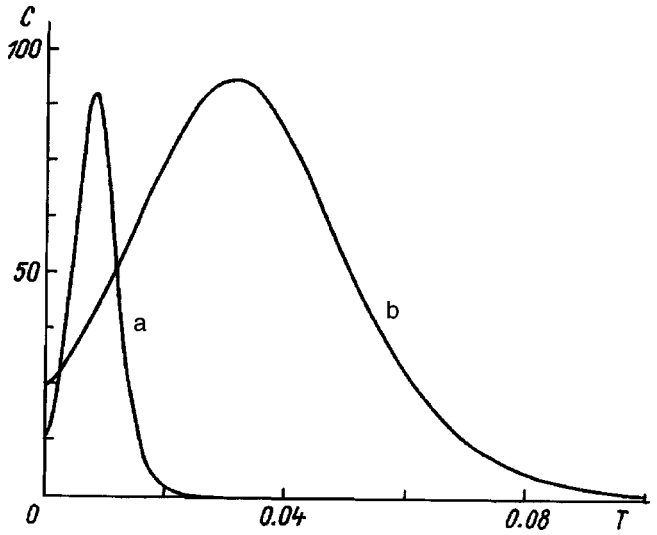

FIG. 6. Heat capacity of the impurity subsystem for $x=3.6\times10^{-4}$, $\nu=1000$, (a) $b=0.5$ and (b) $b=0.8$.

where w_0 is the specific binding energy of defects in a cluster.

Because the quantity w_0 depends on the shape and number of particles in a cluster and increases as one goes over from small clusters to a homogeneous high-concentration b phase, clusterization will occur at different temperatures depending on the cooling rate.

For infinitely slow cooling, where there is enough time for averaging to extend over all of the phase space, there will be a first-order phase transition accompanied by large-scale phase separation. It is characterized by the maximum value of $T_{\rm cl}$ and a sharp peak in heat capacity at $T=T_{\rm cl}$.

For realistic cooling rates, averaging can encompass only a limited part of phase space, whose size increases as the cooling rate decreases. This is accompanied by an increase in $T_{\rm cl}$ and the height of the heat-capacity peak, while the peak width decreases. At $\nu=500$ a large number of small clusters appear (Fig. 5b), to coalesce at $\nu=2000$ into one large cluster (Fig. 5c).

The shape of the resulting clusters and hence the physical characteristics of the impurity system depend substantially on the relative magnitude of the two contributions to the long-range interaction between them, i.e., on the constant b in Eq. (3). Substitution of $b=0.8$ for 0.5 causes the nearest-neighbor impurities in a cluster to occupy adjacent (Fig. 5d) rather than alternate (Fig. 5b) interstitial sites. Figure 6 presents for comparison temperature dependences of heat capacity relating to the same value of ν but different b. A heat capacity peak similar to the one obtained by simulation was observed[8,9] to occur in $ZrCr_2H_x(D_x)$ $(0.27<x<0.45)$ for $T\leqslant60$ K. Note that in the phase diagram this concentration region $(x<0.6)$ remains single phase down to $T=0$,[10] in other words, no large-scale phase separation is observed here. One may thus conclude that it is small hydrogen clusters that form in this concentration region.

3. DIFFUSION COEFFICIENT

Since the distribution of impurities over interstitial sites associated with cooling to $T<T_{\rm cl}$ depends both on their initial distribution and on the cooling rate, simulation produces, generally speaking, not one D/D_0 curve but rather a set of them (Fig. 7). The leftmost curve corresponds to large-scale phase separation ($T_{\rm cl}$ is maximum), and the rightmost, to small-cluster formation and freezeout of single impurities. In this case the diffusion coefficient will drop at a lower temperature.

The averaging of the D/D_0 relation is displayed in Fig. 8 for different values of parameters x, b, and γ. They exhibit a common feature in the decrease of D/D_0 with decreasing temperature from one (high-temperature region) to practically zero $(T\ll T_{cl})$.

Theory yields the following estimate:[2,3]

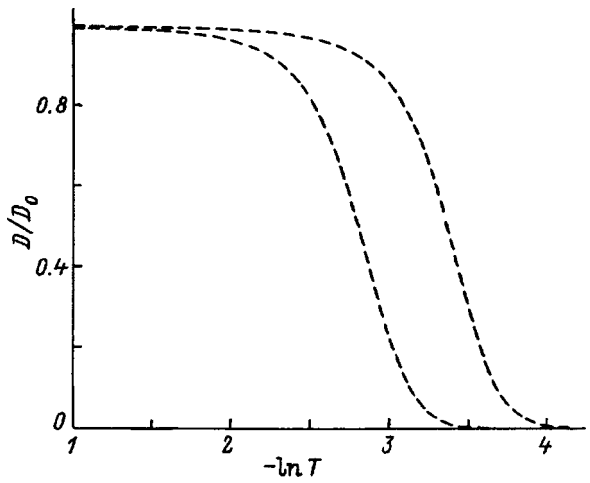

FIG. 7. D/D_0 relations for different initial realizations and cooling rates.

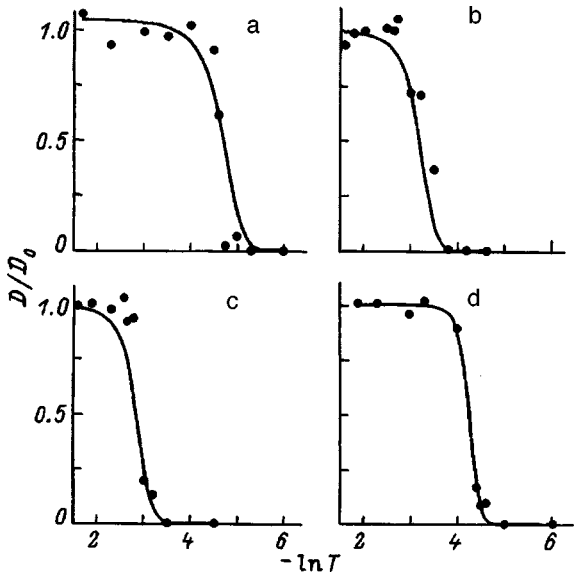

FIG. 8. D/D_0 relations for (a) $x=3.6\times10^{-4}$, $b=0.5$, $\gamma=0.75$; (b) $x=3.6\times10^{-4}$, $b=0.8$, $\gamma=0.75$; (c) $x=3.6\times10^{-4}$, $b=0.8$, $\gamma=1.2$; (d) $x=1.1\times10^{-3}$, $b=0.5$, $\gamma=0.75$.

$$\frac{D}{D_0}=[1+\eta x\ \exp(w_0/T)]^{-1}, \tag{12}$$

where $\eta\sim1$.

The error for the quantity D/D_0 in the high-temperature region, i.e., the scatter in the values obtained for different initial realizations, is 10%. As already mentioned, in the region where D/D_0 drops the error increases. For $T<T_{cl}$ the absolute error of D/D_0 determination is extremely small ($<10^{-4}$), but since different initial realizations give rise to different clusters and different values of w_0, the values of D/D_0 corresponding to different final realizations may differ by more than an order of magnitude.

Estimate (12) was obtained neglecting the cluster mobility. In actual fact, particle transport may occur in two ways:

1. The impurity breaks away from the cluster and diffuses a certain distance, where it is captured by another cluster or another impurity to contribute to formation of another cluster. We shall call this contribution to diffusion the contribution of unclusterized impurities (i.e., of those external to the clusters). Since their fraction decreases exponentially with temperature, the same occurs with the quantity D/D_0.

2. Without breaking away from the cluster, the impurity moves along its boundary. It is followed by another impurity, and so on. This results in a shift of the cluster as a whole without evaporation of impurities out of it and condensation onto it.

Our simulation indicates that both in the clusterization region and for $T>T_{cl}>0.3$ the main contribution to diffusion comes from the unclusterized impurities. For lower temperatures, processes of the second type should dominate, because their activation energy is lower than that of evaporation. In this region, however, diffusion is practically suppressed, and simulation requires a substantially longer time.

We are turning now to a comparison with experiment. Since in the case of quantum impurities $D_0(T)$ in the low-temperature domain grows according to a power law with decreasing temperature,[1] the exponential falloff of the diffusion coefficient is entirely associated here with clusterization processes. Experiments should exhibit a crossover from one activated dependence describing over-barrier transitions at high temperatures to another, with a lower activation energy, which corresponds to quantum diffusion at low temperatures. One may envisage different $D(T)$ relations depending on the relative magnitude of the temperature, at which tunneling begins to dominate over classical diffusion, and T_{cl}.[11]

The activation energy for protium in niobium and tantalum matrices was observed to decrease around 250 K.[12–14] For heavier hydrogen isotopes no such decrease was found to occur, which supports the quantum nature of this phenomenon.[13,15] We recall that J_0 falls off exponentially as the mass of the tunneling particle increases.

A similar effect was observed also in $ZrCr_2H_x$ ($0.25\leqslant x\leqslant0.5$) at 220 K.[16]

Because experiments on volume diffusion of hydrogen were carried out on macroscopic samples, they were not involved with the problem of dependence on initial realization, but the dependence of the final state on cooling rate remains an important aspect from the experimental standpoint.

Thus, clusterization of mobile interstitial impurities in a crystal matrix results, as a rule, not in a large-scale phase separation but rather in the onset of a metastable state characterized by a large number of small clusters. Their shape depends substantially on the cooling rate and parameters of the long-range interaction between impurities.

Clusterization manifests itself in a heat capacity peak, which was observed in a number of experiments.

Clusterization of impurities results in a strong depression of their diffusion coefficient. Therefore even in the case of quantum defects one observes with decreasing temperature not a rise in the diffusion coefficient but rather a replacement of one activated dependence of D by another, with a lower activation energy.

As the temperature is decreased below the clusterization point, the diffusion begins to be dominated by cluster ''creep,'' a process that should be accompanied by still another decrease of activation energy.

Partial support of the Russian Fund for Fundamental Research (Grants 96-02-18563 and 97-02-17627) is gratefully acknowledged.

[1] Y. Fukai and H. Sugimoto, Adv. Phys. **34**, 263 (1985).
[2] A. I. Morozov and A. S. Sigov, Zh. Eksp. Teor. Fiz. **95**, 170 (1989) [Sov. Phys. JETP **68**, 97 (1989)].
[3] A. I. Morozov and A. S. Sigov, Phys. Usp. **164**, 243 (1994).
[4] R. A. Masumura and G. Sines, J. Appl. Phys. **41**, 3930 (1970).
[5] *Monte Carlo Methods in Statistical Physics*, edited by K. Binder (Springer, Berlin 1979; Mir, Moscow, 1982).
[6] Yu. Kagan and N. V. Prokof'ev, Zh. Éksp. Teor. Fiz. **90**, 2176 (1986) [Sov. Phys. JETP **63**, 1276 (1986)].
[7] J. Jäckle, L. Piché, and S. Hunklinger, J. Non-Cryst. Solids **20**, 365 (1976).
[8] A. V. Skripov and A. V. Mirmelstein, J. Phys.: Condens. Matter **5**, L619 (1993).
[9] A. V. Skripov, A. E. Karkin, and A. V. Mirmelstein, J. Phys.: Condens. Matter **9**, 1191 (1997).

[10] V. A. Somenkov and A. V. Rodova, J. Less-Common Met. **101**, 481 (1984).
[11] A. I. Morozov and A. S. Sigov, Fiz. Tverd. Tela (Leningrad) **32**, 639 (1990) [Sov. Phys. Solid State **32**, 376 (1990)].
[12] G. Schaumann, J. Völkl, and G. Alefeld, Phys. Status Solidi **42**, 401 (1970).
[13] H. Wipf and G. Alefeld, Phys. Status Solidi A **23**, 175 (1974).
[14] D. Richter, G. Alefeld, A. Heidemann, and N. Wakabayashi, J. Phys. F **7**, 569 (1977).
[15] Zh. Qi, J. Völkl, R. Lässer, and H. Wenzl, J. Phys. F **13**, 2053 (1983).
[16] W. Renz, G. Majer, A. V. Skripov, and A. Seeger, J. Phys.: Condens. Matter **6**, 6367 (1994).

Translated by G. Skrebtsov

Microhardness anisotropy and the density of atoms in the unit identity volume of crystals

V. N. Gurin, M. M. Korsukova, and L. I. Derkachenko

A. F. Ioffe Physicotechnical Institute, Russian Academy of Sciences, 194021 St. Petersburg, Russia
(Submitted June 20, 1997; resubmitted July 7, 1997)
Fiz. Tverd. Tela (St. Petersburg) **40**, 481–486 (March 1998)

A new criterion of the reticular and polar anisotropy of microhardness is proposed: the density of atoms in the unit identity volume, i.e., the ratio of the number of atoms of one species in the atomic planes (plane) contained within the limits of the unit identity volume to the sum of the areas of these planes (plane) containing atoms of that species. It is shown that these densities of lanthanide, actinide, and boron atoms correlate satisfactorily with the reticular and polar microhardness anisotropy of their tetraborides and hexaborides. This criterion can be used to predict the nature of the variation of the reticular and polar microhardness anisotropy for other classes of compounds as well. © *1998 American Institute of Physics.*
[S1063-7834(98)01703-1]

Many investigations have been devoted to the nature of the anisotropy of microhardness, but it is still not adequately understood.[1–3] Today there are three distinct major approaches to assessing the nature of the anisotropy: chemical (or crystal–chemical), physical and structural (or crystallographic).

The chemical approach looks at the variation of the microhardness (strength) of a material on different faces and the same face of a crystal as a function of the number and type of atoms and the direction and strength of the chemical bond between them in the crystal structure.[1] The difficulties of this approach for many compounds lie in the experimental and theoretical acquisition of accurate data on the nature and strength of the chemical bond.

The physical approach explains the nature of the anisotropy of the lattice structure in terms of primary and secondary processes of plastic deformation, deformation volume, and structures that form around an indentation. These processes are treated at the level of collective lattice phenomena and, in particular, disregard the individual atomic character of the investigated chemical compounds. This approach is the most useful for a highly plastic material.[2–4] The difficulty is that for various classes of compounds, especially the high-melting kind (brittle and low-plasticity materials), the processes of plastic deformation have not yet been adequately studied in relation to their dependence on the temperature, the magnitude and duration of the load, and the presence of impurities.

The structural approach entails calculating the density of atoms on the faces of various simple geometrical forms[2] and establishing the dependence of the anisotropy of the microhardness on this density: The greater the reticular density of atoms, the harder is the face. The implementation of this approach, in application to diamond for example, rests on the concept of the atomic density of planar networks within a cube, a rhombododecahedron, and an octahedron.[5] This is well suited to pure elements, for which all the atomic planes in all directions contain identical atoms. However, when the subject turns to compounds for which atoms of different elements appear on the faces in different crystallographic directions, the same approach falls short and cannot account for the nature of the reticular anisotropy. It is totally inapplicable to polar anisotropy.

However, none of these approaches takes into consideration the role of the volume of the structure beneath the faces of various simple forms and beneath different directions on a face of one given form.

Here we propose to consider the density of atoms in a distinct volume of the crystal structure wherein the characteristic structural motif[2] for the symmetry of the given structure is wholly reproduced. Such volumes will differ in different crystallographic directions, because the structural motifs themselves differ in these directions. Such a volume will be the most representative part of any crystal structure of any element or compound. It will provide a means for more objectively comparing the densities of atoms of elements both on different faces and on a single face in different directions, because the density of the atoms will be calculated in one plane or in a series of planes contained within the given volume and will more accurately characterize the salient features of the structure. In this study we give the results of calculations of the proposed criterion and experimental data on the microhardness of single crystals of lanthanide and actinide hexaborides and tetraborides and also of model materials.

1. CALCULATIONS AND EXPERIMENTAL DATA

In the present article we propose a refined structural approach to the microhardness anisotropy problem. To that end we invoke two new concepts: the unit identity volume and the density of atoms in the unit identity volume.

The unit identity volume V_i is a volume of crystal structure within the limits of a single elementary identity motif defined by the face of simple form and three elementary

 © 1998 American Institute of Physics

translations, or identity periods. It can be established in any crystal structure in any crystallographic direction. For example, in a cubic structure the volume in question for a face of a simple {100} cube can be defined by a translation, or identity period—the shortest possible distance between identical points of the crystal structure (Ref. 7, p. 9). In this case it coincides with the volume of the unit cell. In the general case the volume in question for any crystallographic direction can be obtained in three ways (Ref. 2, p. 11): 1) by three noncoplanar (not in the same plane) translations; 2) by a system of equivalent points that transform from one to another by means of three noncoplanar translations; 3) by a system of identical parallelepipeds that densely fill space and can be made to coincide by three principal translations.

The density of atoms in the unit identity volume ρ_{iv} is the ratio of the number of identical atoms n_i in one atomic plane or Σn_i in all atomic planes containing such atoms and contained within the unit identity volume V_i defined by the face of a simple form of the crystal structure to the area S_i of all such planes containing the identical atoms:

$$\rho_{iv}=n_i/S_i \quad \text{or} \quad \sum n_i \Big/ \sum S_i .$$

This criterion, in contrast with the reticular density of atoms for the plane, is a characteristic volume of the crystal structure of chemical compounds for the face of each simple form. It can therefore be used to describe more completely the response of the structure to an external influence. We shall conditionally consider such influence (e.g., a diamond-pyramid) only on atomic planes contained within the limits of V_i (in the measurement of reticular microhardness) or on one plane contained within the limits V_i (in measurement of the polar microhardness) and not within the limits of the actual deformation volume created around the indentation. We introduce another assumption to facilitate the calculations: All atoms situated on the edges or in the corners of the face (planar network of atoms) are regarded as whole atoms (not fractions as is customary in calculating the reticular density of atoms for a face).

The correlation of the calculated values of ρ_{iv} with microhardness data is an indicator of the presence of reticular (for faces of different simple forms) and polar (for the face of one simple form) anisotropy as a characteristic that depends on the density of atoms of either element (or both) within the limits of V_i. For faces of different simple forms ρ_{iv} is calculated for the atoms of each species from the total area of all planes containing such atoms, contained within V_i, and parallel to the plane of the face of the simple form for which ρ_{iv} is being calculated.

If ρ_{iv} is determined for a specific direction on the plane of the face of one simple form, the area of the atomic plane oriented strictly at a selected angle (0°, 45°, 90°) on this face, perpendicular to the latter, and bounded by V_i is divided by the number of atoms of one (each) species contained in it.

1.1. Density of atoms and reticular anisotropy of the microhardness of hexaborides and tetraborides

It is evident from Fig. 1a that the cross sections of LaB_6 parallel to the faces of a cube and a rhombododecahedron through the atoms within the limits of V_i form a series of parallel planes containing such atoms. The areas of all the planes containing atoms of one species are summed, and ρ_{iv} is calculated as the quotient of their total area divided by the total number of identical atoms in them (see Table I). It is evident from the calculations of ρ_{iv} for the metal and boron atoms that for LaB_6 the face of the cube must be harder than the face of the rhombododecahedron, whereas for ErB_4 the face of the pinacoid is harder than the face of the {100} prism. For the reticular density of atoms, on the other hand, it is impossible to make a complete comparison, because the reticular density has zero values for both the metal atoms and the boron atoms (since their atoms do not emerge to the surface of the face in these cases).

Consequently, the use of ρ_{iv} to exhibit reticular anisotropy of the density of atoms in the crystal structure of compounds (and the properties associated with this density, e.g., microhardness), in contrast with the reticular density of atoms, is more definite and preferable. Table I gives experimental data on the determination of the Knoop microhardness for lanthanide and actinide hexaborides and tetraborides by a procedure described earlier.[7,8]

1.2. Density of atoms and polar anisotropy of the microhardness of hexaborides and tetraborides

An example of the calculation of ρ_{iv} for various directions (e.g., 0°, 45°, 90°) on one plane can be carried out for the face of the LaB_6 rhombododecahedron on the basis of the rule described above (the intermediate direction on the plane is approximately 45° when the long axis of the Knoop pyramid is oriented at the angle of the face, because the face of a rhombododecahedron is a rectangle, not a square). We choose three directions on the rhombododecahedron face $ABCD$ (Fig. 1b): $AD(0°)$, $AC(\sim 45°)$, and $AB(90°)$, whose area, along with the number and species of atoms contained in them, must be known or determined. An analysis shows that the rectangle $ADKL$ contains two La atoms and two B atoms, and the trapezoids $ACNL$ and $ABFL$ contain two and three La atoms, respectively, and no B atoms. The densities ρ_{iv} of La and B atoms for all three directions can be determined by calculating the areas of these figures (see Table I). It is important to note that the $ACNL$ plane passes close to (at least) two boron atoms contained within V_i. All the data of the ρ_{iv} calculations for LaB_6 and ErB_4 are given in the table, where they are compared with experimental data on the microhardness H_k.

2. DISCUSSION OF THE RESULTS

A comparison of ρ_{iv} both for difference faces and for different directions on one face can be made for each species of atoms separately as long as the value of ρ_{iv} is not equal to zero in all cases. If $\rho_{iv}=0$ holds for atoms of one species, the values of ρ_{iv} for atoms of different species must be compared in this case. To explain the reticular anisotropy of the microhardness, we compare the tabulated (Table I) values of ρ_{iv} and H_k for different faces of LaB_6 and ErB_4. Of course, such a comparison is feasible in some direction on the face. This fact leads to the conclusion that the comparison of single

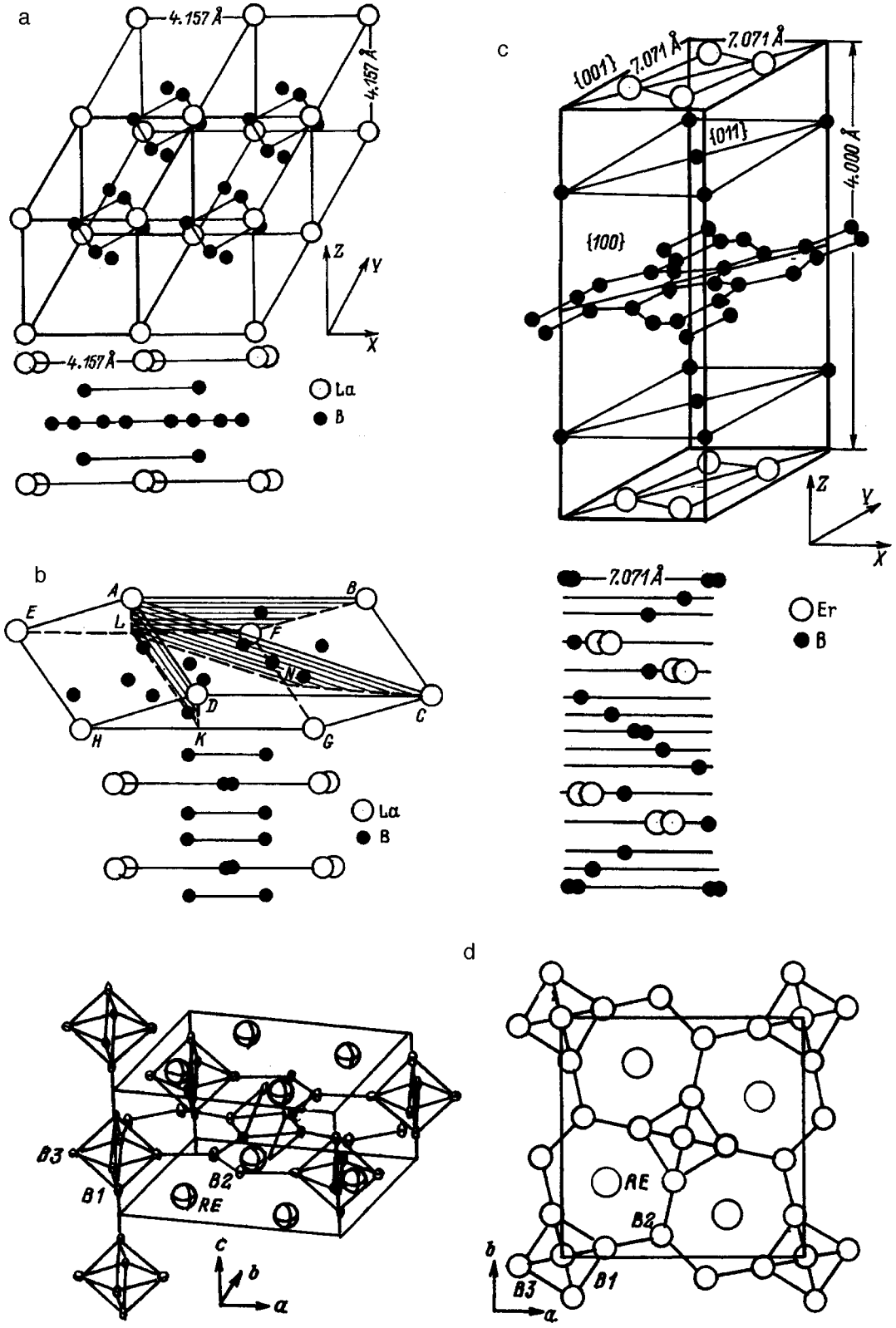

FIG. 1. Schematic diagrams of the crystal lattice of LaB_6 with a habit in form of a cube (a) and a rhombododecahedron (b), unit identity volume of the crystal structure of ErB_4 (c), and general view of the structure of tetraborides (d). a) The bold lines define the unit identity volume V_i (which in this case coincides with the volume of the unit cell); b) the hatched areas represent the planes, perpendicular to three directions on the plane of the rhombododecahedron (0°, 45°, 90°) and contained within V_i, in which ρ_{iv} is determined and the polar microhardness is measured; the lower diagram represents the atomic layers parallel to the faces of the {100} cube and the {110} rhombododecahedron; c) ρ_{iv} coincides for the faces of the (001) pinacoid and the (100) prism (the figure is elongated in the direction of the Z axis as a visual aid); the lower diagram represents the atomic layers parallel to the face of the (100) prism.

TABLE I. Density of metal atoms ρ_{iv} and boron atoms ρ_{iv} B (atoms/AA^2) within the limits of V_i, and microhardness H_k (kg/mm^2, $P=20$ g) in different directions on difference faces of single crystals of LaB_6, ErB_4, and other hexaborides and tetraborides.

	Direction		0°		45°		90°	
$LaB_6(LnB_6)$ cube, {100}	N^a		La—4, B—0		La—4, B—2			
	ρ_{iv} B		0		0.082			
	Crystal	a, Å	H_k	ρ_{iv}	H_k	ρ_{iv}		
	LaB_6	4.1570	2350±260	0.231	2160 ± 160	0.164		
	CeB_6	4.1396	2460 ± 220	0.233	2130 ± 130	0.165		
	PrB_6	4.1327	2460 ± 210	0.234	2220 ± 120	0.166		
	NdB_6	4.1266	2460 ± 190	0.235	2050 ± 120	0.166		
	SmB_6	4.1334	2120 ± 190	0.234	1950 ± 120	0.166		
	EuB_6	4.1844	2330 ± 200	0.228	2100 ± 120	0.162		
	YbB_6	4.1468	2330 ± 200	0.233	2200 ± 130	0.164		
	ThB_6	4.1108	1830 ± 70	0.237	1710 ± 60	0.167		
$LaB_6(LnB_6)$ rhombodo-decahedron, {110}	N^a		La—2, B—2		La—2, B—0		La—3, B—0	
	ρ_{iv} B		0.164		0		0	
	Crystal		H_k	ρ_{iv}	H_k	ρ_{iv}	H_k	ρ_{iv}
	LaB_6		1950 ± 120	0.164	1740 ± 100	0.126	2070 ± 120	0.231
	SmB_6		1500 ± 90	0.166	1740 ± 100	0.127	1600 ± 90	0.234
	YbB_6, $P=50$ g		1850 ± 70	0.165	1700 ± 70	0.127	1990 ± 80	0.233
$ErB_4(LnB_4)$ pinacoid, {001}	N^a		Er—0, B—4		Er—0, B—6			
	ρ_{iv} B		0.080		0.150			
	Crystal		H_k	ρ_{iv} B	H_k	ρ_{iv} B		
	ErB_4		1790 ± 130	0.080	2140 ± 110	0.150		
	SmB_4		2710 ± 150	0.078	1950 ± 110	0.145		
	GdB_4		1740 ± 130	0.078	2190 ± 120	0.147		
	TbB_4		1830 ± 140	0.079	2220 ± 120	0.148		
	DyB_4		2140 ± 160	0.081	2050 ± 110	0.152		
	HoB_4		2070 ± 150	0.080	1600 ± 80	0.149		
	UB_4		2260 ± 110	0.080	2190 ± 130	0.151		
$ErB_4(LnB_4)$ prism, {100}	N^a		Er—4, B—0		Er—2, B—2		Er—0, B—4	
	ρ_{iv} B		0		0.035		0.080	
	Crystal		H_k	ρ_{iv}	H_k	ρ_{iv} B	H_k	ρ_{iv} B
	ErB_4		2570 ± 150	0.141	2800 ± 170	0.035	2330 ± 140	0.080
	SmB_4		2530 ± 150	0.137	2700 ± 160	0.034	2140 ± 130	0.078
	GdB_4		2480 ± 150	0.138	2520 ± 150	0.034	2200 ± 130	0.078
	TbB_4		2050 ± 120	0.139	2580 ± 150	0.034	1950 ± 110	0.079
	DyB_4		1910 ± 100	0.143	2220 ± 120	0.035	1740 ± 90	0.081
	HoB_4		2500 ± 150	0.141	2720 ± 160	0.035	2050 ± 120	0.080
	TmB_4		2280 ± 130	0.142	2420 ± 140	0.035	1950 ± 110	0.080
	LuB_4		2150 ± 120	0.143	2200 ± 130	0.035	1950 ± 110	0.081
	ThB_4		2050 ± 120	0.134	2140 ± 130	0.033	1740 ± 100	0.076

Note: The purity of all the compounds is 99 mass % or better; N^a denotes the number of atoms in planes parallel to the face of interest within the limits of V_i; the 0° and 90° directions are equivalent for the cube and pinacoid.

crystals of compounds by microhardness on different faces or on one face is practical only when data are available for the compared faces in a certain direction (e.g., 0°, 45°, 90°). Otherwise we can only address a certain average microhardness of single crystals.

It follows from the table that for LaB_6 the face of the cube is harder than the face of the rhombododecahedron, corresponding both to the trend of the calculated ρ_{iv} data and to the nature of the variation of H_k. The variation of H_k for other hexaborides is similar [the mutual deviation for all the compounds is $(2-3)\sigma$]. The values of H_k in different directions on the face of the cube for all hexaborides also correlates with the values of ρ_{iv} for the metal atoms [deviation $<(1-2)\sigma$]. For the face of the rhombododecahedron such a correlation is observed for two [$\approx(2-4)\sigma$] of the three investigated hexaborides; the lack of data for all other hexaborides is attributable to the absence of this face or to its imperfection and very small surface area. Consequently, both the reticular and the polar anisotropy of the microhardness of

hexaborides are well described by the proposed criterion ρ_{iv}.

The calculated value of ρ_{iv} for ErB_4 shows that the {001} pinacoid must be harder than the {100} prism in the $\sim 45°$ direction, have approximately equal hardness H_k in the 90° direction, and can be softer in the 0° direction (see Table I). For all the tetraborides, however, H_k is lower in the $\sim 45°$ direction on the pinacoid than for the prism [deviation $(1.5-5)\sigma$]. In the 0° direction the pinacoid is actually softer than the prism (with the exception of SmB_4 and DyB_4, deviation $\approx 1.5\sigma$), and in the 90° direction the pinacoid is softer than the prism for three compounds [deviation $\approx(1-2)\sigma$] and is harder than the prism for three compounds [two of them with a deviation $\approx 2\sigma$, but for HoB_4 the values practically coincide]. This contradiction is easily resolved by taking into account the possibility of error in establishing the simple form (pinacoid or prism) for very small samples (<0.2 mm). The scatter of the data in the 90° direction can be attributed to surface imperfection of the faces of the investigated samples. We therefore regard the interpretation of the reticular microhardness anisotropy of the tetraborides by means of ρ_{iv} as satisfactory.

In regard to polar anisotropy, for the pinacoid form in the tetraborides we observe both a maximum (for three compounds) and a minimum (for four compounds) of H_k in the 45° direction, even though the criterion ρ_{iv} B for boron has a maximum here ($\rho_{iv}=0$ for Er). We can assume that in the event of imprecise orientation of the long diagonal of the Knoop pyramid it is possible for the plane in which it is directed to deviate from the plane containing the maximum number of B atoms. Judging from the large number of tetraborides having a minimum of H_k in the $\approx 45°$ direction, such a deviation is more inevitable than merely probable (Fig. 1d).

In the case of the prism all the tetraborides without exception (including the application of different loads[7]) have a maximum of H_k in the $\sim 45°$ direction, and $\rho_{iv}>0$ for the Er and B atoms, even though the absolute values here are smaller than the values of ρ_{iv} for 0° (Er only) and for 90° (B only). This maximum can be attributed to the fact that the plane in the $\sim 45°$ direction contains at least two boron atoms and two metal ions (our analysis shows that the two boron atoms and the two metal atoms are very close to the plane, perpendicular to this direction and to the face of the prism, in which the microhardness is measured) (Figs. 1c and 1d). Moreover, this plane is also perpendicular to the high spots of the networks of boron atoms formed by the bases of the boron octahedra and linking the boron atoms (Fig. 1d). In these cases the Knoop pyramid hits many chemical bonds, perpendicular to its motion, between boron atoms. Also perpendicular to this motion are the high spots of planes containing metal atoms. Everything here is related to the degree of perfection of this crystal face, which for some tetraborides, according to our observations, has a distinct shading (jointing, cleavage, lamination, and other manifestations of deformation processes in the material).

It is worth noting, in light of the foregoing, that the nature of the variation of ρ_{iv} for all directions on the prism is consistent with the nature of the variation of H_k.

Thus, the proposed criterion ρ_{iv} and the conditions governing its application are helpful in explaining and predicting the variation of microhardness both on different faces and on one face of single crystals of high-melting borides.

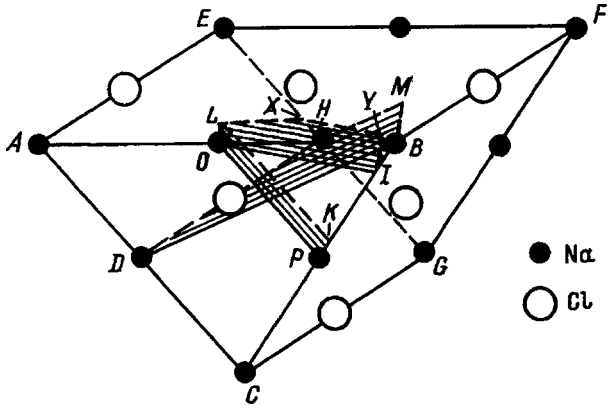

FIG. 2. Unit identity volume of NaCl for the simple form of the {111} octahedron. The hatched areas represent the planes perpendicular to the directions (0°, 45°, 90°) for the determination of ρ_{iv}.

For all hexaborides and tetraborides of lanthanides and actinides the variation of ρ_{iv} is corresponds to the variation of the periods of the lattice of each compound[9] (see Table I). We might also note that in isostructural series of compounds ρ_{iv} is not a ''sensitive'' parameter in that, despite appreciable differences in the lattice periods, ρ_{iv} has the same values for several different compounds (see Table I).

To test the applicability of the proposed criterion to compounds having a different (e.g., ionic) type of bond, we have measured H_k for NaCl and LiF ($a=5.64$ Å and 4.03 Å) in all three directions for the faces of a cube (LiF), a rhombododecahedron, and an octahedron,=and for them we have calculated ρ_{iv} and the reticular density of atoms for each species of atom (Fig. 2). A standard procedure[8] was used for the microhardness measurements. The compounds NaCl (Na 97.8; Mg 1.5; I 0.5 mass %) and LiF (99.99 mass %) were chosen as model materials for the diversity of the polar anisotropy of their microhardness.[2–4,10,11] A comparison of the calculated ρ_{iv} and H_k data ($\sigma \leqslant 3\%$) for all faces in the case of NaCl discloses good correlation. For example, for the face of the octahedron (Fig. 2): 0° ($\rho_{iv}=0.205$ for Na, $H_k=35$ kg/mm^2); 45° (0.108, 32); 90° (0.211, 36). The values of ρ_{iv} for C are less consistent with the experimental data. This pattern is observed for the given choice of unit cell of NaCl (with Na atoms at the vertices of a cube). However, this choice is arbitrary, and Na atoms can be replaced by C atoms. A different pattern is observed in the case of the hexaborides, where the emergence of La atoms to the face of the (100) cube for LaB_6 has been confirmed experimentally.[12] For LiF, on the other hand, the polar anisotropy for the cube (in particular) is very slight, and the results for freshly cleaved chips subjected to light loads ($P=5$ g and 20 g) and short indentation times agree with the data of Refs. 3 and 4. Consequently, LiF is a special material requiring special investigation.

The proposed new criterion can thus be used to interpret and predict reticular and, in particular, polar anisotropy of the microhardness for compounds having different types of chemical bonds.

The unit identity volume and the density of atoms within its limits are new, objective structural characteristics of the solid state of any elements and compounds.

The reticular and polar anisotropy of the microhardness of lanthanide and actinide hexaborides and tetraborides as well as NaCl and LiF can be attributed to a variation of the atomic density within a identity motif of the crystal structure: the unit identity volume.

In closing, the authors express their heartfelt gratitude to S. P. Nikanorov for profitable discussions and are indebted to V. M. Krymov, O. V. Klyavin, and Yu. M. Chernov for assistance and discussion in the course of the study.

[1] A. S. Povarennykh, *Hardness of Minerals* [in Russian] (Izd. AN Ukr. SSR, Kiev, 1963).
[2] M. P. Shaskol'skaya, *Crystallography* [in Russian] (Vysshaya Shkola, Moscow, 1976).
[3] Yu. S. Boyarskaya, D. Z. Grabko, and M. S. Kats, *Physics of Microindentation Processes* [in Russian], Shtiintsa, Kishinev (1986).
[4] S. P. Nikanorov, Doctoral Dissertation [in Russian] (Fiz.-Tekh. Inst. im. A. F. Ioffe Akad. Nauk SSSR, Leningrad, 1976).
[5] I. I. Shafranovskiĭ, *Diamonds* [in Russian], Nauka, Moscow-Leningrad (1964), p. 148.
[6] G. Will, W. Schfer, F. Elf, and J. Etourneau, J. Less-Common Met. **82**, 349 (1981).
[7] V. N. Gurin, L. I. Derkachenko, M. M. Korsukova, S. P. Nikanorov, W. Jung, and R. Müller, Fiz. Tverd. Tela (St. Petersburg) **38**, 2750 (1996) [Phys. Solid State **38**, 1508 (1996)].
[8] B. F. Mott, *Micro-Indentation Hardness Testing* [Butterworths, London, 1956; Gostekhizdat, Moscow, 1960].
[9] T. I. Serebryakova, V. A. Neronov, and P. D. Peshev, *High-Temperature Borides* [in Russian], Metallurgiya-Chelyabinsk Branch, Moscow (1991), pp. 12, 148.
[10] A. A. Vorob'ev, *Mechanical and Thermal Properties of Alkali-Halide Single Crystals* [in Russian] (Vysshaya Shkola, Moscow, 1968).
[11] B. I. Smirnov, *Dislocation Structure and Ordering of Crystals* [in Russian], Nauka, Leningrad (1981).
[12] R. E. Watson and M. L. Perlman Surf. Sci. **122**, 371 (1982).

Translated by James S. Wood

Dynamic mechanism of the temperature dependence of the Portevin–Le Châtelier effect

M. A. Lebedkin and L. R. Dunin-Barkovskiĭ

Institute of Solid-State Physics, Russian Academy of Sciences, 142432 Chernogolovka, Moscow District, Russia

(Submitted July 29, 1997)
Fiz. Tverd. Tela (St. Petersburg) **40**, 487–492 (March 1998)

The influence of temperature on the dynamic and static characteristics of unstable plastic flow due to the Portevin–Le Châtelier effect is investigated experimentally and by numerical modeling. It is concluded that the distinctive features of the complex macroscopic behavior of the plastic instability are determined by collective processes associated with the long-range interaction of dislocations and lead to dynamic effects of mesocopic scale. © *1998 American Institute of Physics.* [S1063-7834(98)01803-6]

The complexity of the macroscopic behavior of plastically deformed solids is attributable to the fact that the ensemble of interacting dislocations represents an extended, nonlinear, dissipative system. The self-organization property of this system is responsible for well-known effects of collective dislocation behavior: the formation of dislocation substructures, abrupt, unstable deformation, and slip propagation or localization.[1,2] Plastic flow therefore takes place at three levels: the microscopic level associated with motions of individual dislocations, the macroscopic level corresponding to the average plastic response in the continuum approximation, and the mesoscopic level, at which the characteristic scale depends on the physical nature of cooperative phenomena. The microscopic and macroscopic descriptions of plasticity, contrary to conventional thinking, are not related one-to-one, but require the investigation of self-organization phenomena in the substructure of defects.

One of the phenomena in which mesoscopic effects stand out most clearly is the discontinuous plastic flow (jerky flow) of molten metal alloys due to the Portevin–Le Châtelier (PLC) effect.[3] This effect refers to the recurrence of localized or propagating deformation bands that induce sudden strain discontinuities in the crystal. In deformation at a constant rate the effect takes place macroscopically in the form of spikes of the deforming stress σ as a result of the elastic response of the machine-sample system. Three main types of spikes are normally distinguished, corresponding to different slip-band dynamics.[4] Type A is characterized by the nucleation of deformation bands near one of the machine clamps and their propagation in the crystal. The spikes occur above a certain average level of σ and, for this reason, are also called locking serrations. In type B each spike of σ is associated with the occurrence of a localized deformation band at a neighboring site relative to the preceding one, and the effect has therefore come to be known as relay strain propagation. This kind of spatial correlation in the localization of strain does not exist in the case of type C, and the corresponding downward-pointing spikes drop below the average level of σ (''unlocking serrations''). The sequential change from type A to type B instability and then to type C is observed as the strain rate $\dot{\varepsilon}_a$ decreases and (or) as the temperature T increases. Other, more specialized types of PLC instability are also discerned. The mixing of different types is customarily observed in a real experiment.

It has been shown[5–7] that certain features of the discontinuous deformation can be explained by the dynamics of a model based on a nonlinear local constitutive equation,[8] which describes the temporal instability of plastic flow, taking into account its inevitable spatial inhomogeneity in a population of dislocations far from equilibrium. The microscopic mechanism of the PLC effect is tied in with the onset of an anomalous part of the negative strain-rate sensitivity of σ as a result of dynamic strain aging, i.e., the diffusion of impurity atoms toward dislocations pinned at obstacles[8,9] (Fig. 1). To within the stress components associated with strain hardening, the phase portrait of the system in $(\sigma,\dot{\varepsilon})$ coordinates, shown in Fig. 1, represents cyclic motion, whereas in (σ,ε) coordinates a periodic, discontinuous (serrated) stress-strain curve should be observed (the strain analog of relaxation oscillations[10]). The inhomogeneity of plastic flow can impart a complex shape to real stress-strain curves. On the other hand, owing to the correlation between neighboring elements of a crystal, the observed curves exhibit a nonrandom character. For example, the observation of a transition to chaotic behavior has been reported,[11] and the possibility of self-organized criticality[12] under the conditions of the PLC effect has been hypothesized.[5]

The influence of temperature on the discontinuous deformation of materials characterized by dynamic strain aging demonstrates what appears to be the richest spectrum of behavior,[13] the investigations of which so far have been of a descriptive nature. In the present study we attempt to probe the mechanism of this influence by experimental investigation and computer modeling of the stress-time curves and the statistics of the jumps in the deforming stress in Al-Mg alloy.

1. PROCEDURE

We investigated polycrystalline samples of the alloy Al–3 at. % Mg and single crystals of Al–4.5 at. % Mg with the axis oriented close to the crystallographic directions ⟨111⟩ or ⟨100⟩, corresponding to multiple slip. The polycrystalline

 © 1998 American Institute of Physics

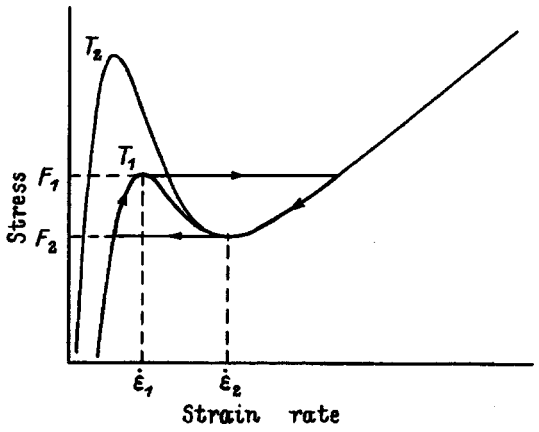

FIG. 1. Schematic plot of the function $F(\dot{\varepsilon})$ representing the strain-rate sensitivity of the deforming stress at two temperatures ($T_1 > T_2$).

samples were annealed for 2 h at 400 °C with subsequent quenching in water. Flat samples in the customary double-ended spade configuration with a working section of length 12–25 mm (single crystals) and 18–36 mm (polycrystals) and with a typical cross section of 5×1.5 mm. The samples were deformed by tension at a constant rate on an Instron testing machine (the machine-sample system had a stiffness $M = 10^7$ N/m) in the temperature interval $T = -30$ °C–160 °C with the loading mechanism moving at a rate of 2.5–5000 μm/min, which for the given sample lengths corresponds to a strain rate $\dot{\varepsilon}_a$ in the range 2×10^{-6}–2.7×10^{-3} s^{-1}.

Several single-crystal and polycrystalline samples were tested at the same temperature. The rate was switched during deformation, so that segments of the stress–time curves were recorded for each sample at the same settings of $\dot{\varepsilon}_a$. The evolution of the distributions in the course of hardening of the deformed crystal was tracked by recording a fragment of the curve for a selected reference value of $\dot{\varepsilon}_a$. A systematic dependence of the average depth of the spikes $\Delta\sigma$ on ε without any change in the nature of their statistics was observed in some of the tests. In the calculation of the distributions this dependence, which to within small error limits was linear in our tests, was taken into account by normalizing the values of $\Delta\sigma$ to the regression line of $\Delta\sigma$ on ε. The statistical sample size for each value of the investigated parameters was $n = 100$–500. The details of the statistical analysis procedure are described in Ref. 5.

2. COMPUTER MODEL

In the model the sample is represented by a one-dimensional chain of N blocks. Each block constitutes the minimum volume in which the strain can be regarded as homogeneous, and it is coupled with the two neighboring blocks by harmonic springs having the same stiffness coefficient K. Using the results of Refs. 6, 7, and 14, we assume that the coupling of adjacent elements of the crystal is elastic and is attributable to inhomogeneous internal stresses in the ensemble of dislocations. Various mechanisms of correlation between the plastic processes are discussed in detail in Refs. 3 and 15. Despite the long-range character of the elastic interaction, the nearest-neighbor approximation is justified by the exponential stress dependence of the plastic flow rate. The choice of a one-dimensional model reflects the fact that the transverse growth of the deformation bands is a much faster process than their axial propagation. Each ith block obeys a nonlinear constitutive equation in the form

$$\sigma = h\varepsilon_i + F(\dot{\varepsilon}_i) + K[(\varepsilon_i - \varepsilon_{i-1}) + (\varepsilon_i - \varepsilon_{i+1})], \tag{1}$$

where h is the work-hardening coefficient, and $F(\dot{\varepsilon})$ is a sawtooth function representing the strain-rate sensitivity of the stress (Fig. 1). The first two terms on the right-hand side of the equation represent the usual local relation in the case of dynamic strain aging.[8] The third term corresponds to the restoring force generated when the blocks are deformed incoherently. The deformation conditions are described by the relation of the rate of movement of the clamps to the rate of elastic deformation of the machine-sample system and the average plastic flow rate of the sample:

$$\dot{\varepsilon}_a = \frac{\dot{\sigma}}{M} + \frac{1}{N}\sum \dot{\varepsilon}_i . \tag{2}$$

The influence of temperature is manifested in the way it affects the coupling constant K and the function $F(\dot{\varepsilon})$. The role of plastic relaxation of the internal stresses diminishes as T decreases, so that the effective coupling constant can be expected to increase (a similar influence should also be observed in strain hardening[14]). The temperature dependence $F(\dot{\varepsilon})$ follows from a relation[7] based on the microscopic theory of dynamic strain aging:

$$F(\dot{\varepsilon}) = S_i \ln\frac{\dot{\varepsilon}}{\dot{\varepsilon}_0} + \beta C_s\left\{1 - \exp\left[-\left(\frac{\dot{\varepsilon}^*}{\dot{\varepsilon}}\right)^p\right]\right\}, \tag{3}$$

$$\dot{\varepsilon}^* = (\Omega/\tau_0)\exp\{-(Q + W/p)/k_B T\}. \tag{4}$$

Here S_i is the impurity-free strain-rate sensitivity of σ, Q is the impurity-diffusion activation energy, W is the binding energy between an impurity atom and a dislocation, $\beta \sim W/b^3$ (b is the Burgers vector) characterizes the pinning force of dislocations by impurity atoms, Ω is the strain corresponding to the elementary event of activation of all mobile dislocations,[9], $\tau = \tau_0 \exp(Q/k_B T)$ is a characteristic time for the diffusion of an impurity toward a dislocation, $C_s = C_0 \exp(W/k_B T)$ is the saturation concentration of impurities at a dislocation, C_0 is the nominal concentration in the bulk of the crystal, and $p = 2/3$ in the classical Cottrell–Bilby theory.[16] Obviously, owing to the increase in C_s and the decrease in $\dot{\varepsilon}^*$ as the temperature decreases, F_1 becomes higher and shifts toward lower values of $\dot{\varepsilon}$, as shown in Fig. 1.

Direct calculations of the temperature dependence $F(\dot{\varepsilon})$ are thwarted by, for example, the considerable arbitrariness encountered in the estimation of the activation parameters at different temperatures T. In contrast, the influence of $\dot{\varepsilon}_a$ on $F(\dot{\varepsilon})$ at a fixed T is simply calculated by adding the term $k\Omega[1 - (\dot{\varepsilon}_a/\dot{\varepsilon}) + \ln(\dot{\varepsilon}_a/\dot{\varepsilon})]$ (Ref. 17). The increase in $\dot{\varepsilon}_a$ is analogous to the influence of an increase in T, so that the

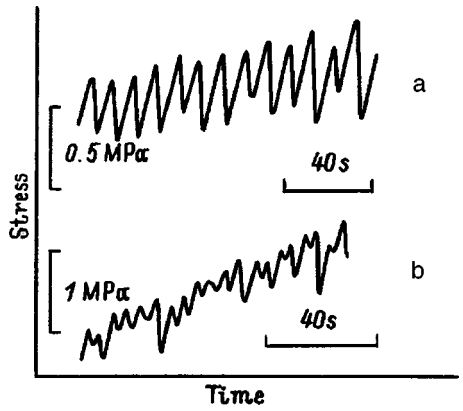

FIG. 2. Typical traces of segments of stress-time curves of Al–Mg alloy at room temperature. a) Polycrystalline sample, strain rate $\dot{\varepsilon}_a = 2.7 \times 10^{-5}$ s^{-1}; b) single crystal, $\dot{\varepsilon}_a = 1.3 \times 10^{-5}$ s^{-1}.

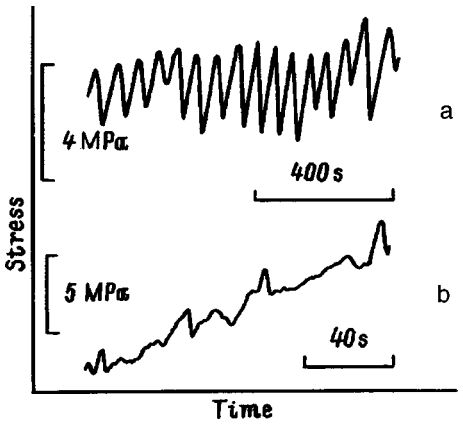

FIG. 3. Segments of stress-time curves of a polycrystalline sample at $T = -20$ °C. a) strain rate $\dot{\varepsilon}_a = 2.1 \times 10^{-5}$ s^{-1}; b) $\dot{\varepsilon}_a = 8.4 \times 10^{-5}$ s^{-1}.

following procedure is used. It has been verified by using trial functions $F(\dot{\varepsilon})$ that the qualitative character of the modeling results do not depend on the differences $F_1 - F_2$ and $\dot{\varepsilon}_2 - \dot{\varepsilon}_1$, but is determined by the position of $\dot{\varepsilon}_a$ relative to $\dot{\varepsilon}_1$ and $\dot{\varepsilon}_2$ and by the value of K. This condition can be used to adjust the model by means of the parameters $\dot{\varepsilon}_a$ and K so as to match the form of the model curve, the statistics of the stress spikes, and the slip dynamics with the experimental data for selected values of T and $\dot{\varepsilon}_a$. The subsequent comparison of experiment and model is based on an investigation of the prominent features of the variation of these deformation characteristics of real and model samples as $\dot{\varepsilon}_a$ is varied or for various values of ε (hardening is simulated in the model by increasing K).

The details of the numerical solution of the system of equations are given in Ref. 7. The parameters of the initial (at $\dot{\varepsilon}_a = 0$) serrated curve are chosen as representative of typical data for alloys deformed by the PLC mechanism: $F_1 = 140$ MPa, $F_2 = 80$ MPa, $\dot{\varepsilon}_1 = 10^{-6}$ m^{-1}, and $\dot{\varepsilon}_2 = 10^{-3}$ s^{-1}. The other parameters of the model are assigned the values $K = (0.02-1.0)M$, $\dot{\varepsilon}_a = (0.01-0.8)\dot{\varepsilon}_2$, $h = 0.01M$, and $N = 300$. Inhomogeneity is introduced into the system by the random sampling of initial values of $\dot{\varepsilon}_i$ with $< 0.05\dot{\varepsilon}_1$ fluctuations. The subsequent evolution of the system is deterministic, without the introduction of additional inhomogeneity.

3. RESULTS AND DISCUSSION

3.1. Form of the stress-time curves

Figure 2 gives typical fragments of type B discontinuous stress–time curves for polycrystalline and single-crystal samples at room temperature and low strain rates. Type C or B spikes characterized by strain localization in slip bands are observed for polycrystals, but when $\dot{\varepsilon}_a$ is raised above 5×10^{-4} s^{-1}, we see a transition to type A instability, corresponding to the propagation of deformation bands in the direction of the tension axis. It is evident from Fig. 2b that the stress-time curves of single crystals have a more regular behavior, i.e., the correlation of the deformation processes taking place in different cross sections of the sample is weaker in them, consistent with its hypothesized elastic nature. As a result, the curves for single crystals are more difficult to classify, but they exhibit a similar kind of evolution when the temperature or the strain rate is varied; we therefore give the data for polycrystalline samples, in which this evolution is not masked by extra features of the stress–time curves.

The variation of the macroscopic characteristics of the discontinuous deformation as the temperature is lowered to -30 °C corresponds to the temperature dependence of the function $F(\dot{\varepsilon})$, which determines the characteristic scale of the stress spikes and the strain-rate interval of plastic flow instability. The qualitative behavior does not change here, and it reflects the transition from slip localization to slip propagation as the strain rate increases. This trend is illustrated by the data shown in Fig. 3: At $T = -20$ °C the stress–time curves acquire very distinct type A behavior even at $\dot{\varepsilon}_a = 8 \times 10^{-5}$ s^{-1}, and type B spikes are observed only at the lowest strain rates in the of interest range. The comparison of Figs. 2a and 3a also discloses a tendency for the average depth of the stress spikes to increase as the temperature decreases. These data are in good agreement with the modeling results. In the framework of the hypothesized elastic nature of the correlation of the deformation processes, the low-temperature interval corresponds to high values of the coupling constant in the model. Indeed, when K lies in the range $K = (0.3-1.0)M$, the nature of the influence of $\dot{\varepsilon}_a$ on the form of the modeled stress-time curves and on their statistics do not depend on K, and they are similar to the experimentally observed influence (Fig. 4). The numerical data also contain information about the deformation-band dynamics. In the model a natural analog of the slip band is found in a group of adjacent blocks whose plastic flow rates correspond to the right ascending branch of the $F(\dot{\varepsilon})$ curve: $\dot{\varepsilon}_i > \dot{\varepsilon}_2$ (Ref. 7). As in real crystals, the dynamics of the model corresponds to the transition from localization to propagation of slip bands as $\dot{\varepsilon}_a$ increases.

In the high-temperature range the variations of the stress–time curves correspond qualitatively to the weakening

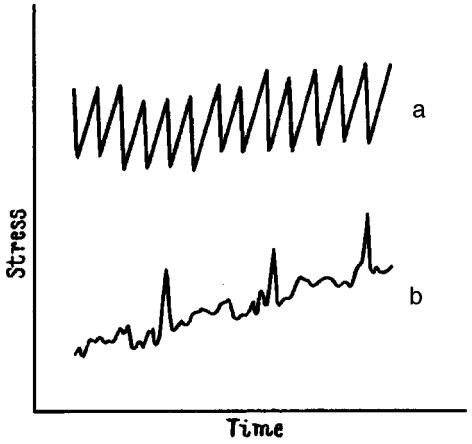

FIG. 4. Form of the model stress–time curves for $k=M$. a) $\dot{\varepsilon}_a=0.05\dot{\varepsilon}_2$; b) $0.4\dot{\varepsilon}_2$.

of the correlation of the deformation processes. Figure 5 shows examples of curves at 100 °C for three strain rates. At a rate below 4×10^{-5} s^{-1} we observe macroscopically smooth stress–time curves, owing to the above-described temperature dependence of $\dot{\varepsilon}_1$. As the strain rate increases, infrequent deep drops appear below the average level of σ (unlocking serrations), separated by long intervals of smooth flow, which are characteristic of type C, or spikes of very minute amplitude, so that these intervals have the appearance of a fine-toothed saw (Fig. 5a). If the strain rate is increased further in the initial stage of deformation, there is a transition to type A instability (locking serrations), bypassing any clearly defined type B stage (Fig. 5b). Hardening of the crystal reverses the transition (Fig. 5c). As deformation progresses, deep stress spikes become more frequent, and the shallow ripples observed in the intervals between them increase in amplitude. The modeling results convey all these

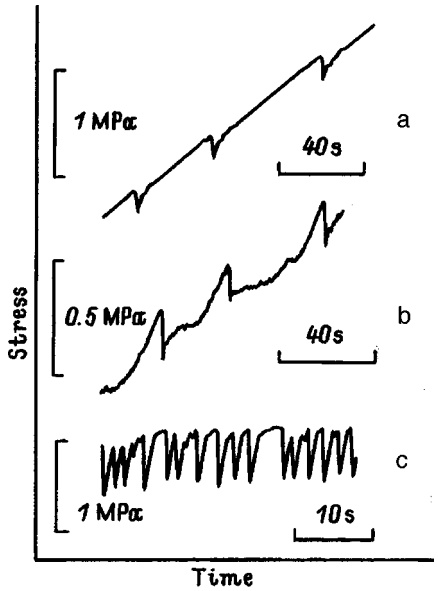

FIG. 5. Examples of stress–time curves for a polycrystalline sample at $T=100$ °C. a) $\dot{\varepsilon}_a=4.7\times10^{-5}$ s^{-1}, $\varepsilon=4.3\%$; b) 9.4×10^{-5} s^{-1}, 6%; c) 9.4×10^{-5} s^{-1}, 14%.

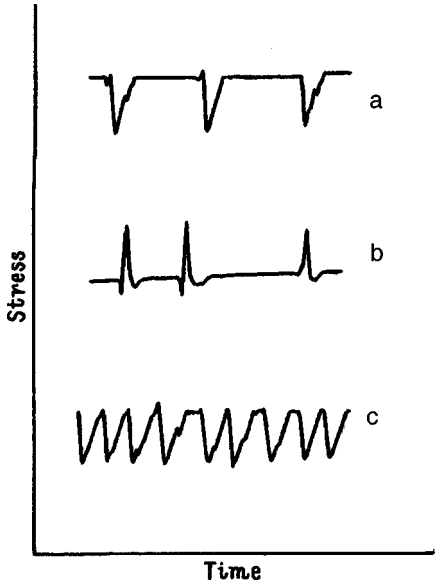

FIG. 6. Form of model stress–time curves. a) $K=0.06M$, $\dot{\varepsilon}_a=0.02\dot{\varepsilon}_2$; b) with the strain rate increased to $\dot{\varepsilon}_a=0.04\dot{\varepsilon}_2$; c) with the coupling constant increased to $K=0.1M$.

features of the experimental observations (Fig. 6). The high-temperature behavior corresponds to numerical results obtained in the range of lower coupling constants $K=(0.03-0.1)M$, corroborating the stated hypotheses about the temperature dependence of K. We note that a further increase in the strain rate in both experiment and model produces irregular curves typical of the recording of nonstationary stochastic processes. This observation runs parallel to recent studies (e.g., Ref. 11), in which the same kind of random behavior of the stress-time curves has been concluded for Al–Mg and Cu–Al single crystals at high $\dot{\varepsilon}_a$.

The high-temperature slip-localization dynamics has not been investigated experimentally. The results of modeling of the dynamics are consistent with general notions that the ''unlocking-locking'' transition with increasing value of $\dot{\varepsilon}_a$ corresponds to the transition from localization to propagation of slip bands. We note that the transition point shifts toward higher values of $\dot{\varepsilon}_a$ as K increases. This result also concurs with the experimental data: A variation such as the curves in Fig. 5 ($T=100$ °C) is already observed at a strain rate twice as high as the left edge of the domain of instability, whereas at room temperature or lower this situation takes place at $\dot{\varepsilon}_a>(10-100)\dot{\varepsilon}_1(T)$ (see, e.g., Fig. 3).

3.2. Stress-spike statistics

The stochastic behavior of the stress–time curves can be characterized by histograms of the amplitude distributions of the deforming-stress spikes. The relatively regular drops corresponding to localized plastic flow and observed at room temperatures and lower and at strain rates close to $\dot{\varepsilon}_1(T)$ reveal bell-shaped distributions with variances that differ depending on the deformation conditions and the microstructure of the samples. The narrowest peaks, close to a normal distribution, are observed for polycrystals (Fig. 7a) and for

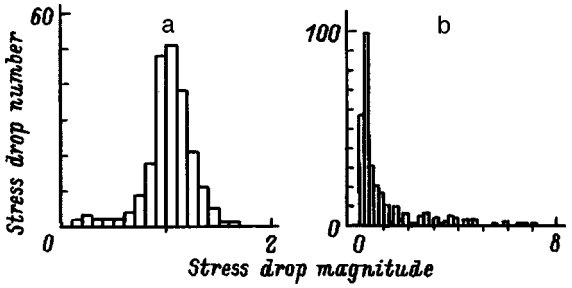

FIG. 7. Histograms of the amplitude distributions of the deforming-stress spikes for polycrystalline samples. a) Samples deformed at $T=20$ °C, $\dot{\varepsilon}_a=9.5\times10^{-6}$ s^{-1}; b) $T=-20$ °C, $\dot{\varepsilon}_a=8.5\times10^{-5}$ s^{-1}.

$K>0.5M$ in the model (Fig. 8a). Single crystals are characterized by broader, asymmetric peaks with their centroid shifted toward lower amplitudes $\Delta\sigma$ (Refs. 6 and 18). This change in the shape of the histograms corresponds to a reduction in the value of K in the model and is probably attributable to an increase in the role of plastic relaxation of inhomogeneous internal stresses. In the range of higher temperatures the distributions have two peaks reflecting the two characteristic scales of the stress spikes (Fig. 5c).

As the strain rate increases or the temperature decreases, the centroids of the distributions shift more and more toward lower spike amplitudes. Above a certain strain rate, which depends on the temperature, the distributions become monotonically decreasing (Figs. 7b and 8b). The distributions exhibit a nontrivial character at strain rates corresponding to the propagation of deformation bands. Figure 9a shows an example of the probability density function $D(s)$ of the distribution of the normalized stress-spike amplitude at $T=-20$ °C. It is evident that this dependence is satisfactorily described by a power law $D(s)\sim s^{\alpha}$ with power exponent $\alpha\approx-1.4$. Numerical simulation gives values of α in the interval $-(1-1.5)$, depending on the choice of parameters. The power-law character of the distributions indicates the lack of a distinctive scale of the processes, as is characteristic of systems in the critical state.

Critical statistics are observed over a wide interval in the range of high strain rates at all the investigated temperatures. It is interesting that raising the temperature at low strain rates $\dot{\varepsilon}_a$ can also lead to irregular stress–time curves characterized by a power-law distribution of $\Delta\sigma$. This behavior sets in only within a narrow range of deformation conditions and, as T or

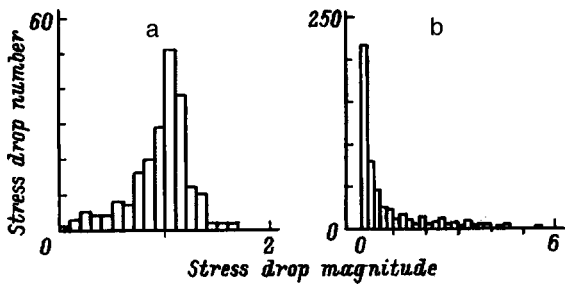

FIG. 8. Histograms of the distribution of $\Delta\sigma$ for model stress–time curves at $K=M$. a) $\dot{\varepsilon}_a=0.07\dot{\varepsilon}_2$; b) $0.5\dot{\varepsilon}_2$.

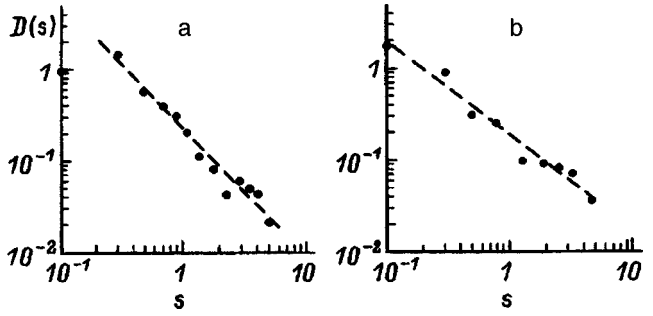

FIG. 9. Probability density functions $D(s)$ of the normalized depth of the deforming-stress spikes (drops) for a polycrystalline sample deformed at $T=-20$ °C and $\dot{\varepsilon}_a=8.4\times10^{-5}$ s^{-1} (a) and for a single crystal deformed at $T=120$ °C and $\dot{\varepsilon}_a=1.3\times10^{-5}$ s^{-1} (b). The dashed lines correspond to the exponent α in the power law $D(s)\sim s^{\alpha}$: a) $\alpha\approx-1.4$; b) $\alpha\approx-1.0$.

$\dot{\varepsilon}_a$ is varied, goes over to one of the above types. This situation is best observed in single crystals (Fig. 9b). An analogous phenomenon is observed in the model with careful selection of the parameters near the localization–propagation transition point. The power-law nature of the distributions in this case is attributable to the emergence of localized deformation bands of any widths allowed in the system. We have previously[14] discussed the analogy of this behavior with avalanche-type earthquake processes used recently as a paradigm of the self-organized criticality phenomenon.[12]

The given examples indicate that the proposed model correctly describes the dynamic and statistical properties of the PLC effect. It can be assumed on the basis of an analysis of the behavior of the model that the evolution of the dynamics of the effect is attributable to competition between two processes. The finite coupling between elements of a deformed crystal stipulates a finite time for equalization of the plastic flow rate throughout the sample, when all of its elements are deformed at the rate $\dot{\varepsilon}_i<\dot{\varepsilon}_1$ corresponding to the left branch of the $F(\dot{\varepsilon})$ curve. On the other hand, the dwell time of a point of the phase trajectory of any one element on this branch depends on the applied strain rate $\dot{\varepsilon}_a$. For large $\dot{\varepsilon}_a$ the homogenization process is not very efficient, and a nonuniformly shifting $\dot{\varepsilon}$ profile (type A) occurs in the crystal. At low rates $\dot{\varepsilon}_a$ neighboring elements are in nearly the same state, so that the cutoff of one of them is capable of initiating an avalanche-type process, which is halted by unloading of the sample. The $\dot{\varepsilon}$ gradient created in this case induces the next such event in the adjacent region of the crystal, i.e., the relay propagation of deformation bands (type B) takes place. But if $\dot{\varepsilon}_a$ is so low that the $\dot{\varepsilon}$ gradient preserved at the instant of attainment of conditions for the next spike is smaller than the level of fluctuations of $\dot{\varepsilon}$, which always occur in a crystal and are associated with fluctuations of the density and velocity of mobile dislocations, slip bands emerge in random locations (type C). When the correlation of deformation in the crystal is suppressed, the pattern described here becomes less regular: the type A at a high strain rate is superseded by curves in the form of noise, and at a low strain rate the macroscopically smooth plastic flow be-

tween deep drops also becomes jerky, with much smaller-scale spikes.

In summary, these investigations justify the assumption that the totality of the prominent features of unstable plastic flow in the presence of the Portevin–Le Châtelier effect can be explained in terms of a single mechanism in the example of the dynamics of a system whose temporal properties follow from the nonlinearity of the strain-rate sensitivity of its flow resistance, while the spatial behavior is determined by mesoscopic-scale inhomogeneity associated with the localization of deformation in slip lines and bands. The investigated influence of temperature on the macroscopic characteristics, statistics, and dynamics of the effect is attributed to the temperature dependence of the strain-rate sensitivity function and the degree of correlation of the deformation processes in the inhomogeneously deformed crystal.

The authors are indebted to V. Ya. Kravchenko for interest and valuable comments, and also to A. P. Ivanov for technical assistance.

This work has received partial support from the Russian Fund for Fundamental Research (Grant No. 96-02-17482) and the International Science Foundation (ISF Grant No. NKV300).

[1] L. P. Kubin, in *Materials Science and Technology: A Comprehensive Treatment*, Vol. 6, edited by R. W. Cahn, P. Haase, and E. J. Kramer (VCH, Weinheim, 1993), p. 138.
[2] G. A. Malygin, Fiz. Tverd. Tela (St. Petersburg) **37**, 3 (1995) [Phys. Solid State **37**, 1 (1995)].
[3] L. P. Kubin and Y. Estrin, in *Continuum Models for Materials with Microstructure*, edited by H.-B. Muhlhaus (Wiley, New York, 1995), p. 395.
[4] P. Rodriguez and S. Venkadesan, Solid State Phenom. **42–43**, 257 (1995).
[5] M. A. Lebyodkin, Y. Bréchet, Y. Estrin, and L. P. Kubin, Phys. Rev. Lett. **74**, 4748 (1995).
[6] M. A. Lebyodkin, Y. Bréchet, Y. Estrin, and L. P. Kubin, Solid State Phenom. **42–43**, 313 (1995).
[7] M. A. Lebyodkin, Y. Estrin, Y. Bréchet, and L. P. Kubin, Acta Metall. Mater. **44**, 4531 (1996).
[8] P. Penning, Acta Metall. **20**, 1169 (1972).
[9] L. P. Kubin and Y. Estrin, Acta Metall. Mater. **38**, 697 (1990).
[10] A. A. Andronov, A. A. Vitt, and S. É. Khaĭkin, *Theory of Oscillations*, 2nd ed. (Pergamon Process, Oxford; Addison-Wesley, Reading, Mass., 1966; Fizmatgiz, Moscow, 1959), Chaps. 4 and 9.
[11] G. Ananthakrishna, C. Fressengeas, M. Grosbras *et al.*, Scr. Metall. **32**, 1731 (1995).
[12] P. Bak, C. Tank, and K. Wiesenfeld, Phys. Rev. A **38**, 364 (1988).
[13] E. Pink and A. Grinberg, Acta Metall. **30**, 2153 (1982).
[14] M. A. Lebedkin and L. R. Dunin-Barkovskiĭ, Zh. Éksp. Teor. Fiz. [JETP] (in press).
[15] P. Hähner, Mater. Sci. Eng., A **164**, 23 (1993).
[16] A. H. Cottrell and B. A. Bilby, Proc. R. Soc. London, Ser. A **62**, 46 (1949).
[17] L. P. Kubin, K. Chibab, and Y. Estrin, Acta Metall. **36**, 2707 (1988).
[18] M. A. Lebyodkin, L. Dunin-Barkowskii, Y. Bréchet, L. P. Kubin, and Y. Estrin, in *Eleventh International Conference on Strength of Materials (ICSMA-11)* (Prague, 1997).

Translated by James S. Wood

Microhardness of the compounds La_2CuO_4 and $La_{1.85}Sr_{0.15}CuO_4$ at temperatures from 81 to 292 K

L. S. Fomenko and S. V. Lubenets

Physicotechnical Institute of Low Temperatures, National Academy of Sciences of Ukraine, 310164 Kharkov, Ukraine

V. S. Bobrov and A. N. Izotov

Institute of Solid-State Physics, Russian Academy of Sciences, 142432 Chernogolovka, Moscow District, Russia

(Submitted August 12, 1997)
Fiz. Tverd. Tela (St. Petersburg) **40**, 493–497 (March 1998)

The microhardness of La_2CuO_4 and $La_{1.85}Sr_{0.15}CuO_4$ crystals is measured in the temperature range 81–292 K, and the influence of various factors on it is investigated. The thermal activation parameters of the plastic deformation process in the vicinity of the indenter impression are estimated. The change of the phase state of the compound $La_{1.85}Sr_{0.15}CuO_4$ at the temperature $T_0=180$ K and the appearance of domain (twin) boundaries formed in the ferroelastic tetra-ortho transition are not seen in the temperature dependence of the microhardness. The results of the study are compared with previously published results for YBa_2CuO_{7-x} crystals. © *1998 American Institute of Physics.* [S1063-7834(98)01903-0]

The objective of the present study is to investigate the micromechanical properties of La_2CuO_4 (LCO) and $La_{1.85}Sr_{0.15}CuO_4$ (LSCO) single crystals in the temperature range 81–292 K. These crystals are typical metal-oxide compounds with a perovskite-type structure. Their investigation is of interest from the standpoint of the high-temperature (high-T_c) superconductivity problem.

Although the high-T_c superconductivity phenomenon was discovered on the lanthanum compound La-Ba-Cu-O ($T_c<40$ K), the plastic and strength characteristics of high-T_c superconducting systems based on lanthanum oxide have scarcely been studied at all. A greater potential for superconductivity was discovered soon afterwards in superconductors based on yttrium and bismuth oxides, which have a substantially higher superconducting transition temperature. The mechanical properties of these materials are the subject of intense study by various methods on single crystals and polycrystalline objects prepared by various technologies, and they span a broad range of temperatures and compositions.[1–16]

The compounds LCO and LSCO undergo a soft-mode tetra→ortho (TO) structural phase transition at temperatures of 530 K and 180 K, respectively.[17] In the temperature range 81–292 K LCO crystals have an orthorhombic lattice, and LSCO has tetragonal and orthorhombic sublattices, setting the stage for investigating the influence of lattice transition on the temperature dependence of the microhardness. The first microhardness measurements of LCO and LSCO at room temperature are reported in Refs. 18 (single crystals) and 19 (ceramics). The results of the measurements reported below are compared with data obtained previously for $YBa_2Cu_3O_{7-x}$ (YBCO) crystals.

1. EXPERIMENTAL PROCEDURE

Single crystals of LCO and LSCO were grown by the method described in Refs. 20 and 21. The As-grown LCO crystals were in the shape of oblique-angled prisms with approximate dimensions $4\times4\times2$ mm and habit planes (001) and {111}, or they were grown as wafers of thickness ~1.5 mm with dimensions $\sim6\times4$ mm in the (001) basal plane. Only the habit plane (110) was clearly defined in the LSCO crystals. The LSCO crystals entered the superconducting state at $T_c\approx25$ K.

The indentation procedure was the same as that described in Ref. 4. The Vickers microhardness was determined from the equation

$$H_V=1.1854P/(2a)^2,$$

where $2a$ is the length of the diagonal of the indenter impression. The load P on the indenter varied in the interval 0.05–1 N. At least ten indentations were made on the sample surface at each temperature. The average values of H_V are given here; the error of their determination was at most 1–2%. The temperature dependence of the microhardness was measured on one sample. The defect structure of the as-grown and indented samples was investigated by means of a metallographic microscope in normal and polarized light. The linear dimensions of the indentations were measured with a PMT-3 hardness-gauging microscope.

2. RESULTS AND DISCUSSION

2.1. Domain structure of LCO crystals and its rearrangement under the influence of mechanical stresses

The as-grown LCO crystals have a domain structure which, viewed in polarized light in the (001) plane, appears as a system of alternating light and dark bands (domains) of

 © 1998 American Institute of Physics

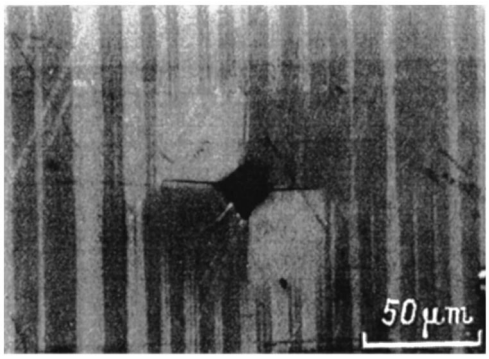

FIG. 1. Domain structure of a La_2CuO_4 crystal, observed in polarized light in the vicinity of the indenter impression. Indentation plane (001), load $P=1.5$ N, $T=292$ K. The light and dark regions are different orientation states existing in twin positions relative to each other.

width $\sim 5-20$ μm parallel to the $\langle 100\rangle$ direction. The coloration of the domains can reverse itself when the position of the analyzer is changed. Occasionally two systems of domains with mutually perpendicular boundaries can be observed.

The as-grown polydomain structure is transformed under the application of a concentrated force (Fig. 1). The direction of motion of the domain boundaries leading to growth of the light or dark domains is determined by the sign of the stresses present near the indenter impression (see the diagram in Fig. 3 of Ref. 2). As a result, the dark domains broaden and absorb the light bands in the first and third quadrants. The opposite effect is observed in the other two quadrants: broadening of the light bands and their absorption of the dark bands. This local conversion to a single-domain state encompasses a small region in the vicinity of the indentation, as seen in Fig. 1.

The transformation of the domain structure takes place within a time of the order of a minute, showing that the boundaries in LCO must be highly mobile even at room temperature. We note that the domain boundaries in YBCO crystals have a much lower mobility: The boundaries of the narrow domain shift at room temperature for a whole day, and loading up to 350–420 K is required to stimulate motion of the boundaries of the wide domains.[2] The motion of the domain (twin) boundaries in YBCO is monitored by the diffusive motion of oxygen atoms[22] and in LCO by the reorientation of the CuO_6 octahedra.[23] The higher mobility of the twin boundaries in LCO implies that the activation energy associated with reorientation of the CuO_6 octahedra is lower than the activation energy of oxygen diffusion, approximately 1 eV, in YBCO.[24,25]

The presence of domains in LCO crystals and their structural transformation under mechanical stresses lead to the classification of these crystals as ferroelastics.[29] The change in the point group $4/mmm$ to mmm in the TO structural phase transition corresponds to one of the 52 types of pure ferroelastic transitions.[30]

The number of such domains partitioning the crystal in transition to the ferroelastic state is determined by the ratio of the order of the point groups of the as-grown and ferroelastic phases,[31] and the geometry of the domain structure formed in the ferroelastic phase transition can be predicted from the condition of minimum elastic energy of the sample.[32] In the $4/mmm \rightarrow mmm$ transition four orientation states are possible in the ferroelastic phase.[31] Two systems of domains can be distinguished here. The domains belonging to one system are in twin positions relative to each other, and the boundary between them has on the (001) plane a direction close to $\langle 100\rangle$ (Ref. 33); the domain boundaries associated with different systems are mutually perpendicular. Our experimental observations of the number, shape, and relative positioning of the domains in LCO fit the above pattern.

It has been shown[34] that the twin boundaries in YBCO create fairly strong barriers to the motion of slip dislocations. However, we have not detected any appreciable variation in the microhardness during the TO transition, which results in the formation of domain structure, either in LSCO crystals as the temperature is lowered or in YBCO crystals as the oxygen concentration is varied.[6] The value of the microhardness is also identical for twinned and untwinned YBCO crystals.[35] Consequently, the twin (domain) structure of high-T_c superconducting oxides obviously has little influence on the resistance to plastic deformation in indentation.

We now consider the influence of other factors on the micromechanical characteristics of the crystals: the indenter load, the anisotropy of the crystal, doping, temperature, and the TO phase transition.

2.2. Influence of the load

For LCO crystals at room temperature we have obtained detailed plots of the length of the indentation diagonal and the length of a radial crack as functions of the indenter load. The linearity of the relation between the quantities $(2a)^2$ and P, indicating constancy of the high-T_c, is preserved for loads $P \leqslant 0.50$ N. At $P \geqslant 0.70$ N we observe a deviation from linearity toward higher indentation diameters, most likely attributable to the accompanying crack formation. This influence of the load on the microhardness of LCO and LSCO crystals has been observed previously.[18] The threshold load above which a visible indentation is left on the crystal surface is close to zero, whereas the threshold for the YBCO crystals investigated in Ref. 3 is approximately 0.01–0.02 N.

The dependence of the length l of the radial crack on the load is well described by the relation $l^{3/2} \sim P$ over the entire load range. The critical stress intensity coefficient (fracture toughness), calculated from the equation[36]

$$K_{1c} = 0.1P/l^{3/2},$$

is found to be equal to 0.96 MPa/m$^{1/2}$. This value is close to one obtained earlier for YBCO (Refs. 1, 3, and 5) and is several times higher than for bismuth-containing high-T_c superconductors.[11,12]

2.3. Microhardness anisotropy

The microhardness of an LCO crystal was measured on the two habit planes (001) and {111} with two positions of the indenter diagonal: aligned with the $\langle 100\rangle$ direction and at

TABLE I. Microhardness of La_2CO_4 crystals for different indentation planes and orientations of the indenter diagonal ($T=292$ K).

Microhardness H_V, GPa	Indentation plane	Orientation of the indenter diagonal
7.44	(001)	⟨110⟩
8.05	(001)	45° from ⟨110⟩
8.24	{111}	⟨110⟩
6.87	{111}	45° from ⟨110⟩

a 45° angle with the ⟨100⟩ direction. The values obtained for H_B are given in Table I. We see that anisotropy of the first kind (the influence of the direction of the indenter diagonal relative to the crystallographic direction in the selected plane on the measured value of H_V, Ref. 37) in LCO crystals is more pronounced than anisotropy of the second kind (the dependence of H_V on the plane of indentation). The anisotropy is more pronounced on the {111} plane, where the measured values of H_V have a spread of approximately 20%, while on the (001) plane this difference does not exceed 8.2%.

Anisotropy of the first kind of the same sign has been observed previously in orthorhombic YBCO crystals,[2] where the ratio $(H_V^{\langle 100\rangle}-H_V^{\langle 110\rangle}/H_V^{\langle 110\rangle}$ in oxygen-saturated crystals attained 50–80%. Anisotropy of the second kind [indentation of the habit planes (100) and (001)] is characterized by values of the ratio $H_V^{(100)}/H_V^{(001)}$ approximately equal to 1.8 for the tetragonal phase of YBCO and to 1.2 for the orthorhombic phase.[38] The latter value is close to our own for orthorhombic LCO crystals with indentation of the (001) and {111} planes.

The microhardness anisotropy occurring in LCO, YBCO (Refs. 2 and 38), and Bi2212 (Ref. 12) crystals is obviously associated with anisotropy of the evolution of plastic shears in these crystals.

2.4. Influence of doping

The replacement of some of the lanthanum atoms by strontium atoms increases the microhardness considerably, by ~20%. This result is not fully consistent with the data of Ref. 19. Although the authors of Ref. 19 acknowledge the hardening effect of doping, they obtained a higher microhardness for LCO ($H_V=9.24$ GPa) than for LSCO ($H_V=8.94$ GPa). This conflict could be attributable to the fact that their ceramic LCO samples had a much smaller grain size than LSCO, and an increase in the grain size, according to Ref. 19, tends to soften the ceramic.

Linear growth of the microhardness with increasing Li and Zn concentration has been observed previously on doped YBCO crystals[39] and was attributed to the dominant role of solid-state hardening. The same cause can account for the increase in the microhardness in doping of our investigated crystals.

2.5. Influence of temperature

It is evident from Fig. 2 that the microhardness of LCO and LSCO crystals, like the YBCO crystals investigated in Refs. 4–6, increases linearly as the temperature is lowered. The relative increase in the microhardness as the temperature is varied from 292 K to 81 K is 37% for LCO crystals and 22% for LSCO crystals. The slopes of the $H_V(T)$ curves are close for LCO and YBCO crystals ($x=0.1$).[6] The microhardness of oxygen-deficient YBCO crystals ($x\geqslant 0.4$) is more sensitive to temperature. The strontium doping of LCO crystals weakens the functional dependence $H_V(T)$.

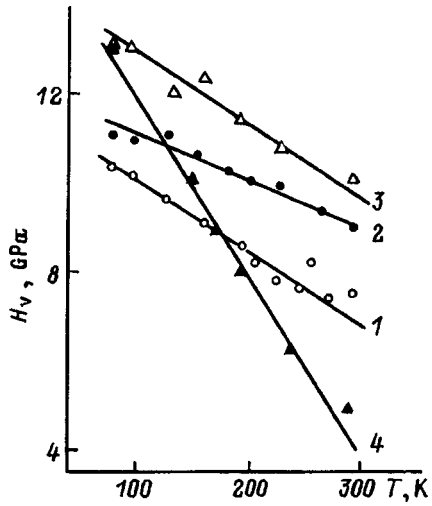

FIG. 2. Microhardness versus temperature for La_2CuO_4 (*1*) and $La_{1.85}Sr_{0.15}CuO_4$ (*2*) crystals with indentation on the (001) plane. Load $P=0.35$ N, indenter diagonal aligned parallel to the ⟨100⟩ direction. Data on the microhardness of $YBa_2Cu_3O_{7-x}$ crystals[6] are shown for comparison: *3*) $x=0.1$; *4*) $x=0.9$.

The dependence $H_V(T)$ of LCO and LSCO crystals is considerably stronger than the temperature dependence of the elastic constants,[27,40] indicating the thermally activated character of microplastic deformation. To estimate the thermal activation parameters of the plastic deformation process near the indenter impression, we use an approximate relation for the temperature dependence of the microhardness in the form given in Refs. 4, 37, and 41:

$$H_V=(U_0-kT)\beta \ln m/\gamma,$$

where U_0 is the activation energy of the deformation process at zero external stress (height of the potential barrier), γ is the activation volume, $\beta=6$ is a factor that incorporates the Schmid factor and the proportionality factor between the microhardness and the yield point, and m is the ratio of the preexponential factor in the Arrhenius equation to the rate of plastic deformation, $\ln m=20$ (Ref. 4). The resulting estimates are given in Table II.

A comparison of the data in Table II for metal oxides of the YBCO and LSCO families and crystals of elemental Ge and Si semiconductors[4,41] leads to the assumption that the plastic deformation mechanisms of these crystals are of a common nature. The most probable candidates are the generation and motion of dislocations in the Peierls relief.

2.6. Influence of the tetra–ortho transition

It is evident from Fig. 2 that the temperature dependence of the microhardness of LSCO crystals is devoid of distinc-

TABLE II. Parameters of the experimental $H_V(T)$ curves and thermal activation parameters of the Arrhenius equations for La_2CuO_4, $La_{2-x}Sr_xCuO_4$, $YBa_2Cu_3O_{7-x}$ (Ref. 6) and Ge (Ref. 41) crystals.

Crystal	Oxygen or strontium concentration x	Parameters of $H_V(T)$ H_V, GPa		Thermal activation parameters		
		292 K	0 K	$\delta H_V/\delta T$, 10^{-2} GPa/K	U_0, eV	$\gamma\cdot 10^{24}$, cm^3
La_2CuO_4		6.9	11.8	1.6	1.27	103.5
$La_{2-x}Sr_xCuO_4$	0.15	9.0	12.2	1.1	1.9	150.5
$YBA_2Cu_3O_{7-x}$	0.1	9.9	14.65	1.6	1.57	103.5
$YBA_2Cu_3O_{7-x}$	0.3					
$YBa_2Cu_3O_{7-x}$	0.4	5.3	17.1	4	0.73	41.4
$YBa_2Cu_3O_{7-x}$	0.9	4	16.45	4.25	0.66	39.0
Ce ($T=550$ K)		7.5	19	4	1.5	80

Note: The values of H_V ($T=0$ K) are the results of extrapolation of the experimental curves. For Ge the linearity of $H_V(T)$ disappears at $T<550$ K.

tive features in the vicinity of the structural phase transition ($T_0\approx 180$ K). A change in the phase state of the YBCO crystal due to a change in the oxygen concentration (TO transition) takes place at $x_c\approx 0.6$ (Ref. 6).

We now consider the possible causes of this behavior of the microhardness in the case of LSCO crystals. The plastic deformation characteristics in the phase transition must first and foremost be compatible with the variation of the elastic properties of the crystal. The elastic constants of the compound LSCO in the vicinity of the phase transition temperature have been investigated in detail in several theoretical[17,42] and experimental[27,43] papers. A symmetry analysis of the $I4/mmm\rightarrow Cmca$ transition in Ref. 17 enabled the authors to calculate the relative jumps of the elastic constants from the values of the lattice parameters. The absolute values of the constants and their variation in phase transition have been measured experimentally on $La_{2-x}Sr_xCuO_4$ crystals for $x=0.13$ (Ref. 27 and $x=0.14$ (Ref. 43). One important conclusion is that C_{44} remains essentially unchanged in the soft-mode TO transition, whereas other constants decrease considerably; the constant C_{66}, in particular, decreases more than 50% (Ref. 27).

Crystals of the LSCO family, like those in the YBCO family, are characterized by two deformation modes: twinning and slip. The literature contains no information on the twinning of the tetragonal modification of LSCO. However, it follows from the preceding discussion that twinning takes place with extreme facility in the orthorhombic phase via two systems: $(110)[1\bar{1}0]$ and $(1\bar{1}0)[110]$. In view of the small twinning shear the twinning fraction in plastic deformation of LSCO crystals is small, not exceeding 1.7%, after complete retwinning of the entire sample. Consequently, the large strains encountered near the indenter impression, amounting to $\sim 7\%$, are mainly attributable to slip.

The types and structure of dislocations in LSCO have not been studied to date, nor have the slip systems been determined; only the observation of growth dislocations of extremely low density has been reported.[28] We can assume by analogy with YBCO that the basal (110) plane is the slip plane in LSCO crystals, and the Burgers vector is in the $\langle 100\rangle$ direction. This means that the elastic properties and mobility of the dislocations determine the elastic constant C_{44}, which, as mentioned above, remains essentially invariant in the TO structural transition. Obviously, the slip systems and structure of the dislocations and, accordingly, the microhardness remain constant as well.

The authors are indebted to V. D. Natsik for support and discussion of the manuscript.

This work has received financial support from the State Committee of Ukraine on Problems of Science, Technology, and Industrial Policy (Project 0.9.01.01/033-92 ''Material'') and from the State Scientific–Technical Program for High-T_c Superconductivity ''Relok.''

[1] R. F. Cook, T. R. Dinger, and D. R. Clarke, Appl. Phys. Lett. **51**, 454 (1987).
[2] V. S. Bobrov, V. K. Vlasko-Vlasov, G. A. Emel'chenko, M. V. Indenbom, M. A. Lebedev, Yu. A. Osip'yan, V. A. Tatarchenko, and B. Ya. Farber, Fiz. Tverd. Tela (Leningrad) **31**, 93 (1989) [Sov. Phys. Solid State **31**, 597 (1989)].
[3] V. V. Demirskiĭ, H. J. Kaufmann, S. V. Lubenets, V. D. Natsik, and L. S. Fomenko, Fiz. Tverd. Tela (Leningrad) **31**, 263 (1989) [Sov. Phys. Solid State **31**, 1065 (1989)].
[4] B. Ya. Farber, N. S. Sidorov, V. I. Kulakov, Yu. A. Iunin, A. N. Izotov, G. A. Emel'chenko, V. S. Bobrov, L. S. Fomenko, V. D. Natsik, and S. V. Lubenets, Sverkhprovodimost' (KIAE) **4**, 2394 (1991).
[5] S. V. Lubenets, V. D. Natsik, L. S. Fomenko, N. M. Sorin, N. M. Chaĭkovskaya, V. S. Bobrov, A. N. Izotov, and A. A. Zhokhov, Sverkhprovodimost' (KIAE) **6**, 1406 (1993).
[6] S. V. Lubenets, V. D. Natsik, L. S. Fomenko, V. S. Bobrov, and A. N. Izotov, Fiz. Nizk. Temp. **21**, 324 (1995) [Low Temp. Phys. **21**, 247 (1995)].
[7] N. N. Peschanskaya, B. I. Smirnov, V. V. Shpeĭzman, and P. N. Yakushev, Fiz. Tverd. Tela (Leningrad) **30**, 3503 (1988) [Sov. Phys. Solid State **30**, 2014 (1988)].
[8] N. N. Peschanskaya, B. I. Smirnov, Yu. P. Stepanov, V. V. Shpeĭzman, and P. N. Yakushev, Fiz. Tverd. Tela (Leningrad) **31**, 271 (1989) [Sov. Phys. Solid State **31**, 703 (1989)].
[9] N. N. Peschanskaya, B. I. Smirnov, and V. V. Shpeĭzman, Fiz. Tverd. Tela (Leningrad) **31**, 292 (1989) [Sov. Phys. Solid State **31**, 1446 (1989)].
[10] V. V. Shpeĭzman, B. I. Smirnov, N. N. Peschanskaya, and L. K. Markov, Fiz. Tverd. Tela (Leningrad) **33**, 2198 (1991) [Sov. Phys. Solid State **33**, 1238 (1991)].
[11] S. V. Lubenets, V. D. Natsik, N. M. Sorin, L. S. Fomenko, N. M. Chaĭkovskaya, H. J. Kaufmann, and K. Fischer, Sverkhprovodimost' (KIAE) **3**, 1857 (1990).
[12] J. H. Jia and Q. P. Kong, Phys. Status Solidi A **145**, K51 (1994).
[13] M. Muralidhar, K. Narasimha Reddy, and V. Hari Badu, Phys. Status Solidi A **126**, 115 (1991).
[14] J. Rabier and M. F. Denanot, J. Less-Common Met. **164–165**, 223 (1990).

[15] M. F. Imaev, F. F. Musin, R. O. Kaĭbyshev, and M. R. Shagiev, Dokl. Akad. Nauk **338**, 184 (1994) [Phys. Dokl. **39**, 639 (1994)].
[16] K. C. Goretta, E. J. Zamirowski, J. M. Calderon-Moreno, D. J. Miller, Nan Chen, T. G. Holesinger, and J. L. Routbort, J. Mater. Res. **9**, 541 (1994).
[17] N. M. Plakida and V. S. Shakhmatov, Sverkhprovodimost' (KIAE) **6**, 669 (1993).
[18] L. S. Fomenko, J.-J. Kaufmann, S. V. Lubenets, V. D. Natsik, T. S. Orlova, N. N. Peschanskaya, V. V. Shpeizmann, and V. I. Smirnov, Acta Univ. Carolinae Math. Phys. **32**, 131 (1991).
[19] M. Stubičar, M. Tudja, V. Žerjav, N. Stubičar, M. Prester, and N. Brničevic, J. Cryst. Growth **91**, 423 (1988).
[20] V. V. Tatarchenko, G. A. Emelchenko, N. V. Abrosimov, V. A. Borodin, L. Ya. Vinnikov, O. V. Zharikov, A. A. Zhokhov, P. A. Kononovich, V. M. Masalov, I. M. Romanenko, V. V. Ryazanov, and L. I. Chernyshova, Int. J. Mod. Phys. B **3**, 289 (1989).
[21] A. N. Maljuk, A. A. Zhokhov, G. A. Emelchenko, I. I. Zverkova, A. N. Turanov, and V. Sh. Shekhtman, Physica C **214**, 93 (1993).
[22] L. A. Dorosinskiĭ, M. V. Indenbom, V. I. Nikitenko, and B. Ya. Farber, JETP Lett. **49**, 182 (1989).
[23] V. V. Zonikashvili, V. I. Serdobintsev, I. A. Naskidashvili, L. M. Kolesnikova, and N. M. Yastrebova, Fiz. Tverd. Tela (Leningrad) **33**, 2806 (1991) [Sov. Phys. Solid State **33**, 1586 (1991)].
[24] S. J. Rothman, J. L. Routbort, and J. E. Baker, Phys. Rev. B **44**, 2326 (1991).
[25] J. R. Cost and J. T. Stanley, Scr. Metall. Mater. **28**, 773 (1993).
[26] A. Sawada, Y, Nishihata, K. Oka, and H. Unoki, Jpn. J. Appl. Phys. **28**, L1787 (1989).
[27] E. V. Bezuglyĭ, N. G. Burma, I. G. Kolobov, V. D. Fil', I. M. Vitebskiĭ, A. N. Knigavko, N. M. Lavrinenko, S. N. Barilo, D. I. Zhigunov, and L. E. Soshnikov, Fiz. Nizk. Temp. **21**, 86 (1995) [Low Temp. Phys. **21**, 65 (1995)].
[28] V. A. Goncharov, Yu. A. Osip'yan, É. V. Suvorov, and A. A. Sergeev, Izv. Ross. Akad. Nauk, Ser. Fiz. **59**, 133 (1995).
[29] L. A. Shuvalov, Izv. Akad. Nauk Ser. Fiz. **43**, 1554 (1979).
[30] K. Aizu, J. Phys. Soc. Jpn. **27**, 387 (1969).
[31] K. Aizu, Phys. Rev. B **2**, 754 (1970).
[32] A. L. Roĭtburd, Usp. Fiz. Nauk **113**, 69 (1974) [Sov. Phys. Usp. **17**, (1974)].
[33] J. Sapriel, Phys. Rev. B **12**, 5128 (1975).
[34] J. Rabier and M. F. Denanot, J. Appl. Phys. **65**, 427 (1992).
[35] A. S. Raynes, S. W. Freiman, F. W. Cayle, and D. L. Kaiser, J. Appl. Phys. **70**, 5254 (1991).
[36] G. R. Anstis, P. Chantikul, V. R. Lawn, and D. R. Marshall, J. Am. Ceram. Soc. **64**, 533 (1981).
[37] Yu. S. Boyarskaya, D. Z. Grabko, and M. S. Kats, *Physics of Microindentation Processes* [in Russian] (Kishinev, 1986).
[38] E. Cruceanu, J. Deutz, H. Klein, W. Schmitz, and H. Ullmaier, Mater. Sci. Eng. **169**, L9 (1993).
[39] H. C. Ling and M. F. Yan, J. Appl. Phys. **64**, 1307 (1988).
[40] S. V. Lubenets, V. D. Natsik, and L. S. Fomenko, Fiz. Nizk. Temp. **21**, 475 (1995) [Low Temp. Phys. **21**, 367 (1995)].
[41] V. I. Trefilov, Yu. V. Mil'man, and S. A. Firstov, *Physical Principles of the Strength of Refractory Metals* [in Russian] (Kiev, 1975).
[42] Wu Ting and K. Fossheim, Phys. Rev. B **48**, 16751 (1993).
[43] A. Migliory, J. L. Sarrao, W. M. Visscher, M. William, T. M. Bell, Lei Ming, Z. Fisk, and R. G. Leisure, Physica B **183**, 1 (1993).

Translated by James S. Wood

Softening processes in single-crystal tungsten ribbons

L. N. Pronina, A. A. Mazilkin, and I. M. Aristova

Institute of Solid-State Physics, Russian Academy of Sciences, 142432 Chernogolovka, Moscow District, Russia

(Submitted May 20, 1997; resubmitted September 15, 1997)
Fiz. Tverd. Tela (St. Petersburg) **40**, 498–502 (March 1998)

Recovery processes in rolling-deformed (001)[110] tungsten single crystals having various degrees of purity are investigated. It is shown that the dislocation structure formed in the plastic deformation of tungsten single crystals is transformed in subsequent high-temperature anneals to a system of dislocation subboundaries; only polygonization, which preserves the single-crystal structure, takes place in samples heated to a temperature close to the melting point. The formation of subboundaries proceeds in two stages with subsequent transformation of the unstable structure to a configuration having an energy minimum. The decisive factor affecting the polygonization rate is the stacking fault energy; the presence of impurities also has a significant influence. © *1998 American Institute of Physics.* [S1063-7834(98)02003-6]

We have investigated recovery processes in highly deformed single crystals of refractory body-centered cubic metals in the examples of molybdenum and tungsten.[1–3] We have shown that specially deformed molybdenum single crystals preserve their single-crystal structure in high-temperature anneals. The dislocation recovery in these single crystals takes place in several stages, where a 3-min anneal of molybdenum single crystals at 2000 °C produces a structure of parallel $a[001]$ edge dislocations identical to the structure obtained by a prolonged (2 h) anneal at the same temperature. It is of interest to compare the molybdenum data with data on the behavior of other refractory bcc metals subjected to heating. In this paper we report an investigation of recovery processes in single-crystal tungsten ribbons with various degrees of purity.

1. PROCEDURE

Tungsten single crystals with the growth axis oriented along [110] were grown by electron-beam zone melting with resistance ratios $R_{300\ \mathrm{K}}/R_{4.2\ \mathrm{K}}=RRR=50\,000$ and 200 000. Samples for rolling were cut by spark machining and were then polished mechanically and chemically in NaOH solution. The investigation was carried out on single crystals rolled in the (001) plane and in the [110] direction. The rolled single crystals were subjected to $\sim 80\%$ deformation. The samples were annealed by passing current through them in oilless vacuum, 10^{-8} Torr, at a temperature of 2300 °C. Samples for electron microscopy were prepared by jet electropolishing in 1.5% NaOH solution. The electron-microscope examinations were carried out on JEM-100CX and JEM-2000FX electron microscopes.

2. RESULTS

2.1. Postdeformation structure

We have previously reported[4] a detailed investigation of the structure formed by the rolling deformation of (001)[001] single crystals. It was shown that $a/2\langle 111\rangle$ screw dislocations present in the structure of single crystals with a total reduction $\varepsilon=0.5\%$ form a planar dislocation network as a result of interaction according to the reaction (Fig. 1)

$$a/2[111]+a/2[\overline{1}\,\overline{1}1]=a[011].$$

Increased deformation leads to the development of transverse slip processes as a mechanism for overcoming the resulting $a\langle 001\rangle$ barriers and hence to the formation of a three-dimensional (bulk) dislocation network.

As a result of rolling with reductions up to $\varepsilon=80\%$, the (001)[110] tungsten samples preserve the single-crystal structure of the as-grown orientation with a uniform distribution of dislocations (Fig. 2). Such a structure is characteristic of deformed single crystals of refractory bcc metals of the given orientation in connection with the influence of the longitudinal slip systems (101)[111], (101)[1 11], (011)[111], and (011)[1 11].

2.2. Anneal-induced structure

As a result of high-temperature anneal, the dislocation structure formed in (001)[110] tungsten single crystals in rolling is transformed into a system of dislocation subboundaries, which differ in structure and composition, the material retaining its single-crystal character and its as-grown orientation.

The heating of rolled tungsten single crystals with a resistance ratio of 50 000 to 2300 °C in just 10 s causes subboundaries to form in them. Some of the subboundaries are dislocation networks. Two types of network are observed: 1) a hexagonal network consisting of two families of $a/2\langle 111\rangle$ dislocations, at whose points of intersection are formed dislocations with Burgers vectors $a[001]$ (Fig. 3); 2) a network formed at the intersection of two families of dislocations with $b=a\langle 100\rangle$. One would expect $a\langle 110\rangle$ dislocations to be formed at their points of intersection, but inasmuch as dislocations with such a Burgers vector are unstable

 © 1998 American Institute of Physics

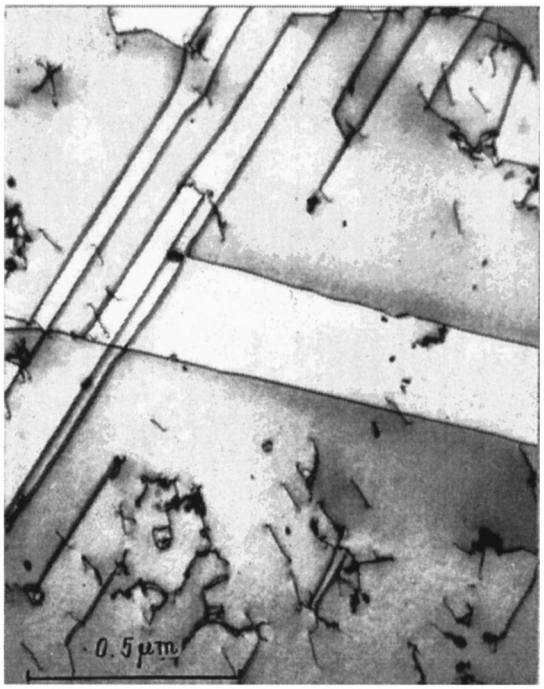

FIG. 1. Structure of a slightly deformed tungsten single crystal ($\varepsilon = 0.5\%$).

in a bcc structure, a bundle of four ternary nodes is formed, where one of the dislocations at each site is $a\langle 100\rangle$, and the other two are $a/2\langle 111\rangle$ (Fig. 4).

The dislocations constituting these networks have an edge or mixed orientation, and the networks themselves are mixed-type subboundaries.

Another type of subboundary is also observed in the structure (Fig. 5). An analysis of the behavior of the diffraction contrast at the dislocations forming the subboundary leads to the conclusion that these dislocations are the edge type with Burgers vector $a[001]$, and the subboundary represents a vertical wall of edge dislocations, which is a tilt boundary. The dislocation lines extend in a direction that coincides with the rolling direction [110].

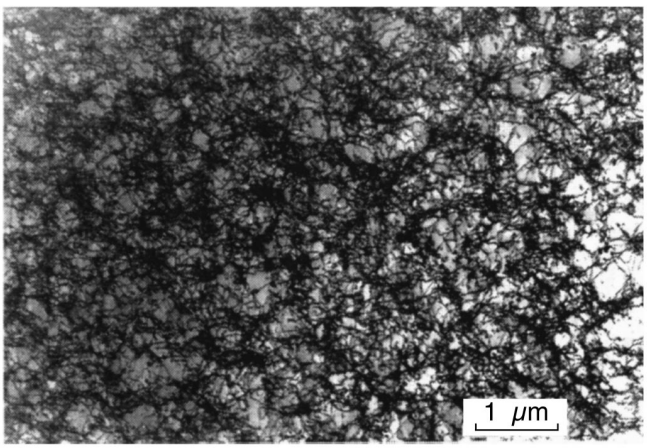

FIG. 2. Structure of a single crystal rolled to full 80% reduction.

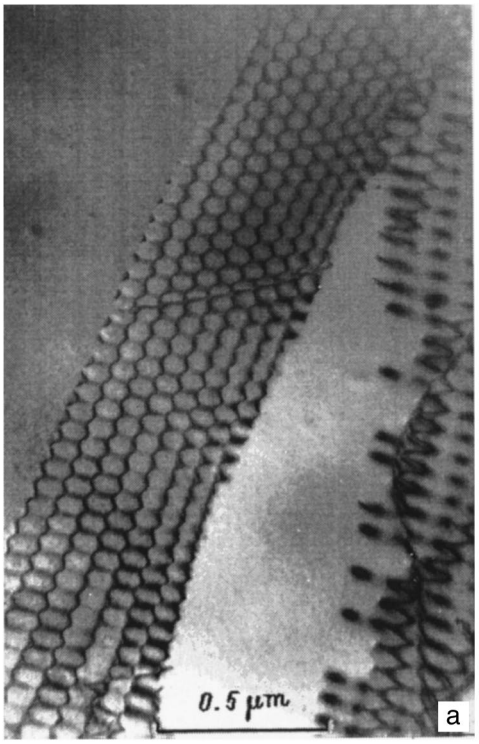

FIG. 3. a) Hexagonal network in tungsten after rolling and annealing, $RRR = 50\,000$, 2300 °C, 10 s; b) schematic diagram of a subboundary with analysis of the dislocation Burgers vectors: $b_1 = a[001]$, $b_2 = a/2[\overline{1}11]$, $b_3 = a/2[111]$.

After a 60-s anneal the structure consists predominantly of walls of long $a[001]$ edge dislocations, and it is essentially devoid of dislocation networks.

An investigation of the structure of tungsten single crystals with a ratio $RRR = 200\,000$ has shown that tilt subboundaries are formed in them even in the briefest (no more than 3 s) anneals. They consist of long, parallel $a[001]$ edge dislocations and are identical to those observed in single crystals with $RRR = 50\,000$ (Fig. 6). There is no dislocation network-forming stage.

3. DISCUSSION OF THE RESULTS

The evolution of structure in tungsten single crystals includes a dislocation network-forming stage. The stability of dislocation boundaries is known to be associated with the stress fields created by them. Previous calculations[5] show

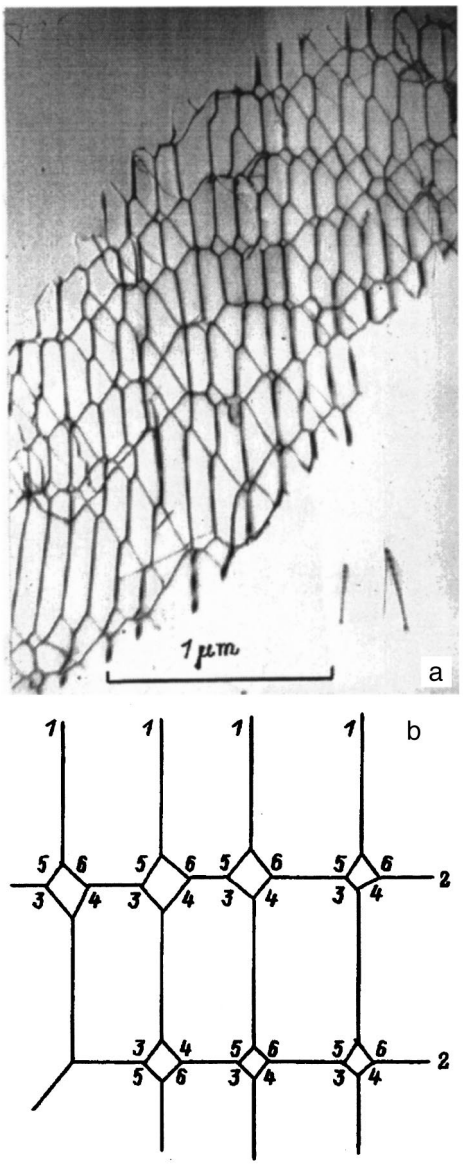

FIG. 4. a) Dislocation subboundary in tungsten after rolling and annealing, containing bundles of four ternary nodes, $RRR = 50\,000$, 2300 °C, 10 s; b) schematic diagram of a subboundary with analysis of the dislocation Burgers vectors: $b_1 = a[001]$, $b_2 = a[100]$, $b_3 = a/2[\bar{1}11]$, $b_4 = a/2[1\bar{1}1]$, $b_5 = a/2[111]$, $b_6 = a/2[11\bar{1}]$.

that edge-dislocation walls, representing tilt boundaries, or networks of pure screw dislocations, which are twist boundaries, can be stable dislocation boundaries, because long-range stress fields do not exist in them. According to the same calculations, networks formed by the anneal of tungsten single crystals are nonequilibrium structures (they do not have an energy minimum) because their constituent dislocations have a large edge component, and as the anneal time is increased, they are transformed into a configuration with an energy minimum: walls of edge dislocations.

The rearrangement of the dislocation structure in connection with polygonization entails slip in the shear plane, the climb of edge components into adjacent planes, and the cross slip of screw components. The rate of the whole process is obviously limited by climb, i.e., the influx of vacancies to dislocations or the emergence of new vacancies at dislocations. Vacancies attach most easily to dislocations (or are newly formed) on steps. A high density of steps at dislocations therefore facilitates the polygonization process.

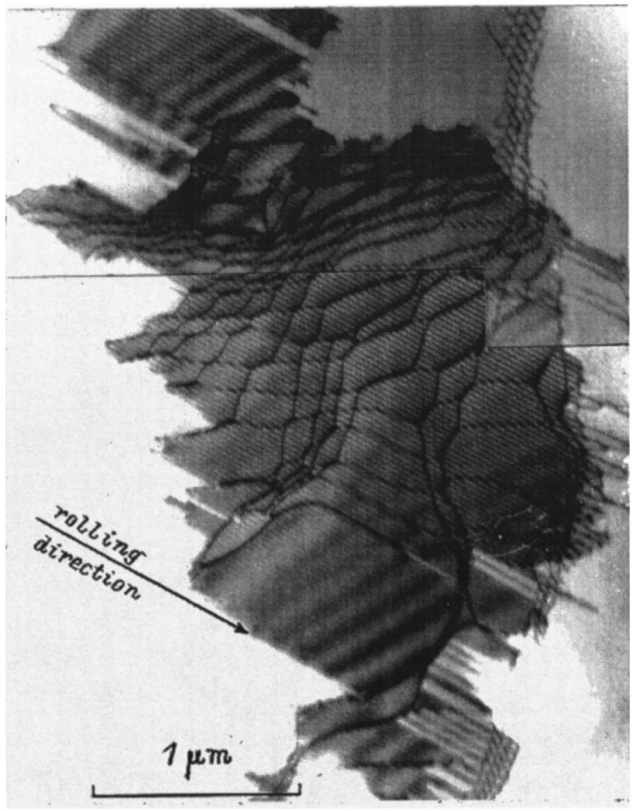

FIG. 5. Tilt subboundary in tungsten after rolling and annealing, $RRR = 50\,000$, 2300 °C, 10 s.

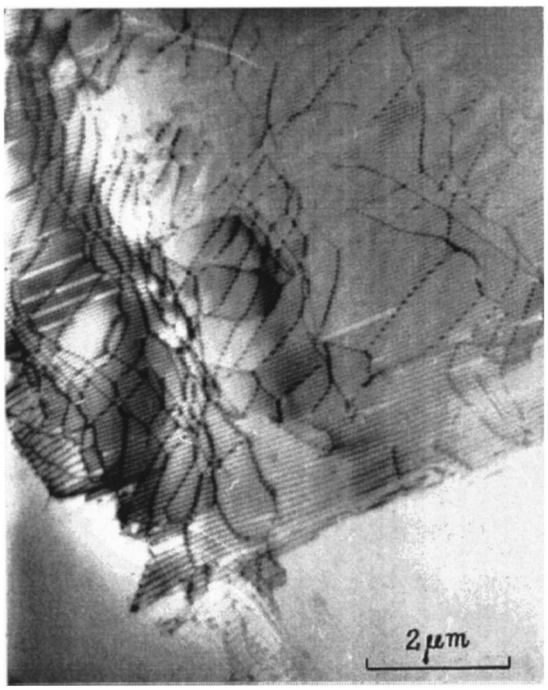

FIG. 6. Tilt subboundary in tungsten after rolling and annealing, $RRR = 200\,000$, 2300 °C, ~3 s.

TABLE I. Self-diffusion activation energy Q_f+Q_m and stacking fault energy of refractory bcc metals.

Metal	Q_f+Q_m, kJ/mol	γ, erg/cm^2
Nb	397.7	150
Mo	464.7	430
W	641	500

Since climb is a thermally activated process,[6] the rate of polygonization v_p can be determined from the expression

$$v_p \sim \exp(-Q_p/kT), \tag{1}$$

where $Q_p=Q_j+Q_f+Q_m$ is the polygonization activation energy. In the latter expression Q_j is the activation energy of step formation, Q_f is the activation of vacancy formation, and Q_m is the activation energy of vacancy migration. The sum Q_f+Q_m is equal to the self-diffusion activation energy.

The self-diffusion activation energies for molybdenum, tungsten, and niobium are given in Table I.[7] Also shown in the table are the stacking fault energies γ. The values of γ obtained by different investigators for the same material differ, obviously because of idiosyncrasies of the method of determination, but they have in common the fact that the stacking fault energy increases in the order Nb–Mo–W. The values of γ obtained by Hartley from theoretical calculations[8] are given in the table.

It is instructive to compare the data obtained here with data from investigations of single-crystal molybdenum and niobium ribbons.[1–3] All three materials are characterized by the formation of walls of edge dislocations with Burgers vector $a[001]$. The time for complete polygonization to take place in molybdenum is of the order of 3 min. In niobium dislocation networks are observed together with the walls even after more than two hours of annealing. If only the self-diffusion activation energy is included in the expression for the polygonization rate (1), the polygonization rate should be the highest in niobium and decrease in sequence to molybdenum and then tungsten, but the results contradict this reasoning. Consequently, the activation energy Q_j of step formation plays a decisive role in (1). We know that Q_j is related to the stacking fault energy γ of the material, decreasing as γ increases. The equilibrium density of steps also depends exponentially on the temperature:

$$n_j \sim \exp(-Q_j/kT). \tag{2}$$

The step density decreases for large Q_j; consequently, the number of vacancies formed at them is reduced, and the polygonization rate association with dislocation climb decreases. On the other hand, the stacking fault energy governs the dislocation splitting width. An extended dislocation can slip only in the plane of a stacking fault. The transition from one slip plane to another requires the preliminary contraction of partial dislocations into a whole. This process hinders cross slip and therefore lowers the polygonization rate, especially in the presence of low stacking fault energy.

It is also known that impurities exert a major influence on diffusion processes and polygonization in particular. In the presence of a low-mobility impurity, which has a high binding energy with vacancies, not all the vacancies are capable of moving about freely, and some of them become trapped by impurity atoms. Atmospheres of impurities formed around dislocations hinder their motion and can have the effect of lowering the stacking fault energy. It is also necessary to take into account the role of steps: In the interaction of impurities with steps, which is stronger than with all other dislocations, the steps adsorb impurities and, in so doing, sacrifice their effectiveness as sources and sinks of vacancies, and the climb rate diminishes.[6]

The results of an investigation of the anneal of high-purity tungsten single crystals confirms the well-known strong influence that impurities have on diffusion processes. The impurity atmospheres formed around dislocations hinder their motion, and in single crystals with $RRR=50\,000$ we observe two stages of the polygonization process, whereas in single crystals with a resistance ratio $RRR=200\,000$ an intermediate stage is not established, owing to the higher rate of polygonization.

The authors are deeply grateful to Dr. Prof. G. Gottstein for a profitable discussion and valuable comments, and also for affording the opportunity to perform experiments on the electron microscope at the Institut für Metallkunde und Metallphysik, RWTH, Aachen, Germany.

The authors are also grateful to the Deutsche Forschungsgemeinschaft and to the Russian Fund for Fundamental Research (RFFI Grant 96-02-17536) for financial support.

[1] L. N. Pronina, S. Takeuchi, K Suzuki, and M. Ichihara, Philos. Mag. A **45**, 859 (1982).
[2] L. N. Pronina and I. M. Aristova, Fiz. Tverd. Tela (St. Petersburg) **35**, 2701 (1993) [Phys. Solid State **35**, 1336 (1993)].
[3] L. N. Pronina, M. V. Bayazitova, and A. A. Mazilkin, Fiz. Tverd. Tela (St. Petersburg) **38**, 792 (1996) [Phys. Solid State **38**, 437 (1996)].
[4] L. N. Pronina, I. M. Aristova, and A. A. Mazilkin, Fiz. Tverd. Tela (St. Petersburg) **38**, 800 (1996) [Phys. Solid State **38**, 442 (1996)].
[5] J. C. M. Li, in *Electron Microscopy and Strength of Crystals* (New York, 1963), pp. 713–779.
[6] J. P. Hirth and J. Lothe, *Theory of Dislocations*, McGraw-Hill, New York (1968) [Russ. transl., Atomizdat, Moscow (1972)].
[7] *Diffusion in Solid Metals and Alloys*, edited by H. Mehrer (Springer-Verlag, Berlin-New York, 1990).
[8] C. S. Hartley, Acta Metall. **14**, 1133 (1966).

Translated by James S. Wood

Influence of indentation-forming conditions on the estimation of the photomechanical effect

A. B. Gerasimov, G. D. Chiradze, N. G. Kutivadze, A. P. Bibilashvili, and Z. G. Bokhochadze

Tbilisi State University, 380028 Tbilisi, Georgia
(Submitted July 17, 1997; resubmitted September 26, 1997)
Fiz. Tverd. Tela (St. Petersburg) **40**, 503–504 (March 1998)

The anisotropy, spectral dependence, and time dependence of relaxation of the dimensions of microhardness indentations in silicon are investigated. It is shown that the time and spectral dependences correlate with the density of excited carriers in the (defective and elastically deformed) region in which they are excited, and the anisotropy is determined by various types of deformations of the chemical bonds for different positions of the indenter. © *1998 American Institute of Physics.* [S1063-7834(98)02103-0]

In the measurement of hardness of indentation the ingress of the indenter into the investigated material is accompanied by plastic deformation of the region immediately adjacent to the indentation, and part of the contiguous defect-free region exists in the elastically deformed state.[1,2] When the load is removed, this deformation partially relaxes, but for crystals with a covalent bond, which have a high hardness rating, pronounced brittleness, and low plasticity,[3] the relaxation under ordinary conditions is disregarded. It has been found, however, that to correctly determine the illumination microhardness, i.e., the magnitude of the photomechanical effect,[4] this relaxation must be taken into account.[5]

It has been established for the case of a silicon single crystal that if the load is removed from the illuminated surface, the trace of the indentation (length of the diagonal) is shorter (and, hence, the magnitude of the photomechanical effect is lower) than when the illumination is turned off first, and the load is lifted after a certain time interval. Under equal experimental conditions this difference is greater for small loads and high illumination.[5]

Here we give the results of investigations of the time and spectral dependence and the anisotropy[1)] of the relaxation of microhardness indentation size.

The experiments were performed on the (100) face of dislocation-free, single-crystal n-type Si with a resistivity of 200 $\Omega\cdot$cm. Prior to microhardness measurement the samples were subjected to mechanical and chemical processing and were then subjected to vacuum anneal followed by slow cooldown. The microhardness measurements were performed on a Durimet machine by an indentation technique using a standard tetrahedral Knoop pyramid indenter. The load on the indenter was set equal to 25 g. The illumination had two different spectral compositions: with photon energies greater ($h\nu > \Delta E_g$, regime 1) and smaller ($h\nu < \Delta E_g$, regime 2) than the width of the bandgap of Si. The radiation intensities were chosen so that the magnitudes of the photomechanical effect in both regimes, taking into account elastic recovery of the indentations, would coincide.

The experiments showed that in regime 1, irrespective of the indenter position on the investigated face, the illumination microhardness depends exponentially on the time that the load is maintained on the sample after the cessation of illumination (see Fig. 1a). Control measurements have shown that increasing this dark-loading time of the investigated crystal to the times used in the illumination experiments does not influence the dimensions of the indentation. In addition, it has been found that the relaxation of the indentation dimensions in regime 1 exhibits an anisotropic character (see Table I). The magnitude of the relaxation for the (100) direction is greater than for the (110) direction. It is important to note that the magnitude of the relaxation is always greater in regime 1 than in regime 2, regardless of the indenter position on the investigated face (see Table I). The weakness of the effect in regime 2 (even though relaxation of the indentation dimensions is observed) might conceivably make it impossible to detect any time dependence and anisotropy.

These results can be interpreted on the basis of considerations set forth in Refs. 5, 7, and 8, according to which nonequilibrium carriers excited from the valence band, or so-called antibonding quasiparticles—a free electron in the conduction band and a hole in the valence band—are responsible for the softening of crystals with covalent chemical bonds. A relationship has been shown[5] to exist between the magnitudes of the photomechanical effect and the corresponding densities of antibonding quasiparticles. The relaxation of the indentation decreases with time elapsed after the light is turned off (see Fig. 1a), i.e., the softening of the surface layer relaxes because this layer harbors residual concentrations of antibonding quasiparticles at the energy minima, i.e., repeatedly bending energy bands for electrons and holes (see Fig. 1b). This inhomogeneous bending in the surface layer is caused by the presence of various types of inhomogeneities in the surface layer.[9] After illumination ceases, carriers recombine rapidly in the homogeneous regions of the crystal, and electrons and holes arriving at the corresponding spatially separated minima can recombine by an activation scenario after overcoming the corresponding barrier (see Fig. 1b). This is why softening persists for a certain length of time after the cessation of illumination of

 © 1998 American Institute of Physics

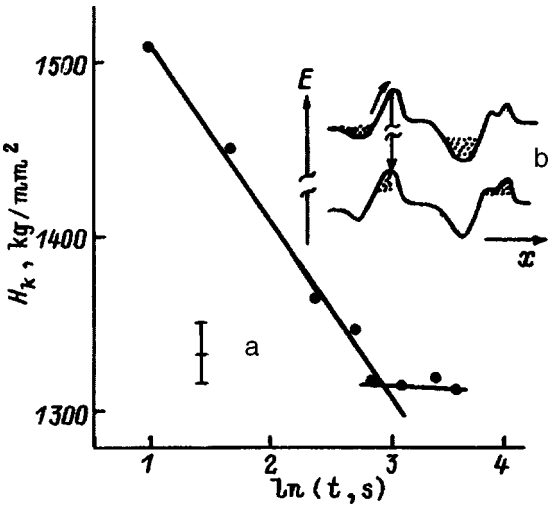

FIG. 1. a) Reduction in the illumination microhardness during the time that the sample remains loaded after the cessation of illumination (in this situation the large diagonal of the Knoop pyramid coincides with the ⟨100⟩ direction); b) recombination transitions in the surface layer of a crystal between bent bands. Here E is the energy, and x is the coordinate along the surface.

the surface layer.[5] The same process explains why, as the load is increased, the magnitude of the relaxation effect decreases and becomes unmeasurable, i.e., at the indentation depth in the crystal to which the inhomogeneous band bending of the surface layer extends.

The magnitude of the relaxation in regime 1 is always greater than in regime 2 because light is absorbed predominantly in the defect-free zone of the indentation in regime 1,

TABLE I. Anisotropy of relaxation of the indenter dimensions.

Radiation spectral composition	$\Delta[(H_d-H_l)/H_d]$, %	
	$\parallel \langle 100\rangle$	$\parallel \langle 110\rangle$
$h\nu > \Delta E_g$ (regime 1)	11	9
$h\nu < \Delta E_g$ (regime 2)	6	6

The magnitude of the relaxation is expressed as the difference between the magnitudes of the photomechanical effect: $\Delta[(H_d-H_l)/H_d]$, %, where H_d and H_l are the microhardnesses in darkness and during illumination, respectively.

so that the elastic deformation in the illuminated crystal propagates to a much greater distance from the indenter than in darkness, whereas in regime 2 light-induced softening sets in only for the defective zone, in which the fraction of elastic deformation is small. Consequently, when the load is removed, the elastic recovery of the indentation in regime 1 is a more efficient process than in regime 2.

The contraction, extension, and rotation of chemical bonds take place in a covalent crystal as the indentation forms under the indenter. This behavior accounts for the anisotropic character of the relaxation of the indentation size. When the indenter is in the position of maximum microhardness on a given face, contraction is the dominant process, and when the microhardness is a minimum, extension and rotation of the chemical bonds are dominant.[10] During removal of the load from the illuminated surface of a crystal (in regime 1), when relaxation of the elastic stresses takes place, the force exerted by the elastically deformed region (in which the chemical bonds are predominantly in the contracted state) on the defective region is naturally greater than when the chemical bonds are weakened by tensile and rotational strains.

[1)]Microhardness anisotropy refers to the variation of the microhardness (usually measured by means of an elongated Knoop indenter) as a function of the indenter orientation on the face of a single crystal.[6]

[1] Yu. S. Boyarskaya and M. I. Val'kovskaya, *Microhardness* [in Russian] (Shtiintsa, Kishinev, 1981), p 67.
[2] V. P. Alekhin and A. P. Ternovskiĭ, in *The Latest in Microhardness Testing* (Nauka, Moscow, 1974), p. 29.
[3] M. I. Val'kovskaya, B. M. Pushkash, and É. E. Maronchuk, *Plasticity and Brittleness of Semiconductor Materials in Microhardness Tests* [in Russian] (Shtiintsa, Kishinev, 1984), p. 100.
[4] G. K. Kuczynski and R. H. Hochman, Phys. Rev. **108**, 946 (1957).
[5] A. B. Gerasimov, Z. V. Dzhibuti, and G. D. Chiradze, Soobshch. Akad. Nauk Gruz. SSR **142**, 53 (1991).
[6] P. D. Warren, S. G. Roberts, and P. B. Hirsch, Izv. Akad. Nauk Ser. Fiz. **51**, 812 (1987).
[7] I. G. Gverdtsiteli, A. B. Gerasimov, Z. V. Dzhibuti, and M. G. Pkhakadze, Poverkhnost', No. 11, 132 (1985).
[8] A. B. Gerasimov, in *Proceedings of the Fourth International Conference on Shallow Impurities in Semiconductors* (Trans Tech Publ., Zurich, 1990): Mater. Sci. Forum **65–66**, 47 (1990).
[9] *Problems in the Radiation Technology of Semiconductors* [in Russian], edited by L. S. Smirnov (Nauka, Novosibirsk, 1980), p. 149.
[10] A. B. Gerasimov, G. D. Chiradze, and N. G. Kutivadze, Bull. Kutaisi Univ., No. 2, 196 (1996).

Translated by James S. Wood

MAGNETISM AND FERROELECTRICITY

Influence of a strong microwave electric field on the spectrum and damping of magnetostatic waves in the magnetic semiconductor p-$HgCr_2Se_4$

N. I. Solin, A. A. Samokhvalov, and V. S. Babushkin

Institute of Metal Physics, Ural Branch of the Russian Academy of Sciences, 620219 Ekaterinburg, Russia
(Submitted July 14, 1997)
Fiz. Tverd. Tela (St. Petersburg) **40**, 505–507 (March 1998)

Variations in the spectrum and damping of magnetostatic waves are observed in p-$HgCr_2Se_4$ irradiated by a strong microwave electric field. The variations depend on the magnetostatic wavenumber and the electrical conductivity of the crystal. The results are discussed in the model of magnon heating by high-energy carriers. © *1998 American Institute of Physics.* [S1063-7834(98)02203-5]

One of the central problems of the physics of magnetic semiconductors is the study of the interaction of charge carriers (electrons and holes) with spin waves. Strong electron–magnon interaction in magnetic semiconductors governs the variations of the magnetic properties of magnetic semiconductors in an electric field,[1,2] In n-$HgCr_2Se_4$ samples exhibiting metal-type conductivity, substantial (up to tenfold) reductions in the damping of magnetostatic waves (MSWs) in an external electric field[3,4] are attributed[5] to variation of the band structure of $HgCr_2Se_4$ as a result of a decrease in the magnetization when magnons are heated by high-energy electrons.[2,6]

Studies of electron–magnon interaction in ρ-$HgCr_2Se_4$ are nonexistent, because holes are known to interact weakly with the magnetic subsystem. In this article we give the results of investigations of the influence of an external microwave electric field on the propagation of backward-traveling volume magnetostatic waves in p-$HgCr_2Se_4$.

The experiments known to us on magnetic semiconductors in strong electric fields have been carried out with direct current. Carrier injection and other contact effects can be eliminated by using a noncontact method. Our measurements were performed by a resonator method. A $HgCr_2Se_4$ sample in the form of a right parallelepiped of dimensions $1.4\times1.4\times0.28$ mm was placed in the center of a rectangular, dual-mode, beam resonator. Microwaves from two sources were fed to the resonator. One source (operating at a frequency of 8 GHz and low power) was used to excite and record MSWs in the sample (TE_{102} mode). A magnetron source operating at a frequency of 9.4 GHz with power up to 5 kW was used to irradiate the sample with an electric field up to 3 kV/cm (TE_{103} mode). To eliminate Joule heat, the investigations were carried out in the pulsed regime. The MSWs were recorded by a stroboscopic voltmeter using a strobe pulse of duration 20 ns. The microwave measurement procedure and apparatus were similar to those described in Ref. 7.

The samples were prepared by the technology described in Ref. 8 and had a semiconductor-type temperature dependence of the microwave conductivity σ with activation energies $\Delta E_a = 0.07$ eV and 0.03 eV in the ferromagnetic and paramagnetic regions, respectively. The electrical properties and thermal emf of p-$HgCr_2Se_4$ have been investigated previously.[9]

1. RESULTS

It is evident from Fig. 1 that the values of the MSW resonance field H_r and linewidth ΔH_k increase in proportion to the electric field above a certain critical value $E \cong 0.7$ kV/cm of the latter. The variations of $\Delta H_k(E)$ and $H_r(E)$ are approximately inversely proportional to the square of the MSW wavenumber k. In samples of lower conductivity ($\sigma \leqslant m\Omega^{-1}\cdot cm^{-1}$) the electric field is not observed to have any influence on MSW propagation.

Figure 2 shows typical plots of the MSW characteristics H_r and ΔH_k as functions of the microwave-pulse input time. We see that within the duration of the microwave pulse, $\tau \cong 1$ μs, the MSW line broadens, and H_r shifts toward higher resonant fields, and then, upon termination of the microwave pulse, the MSW characteristics ΔH_k and H_r return to the original values after a characteristic time $\tau = 2-3$ μs.

Thus, the MSW damping and resonance fields increase in p-$HgCr_2Se_4$ samples in an electric field instead of decreasing as in n-type samples,[4] and the time variations of the H_r and ΔH_k in p-$HgCr_2Se_4$ are an order of magnitude faster.

To determine the nature of the observed MSW variations, the MSW characteristics ΔH_k and H_r and the microwave conductivity at 9.4 GHz of the investigated $HgCr_2Se_4$ sample were measured as functions of the temperature (Fig. 3). Clearly, H_r and ΔH_k and the conductivity increase with the temperature. At high temperatures the MSW damping decreases as the MSW wavenumber k increases, and at 77 K the variation of $\Delta H_k(k)$ is monotonic.

2. DISCUSSION OF THE RESULTS

The spectrum and damping of MSWs in magnetic dielectrics are determined by the magnetization of the

 © 1998 American Institute of Physics

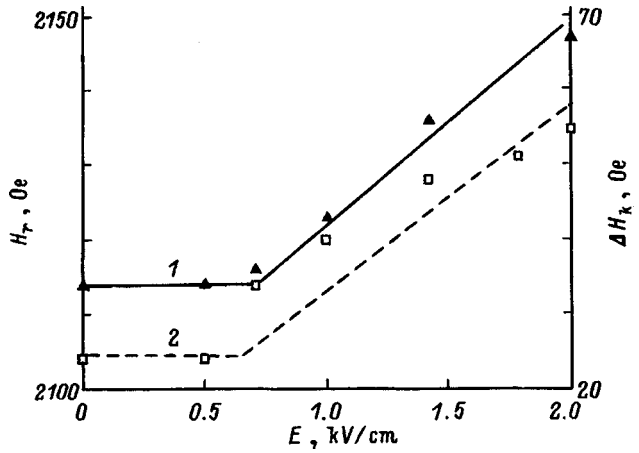

FIG. 1. Resonant field (graph *1*) and linewidth (graph *2*) of magnetostatic waves versus microwave electric field, $T=77$ K, $k=20$ cm^{-1}.

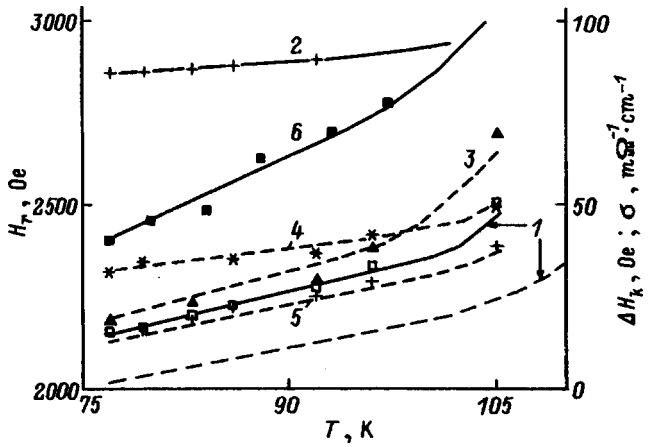

FIG. 3. Resonant fields (graphs *1* and *2*) and linewidths (graphs *3*–*5*) of magnetostatic waves and microwave conductivity (graph *6*) of p-$HgCr_2Se_4$ versus temperature. *1, 3*) $k=20$ cm^{-1}; *2, 4*) 65 cm^{-1}; *5*) 110–150 cm^{-1}.

crystal.[10] To describe MSW propagation in conducting magnets, the electrical conductivity of the crystal must be taken into account; calculations have shown[4] that it mainly influences (through an induction mechanism) only the damping of the waves. It is well known[11] that the MSW resonance fields $H_r(k)$ for a plate in free space are described by the Damon-Eshbach equations[10] only for large $k \gg k_0 = 7$ cm^{-1}, where k_0 is the electromagnetic wavelength in the medium. The temperature dependence of H_r for the MSW fundamental ($k=22$ cm^{-1}) can be explained on the basis of the Kittel equation for an ellipsoid

$$(\omega/\gamma)^2=[H_r+(N_x-N_z)][H_r+(N_y-N_z)M], \qquad (1)$$

where ω is the frequency, and N is the demagnetization factor. Clearly, calculations based on (1) for a g factor equal to 2 (dashed curve *1* in Fig. 3) provide a good explanation of $H_r(T)$ as the result of the temperature dependence of the magnetization M of $HgCr_2Se_4$ (Ref. 4).

The contribution of internal processes to the damping of spin waves of $HgCr_2Se_4$ with $k \cong 0$ is small.[12] At 77 K the contributions of fast-relaxing impurity ions of the Cr^{+2} type to the damping are also small and decrease as the temperature increases.[13] The increase of ΔH_k with $k>110$ cm^{-1} (curve 5 in Fig. 3) as the temperature approaches the Curie point $T_C=106$ K (Ref. 9) agrees with ferromagnetic linewidth (ΔH) data for nonconducting $HgCr_2Se_4$ crystals[14] and can be attributed to the influence of spin fluctuations. The k-dependent part of the MSW attenuation (curves *3*–*5* in Fig. 3) can be attributed to the influence of the electrical conductivity of the crystal. The oscillations of the alternating magnetization induce an electric field, and the Joule heating induces additional MSW damping, whose contribution at $k \gg k_0$ has the form[4]

$$\Delta H_k = 4\pi M k_c^2/k^2, \qquad (2)$$

where $k_c^2=4\pi\sigma\omega/c^2=1/\delta^2$, and δ is the skin depth.

For small k the conductivity contribution to the MSW damping can only be determined numerically from the solution of a system of equations,[4] and Eq. (2) can only be used for estimates, which give $\Delta H_k \cong 20$ Oe for the MSW fundamental at 77 K. The nonmonotonic behavior of $\Delta H_k(k)$ at 77 K (Fig. 3) can be attributed to the fact that the fundamental mode is observed in the region of surface MSW propagation, because $H_r < H_r^a \equiv [(\omega/\gamma)^2+(2\pi M)^2]^{1/2}-2\pi M$, where H_r^a is the antiresonance field (magnetic permeability $\mu'=0$).[10] The damping of surface waves can be expected not to depend as strongly on the conductivity of the magnet as the damping of volume MSWs.[11]

Thus, the variations of H_r and ΔH_k in an electric field, like the temperature variations, are probably caused by variations of M and σ in $HgCr_2Se_4$. The variations of $\Delta H_k(E)$ and $H_r(E)$ (Figs. 1 and 2), estimated from their temperature dependences, correspond to a (5–10)-K increase in the temperature. The short durations of the aftereffect of ΔH_k and H_r (Fig. 2) and estimates of the Joule heating in the adiabatic regime (less than 0.5 K) show that the observed variations of MSWs in an electric field are associated with interaction between the magnetic and electronic systems. The decrease in the magnetization is well explained in the model of magnon heating[2] by high-energy carriers. Carriers heated in the electric field transfer energy to magnons. In $HgCr_2Se_4$, however,

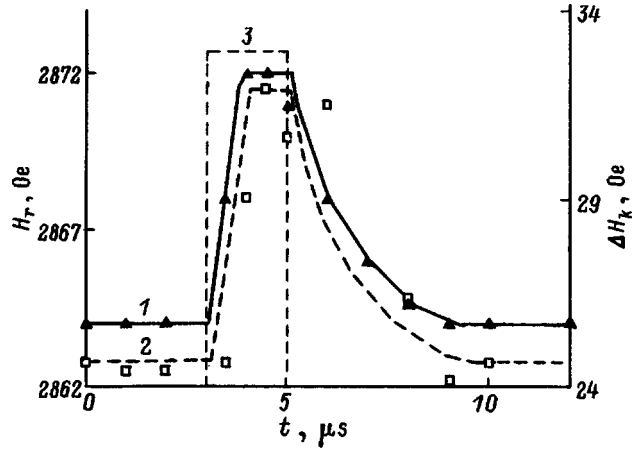

FIG. 2. Resonant field (graph *1*) and linewidth (graph *2*) of magnetostatic waves versus time, $T=77$ K, $k=65$ cm^{-1}, $E=2$ kV/cm. *3*) Profile of the microwave pulse.

the magnons are weakly coupled with phonons, because the Debye temperature[15] is $T_D = 220\ \mathrm{K} < T_C$. This is why magnons are also heated in the electric field.

The increase of ΔH_k in an electric field and its dependence on k (Figs. 1 and 2) are consistent with the induction mechanism of MSW damping and with the increase in the conductivity of $HgCr_2Se_4$ in an electric field.[16] The increase of $\sigma(E)$ in an electric field has been explained[16] by the delocalization of electrons around the bottom of the valence band as the carriers heat up. The identical behavior of the $H_r(E)$ and $\Delta H_k(E)$ curves, which implies the common nature of these variations, can also be explained in the magnon-heating model.

The electrical conductivity of $HgCr_2Se_4$ is attributed[17] to nonstoichiometric composition, specifically deficiencies in both Se (donors) and in Hg (acceptors). We postulate that in the paramagnetic region, owing to strong $s-d$ exchange interaction, electrons bound to Se vacancies become localized at neighboring chromium ions, forming magnetization-dependent impurity states of the ferron type[18] and are involved only in hopping conduction. In the ferromagnetic region the gain in exchange energy disappears, and the electrons become delocalized. The released electrons compensate acceptors, thereby increasing the resistance. This phenomenon can account for the positive magnetoresistance in p-$HgCr_2Se_4$ (Ref. 19) and the increase in the activation energy close to T_C (Ref. 9). This model explains the variations of the conductivity as a function of the temperature and the magnetic and electric fields, along with other properties of n-$HgCr_2Se_4$ (Refs. 5, 7, and 20). The difference is probably that the densities of Se and Hg vacancies in the investigated p-$HgCr_2Se_4$ are approximately equal or have values such that hole compensation and the change of conductivity type take place at $T \cong 18\ \mathrm{K} \ll T_C$ (Ref. 9). According to x-ray data,[8] there are more Se vacancies than Hg vacancies in undoped crystals, but the ratio between them is technology-dependent and can be modified by annealing in various atmospheres.[9,21] The approximately 10-K variation of the magnetization of such a crystal at a temperature of 77 K (close to T_C) as a result of magnon heating is potentially conducive to the transfer of electrons into localized states and lowering of the conductivity.

The duration of the aftereffect (Fig. 2) is governed by magnon-phonon interaction in the magnon-heating model.[2,6] The variation of this time as a function of the conductivity type indicates indirect relaxation of the magnon energy into the lattice by way of carriers.

Thus, the model of magnon heating by high-energy carriers in connection with the nature of the electrical conductivity of p-$HgCr_2Se_4$ explains the main features of the changes in the spectrum and damping of magnetostatic waves in a strong electric field.

This work has been carried out as part of the Federal Program ''Surface Atomic Structures'' (Project No. 95-2.10).

[1] A. A. Samokhvalov, N. I. Solin, N. A. Viglin, V. A. Kostylev, V. V. Osipov, and V. S. Babushkin, Phys. Status Solidi B **169**, K93 (1992).
[2] I. Ya. Korenblit, A. A. Samokhvalov, and V. V. Osipov, Sov. Sci. Rev. Phys. A **8**, 447 (1987).
[3] N. A. Viglin, V. V. Osipov, and A. A. Samokhvalov, Fiz. Tverd. Tela (Leningrad) **33**, 2695 (1991) [Sov. Phys. Solid State **33**, 1523 (1991)].
[4] N. I. Solin, B. N. Filippov, I. Yu. Shumilov, and A. A. Samokhvalov, Fiz. Tverd. Tela (St. Petersburg) **35**, 1613 (1993) [Phys. Solid State **35**, 812 (1993)].
[5] N. I. Solin, A. A. Samokhvalov, and S. V. Naumov, Fiz. Tverd. Tela (St. Petersburg) **39**, 664 (1997) [Phys. Solid State **39**, 580 (1997)].
[6] I. Ya. Korenblit and B. G. Tankhilevich, Fiz. Tverd. Tela (Leningrad) **18**, 62 (1976) [Sov. Phys. Solid State **18**, 34 (1976)].
[7] N. I. Solin, A. A. Samokhvalov, and S. V. Naumov, Fiz. Tverd. Tela (St. Petersburg) **37**, 2100 (1995) [Phys. Solid State **37**, 1142 (1995)].
[8] N. M. Chebotaev, M. I. Simonova, T. I. Arbuzova, and B. A. Gizhevskiĭ, Izv. Akad. Nauk SSSR, Neorg. Mater. **21**, 1468 (1985).
[9] V. A. Kostylev, B. A. Gizhevskiĭ, A. A. Samokhvalov, and N. M. Chebotaev, Fiz. Tverd. Tela (Leningrad) **32**, 38 (1990) [Sov. Phys. Solid State **32**, 20 (1990)].
[10] R. M. Damon and J. R. Eshbach, J. Phys. Chem. Solids **19**, 308 (1961).
[11] N. I. Solin, A. A. Samokhvalov, I. Yu. Shumilov, and A. B. Zolotovitskiĭ, Zh. Tekh. Fiz. **57**, 2250 (1987) [Sov. Phys. Tech. Phys. **32**, 1361 (1987)].
[12] N. I. Solin, A. A. Samokhvalov, and I. Yu. Shumilov, Fiz. Tverd. Tela (Leningrad) **30**, 2246 (1988) [Sov. Phys. Solid State **30**, 1298 (1988)].
[13] N. I. Solin, L. D. Fal'kovskaya, and A. A. Samokhvalov, Fiz. Tverd. Tela (St. Petersburg) **36**, 3090 (1994) [Phys. Solid State **36**, 1643 (1994)].
[14] N. I. Solin, A. A. Samokhvalov, I. Yu. Shumilov, N. M. Chebotaev, and S. V. Naumov, Fiz. Tverd. Tela (Leningrad) **30**, 2188 (1988) [Sov. Phys. Solid State **30**, 1260 (1988)].
[15] M. A. Ivanov, N. I. Kourov, Kh. Medge, M. I. Simonova, L. D. Fal'kovskaya, and A. Ya. Fishman, Fiz. Tverd. Tela (Leningrad) **28**, 1585 (1986) [Sov. Phys. Solid State **28**, 899 (1986)].
[16] A. Gal'dikas, V. Viktorovichyus, I. Matulenene, S. Mitskyavichyus, I. S. Kovaleva, Z. Martunas, and A. Shyatkus, Fiz. Tverd. Tela (Leningrad) **26**, 2906 (1984) [Sov. Phys. Solid State **26**, 1757 (1984)].
[17] V. G. Veselago, K. M. Golant, I. S. Kovaleva, and I. M. Yurin, Zh. Éksp. Teor. Fiz. **86**, 1857 (1984) [Sov. Phys. JETP **59**, 1079 (1984)].
[18] É. L. Nagaev, *Physics of Magnetic Semiconductors* (Mir, Moscow, 1983; Nauka, Moscow, 1979).
[19] V. A. Kostylev, B. A. Gizhevskii, A. A. Samokhvalov, M. I. Auslender, and N. G. Bebenin, Phys. Status Solidi B **158**, 307 (1990).
[20] N. I. Solin and N. M. Chebotaev, Fiz. Tverd. Tela (St. Petersburg) **39**, 848 (1997) [Phys. Solid State **39**, 754 (1997)].
[21] L. Goldstein, P. Gibart, and A. Selmi, J. Appl. Phys. **49**, 1474 (1978).

Translated by James S. Wood

Long-time relaxation of an ordered magnetic structure

S. K. Godovikov

Nuclear Physics Scientific-Research Institute, M. V. Lomonosov Moscow State University, 119899 Moscow, Russia

Yu. D. Perfil'ev and Yu. F. Popov

M. V. Lomonosov Moscow State University, 119899 Moscow, Russia

A. I. Firov

A. A. Baĭkov Institute of Metallurgy, Russian Academy of Sciences, 117911 Moscow, Russia
(Submitted July 1, 1997; resubmitted September 30, 1997)
Fiz. Tverd. Tela (St. Petersburg) **40**, 508–512 (March 1998)

In a Mössbauer investigation of the parameters of the hyperfine interactions on Fe^{57} nuclei in the ferromagnetic $Tb_{0.8}Y_{0.2}Fe_2$, we have made the first observation of long-time (days, months) relaxation of an ordered magnetic structure. In this effect the orientation of some moments in a sample changes under the action of a pulsed magnetic field (up to 250 kOe) and then slowly reverts to the initial state by means of gradual decomposition of clusters of the reoriented moments. A theoretical estimate of the relaxation time is made. © *1998 American Institute of Physics.* [S1063-7834(98)02303-X]

Giant magnetic anisotropy and giant magnetostriction, which were discovered in the 1960s in rare-earth magnets, are apparently not the only giant magnetic properties characteristic of lanthanides. Separate studies performed in the last 30 years indicate the possible existence of another such property, associated with the time dependence of some macroscopic magnetic parameters. For example, it is known[1] that the relaxation time for Tb containing 0.5 at. % of different impurities can reach 160 s near a transition into the ferromagnetic state. In Ref. 2 it was observed that in Tb at temperatures above 135 K the initial susceptibility decays over $\sim$320 min. This was attributed to a property of Tb and not the presence of impurities. An elastic aftereffect corresponding to the high magnetic viscosity of some compounds of Tb with Gs and Dy was discovered in Ref. 3. The characteristic relaxation times were $\sim 10^2$ s. Long-period decay of the induced magnetization is also well known in spin glasses containing rare-earth elements. For example, the magnetization in the system Y+3 at. % Tb (Ref. 4) decays over a time $\sim$400 s. This is because the spin-glass system is multiply degenerate, as a result of which a slow wandering between energy valleys occurs. However, in the above-mentioned works the microscopic mechanism for the decay of the magnetization and of other parameters was not known, and the problem had not even been formulated.

The first step in understanding the microscopic mechanism was taken in Ref. 5, where the hyperfine interactions on impurity Sn^{119} in Tb metal were discovered to be time-dependent and their time dependence was investigated. It was found that under some conditions (ordinarily, near the Néel point) the magnetic environment surrounding a Sn atom becomes unstable and decays into a structure with a lower local magnetization. The characteristic decay times were hours and days. The decay slows down when a magnetic field is applied. It was conjectured that the phenomenon is of a cluster, microcollective character. It would be appropriate to call the phenomenon a giant viscosity of the magnetic structure of a rare-earth magnet, by analogy to other specific properties of materials in this class. It would be extremely interesting to determine the boundaries of the region within which this phenomenon occurs. The present investigation was undertaken in this connection, but this time on the compound $Tb_{0.8}Y_{0.2}Fe_2$ by the Mössbauer spectroscopy method (Fe^{57}).

The intermetallide $TbFe_2$ is a ferrimagnet with a high Curie point (682 K). Its magnetic anisotropy constants $K_1 = -7\times10^7$ ergs/cm^3 and magnetostriction $\lambda_s = 2\times10^{-3}$ at 300 K are very large.[6] Substitution of yttrium for Tb introduces some disorder into the periodic arrangement of the magnetic Tb ions and creates the prerequisites for an imbalance of the exchange energy, magnetic anisotropy, and magnetostriction in a direction favorable for the appearance of metastability.

1. EXPERIMENTAL PROCEDURE

Pulsed magnetic fields with intensity up to 50 kOe and pulse durations of several milliseconds were used to produce a perturbation in the system of magnetic moments. The fields were produced in the gap of a solenoid by discharging a capacitor bank. A field of 125 kOe was produced at room temperature and a field at 250 kOe was produced with the solenoid and samples cooled by liquid nitrogen. The main method of investigation was Mössbauer spectroscopy on Fe^{57} nuclei. The ''Perseĭ'' apparatus, which makes it possible to measure the parameters of the hyperfine interactions to within 10^{-3} mm/s, and a $\sim$10 mCi source consisting of Co^{57} in Cr were used. The magnetic parameters were mea-

 © 1998 American Institute of Physics

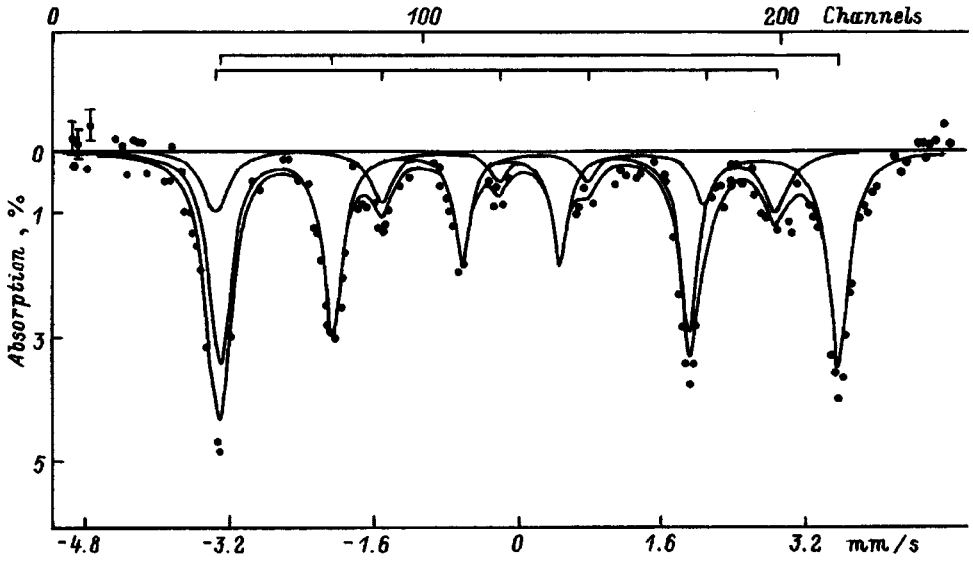

FIG. 1. Mössbauer (Fe^{57}) spectrum of $Tb_{0.8}Y_{0.2}Fe_2$. $T=293$ K. The spectrum was analyzed in the model of two sextets of lines.

sured in a high-precision magnetometer. The x-ray crystallographic analysis was performed on a DRON-3 apparatus.

2. EXPERIMENTAL RESULTS

The Mössbauer spectrum of the $Tb_{0.8}Y_{0.2}Fe_2$ sample at 293 K is displayed in Fig. 1. The spectrum corresponds well to the parameters characteristic of compounds of the RFe_2 series.[7,8] It decomposes into two sextets of lines with different hyperfine magnetic fields (H_1 and H_2), isomeric shifts (δ_1 and δ_2), quadrupole splittings (Q_1 and Q_2), line widths ($\Gamma 1$ and Γ_2), and populations A_1 and A_2 (A_1/A_2). The parameters are summarized in Table I. The first row of the table contains the parameters of the initial spectrum, and the second row contains the parameters of the spectrum that was obtained immediately after application of a 125 kOe field (one pulse). The spectrum was obtained in a time of 10–12 h. One can see from Table I that the field changes substantially only one parameter, A_1/A_2. Except possibly Γ_2, which increases slightly, the other parameters are stable within the limits of the experimental error. Hence, the field gives rise to hysteresis of the magnetic structure of the sample that lasts long enough to obtain at least a spectrum. It was of interest to check how stable the hysteresis state is.

We found that the parameter A_1/A_2 relaxes to the initial level over a time of order 1 month (Fig. 2a). Repeated application of a magnetic field produces the same hysteresis effect, but the relaxation time decreases to 1 week (Fig. 2b).

It was very important to determine the conditions under which the hysteresis state does not decay, i.e., the state exhibits absolute temporal stability. For this, a sample with no magnetic past history was prepared from the same piece of material. The sample was subjected to a 250 kOe magnetic field applied in a series of five pulses, repeated every 10 min. The result is displayed in Fig. 2c. One can see that here the degree of rearrangement of the structure is the same as in the cases presented in Figs. 2a and 2b, but there is no relaxation for at least two months.

Measurements of the magnetic hysteresis loops showed that $Tb_{0.8}Y_{0.2}Fe_2$ is a quite soft material magnetically. Its coercivity is ~ 250 Oe in the initial state and decreases to ~ 190 Oe after the 125 kOe field is applied (the case shown in Fig. 2a). X-ray crystallographic analysis revealed that the initial value of the lattice parameter $a=7.345\pm 0.001$ Å of the fcc structure does not change after the application of the 250 kOe field.

An experiment searching for hysteresis of the parameter A_1/A_2 was also conducted in a weak 4.7 kOe field. This field was produced with an electromagnet in a time of 10 min at 293 K. No changes in A_1/A_2 or other parameters of the spectrum were observed.

3. DISCUSSION

It should be noted, first and foremost, that the observed phenomena are in no way associated with macroscopic magnetization and demagnetization of $Tb_{0.8}Y_{0.2}Fe_2$. A pulsed field does not convert the sample into a permanent magnet, since the coercivity of the sample is very low. Moreover, residual magnetization would result in an appreciable magnetostriction effect, which is absent to within 0.001 Å. Finally, the parameters H_1 and H_2 are identical before and

TABLE I. Parameters of Mössbauer spectra of $Tb_{0.8}Y_{0.2}Fe_2$ ($T=293$ K).

	H_1, kOe	H_2, kOe	δ_1, mm/s	δ_2, mm/s	Q_1, mm/s	Q_2, mm/s	A_1/A_2	Γ_1, mm/s	Γ_2, mm/s
Initial	212.9	193.2	0.016	0.011	0.204	−0.534	3.1	0.30	0.34
state	(0.2)	(0.7)	(0.002)	(0.008)	(0.004)	(0.017)	(0.1)	(0.01)	(0.03)
After the application	212.9	193.8	0.017	0.0101	0.206	−0.555	2.4	0.31	0.41
of a 125 kOe field	(0.2)	(0.7)	(0.002)	(0.008)	(0.004)	(0.016)	(0.1)	(0.01)	(0.03)

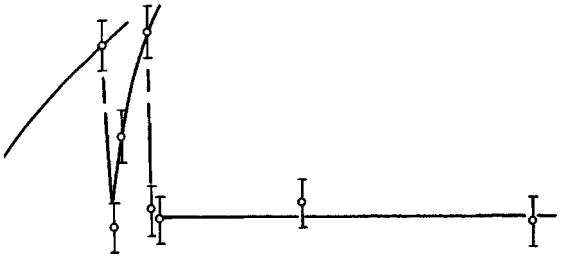

FIG. 2. Long-time relaxation in $Tb_{0.8}Y_{0.2}Fe_2$. a—After the application of a 125 kOe field, b—after repeated application of a 125 kOe field, c—after the application of a 150 kOe field.

after a field is applied, i.e., the internal field induced in the sample by the external field is negligibly small. The reason for the hysteresis and relaxation of A_1/A_2 must be sought in the microscopic arrangement of the intrinsic magnetic structure of the experimental material.

We now direct our attention to the nature of the fields H_1 and H_2, which is considered to be quite well studied in RFe_2 compounds.[7,8] These compounds have a structure of the Laves phases type, the iron atoms occupy the vertices of tetrahedra, and the symmetry is $\bar{3}m$. The three-fold axes lie in the directions [111]. The R atoms form a diamond lattice. The unit cell possesses four tetrahedra of Fe atoms, the tetrahedra being aligned in the same direction. A fragment of the structure of RFe_2 is displayed in Fig. 3.

If the crystal is not magnetized, the iron atoms are crystallographically absolutely equivalent. The presence of a magnetic axis produces a difference between the iron atoms, since the angle θ between the axis of the axisymmetric electric-field gradient and the magnetic field, generally speaking, will not be the same for all iron atoms (Fig. 3). If the magnetization is directed along [111], then there exist

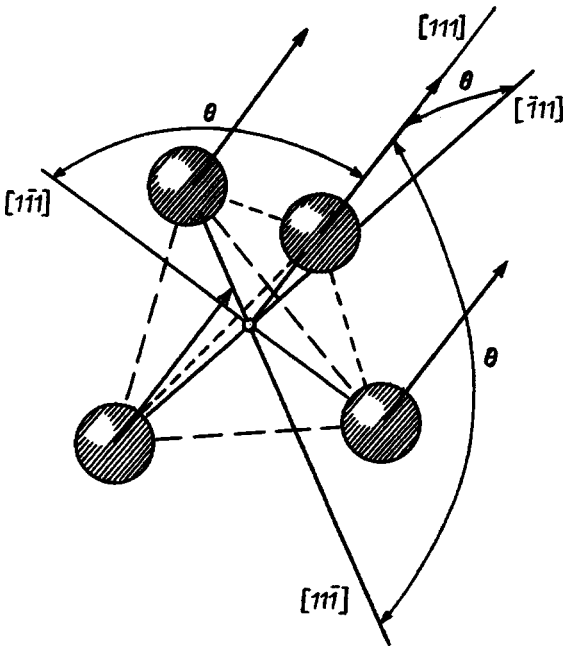

FIG. 3. Arrangement of Fe atoms in the RFe_2 structure. The arrows indicate the magnetic moments of Fe.

two classes of distinguishable iron atoms: those for which $\theta=0$ and those for which $\theta=70°32'$. They are present in a 1:3 ratio (Fig. 3) and can be distinguished in a Mössbauer experiment, since the combined effect of the magnetic dipole and electric quadrupole interactions depends on the angle θ. Two other cases are also possible: easy magnetization in the [110] direction (two pairs of nonequivalent sites and a 1:1 ratio of intensities of the spectra) and easy magnetization in the [100] direction (all sites equivalent and only one Mössbauer spectrum).

In the $TbFe_2$ structure the easy axis is [111], i.e., the parameter A_1/A_2 must equal 3, as is observed in our case. Thus, the parameter A_1/A_2 is the ratio of the populations of the two magnetically nonequivalent positions shown in Fig. 3. We shall examine the most likely reason why an external field changes A_1/A_2.

In a cubic lattice there exist four directions of easy magnetization of the type [111] (diagonals of the cube). They are absolutely equivalent energetically, but they are separated from one another by quite high barriers. In each unit cell the moments align along one of the [111] axes, as a result of which $A_1/A_2=\text{const}$ holds over all cells. However, a strong external field can destroy this constancy. Within a given cell some moments can be reoriented to a different [111] axis. For example, if in the fragment of the structure shown in Fig. 3 only one moment undergoes such a transition with the angle θ changing from $72°32'$ to 0°, then A_1/A_2 becomes equal to $2/2=1$. The fields H_1 and H_2 and the other parameters of the spectrum should not change in the process, since the configuration with a collinear arrangement of the moments and the ''defective'' configuration are energetically equivalent. Since the experimental material is a polycrystal, transitions of the moments in the [111] axes are random. If it is assumed that of the 16 moments of the Fe atoms per unit cell only one, on the average, changes orientation, then the result is that A_1/A_2 changes from $12/4=3$ to $11/5=2.2$, which is very close to the experimentally observed value (Fig. 2).

There arise the obvious questions: How will the defective configuration behave as a function of time? Will it relax into the initial state and if so, then how long is this relaxation time?

It is obvious that a single moment cannot revert to the initial state, since this involves an increase in energy by an amount at least of the order of the exchange energy per lattice site. All moments united by the exchange interaction forces into a cluster must relax simultaneously. Let us estimate the number of moments that can participate in this formation. For this, we employ the physical considerations and results of Ref. 9, where relaxation of the hyperfine fields for a Sn impurity in Tb is discussed.

Following Ref. 9, let us assume that an energy ΔE is required for a moment to rotate from a defective state into the normal state. Then the rotation will occur over the time

$$\tau_0 \simeq \hbar/\Delta E. \tag{1}$$

The probability of finding this moment in a time interval τ_0 in the rotated state is

TABLE II. Computed relaxation times τ of the moments as a function of the average number N of moments in a cluster.

x	N	τ
5	2.14	7.7×10^{-13} s
30	12.87	0.93×10^{-2} s
35	15.02	1.18 s
40	17.17	2.5 min
45	19.31	5.6 h
48.5	20.81	7.19 days
50	21.46	31.25 days
51	21.89	83.3 days
52	22.32	222.2 days

$$W_0=\exp(-\Delta E/kT). \tag{2}$$

The probability that N moments (one cluster) will rotate simultaneously over time τ_0 is

$$W=W_0^N=\exp(-N\Delta E/kT). \tag{3}$$

The time for N moments comprising one cluster to rotate simultaneously is

$$\tau=\tau_0/NW=(\tau_0/N)\exp(N\Delta E/kT). \tag{4}$$

Introducing $x=n\Delta E/kT$ we obtain

$$\tau=\frac{\hbar}{xkT}e^x. \tag{5}$$

Since the measurements in the present work were performed at $T=293$ K

$$\tau\cdot 3.84\times10^{13}=\frac{e^x}{x}. \tag{6}$$

The equation (6) establishes a relation between τ and N, if we take into account the fact that $\Delta E/kT\simeq2.33$ for $TbFe_2$, whose Curie point is 682 K.

One can see from Table II, where computational results are presented, that the dependence of τ on N is of a ''catastrophic'' character: A cluster of two moments decays over 10^{-13} s and a cluster of 22 moments decays in 222 days. The experimentally observed relaxation times correspond to a cluster consisting of 20–22 moments, the dependence of τ on N being extremely sharp even in this narrow range: Changing N by 7% increases τ from 7 to 222 days.

The calculation performed above is, of course, very general and approximate, since many parameters of the material in question have been neglected. On the other hand, however, the main features of the observed effects are completely described by Eq. (6). It is obvious that the main parameter here is the cluster size N. This explains almost all experimental results.

Indeed, it is obvious why a 250 kOe field in a series of five pulses virtually freezes out the hysteresis state. Such a strong action forms very many defects, which are described above, in the magnetic structure, and this promotes the formation of large, very stable clusters ($N>22$). The weaker effect of a 125 kOe field forms smaller clusters ($N<22$), which decay over a time of the order of weeks or months (Fig. 2). For a very weak field of 4.7 kOe, even if it does form defects in the magnetic structure, the defects are impossible to notice because very small clusters decay rapidly ($N\ll22$). It is also obvious that the magnetic past history of a sample influences the relaxation time, since when the coercivity decreases from 250 to 190 Oe with a transition from the cycle corresponding to Fig. 2a to the cycle corresponding to Fig. 2b, the magnetization curve shifts upward, as a result of which the exchange energy, the parameter ΔE, increases and N decreases.

Analysis of Eq. (6) shows that when the temperature at which the experiments are performed decreases, the existence of much smaller clusters becomes admissable, which nonetheless give long relaxation times. For example, cooling to 77 K permits clusters consisting of 5–6 moments. Indeed, preliminary experiments at 77 K with a 4.7 kOe field that does not give any effects at 293 K showed the presence of hysteresis and long-time relaxation.

Finally, let us consider the role of Y in the phenomena discussed above. Yttrium, being a nonmagnetic impurity, produces a magnetic perturbation in its vicinity and gives rise to tilting, disorientation, of the Fe moments. For this reason, the structure of $Tb_{0.8}Y_{0.2}Fe_2$ apparently is not completely collinear, which is why the height of the barrier between the [111] magnetic axes is lower than in pure $TbFe_2$. Moreover, Y decreases the exchange interaction in the matrix. The result of these processes is a decrease of ΔE, i.e., a shift in the direction of long (observable, at least) relaxation times.

The results obtained in the present work have much in common with the results obtained for the Tb+0.5 at. % Sn^{119} system.[5] Both sets of results can be described successfully by a two-level cluster model of the decay of the excited magnetic structure. Further experimental and theoretical investigations must be performed in order to understand better the long-time relaxation effects.

We thank A. S. Andreenko for providing the $Tb_{0.8}Y_{0.2}Fe_2$ sample.

This work was supported by Russian Fund for Fundamental Research Grant No. 95-02-16999a.

[1] K. P. Belov, S. A. Nikitin, and K. G. Kurtovoĭ, Zh. Éksp. Teor. Fiz. **55**, 157 (1968) [Sov. Phys. JETP **28**, 84 (1969)].
[2] A. del Moral and E. W. Lee, J. Phys. F: Metal Phys. **4**, 280 (1974).
[3] M. K. Kubkin, G. I. Kataev, T. A. Mamatova, V. G. Prokoshev, and V. V. Shubin, Fiz. Met. Metalloved. **64**, 480 (1987).
[4] Y. Yeshurun, L. J. P. Ketelsen, and S. Salamon, Phys. Rev. B **32**, 7425 (1985).
[5] S. K. Godovikov, N. I. Moreva, and A. I. Firov, Izv. Akad. Nauk SSSR, Ser. Fiz. **52**, 1683 (1988).
[6] K. P. Belov, *Rare-Earth Magnets and Their Applications* [in Russian], Nauka, Moscow, 1980.
[7] G. K. Wertheim, V. Jaccarino, and J. H. Wernick, Phys. Rev. **135**, 151 (1964).
[8] G. Meyer, F. Hartmann-Boutron, Y. Gros, and Y. Berthier, J. de Phys. **42**, 605 (1981).
[9] Yu. P. Irkin and E. V. Rozenfel'd, Izv. Akad. Nauk SSSR, Ser. Fiz. **52**, 1678 (1988).

Translated by M. E. Alferieff

Investigation of the effect of uniaxial pressure on antiferromagnetic resonance in $KFe_{11}O_{17}$ Crystals

V. N. Vasil'ev and E. N. Matveĭko

L. V. Kirenskiĭ Institute of Physics, Siberian Branch of the Russia Academy of Sciences, 660036 Krasnoyarsk, Russia

(Submitted September 30, 1997)
Fiz. Tverd. Tela (St. Petersburg) **40**, 513–515 (March 1998)

The deformation dependence of the resonance field in $KFe_{11}O_{17}$ single crystals was investigated by the AFMR method. The measurements were performed at $T=77$ K and $\nu=47.52$ GHz for two orientations of the external pressure. The experimental data are discussed in terms of a model of a very simple easy-plane antiferromagnet taking account of the elastic and magnetoelastic contributions to the thermodynamic potential. The magnetostriction, magnetoelastic, and elastic contants are calculated and the results are $\lambda=1.94\times10^{-5}$, $B_1=2.75\times10^8$ erg/cm^3, and $C_{11}-C_{12}=1.42\times10^{13}$ erg/cm^3, respectively. The values of these constants imply that the origin of the initial gap in the AFMR spectrum is not of magnetoelastic origin. © *1998 American Institute of Physics.* [S1063-7834(98)02403-4]

$KFe_{11}O_{17}$ has a hexagonal layered structure, belonging to the space symmetry group D_{6h}^4, like that observed in β-Al_2O_3.[1] Below the Néel temperature 800 K potassium ferrite is an easy-plane (EP) antiferromagnet.[2] In investigations of the orientational dependence of the low-frequency (LF) branch of the antiferromagnetic resonance (AFMR) in the basal plane of potassium ferrite crystals, it was observed that the amplitude and periodicity of the variation of the resonance field differed from sample to sample.[3] It was established that this is due to nonuniform strains induced in samples when they are glued to the quartz holder and to residual deformations arising when the solution in a melt cools during synthesis of the crystals. Moreover, the spectrum of the LF branch of AFMR has an isotropic energy gap, which, just as in other easy-plane antiferromagnets,[4] can be of magnetoelastic origin. For this reason, in the present work we investigated theoretically and experimentally the effect of uniaxial pressure on AFMR in potassium ferrite.

1. SAMPLES, EXPERIMENTAL CONDITIONS, AND RESULTS

The measurements were performed in an AFMR spectrometer with a pulsed magnetic field. The measuring section of the spectrometer was equipped with an apparatus that made it possible to apply a uniaxial pressure to the sample.[5] Single crystals grown by spontaneous crystallization from a solution in a melt[3] and prepared in the form of 1×0.3 mm rectangular wafers with plane parallel end planes were used as samples. To remove the induced residual strains, the samples were annealed for 7 h at 720 °C in air. The pressure on a sample placed in a quartz ampul was transmitted through a quartz rod. The ampul itself was placed inside a transmission-type resonator so that the sample was located at the antinode of the microwave field, whose flux lines were parallel to the applied pressure and perpendicular to the external magnetic field.

The deformation dependence of the LF AFMR was investigated at temperature 77 K and frequency 47.52 GHz for two orientations of the pressure relative to the crystallographic axes: $\mathbf{p}\|C_6$ and $\mathbf{p}\|C_2$, where C_6 is a six-fold principal axis of the crystal and C_2 is one of the two-fold axes passing through opposite sides of the hexagon characterizing the symmetry in the basal plane. In both cases the external magnetic field was oriented in the basal plane of the crystal along the other two-fold axis U_2, which was perpendicular to C_6 and C_2.

It was established that, to within the accuracy of the measurements, the pressure applied along the C_6 axis does not produce a shift of the resonance field, up to 4×10^8 dyn/cm^2. The figure displays the AFMR field versus pressure applied along C_2. This dependence can be described by a linear law.

2. DISCUSSION

The experimental data were analyzed using a phenomenological model of a two-sublattice antiferromagnet with

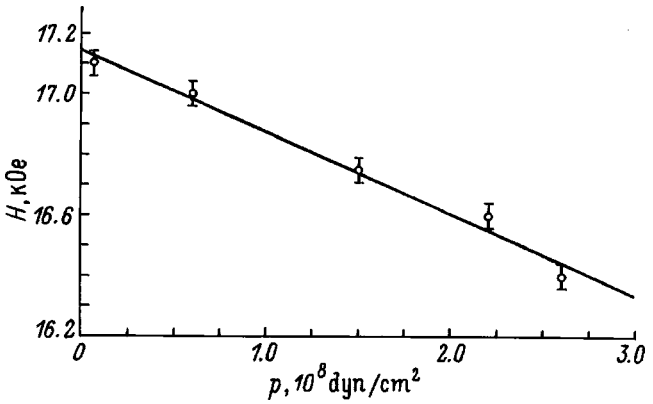

FIG. 1. Resonance field H versus external pressure p applied along one of the axes U_2.

 © 1998 American Institute of Physics

easy-plane magnetic anisotropy. The thermodynamic potential for the experimental crystal can be written, on the basis of symmetry considerations, in the form

$$F=F_M+F_{ME}+F_E+F_{ES}, \tag{1}$$

where

$$F_M=1/2(A\mathbf{m}^2)+1/2(a_1l_z^2)-\mathbf{m}\cdot\mathbf{h} \tag{2}$$

is the magnetic part of the thermodynamic potential, including the intersublattice exchange interaction, a second-order anisotropic invariant, and the Zeeman interaction, respectively, $\mathbf{m}=(\mathbf{M}_1+\mathbf{M}_2)/2M_0$ and $\mathbf{l}=(\mathbf{M}_1-\mathbf{M}_2)/2M_0$ are ferromagnetism and antiferromagnetism vectors, $\mathbf{M}_i$ are the sublattice magnetizations, $M_0=|\mathbf{M}_1|=|\mathbf{M}_2|$ is the saturation magnetization of the sublattices (the latter equalities are equivalent to the conditions $\mathbf{m}^2+\mathbf{l}^2=1$ and $\mathbf{m}\cdot\mathbf{l}=0$),

$$\begin{aligned}F_{ME}=&B_1(U_{XX}l_X^2+U_{YY}l_Y^2+2U_{XY}l_Xl_Y)+B_2\\&\times(U_{XX}+U_{YY})l_Z^2+B_3U_{ZZ}l_Z^2+B_4(U_{XZ}l_Xl_Z\\&+U_{YZ}l_Yl_Z)\end{aligned} \tag{3}$$

is the magnetoelastic part of the potential, B_i are magnetoelastic constants, u_{ij} are the strain,

$$\begin{aligned}F_E=&C_{11}(U_{XX}^2+U_{YY}^2)/2+C_{12}U_{XX}U_{YY}+C_{13}(U_{XX}U_{ZZ}\\&+U_{YY}U_{ZZ})+(C_{11}-C_{12})U_{XY}^2+C_{33}U_{ZZ}^2/2\\&+2C_{44}(U_{XZ}^2+U_{YZ}^2\end{aligned} \tag{4}$$

is the elastic part of the potential, C_{ij} are the elastic constants,

$$E_{ES}=-\sigma_{ij}U_{ij} \tag{5}$$

is the potential of the external stresses, $\sigma_{ij}=-|\mathbf{p}|\alpha_i\alpha_j$ is the stress tensor, and α_i and α_j are the direction cosines of the pressure vector. All phenomenological constants in the expression for the thermodynamic potential have the dimension of energy. The effective fields are expressed as follows: $H_E=A/2M_0$ is the effective exchange field, $H_{a2}=a_1/2M_0$ is the anisotropy field, $H=h/2M_0$ is the external magnetic field, and so on. The coordinate system of the problem was chosen so that $X\|U_2$, $Y\|C_2$, and $Z\|C_6$.

Let us examine the equilibrium states of the system for an external magnetic field directed along $U_2\|X$, using the standard procedure of minimizing the thermodynamic potential with respect to the components of the vectors $\mathbf{m}$ and $\mathbf{l}$ and the deformations u_{ij}. For the case $\mathbf{p}\|C_6$ ($\sigma=\sigma_{ZZ}$) we have

$$\begin{aligned}&m_{OY}=0,\quad m_{OZ}=0,\quad l_{OX}=0,\\&l_{OY}=(1-H_X^2/H_E^2)^{1/2},\quad l_{OZ}=0,\\&(U_{XX}-U_{YY})^{(0)}=B_1l_{OY}^2/(C_{11}-C_{12}),\\&U_{XY}^{(0)}=0,\quad U_{XZ}^{(0)}=0,\quad U_{YZ}^{(0)}=0,\\&U_{ZZ}^{(0)}=[B_1C_{13}l_{OY}^2+(C_{11}+C_{12})\sigma_{ZZ}]/\\&\qquad[C_{33}(C_{11}+C_{12})-2C_{13}].\end{aligned} \tag{6}$$

For the case $\mathbf{p}\|C_2$ ($\sigma=\sigma_{YY}$) we have

$$\begin{aligned}&m_{OX}=H_X/H_E,\quad m_{OY}=0,\quad m_{OZ}=0,\quad l_{OX}=0,\\&l_{OY}=(1-H_X^2/H_E^2)^{1/2},\quad l_{OZ}=0,\\&(U_{XX}-U_{YY})^{(0)}=(B_1l_{OY}^2-\sigma_{YY})/(C_{11}-C_{12}),\\&U_{XY}^{(0)}=0,\quad U_{XZ}^{(0)}=0,\quad U_{YZ}^{(0)}=0,\\&U_{ZZ}^{(0)}=(B_1C_{13}l_{OY}^2-C_{13}\sigma_{YY})/[C_{33}(C_{11}+C_{12})-2C_{13}].\end{aligned} \tag{7}$$

Solving the linearized Landau–Lifshitz equations for small uniform oscillations around a position of equilibrium and for an external magnetic field directed along the axis $U_2\|X$, we obtain for the characteristic frequencies of these oscillations

$$\begin{aligned}(\omega_1/\gamma)^2=&(1-H_{a1}/2H_E)H_X^2+2H_EB_1\\&\times(u_{XX}-u_{YY})^{(0)}l_{OY}^2,\end{aligned} \tag{8}$$

$$\begin{aligned}(\omega_2/\gamma)^2=&H_E[H_{a1}-2B_1U_{YY}^{(0)}+2B_2(u_{XX}-u_{YY})^{(0)}\\&+2B_3U_{ZZ}^{(0)}]l_{OY}^2.\end{aligned} \tag{9}$$

In what follows we shall be interested only in the LF branch of AFMR and the particular cases of the equilibrium states (6) and (7) that are realized in the experiment.

If $\mathbf{p}\|C_6$, then

$$(\omega_1/\gamma)^2=(1-H_{a1}/2H_E)H_X^2+2H_EH_{MS}, \tag{10}$$

where

$$H_{MS}=B_1^2/2M_0(C_{11}-C_{12})=\lambda_1B_1/2M_0 \tag{11}$$

is the effective magnetoelastic field of spontaneous deformations and $\lambda_1=B_1/(C_{11}-C_{12})$ is one of four magnetostriction constants. In this case the pressure does not affect the AFMR parameters of the crystal, but spontaneous deformations make an isotropic contribution $2H_EH_{MS}$ to the initial gap. The frequency–field relation (10) is formally identical to the experimentally observed relation

$$(\omega/\gamma)^2=(1-H_{a1}/2H_E)H_X^2+\Delta^2, \tag{12}$$

where $\Delta=4500$ Oe is the isotropic gap in the AFMR spectrum.

If $\mathbf{p}\|C_2$, then

$$(\omega_1/\gamma)^2=(1-H_{a1}/2H_E)H_X^2+2H_EH_{MS}+H_EH_\sigma, \tag{13}$$

where

$$H_\sigma=-B_1\sigma_{YY}/2M_0(C_{11}-C_{12})=-\lambda_1\sigma_{YY}/2M_0 \tag{14}$$

is the effective magnetoelastic field of the external stresses. In this case there is an external-pressure dependent additional anisotropic contribution $2H_EH_\sigma$ in the AFMR spectrum. It follows from Eqs. (13) and (14) that the external stress dependence of the resonance field has the form

$$\begin{aligned}H_X(\sigma)=&[H_X^2(0)-H_E\lambda_1|\sigma_{YY}|/2M_0(1-H_{a1}/2H_E)]^{1/2}\\\approx&H_X(0)-H_E\lambda_1|\sigma_{YY}|/2M_0H_X(0)\\&\times(1-H_{a1}/2H_E),\end{aligned} \tag{15}$$

i.e., just as in the case of rhombohedral easy-plane antiferromagnets,[4,5] it is an approximately linear function of the applied stress (pressure).

Thus, in both cases the experimental pressure dependence of the resonance field is in complete qualitative agreement with the theoretical dependence. Comparing the relation (15) with the experimental data in the figure, we estimated the magnetostriction constant as $\lambda_1 = 1.94 \times 10^{-5}$. In so doing, we use the computed value $M_0 = 706$ G of the sublattice saturation magnetization and the values $H_{a1}/2H_E = 0.031$ and $H_E = 2.75 \times 10^6$ Oe obtained from the resonance and static magnetic measurements.[3,6] Next, using the value obtained for λ_1 and making the assumption that the initial splitting in the LF AFMR spectrum is of a purely magnetoelastic origin (i.e., the frequency versus field relation in the absence of external stresses is described by Eqs. (10)–(11)), we estimated the magnetoelastic and elastic constants $B_1 = 2.75 \times 10^8$ erg/cm^2 and $C_{11} - C_{12} = 1.42 \times 10^{13}$ erg/cm^3. It is evident from the estimates presented that each constant is approximately an order of magnitude greater than its typical value for related crystalline oxide compounds.[7] If these typical values ($B_1 \sim 10^7$ and $C_{ij} \sim 10^{12}$) are substituted back into the expression for H_{ME}, then it is found that only a fraction $\sim 1/7$ of the experimentally observed magnitude of the gap can be attributed to the magnetoelastic coupling.

In summary, LF AFMR in potassium ferrite is indeed very sensitive to the interaction of the spin and elastic subsystems of the crystal, but the existence of an initial splitting in the AFMR spectrum cannot be explained only by the magnetoelastic interaction.

[1] C. A. Beevers and M. A. Ross, Z. Krist. **97**, 59 (1937).
[2] E. W. Gorter, J. Appl. Phys. **34**, 1253 (1963).
[3] V. N. Vasil'ev, E. N. Matveĭko, A. I. Kruglik, A. I. Pankrats, G. A. Petrakovskiĭ, and K. A. Sablina, Fiz. Tverd. Tela (Leningrad) **34**, 3047 (1992) [Sov. Phys. Solid State **34**, 1632 (1992)].
[4] A. S. Borovik-Romanov and E. G. Rudashevskiĭ, Zh. Éksp. Teor. Fiz. **47**, 2095 (1964) [Sov. Phys. JETP **20**, 1407 (1965)].
[5] A. I. Pankrats V. N. Vasil'ev, and G. A. Petrakovskiĭ, Fiz. Tverd. Tela (Leningrad) **19**, 1475 (1977) [Sov. Phys. JETP **19**, 860 (1977)].
[6] A. D. Valaev, V. N. Vasil'ev, and E. N. Matveĭko, Fiz. Tverd. Tela (St. Petersburg) **38**, 3427 (1996) [Phys. Solid State **38**, 1869 (1996)].
[7] E. V. Kuz'min, G. A. Petrakovskiĭ, and É. A. Zavadskiĭ, *The Physics of Magnetically Ordered Materials* [in Russian], Novosibirsk, 1976.

Translated by M. E. Alferieff

On the theory of quantum stochastic resonance in single-domain magnetic particles

É. K. Sadykov, A. G. Isavnin, and A. B. Boldenkov

Kazan' State University, 420008 Kazan', Russia
(Submitted July 29, 1997)
Fiz. Tverd. Tela (St. Petersburg) **40**, 516–518 (March 1998)

The phenomenon of stochastic resonance in a system of small magnetic particles with easy-axis anisotropy, where stochastic magnetization reversal in such particles occurs by macroscopic quantum tunneling of the magnetization, is investigated theoretically. An analytical model in the approximation of discrete orientations is proposed for calculating the dynamic (rf) susceptibility of easy-axis single-domain particles in a constant magnetic field applied perpendicular to the easy axis. The new contribution of this model lies in a more accurate description of quantum tunneling under conditions of rf modulation at temperatures close to absolute zero. The adequacy of the proposed approximation is checked by numerical modeling and by comparing the results with the published results on quantum tunneling and stochastic resonance. © *1998 American Institute of Physics.* [S1063-7834(98)02503-9]

1. Superparamagnetic particles with easy-axis (EA) anisotropy have been investigated previously[1,2] as systems that can exhibit a stochastic resonance (SR)[3]—a nonmonotonic dependence of the output signal of the system on an external periodic signal with monotonically increasing noise in the system. Thermal fluctuations of the magnetization were treated as a stochastic component of the dynamics of the system, and it was shown, specifically, that the dynamic magnetic susceptibility of such systems increases substantially in a certain temperature interval.[4] The idea of treating SR on the basis of quantum fluctuations of the magnetic moment vector in a single-domain particle under the influence of macroscopic quantum tunneling[6] was first suggested in Ref. 5. We note that quantum SR was also investigated in Ref. 7 for tunneling transitions in mesoscopic contacts. In the present paper we elaborate further the basic premises stated in Ref. 5 and we propose an analytical model for describing the dynamics of tunneling transitions of the magnetization vector through a potential barrier under the conditions of rf modulation of a bistable potential. We use this model to study quantum SR for magnetic particles at temperatures near absolute zero.

2. In a spherical coordinate system, the energy of the system—a single-domain particle with EA magnetic anisotropy—is given by

$$E(t)=Kv\ \sin^2\ \theta-\mu_0 HVv\ \sin\ \theta\ \cos\ \varphi + \mu_0(\pi/2)H_1 Mv\ \cos\ \theta\ \sin(\Omega t+\psi_0). \tag{1}$$

Here θ and φ are, respectively, the polar and azimuthal angles, K is the anisotropy constant, M and ν are, respectively, the saturation magnetization and the volume of the particle, $(\pi/2)H_1$ is the amplitude of the ac magnetic field, which is directed along the EA, and H is a constant magnetic field applied in a direction perpendicular to the easy axis of the particle. Such a constant field is necessary for the appearance of quantum fluctuations of the magnetization, since under conditions preserving the axial symmetry of the Hamiltonian the projection of the magnetization vector on the easy axis commutes with the Hamiltonian, i.e., quantum number is conserved and therefore tunneling is impossible.[6] The magnitude of this field determines the average subbarrier transition rate, i.e., the noise level in the system. The rate of tunneling of the magnetic moment vector out of a metastable state is determined by the extremal (Euclidean) action S_e in an imaginary time along the trajectory of the transition from one stable orientation to another[6]

$$W=\omega_0\ \exp(-S_e\hbar) = \omega_0 \exp\left(-i\int dt\{(Mv/\gamma)\dot{\varphi}\ \cos\ \theta - E(\theta,\varphi)\}/\hbar\right). \tag{2}$$

Here ω_0 is the frequency of attempts, which ordinarily is of the order of magnitude of the ferromagnetic resonance frequency $\omega_0 \sim 10^9-10^{10}\ \mathrm{s}^{-1}$, and γ is the gyromagnetic ratio. To obtain an analytical expression for the tunneling rate we consider the static metastable potential obtained by averaging over a half-period of the modulation,

$$E=Kv\ \sin^2\ \theta-\mu_0 HMv\ \sin\ \theta\ \cos\ \varphi + \mu_0 H_1 Mv\ \cos\ \theta. \tag{3}$$

The averaging must be performed over a half-period because during the other half-period of the modulation the potential is no longer metastable and the probability of tunneling through an infinitely wide barrier approaches zero, i.e., transitions from a lower to a higher minimum, are impossible at temperatures close to absolute zero.

3. The dynamics of the magnetic-moment vector is described by the Gilbert equation, which in a spherical coordinate system and neglecting dissipation is[6]

$$\dot{\theta}\ \sin\ \theta=(\gamma/Mv)\partial E/\partial\varphi,$$

 © 1998 American Institute of Physics

$$\dot{\varphi}\ \sin\ \theta = -(\gamma/Mv)\partial E/\partial\theta. \tag{4}$$

Substituting the expression (3) into the system (4) yields a second-order differential equation

$$d^2\theta/d\tau^2 = w_h^2\frac{H_c}{H}\cos\ \theta[1+(d\theta/d\tau)^2/w_h^2]^{1/2} - w_h^2\cos\ \theta[1+(d\theta/d\tau)^2/w_h^2] - w_h^2\frac{H_1}{H}[1+(d\theta/d\tau)^2/w_h^2]^{1/2}, \tag{5}$$

where $\tau = it$ is the imaginary time, $w_h = \gamma\mu_0 H$, and $H_c = 2K/\mu_0 M$.

In the limit $H \to H_c$ directions close to H correspond to stable orientations of the vector **M**. Making the substitution $\delta = \pi/2 - \theta \ll 1$, we obtain from Eq. (5)

$$d^2\delta/d\tau^2 = w_h^2(\delta^3 + H_1/H\delta^2 - 2\varepsilon\delta + 2H_1/H)/2,$$

$$\varepsilon = 1 - H/H_c \ll 1. \tag{6}$$

The solution of Eq. (6) in the limit of a low potential barrier is

$$\delta(\tau) = \delta_0 + \frac{2[(\delta_0-a)(\delta_0-b)]}{(a-b)\cosh[\{(\delta_0-a)(\delta_0-b)\}^{1/2}w_h\tau/2] - (2\delta_0-a-b)}, \tag{7}$$

where $\delta_0 = H_1/(3H_c) + 2[2\varepsilon/3]^{1/2}\cos(\Phi/3)$ is the position of the metastable minimum of the potential (3),[8] $\cos\Phi = -H_1/H_c[2/3\varepsilon]^{-3/2}$, $a = -2H_1/(3H) - \delta_0 + [4\varepsilon - 2\delta_0^2]^{1/2}$, and $b = -2H_1/(3H) - \delta_0 - [4\varepsilon - 2\delta_0^2]^{1/2}$. The system (3) remains bistable in perpendicular fields $H < H_{c1} = (1 - 3/2 \times [H_1/H_c]^{2/3})H_c$. The minimum action is given by

$$S_e = -\frac{1}{w_h}\left[\left(2(K-\mu_0 MH)v\varepsilon\left(\delta_0 + \frac{a+b}{2}\right) + \frac{2\mu_0 MH - K}{2}vC_1\right) \times \ln\left(\frac{a-b}{2\delta_0 - a - b + 2[(\delta_0-a)(\delta_0-b)]^{1/2}}\right) - \left(2(K-\mu_0 MH)v\varepsilon + \frac{2\mu_0 MH - K}{2} \times v\left(\frac{1}{3}\delta_0^2 + C_2\delta_0 + C_3\right)\right)[(\delta_0-a)(\delta_0-b)]^{1/2}\right], \tag{8}$$

where

$$C_1 = \delta_0^3 - (\delta_0/2 + 5(a+b)/12)ab + C_3(a+b)/2,$$

$$C_2 = \delta_0/2 + 5(a+b)/12,$$

$$C_3 = \delta_0^2 + 3\delta_0(a+b)/4 + 15(a^2+b^2)/24 + 7ab/12.$$

In Fig. 1 we present for comparison the computational results, obtained using different models and methods, for the dimensionless action $S_e/\hbar$ for tunneling out of a metastable minimum of the potential (3) in the limit $H \to H_c$. Thus, the curve *a* was obtained using our analytical expression (8). The curve *b* was obtained using the Zaslavskiĭ model.[9] In the present case, the two-dimensional problem (49) can be reduced to a one-dimensional problem by switching to the so-called effective potential. Since such an effective potential makes it possible to obtain only an approximate analytical expression for the action in the case of a small potential barrier, we constructed the curve *b* using the numerical solution of the corresponding problem without expanding the effective potential into a cubic parabola.[9] The curve *c* was constructed on the basis of our numerical solution of Eq. (5). The curve *d* reflects the result of the model proposed in Ref. 5. In such a model the rate of tunneling out of an asymmetric metastable potential can be expressed in terms of the rate of tunneling in a bistable symmetric potential[6] taking account of the correction introduced by the application of the field H_1.

4. Under the conditions of rf modulation, $H_1(t) = H_1 \sin\Omega t$, the rate of tunneling of the magnetic moment vector in a bistable potential at $T = 0$ K is a square wave

$$W(t) = \begin{cases} \omega_0\ \exp(-S_e/\hbar), & 2\pi m < \Omega t < (2m+1)\pi, \\ 0, & (2m+1)\pi < \Omega t < 2m\pi, \\ & m = 0,1,2,\ldots. \end{cases} \tag{9}$$

We propose as an analytical model the following expres-

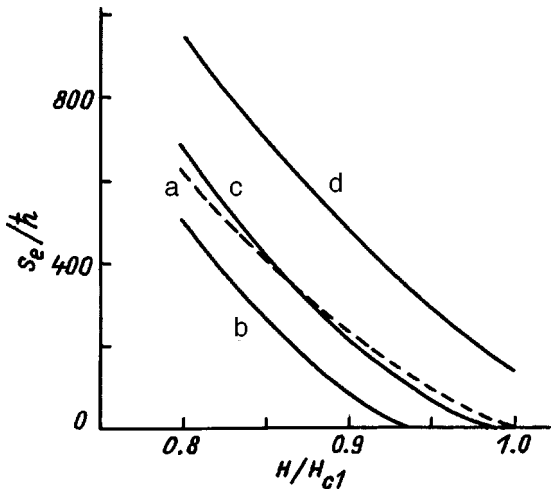

FIG. 1. Euclidean action versus constant field applied perpendicular to the easy axis of a single-domain iron particle. $K = 4\times10^4$ J/m^3, $M = 1.72\times10^6$ A/m, $H_1/H_c = 0.01$, $\nu = 10^{-26}$ m^3. a—Analytical result (8), b—result obtained in Ref. 9, c—result of our numerical calculations, d—result obtained in Ref. 5.

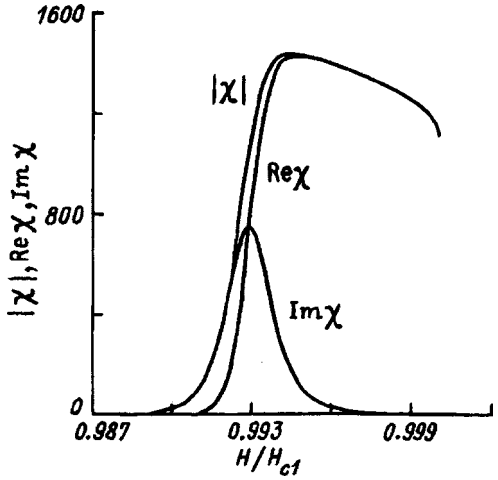

FIG. 2. Dynamic magnetic susceptibility and its components for a single-domain iron particle. The system parameters are the same as for Fig. 1; $\Omega = 10^5\ s^{-1}$.

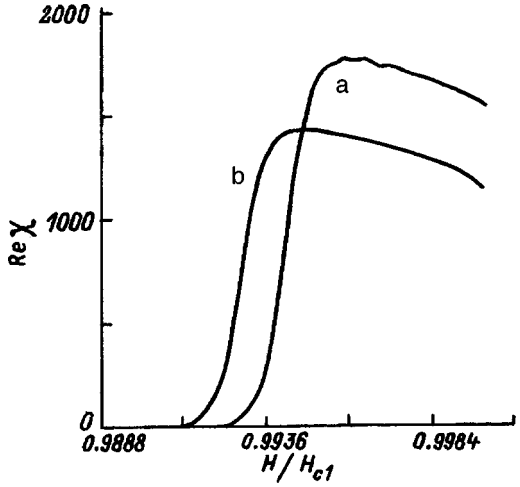

FIG. 3. Comparison of the numerical results and the analytical expression (10). The system parameters are the same as in Fig. 1. a—Numerical result, b—analytical result (12).

sion for the dynamical transition rate (9), i.e., the rate of subbarrier transitions in the modulated bistable system:

$$W(t) = \omega_0 \exp(-S_e/\hbar)(1+\sin \Omega t)/2 = 1/2(W_0 + W_0 \sin \Omega t). \quad (10)$$

Having obtained an analytical expression for the subbarrier transition rate, we employ next the apparatus of the control equation describing the dynamics of a bistable system:

$$\frac{dn_+}{dt} = -\frac{dn_-}{dt} = W_-(t)n_- - W_+(t)n_+ = W_-(t) - [W_-(t) + W_+(t)]n_+ . \quad (11)$$

Here $n_\pm$ is the probability that the discrete dynamical variable $x = M \cos \theta$ assumes a value corresponding to one of the minima (+ or −) of the bistable potential and $W_\pm(t)$ is the rate of tunneling out of the $\pm$ states. This control equation can be solved exactly in the quasiadiabatic limit.[3]

On the basis of Refs. 3 and 4 we write expressions determining the dynamic magnetic susceptibility of the system

$$\mathrm{Re}\ \chi = \frac{M \sin \delta_0 W_0^2}{H_1(W_0^2+\Omega^2)}, \quad \mathrm{Im}\ \chi = \frac{M \sin \delta_0 W_0 \Omega}{H_1(W_0^2+\Omega^2)},$$

$$|\chi| = \frac{M \sin \delta_0 W_0}{H_1(W_0^2+\Omega^2)^{1/2}}. \quad (12)$$

The curves presented in Fig. 2 reflect the dynamic magnetic susceptibility as a function of the perpendicular field H.

We also solved the control equation (11) numerically for the square-wave tunneling rate (9) calculated with a time varying energy of the system (1). The results (Fig. 3) confirm the validity of the model (10) describing the tunneling rate in the case of external modulation. In calculating the components of the dynamic magnetic susceptibility near absolute zero temperature, the model (10) gives results which are at least an order of magnitude greater than those obtained using the model proposed in Ref. 5.

5. In conclusion, we note that subbarrier tunneling of magnetization reversal appears only at temperatures below a critical value which is ordinarily determined from the relation $T_c \sim \hbar U/S_e k$,[6] where U is the height of the potential barrier and k is Boltzmann's constant. Usually, this critical temperature does not exceed tenths of a Kelvin. To study stochastic resonance at nonzero, finite temperatures it is necessary to take into account the possibility of tunneling not only from the bottom of the potential well but also from higher levels.

Together with that described in Ref. 5, a possible experimental method for observing the predicted effects is to use the SQUID-based apparatus, similar to that used in Ref. 10.

[1] É. K. Sadykov, Fiz. Tverd. Tela (Leningrad) **33**, 3302 (1991) [Sov. Phys. Solid State **33**, 1544 (1991)].
[2] É. K. Sadykov and A. I. Skvortsov, JETP Lett. **52**, 113 (1990).
[3] B. McNamara and K. Wiesenfeld, Phys. Rev. A **39**, 4854 (1989).
[4] É. K. Sadykov and A. G. Isavnin, Fiz. Tverd. Tela (St. Petersburg) **36**, 3473 (1994) [Phys. Solid State **36**, 1843 (1994)].
[5] A. N. Grigorenko, V. I. Konov, and P. I. Nikitin, JETP Lett. **52**, 593 (1990).
[6] E. M. Chudnovsky and L. Cunther, Phys. Rev. Lett. **60**, 661 (1988).
[7] R. Lofstedt and S. N. Coppersmith, Phys. Rev. Lett. **72**, 1974 (1994).
[8] E. Madelung, *Die Mathematischen Hilfsmittel des Physikers*, Springer, Berlin, 1964, 7th edition [Russian translation, Moscow, 1961].
[9] O. B. Zaslavskii, Phys. Rev. B **42**, 992 (1990).
[10] W. Wernsdorfer, K. Hasselbach, D. Mailly, B. Barbara, A. Benoit, L. Thomas, and G. Suran, J. Magn. Magn. Mater. **145**, 33 (1995).

Translated by M. E. Alferieff

Microkinetics of the Ising–Glauber model in the binary approximation

V. A. Murav'ev, V. M. Vorob'ev, and A. S. Garevskiĭ

Nizhegorod State University, 603600 Nizhniĭ Novgorod, Russia
(Submitted October 2, 1997)
Fiz. Tverd. Tela (St. Petersburg) **40**, 519–523 (March 1998)

Phase transitions in ferromagnets described by the Ising model are investigated in terms of the solution of a hierarchy of microscopic equations for unary and binary distribution functions. A dynamical procedure for making the equations self-consistent is developed. For cubic crystals, an equation of state relating the long-range order parameter to temperature and magnetic field is obtained in analytic form. The temperature dependence of the magnetic susceptibility and of the specific heat are calculated. A stability criterion is obtained for the stationary states of the system is obtained. The dynamics of magnetization reversal by constant and ac external fields are investigated. © *1998 American Institute of Physics.* [S1063-7834(98)02603-3]

Interesting results concerning the micro- and macrokinetics of second-order phase transitions were obtained even in the early works which were devoted to the study of the stochastic dynamics of such transitions in the Ising model. Some of these results were described by Glauber[1,2] in the mean-field approximation.

In years following, interest in the approximate microkinetic approach in the theory of phase transitions waned somewhat as a result of the development of field-theoretic methods for solving this problem (renormalization-group and ε-expansion methods[3]). However, the exact results obtained by modern methods describe the situation only near the critical point. The microkinetic approach, on the other hand, makes it possible to describe, about approximately, the entire picture and not only in the state of thermodynamic equilibrium.

In the present paper we propose a method for solving self-consistently a hierarchy of coupled equations for the low-order distribution functions. This approach is similar to the Bogolyubov method in the kinetic theory of the liquid state and is, of course, approximate, since we do not work with the complete distribution function of the spins over the lattice sites and we truncate the hierarchy at the binary functions. We employed this technique earlier to study the correlation effects of diffusion in semiconductors.[5–9]

For conceptual clarity, we expound the essentials of the procedure for the example of a cubic lattice.

1. MICROKINETIC EQUATIONS AND SELF-CONSISTENCY PROCEDURE

For a microscopic description of the state of the crystal, we introduce the distribution functions p^{α} and $f^{\alpha\beta}$. The unary function p^{α} gives the probability of observing a spin α at a lattice site and the binary function $f^{\alpha\beta}$ determines the probability of finding a pair of spins α and β at adjacent sites. The indices $\alpha, \beta, \gamma, \cdots$ assume the values $+$ and $-$, corresponding to spins $+1$ and -1.

The functions p^{α} and $f^{\alpha\beta}$ are related by the obvious normalization conditions

$$p^{+}+p^{-}=1, \quad f^{\alpha+}+f^{\alpha-}=p^{\alpha}, \quad f^{+\beta}+f^{-\beta}=p^{\beta}. \tag{1}$$

We take as the independent functions, for example, $p^{+}\equiv P$ and $f^{++}\equiv S$. We express the remaining functions from Eq. (1) as

$$p^{-}=1-P, \quad f^{+-}=f^{-+}=P-S,$$
$$f^{--}=1-2P+S. \tag{2}$$

We shall assume that the stochastic dynamics of the system, which is determined by the interaction of the system with a thermostat, can be described by random spin flips. Following Suzuki and Kubo,[2,10] we represent the spin-flip probability Ω per unit time as

$$\tau\Omega=\frac{1}{1+\exp(\Delta E)}, \tag{3}$$

where τ is the characteristic flip time and $\Delta E=E_f-E_i$ is the increment to the energy of the crystal as a result of such a flip (here and below all energy parameters are given in units of kT).

The equation expressing the balance of probabilities for the unary function is

$$\tau\dot{P}=\Omega_{-}p^{-}-\Omega_{+}p^{+}=\frac{1-P}{1+\exp(\Delta E)}-\frac{P}{1+\exp(-\Delta E)}. \tag{4}$$

To calculate E_f and E_i, strictly speaking, one would have to sum the probabilities of all possible spin configurations in the environment surrounding a given site, multiplied by the corresponding binding energies. However, this path requires introducing higher-order distribution functions, which makes solving the problem virtually hopeless.

Instead, we introduce the effective interaction energies φ_{α} for a known spin α with its environment per bond and we denote their difference by $\psi=\varphi_{+}-\varphi_{-}$. In this notation $E_f=Z\varphi_{+}-JH$, $E_i=Z\varphi_{-}+JH$, and $\Delta E=Z\psi-2JH$. Here Z

 © 1998 American Institute of Physics

is the coordination number, $J=\Upsilon/kT$ is the dimensionless exchange integral, $H=\mu h/\Upsilon$ is the dimensionless magnetic field (whose direction is the same as that of the + spin), and μ is the magnetic moment of an atom.

Let us now turn to the equation expressing the balance of probabilities for the binary function

$$\tau\dot{S}=\Omega_{-+}f^{-+}-\Omega_{++}f^{++}+\Omega_{+-}f^{+-}-\Omega_{++}f^{++}$$
$$=2\left(\frac{P-S}{1+\exp(\delta E)}-\frac{S}{1+\exp(-\delta E)}\right), \quad (5)$$

where $\delta E=-2J+(Z-1)\psi-2JH$. This formula differs from the expression for ΔE by the fixed orientations of two spins.

The system of equations (4) and (5) is still not closed, since it contains the two unknown functions P and S and the undefined self-consistency parameter ψ.

The missing equation can be obtained from the following considerations. The structure of the right-hand sides of the probability balance equations must be consistent with the normalization conditions. Therefore the relation

$$\tau\frac{d}{dt}(f^{--})=\Omega^{-+}f^{-+}-\Omega^{--}f^{--}+\Omega^{+-}f^{+-}-\Omega^{--}f^{--}$$
$$=2\left(\frac{P-S}{1+\exp(-\delta F)}-\frac{1-2P+S}{1+\exp(\delta F)}\right)$$
$$\equiv\tau\frac{d}{dt}(1-2P+S), \quad (6)$$

where $\delta F=2J+(Z-1)\psi-2JH$, must be satisfied. The derivatives $\dot{S}$ and $\dot{P}$ on the right-hand side of Eq. (6) are determined by Eqs. (4) and (5), and we therefore obtain the algebraic equation

$$\frac{P}{1+\exp(\delta E)}+\frac{1-P}{1+\exp(\delta F)}=\frac{1}{1+\exp(\Delta E)}, \quad (7)$$

which determines ψ implicitly as a function of P, J, and H. This completes the self-consistency procedure for the system of microkinetic equations. We call this system dynamic because the problem now reduces to analyzing the two ordinary differential equations (4) and (5), supplemented by the algebraic equation (7), which together describe the kinetics of a ferromagnet.[1)]

Despite the strong nonlinearity of this system, the problem nonetheless can be solved in quadratures. Indeed, the function $P(\psi)$ can be easily found from Eq. (7) (for any values of the thermodynamic parameters J and H), after which Eq. (4) becomes

$$\tau\frac{dP}{d\psi}\dot{\psi}+P(\psi)=\frac{1}{1+\exp(\Delta E)}. \quad (8)$$

Separating variables here makes it possible to find the function $t(\psi)$ in the form of an integral. The function $P(t)$ is thereby determined in a parametric form (ψ is the parameter). However, it is more convenient here to solve the equations numerically. We note that the dynamics of long-range order, determined by the function $P(t)$, does not depend on the behavior of the parameter $S(t)$ (characterizing the short-range order). The behavior of the function $S(t)$, however, is described by the linear differential equation (5).

2. STATIONARY SOLUTION

Let $\dot{P}=0$ and $\dot{S}=0$. Then the system of equations (4), (5), and (7) acquires the form

$$P=\frac{1}{1+\exp(Z\psi-2JH)}, \quad (9)$$

$$S=\frac{P}{1+\exp((Z-1)\psi-2J(H+1))}, \quad (10)$$

$$\frac{P-S}{1-P}=\frac{1}{1+\exp((Z-1)\psi-2J(H-1))}. \quad (11)$$

Let us consider first the case when $H=0$. It is immediately seen that this system always possesses the trivial solution

$$\psi=0, \quad P=\frac{1}{2}, \quad S=\frac{1}{2(1+\exp(-2J))}. \quad (12)$$

The long-range order parameter defined as $L=2P-1$ then equals zero. Such a solution exists for any temperature, but it is not always stable, as will be shown below.

This system also possesses a nontrivial solution, which can be easily found by eliminating ψ, specifically,

$$S(L)=\frac{L(1+L)^m}{(1+L)^m-(1-L)^m}, \quad m=\frac{2(Z-1)}{Z}, \quad (13)$$

$$\exp(4J)=\frac{4S(S-L)}{(1+L-2S)^2}. \quad (14)$$

The last two expressions determine the dimensionless temperature $\Theta\equiv 1/J$ as a function of L, i.e., they solve the problem of spontaneous magnetization. It is obvious that the second solution will be stable below the Curie point Θ_c. This point is found as follows. Expanding the indefinite term in Eq. (13) in the limit $L\to 0$, we obtain $S(0)\to Z/4(Z-1)$. But this value must agee with the expression (12) for $J=J_c=1/\Theta_c$. Hence

$$\Theta_c=\frac{2}{\ln(Z/(Z-2))}. \quad (15)$$

Of course, the same result is also obtained from Eq. (14). The present result is identical to that obtained in the Bethe–Peierls (BP) approximation,[11–13] but the agreement ends here; in our case, the temperature dependences $L(\Theta)$ and $S(\Theta)$ below Θ_c differ somewhat from BP, specifically, by the fact that we have the explicit function $\Theta(L)$. Above Θ_c the agreement of the curves with BP is complete.

In the general case, $H\neq 0$, we proceed similarly: Eliminating ψ from Eqs. (4), (5), and (7) we arrive at the relation

$$S(L,H,J)=\frac{L(1+L)^m}{(1+L)^m-(1-L)^m\exp(-4JH/Z)}. \quad (16)$$

Let us solve Eq. (14) for S^2

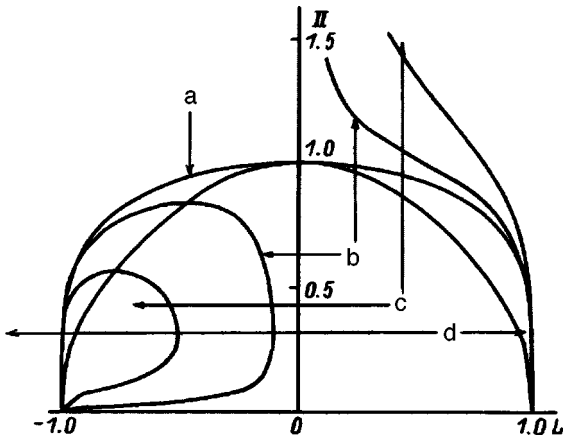

FIG. 1. Curves of the equation of state for external fields $H=0$ (a) 0.2 (b), and 1 (c). d—Spinodal curve. $Z=6$.

$$S(L,J)=\frac{1}{2K}(1+KL-\sqrt{(1+KL)^2-K(1+L)^2}). \quad (17)$$

Here, for conciseness, we have set $K=1-\exp(-4J)$.[2)]

Equating the expressions (16) and (17), we obtain the equation of state of a ferromagnet. This equation provides an implicit relation between Θ, L, and H. The numerical results for the temperature $\Pi\equiv\Theta/\Theta_c$ as a function of L are displayed in Fig. 1.

It is obvious that hysteresis exists in the system, since three values of the magnetization exist at sufficiently low temperatures. It will be shown below that one of these values is absolutely unstable and another is metastable.

3. MAGNETIC SUSCEPTIBILITY AND SPECIFIC HEAT

Let us solve Eq. (16) for the field factor

$$\exp\left(\frac{-4JH}{Z}\right)=\left(\frac{S-L}{S}\right)\left(\frac{1+L}{1-L}\right)^m. \quad (18)$$

Differentiating this expression with respect to H, we obtain for the reciprocal of the magnetic susceptibility $\chi^{-1}|_{H=0}=\partial H/\partial L$ the relation

$$-\frac{4J}{Z}\chi^{-1}=\left(\frac{1+L}{1-L}\right)^m\left(\frac{LS_L-S}{S^2}+\frac{2m(S-L)}{S(1-L)^2}\right), \quad (19)$$

where

$$S_L=\frac{\partial S}{\partial L}=\frac{1}{2}\left(1-\frac{L(K-1)}{2\sqrt{(1+KL)^2-K(1+L)^2}}\right).$$

These expressions simplify substantially for $\Theta>\Theta_c$

$$\chi^{-1}=\Theta\left[1+\frac{Z}{2}\left(\exp\left(\frac{-2}{\Theta}\right)-1\right)\right].$$

Hence one can see [taking account of Eq. (15)] that $\chi^{-1}=0$ for $\Theta=\Theta_c$, while $\chi^{-1}\approx\Theta$ as $\Theta\to\infty$, in complete accord with the Curie–Weiss law.

It can also be shown that the temperature curve of the reciprocal of the susceptibility to the left of Θ_c is two times steeper than to the right of Θ_c. This result is in complete agreement with the predictions of the Landau theory.[14]

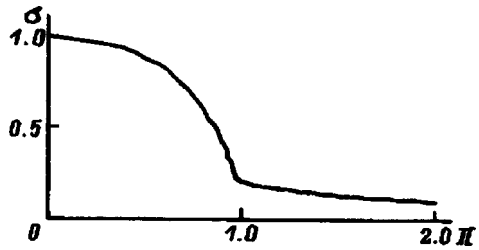

FIG. 2. Parameter σ as a function of temperature with $Z=6$, $H=0$.

We shall now briefly discuss the question of the specific heat. At $H=0$ the energy of the system and the specific heat C per spin (in the conventional units) are given by the expressions

$$E=(1/2)Z\Upsilon(f^{++}+f^{--}-2f^{+-})=Z\Upsilon(2S-L-1/2),$$

$$C=\frac{dE}{dT}=kZ\frac{d}{d\Theta}(2S-L)=kZ\frac{d}{d\Theta}\left(\frac{1+\sigma}{2}\right), \quad (20)$$

where $\sigma\equiv f^{++}+f^{--}-2f^{+-}=1+4(S-P)$ is the short-range order parameter. Figure 2 shows the function $\sigma(\Pi)$, calculated according to Eqs. (16) and (17) for $\Pi<1$ [for $\Pi>1$ it is simply the function (12). One can see that the curve has an inflection at the critical point.[12] According to Eq. (20), this means that the specific heat undergoes a jump at the transition through Θ_c. The relative magnitude of the jump equals $\Delta C/C_c=3(Z-1)$, where C_c is the specific heat to the right of Θ_c.

4. KINETICS OF NONEQUILIBRIUM PROCESSES

Turning now to the dynamic aspects of the problem, let us examine the behavior of the system for small deviations from equilibrium. We write the dynamical variables in the form $\tilde{L}=L+x$, $\tilde{S}=S+y$, $\tilde{\psi}=\psi+u$, where x, y, and u are small corrections to the equilibrium values of L, S, and ψ, and linearize the system (4), (5), and (7). Using Eqs. (9)–(11) we obtain

$$\tau\dot{x}+a_{11}x=0, \quad (21)$$

$$\tau\dot{y}+a_{22}y+a_{21}x=0, \quad (22)$$

where[3)]

$$a_{22}=2,$$

$$a_{11}=\frac{2(L+1-2S)[(L+1)(Z+(Z-2)L)-4(Z-1)S]}{Z(1-L^2)^2+4(Z-1)(L+1-2S)(L(1+L)-2S)}.$$

The equations (21) and (22) do not contain u because of the linear relation $u\sim x$ following from Eq. (7).

The determinant of the coefficients of this system is $\Delta=a_{11}a_{22}$, and the roots of the characteristic equation are $\lambda_1=-a_{11}$ and $\lambda_2=-a_{22}$. Under these conditions, the types of singularities in the phase plane (L,S) and hence the character of the stationary solutions are determined only by the sign of a_{11}. The stability criterion $a_{11}>0$ for a stationary state becomes

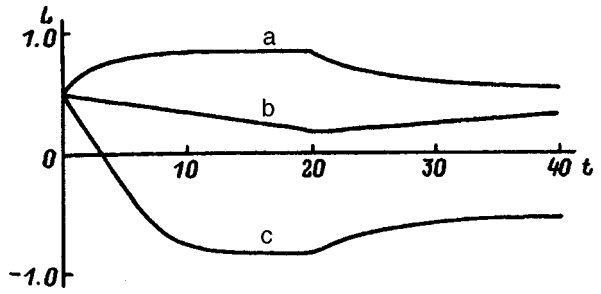

FIG. 3. Magnetization reversal curves for external fields $H=1$ (a), -0.15 (b), and -1 (c). $Z=6$.

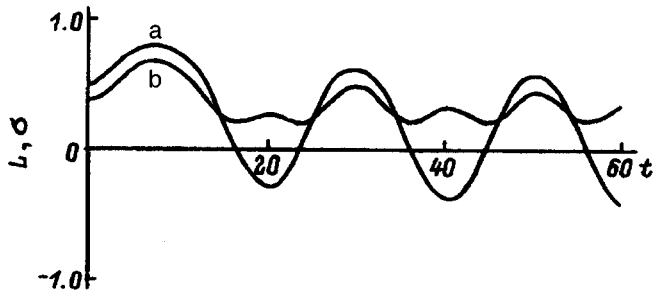

FIG. 5. Dynamics of long- and short-range orders in a periodic field. a—$L(t)$, b—$\sigma(t)$. $Z=6$, period $T_0=20\tau$.

$$S<\frac{(L+1)(Z+(Z-2)L)}{4(Z-1)}. \tag{23}$$

We note here that the quantity τ/a_{11} is the characteristic relaxation time of long-range order, which increases without bound near Θ_c (critical retardation[14]). At a transition through the critical point a_{11} changes sign. The types of singularities also change at the same time: When the condition (23) holds, the singularities are stable nodes, otherwise they are saddle-points (where the angular coefficients of the separatrices are $k_1=0$ and $k_2=1$). The change in form occurs via a complicated ''saddle–node'' singularity, which lies at the apex of the left-hand closed loop, separating stable and unstable states of the system (Fig. 1). The formula (23) together with Eq. (14) determine the region of metastable states corresponding to the left-hand sections of the loop-shaped curves in Fig. 1. The curve d passing through the apex of the loops and separating the metastable region from the region of absolute instability can be called spinodal (by analogy to this concept in the theory of solid solutions[15]). This analogy is valid because of the isomorphic nature of the Ising model, making it possible to describe both ferromagnets and decomposing solid solutions in an identical manner.[16] Here, the degree of deviation of the crystal from a stoichiometric composition is the analog of the magnetic field.

In Sec. 1 we indicated that the dynamic problem can in principle be solved in quadratures, but the integrals arising here cannot be calculated and it is necessary to resort to numerical modeling. As an example let us take a system in a state of spontaneous magnetization $L_0=0.5$ and let us study its behavior under the action of a square-shaped magnetic field pulse with duration $t_0=20$ (time is measured in units of τ). The processes occurring here are illustrated in Figs. 3 and 4. The curves shown were obtained by simultaneously numerically integrating Eqs. (8) and (5) for the functions $\psi(t)$ and $\sigma(t)$; the expression for $L(t)$ was calculated at each step according to Eq. (7).

We note the following features. The characteristic magnetization reversal time is ≈ 10 at the temperature chosen. This time, of course, depends on the starting value of L_0 and hence the temperature, increasing as the Curie temperature is approached. It is noteworthy that in a weak field $H=-0.15$ magnetization reversal does not occur and $L(t)$ only decreases. This is what makes it possible to talk about the metastability of the states. The nonmonotonicity of the curve $\sigma(t)$ with $H=-1$ is also interesting.

We underscore once again that in the binary approximation the long-range order dynamics completely dictates the short-range order dynamics.

Figures 5 and 6 show the behavior of the parameters L and σ under the action of an ac field $H=H_0\sin(2\pi t/T_0)$, where T_0 is the period of the field and $H_0=1$. One can see that the character of the process depends on the period, as expected, bearing in mind the processes shown in Figs. 3 and 4. A run for long times leads to a periodic state.

In summary, although more accurate methods for performing an approximate calculation of the critical parameters, for example, the Kikuchi technique,[17,18] do exist now, the microkinetic approach to the problem seems promising to us mainly because of the possibility of analyzing the dynamics of critical phenomena.

The method developed can also be extended to the nonuniform situation, where the order parameter depends on the position and time. This possibility is especially interesting in

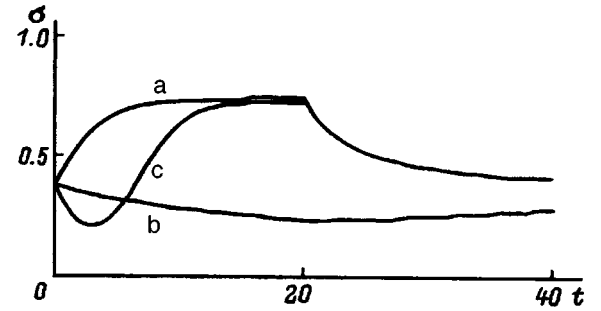

FIG. 4. Dynamics of short-range order σ for external fields $H=1$ (a), -0.15 (b), and -1 (c). $Z=6$.

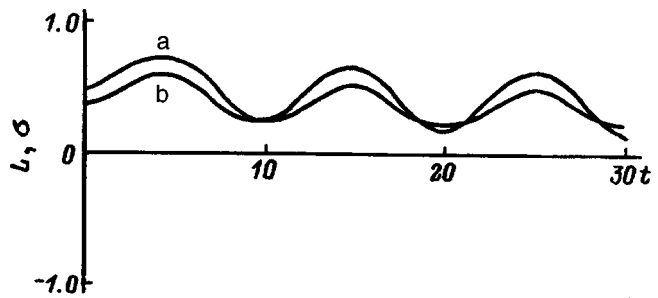

FIG. 6. Dynamics of long- and short-range orders in a periodic field. a—$L(t)$, b—$\sigma(t)$. $Z=6$, period $T_0=10\tau$.

connection with the description of spinodal decomposition and order–disorder phase transitions in binary alloys.

We also call attention to the obvious possibility of improving the method by including higher-order distribution functions in the chain of microkinetic equations.

This work was supported in part by the Russian Fund for Fundamental Research (Grant 96-02-18852).

[1)]It is easy to verify that the equations of stochastic dynamics for the functions f^{+-} and f^{-+} are identical to the equations following from Eqs. (4)–(6).

[2)]The sign in front of the square root in Eq. (17) is chosen so that $S \to 1/4$ is obtained in the limit $\Theta = 1/J \to \infty$.

[3)]We do not write out the coefficient a_{21}, since it is not required below.

[1] R. J. Glauber, J. Math. Phys. **4**, 294 (1963).
[2] H. Stanley, *Introduction to Phase Transitions and Critical Phenomena* [Clarendon Press, Oxford, 1971; Mir, Moscow, 1973].
[3] S. Ma, *Modern Theory of Critical Phenomena* [Benjamin, Reading, MA, 1976; Mir, Moscow, 1980].
[4] N. N. Bogolyubov, J. de Boer and G. E. Uhlenbech (Eds.), in *Studies in Statistical Mechanics*, Vol. 1, Wiley, New York, 1961; Moscow State University Press, Moscow, 1979.
[5] V. A. Murav'ev and V. A. Panteleev, Fiz. Tverd. Tela (Leningrad) **20**, 3245 (1978) [Sov. Phys. Solid State **20**, 1871 (1978)].
[6] V. A. Murav'ev and V. A. Panteleev, Fiz. Tverd. Tela (Leningrad) **21**, 1663 (1979) [Sov. Phys. Solid State **21**, 954 (1979)].
[7] V. A. Murav'ev and V. A. Panteleev, Fiz. Tverd. Tela (Leningrad) **22**, 780 (1980) [Sov. Phys. Solid State **22**, 455 (1980)].
[8] V. M. Vorob'ev, V. A. Murav'ev, and V. A. Panteleev, Fiz. Tverd. Tela (Leningrad) **23**, 1125 (1981) [Sov. Phys. Solid State **23**, 653 (1981)].
[9] V. M. Vorob'ev, V. A. Murav'ev, and V. A. Panteleev, Izv. Akad. Nauk SSSR, Neorg. Mater. **18**, 1765 (1982).
[10] K. Binder (Ed.), *Monte Carlo Methods in Statistical Physics*, Springer, Berlin, 1979; G. I. Marchuk and G. A. Mikhaĭlov [Eds.], *Monte Carlo Methods in Statistical Physics* [Russian translation], Mir, Moscow, 1982.
[11] L. A. Girifalco, *Statistical Physics of Materials*, Wiley, N.Y., 1973 [Mir, Moscow, 1975].
[12] S. V. Vonsovskiĭ, *Magnetism* [Wiley, N.Y., 1974; Nauka, Moscow, 1971].
[13] K. Huang, *Statistical Mechanics* [Wiley, N.Y., 1963; Mir, Moscow, 1966].
[14] L. D. Landau and E. M. Lifshitz, *Statistical Physics*, Pergamon Press, N.Y. (1980).
[15] K. Binder, in *Synergetics* [Russian translation], Mir, Moscow, 1984.
[16] F. Dyson, E. Montroll, M. Kac, and M. Fisher, *Stability and Phase Transitions* [Russian translation], Mir, Moscow, 1973.
[17] R. Kikuchi, Suppl. Prog. Theor. Phys. **35**, 1 (1966).
[18] J. Ziman, *Models of Disorder*, Cambridge University Press, N.Y., 1979; Mir, Moscow, 1966].

Translated by M. E. Alferieff

Observation of diamagnetic domains in beryllium

V. S. Egorov, E. P. Krasnoperov, F. V. Lykov, and U. Zimmermann

Russian Science Center ''Kurchatov Institute,'' 123182 Moscow, Russia

G. Solt, C. Baines, and D. Herlach

Paul Scherrer Institute CH-5232, Villigen, Switzerland
(Submitted October 9, 1997)
Fiz. Tverd. Tela (St. Petersburg) **40**, 524–526 (March 1998)

We have observed diamagnetic domains (Condon domains) in a beryllium single crystal in magnetic fields $H \leqslant 3$ T ($\mathbf{H} \| [0001]$) at liquid-helium temperatures. The formation of the domain structure was determined according to magnetic-breakdown quantum oscillations of the resistance thermoelectric power as well as according to the splitting of the resonance peak of the free spin precession frequency of muons (μSR). The alternation of a uniform state (with one μSR peak) and a state with domain structure (with two peaks) is consistent as regards the periodicity with the de Haas–van Alphen effect, the period is $\Delta H \cong 78$ Oe, and the range of existence of domains and the difference in their magnetizations are $\Delta B = 4\pi\Delta M = B_2 - B_1 \cong 30$ Oe. © *1998 American Institute of Physics.* [S1063-7834(98)02703-8]

The question of the appearance of diamagnetic domains was first considered by Condon.[1] Under the conditions such that narrow Landau levels form, for which the value of $\hbar/\tau$ is much less than the splitting $\hbar\omega_c$ between the levels, i.e., $\omega_c\tau \gg 1$, and at low temperatures, for which $kT < \hbar\omega_c$, oscillations corresponding to the extremal sections of the Fermi surface arise in the energy spectrum of the metal. As a result, the energy $\varepsilon(B)$ of the electron gas oscillates as a function of the magnetic field, and oscillations of the magnetic moment $M = -\partial\varepsilon/\partial B$, i.e., the de Haas–van Alphen (dHvA) effect, are observed in experiments. Since the induction B in a sample with demagnetizing factor $N \cong 0$ differs from the external magnetic field H by the amount $4\pi M$, in an experiment one observes instead of a harmonic signal $M(B)$, as follows from the Lifshitz–Kosevich theory,[2] an oscillating signal $M(H)$ whose amplitude is the same and whose shape approaches a saw-tooth shape as the amplitude increases. The rising sections with a paramagnetic sign of the differential susceptibility ($dM/dH > 0$) become steeper and the sections with a diamagnetic sign ($dM/dH < 0$) become flatter. Shoenberg, analyzing his measurements of the dHvA effect in precious metals, was the first to call attention to this.[3]

The period P of the oscillations in the dHvA effect is constant in the reciprocal magnetic field and is determined by the area A of the extremal section of the Fermi surface according to the Lifshitz–Onsager formula $P^{-1} = F = (c\hbar/2\pi e)A$, where F is the magnetic frequency of the oscillations. Depending on the magnetic field H, the n-th period of the oscillations decreases as $\Delta H_n = F/n^2 = H^2/F$ (n is the number of the Landau level). Therefore, the differential susceptibility $|\partial^2\varepsilon/\partial B^2|$ increases with decreasing H and at some magnetic field (and in weaker fields) it can exceed $1/4\pi$. This means that the region ΔB of values of the magnetic field close to this maximum of $\varepsilon(B)$ becomes a region of absolute instability and is not realized in the sample at all, while a corresponding jump $4\pi\Delta M = \Delta B$ is observed experimentally. The signal $M(H)$ becomes completely saw-toothed, and only sharp positive peaks are present in dM/dH.[3] In other words, as the external magnetic field H is continuously scanned, the induction in the sample ''is held back'' near values of B corresponding to the minimum of the energy $\varepsilon(B)$, while the regions ΔB near the maxima ''slip through'' on account of the abrupt change in magnetization.

At first glance, however, this may not happen, if the sample is plate-shaped and arranged perpendicular to the magnetic field. Such a sample can not longer be magnetized uniformly so that the values of B would correspond to a minimum of the energy, since the boundary condition $B = H$ must also be satisfied. In the region of instability $\delta H = \Delta B$ in question, it is found that all values of B within this range are also absent, and the metal separates into domains with the extreme values B_1 and B_2 of this range ($B_2 - B_1 = \Delta B$), so that the condition $B = H$ holds on the average, i.e., as H varies, only the ratio of the phase volumes with constant values of B_1 and B_2 changes.[1]

The first direct experimental observation of domains of this kind was made by Condon and Walstedt.[4] Nuclear magnetic resonance (NMR) was measured in a silver plate arranged perpendicular to the magnetic field. The appearance of domains was established according to the beat signal corresponding to splitting of the NMR line. The magnitude of the splitting was $\Delta B = 12$ Oe in a 9 T magnetic field. In the same work an attempt was made to observe a similar effect in beryllium at $H = 1.9$ T, but the results obtained were not understood well enough to make an interpretation. This was apparently due to both the very long nuclear spin–lattice relaxation time and the quadrupole broadening of the NMR line. Nonetheless, despite this unsuccessful result, it could be assumed, with a high degree of confidence, that in beryllium diamagnetic domains form in magnetic fields less than 4–5 T. This certainty was based on the fact that in a number of

 © 1998 American Institute of Physics

works on the observation of the quantum oscillations of the thermoelectric power and resistance in beryllium[3,5,6] a unique behavior of the amplitude of these oscillations was observed, attesting to the appearance of domains.

In the present paper we describe the observation of Condon domain formation in a beryllium single crystal simultaneously with respect to magnetic-breakdown quantum oscillations of the resistance and thermoelectric power and with respect to splitting of the resonance peak of free precession muons (μSR). The μSR method, as a method for performing local measurements of the magnetic field, is not influenced by the skin effect, so that in pure metals (and the dHvA effect exists only in such metals) it seems to us to be in principle preferable to NMR. This method is completely free of the above-noted drawbacks of NMR due to the long nuclear spin-lattice relaxation time and the quadrupole broadening of the resonance, if the nuclear spin is different from 1/2.[7]

The experimental sample consisted of a $9\times14\times1.8$ mm beryllium single crystal. The hexagonal axis of the crystal was perpendicular to the plane of the plate. The resistance ratio is $\rho_{300}/\rho_{4.2}\cong300$. Preliminary muon precession measurements on this sample in weak fields showed that at liquid-helium temperatures the damping of the muon spin precession is small[4] on account of quantum tunneling of the muon and the corresponding μSR line width does not exceed 1.5 Oe in fields $H\sim1$ kOe. This dictated the choice of the range of magnetic fields for the present investigations: $H\approx25-30$ kOe. The period of the dHvA oscillations (and, correspondingly, the order of magnitude of the difference of the inductions in the expected domain structure) in this field equals $\Delta H\cong10^2$ Oe, which is much greater than the line width. On the other hand, the muon precession frequency in this field is $f\cong300$ MHz and analysis of the spectrum is still possible with a 0.7 ns wide time channel. This gave a basis for resolving the expected domain structure.

Quantum oscillations of the magnetoresistance and thermoelectric power were measured in the indicated range of magnetic fields at temperatures $T\cong1.5$ K, making it possible to observe domains indirectly. The measurements were performed using clamped beryllium bronze contacts. A section of the curve of the thermoelectric power $\alpha(H)$ versus the magnetic field at $T=1.6$ K is displayed in Fig. 1. The inset shows schematically the sample together with the contacts. Local heating was performed with current contacts *1–2*, and the thermoelectric power was measured with the two other contacts *3–4*. To obtain a large temperature gradient, the edge of the sample was glued to a copper cold duct.

A low frequency is superposed on the high-frequency magnetic-breakdown oscillations of the thermoelectric power shown in Fig. 1. This is a consequence of domain formation. This result for $\alpha(H)$ is due to the unique shape of the Fermi surface of beryllium, specifically, an electronic ''cigar,'' possessing for this orientation of the magnetic field three extremal sections. The two noncentral sections with frequency F_1 dominate the dHvA effect, while the central section determines the frequency F_2 of oscillations of the magnetoresistance $\rho(B)$ and thermoelectric power $\alpha(B)$ due to magnetic breakdown in the basal plane. The amplitude of these

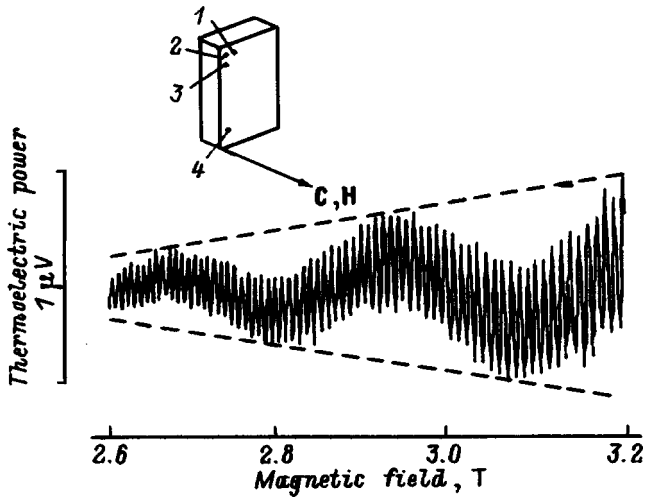

FIG. 1. Thermoelectric power $\alpha(H)$ versus magnetic field at $T=1.6$ K. The dashed lines show the expected variation of the amplitude assuming no magnetization. Inset: Schematic diagram showing the sample together with clamping contacts for measuring the thermoelectric power: *1* and *2*— current contacts producing local overheating; *3* and *4*—potential contacts.

oscillations by itself (neglecting the magnetization, i.e. as if $B\equiv H$ everywhere) should grow monotonically as a function of the magnetic field, as shown by the dashed lines in Fig. 1. However, the picture changes radically when domains appear periodically. On account of the small difference between the frequencies F_1 and F_2 ($F_1=9709\pm5$ kOe, $F_2=9422\pm3$ kOe, $F_1-F_2=287\pm2$ kOe[9]), maxima and minima of the oscillating function alternately coincide with the intervals ΔB. If the maxima (or minima) of the function coincide with these intervals ΔB, then the values of ρ (or α) near such a maximum (or minimum) that fall in the interval ΔB are not realized. As a result, a unique envelope is obtained, where maxima and minima are alternately ''cut out.'' This is what indicates the presence of domains. Moreover, the magnitude of ΔB for the domain structure formed can be judged from the depth of the cutting out. In the section of the thermoelectric power versus magnetic field presented in Fig. 1, the depth of cutting out of the amplitude of the oscillations equals almost half the amplitude. Hence it can be concluded that in this sample a domain structure arises near $H\approx3$ T with intervals $\Delta B=B_2-B_1$ slightly less than half the period. Exactly the same result was also obtained from measurements of the magnetoresistance on the same sample, but it was found that under the present conditions less heat was released in the thermoelectric power measurements. These experiments were found to be extremely helpful for making reliable predictions of the results in the complicated and laborious muon experiment.

A surface muon beam with momentum 28 MeV/s was used in the μSR experiment. The beam was parallel to the magnetic field and penetrated into the plate, arranged perpendicular to the beam, to a depth of approximately 0.6 mm, i.e., quite far from the boundary near which the domain structure can be distorted. To observe precession, the muon spin was rotated by an angle $\approx50°$ from the direction of its momentum. The histograms were recorded with two detectors, placed to the left and right of the sample. As it turned out,[8]

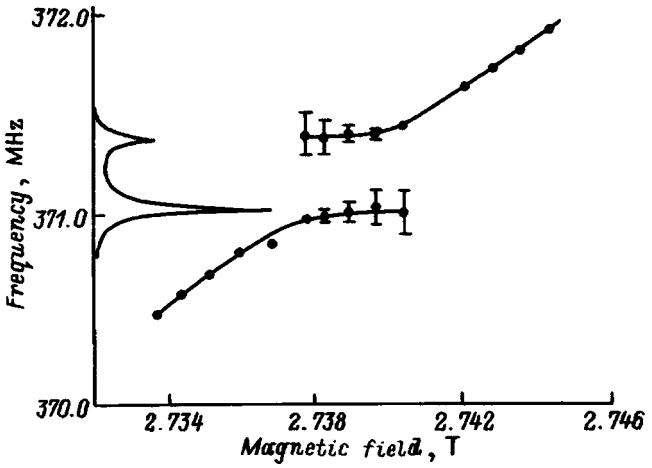

FIG. 2. Position of μSR peaks accompanying variation of the magnetic field within one dHvA period. In the magnetic field range $27.38 \leqslant H \leqslant 27.41$ kOe there are two well-resolved peaks whose amplitudes vary: As the field increases, the amplitude of the upper peak increases while the amplitude of the lower peak decreases. A section of a filtered spectrum, illustrating the splitting into two peaks near the center of the region of the domain structure, is displayed on the left.

for this beryllium single crystal the waiting time for a muon hop was $\tau \approx 10^{-7}$ s, and over its lifetime τ_μ the muon diffuses over a distance of order $a\sqrt{\tau_\mu/\tau}$, which equals about 10 Å. It can be assumed that at such distances the dynamic effects average out the interaction of the muon with the nuclear magnetic moments but do not influence the measurement of the field in a domain whose size is much greater than the muon diffusion length.

Measurements of the decay rate, $\lambda(H)$, of the μSR precession as a function of the magnetic field in the interval $H = 27.3-27.5$ kOe showed oscillations of the line width with period $\Delta H = 76 \pm 3$ Oe.[10] This equals the dHvA period, which for the magnetic frequency F_1 equals $\Delta H = 77.4$ Oe here. Fourier analysis showed that for large values of λ the μSR spectrum is split into two lines, while one line with $\lambda = 0.15\ \mu s^{-1}$ is observed near the minimum. The magnetic field dependence of the positions of these lines is shown in Fig. 2. The frequency of the single μSR peak grows linearly with H, and a second peak appears when $H = 27.38$ kOe is reached. As H increases further, the amplitude of the first peak decreases and that of the second peak increases but the positions of the peaks remain unchanged, and the difference of the fields at the peaks equals $\Delta B = 30 \pm 2$ Oe. The region within which two peaks coexist likewise is $\delta H \cong 30$ Oe. The observed picture corresponds completely to the Condon domain picture: The field in a domain is constant, and only the ratio of the phase volumes with different inductions changes. Thus, it can be stated with confidence that the observations of the diamagnetic domains in beryllium by the μSR method are in good qualitative and quantitative agreement with the same observations made by the quantum oscillation method. A more detailed analysis of the split μSR spectra will make it possible to determine the size (volume) of the interdomain region and possibly the character of the changes of the field in it.

The Russian authors thank the Russian Fund for Fundamental Research (Grant 95-02-06015) for supporting this work.

[1] J. H. Condon, Phys. Rev. **145**, 526 (1966).
[2] I. M. Lifshitz and A. M. Kosevich, Zh. Éksp. Teor. Fiz. **29**, 730 (1956) [Sov. Phys. JETP **2**, 636 (1956)].
[3] D. Shoenberg, *Magnetic Oscillations in Metals* [Cambridge University Press, N.Y., 1984; Mir, Moscow, 1986].
[4] J. H. Condon and R. E. Walstedt, Phys. Rev. Lett. **21**, 612 (1968).
[5] W. A. Reed and J. H. Condon, Phys. Rev. B **1**, 3504 (1970).
[6] V. S. Egorov, Zh. Éksp. Teor. Fiz. **72**, 2210 (1977) [Sov. Phys. JETP **45**, 1161 (1977)].
[7] Yu. M. Belousov and V. L. Smilga, Fiz. Tverd. Tela (Leningrad) **21**, 2459 (1979) [Sov. Phys. Solid State **21**, 1416 (1979)].
[8] G. Solt, C. Baines, X. Donathm, V. S. Egorov, D. Herlach, E. P. Krasnoperov, I. Reid, and U. Zimmermann, Annual Report, PSI, Villigen, Switzerland, 1994, Annex I, p. 77.
[9] V. S. Egorov, Zh. Éksp. Teor. Fiz. **69**, 2231 (1975) [Sov. Phys. JETP **42**, 1135 (1975)].
[10] G. Solt, C. Bames, and V. S. Egorov *et al.*, Phys. Rev. Lett. **76**, 2575 (1996).

Translated by M. E. Alferieff

Electric-field-induced phase transition in single-crystal lead zinc niobate

L. S. Kamzina and N. N. Kraĭnik

A. F. Ioffe Physicotechnical Institute, Russian Academy of Sciences, 194021 St. Petersburg, Russia
(Submitted July 8, 1997; resubmitted September 16, 1997)
Fiz. Tverd. Tela (St. Petersburg) **40**, 527–530 (March 1998)

The behavior of lead zinc niobate, a relaxor ferroelectric, in electric fields has been studied by dielectric, optical transmittance, and small-angle light scattering techniques. A field-induced transition from an averaged cubic to macrodomain ferroelectric phase has been found. A comparison is made with the properties of the phase induced in lead magnoniobate, a classical relaxor. © *1998 American Institute of Physics.* [S1063-7834(98)02803-2]

Crystalline lead zinc niobate, $PbZn_{1/3}Nb_{2/3}O_3$ (PZN), belongs to the class of relaxor ferroelectrics and exhibits all properties characteristic of this class, such as a broad maximum in the temperature dependence of the dielectric permittivity $\varepsilon(T)$ and the dependence of the position of this peak and of the maximum value of ε on frequency, dielectric hysteresis above the maximum in ε, the absence of spontaneous birefringence down to liquid nitrogen temperature, and a number of other properties.

Although the physical properties of relaxor ferroelectrics have been studied already for more than 40 years, there is still no unambiguous interpretation of the nature of the low-temperature phases. The numerous studies of the dielectric, optical, and other properties of the phases appearing below T_{max} were carried out primarily on lead magnoniobate $PbMg_{1/3}Nb_{2/3}O_3$ (PMN), a typical relaxor compound.[1–5] In the absence of an electric field, no transition from the relaxor to ferroelectric phase, which would be accompanied by a change in symmetry and formation of ferroelectric domains, was observed to occur in PMN. Application to a PMN crystal of a small constant electric field ($E_{cr}>1.7$ kV/cm) along the $\langle 111\rangle$ direction induces a ferroelectric transition accompanied by the appearance of additional anomalies in the temperature dependence of the permittivity and in some optical properties, with the character of these anomalies depending essentially both on the strength and direction of the electric field and on the regime of its application.[4,6–8]

Our experimental study of small-angle light scattering in PMN crystals revealed narrow peaks in the scattered intensity which suggest the field-induced transition from the relaxor to ferroelectric phase to be percolative.[9] It was shown that the large-scale spatially inhomogeneous structure appearing in the vicinity of this transition is a fractal.

While all the above phenomena have been adequately studied in PMN crystals, for PZN there is practically no information on an electric-field induced phase transition. The existence of an induced ferroelectric transition in PZN crystals with the maximum temperature $T_{max}\cong 400$ K was first mentioned in Ref. 10. When a crystal was cooled in an electric field exceeding some critical level ($E_{cr}\geqslant 20$ kV/cm) and subsequently heated in a weaker field, a maximum in the small-angle scattering intensity was observed at ~ 375 K. This phenomenon was attributed to the onset in the cooling crystal of a homogeneous macrodomain ferroelectric state, which breaks down under heating by the pattern of a percolative phase transition to form an ''infinite'' cluster. A study[11] of the domain structure and birefringence in a similar PZN crystal cut along the $\langle 111\rangle$ direction revealed the existence of four phase regions, namely, paraelectric, ferroelectric microdomain, ferroelectric macrodomain, and ferroelectric ''frozen'' macrodomain phase. Dielectric measurements confirmed the existence of a transition at a frequency-independent temperature from the micro- to macrodomain phase in fields above 15 kV/cm.[11]

These few available papers related to a field-induced phase transition in PZN crystals for which the temperature of the maximum in $\varepsilon(T)$ is $\sim 400-410$ K. PZN crystals studied in Refs. 12 and 13 had the maximum in $\varepsilon(T)$ around ~ 323 K. Optical and dielectric measurements suggest that the difference in position of the maximum in $\varepsilon(T)$ is due to a different degree of ordering of Zn and Nb ions.[12] PZN crystals with a higher temperature of the maximum in $\varepsilon(T)$ exhibit a more pronounced phase transition. Field-induced phase transitions in crystals with a lower T_{max} have not been studied at all.

The objective of this work was to study the possible existence of an electric-field-induced ferroelectric phase transition in PZN crystals with $T_{max}=323$ K (PZNI) by dielectric and optical methods, and to compare these results with measurements performed on PZN crystals with $T_{max}\sim 400$ K (PZNII) and on the classical relaxor PMN in order to reveal general features in the onset and properties of the field-induced low-temperature ferroelectric phase observed in ferroelectrics with a diffuse phase transition. Dielectric studies, as well as measurements of optical transmittance and small-angle light scattering, may yield valuable information on the nucleation and destruction of new-phase clusters as one crosses the phase transition.

1. EXPERIMENTAL RESULTS AND THEIR DISCUSSION

We investigated the dielectric properties, optical transmittance, and small-angle light scattering in PZNI crystals in constant external bias fields of up to 15 kV/cm. The single crystals were grown by spontaneous crystallization from solution in a PbO melt to which 3% sodium tetraborate[13] was

 © 1998 American Institute of Physics

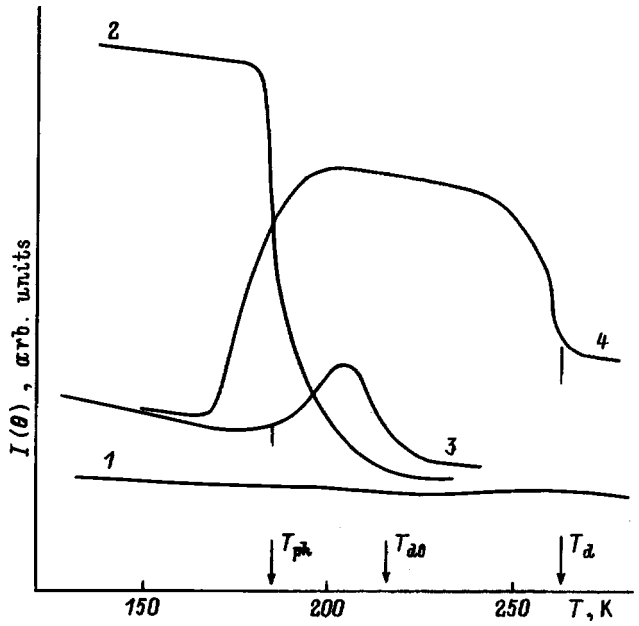

FIG. 1. Temperature dependence of small-angle scattering intensity (scattering angle 20′) in PZNI crystal obtained in different [111]-oriented electric fields in two modes: *1,2*—ZFHaFC, and *3,4*—FHaZFC. E(kV/cm): *1*—2.5, *2,4*—10, *3*—5.

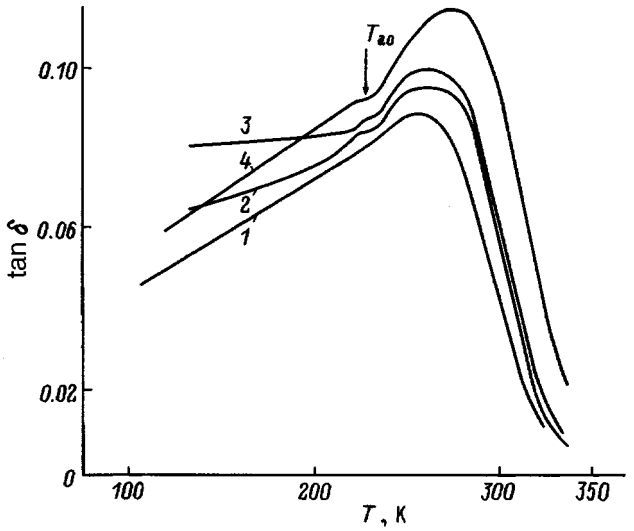

FIG. 2. Temperature dependence of the dielectric loss factor of PZNI crystal obtained at 50 kHz (*1–3*) and 450 kHz (*4*) in different [111]-oriented electric fields in the ZFHaFC mode. E(kV/cm): *1*—0, *2,4*—12, *3*—14.

added. The measurements were carried out on $2\times1.5\times1$ mm parallelepipeds cut from a single crystal. Silver electrodes were deposited on the face oriented perpendicular to the ⟨111⟩ axis. Light propagated along ⟨110⟩. The setup used to measure the temperature and field dependences of the small-angle scattering intensity are described elsewhere.[14] The dielectric characteristics were measured in the frequency range 30–500 kHz. The electric field was applied in different modes: (1) field cooling (FC), (2) zero-field heating after field cooling (ZFHaFC), (3) field heating after zero-field cooling (FHaZFC), and (4) field heating after field cooling (FHaFC). To avoid residual effects, the sample was annealed to 450 K before each measurement. Depending on the actual measurement regime, the electric field was applied to the sample either at 100 or 450 K.

Figure 1 presents the temperature dependence of the small-angle scattering intensity (scattering angle 20′) measured in FHaZFC and ZFHaFC modes. Below 2.8 kV/cm, no significant changes in small-angle scattering intensity were observed to occur with temperature, irrespective of the field application regime used (curve *1*). In fields above 3 kV/cm, one clearly sees a change in small-angle scattering intensity within a certain temperature interval. Indeed, curve *2* obtained under ZFHaFC conditions (10 kV/cm) exhibits a pronounced drop in scattering intensity within an interval from 180 K up to the temperature $T_{d0}=\sim230$ K, above which the scattering intensity practically does not change. This temperature corresponds to the sample depolarization point. This suggests that cooling a crystal in a field above a certain threshold level induces a polar macrodomain phase, which remains frozen after field removal at 100 K. When the crystal is heated in this polar state at zero field, the sample undergoes thermal depolarization at $T_{d0}\sim230$ K. This temperature does not depend on the electric field applied under cooling, and it coincides with the temperature determined from the temperature dependence of optical transmittance of the preliminarily polarized sample, which was measured in crossed Nicol prisms.

Curves *3* and *4* illustrate the temperature dependence of the small-angle scattering intensity obtained under FHaZFC conditions. We see that application of an electric field of 5 kV/cm and more at 100 K, followed by field-heating, does not change this intensity up to T_{ph} (curve *3*). At this temperature, which depends on the applied field, one observes an increase in the scattered intensity associated apparently with the onset of an inhomogeneous macrodomain polar state. The interval within which this macrodomain state persists depends on the electric field, namely, the higher this field, the broader the interval (curve *4*). The change in small-angle scattering intensity observed to occur within a certain temperature interval argues for the appearance of a ferroelectric phase with sufficiently large macrodomain regions. At the temperature T_d this state breaks down, which reduces the scattering intensity. The nature of the phase forming above T_d remains unclear. This may be either a paraelectric phase, or, as was suggested[11] for the PZNII crystal, a ferroelectric microdomain phase.

The temperatures of the anomalies determined from light scattering measurements are supported by dielectric studies. Figure 2 shows the typical temperature dependence of the dielectric loss factor for a PZN crystal obtained in various electric fields (ZFHaFC mode) at 50 and 450 kHz. With no electric field applied (curve *1*), no anomalies in addition to the main peak were observed. Curves *2–4* obtained in ZFHaFC conditions show clearly an additional, field-independent anomaly at $T_{d0}\sim230$ K. At this temperature the sample undergoes thermal depolarization. This temperature also does not depend on measuring-field frequency (curve *4*).

Let us compare the results on light scattering in a PZNI crystal with our earlier data[9,10] for the PMN and PZNII crys-

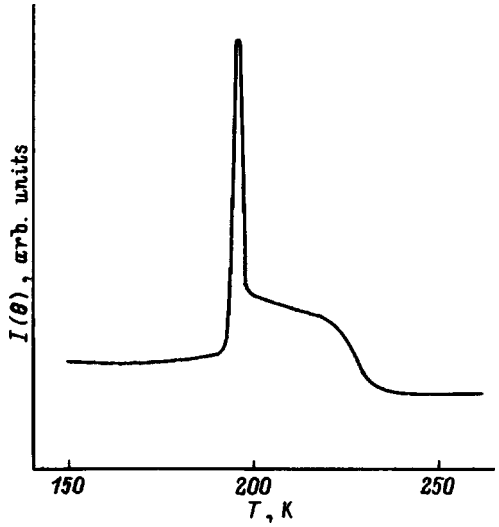

FIG. 3. Temperature dependence of small-angle scattering intensity in PMN crystal obtained in a [111]-oriented 3-kV/cm electric field in the FHaZFC conditions (scattering angle 30′).

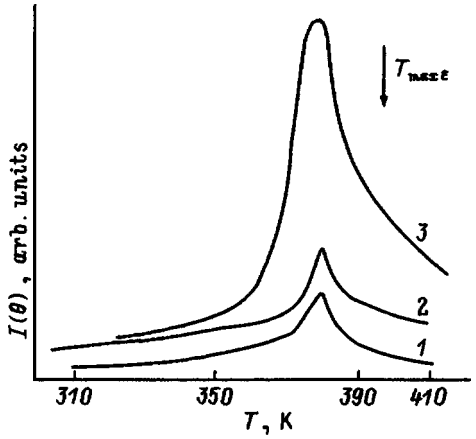

FIG. 4. Temperature dependence of the small-angle scattering intensity in PZNII crystal obtained in different [100]-oriented electric fields in two modes: *1*—ZFHaFC, and *2*,*3*—FHaFC. The field cooling was done at 20 kV/cm. Scattering angle 30′. E(kV/cm): *1*—0, *2*—2, *3*—10.

tals. Figure 3 displays a temperature dependence of small-angle scattering intensity for a PMN crystal obtained at 3 kV/cm (FHaZFC mode, scattering angle 30′). In contrast to PZN, the PMN crystal exhibits clearly a narrow peak in small-angle scattering intensity at the onset temperature of the ferroelectric phase, which argues for the percolative nature of the formation of this phase. As is evident from Fig. 3, breakdown of the induced ferroelectric state occurs more smoothly. In the PZNI crystal studied by us (Fig. 1), nucleation and destruction of the ferroelectric state follows a more symmetric pattern; indeed, no narrow peaks were observed in any regime of application of electric fields of up to 10 kV/cm. One possible reason for this difference in the behavior of the small-angle scattering intensity in PMN and PZN crystals is that the ferroelectric phase induced in PZN crystals is less homogeneous in structure. The macrodomain regions of this phase forming in electric fields below 10 kV/cm are still not large enough to produce an infinite macrodomain cluster capable of generating peaks in small-angle scattering intensity in the heterophase region. As the electric field increases, a homogeneous macrodomain state may possibly set in in PZNI crystals, and the development and/or destruction of this state will occur as a percolative phase transition involving formation of an infinite cluster. Indeed, we observed such a pattern in PZNII crystals. Figure 4 presents the temperature dependence of the small-angle scattering intensity for a PZNII crystal in different electric fields applied along [100] under the ZFHaFC (curve *1*) and FHaFC (curves *2* and *3*) conditions. After the crystal was cooled in fields $\sim$20 kV/cm, a peak appeared in the temperature dependence of the small-angle scattering intensity taken under heating. As the field applied to the crystal under heating increases, the small-angle scattering intensity at the maximum grows, and the maximum itself spreads out.

PZNI crystals studied in this work are more disordered and exhibit a larger difference between the temperatures of the maxima, $\varepsilon(T)$, and of depolarization, T_{d0}, than is typical of PZNII (Refs. 11 and 12). There are therefore grounds to assume that formation of an infinite macrodomain cluster would require electric fields in excess of those used here, namely, up to 15 kV/cm and applied along [111]. Using such high fields meets with experimental difficulties. Moreover, high fields diffuse the phase transition, so that one would hardly expect to observe narrow small-angle scattering peaks here.

Thus, our measurements on PZNI crystals indicate an induced transition to the ferroelectric phase in electric fields in excess of a certain critical level. The region in which this phase exists depends on the strength and actual regime of application of the field. This induced state is probably a inhomogeneous macrodomain. The increase in small-angle scattering intensity observed to occur in this phase argues for the formation of large macrodomain regions, possibly separated by microdomain ferroelectric layers. The nature of the high-temperature phase that sets in when the macrodomain state breaks down is unclear and requires further investigation. It could be a microdomain ferroelectric phase.

The numerous small-angle scattering studies of a broad class of disordered ferroelectrics carried out by us in recent years permit identification of three paths for a phase transition to a macrodomain ferroelectric state in these compounds:

1. In $PbB'_{1/2}B''_{1/2}O_3$ crystals with weakly disordered ions B′ and B″ (degree of ordering $s>0.7$), the ferroelectric transition is percolative and is accompanied by the appearance of anomalously narrow small-angle scattering intensity peaks with no external electric field applied.

2. In PMN, which are more disordered crystals, a percolative transition to macrodomain ferroelectric state is observed to occur only in an electric field exceeding a threshold of 2–2.5 kV/cm.

3. In PZN crystals, percolative ferroelectric transition takes place under conditions different from those for PMN. In the more ordered crystals, PZNII, in which the temperatures of the maxima in $\varepsilon(T)$ are higher, we succeeded in observing a percolative phase transition involving destruc-

tion of the macrodomain ferroelectric state by heating the crystal following its preliminary cooling in a [100] electric field in excess of 20 kV/cm. In PZNI crystals, characterized by a lesser degree of ordering and lower temperatures of $\varepsilon(T)$ maxima, application of electric fields of up to 15 kV/cm even in the direction of spontaneous polarization, [111], while inducing a transition to macrodomain ferroelectric state, does not result in formation of an infinite cluster and, as a consequence, in a percolative phase transition.

The difference between the conditions in which a percolative phase transition sets in in PMN and PZN may be due to the different nature of the high-temperature phases in these crystals; indeed, there are indications that regions of antiferroelectric phase form in PMN,[15] whereas in PZN nucleation of a microdomain ferroelectric phase is presumed.

The reason for the variety of paths by which the ferroelectric phase transition can set in in disordered ferroelectrics should probably be sought in the elastic subsystem of the crystals under study.

Support of the Russian Fund for Fundamental Research (Grants 96-02-16958 and 96-02-16893) and of the Laser Optics Program is gratefully acknowledged.

[1] V. A. Bokov and I. E. Myl'nikova, Fiz. Tverd. Tela (Leningrad) **3**, 841 (1961) [Sov. Phys. Solid State **3**, 613 (1961)].
[2] S. N. Dorogovtsev and N. K. Yushin, Ferroelectrics **112**, 27 (1990).
[3] L. A. Markova, N. N. Kraĭnik, and R. N. Kütt, Fiz. Tverd. Tela (Leningrad) **33**, 35 (1991) [Sov. Phys. Solid State **33**, 18 (1991)].
[4] E. V. Colla, S. B. Vakhrushev, E. Yu. Koroleva, and N. M. Okuneva, Fiz. Tverd. Tela (St. Petersburg) **38**, 2183 (1996) [Phys. Solid State **38**, 1202 (1996)].
[5] V. Westphal, W. Kleemann, and M. D. Glinchuk, Phys. Rev. Lett. **68**, 847 (1992).
[6] Z.-G. Ye and H. Schmid, Ferroelectrics **145**, 83 (1993).
[7] H. Arndt, F. Sauerbier, G. Schmidt, and L. A. Shebanov, Ferroelectrics **79**, 145 (1988).
[8] R. Sommer, N. K. Yushin, and J. J. van Klink, Phys. Rev. B **48**, 13230 (1993).
[9] L. S. Kamzina, N. N. Kraĭnik, and O. Yu. Korshunov, Fiz. Tverd. Tela (St. Petersburg) **37**, 2765 (1995) [Phys. Solid State **37**, 1523 (1995)].
[10] L. S. Kamzina, N. N. Kraĭnik, and A. L. Korzhenevskiĭ, JETP Lett. **56**, 519 (1992).
[11] M. L. Mulvihill, L. E. Cross, and K. Uchino, Ferroelectrics **186**, 325 (1996).
[12] L. S. Kamzina, N. N. Kraĭnik, L. M. Sapozhnikova, and S. V. Ivanova, Fiz. Tverd. Tela (Leningrad) **33**, 2078 (1991) [Sov. Phys. Solid State **33**, 1169 (1991)].
[13] A. A. Berezhnoĭ, V. N. Bukhman, L. T. Kudinova, and I. A. Myl'nikova, Fiz. Tverd. Tela (Leningrad) **10**, 255 (1968) [Sov. Phys. Solid State **10**, 192 (1968)].
[14] L. S. Kamzina and A. L. Korzhenevskiĭ, JETP Lett. **50**, 163 (1989).
[15] Q. M. Zhang, H. You, M. L. Mulvihill, and S. J. Jang, Solid State Commun. **97**, 693 (1996).

Translated by G. Skrebtsov

Photoinduced domains in lithium niobate

A. V. Golenitsev-Kutuzov and R. I. Kalimullin

Kazan' Affiliate of the Moscow Power Engineering Institute, 420066 Kazan', Russia
(Submitted April 3, 1997; resubmitted September 30, 1997)
Fiz. Tverd. Tela (St. Petersburg) **40**, 531–533 (March 1998)

We have observed the optically induced occurrence of domain structure with polarization opposite to the spontaneous polarization of a single-domain sample of lithium niobate. The appearance of the domains can be explained by a redistribution of the density of the Fe^{2+} and Fe^{3+} impurity ions under the action of the photoinduced field and subsequent additional inverse polarization of the environment surrounding the Fe^{2+} ions. © *1998 American Institute of Physics.* [S1063-7834(98)02903-7]

There is an extensive literature on the development of microscopic models of the photoinduced variation of the index of refraction, called the photorefractive effect. Most of these works are incorporated in the monographs Refs. 1 and 2. Attempts to describe all features of the photorefractive effect on the basis for the most widely accepted photovoltaic mechanism have not always been successful. Specifically, the mechanism of the fixation of holographic gratings by optical irradiation in the temperature range 140–160 °C has never been adequately explained. According to one of these models,[3] drift of ions present in the photorefractive material in a photoinduced electric field starts on heating. After completion of fixation and cooling to room temperature, optical irradiation can completely or partially remove the distribution of electronic charges, but then an ionic ''replica'' of the previously recorded hologram will remain. To explain this process it was assumed that lithium niobate contains OH^- ions, which can enter the lattice of the crystal during the growth process.[3] However, the proposed mechanism requires the existence of at least three lattice positions for protons and poorly agrees with a number of experimental data.

According to a different model,[4,5] fixation of holograms occurs as a result of the formation of microscopic photoelectric domains with polarization opposite to that of a single-domain sample. Such domains were experimentally observed earlier in (Sr,Ba)Nb_2O_6 crystals.[5] However, this model has not been adequately confirmed experimentally in the case of lithium niobate.

To obtain more precise substantiation of the model of photoinduced formation of domains, we investigated the optical characteristics of a lithium niobate single crystal whose surface was irradiated with the second harmonic ($\lambda = 0.53$ μm) of the radiation from an yttrium-aluminum garnet laser (LTI-709). Optical and ESR spectroscopy showed that the $10\times1.5\times10$ mm (along the X, Y, and Z axes, respectively) sample contained ~0.05 at. % iron ions. The sample was annealed in helium at 450 °C until the relative Fe^{2+} ion density increased to 25–35%. A pulsed regime with $\tau_i \approx 60$ ns and power density per pulse of approximately 10^5 cm^2 with a pulse repetition frequency on the order of 1 kHz was used for optical irradiation of the YZ surface. The irradiation time up to completion of the photorefractive process was equal to 5–10 s. A narrow (10×0.2 mm^2) strip was irradiated while the temperature of the sample varied from room temperature up to 200 °C.

After completion of the photorefractive process, which was monitored by an optical compensation method, and the sample cooled down to room temperature, it was observed visually that near the region of optical irradiation a darkening of the sample occurred at a location 0.3 mm from the center of the irradiation strip toward the positive end of the polarization axis. The photoinduced change δn of the refractive index was equal to 6×10^{-4}, which corresponds to a photoinduced field of order 5×10^6 V/m.

It is quite difficult to identify 180° domains in ferroelectrics. Etching of the surface of the sample[1)] in a mixture of nitric and hydrofluoric acids at 80 °C for 10 h showed that the near-surface relief did indeed change somewhat in the region of interest. The lack of sharpness of the picture and the presence of individual regions are most likely due to the nonuniform distribution of iron ions in the sample.

It is known that for neighboring 180° domains only odd-rank tensors, describing some interactions, specifically, the electro-optic tensor, will have different signs. Therefore, when an electric field is applied to the crystal, the values of the birefringence tensor will be determined by the sign of the polarization of a given part of the sample. This is the principle on which the interferometric method of identifying antiparallel domains, which has been successfully employed for lithium niobate,[6] is based.

This method was used to determine the change in sign of the polarization in the region of darkening of the sample by scanning along the XY surface a focused, low-power beam (20 μm in diameter) from a helium-neon laser and applying an electric field along the Z axis (Fig. 1). The strip of inverse polarization was 100–150 μm wide (Fig. 2). When the temperature of the experiment decreased below 120 °C, an inverse polarization did not arise, but rather only a photoinduced change δn of the refractive index was produced. An identical pattern in which only δn appeared was also observed when the sample was irradiated with an intense beam from a He–Ne laser (LG-38) with a power density of 10 W/cm^2. The character of the photoinduced processes dif-

 © 1998 American Institute of Physics

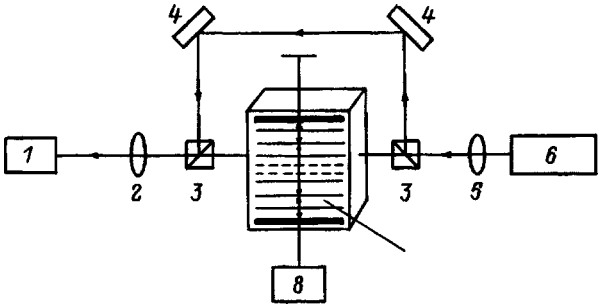

FIG. 1. Block diagram of the apparatus. *1*—Photodetector, *2, 5*—lenses, *3*—biprism, *4*—mirror, *6*—laser, *7*—structure of inverted domains, *8*—regulatable voltage source.

fered in that the induced inverse polarization was not erased even by heating up to 500 °C or by irradiation with an intense ultraviolet beam, while the induced δn was erased at $T \sim 180$ °C and by UV irradiation.

Thus, these features, just as the displacement itself of the domain region relative to the center of the irradiation strip, point to a mechanism connected with a change in the valence of the impurity iron ions and not with the formation of a strong photoinduced field, since the latter is distributed symmetrically in the irradiation strip.

The appearance of a domain structure can be explained on the microscopic level by analyzing the nature of the impurity iron ions. Under optical irradiation the photoinduced electrons from Fe^{2+} ions will drift, as a result of the photovoltaic effect, out of the region of illumination in the direction of the positive pole of the spontaneous-polarization field and Fe^{3+} ions will be absorbed in the nonilluminated region. Thus, impurity ions which earlier were randomly distributed become separated: Mainly Fe^{3+} ions remain in the illuminated region and mainly Fe^{2+} ions remain in the nonilluminated region. It is well known[7,8] that Fe^{2+} and Fe^{3+} ions, replacing the lithium ions, occupy the same positions in the crystal lattice. As a result of the conditions of charge neutralization, the iron ions are displaced somewhat along the polarization axis **C** relative to the positions of the lithium ions. The Fe^{3+} ions possess spherical symmetry and are weakly bound with the crystal lattice, so that their influence on the crystal field can be neglected. The Fe^{2+} ions are Jahn–Teller ions, and they are strongly coupled with the nearest-neighbor lattice environment and do not possess spherical symmetry. Large electric-field gradients, directed antiparallel to the **C** axis, are formed around the Fe^{2+} ions.

On the other hand, a change in the valence of the Fe^{2+} and Fe^{3+} ions under optical irradiation results in new displacements of these ions relative to their initial positions. This fact has been confirmed directly in observations of optically induced distortions of the unit cell.[9] The displacement of ions which arises with the photophysical reaction $Fe^{+} \leftrightarrow Fe^{3+}$ causes additional polarization p of the crystalline environment by the field of a charged center. The approximate magnitude of p can be estimated by using the model of charged centers.[10] In this case

$$p = \frac{q \cdot u}{a^3},$$

where q is the ion charge, a is the size of a unit cell, and u is the elastic displacement.

For $u \sim 0.2$ nm we have $p \sim 2 \times 10^{-2}$ C/cm^2, which corresponds to the appearance of an electric field of order 10^6 V/m. Such a field is sufficient for reversing the polarization of the volume around a Fe^{2+} ion.

One would think that the formation of microdomains around Fe^{2+} ions is limited to the first coordination sphere. However, in ferroelectrics, especially at high temperature (150 °C), domains can increase in size as a result of the easy polarizability, and a quasicooperative effect accompanied by the formation of macroscopic domains can appear if the impurity ion density is sufficiently high. As has already been established,[11] the polarization field decreases by two orders of magnitude when the temperature increases from room temperature up to 150 °C, while the formation of clusters of iron ions has been observed even in Mössbauer experiments.[7]

This work was supported by the Russian Fund for Fundamental Research (Grant 96-02-18229).

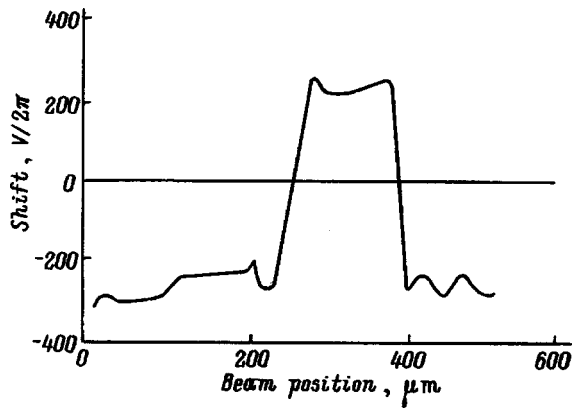

FIG. 2. Phase-shift voltage versus position of the scanning optical beam.

[1)]We thank the staff at the Scientific Research Institute of the Chemical Industry at Kazan' State University for etching the lithium niobate crystal.

[1] Yu. S. Kuz'min, *Electro- and Nonlinearly-Optical Lithium Niobate Crystal* [in Russian], Nauka, Moscow, 1987.
[2] M. P. Petrov, S. M. Stepanov, and A. V. Khomenko, *Photorefractive Crystals in Coherent Optics* [in Russian], Nauka, St. Petersburg, 1992.
[3] M. Carrascoca and L. Arizmendi, J. Appl. Phys. **73**, 2709 (1993).
[4] R. Matull and R. Rupp, J. Phys. D **21**, 1556 (1988).
[5] B. Williams, W. Burk, and D. Staebler, Appl. Phys. Lett. **28**, 224 (1976).
[6] Q. Chen and D. Stancil, Appl. Opt. **33**, 7496 (1994).
[7] H. Engelman, I. Dezsi, and U. Gonser, Appl. Phys. A **48**, 211 (1989).
[8] I. Sh. Akhmadullin, V. A. Golenhishchev-Kutuzov, and S. A. Migachev, Fiz. Tverd. Tela (Leningrad) **32**, 1854 (1990) [Sov. Phys. Solid State **32**, 1080 (1990)].
[9] I. A. Abramov and V. V. Voronov, Fiz. Tverd. Tela (Leningrad) **21**, 1234 (1979) [Sov. Phys. Solid State **21**, 716 (1979)].
[10] A. Stoneham, *Theory of Defects in Solids*, [Clarendon Press, Oxford, 1975; Mir, Moscow, 1979].
[11] V. Kovalevich, L. Shuvalov, and T. Volk, Phys. Status Solidi **45**, 249 (1978).

Translated by M. E. Alferieff

ESR of V^{4+} in α-$RbTiOPO_4$ single crystals

I. N. Geĭfman and I. S. Golovina

Institute of Semiconductor Physics, Ukrainian Academy of Sciences, 252650 Kiev, Ukraine

P. G. Nagornyĭ

Kiev State University, 252000 Kiev, Ukraine

(Submitted June 23, 1997; resubmitted October 23, 1997)
Fiz. Tverd. Tela (St. Petersburg) **40**, 534–536 (March 1998)

We have recorded and investigated the ESR spectrum of vanadium-doped α-$RbTiOPO_4$ single crystals in the temperature interval 77–300 K. Two types of structurally distinct centers, V1 and V2, with a 4:1 ratio of the peak intensities were observed. The angular dependences of the resonance magnetic fields are described by a spin Hamiltonian corresponding to axial symmetry with the parameters $g_{\|1}=1.9305$, $g_{\perp 1}=1.9565$, $A_{\|1}=-168.2\times10^{-4}$ cm^{-1}, and $A_{\perp 1}=-54.3\times10^{-4}$ cm^{-1} for V1 centers and $g_{\|2}=1.9340$, $g_{\perp 2}=1.9523$, $A_{\|2}=-169.0\times10^{-4}$ cm^{-1}, and $A_{\perp 2}=-55.2\times10^{-4}$ cm^{-1} for V2 centers. A model of a paramagnetic center is proposed: The vanadium ions replace titanium ions in two structurally distinct positions Ti1 and Ti2 (V1 and V2 centers, respectively). The possibility that a VO^{2+} ion forms when α-$RbTiOPO_4$ crystals and crystals of the KTP group ($KTiOPO_4$, $NaTiOPO_4$, α- and β-$LiTiOPO_4$), studied earlier, are doped with vanadium is discussed. © *1998 American Institute of Physics.* [S1063-7834(98)03003-2]

Rubidium titanyl phosphate $RbTiOPO_4$ (RPT) crystallizes in two polymorphic modifications: α-$RbTiOPO_4$ (rhombic system) and β-$RbTiOPO_4$ (cubic system).[1] The α-$RbTiOPO_4$ crystals, belonging to complex phosphates of the $KTiPOPO_4$ (KTP) group, possess high nonlinear optical characteristics and anomalously high ionic conductivity.[2] They are classified as ferroelectrics—superionic conductors.[3] To obtain RTP single crystals of high optical quality, vanadium oxide (V_2O_5) and rubidium vanadate ($RbVO_3$), which lower the viscosity of the melt, are added at the time the crystals are grown. Investigations have shown that centers of two types can form: individual V^{4+} ions[4–7] or the complexes VO^{2+}.[8–10]

In the present work, the ESR of vanadium atoms in RTP crystals is investigated for the purpose of determining the structure of the paramagnetic defect. The results obtained are compared with existing results as well as with the characteristics which we computed for vanadium-doped crystals of the KTP group.

1. PRODUCTION AND STRUCTURE OF THE CRYSTALS

Vanadium-doped RTP single crystals were obtained as the result of the interaction of titanium dioxide in (1) $RbPO_3$–$RbVO_3$–TiO_2 and (2) $RbPO_3$–$Rb_4P_2O_7$–TiO_2–V_2O_5 systems. Melts of the system (1) with a $RbPO_3$:$RbVO_3$ ratio 80:20 mole % and with 18–20% TiO_2 were homogenized at 1080–1100 °C for 4–5 h with periodic mixing in a platinum crucible. Next, the homogeneous melt was cooled to 850–820 °C at a rate of 1–1.5 deg/h. This yielded $3\times4\times5$ mm RTP:V single crystals containing 0.08–0.12% vanadium (IV). Melts in the system (2) with Rb_2O:P_2O_5 molar ratio 1.25 and with 2.0% V_2O_5 were used for the same purpose. The cooling rate in the temperature interval 800–1000 °C was 1 deg/h.

RTP crystals in the ferroelectric phase ($T_c=789$ °C) are orthorhombic and belong to the noncentrosymmetric point group C_1 (space group $Pna2_1$). The unit cell contains eight formula units ($a=12.974$ Å, $b=6.494$ Å, $c=10.564$ Å[12]). Similarly, the KTP structure of RTP crystals consists of a three-dimensional network of chains of distorted TiO_6 octahedra and almost regular PO_4 tetrahedra. A unit cell contains two crystallographically nonequivalent positions: Ti1 and Ti2. Below T_c the Ti atoms are displaced along the c axis away from the centrosymmetric position and form in each TiO_6 octahedron one short (Ti1–OT2 = 1.714 Å, Ti2–OT1 = 1.737 Å), one long (Ti1–O1 = 2.146 Å, Ti2–OT2 = 2.094 Å), and four midlength (in the interval 1.95–2.07 Å) Ti–O bonds.[12] Thus, the titanium ions in the RTP lattice are surrounded by oxygen ions forming distorted oxygen octahedra.

2. ESR SPECTRA

The ESR spectra were recorded in the 3-cm wavelength range in the temperature interval 77–300 K on a RÉ-1307 radio-spectrometer. The ESR signal consists of two groups of lines (I and II) (Fig. 1). Each group contains four spectra consisting of an octet of lines. This octet of lines is the hyperfine structure corresponding to the interaction of unpaired electrons of V^{4+} ions (electronic configuration $3d^1-{}^2D_{3/2}$, $S=1/2$) with natural nuclei of the isotope V^{51} (nuclear spin $I=7/2$). Therefore, the crystal contains two structurally non-

 © 1998 American Institute of Physics

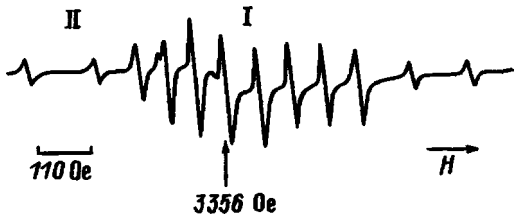

FIG. 1. ESR spectrum of V^{4+} in a α-$RbTiOPO_4$ single crystal with $\mathbf{H}\|[010]$ ($\nu=9378$ MHz). The lines I and II belong to vanadium ions in the Ti1 and Ti2 positions, respectively.

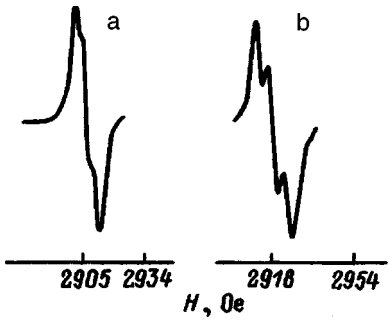

FIG. 2. Hyperfine structure of V2 centers which is observed with rotation of the crystal planes close to (001) (a) and (010) (b).

equivalent centers (which we denote as V1 and V2), each of which is associated with four magnetically nonequivalent centers.

The peak intensities of the ESR lines of the V1 and V2 centers are in the ratio 4:1, and the line widths of these centers equal 5.6 and 14 Oe, respectively.

Splitting of the ESR lines of the V2 centers, which depends on the orientation of the crystal in the magnetic field, was observed in the entire experimental temperature interval (Fig. 2). This splitting is probably due to the superhyperfine interaction.

We note that for $\mathbf{H}\|[001]$ only one octet is observed. This attests to the fact that the principal magnetic axes of all centers make the same angle with the [001] direction of the crystal. One octet of lines for each orientation $\mathbf{H}\|[100]$ and $\mathbf{H}\|[010]$ of the crystal is observed for each center V1 and V2. Therefore, the four magnetically nonequivalent centers of each type of center V1 and V2 make identical angles with the crystallographic directions of the type [100] and [010]. For an arbitrary orientation of the crystal, lines of all eight types of paramagnetic centers are observed.

The angular dependences of the resonance magnetic fields are described by the spin Hamiltonian

$$\mathcal{H}=g_{\|}\beta H_z S_z+g_{\perp}\beta(H_z S_z+H_y S_y)+A_{\|}I_z S_z+A_{\perp}(I_x S_x+I_y S_y) \quad (1)$$

with the parameters $g_{\|1}=1.9305$, $g_{\perp 1}=1.9565$, $A_{\|1}=-168.2\cdot 10^{-4}$ cm^{-1}, and $A_{\perp 1}=-54.3\times 10^{-4}$ cm^{-1} for V1 centers and $g_{\|2}=1.9340$, $g_{\perp 2}=1.9523$, $A_{\|2}=-169.0\times 10^{-4}$ cm^{-1}, and $A_{\perp 2}=-55.2\times 10^{-4}$ cm^{-1} for V2 centers.

Let us examine the position of the V^{4+} ions in the RTP lattice. Since the number of spectra which we observed corresponds to the number of structurally and magnetically nonequivalent positions of the titanium ions in the unit cell of RTP, we assume that in RTP crystals the V^{4+} ions isomorphically replace Ti^{4+} ions. The facts that the V^{4+} and Ti^{4+} ions have the same valence and their ionic radii are close support this conjecture.

The direction cosines of the magnetic axes Z of the centers V1 and V2 with respect to the crystallographic axes were determined by studying the angular dependences of the spectra of all centers. (See Table I). This table also gives the direction cosines of the shortest bonds in the $Ti1O_6$ and $Ti2O_6$ octahedra in RTP crystals. Comparing the values obtained for the direction cosines, we can conclude that the V1 centers correspond to vanadium ions occupying Ti1 positions and the V2 centers correspond to V^{4+} ions occupying Ti2 positions. The angles between the directions of the magnetic axes Z of the V1 and V2 centers and the directions from the Ti site to the nearest oxygen in the $Ti1O_6$ and $Ti2O_6$ octahedra are 4 and 5°, respectively. The analogous angles in the isostructural KTP crystal are 3 and 4°. It should be noted that the peak intensities and widths of the ESR lines of V1 and V2 centers in the RTP crystal correspond to the situation where V^{4+} ions occupy structurally nonequivalent positions with equal probability. In the KTP crystals investigated earlier more than twice as many V^{4+} ions occupy Ti1 positions (2.1 in Ref. 13 and 2.4 in Ref. 14) as Ti2 positions. This is

TABLE I. Direction cosines of the principal axes of V1 and V2 paramagnetic centers and the shortest Ti–O bonds in RTP and KTP crystals.

Center or bond	cos α	cos β	cos γ	Space group	Reference
		RTP			
V1	0.6884	−0.1564	−0.7071	$Pna2_1$	This
V2	0.1737	−0.6947	−0.7071	$Pna2_1$	work
Ti1–OT2	0.7223*	−0.1663*	−0.6710*	$Pna2_1$	12
Ti2–OT1	0.2228*	−0.7211*	−0.6556*	$Pna2_1$	12
		KTP			
V^{4+}(1)	−0.6933	0.1260	−0.7096	$Pna2_1$	13
V^{4+}(2)	−0.1651	0.6874	−0.7071	$Pna2_1$	13
V^{4+}(I)	−0.2588	−0.6802	−0.7330	$Pna2_1$	14
V^{4+}(II)	−0.6946	0.1737	0.7193	$Pna2_1$	14
Ti1–OT2	−0.7216	0.1507	−0.6757	$Pna2_1$	13
Ti2–OT1	−0.1943	0.7304	−0.6547	$Pna2_1$	13

*Values of the direction cosines which we calculated from the x-ray crystallographic data of Ref. 12.

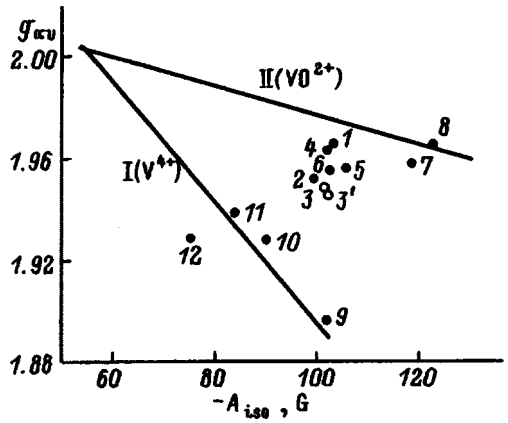

FIG. 3. Average g factor (g_{av}) versus the isotropic hyperfine interaction constant (A_{iso}). Data employed: *1*—KTP,[8] *2*—KTP,[13] *3* and *3′*—V1 and V2 centers in RTP crystals, *4*—$NaTiOPO_4$,[16] *5*—α-$LiTiOPO_4$,[17] *6*—β-$LiTiOPO_4$,[17] *7*—KDP,[9] *8*—$(NH_4)_2SO_4$,[10] *9*—WO_3,[5] *10*—TiO_2,[6] *11*—$ThSiO_4$,[7] *12*—SnO_2.[4]

probably due to the smaller distortion of the TiO_6 octahedra in RTP crystals than in KTP crystals.

As we have noted above, two types of centers are observed in vanadium-doped crystals: V^{4+} ions or VO^{2+} complexes. The value of the parameter K characterizing the polarization of the shell of a paramagnetic impurity is 1.6 times larger for VO^{2+} complexes $[(100-118)\times10^{-4}\ \mathrm{cm}^{-1}]$ than for V^{4+} ions $[(68-78)\times10^{-4}\ \mathrm{cm}^{-1}]$.[5] A similar situation is observed for Nb^{4+} and Mo^{5+} impurity ions and NbO^{2+} and MoO^{3+} complexes.[15] Therefore, the values of K for ions and the corresponding oxide complexes make it possible to determine the type of defect. The value of K was determined from the following formulas:[5]

$$A_{\parallel}=-K+P\{\Delta g_{\parallel}-(4/7)(1-0.75\Delta g_{\perp})\},$$
$$A_{\perp}=-K+P\{\Delta g_{\perp}+(2/7)(1-0.75\Delta g_{\perp})\}, \qquad (2)$$

where $\Delta g_{\parallel}=g_{\parallel}-2.0023$, $\Delta g_{\perp}=g_{\perp}-2.0023$. Hence $K=86\times10^{-4}\ \mathrm{cm}^{-1}$. We note that for other crystals of the KTP group ($KTiOPO_4$, $NaTiOPO_4$, and α- and β-$LiTiOPO_4$) the values of K likewise fall in the interval $(85-91)\times10^{-4}\ \mathrm{cm}^{-1}$.

A different method was developed in Ref. 5. In this method the values of the isotropic hyperfine constant ($A_{iso}=(A_{\parallel}+2A_{\perp})/3$) and the average g-factor ($g_{av}=(g_{\parallel}+2g_{\perp})/3$) are calculated from the experimental ESR data. As shown in Ref. 5, the points on the plot $g_{av}(A_{iso})$ are described well by two straight lines (for V^{4+} ions and VO^{2+} complexes) with the general formula

$$g_{av}=(-|A_{iso}|+K_0)/P_i+2.0023, \qquad (3)$$

where $K_0=55.2$ G, $P_1=418$ G (for V^{4+} ions), and $P_2=1763$ G (for VO^{2+} complexes).

We calculated the values of g_{av} and A_{iso} for crystals in the KTP group. These data are displayed in Fig. 3. The straight lines corresponding to the formula (3) are also presented in this figure. One can see that for V1 and V2 centers in RTP crystals, just as for the KTP crystals $NaTiOPO_4$ and α- and β-$LiTiOPO_4$ which we investigated earlier, the points fall between the straight lines I and II. Therefore, the results obtained by both methods agree with one another. In these crystals the bond between the vanadium and oxygen ions is probably strong and the earlier suggestion that centers of the type V^{4+} (and not VO^{2+}) form is ambiguous.

[1] A. S. Lyakhov, A. F. Selevich, and A. I. Verenich, Zh. Neorg. Khim. **33**, 1121 (1993).
[2] V. I. Voronkova and V. K. Yanovskiĭ, Izv. Akad. Nauk SSSR, Neorg. Mater. **24**, 2062 (1988).
[3] S. Yu. Stefanovich, L. A. Ivanova, and A. V. Astaf'ev, *Review Series on Scientific and Technical Forecasts in Physicochemical Research* [in Russian], Moscow, 1989.
[4] C. Kikuchi, I. Chen, W. H. From, and P. B. Dorain, J. Chem. Phys. **42**, 181 (1965).
[5] T. Hirose, M. Kawaminami, and M. Arakawa, J. Phys. Soc. Jpn. **54**, 3584 (1985).
[6] V. A. Grunin, V. A. Ioffe, I. B. Patrina, and G. D. Davtyan, Fiz. Tverd. Tela (Leningrad) **17**, 3034 (1975) [Sov. Phys. Solid State **17**, 2012 (1975)].
[7] S. D. Greorio, M. Greenblatt, J. H. Pifer, and M. D. Sturge, J. Chem. Phys. **76**, 2931 (1982).
[8] A. B. Vassilikou-Dova, S. Jansen, F. Wallrafen, and G. Z. Lenmann, Z. Naturforsch. A **44**, 711 (1989).
[9] R. P. Kohin, J. Zakelj, and V. K. Jain, J. Chem. Phys. **68**, 778 (1978).
[10] V. K. Jain, J. Phys. Soc. Jpn. **46**, 1250 (1979).
[11] V. K. Yanovskiĭ, V. I. Voronkova, A. P. Leonov, and S. Yu. Stefanovich, Fiz. Tverd. Tela (Leningrad) **27**, 2516 (1985) [Sov. Phys. Solid State **27**, 1508 (1985)].
[12] P. A. Thomas, S. C. Mayo, and B. E. Watts, Acta Cryst. B **48**, 401 (1992).
[13] K. T. Liu, J. T. Yu, S. H. Lou, C. H. Lee, Y. Huang, and K. H. Lii, Phys. Chem. Solids **55**, 1221 (1994).
[14] I. N. Geĭfman, P. G. Nagornyĭ, A. N. Usov, and Pham za Ngy, Fiz. Tverd. Tela (Leningrad) **33**, 2716 (1991) [Sov. Phys. Solid State **33**, 1535 (1991)].
[15] D. R. McGarvey, J. Phys. C **71**, 51 (1967).
[16] I. N. Geĭfman, P. G. Nagornyĭ, and M. V. Rotenfel'd, Fiz. Tverd. Tela (St. Petersburg) **36**, 3550 (1994) [Phys. Solid State **36**, 1888 (1994)].
[17] I. N. Geĭfman, N. G. Furmanova, P. G. Nagornyĭ, L. D. Yun, and M. V. Rotenfel'd, Kristallografiya **38**, 88 (1993) [Crystallogr. Rep. **38**, 259 (1993)].

Translated by M. E. Alferieff

LATTICE DYNAMICS. PHASE TRANSITIONS

Phonons in red HgI_2

S. I. Skachkov and V. G. Tyuterev

Siberian Physicotechnical Institute, Tomsk State University, 634050 Tomsk, Russia
(Submitted September 22, 1997)
Fiz. Tverd. Tela (St. Petersburg) **40**, 537–541 (March 1998)

A critical analysis of existing experimental and theoretical information on the lattice dynamics of the layered crystal α-HgI_2 is performed. It is shown that a satisfactory understanding of the character of the interatomic interaction and characteristic features of the phonon spectrum of this material can be obtained in a simple phenomenological model with eight parameters, assuming that E_g/B_{1g} degeneracy of the 29 cm^{-1} Raman line is of a two-phonon nature. © *1998 American Institute of Physics.* [S1063-7834(98)03103-7]

Crystalline HgI_2 in the red modification is a photoactive semiconductor with a room-temperature band gap of about 2.1 eV.[1,2] Earlier, it was of interest to study its optical properties, primarily the exciton spectrum, whereas now it is more important to investigate its transport properties. This change is due to the promising applications of α-HgI_2 as a working material for high-resolution x- and γ-ray spectrometers.[2,3] In Ref. 4 data were also obtained on the photoacoustic effect. A bar to wide application of HgI_2 is the quite low hole mobility ($\sim 4\ cm^2/V\cdot s$ at room temperature[5]). The key to understanding the reasons for such behavior could be the role of scattering by phonons.

An investigation of the phonon spectrum of HgI_2 was presented in a recent work,[6] where 18 branches of the phonon spectrum were calculated on the basis of the hard-ion model, the 27 parameters of which were determined by fitting neutron-scattering,[7] infrared-reflection,[8] and Raman-scattering[9] data. The proposed interpretation of experiment is quite reasonable on the whole, but a careful analysis reveals a number of weak spots that merit a more careful analysis.

First and foremost, the phonon frequencies were apparently calculated neglecting the conditions for stability of the crystal. This is obvious from the results presented in Table 3 of Ref. 6. The computed values of the sound velocities $\nu(001)_{xy}$ and $\nu(100)_z$ are substantially different (0.67×10^5 and 1.01×10^5 cm/s, respectively), while the symmetry implies that in the absence of mechanical stresses they should be equal.

The second problem concerns the analysis of phonon frequencies near 29 cm^{-1}. It follows from the computational results in Ref. 6 that there is an accidental degeneracy of the frequencies with the symmetries E_g and B_{1g}. It appears that the experiments performed do not unequivocally confirm this feature. While most of the Raman measurements that have been performed can indeed be interpreted on the basis of an accidental degeneracy, the neutron-diffraction data of Ref. 7 identify only the nondegenerate frequency B_{1g}. The Raman measurements in Ref. 10 do not show E_g/B_{1g} splitting with temperature and pressure. The experimental results on Raman scattering in the solid solution $Cd_{1-x}Hg_xI_2$[11] likewise do not agree with an accidental E_g/B_{1g} degeneracy. For this reason, the picture proposed in Ref. 6 for the phonon spectrum in red HgI_2 is not entirely satisfactory. In the absence of additional experimental data, specifically, for the phonon branches lying in the high-frequency region of the spectrum, the best way out, apart from, of course, first-principles calculations, could be a theoretical analysis in a phenomenological model with the minimum possible number of parameters. Such an approach has the advantage that the physical interpretation is clear, which promotes better understanding, though at the expense of, possibly, some loss of accuracy in reproducing the experiments. Our hard-ion model, combined with the Keating valence force field model,[12,13] it seems, makes it possible to give a physically well-grounded consistent interpretation of existing experimental data.

1. INTERATOMIC FORCE FIELD MODEL

The layered tetragonal structure of α-HgI_2[14] possesses D_{4h}^{15} group symmetry with six atoms per unit cell: iodine coordinates $[a/2, a/2, c/4-uc]$, $[0, a, c/4+uc]$, $[a/2, a/2, 3c/4-uc]$, $[0, a, 3c/4+uc]$ and mercury coordinates $[0, a/2, c/4]$, $[a/2, a, 3c/4]$ (Fig. 1). Here $a=4.37$ Å, $c=12.44$ Å, $u=0.14$ are the lattice parameters.

In the hard-ion model the Coulomb part of the energy is described by the interaction of the point charges of the ions, while the short-range forces are limited by the interaction of nearest neighbors. A central interaction with the force matrix

$$\Phi_{\alpha\beta}^{nm} = -A^{nm}\frac{R_\alpha^{nm}R_\beta^{nm}}{|R^{nm}|^2}. \tag{1}$$

is taken for the first neighbors. Here $R_\alpha^{nm}=R_\alpha^n-R_\alpha^m$, where R^n is the position of the n-th atom in the lattice, α and β are Cartesian indices, and A^{nm} is a force constant. In our case there are only two independent parameters $A^{\mathrm{Hg-I}}\equiv 3A$ and $A^{\mathrm{I-I}}\equiv F$. Since each Hg ion in the structure of HgI_2 possesses a quite regular tetrahedral environment consisting of I

 © 1998 American Institute of Physics

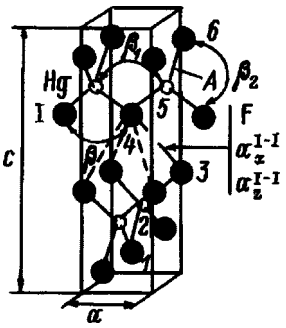

FIG. 1. Structure of α-HgI_2. The numbers indicate the ions appearing in the unit cell.

ions, it is reasonable to adopt for the interaction of the second neighbors the Keating variant[12] of the valence force field model. This model has been successfully used to describe phonons in ionic-covalent crystals with III–V structure.[13] The Keating contributions to the interaction of the first and second neighbors can be written, respectively, in the form

$$\Phi_{\alpha\beta}^{nm}=-\frac{3}{4|R^{nm}|^2}\sum_k\{B_n^{mk}[R_\alpha^{nk}R_\beta^{nk}+R_\alpha^{nm}R_\beta^{nk}]+B_m^{nk}[R_\alpha^{mk}R_\beta^{mk}+R_\alpha^{mk}R_\beta^{mn}]\},$$

$$\Phi_{\alpha\beta}^{nm}=\frac{3}{4}\sum_k B_k^{nm}\frac{R_\alpha^{km}R_\beta^{km}}{|R^{nm}|^2}. \qquad (2)$$

Here B_k^{mn} is the force constant corresponding to a change in angle between the covalent bonds with a vertex at the k-th ion; the pairs (kn) and (km) are nearest neighbors and the pairs (nm) are second nearest neighbors. Assuming a definite rigidity in the preservation of the tetrahedral symmetry around Hg, only three independent angular constants need be considered: $\beta_1\equiv B_{\mathrm{I}}^{\mathrm{Hg-Hg}}$, $\beta\equiv B_{\mathrm{Hg}}^{\mathrm{I-I}}$ (both iodine ions lie in the same xy plane), and $\beta_2\equiv B_{\mathrm{Hg}}^{\mathrm{I-I}}$ (the iodine ions lie in different xy planes). The Coulomb part of the dynamical matrix can be calculated by the conventional Ewald method,[15] and the condition of electric neutrality reduces the number of independent parameters to one: $Z_{\mathrm{Hg}}\equiv z$, $Z_{\mathrm{I}}\equiv -z/2$.

The dynamical matrix must be invariant under a small rotation of the coordinate system and satisfy the condition of no internal stresses.[15] The Keating component is automatically invariant, while the electrostatic contribution does not satisfy these conditions, as a result of which, the permutational symmetry of the indices for the elastic moduli, which in the tetragonal crystal should have the form $C_{zzxx}=C_{xxzz}$ and $C_{xzxz}=C_{zxxz}=C_{zxzx}=C_{xzzx}$, breaks down. The above-noted difference of the sound velocities in the calculation performed in Ref. 6 is apparently a consequence of the fact that this circumstance was neglected. To restore the invariance properties of the complete dynamical matrix, compensating terms must be introduced in the short-range part. In the simplest variant diagonal terms of the form $\Phi_{\alpha\beta}^{nm}=-\delta_{\alpha\beta}a_\alpha^{nm}$ are added to the first-neighbors matrix.[16] Only two of the six additional parameters are independent, since by symmetry $a_x^{\mathrm{I-I}}=a_y^{\mathrm{I-I}}$ and $a_x^{\mathrm{Hg-Hg}}=a_y^{\mathrm{Hg-Hg}}$ and the conditions of invariance imply

TABLE I. Frequencies of long-wavelength phonons in HgI_2.

Phonon symmetry	Frequency, cm^{-1}			
			Our calculation	
	Experiment	Theory[6]	*a*	*b*
B_{1g}	143 [Ref. 11]	148	146	143
$A_{2u}(L)$	139.23 [Ref. 8]	-	144	140
$A_{2u}(T)$	125.29 [Ref. 8]	119	131	127
$E_u(L)$	128.99 [Ref. 8]	-	122	123
B_{2u}	-	-	100	107
$E_u(T)$	104.84 [Ref. 8]	104	111	110
E_g	115 [Ref. 11]	142	113	112
A_{1g}	115 [Ref. 11]	112	108	114
$E_u(L)$	32.15 [Ref. 8]	-	33.4	53.6
B_{1g}	28.8 [Ref. 11]	29.6	29.3	28.9
E_g	28.8 [Ref. 11]	29.4	29.4	53.4
E_g	17.9 [Ref. 11]	18.5	17.5	18.5
$E_u(T)$	17.46 [Ref. 8]	19.6	15.7	47.5

$$\frac{c}{2}[2ua_x^{\mathrm{Hg-I}}+(4u-1)a_x^{\mathrm{I-I}}]=-\frac{ae_0^2z^2}{v_a}\cdot 1.76445,$$

$$\frac{c}{2}[4u^2a_x^{\mathrm{Hg-I}}+(4u-1)^2a_x^{\mathrm{I-I}}]-\frac{a^2}{4}(a_z^{\mathrm{Hg-I}}+a_z^{\mathrm{I-I}})=\frac{a^2e_0^2z^2}{8\pi v_a}\cdot 31.496. \qquad (3)$$

Here e_0 is the electron charge and ν_a is the cell volume. The values of the first and second derivatives of the electrostatic contribution with respect to the wave vector which appear in Eq. (3) were calculated by the Ewald method.[15] The self-action matrices $\Phi_{\alpha,\beta}^{nm}$ can be expressed completely in terms of the independent parameters, already introduced, from the condition of translational invariance. This completes the definition of the force-field model.

2. RESULTS AND DISCUSSION

In the discussion below we employ the group-theoretic classification, presented in Ref. 7, of the spectrum of HgI_2. Eight parameters of the theory were determined by least-squares fitting for known values of the long-wavelength frequencies observed in Raman[9,11,17–19] and IR experiments.[7,8] The results are presented in column *a* in Table I and on the whole agree well with experiment. There is a discrepancy of $\sim 7\ cm^{-1}$ for the most intense Raman mode with symmetry A_{1g}. The elastic moduli calculated in this variant (column *a* in Table II) agree with experiment,[7,20] excepting C_{13}, C_{44}, and C_{66}, the latter value being an order of magnitude lower than the observed value, signifying that the value of the transverse sound velocity $[100]_y$ is too low (the direction of the wave vector is shown in brackets and the index denotes the polarization).

Though not included in the fitting procedure, the dispersion curves of the phonons along [100] and [001] (Fig. 2a) nonetheless agree with experiment[7] and the computed dispersion in the 27-parameter model.[6] Just as in Ref. 6, together with six branches of the interlayer vibrations which are observed in the neutron experiment, our calculation shows a

TABLE II. Elastic constants of HgI_2 (10^{11} dynes/cm^2).

Elastic constant	Experiment		Theory	
	Ref. 7	Ref. 20	*a*	*b*
C_{11}	3.16	3.303	4.32	4.08
C_{33}	1.526	1.634	1.70	1.69
C_{44}	0.727	0.723	0.257	0.612
C_{66}	0.35	0.231	0.038	0.490
C_{12}	-	0.559	0.547	0.538
C_{13}	-	1.168	0.544	0.485

coupling between two additional branches, which penetrate into the low-frequency part of the spectrum and have no experimental analog. The absence of these branches in the experiment is explained in Ref. 6 by the specific form of the atomic displacements, which effectively leads to small neutron-scattering cross sections.

The experimental data of Ref. 11 for the solid solution $Cd_xHg_{1-x}I_2$ present an additional way to assess the quality of the theory. According to the form of the computed polarization vectors, the low-frequency part of the HgI_2 spectrum corresponds to a rigid relative displacement of the layers, so that the virtual crystal approximation can be used to investigate the concentration dependence of the vibrations in the solid solution. Calculations (dashed lines in Fig. 3) show a linear variation as a function of concentration for the lowest-frequency mode with B_{1g} symmetry, while the E_g mode degenerate with B_{1g} at $x=0$ shows virtually no variation with concentration. The experimental data of Ref. 11 do not show any indications of such a splitting of the E_g and B_{1g} modes with concentration, which casts doubt on their interpretation based on accidental degeneracy. In this connection, we note that in Ref. 10 lifting of E_g/B_{1g} degeneracy under the action of pressure or as a function of temperature was not observed.

In the high-frequency part of the spectrum the solid solution exhibits bimodal behavior, so that for interpretation of the experiment it is reasonable to use the calculations of

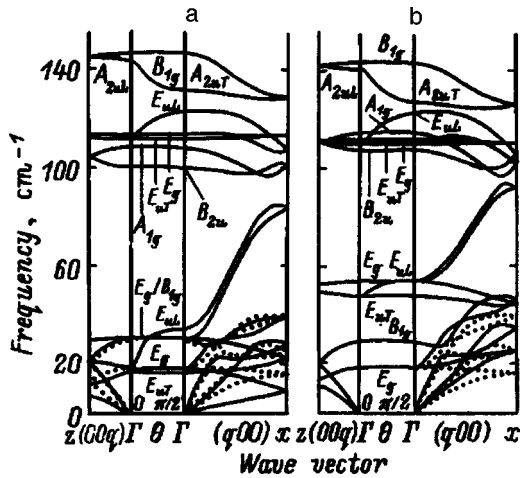

FIG. 2. Phonon spectrum of α-HgI_2, calculated for two sets of the interatomic interaction parameters (a, b). Solid lines—calculation, dotted lines—neutron diffraction data.[7] The dependence of the long-wavelength frequencies on the angle θ between the phonon wave vector and the tetragonal axis C is presented in the central part of the figure (Γ–Γ).

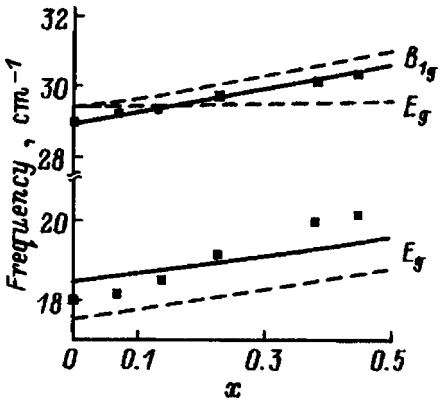

FIG. 3. Concentration dependence of low-frequency long-wavelength phonons in $Cd_xHg_{1-x}I_2$. The dots represent experimental data.[11] The dashed and solid lines correspond to calculations in the virtual crystal approximation in the variants *a* and *b* of the theory.

frequencies in the hypothetical crystal CdI_2 in the structure of red mercury iodide. Taking the same parameters of the force field, we obtained $\omega_{B_{1g}}(CdI_2)=173\ \mathrm{cm}^{-1}$ and $\omega_{E_g}(CdI_2)=128\ \mathrm{cm}^{-1}$, in good agreement with the observed values 168 ± 3 and $130\ \mathrm{cm}^{-1}$.[11] Since the completely symmetric mode A_{1g} contains only displacements of iodine, the corresponding frequency in the solid solution does not depend on concentration (108 and $115\ \mathrm{cm}^{-1}$ in the calculation and experiment of Ref. 11, respectively).

Analysis of the values of the model parameters (the variant *a* in Table III) shows that the force constant F is small, in agreement with the idea of a van der Waals interaction between the layers.[10] The constants $a_x^{\mathrm{I-I}}$ and $a_z^{\mathrm{I-I}}$ are small, but they give equal transverse sound velocities $[100]_z$ and $[001]_{x,y}$, as the crystal symmetry requires. The values of the charge of the Hg ion are close to those given in Ref. 6. The value of the force constant A is typical for III–V crystals. Interestingly, the angular constants for the Hg–I–Hg angle are unusually large, compared with the values in the III–V group. At the same time, the intralayer constant $\beta_2 \equiv B_{\mathrm{Hg}}^{\mathrm{I-I}}$ is half the value of the constant $\beta \equiv B_{\mathrm{Hg}}^{\mathrm{I-I}}$, signifying a weak rigidity of the corresponding angles and HgI_4 tetrahedra as a whole with respect to stresses oriented in a direction transverse to a layer. It is difficult to explain such a large difference in the rigidities of the different valence angles in the presence of a regular tetrahedral coordination.

We attempted to resolve the contradictions noted above by attributing them to the rejection of the hypothesis of accidental degeneracy of the ω_{E_g} and $\omega_{B_{1g}}$ modes at $29\ \mathrm{cm}^{-1}$ by eliminating ω_{E_g} from the set of fitted frequencies. The results presented in column *b* in Table I show much better agreement with experiment, including also A_{1g}, but the lowest frequency ω_{E_u} and the next highest frequency ω_{E_g} increase substantially. The result is that the pair of phonon branches which is associated with them is displaced out of the region of interlayer vibrations covered by the neutron-diffraction experiment (Fig. 2b). The quantitative agreement with the experimental dispersion of the phonons in the [100] direction is somewhat worse, but the qualitative picture of the spectrum seems to be even better. At the same time, the

TABLE III. Parameters of the interatomic force field in HgI_2 (10^3 dynes/cm) and effective charges (in a.u.).

A	$B_{\mathrm{I}}^{\mathrm{Hg-Hg}}$	$B_{\mathrm{Hg}}^{\mathrm{I-I}}$	$B_{\mathrm{Hg}}^{\mathrm{I-I}'}$	F	$a_x^{\mathrm{I-I}}$	$a_z^{\mathrm{I-I}}$	z_{Hg}	Fitting variant
20.93	13.50	5.11	3.27	2.28	−0.21	0.85	0.975	*a*
20.14	8.53	8.53	9.41	2.10	−0.17	0.90	0.990	*b*

agreement for the [001] phonon branches is excellent. We recall that the neutron-diffraction data were not included in the least-squares scheme. The elastic constants, likewise not specially fit, agree much better with experiment in this variant (column *b* in Table II). The agreement with the experimental concentration dependence of the low-frequency modes ω_{E_g} and $\omega_{B_{1g}}$ in $Cd_xHg_{1-x}I_2$ (solid curves in Fig. 3) is as good as in the preceding variant of the fit, except that the problem of the absence of a concentration splitting does not arise at all. The computed values $\omega_{B_{1g}}(CdI_2)=170\ \mathrm{cm}^{-1}$, $\omega_{E_g}(CdI_2)=129\ \mathrm{cm}^{-1}$, and $\omega_{A_{1g}}(CdI_2)=114\ \mathrm{cm}^{-1}$ likewise agree excellently with experiment.[11] The values of the central constants, just as $a_x^{\mathrm{I-I}}$ and $a_z^{\mathrm{I-I}}$, in both variants (*a* and *b*) differ very little (Table III), while the angular constants are closer to one another, falling into the range of values of these constants for III–V compounds, which appears to be more reasonable, bearing in mind that the tetrahedral environment of Hg is preserved.

In this variant of the calculation of the phonon spectrum of HgI_2 there are a number of discrepancies with the traditional interpretation. Most importantly, the poor agreement between the phonon frequencies at the point *X* and the experimental values is apparently of the same origin as for the calculations for III–V crystals in the Keating model,[13] and the agreement can be improved in a model that takes account of the bond polarizability.

The most serious problem arises with the frequency $29\ \mathrm{cm}^{-1}$, which in all Raman experiments is observed simultaneously in the E_g and B_{1g} geometries, which served as the basis for the idea of accidental degeneracy. The LO/TO infrared frequencies $18\ \mathrm{cm}^{-1}/32\ \mathrm{cm}^{-1}$ observed experimentally in the E_u geometry also require explanation.[8]

Our calculations show that the three phonons at the point *Z* have the frequencies $\omega_{Z_1}=11\ \mathrm{cm}^{-1}$, $\omega_{Z_2}=13\ \mathrm{cm}^{-1}$, and $\omega_{Z_3}=20\ \mathrm{cm}^{-1}$, respectively, so that the two-phonon overtones $2\omega_{Z_1}$ and $2\omega_{Z_2}$ and the combination frequencies $\omega_{Z_1}+\omega_{Z_2}$, $\omega_{Z_1}+\omega_{Z_3}$, and $\omega_{Z_2}+\omega_{Z_3}$ turn out to be close to the computed single-phonon frequencies $\omega_{E_g}=18\ \mathrm{cm}^{-1}$ and $\omega_{B_{1g}}=29\ \mathrm{cm}^{-1}$. The direct product of the representations $Z_1\otimes Z_3$ and $Z_2\otimes Z_3$ does indeed contain both the IR and RS active representations of the point Γ, while for other combinations this is not valid. We note in this connection that it is not obvious that the standard group-theoretic methods are applicable under conditions of a Fermi resonance of two- and one-phonon frequencies. For this reason, the interpretation of the observed frequencies $\omega_{E_u}(T)=18\ \mathrm{cm}^{-1}$, $\omega_{E_u}(L)=32\ \mathrm{cm}^{-1}$, and $\omega_{E_g}=29\ \mathrm{cm}^{-1}$, conventionally treated in the one-phonon sense, as manifestations of a resonance between first- and second-order processes in the optical experiment seems admissable. It is interesting that in $Cd_xHg_{1-x}I_2$ the concentration dependence of the low-frequency *Z*-phonon frequencies (and therefore also their combinations) is identical to that for Γ phonons, which explains the reason why the E_g/B_{1g} degeneracy remains, at least in this case.

Indirect evidence of the multiphonon nature of the lines 18, 32, and $29\ \mathrm{cm}^{-1}$ could be the fact that none of these frequencies is observed in neutron experiments in the $E_{uLO/TO}$ and E_g geometries.[7] The entire phonon branches $Z_2-\Delta_5-E_u-\Delta_1$, Δ_2 and $Z_1-\Delta_5-E_g-\Delta_3$, Δ_4, which are topologically coupled with them by symmetry, are also not observed (see the compatibility relations in Ref. 7). Doubts as to the single-phonon nature of the oscillator $18\ \mathrm{cm}^{-1}/32\ \mathrm{cm}^{-1}$ are also bolstered by their unusual properties observed in Ref. 8—almost complete absence of temperature dependence of the reflection coefficient, negative temperature shift of the frequency, and unusually large oscillator strength, which lead to an anomalously large anisotropy of the low-frequency permittivity tensor with moderate anisotropy of its high-frequency part. A substantial variance in the values of the low-energy branch $\omega_{E_u}(LO,TO)$ in IR experiments performed by other groups and an unusual pressure dependence of the branch $\omega_{E_u}(TO)$ are also observed.[9,10]

The computed value $\omega_{E_g}=53\ \mathrm{cm}^{-1}$ appears not to agree with experiment, but it falls into the frequency range $37-55\ \mathrm{cm}^{-1}$, where Prevot *et al.*[19] observed features in the Raman spectra, interpreting them from the standpoint of second-order processes. The computed polar mode $\omega_{E_u}=47\ \mathrm{cm}^{-1}/54\ \mathrm{cm}^{-1}$ has a quite small longitudinal–transverse splitting ($6\ \mathrm{cm}^{-1}$), as a result of which it should have a relatively small oscillator strength and, correspondingly, a low intensity in IR absorption.

Although the existing experimental data do not permit making a definite choice between the two interpretations, the second set of model parameters appears to be preferable both from the standpoint of the neutron-diffraction experiment and the behavior of phonons in the solid solution and in the sense of the interpretation of the character of the chemical bond.

In summary, we have performed calculations of the phonon spectrum of red HgI_2 in a simple model of interatomic forces with eight parameters. In the conventional interpretation of the experimentally observed frequency $29\ \mathrm{cm}^{-1}$ as an accidentally degenerate combination of single-phonon frequencies $\omega_{E_g}/\omega_{B_g}$, the model underestimates the transverse sound velocity, leads to the appearance of two extra branches in the interlayer part of the phonon spectrum, and contradicts

the results of Raman experiments on $Cd_xHg_{1-x}I_2$. We believe that the two-phonon interpretation of both the Raman frequency $\omega_{E_g}=29\ \mathrm{cm}^{-1}$ and the lowest polar frequency ω_{E_u} is more consistent with the character of the interatomic interaction in red HgI_2.

We thank Professor A. Anedda and J. Mul for formulating the problem and for a discussion of the results.

[1] Yia-Chung Chang and R. B. James, Phys. Rev. B **46**, 15040 (1992).
[2] X. J. Bao, T. E. Schisinger, R. B. James, R. H. Stulen, C. Ortale, and A. Y. Cheng, J. Appl. Phys. **68**, 86 (1990); X. J. Bao, T. E. Schisinger, R. B. James, G. L. Gentry, A. Y. Cheng, C. Ortale, J. Appl. Phys. **69**, 4247 (1991).
[3] S. P. Swierkowski, G. A. Armantrout, and R. Wichner, Appl. Phys. Lett. **23**, 281 (1973).
[4] B. K. Kardashev, A. V. Rezvushkin, P. A. Stepanov, V. A. Stepanov, V. M. Chernov, and V. M. Zaletin, Fiz. Tverd. Tela (St. Petersburg) **38**, 1511 (1996) [Phys. Solid State **38**, 832 (1996)].
[5] R. Minder, G. Ottaviani, and C. Canali, J. Phys. C **37**, 417 (1976).
[6] Hock-Kee Sim, Yia-Chung Chang, and R. B. James, Phys. Rev. B **49**, 4559 (1994).
[7] B. Prevot, C. Schwab, and B. Dorner, Phys. Status Solidi B **88**, 327 (1978).
[8] J. Biellmann and B. Prevot, Infrared Phys. **20**, 99 (1980).
[9] N. Kuroda, T. Iwabuchi, and Y. Nishina, J. Phys. Soc. Jpn. **52**, 2419 (1983).
[10] N. Kuroda, M. Sakai, and Y. Nishina, J. Phys. Soc. Jpn. **54**, 1423 (1985).
[11] A. Anedda, G. Bongiovanni, and E. Fortin, Phys. Status Solidi B **146**, 757 (1988).
[12] P. N. Keating, Phys. Rev. **145**, 637 (1966).
[13] R. M. Martin, Phys. Rev. B **1**, 4005 (1970).
[14] R. W. G. Wyskoff, *Crystal Structures*, Interscience Publishers, N.Y., 1965, Vol. 1, p. 309.
[15] M. Born and K. Huang, *Dynamical Theory of Crystal Lattices* [Clarendon Press, Oxford, 1954; Inostr. Lit., Moscow, 1958].
[16] V. G. Tyuterev and S. I. Skachkov, Nuovo Cim. **140**, 1097 (1992).
[17] V. A. Haisler, V. M. Zaletin, and A. F. Kravchenko, Phys. Status Solidi B **125**, K103 (1984).
[18] V. A. Haisler, V. M. Zaletin, A. F. Kravchenko, and G. Y. Yashin, Phys. Status Solidi B **121**, K13 (1984).
[19] B. Prevot and J. Biellmann, Phys. Status Solidi B **95**, 601 (1979).
[20] S. Haussuhl and S. H. Scholz, Krist. Tech. **10**, 1175 (1975).

Translated by M. E. Alferieff

LOW-DIMENSIONAL SYSTEMS AND SURFACE PHYSICS

Low-frequency plasmons in coupled electronic microstructures

A. O. Govorov and S. A. Studenikin

Institute of Semiconductor Physics, Siberian Branch of the Russian Academy of Sciences, 630090 Novosibirsk, Russia

W. R. Frank

University of Munich, 80539 Munich, Germany

(Submitted August 6, 1997)
Fiz. Tverd. Tela (St. Petersburg) **40**, 542–545 (March 1998)

The plasmon spectrum and the absorption of an electromagnetic wave in an electronic two-dimensional plasma with strongly modulated density are studied. The appearance of additional plasmon modes in a system of electronic wires and islands with weak current coupling is described in a model of an electronic system covered with metallic gates. Such plasmon modes appear in the low-frequency region of the spectrum, as compared with the conventional plasma oscillations, and have recently been observed experimentally in paired wires. © *1998 American Institute of Physics.* [S1063-7834(98)03203-1]

Systems of interacting electronic wires and dots are objects of intense investigation. The interaction between electronic wires and dots, for example, as a result of Coulomb forces or a current, can result in new physical phenomena.[1] It has recently been shown that current coupling in pairs of electronic wires strongly modifies their absorption spectrum.[2] In the present paper the case when a weak current coupling in a pair of electronic wires or dots results in the appearance of new plasma modes and substantially alters the optical response of the system is described. The spectrum of plasma oscillations in systems with periodically modulated density has been investigated theoretically in a number of studies by means of perturbation theory[3] and by numerical methods.[4,5] Perturbation theory makes it possible to describe analytically the case of weak modulation of the electron density. The numerical results presented in Refs. 4 and 5 do not give a complete picture of all regimes of interaction between electronic wires. For example, new plasma modes are observed when a weak current coupling arises between wires (the case of strong modulation of the density).[2] Such a regime was not described in detail earlier in Refs. 4 and 5.

In the present paper the spectrum of electronic wires with an arbitrary degree of coupling is investigated. The model of a two-dimensional ($2D$) system with metallic gates makes it possible to describe analytically the spectrum and optical response of the wires. Low-frequency plasmons in two electronic islands coupled by a narrow neck are also studied.

1. PLASMON SPECTRUM OF A $2D$ SYSTEM WITH NONUNIFORM DENSITY

We consider a structure with metallic finger-shaped gates in the form of strips (Fig. 1), similar to that investigated in Ref. 2. A quantum well (QW), formed at the heteroboundary of the GaAs layer and a short-period AlAs–GaAs superlattice, is located between the system of gates on the surface of the sample and the bottom embedded contact in the form of a strongly doped GaAs layer. When a positive voltage is applied to the surface gates, the electrons of the reverse contact tunnel into the QW, forming a $2D$ electronic system with modulated density. The equilibrium electron density distribution $N_s(x)$ (x is the coordinate axis in the plane of $2D$ layer, perpendicular to the wires) is controlled by the voltages V_1 and V_2 applied to the metal strips.

The response of the system to a uniform external electric field $\mathbf{f}_0 e^{-i\omega t}$ is described by the conventional expression for the surface current $\sigma(x)[\mathbf{f}_0+\mathbf{f}_{\rm ind}(\mathbf{r})]e^{-i\omega t}$, where $\mathbf{r}=(x,y)$ is the $2D$ radius vector, $\mathbf{f}_{\rm ind}$ is the amplitude of the electric field induced by the plasma, $\sigma(x)=e^2N_s(x)/[m^*(-i\omega+\Gamma)]$, m^* is the electron mass, and $1/\Gamma$ is the relaxation time. The electric field $\mathbf{f}_{\rm ind}$ can be expressed in terms of the perturbation $\delta\varphi$ induced in the potential by the plasma: $\mathbf{f}_{\rm ind}e^{-i\omega t}=-\nabla\delta\varphi(\mathbf{r},t)$. If the distance d from the surface gate to the quantum well is much less than the width a of the metal strips, the induced potential in the plane of the QW is proportional to the perturbation of the electron density (the flat capacitor approximation):

$$\delta\varphi(\mathbf{r},t)=-\frac{4\pi|e|d}{\varepsilon}\delta n_s(\mathbf{r},t). \tag{1}$$

Here $\delta n_s(\mathbf{r},t)=\delta n(\mathbf{r})e^{-i\omega t}$ is the nonequilibrium correction to the electron density and $e=-|e|$ is the electron charge. The expression (1) makes it possible to obtain a differential equation for the current.[6] Let the external field be directed along the x axis: $\mathbf{f}_0=(f_0,0)$. Using the continuity equation, in the linear approximation we arrive at an expression for the amplitude of the x component of the current $j_s=j(x)e^{-i\omega t}$:

 © 1998 American Institute of Physics

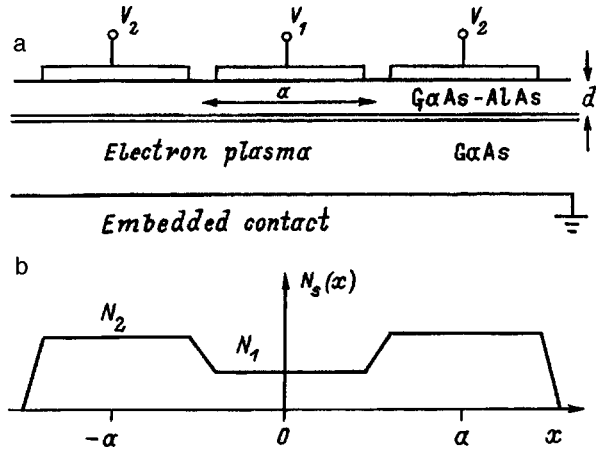

FIG. 1. a) Transverse section of a system with two electronic wires coupled by a region with low electron density. The electrons tunnel into the quantum well from the embedded contact when voltages are applied to the surface gates. b) Schematic diagram of the electron density distribution in the plane of the quantum well for $V_1>0$, $V_2>0$.

$$\frac{d^2j(x)}{dx^2}+\frac{i\varepsilon\omega}{4\pi\sigma(x)d}j(x)=f_0\frac{i\omega\varepsilon}{4\pi d}. \tag{2}$$

Without the expression on the right-hand side this equation has the form of a Schrödinger equation with zero energy. Let us write the expression (2) without the right-hand side and introduce formally an ''energy'' E: $j''+[\Phi(x,\omega)-E(\omega)]j=0$. The ''potential'' $\Phi(x,\omega)$ in this equation is proportional to $1/N_s(x)$. The characteristic values of the energy of this equation determine the plasma frequencies of the system: $E_n(\omega)=0$. Under the condition $E_n(\omega)=0$ the eigenfunctions $j_n(x)$ are orthogonal to each other with weight $1/N_s(x)$: $\int dx j_n j_m/N_s(x)=\delta_{nm}$.

Let us examine the simplest case of a strip with a uniform electron density $N_s(x)=N_x$ for $|x|<a/2$ and $N_s(x)=0$ for $|x|>a/2$. The boundary conditions for the current are $j(x=\pm a/2)=0$. The plasmon spectrum is obvious: $\omega_n^2=(4\pi e^2 dN_s/m^*\varepsilon)q_n^2$,[4] where $q_n=\pi n/a$ and ε is the permittivity of the semiconductor.

2. COUPLED ELECTRONIC WIRES

In a system with three metal gates (Fig. 1a) the electron density can be written in the form $N_s(x)=N_1$ for $|x|<a/2$ and $N_s(x)=N_2$ for $a/2<x<3/2a$, $-3/2a<x<-1/2a$. It is convenient to describe the quantities N_1 and N_2 in the approximation $N_1=C_0V_1$ and $N_2=C_0V_2$, where C_0 is the specific capacitance of the gate with respect to the electronic layer. In this system it can be assumed that electrons flow into the layer with the QW for positive values of V_1 and V_2, i.e., $N_1\neq 0$ ($N_2\neq 0$), if $V_1>0$ ($V_2>0$). Moreover, we assume that the sections with a free surface between the gates are narrow compared with the gates, while the density profile $N_s(x)$ is a step function. Thus, the expression for the potential (1) will be used for the entire surface in the interval $-3/2a<x<3/2a$.

The quantities $j(x)$ and $\delta n(x)$ in our model are combinations of the functions $A_i\cos(k_ix)$ and $B_i(k_ix)$, where $k_i=\omega/\nu_i$ and $\nu_i=\sqrt{4\pi e^2 dN_i/m^*\varepsilon}$ is the plasmon velocity

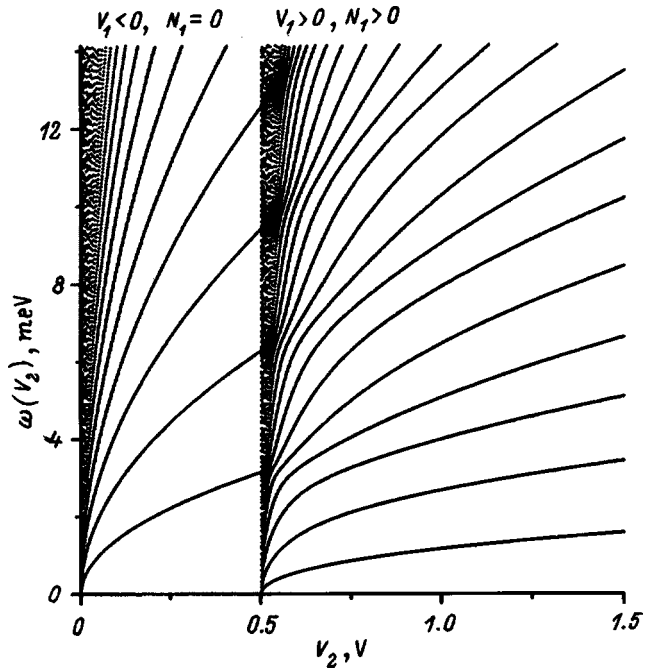

FIG. 2. Plasmon spectrum of a system of two coupled wires as a function of the voltage V_2 with fixed potential difference $\Delta V=V_1-V_2=-0.5$V. Current coupling between the wires appears for voltages $V_2>0.5$V ($V_1>0$). Parameters of the structure: $a=1000$ Å, $d=600$ Å, $\varepsilon=12.5$, and $m^*=0.07m_0$ (m_0—free-electron mass).

in regions with densities $N_{i=1,2}$. The coefficients A_i and B_i can be found from the continuity of the functions $j(x)$ and $\delta n(x)$ at the points $x=\pm 1/2a$ and from the condition $j(x)=0$ at $x=\pm 3/2a$. From these boundary conditions follow equations for the plasmon frequencies

$$\frac{v_2}{v_1}\tan\left(\frac{k_1a}{2}\right)=\cot(k_2a),\quad \frac{v_2}{v_1}\cot\left(\frac{k_1a}{2}\right)=\cot(k_2a). \tag{3}$$

These equations describe the frequencies of the antisymmetric and symmetric plasma oscillations, respectively.

Figure 2 shows the plasmon spectrum with zero longitudinal momentum as a function of the voltage V_2 with a constant potential difference $\Delta V=V_1-V_2=-0.5$ V. Actually, Fig. 2 shows the spectrum for different values of the parameter $\gamma=N_1/N_2$. For $V_2<0.5$ V ($V_1<0$, $N_1=0$) the spectrum consists of plasmons localized in separate wires. The point $V_2=0.5$ V ($V_1=0$) is a singular point. The branches of the spectrum condense at this point on account of the appearance of current coupling between the electronic wires under the side gates. Near and to the right of the point $V_2=0.5$ V ($V_1=0$) the distance between the branches of the spectrum is of the order of $\nu_1/a\propto\sqrt{N_1}\propto\sqrt{V_1}$. When the voltage V_2 approaches the value 0.5 V from the right-hand side, all branches of the spectrum approach zero. If the voltage V_2 is only slightly above 0.5 V, the spectrum in Fig. 2 has points of condensation opposite the frequencies of the plasmons localized in individual side wires with $V_2=0.5$ V.

Let us examine the lowest branch of the spectrum in Fig. 2 in a small neighborhood to the right of the point $V_2=0.5$ V. This branch has the frequency $\Omega_0\simeq 1.31\nu_1/a$ and corresponds to an oscillation in which charge flows be-

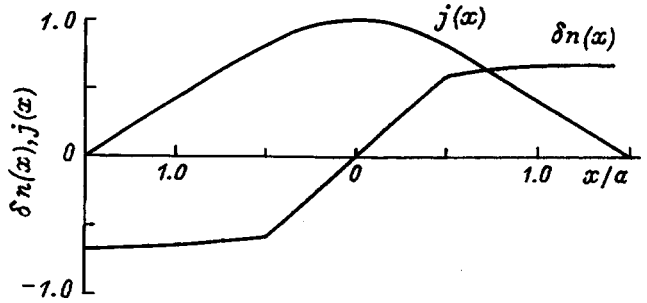

FIG. 3. Nonequilibrium charge density and current distributions ($\delta n(x)$ and $j(x)$) in the low-frequency mode.

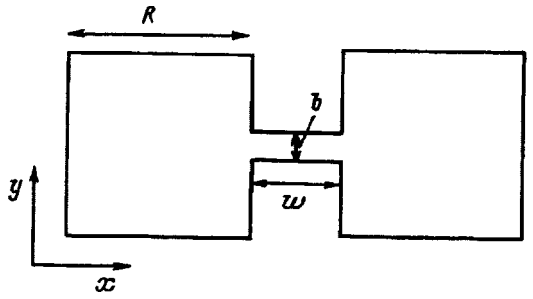

FIG. 5. Geometry of a system with two coupled electronic islands.

tween two side wires (Fig. 3). Note that the frequency of this mode is much lower than the characteristic plasma frequency ν_2/a of the individual wires with voltage $V_2=0.5$ V.

The current in the presence of an external force can be obtained from Eq. (2) as

$$j(x)=\sum_n j_n(x)\frac{A_n}{\omega(\omega+i\Gamma)-\omega_n^2},$$

$$A_n=-f_0\left(\frac{i\omega e^2}{m^*}\right)\int j_n(x)dx. \tag{4}$$

The intensity of IR absorption $I(\omega)=(1/2)f_0\ \mathrm{Re}[\int j(x)dx]$ is shown in Fig. 4. The spectra *1* and *2* in Fig. 4 are presented for voltages near $V_1=0$. The spectra *3* and *4* are presented for comparatively high voltages V_1, when the system consists of one wide wire with modulation of the density. Only modes with an antisymmetric density distribution are active in the IR absorption spectrum. One can see that the IR absorption spectrum near the point $V_2=0.5$ V ($\gamma=0$) is modified and acquires a low-frequency structure. The number of modes in a unit interval of the spectrum for small values of γ (Fig. 2) is large, but the intensity of most of them is low. When plasmon damping is taken into account, the IR spectrum changes continuously from a regime of uncoupled wires ($\gamma=0$) into a regime of coupled oscillations ($\gamma>0$). For low values of V_1 the low-frequency mode, marked by the asterisk in Fig. 4, has a low oscillator strength, since this mode is due to charge flowing over through the region with a low density $N_1\propto V_1$. As V_1 increases, the low-frequency mode becomes dominant in the spectrum, since in a single wire with almost uniform density it has the largest dipole moment. The second low-frequency mode, which is marked by two asterisks in Fig. 4, also acquires a substantial oscillator strength as the voltage increases.

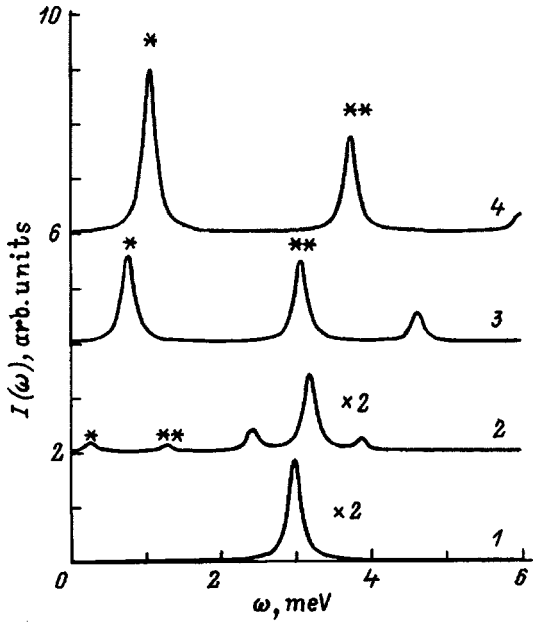

FIG. 4. Absorption spectrum of coupled wires for different voltages (in V) applied to the gates. V_1 and V_2: *1*—0.05 and 0.45, *2*—0.02 and 0.52, *3*—0.2 and 0.7, *4*—0.4 and 0.9. Potential differences $\Delta V=V_1-V_2=-0.5$ V and $\Gamma=0.1$ meV. The asterisks mark the low-frequency modes arising when $V_1>0$.

A similar behavior of the IR absorption spectrum was observed experimentally in Ref. 2, where the experiment was performed in a system with paired wires. The electron density in these wires was varied by applying voltages to two metal strips on the surface of the sample. As the voltages increased, the electronic wires merged, forming one wide channel with a barrier in the middle. In other words, the current coupling between the wires was controlled by the voltage. In the experiment of Ref. 2, a free surface was present between the metal strips, and therefore the current coupling between the wires was also determined by the surface charges. In our approach we introduce a third gate in the middle in order to model the effect of surface charges. Comparison of our theoretical results and the experimental data of Ref. 2 shows that our model reproduces the qualitative behavior of the experimental spectra. In addition, the experiments of Ref. 7 showed that the intensity of the low-frequency mode in the IR absorption spectrum varies with charge transfer on the surface between the metal strips. Thus, the low-frequency plasmons arising on account of the current coupling between the microstructures can be used to obtain information about the charge state of the surface.

3. COUPLED ELECTRONIC ISLANDS

Let us examine the spectrum of two square, electronic islands coupled by a narrow neck (Fig. 5). The width b of the neck is much smaller than the length R of the edge of the square-shaped island. The entire system is covered with a

dielectric layer of thickness d and an uniform metal gate. From the expression (1) and the continuity equation we obtain

$$\nabla^2 \delta n(\mathbf{r}) + \frac{\omega^2}{v_p^2} \delta n(\mathbf{r}) = 0, \tag{5}$$

where $\nu_p = \sqrt{4\pi e^2 dN_s/m^*\varepsilon}$ is the phase velocity of a plasmon and N_s is the electron density, which is the same in all regions of the microstructure, including the neck. Here we neglect the damping of the plasmons. The boundary condition is vanishing of the component of the current perpendicular to the boundary, $\mathbf{j}\cdot\mathbf{s} \propto \nabla n \cdot \mathbf{s} = 0$ ($\mathbf{s}$ is the normal to the boundary).

Let us examine first the solution of Eq. (5) for a single electronic island. For zero boundary, conditions $\mathbf{j}\cdot\mathbf{s}=0$ the solutions of Eq. (5) for a single square island are the normalized functions $\psi_{n,m}(x,y) = A_{n,m} \cos(k_n x)\cos(k_m y)$, where $k_n = \pi n/R$, $k_m = \pi m/R$, $n,m = 0,1,2,\ldots$. Here we assume that the origin of the coordinates is located at the left-hand bottom corner of the square island. We describe the inflow or outflow of electrons from the neck into the island by introducing a term on the right-hand side of the continuity equation, which we shall write down, for example, only for the left-hand island $-i\omega e\,\delta n + \mathrm{div}\,\mathbf{j}(\mathbf{r}) = J_0 \delta(x-R) f(y)$, where J_0 is the amplitude of the total current inflowing from the neck. The function $f(y)$ is normalized to 1 and is nonvanishing only in the interval $R/2 - b/2 < y < R/2 + b/2$. Therefore the function $J_0\delta(x-R)f(y)$ describes the current coupling between the islands and the neck. The solution of the continuity equation, taking account of the right-hand side, can be written in the form

$$\delta n(x,y) = \sum_{n,m} B_{n,m}\psi_{n,m}(x,y),$$

$$B_{n,m} = \frac{i\omega J_0}{|e|(\omega^2 - \omega_{n,m}^2)} \int f(y)\psi_{n,m}(R,y)\,dy, \tag{6}$$

where $\omega_{n,m} = \nu_p\sqrt{k_n^2 + k_m^2}$.

We shall now examine the density oscillations near the neck. We write Eq. (5) for the density $\delta\tilde{n}(x) = (1/b)\int \delta n(x,y)\,dy$, averaged over the cross section of the neck. Taking account of the boundary condition on the current, we obtain $d^2\tilde{n}/dx^2 + (\omega^2/\nu_p^2)\tilde{n} = 0$. The solutions of this equation are obvious: $\tilde{n}(x) \propto \sin(qx)$, where $q = \omega/\nu_p$. Here we examine only the antisymmetric oscillations with nonzero dipole moment along the x axis of the system and zero dipole moment along the y axis. The equation for the frequencies is found from the continuity of the functions $\tilde{n}$ and $\tilde{j}$ at the points where the neck joins the islands. The result is

$$b\omega v_p \cot\left(\frac{\omega w}{2v_p}\right) \sum_{n,m} \frac{1}{(\omega^2 - \omega_{n,m}^2)} \int f(y)\psi_{n,m}(R,y)\,dy \times \int_{R/2-b/2}^{R/2+b/2} \psi_{n,m}(R,y)\frac{dy}{b} = 1. \tag{7}$$

In the limit $\omega \to 0$ the term with $n=m=0$ in Eq. (7) plays the main role. Thus, taking into account only the first term in Eq. (7) we see that the spectrum in the limit $b/R \to 0$ has a low-frequency mode. The frequency of this mode is $\Omega_0 = \sqrt{(2b/R)(\nu_p^2/Rw)} \ll \nu_p/R$ $(b/R \to 0)$. The current and density distributions in a low-frequency plasmon are similar to those shown in Fig. 3. This mode corresponds to an oscillation in which charge flows between the islands through the narrow neck.

The problem can also be solved for the case of two disks coupled by a narrow neck. In this case the frequency of the fundamental mode is $\Omega_0 = \sqrt{(2b/\pi R_d)(\nu_p^2/R_d w)}$, where R_d is the radius of the disk.

In closing, we note that the plasmon mode investigated in the present paper, which results from charge transfer between electronic reservoirs is a characteristic property of weakly coupled microstructures. This mode determines the low-frequency response of the system. Its frequency satisfies $\Omega_0 \ll \omega_p$, where ω_p are the characteristic plasma frequencies of individual wires or islands.

We thank W. Hansen, J. P. Kotthaus, and A. V. Chaplik for helpful remarks.

This work was supported by the Russian Fund for Fundamental Research (Grant 96-02-19555) and INTAS.

[1] J. P. Kotthaus, W. Hansen, and D. Wharam, Physica B **227**, 1 (1996).
[2] F. R. Frank, A. O. Govorov, J. P. Kotthaus, C. Steinebach, V. Gudmundsson, W. Hansen, and M. Holland, Phys. Rev. B **55**, 1950 (1997).
[3] M. V. Krasheninnikov and A. V. Chaplik, Fiz. Tekh. Poluprovodn. **15**, 32 (1981) [Sov. Phys. Semicond. **15**, 19 (1981)].
[4] G. Eliasson, P. Hawrylak, J. W. Wu, and J. J. Quinn, Solid State Commun. **60**, 3 (1986); G. Eliasson, J. W. Wu, P. Hawrylak, and J. J. Quinn, *ibid.* **60**, 41 (1986).
[5] D. Richards, H. Hüsken, D. Bangert, H. P. Hughes, D. A. Ritchie, A. C. Churchill, M. P. Grimshaw, and G. A. C. Jones, Solid-State Electron. **40**, 203 (1996).
[6] A. O. Govorov and A. V. Chaplik, Poverkhnost', No. 12, 1 (1987).
[7] F. R. Frank, W. Hansen, A. O. Govorov, J. P. Kotthaus, and M. Holland, in *Proceedings of the 12th International Conference on Applications of High Magnetic Fields in the Physics of Semiconductors*, Würzburg, Germany, 1996, edited by G. Landwehr and W. Ossau, World Scientific, Singapore, 1997, Vol. 2, p. 677.

Translated by M. E. Alferieff

Effect of deformation on spin splitting in quasi-2D hole systems

V. E. Bisti

Institute of Solid State Physics, Russian Academy of Sciences, 142432 Chernogolovka, Moscow District, Russia

(Submitted May 12, 1997; resubmitted September 23, 1997)
Fiz. Tverd. Tela (St. Petersburg) **40**, 546–549 (March 1998)

The effective Hamiltonian for holes in a 2D channel with in-plane uniaxial deformation is obtained. Two-dimensional channels on a Si surface are studied in the approximation of a spherically symmetric valence band and on the (100) and (110) surfaces taking account of the cubic symmetry. It is shown that the shift of the positions of the beats of the Shubnikov–de Haas oscillations that is linear in the deformation is due to the nonequivalence of the compression–tension axis and the direction perpendicular to it in the plane on the (110) surface.
© *1998 American Institute of Physics.* [S1063-7834(98)03303-6]

It is well known that in systems without a center of inversion the spin–orbit interaction should remove the spin degeneracy in the electronic spectrum for $\mathbf{k}\neq 0$.[1,2] Examples of such systems are quasi-2D channels in silicon MIS structures, heterojunctions, and asymmetric quantum wells based on GaAs. Observations of the Shubnikov–de Haas (ShdH) oscillations are used to study the spin splitting of the levels. Spin splitting results in phase interruption (beats) in these oscillations, as has been shown experimentally[3–5] and theoretically[6] for both electrons in GaAs heterojunctions and holes in Si MIS structures. In Ref. 6 an effective two-dimensional Hamiltonian for holes in an asymmetric quantum well was obtained and a spin splitting proportional to k^3 was found. The behavior of the ShdH oscillations under uniaxial tension or compression along the [001] axis in the plane of two-dimensional hole channels ((110) surface) in silicon field-effect transistors was studied experimentally in Ref. 7; a shift of the position of the beats that depends on the sign of the deformation was found. An attempt has also been made to analyze these experiments numerically.[8]

In the present paper the effect of deformation in the plane of a hole channel on the ShdH oscillations is studied analytically. An explicit form of the effective Hamiltonian for holes in a 2D channel (asymmetric quantum well) is obtained under the condition that the in-plane deformation can be regarded as a perturbation. The following cases are studied: a) deformation in the plane of the 2D channel in the approximation of a spherically symmetric valence band (i.e., neglecting rippling); b) the plane of the 2D channel is (100) and the deformation is along the [001] axis; c) the plane of the 2D channel is (110) and the deformation is along the [001] axis. The designations a–c for the cases listed above are used throughout this paper.

It is shown that, besides a cubic term, the Hamiltonian contains a term linear in k that is proportional to the deformation. It is established that the correction to the Landau levels that is linearly dependent on the deformation and therefore the shift in the position of the beats in the ShdH oscillations arise only when rippling is taken into account and only when the surface symmetry is lowered (the compression–tension axis must not be equivalent to a direction perpendicular to it in the plane, as, for example, for the (110) surface).

1. EFFECTIVE HAMILTONIAN AND THE SPIN SPLITTING OF HOLES IN A TWO-DIMENSIONAL CHANNEL IN THE PRESENCE OF AN IN-PLANE UNIAXIAL DEFORMATION

Let us examine a system of particles with a degenerate energy band (holes) described by the Luttinger Hamiltonian.[9,10] The holes are located in an asymmetric quantum well $V(z)$ near the surface (the z axis is directed along the normal to the surface). In addition, the system can be placed in a magnetic field $\mathbf{H}$ directed along the z axis and subjected to a uniaxial compression or tension along the x axis along the surface.

The Hamiltonian $H(\hat{\mathbf{k}},\mathbf{H},\varepsilon)$ of the system in the basis $|j_z\rangle$ has the form

$$H(\hat{\mathbf{k}},\mathbf{H},\varepsilon)=H_0(\hat{\mathbf{k}})+\mu_0 g_0 \mathscr{H}\mathbf{H}\cdot\mathbf{J}+H(\varepsilon)+V(z), \qquad (1)$$

where $\mathbf{J}$ is the spin-3/2 matrix, $\hat{\mathbf{k}}=\mathbf{k}+e\mathbf{A}/\hbar c$ ($\mathbf{A}$ is the vector potential), and $H_0(\mathbf{k})$ is the Luttinger Hamiltonian

$$H_0(\mathbf{k})=\frac{\hbar^2}{2m_0}\begin{vmatrix} P+Q & -S & R & 0 \\ -S^+ & P-Q & 0 & R \\ R^* & 0 & P-Q & S \\ 0 & R^* & S^* & P+Q \end{vmatrix}. \qquad (2)$$

a) In a spherical approximation for the valence band ($\gamma_2=\gamma_3$) the elements of the Hamiltonian matrix $H_0(\mathbf{k})$ have the form

$$P=\gamma_1(k_z^2+k^2),\quad Q=\gamma_2(-2k_z^2+k^2),$$
$$S=2\sqrt{3}\,\gamma_2 k_z k_-,\quad R=-\sqrt{3}\,\gamma_2 k_-^2,$$
$$k_\pm=k_x\pm ik_y,\quad k^2=k_x^2+k_y^2. \qquad (3)$$

b) If the z axis is directed along [100] and the x axis along [001], then P and Q are the same as in the spherical approximation (3),

 © 1998 American Institute of Physics

$$S=2\sqrt{3}\,\gamma_3 k_z k_-,$$

$$R=-\frac{\sqrt{3}}{2}[(\gamma_2+\gamma_3)k^2+(\gamma_2-\gamma_3)k_+^2]$$

$$=-\sqrt{3}\,\gamma_2(k_-^2+\delta k_+^2), \tag{4}$$

where $\widetilde{\gamma}_2=(\gamma_2+\gamma_3)/2$ and $\delta=(\gamma_2-\gamma_3)/(\gamma_2+\gamma_3)$.

c) If $z\|[110]$ and $x\|[001]$, according to Ref. 11, we have

$$P=\gamma_1(k_z^2+k^2),$$

$$Q=-\frac{3\gamma_3+\gamma_2}{2}2k_z^2+\gamma_2 k_x^2+\frac{3\gamma_3-\gamma_2}{2}k_y^2,$$

$$R=-\sqrt{3}\left(\frac{\gamma_3-\gamma_2}{2}k_z^2+\gamma_2 k_x^2-\frac{\gamma_3+\gamma_2}{2}k_y^2+2i\gamma_3 k_x k_y\right),$$

$$S=2\sqrt{3}k_z(\gamma_3 k_x-i\gamma_2 k_y), \tag{5}$$

where γ_1, γ_2, and γ_3 are the Luttinger parameters.

The term $H(\varepsilon)$ describes the effect of the deformation. If the x, y, and z axes are the crystallographic axes, then

$$H(\varepsilon)=\begin{vmatrix} p+q & h & j & 0 \\ h^* & p-q & 0 & j \\ j^* & 0 & p-q & -h \\ 0 & j^* & -h^* & p+q \end{vmatrix}, \tag{6}$$

$$p=a(\varepsilon_{xx}+\varepsilon_{yy}+\varepsilon_{zz}),\quad q=\frac{b}{2}(\varepsilon_{xx}+\varepsilon_{yy}-2\varepsilon_{zz}),$$

$$h=-(i\varepsilon_{xz}+\varepsilon_{yz}),\quad j=-\frac{\sqrt{3}}{2}b(\varepsilon_{xx}-\varepsilon_{yy})-id\varepsilon_{xy}, \tag{7}$$

a, b, and d are constants in the deformation potential.[12] The spherical approximation corresponds to $d=\sqrt{3}b$; the form of $H(\varepsilon)$ does not depend on the orientation of the axes. In what follows $H(\varepsilon)$ will be studied only in the spherical approximation.

We take into account exactly the dependence of the deformation on the applied stress. Stretching and compression occur along the [001] crystallographic axis (x axis). For both $z\|[110]$ and $z\|[100]$ the deformation tensor possesses three nonvanishing components $z\|[110]$ ε_{xx}, ε_{yy}, and ε_{zz}, where

$$\varepsilon_{yy}=\varepsilon_{zz}=-t\varepsilon_{xx},\quad t=\frac{C_{12}'}{C_{11}'+C_{12}'}, \tag{8}$$

and C_{ij}' are the elastic constants (for Si $C_{11}'=169$ GPa and $C_{12}'=65$ GPa). Then $h=0$ and $j=-\sqrt{3}/2b\varepsilon_{xx}(1+t)$.

In Ref. 6 the effective Hamiltonian of quasi-2D holes for the (001) surface in a magnetic field but with no deformation was obtained using perturbation theory. The Hamiltonian $H_0(k_z)+V(z)$, giving a set of doubly degenerate levels E_m and E_n for light and heavy holes, respectively, was used as the zeroth approximation. The quasi-2D motion near each level is described by the effective 2D Hamiltonian $H_{n(m)}(\hat{k}_x,\hat{k}_y,\mathbf{H})$. Proceeding similarly, we obtain in perturbation theory a Hamiltonian for the ground state of the heavy holes in the presence of a deformation

$$H_{0h}=E_{0h}(\varepsilon)+\frac{\hbar^2}{2m_{0h}}\hat{k}^2+\frac{3}{2}g_{0h}H_z\sigma_z+\beta_{0h}$$

$$\times\left[\left(\frac{\hbar^2}{2m_0}\hat{R}+j\right)\hat{S}\sigma_+-\left(\frac{\hbar^2}{2m_0}\hat{R}^*+j\right)\hat{S}^*\sigma_-\right], \tag{9}$$

where σ_x, σ_y, and σ_z are the Pauli matrices, $\sigma_\pm=(\sigma_x\pm i\sigma_y)/2$,

$$E_{0h}(\varepsilon)=E_{0h}+p+q,\quad \frac{1}{m_{0h}}=\frac{1}{m_0}(\gamma_1+\gamma_2+\gamma_{0h}),$$

$$g_{0h}=g_0 k+\frac{2}{3}\gamma_{0h},\quad \gamma_{0h}=\frac{\hbar^2}{2m_0}\sum_m 3\gamma_3^2\frac{|\langle 0h|k_z|m\rangle|^2}{E_{0h}-E_m},$$

$$\beta_{0h}=\frac{\hbar_2}{2m_0}\sum_m\frac{\langle 0h|m\rangle\langle m|k_z|0h\rangle}{E_{0h}-E_m}. \tag{10}$$

For a triangular well with $V(z)=2n_s ez/\varepsilon_0$ (n_s is the two-dimensional density and ε_0 is the permittivity) calculations give

$$\gamma_{0h}=-0.575(\gamma_1-2\gamma_2),$$

$$\beta'=i\sqrt{3}\gamma_3\beta_{0h}=(\gamma_1-2\gamma_2)^{4/3}(n_0/n_s)^{1/3}\times 0.644\ 10^{-5}\ \text{(cm)}$$

$(n_0=10^{12}\ \text{cm}^{-2})$.

We shall consider the specific form of the energy levels in different cases.

a) Neglecting rippling and performing a unitary transformation $H_{0h}=U^+H_{0h}^2U$, where $U=\frac{1}{2}(1+\sigma_z)$, the 2D Hamiltonian assumes the form

$$H_h=E_{0h}(\varepsilon)+\frac{\hbar^2}{2m_{0h}}\hat{k}^2+\frac{3}{2}g_{0h}H_z\sigma_z+\beta' j\boldsymbol{\sigma}\times\hat{\mathbf{k}}\cdot\mathbf{n}$$

$$+\beta''\boldsymbol{\sigma}\times\boldsymbol{\kappa}\cdot\mathbf{n}, \tag{11}$$

where $\boldsymbol{\kappa}=\{k_x(k_x^2-3k_y^2),\ -k_y(k_y^2-3k_x^2),0\}$ and $\beta''=\hbar^2/2m_0\sqrt{3}\gamma_2\beta'$. Here the linear term is of the same form as in the Bychkov–Rashba case.[1]

In the absence of a magnetic field the Hamiltonian (9) gives energy levels

$$E_{0h}^2=\frac{\hbar^2}{2m_{0h}}k^2\pm k\beta'\sqrt{\beta''^2k^4+j^2+2\beta'' jk^2\cos 2\varphi}. \tag{12}$$

b) For the (100) surface the energy levels are given by

$$E_{0h}^2=\frac{\hbar^2}{2m_{0h}}k^2\pm k\beta'\sqrt{\beta''^2k^4(1+\delta^2+2\delta\cos 4\varphi)+j^2+2\beta'' j(1+\delta)k^2\cos 2\varphi}. \tag{13}$$

c) For the (110) surface the Hamiltonian $H_0(\mathbf{k})$ at first is put into a diagonal form at $k=0$, since the terms depending only on k_z are included in the zeroth approximation and are taken into account exactly. The diagonal Hamiltonian $H_0'(\mathbf{k})$ has a form similar to Eq. (2) with the elements P', Q', S', and R':

$$P'=P, \quad S'=S,$$

$$Q'=-\sqrt{3\gamma_3^2+\gamma_2^2}k_z^2+\left(\frac{\gamma_2(3\gamma_3+\gamma_2)}{2\sqrt{3\gamma_3^2+\gamma_2^2}}-\frac{3\gamma_2(\gamma_3-\gamma_2)}{2\sqrt{3\gamma_3^2-\gamma_2^2}}\right)k_x^2+\left(\frac{(3\gamma_3-\gamma_2)(3\gamma_3+\gamma_2)}{4\sqrt{3\gamma_3^2+\gamma_2^2}}+\frac{3(\gamma_3+\gamma_2)(\gamma_3-\gamma_2)}{4\sqrt{3\gamma_3^2+\gamma_2^2}}\right)k_y^2,$$

$$R'=-\sqrt{3}\left(\frac{(\gamma_2)(3\gamma_3+\gamma_2)}{2\sqrt{3\gamma_3^2+\gamma_2^2}}k_x^2-\frac{(\gamma_3+\gamma_2)(3\gamma_3+\gamma_2)}{4\sqrt{3\gamma_3^2+\gamma_2^2}}k_y^2+2i\gamma_3k_xk_y\right). \tag{14}$$

Next, an effective Hamiltonian of the form (9) is determined according to the scheme of Ref. 6 and gives the following energy levels for the ground state of heavy holes:

$$E_{0h}=\frac{\hbar^2}{2}\left(\frac{k_x^2}{m_{0x}}+\frac{k_y^2}{m_{0y}}\right)\pm|\beta_{0h}|\sqrt{|S|^2(R'+j)(R'^*+j)}. \tag{15}$$

It is convenient to transfer the anisotropy in the term quadratic in k to the second term by a scale transformation

$$k_x=k_x'\left(\frac{m_{0x}}{m_{0y}}\right)^{1/4}, \quad k_y=k_{y'}\left(\frac{m_{0x}}{m_{0y}}\right)^{1/4} \tag{16}$$

(for calculations using the potential (9) $m_{0x}/m_{0y}\approx 2$). After this, the anisotropy in the terms R' is substantially smaller, and it can be neglected in the further calculations. Conversely, however, the anisotropy in the S terms increases:

$$E_{0h}\approx\frac{\hbar^2k'^2}{2\sqrt{m_{0x}m_{0y}}}\pm\beta'k'\times\sqrt{(\cos^2\varphi+\tilde{\delta}\sin^2\varphi)(\beta''^2k'^4+j^2+2\beta''jk'^2\cos 2\varphi)},$$

$$\tilde{\delta}=(\gamma_2/\gamma_3)^2(m_{0y}/m_{0x})\sim 0.1\ll 1. \tag{17}$$

2. EFFECT OF DEFORMATION ON THE LANDAU LEVELS

In a magnetic field the energy levels can be found analytically for an isotropic 2D Hamiltonian in the case of only the linear[1] or only the cubic[6] term responsible for the spin splitting. The wave functions then have the form χ_N (for linear splitting) or ϕ_n (for cubic splitting), where

$$\chi_N=\begin{pmatrix}Au_{N-1}\\ Bu_N\end{pmatrix}, \quad \phi_N=\begin{pmatrix}Cu_{N-3}\\ Du_N\end{pmatrix} \tag{18}$$

(u_N is a harmonic oscillator function).

We shall analyze the effect of the deformation-dependent term in the Hamiltonian (9) on the Landau levels for the three cases studied, assuming that it is small compared to the cubic term.

a) The Hamiltonian (11) with $j=0$ has an analytical solution, and the wave functions have the form ϕ_N. Adding the term $\beta' j\boldsymbol{\sigma}\times\hat{\mathbf{k}}\cdot\mathbf{n}$ does not give first-order corrections to the energy levels in a magnetic field.

b) For the (100) surface, rippling mixes the states ϕ_N and $\phi_{N\pm 4}$, which once again does not give corrections linear in j to the Landau levels. Therefore, in these two cases there will be no deformation-sign dependent shift in the positions of the beats.

c) The anisotropy of the (110) surface ''couples'' the states ϕ_N and $\phi_{N\pm 2}$, which leads to terms of the form χ_N in the wave function when $j=0$. Therefore, there arises a correction ΔE_j^N to the Landau levels that is linear in j:

$$\Delta E_j^N\sim(1-\tilde{\delta})\beta' j\lambda_H^{-1}(N)^{1/2} \tag{19}$$

(where $\lambda_H=(\hbar c/eH)^{1/2}$), leading to a shift in the positions of the nodes of the beats in the ShdH oscillations that is proportional to the deformation.

3. DISCUSSION

The results obtained for the (110) surface agree qualitatively with the experimental data of Ref. 7 and the results of numerical calculations.[8] Moreover, the analysis performed above makes it possible to draw the new conclusion that the shift in the positions of the beats that is linearly in the deformation exists only when rippling is taken into account and only as a result of the lower symmetry of the (110) surface. It is impossible to draw this conclusion from numerical calculations. An analytical analysis also explains the sensitivity of the numerical results to the choice of the Luttinger parameters: The linear deformation-dependence of the position of the beats exists to the extent of the anisotropy (19). The quantitative discrepancy between Refs. 7 and 8 can likewise be partially explained, aside from the differences in the Luttinger parameters and the constants in the deformation potential which are presented by in Ref. 7, by the influence of the deformation arising as a result of the difference between the thermal expansion coefficients of Si and SiO_2.[13] This hydrostatic tension with characteristic stress 0.1 kbar in the plane, which is equivalent to a compression along the (110) axis, leads to a correction in the Hamiltonian $H(\varepsilon)$ given by (6), where $q=-b\varepsilon_{zz}(1+2t)=\Delta\sim 5$ meV. The distance between the subbands and, in consequence, the spin splitting determined by the coefficient β', changes. When anisotropy is taken into account, a term linear in k also arises, but the magnitude of this term is much smaller than that of the term arising as a result of applied external stresses, and for this reason it cannot play a large role in the explanation of the experiments of Ref. 7.

I wish to thank S. I. Dorozhkin and V. M. Édel'shteĭn for helpful discussions and his unflagging interest in this work.

This work was supported in part by Russian Fund for Fundamental Research (Project 95-02-06107).

[1] Yu. A. Bychkov and É. I. Rashba, JETP Lett. **39**, 78 (1984).
[2] F. T. Vas'ko, JETP Lett. **30**, 541 (1979).
[3] S. I. Dorozhkin, Phys. Rev. B **41**, 3225 (1990).
[4] S. I. Dorozhkin and E. B. Ol'shanetskiĭ, JETP Lett. **48**, 588 (1988).
[5] K. von Klitzing, G. Landwehr, and G. Dorda, Solid State Commun. **14**, 387 (1974).
[6] V. E. Bisti, Superlattices Microstruct. **10**, 485 (1991).
[7] S. I. Dorozhkin and G. Landver, JETP Lett. **64**, 677 (1966).
[8] W. O. G. Schmitt, Phys. Rev. B **50**, 15 239 (1994).
[9] J. M. Luttinger and W. Kohn, Phys. Rev. **97**, 869 (1955).
[10] J. M. Luttinger, Phys. Rev. **102**, 1030 (1956).
[11] W. O. G. Schmitt, Phys. Rev. **50**, 15 221 (1994).
[12] G. L. Bir and G. E. Pikus, *Symmetry and Strain-Induced Effects in Semiconductors*, Wiley, New York (1975); Nauka, Moscow (1972).
[13] M. V. Whelan, A. N. Goemans, and L. M. C. Goossens, Appl. Phys. Lett. **10**, 262 (1967).

Translated by M. E. Alferieff

Localized optical phonons in GaAs/AlAs superlattices grown on (311)*A* and (311)*B* surfaces

A. Milekhin, Yu. Pusep, Yu. Yanovskiĭ, V. Preobrazhenskiĭ, and B. Semyagin

Institute for Semiconductor Physics, Siberian Branch of the Russian Academy of Sciences, 630090 Novosibirsk, Russia

(Submitted September 23, 1997)
Fiz. Tverd. Tela (St. Petersburg) **40**, 550–552 (March 1998)

A study is reported of optical vibrational modes in [311]-grown GaAs/AlAs superlattices. An analysis of the *TO* and *LO* localized modes observed in IR reflectance spectra showed that the difference between the *TO* and *LO* mode frequencies in superlattices grown on (311)*A* and (311)*B* surfaces is due to the different localization lengths of these modes. The dispersion of transverse optical phonons in GaAs derived from IR reflectance spectra is in a good agreement with Raman scattering data. © *1998 American Institute of Physics.* [S1063-7834(98)03403-0]

(311)-oriented GaAs/AlAs superlattices (SL) with anisotropic electronic and optical properties have recently been made.[1–3] The anisotropy was found to be due to surface faceting.[4] At the same time recent Raman studies of these SLs did not reveal surface faceting.[5] While a large number of papers dealing with electronic properties of (311) SLs are presently available, there are only a few works devoted to investigation of optical properties.[5–7]

This work presents a study of the vibrational spectrum of (311)-oriented GaAs/AlAs SLs by IR Fourier spectroscopy.

The lowering of symmetry of (311) SLs compared to the [100]-grown SLs interferes with identification of the vibrational modes localized in SL layers and gives rise to optical modes in (311) SLs which may have either pure transverse (A'') or mixed, longitudinal/transverse (A'), character.[6] Besides, surface faceting in (311)*A* SLs with a 32-Å period may result in splitting of localized vibrational modes. According to the selection rules, all modes (A' and A'') can be IR-active. The wave number of the localized modes can be defined as

$$q_m = m\pi/[(n+\delta)d], \tag{1}$$

where n is the number of monolayers, $d = a/\sqrt{11}$ is the thickness of one monolayer in the [311] direction, a is the lattice parameter in the (100) direction, and m is the number of the localized mode. The parameter δ describes penetration of localized modes into the neighboring layers. The assignment of mixed localized modes with small wave numbers is simplified by the corresponding localized modes being either *LO* or *TO* polarized.[7]

We studied $(GaAs)_n/(AlAs)_m$ superlattices (where $n=7$, 10, 12, 28 and $m=7$, 16, 17, 24 monolayers) grown simultaneously on (311)*A* and (311)*B* surfaces. The layer thickness was chosen so as to ensure optimum conditions to observe optical phonon localization in these layers. The thicknesses of the GaAs and AlAs layers were monitored by RHEED oscillations using SLs grown in the same process on (100)GaAs substrates. The number of layer sequences was 100.

IR spectra were obtained at 80 K with a Bruker IFS-113V IR Fourier spectrometer equipped with an Oxford Instruments cryostat. The resolution was 0.5 cm^{-1} throughout the spectral range covered. We analyzed reflectance spectra measured at normal incidence together with those taken in

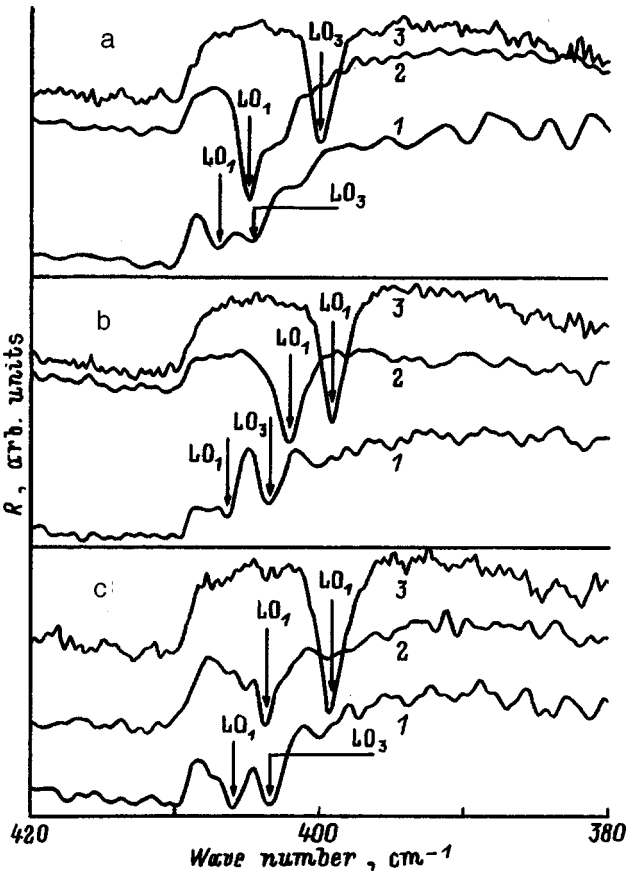

FIG. 1. Experimental IR reflectance spectra measured in *p* polarized light in the AlAs *LO* phonon spectral range. (a) (100) superlattices: *1*—$(GaAs)_{17}/(AlAs)_{15}$, *2*—$(GaAs)_7/(AlAs)_9$, *3*—$(GaAs)_4/(AlAs)_4$; (b,c) for the (311)*A* and (31)*B* superlattices, respectively: *1*—$(GaAs)_{28}/(AlAs)_{24}$, *2*—$(GaAs)_{12}/(AlAs)_{17}$, *3*—$(GaAs)_7/(AlAs)_7$.

 © 1998 American Institute of Physics

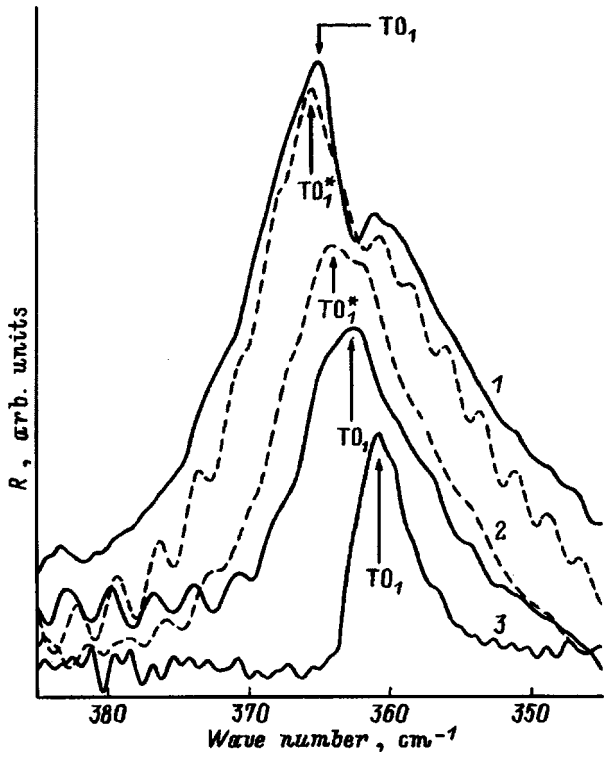

FIG. 2. Experimental IR reflectance spectra of (311)*A* GaAs/AlAs (solid traces) and of (311)*B* GaAs/AlAs superlattices (dashed traces) measured at normal incidence in the AlAs *TO* phonon spectral range. *1*—$(GaAs)_{28}/(AlAs)_{24}$, *2*—$(GaAs)_{12}/(AlAs)_{17}$, *3*—$(GaAs)_{10}/(AlAs)_{16}$.

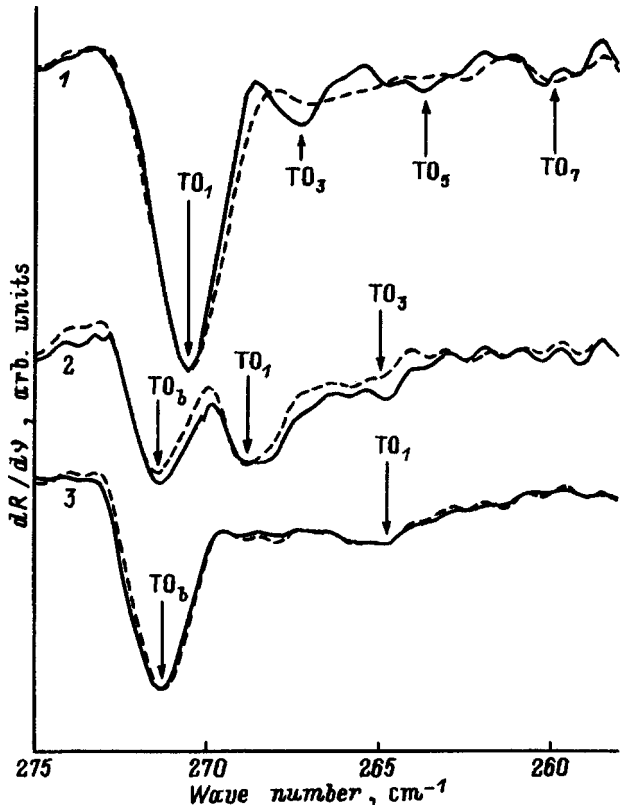

FIG. 3. Experimental IR reflectance spectra of (311)*A* GaAs/AlAs (solid traces) and of (311)*B* GaAs/AlAs superlattices (dashed traces) measured at normal incidence in the GaAs *TO* phonon spectral range. *1*—$(GaAs)_{28}/(AlAs)_{24}$, *2*—$(GaAs)_{12}/(AlAs)_{17}$, *3*—$(GaAs)_{7}/(AlAs)_{7}$.

p polarized light at an angle of incidence $\theta = 70°$. Normal-incidence spectra permit observation of *TO* phonons in SLs, whereas *p* polarized spectra reveal also *LO* phonons due to the effect of Berreman.[8]

Figure 1 shows *p*-polarized spectra of (311)*A* and (311)*B* SLs together with spectra of (100) SLs measured in the spectral range containing AlAs *LO* phonons. The features identified by arrows correspond to the *LO* modes localized in the AlAs layers. As seen from Fig. 1, the fundamental mode frequency in all SLs decreases with decreasing AlAs layer thickness as a result of AlAs phonon dispersion. Moreover, the reflectance spectra exhibit higher-order LO_3 modes, which confirms the high crystalline perfection of the samples. We detected, however, neither any significant difference between the spectra of the (100) and (311) SLs nor an additional splitting of the localized modes in (311)*A* SLs, which would be an indication of phonon localization in the narrow and broad parts of the faceted layer. The change in the vibrational mode frequencies in SLs of different thickness is due only to different localization length of the corresponding vibrational modes.

As already mentioned, SL reflectance spectra taken at normal incidence carry information on *TO* phonons. Figure 2 displays reflectance spectra of the (311)*A* and (311)*B* SLs exhibiting fundamental *TO* and *TO** modes localized in the AlAs layers which were grown on the (311)*A* and (311)*B* surfaces, respectively. As in the case of *LO* phonons in AlAs, we did not observe any change in the frequency of vibrational *TO* modes in the (311)*A* SL relative to the corresponding modes in the (311)*B* SL.

In order to determine more accurately the frequencies of the GaAs-localized *TO* modes, we analyzed the derivative of the reflectance spectra, $dR/d\nu$, for the (311)*A* and (311)*B* SLs (Fig. 3). The minima identified by arrows correspond to odd localized TO_i modes, because only these modes are active in the IR spectra of the SLs (as a result of the nonzero dipole moment). The high-frequency TO_b mode corresponds to the bulk *TO* phonon frequency in the GaAs substrate. The dependence of the localized *TO* mode frequencies in (311)*A* and (311)*B* SLs with different layer thicknesses on the corresponding wave numbers given by Eq. (1) is shown in Fig. 4. The parameter δ was taken equal to unity. We do not see any substantial difference between the SLs grown on the (311)*A* and (311)*B* surfaces.

We note also that the (311)*A* and (311)*B* GaAs/AlAs SLs studied in this work did not reveal any in-plane optical phonon anisotropy when the sample was rotated about the growth axis at a fixed light polarization. As possible reasons for the absence of anisotropy one could suggest segregation and interdiffusion of atoms at interfaces, which depend essentially on sample growth conditions.

Thus, we have studied optical localized vibrational modes in (311)*A* and (311)*B* GaAs/AlAs superlattices by IR Fourier spectroscopy. The GaAs *TO* phonon dispersion in (311) superlattices derived from IR spectra is in good

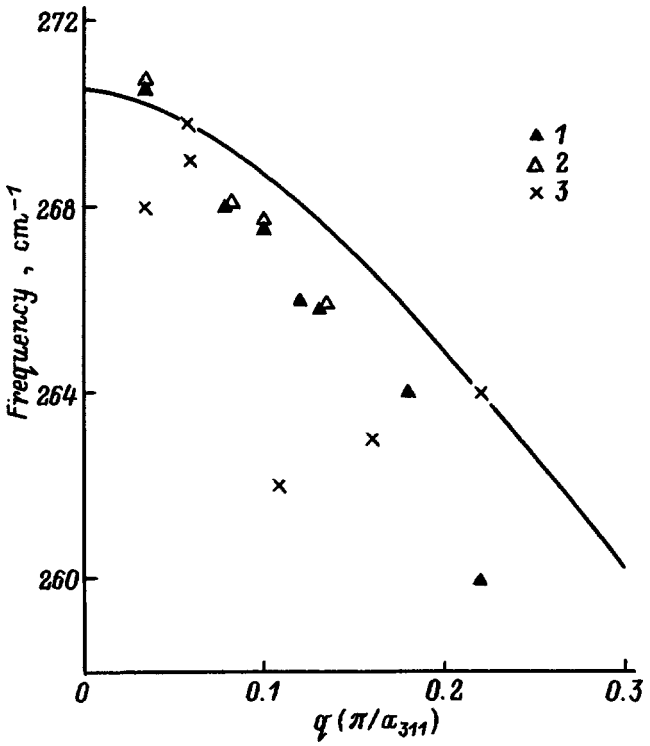

FIG. 4. Wave number dependence of the localized *TO* mode frequencies measured for (*1*) (311)*A* and (*2*) (311)*B* superlattices with different layer thickness. Shown for comparison (curve) is the GaAs *TO* phonon dispersion in the (100) direction; (*3*) Raman scattering data.[5]

agreement with Raman scattering data. The experimental data do not reveal any optical anisotropy which could be induced by optical phonon localization as a result of surface faceting.

Support of the Russian Fund for Fundamental Research (Grant 95-02-04431) and of the Committee of the Russian Federation for Higher Education (Project 3H-249-96/231 MP 2-5) is gratefully acknowledged.

[1] R. Nötzel, L. Däweritz, and K. Ploog, Phys. Rev. B **46**, 4736 (1992).
[2] R. Nötzel, N. N. Ledentsov, L. Däweritz, M. Hohenstein, and K. Ploog, Phys. Rev. Lett. **67**, 3812 (1991).
[3] R. Nötzel and K. Ploog, J. Vac. Sci. Technol. A **10**, 617 (1992).
[4] R. Nötzel, N. N. Ledentsov, L. Däweritz, K. Ploog, and M. Hohenstein, Phys. Rev. B **45**, 3507 (1992).
[5] Yu. A. Pusep, S. W. da Silva, J. C. Galzerani, D. I. Lubyshev, V. Preobrazhenskii, and P. Basmaji, Phys. Rev. B **51**, 5473 (1995).
[6] Z. V. Popovich, E. Richter, J. Spitzer, M. Cardona, A. J. Shield, R. Nötzel, and K. Ploog, Phys. Rev. B **49**, 7577 (1994).
[7] P. Castrillo, L. Colombo, and G. Armelles, Phys. Rev. B **49**, 10362 (1994).
[8] D. W. Berreman, Phys. Rev. **130**, 2193 (1963).

Translated by G. Skrebtsov

Effect of Coulomb correlations in a variable-valence impurity system and phonon drag on the thermoelectric constants in two-dimensional systems

I. I. Lyapilin

Institute of Metal Physics, Ural Branch of the Russian Academy of Sciences, 620219 Ekaterinburg, Russia
(Submitted July 14, 1997; resubmitted September 30, 1997)
Fiz. Tverd. Tela (St. Petersburg) **40**, 553–556 (March 1998)

The temperature behavior of the longitudinal Nernst–Ettingshausen coefficient in 2D systems is studied theoretically taking account of phonon drag and Coulomb correlations in a system of mixed-valence impurities at low temperatures. It is shown that the effect changes sign at the transition from entrainment to scattering by a correlated system of impurity centers. A sign change does not occur in the case of scattering by randomly distributed impurity centers. This temperature behavior of the Nernst–Ettingshausen coefficient is due to the radical rearrangement of the impurity system as a result of strong Coulomb correlations present in a system of impurities with mixed valence. As a result, the character of the scattering of charge carriers by the correlated system of charge centers changes substantially. © *1998 American Institute of Physics.* [S1063-7834(98)03503-5]

In Ref. 1 it was shown that in both HgSe:Fe films and in HgSe–HgSe:Fe multilayer structures, grown using molecular-beam epitaxy, the mobility of itinerant charge carriers increases with decreasing temperature, the increase amounting to several factors. This effect, discovered earlier in an investigation of bulk HgSe:Fe crystals, had been shown in a number of works[2–4] to be due to the scattering of itinerant carriers by a collection of charged centers as temperature decreases, if the density of the centers is such that the Fermi level is stabilized at an impurity level located in the conduction band. The impurity centers form a system where the Coulomb repulsion between the charged donors leads to strong correlations in their spatial arrangement, which is the reason why the scattering of the itinerant charge carriers by them is appreciably weakened.

It should be noted that ''anomalous'' dependences (both temperature and concentration) have also been observed in an investigation of transport coefficients arising from the presence of temperature gradients in the experimental samples.[4]

It is of interest to study the thermomagnetic coefficient (TMC) at low temperatures in 2D systems with a mixed-valence impurity, where the effect due to spatial correlation in a system of impurity centers will be strongest. In so doing, it should be kept in mind that together with scattering of $2d$ electrons by impurity centers, the behavior of the TMC at low temperatures is also determined by other effects, for example, phonon drag of electrons. The contribution of the latter effect to the conductivity is negligibly small but it can dominate the behavior of the TMC.

In the present paper we shall examine the longitudinal Nernst–Ettingshausen (NE) effect in a classically strong magnetic field for 2D charge carriers at low temperatures. Together with scattering of the 2D charge carriers by a correlated system of impurity centers, we shall also take account of phonon drag of electrons.

As the 2D system we shall study a quantum well (QW) of width W. For simplicity, we shall assume that the well is infinitely deep. In this case the wave functions of the 2D electrons have the conventional form

$$\psi_\nu(R_j,z_j)=\psi_{kL}(R_j,z_j)=\frac{1}{(L_xL_y)^{1/2}}\exp(ikR_j)\varphi_L(z_j). \tag{1}$$

Here $\varphi_L(z)$ is the envelope wave function,

$$\varphi_L(z_j)=\left(\frac{2}{W}\right)^{1/2}\sin\left(\frac{Lz}{W}+\frac{L\pi}{2}\right),\quad z\in\left[-\frac{W}{2};\frac{W}{2}\right],$$
$$R=(x,y),\quad \nu=(k,L),\quad L=1,2,3..., \tag{2}$$

and L characterizes the number of the size-quantized level that can be realized in the QW.

We shall assume that the dispersion law of the $2d$ conduction electrons is quadratic and isotropic

$$\varepsilon_\nu=\varepsilon_{kL}=\frac{\hbar^2k^2}{2m}+E_L,\quad E_L=E_0L^2,\quad E_0=\frac{\pi^2}{2m}\frac{\hbar^2}{W^2}, \tag{3}$$

where E_L is the energy of the size-quantized level and m is the electron effective mass. We note that neither the finite depth of the QW nor the nonparabolicity of the conduction band results in any qualitative changes in the calculations.

1. CALCULATION OF THE ELECTRONIC COMPONENTS OF THE THERMOELECTRIC POWER

We start from the fact that the longitudinal NE coefficient $\Delta\alpha(H,T)=\alpha(H,T)-\alpha(0,T)$ at low temperatures is determined by the sum of the electronic and phonon components

$$\Delta\alpha(H,T)=\Delta\alpha_e(H,T)+\Delta\alpha_p(H,T), \tag{4}$$

where the indices e and p refer to the electronic and phonon components of the transport coefficients.

 © 1998 American Institute of Physics

In the case of a 2D gas the expression for the electronic component can be easily obtained by generalizing the well-known expressions for the thermogalvanomagnetic coefficients for a 3D electron gas,[4]

$$\alpha(0,T)=C(1+P),$$

$$\alpha(H,T)=C\left(1+\frac{P}{1+v^2}\right), \quad v=\omega\tau,$$

$$P=\varepsilon_F\left(\frac{dLn\,\tau}{d\varepsilon}\right)_{\varepsilon=\varepsilon_F}, \quad C=-\frac{\pi^2 k_0}{3|e|}\frac{k_0 T}{\varepsilon_F}. \tag{5}$$

Here k_0 is Boltzmann's constant, ω is the cyclotron frequency, e is the electron charge, τ is the total relaxation time of 2D electrons, and ε_F is the Fermi energy.

We shall treat the Fe(3+)–Fe(2+) impurity system of iron ions in the QW as a binary alloy consisting of charged Fe(3+) and neutral Fe(2+) centers. We confine our attention below to scattering of electrons only by pairs of Fe(3+)–Fe(3+) ions distributed in a correlated manner. This case is of greatest interest.

We represent the relaxation time of $2d$ electrons in the Born approximation with respect to the interaction with scatterers in the form

$$\tau^{-1}=\frac{\hbar N_{\mathrm{Fe}}}{mnkT}\sum_{q\nu\nu'} q_x^2 S(q) V_q^2 I_{\nu\nu'}^2 f(\varepsilon_\nu) \times[1-f(\varepsilon_{\nu'})]\delta(\varepsilon_{\nu'}-\varepsilon_\nu),$$

$$I_{\nu\nu'}=\langle\nu'|e^{iqr}|\nu\rangle. \tag{6}$$

Here $V_q(z_i)$ is the Fourier transform of the potential of an ionized impurity located at the point z_i,

$$V_q(z_i)=\frac{2\pi e^2}{\chi}\frac{F(q,z_i)}{q+q_s F(q)}, \tag{7}$$

χ is the permittivity of the medium (QW), $q_s^{-1}=r_s$ is the screening radius, n is the $2d$-electron density, and $f(\varepsilon)$ is the Fermi distribution function. Next, following Ref. 6 we have

$$F(q,z_i)=\int_0^W \varphi^*(z)e^{-q|z-z_i|}\varphi(z)dz,$$

$$F(q)=\int_0^W\int_0^W |\varphi(z)|^2 e^{-q|z-z_i|}|\varphi(z')|^2 dz dz'. \tag{8}$$

In the linear approximation in x, to which we confine our attention, we have $F(q)\approx 1+5x/4\pi^2$, while $F(q,z_i)\approx 1$.

The degree of the spatial correlations in the system of charged iron ions is determined by the structure factor $S(q)$, which depends on the iron concentration and temperature. For randomly distributed impurity centers $S(q)=1$.

The matrix element in the expression (7) can be rewritten in the form[7]

$$\langle\nu'|e^{iqr}|\nu\rangle=\langle k'|e^{iq_\perp r_\perp}|k\rangle\langle L'|e^{iq_z z}|L\rangle, \quad q_\perp=(q_x,q_y),$$

$$\sum_{q_z}|\langle L'|e^{iq_z z}|L\rangle|^2=\int_{-\infty}^{+\infty}\varphi_L^4(z)dz=\frac{3}{2}. \tag{9}$$

Simple calculations give for the relaxation time

$$\tau^{-1}=\frac{16\pi N(\mathrm{Fe}^{3+})W\varepsilon_F}{\hbar k_F b^2}M_c,$$

$$M_c=\int_0^1 dx\frac{x^2 S(2k_F x)}{\left(x^2+\dfrac{Q_s}{2k_F}\right)^2[1-x^2]^{1/2}},$$

$$Q_s=\frac{q_s}{b}, \quad b=1+\frac{5q_s W}{4\pi^2}. \tag{10}$$

It should be stressed that the specific nature of the QW that we are studying is such that the scattering centers are located in the QW. The average distance between them is much smaller than the width of the QW. In this case, the structure factor can be expressed in terms of the pair correlation function $g(r)$ for Fe(3+) ions.[3]

2. CONTRIBUTION OF THE PHONON COMPONENT

We shall now calculate the component due to entrainment effects. We represent it in the form[6]

$$\alpha_p=-\frac{k_0}{eU}(\langle\tau R\rangle\langle\tau A_p R\rangle+\langle\tau v R\rangle\langle\tau v A_p R\rangle),$$

$$U=\langle\tau R\rangle^2+\langle\tau v R\rangle^2, \quad R=[m(1+v^2)]^{-1}. \tag{11}$$

Here the brackets $\langle A\rangle$ are defined as

$$\langle A\rangle=\frac{1}{\pi n}\int_0^\infty k^2(\varepsilon)\left(-\frac{\partial f_0}{\partial\varepsilon}\right)A(\varepsilon)d\varepsilon. \tag{12}$$

For a strongly degenerate 2D electron gas the expression (12) can be represented in the form

$$\langle A\rangle=A(\varepsilon_F)+\gamma\frac{\partial^2}{\partial\varepsilon^2}(k^2(\varepsilon)A(\varepsilon))_{\varepsilon=\varepsilon_F},$$

$$\gamma=\frac{\pi^2}{6}(k_0T)^2\frac{1}{\pi n}. \tag{13}$$

The quantity A_p determines the contribution of phonon drag and will be determined below.

Using the definition (12) and Eq. (13), the expression for the phonon component can be represented in the form

$$\alpha_p(H,T)=-\frac{k_0}{|e|}\left\{A_p+\frac{\pi^2}{3}\frac{(k_0T)^2}{\varepsilon_F}\left(\frac{\partial A_p}{\partial\varepsilon}\right)_{\varepsilon=\varepsilon_F}\times\left[1+\frac{P}{1+v^2}\right]\right\}. \tag{14}$$

Thus, the final expression for the longitudinal NE coefficient following from Eqs. (5) and (14) can be represented as

$$\Delta\alpha(H,T)=-\frac{\pi^2}{3|e|}\frac{k_0^2T}{\varepsilon_F}\frac{Pv^2}{1+v^2}\left[1+\frac{k_0T}{\varepsilon_F}\left(\frac{\partial A_p}{\partial\varepsilon}\right)_{\varepsilon=\varepsilon_F}\right]. \tag{15}$$

We shall now find the phonon drag in the case of a 2D system. We assume that the phonon–phonon collision fre-

quency is much higher than the frequency of collisions between phonons and charge carriers. In this case phonon relaxation is determined mainly by scattering of phonons by one another. This makes it possible to introduce a relaxation time $\tau_p(Q)$ for long-wavelength acoustic phonons (Q is the phonon wave vector). In this approximation the nonequilibrium phonon distribution function N_Q can be found from an independent equation for the nonequilibrium phonon distribution function. When the temperature gradient is directed long the x axis, the statistical drag force can be represented in the conventional form

$$F_p = -A_p(\varepsilon)\nabla_x T, \tag{16}$$

where

$$A_p(\varepsilon) = \frac{2mv_p}{k_0}\sum_{k'Q} W(Q)\tau_p(Q)\frac{dN_Q^0}{dT}\left(1-\frac{\mathbf{k}\cdot\mathbf{k}'}{k^2}\right)\delta(\varepsilon_{k'} - \varepsilon_k)\delta_{k',k+Q_\perp}. \tag{17}$$

Here ν_p is the group velocity of the phonons, $Q_\perp$ is the wave vector of a phonon in the xy plane, N_Q^0 is the equilibrium phonon distribution function, and

$$W(Q) = \frac{\pi E_1^2 Q}{\rho \nu_p} J^2(q_z),$$

$$J^2(q_z) = \left|\int \varphi^2(z)\exp(iQ_z z)dz\right|^2. \tag{18}$$

We note that the squared matrix element appearing in the expression (18) determines the phonon contribution in the dependence on the parameters of the QW.[8] For narrow QWs it equals 1 for all values of Q_z, while for wide QWs it equals $Z-\delta_{Q_z',0}$. For QWs with infinitely high walls it equals

$$J^2(q_z) = \pi^2 \sin^2 u/[u^2(u^2-\pi^2)^2], \quad u = q_z W/2. \tag{19}$$

We shall assume that the long-wavelength phonons at low temperatures relax mainly by scattering at the boundaries of the sample

$$\tau_{pL}^{-1} = v_p/L, \tag{20}$$

where L is the size of the sample.

Switching in Eq. (17) from summation to integration, we obtain

$$A_p = D\int dq_z Z\int (q^2 + q_z^2)qdq\int \frac{(-kq\cos\vartheta)}{\mathrm{sh}^2(\gamma)}\delta\left(kq\cos\vartheta + \frac{q^2}{2}\right)d\vartheta,$$

$$\gamma = \hbar\omega_Q/2k_0T, \quad D = \frac{m^2 v_p^2 \pi E_1^2 \tau_p}{2\rho(k_0T^2)\hbar k^2(2\pi)^3}. \tag{21}$$

After integration over angles, the expression (21) assumes the form

$$A_p = D\int dq_z Z\int_0^{2k}\frac{(q^2+q_z^2)q^2}{\mathrm{sh}^2(\gamma)[(2k)^2-q^2]^{1/2}}dq. \tag{22}$$

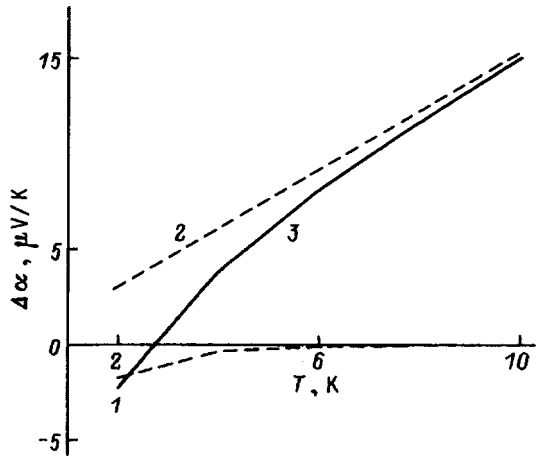

FIG. 1. Temperature dependence of the longitudinal Nernst–Ettingshausen coefficient (''hard-sphere'' approximation). *1*—drag contribution, *2*—contribution of scattering by the impurity system, *3*—resulting contribution.

As one can see from the expression (22), the integral over q diverges at the upper limit at $q=2k_F$. This divergence can be eliminated by, for example, taking into account inelastic electron scattering processes.

Thus, to calculate $\Delta\alpha(H,T)$ numerically it remains to find the energy derivative of the expression determined by Eq. (22). Simple calculations give

$$A_p'(\varepsilon_F) = A_p(\varepsilon_F)\left[-\frac{1}{\varepsilon_F} + \frac{x_{2k_F}}{2\varepsilon_F}\frac{J_1-J_2}{J}\right]. \tag{23}$$

Here

$$J = \int_0^{q_D^*}dy\int_0^{x_{2k_F}}\frac{F(x,y)}{(x_{2k_F}^2-x^2)^{1/2}}dx,$$

$$J_1 = \int_0^{q_D^*}dy\frac{F(x_{2k_F},y)}{\delta_{\min}},$$

$$J_2 = x_{2k_F}\int_0^{q_D^*}dy\int_0^{x_{2k_F}}\frac{F(x,y)}{(x_{2k_F}^2-x^2)^{3/2}}dx,$$

$$x_{2k_F} = \frac{2\hbar v_p k_F}{k_0 F}, \quad q_D^* = \frac{\hbar v_p q_D}{k_0 T},$$

$$F(x,y) = \frac{x^2(x^2+y^2)e^{(x^2+y^2)^{1/2}}}{(e^{(x^2+y^2)^{1/2}}-1)^2},$$

q_D is the Debye wave vector, and $\delta_{\min}\approx k_0T$.

The expressions (15) and (23) make it possible to calculate numerically the contribution of phonon drag to the longitudinal NE effect. The conputational results obtained for the longitudinal NE coefficient using the following parameters are presented in the figures: $W=90$ Å ($E_0=64$ K), $H=2$ kOe, $\nu_p=3\times10^5$ cm·s^{-1}, $m=0.067m_0$ (m_0 is the mass of a free electron), and $E_1=7$ eV. Figure 1 displays the temperature dependence of the longitudinal NE coefficient, calculated assuming that the Coulomb correlations in a mixed-valence system at low temperatures have reached their maximum magnitude and the degree of ordering in the impurity system does not change with temperature (''hard-

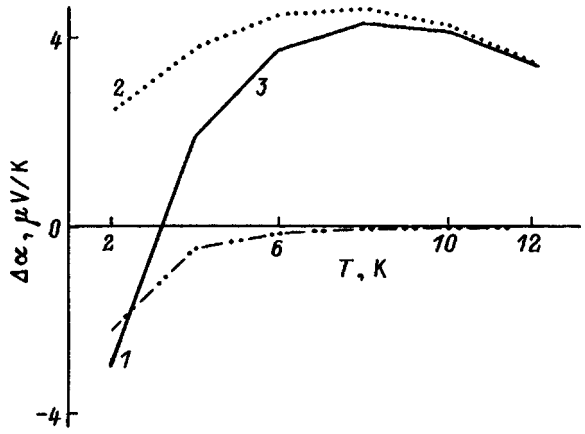

FIG. 2. Temperature dependence of the longitudinal Nernst–Ettingshausen coefficient (''soft-sphere'' approximation). *1*—drag contribution, *2*—contribution of scattering by the impurity system, *3*—resulting contribution.

sphere'' approximation). This situation corresponds to the case when as the temperature decreases, the electron mobility becomes constant and does not change with a further decrease of temperature. As follows from the numerical calculations, at low temperatures ($T<5$ K) the entrainment effect dominates and the NE coefficient is negative. The effect changes sign at temperatures $T\sim 5-8$ K. Scattering of $2d$ electrons is then determined mainly by the strongly correlated system of charged impurity centers. Figure 2 shows the computational results for the case when correlations in the impurity system vary with temperature in the temperature interval investigated. In examining this case, it should be kept in mind that the correlations in the system of charged centers change with temperature (''soft-sphere'' approximation[3]). As one can see, the effect changes sign even in this case. However, as the temperature increases further, the effect diminishes as a result of weakening of the correlation in the impurity system—increase of chaos in the impurity system.

We note that in the case scattering by completely randomly distributed impurity centers the effect remains negative right up to temperatures $T\sim 30$ K. The effect changes sign when the charge carriers are scattered mainly by acoustic phonons.

This work was supported by INTAS (Grant 93-3657).

[1] T. Widmer, V. Shikora, G. Hendorfer, S. Luther, W. Jantsch, K. Lischka, and M. von Ortenberg, Mater. Sci. Forum **182**, 395 (1995).
[2] I. I. Kuleev, I. I. Lyapilin, and I. M. Tsidil'kovskiĭ, Zh. Éksp. Teor. Fiz. **102**, 1652 (1992) [Sov. Phys. JETP **75**, 893 (1992)]; Zh. Éksp. Teor. Fiz. **106**, 1205 (1994) [J. Exp. Theor. Phys. **79**, 653 (1994)].
[3] I. G. Kuleev, I. I. Lyapilin, A. T. Lonchakoy, and I. M. Tsidilkovski, Semicond. Sci. Technol. **10**, 314 (1995); Zh. Eksp. Teor. Fiz. **103**, 1447 (1993) [J. Exp. Theor. Phys. **76**, 707 (1993)].
[4] I. I. Kuleev, I. I. Lyapilin, and I. M. Tsidil'kovskiĭ, Fiz. Tekh. Poluprovodn. **28**, 937 (1994) [Semiconductors **28**, 544 (1994)].
[5] B. M. Askerov, *Electron Transport Phenomena in Semiconductors*, World Scientific, Singapore, 1994; Nauka, Moscow, 1985 [in Russian].
[6] T. Ando, A. B. Fowler, and F. Stern, Rev. Mod. Phys. **54**, 437 (1982).
[7] A. K. Vijay and A. G. Fawry, Phys. Rev. B **23**, 5570 (1981).
[8] D. G. Cantrell and P. N. Butcher, J. Phys. C: Sol. State **20**, 1993 (1987).

Translated by M. E. Alferieff

Electron spectrum in a quantum superlattice with cylindrical symmetry

N. V. Tkach, I. V. Pronishin, and A. M. Makhanets

Chernovtsy State University, 274012 Chernovtsy, Ukraine
(Submitted July 17, 1997; resubmitted September 30, 1997)
Fiz. Tverd. Tela (St. Petersburg) **40**, 557–561 (March 1998)

A quantum superlattice with axial symmetry, a heterostructure in which two semiconductor materials in the form of coaxial wires with a nanosize cross section are in contact with one another and form a periodic structure in the radial direction, is studied. It is shown that the electron energy spectrum consists of alternating allowed and forbidden bands. The electron dispersion law is studied for different values of the period of the potential, thicknesses of the semiconductor layers, and radius of the inner crystal of the system. It is shown that the coherent electron effective mass of the quantum superlattice is a tensor: The longitudinal component is close in value to the electron effective mass of the semiconductor material characterizing the quantum well of the superlattice and the radial component depends strongly on the period of the potential, the thicknesses of the coaxial semiconductor layers, and the core radius of the heterosystem, taking on positive or negative values in different allowed bands. © *1998 American Institute of Physics.* [S1063-7834(98)03603-X]

Nanosize heterogeneous semiconductor systems are important objects of research in solid-state physics in connection with their possible applications in the components of next-generation computers and in laser technology. Investigations of quasi-1D (quantum wires) and 0D (quantum dots) heterostructures are of great interest,[1–6] since unique optical and transport properties that are not characteristic of bulk crystals can be observed in these systems.

In the overwhelming majority of the studies,[1–3,7] the quasiparticle spectra in simple heterosystems—a semiconductor nanocrystal of definite geometry inserted in a dielectric medium—were investigated experimentally and theoretically. It is obviously of interest to investigate the quasiparticle spectra in inhomogeneous semiconductor heterostructures consisting of cylindrical quantum wires, one inserted into another and forming a periodic structure in a plane perpendicular to the axis of the system. Since such a system has a nanosize radial period, it is an axisymmetric quantum superlattice with specific properties distinguishing it from 3D analogs. A spherical heterostructure with several semiconductor layers CdS/HgS/CdS/H_2O has now been achieved experimentally,[6] so that the development of a cylindrical quantum superlattice is entirely realistic.

Our objective in the present work is to investigate the electron spectrum in an axisymmetric quantum superlattice whose radial period contains two semiconductor materials in contact with one another.

1. QUANTUM CYLINDRICAL SUPERLATTICE

We shall investigate a heterosystem in which two semiconductor materials in the form of coaxial wires with a nanosize cross section are in contact with one another, forming a periodic structure in a plane perpendicular to the axis of the system (Fig. 1a). Such a cylindrical quantum superlattice produces for an electron a periodic radially symmetric field (Fig. 1b); the energy is measured from the top to the bottom of the potential well

$$U(\rho)=\begin{cases} U_0, & \rho_0+pL\leqslant\rho\leqslant\rho_0+a+pL, \\ 0, & \rho\leqslant\rho_0,\ \ \rho_0+a+pL\leqslant\rho\leqslant\rho_0+(p+1)L, \end{cases}$$

$$p=0,1,2,\ldots\ . \tag{1}$$

The period of the potential is $L=a+b$, where a is the width of the barrier (material 1), b is the width of the quantum well (material 2), and ρ_0 is the radius of the inner cylinder (material 2). In each medium an electron is characterized by an effective mass, so that

$$\mu(\rho)=\begin{cases} \mu_1, & \rho_0+pL\leqslant\rho\leqslant\rho_0+a+pL, \\ \mu_2, & \rho\leqslant\rho_0,\ \ \rho_0+a+pL\leqslant\rho\leqslant\rho_0+(p+1)L, \end{cases}$$

$$p=0,1,2,\ldots\ . \tag{2}$$

Because of the dependence $\mu(\rho)$, the variables ρ and z in the Schrödinger equation do not separate, so we shall use perturbation theory to solve this equation. We represent the Hamiltonian of an electron in a cylindrical coordinate system as

$$\hat{H}=\hat{H}_0(\rho,\varphi,z)+\Delta\hat{H}(\rho,z), \tag{3}$$

where the unperturbed Hamiltonian is

$$\hat{H}(\rho,\varphi,z)=-\frac{\hbar^2}{2}\left(\nabla_{\rho,\varphi}\frac{1}{\mu(\rho)}\nabla_{\rho,\varphi}+\frac{1}{\mu}\frac{\partial^2}{\partial z^2}\right)+U(\rho), \tag{4}$$

and the perturbation is

$$\Delta\hat{H}(\rho,z)=-\frac{\hbar^2}{2}\left(\frac{1}{\mu(\rho)}-\frac{1}{\mu}\right)\frac{\partial^2}{\partial z^2}, \tag{5}$$

 © 1998 American Institute of Physics

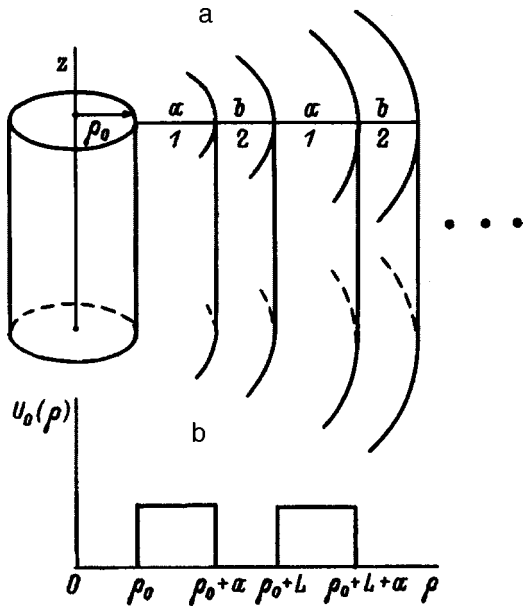

FIG. 1. Geometry of a cylindrical superlattice (a) and the potential energy of an electron in the superlattice as a function of the radius ρ (b).

$$\overline{\mu}=\frac{1}{2}(\mu_1+\mu_2). \tag{6}$$

From the Schrödinger equation

$$\{\hat{H}_0(\rho,\varphi,z)-E^0_{nmk}\}\Psi^0_{nmk}(\rho,\varphi,z)=0 \tag{7}$$

we determine the energy spectrum and wave functions of the electron in the zeroth approximation

$$E^0_{nmk}=E_{nm}+\frac{\hbar^2k^2}{2\overline{\mu}}, \tag{8}$$

$$\Psi^0_{nmk}(\rho,\varphi,z)=(2\pi h)^{-1/2}e^{i(m\varphi+kz)}\Psi_{nm}(\rho), \tag{9}$$

where $n=0,1,2,\ldots$ is the radial quantum number, $m=0,\pm1,\pm2,\ldots$ is the magnetic quantum number, k is the quasimomentum of an electron in the longitudinal direction, E_{nm} is the energy spectrum of the radial motion of an electron, $\Psi_{nm}(\rho)$ is the radial wave function, and h is the length of the main region of the wire along the $0z$ axis.

The energy of an electron in the first approximation is

$$E^{(1)}_{nmk}=E^0_{nmk}+\langle nmk|\Delta\hat{H}|nmk\rangle. \tag{10}$$

After manipulations, the relation (10) assumes the form

$$E^{(1)}_{nmk}=E^0_{nmk}+\frac{\hbar^2k^2}{2\mu_\parallel}. \tag{11}$$

Here $\mu_\parallel$ is the longitudinal component of the coherent effective mass of an electron in a quantum cylindrical superlattice in the first approximation,

$$\mu_\parallel=\frac{\overline{\mu}}{1+I\overline{\mu}}, \tag{12}$$

where

$$I=\left\langle nm\left|\frac{1}{\mu(\rho)}-\frac{1}{\overline{\mu}}\right|nm\right\rangle. \tag{13}$$

Since the potential energy $U(\rho)$ is a periodic function (with period L), the radial Schrödinger equation is invariant with respect to all translations that are multiples of L

$$U(\rho+L)=U(\rho),\quad \rho\to\rho+pL,\quad p=1,2,3,\ldots. \tag{14}$$

According to the Floquet theorem,[8] the radial wave function of an electron in the region of periodicity of the potential $\rho\geqslant\rho_0$ has the form

$$\Psi_{nm}(\rho+pL)=e^{ipqL}\Psi_{nm}(\rho), \tag{15}$$

where q is a real number, whose values lie in the interval $-\pi/L\leqslant q\leqslant\pi/L$. The relation (15) is possible only if

$$\Psi_{nm}(\rho)=e^{iq\rho}f_{nmq}(\rho), \tag{16}$$

where $f_{nmq}(\rho)$ is a periodic function, i.e.,

$$f_{nmq}(\rho)=f_{nmq}(\rho+L). \tag{17}$$

On this basis and using the solutions of the radial Schrödinger equations for the corresponding regions of the heterostructure and boundary conditions, which require continuity of the radial wave functions and their flux densities at the boundaries of the regions

$$\Psi_{nmp}(\rho_p)=\Psi_{nm,p+1}(\rho_p), \tag{18}$$

$$\frac{1}{\mu_p}\frac{\partial}{\partial\rho}\Psi_{nmp}(\rho_p)=\frac{1}{\mu_{p+1}}\frac{\partial}{\partial\rho}\Psi_{nm,p+1}(\rho_p), \tag{19}$$

we obtain the radial wave function in the form

$$\Psi_{nm}(\rho)=\begin{cases}A_0J_{|m|}(\alpha\rho), & \rho\leqslant\rho_0,\\ A_0e^{iq\rho}\begin{cases}\Gamma_1I_{|m|}(\alpha\rho)+\Gamma_2K_{|m|}(\alpha\rho), & \rho_0+pL\leqslant\rho\leqslant\rho_0+a+pL,\\ \Gamma_3I_{|m|}(\beta\rho)+\Gamma_4N_{|m|}(\beta\rho), & \rho_0+a+pL\leqslant\rho\leqslant\rho_0+(p+1)L.\end{cases}\end{cases} \tag{20}$$

In the expression (20) $J_{|m|}(\rho)$ and $N_{|m|}(\rho)$ are Bessel functions of the first and second kinds, $I_{|m|}(\rho)$ and $K_{|m|}(\rho)$ are modified Bessel functions, and Γ_i $(i=1-4)$ are coefficients determined from the system of equations (18) and (19) and are not presented here because of their complexity; the quantities

$$\alpha\equiv\alpha_{nm}=\hbar^{-1}\sqrt{2\mu_1(U_0-E_{nm})},$$
$$\beta\equiv\beta_{nm}=\hbar^{-1}\sqrt{2\mu_2E_{nm}} \tag{21}$$

determine the spectrum of the system.

The normalization of the radial wave function (20) determines the coefficient A_0

$$A_0=\left[\int_0^\infty|\Psi_{nm}(\rho)|^2\rho d\rho\right]^{-1/2}. \tag{22}$$

We represent the solutions of the radial Schrödinger equations for the corresponding regions of the heterosystem, taking account of the relations (15), in the form

$$\Psi_{nm}(\rho)=\begin{cases} A_0 J_{|m|}(\beta\rho), & \rho\leqslant\rho_0, \\ A_1 I_{|m|}(\alpha\rho)+B_1 K_{|m|}(\alpha\rho), & \rho_0\leqslant\rho\leqslant\rho_1, \\ A_2 J_{|m|}(\beta\rho)+B_2 N_{|m|}(\beta\rho), & \rho_1\leqslant\rho\leqslant\rho_2, \\ e^{iqL}\left[A_1\dfrac{I_{|m|}(\alpha\rho_0)}{I_{|m|}(\alpha\rho_2)}I_{|m|}(\alpha\rho)+B_1\dfrac{K_{|m|}(\alpha\rho_0)}{K_{|m|}(\alpha\rho_2)}K_{|m|}(\alpha\rho)\right], & \rho_2\leqslant\rho\leqslant\rho_2+a, \end{cases} \tag{23}$$

where $\rho_1=\rho_0+a$ and $\rho_2=\rho_0+L$.

Applying the boundary conditions (18) and (19) for the wave functions (23),b we obtain a system of linear homogeneous equations for the coefficients A_s and B_s $(s=0,1,2)$ and the dispersion equation

$$F(E_{nm})=\cos(qL) \tag{24}$$

for determining the energy spectrum, where the function F is given by the expression

$$\begin{aligned} F(E_{nm}) &= \frac{\pi\alpha\beta\rho_1\rho_2}{2}\Bigg\{[J_{|m|}(\beta\rho_2)N'_{|m|}(\beta\rho_1)-N_{|m|}(\beta\rho_2)J'_{|m|}(\beta\rho_1)] \\ &\times\Bigg[I_{|m|}(\alpha\rho_1)K_{|m|}(\alpha\rho_0)\,\frac{K'_{|m|}(\alpha\rho_2)}{K_{|m|}(\alpha\rho_2)} \\ &-K_{|m|}(\alpha\rho_1)I_{|m|}(\alpha\rho_0)\,\frac{I'_m(\alpha\rho_2)}{I_{|m|}(\alpha\rho_2)}\Bigg] \\ &+[J_{|m|}(\beta\rho_1)N'_{|m|}(\beta\rho_2)-N_{|m|}(\beta\rho_1)J'_{|m|}(\beta\rho_2)] \\ &\times[I_{|m|}(\alpha\rho_0)K_{|m|}(\alpha\rho_1)-K_{|m|}(\alpha\rho_0)I_{|m|}(\alpha\rho_1)] \\ &+\frac{\mu_1\beta}{\mu_2\alpha}[J'_{|m|}(\beta\rho_1)N'_{|m|}(\beta\rho_2)-N'_{|m|}(\beta\rho_1)J'_{|m|}(\beta\rho_2)] \\ &\times[I_{|m|}(\alpha\rho_1)K_{|m|}(\alpha\rho_0)-K_{|m|}(\alpha\rho_1)I_{|m|}(\alpha\rho_0)] \\ &+\frac{\mu_2\alpha}{\mu_1\beta}\Bigg[K_{|m|}(\alpha\rho_0)I'_{|m|}(\alpha\rho_1)\,\frac{K'_{|m|}(\alpha\rho_2)}{K_{|m|}(\alpha\rho_2)} \\ &-I_{|m|}(\alpha\rho_0)K'_{|m|}(\alpha\rho_1)\,\frac{I'_{|m|}(\alpha\rho_2)}{I_{|m|}(\alpha\rho_2)}\Bigg][J_{|m|}(\beta\rho_1)N_{|m|}(\beta\rho_2) \\ &-N_{|m|}(\beta\rho_1)J_{|m|}(\beta\rho_2)]\Bigg\} \end{aligned} \tag{25}$$

If

$$|F(E_{nm})|\leqslant 1, \tag{26}$$

Eq. (24) possesses real solutions, and the energy E_{nm} is a function of the quantum number q, which plays the role of a radial quasimomentum. In the opposite case, band gaps appear. As a result, the electron energy spectrum E_{nm} consists of alternating allowed and forbidden bands.

2. DISCUSSION

We choose as the materials for the structure, which is periodic in the radial direction, semiconductors that are widely employed by experimentors:[6] CdS (material 1), HgS (material 2), and a cubic face-centered modification (β). The parameters of these crystals are as follows:[6] $U_0=1.2$ eV, the electron effective masses are $\mu_1=\mu_{\mathrm{CdS}}=0.2\ \mu_0$, $\mu_2=\mu_{\mathrm{HgS}}=0.036\ \mu_0$, where μ_0 is the electron mass in vacuum, and the lattice constants $c_1=c_{\mathrm{CdS}}=5.818$ Å and $c_2=c_{\mathrm{HgS}}=5.851$ Å.

Let us now analyze the electron energy spectrum in a CdS/HgS cylindrical superlattice with a nanosize radial period. The electron dispersion law $E_{nm}(q)$ in this heterostructure with $m=0$, fixed radius of the inner crystal (HgS) $\rho_0=20c_2$, and different thicknesses a and b of the semiconductor layers is displayed in Fig. 2. The heterosystem is characterized by a barrier U_0 of finite height, so that a finite number of allowed energy bands exists in the quantum well. The series of curves in Fig. 2 with fixed m, starting with the lowest curve, correspond to values of the radial quantum number $n=0,1,2,\ldots$. For small values of b there is one allowed band in the energy range $0\leqslant E_{nm}\leqslant U_0$ (ground state—$n=0$, $m=0$). The energy of this band is determined by the dimensions of the HgS well. The next allowed band appears in this region as the width b of the HgS potential well increases and the width a of the CdS barrier decreases, and it shifts monotonically in the direction of the bottom of the well, broadening as it does so. The larger the dimension b of the HgS well, the larger the number of allowed bands present in it.

The investigations show that the longer the period L of the potential, the larger the number of allowed bands present in the energy range $0\leqslant E_{nm}\leqslant U_0$ is.

One feature of the bands displayed in Fig. 2 is that the functions $E_{nm}(q)$ at the bottom and top of each band satisfy $dE_{nm}/dq=0$ and $d^2E^2_{nm}/dq^2\neq 0$. In the allowed bands, which correspond to the quantum number $n=0,2,4,\ldots$ $(n=1,3,5,\ldots)$, the curvature of the function $E_{nm}(q)$ is such that the radial component of the electron effective mass in the quantum superlattice (coherent state) μ_{nm} assumes positive (negative) values. These features are characteristic of all allowed bands of the system.

Figure 3 shows the energy E_{nm} as a function of the radial wave number q with $m=0$ and fixed period of the potential $L=a+b$, $a=1c_1$, and $b=9c_2$ for different values of the radius ρ_0 of the inner HgS crystal. For this value of L and $\rho_0=0$ (Fig. 3a) two allowed electron energy bands exist in the HgS quantum well of the superlattice: the ground state $(n=0,\ m=0)$ and an excited state $(n=1,\ m=0)$. The ener-

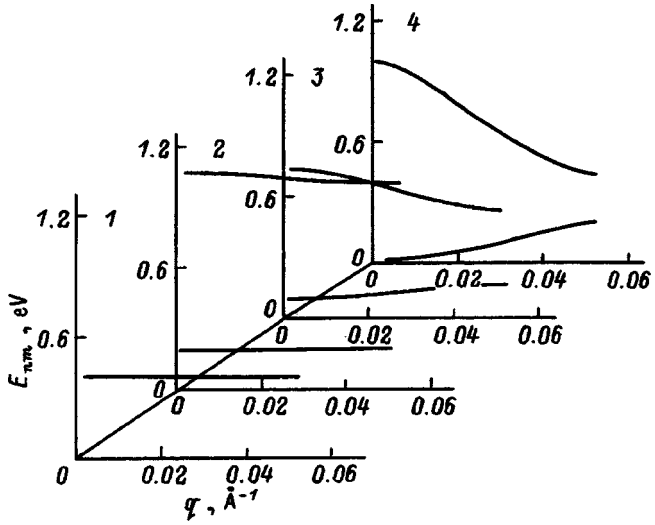

FIG. 2. Dispersion law of an electron with $m=0$, $\rho_0=20c_2$, and different widths of the barrier and quantum well. *1*—$a=6c_1$, $b=4c_2$; *2*—$a=3c_1$, $b=7c_2$; *3*—$a=2c_1$, $b=8c_2$; *4*—$a=0$, $b=10c_2$.

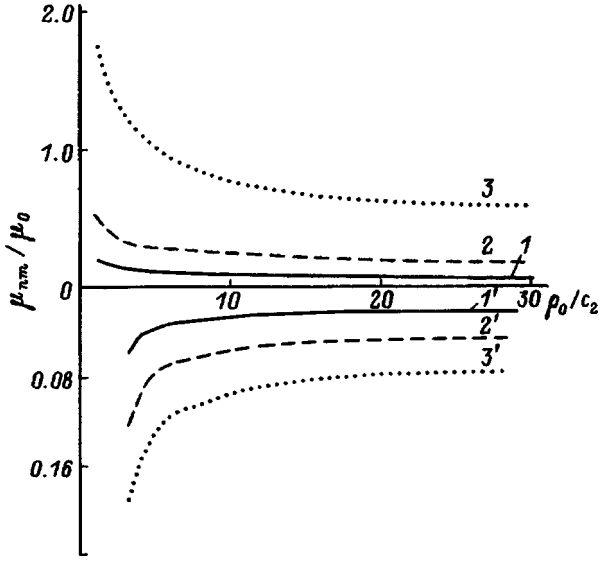

FIG. 4. Radial component of the electron effective mass in the superlattice versus the radius of the inner crystal. $n=0$ (*1–3*) and 1 (*1′–3′*). $L=1c_1+9c_2$ (*1,1′*), $2c_1+8c_2$ (*2,2′*), and $3c_1+7c_2$ (*3,3′*).

gies of these states are constant over the entire Brillouin zone (energy levels), and an electron in them is characterized by an infinite effective mass μ_{nm}. The dimensions of the core of the heterosystem strongly affect the width of the allowed bands, the curvature of the dispersion law $E_{nm}(q)$, and hence also the electron effective mass μ_{nm}. As ρ_0 increases, the boundary of the cylindrical surfaces becomes increasingly rectified, both bands broaden, and the radial component of the electron effective mass decreases. Figure 4 shows the functions $\mu_{nm}(\rho_0)$ for different thicknesses of the layers of semiconductor materials *a* (CdS) and *b* (HgS) with the same period L of the potential. The electron effective mass μ_{nm} is positive in the ground state ($n=0$, $m=0$) and negative in the excited state ($n=1$, $m=0$). The larger the width *b* of the quantum well (HgS) and the smaller the width *a* of the barrier (CdS) (the period $L=a+b$ is constant), the smaller in magnitude the limiting values (at $\rho_0=1c_2$ and $30c_2$) of the electron effective masses μ_{nm} of the quantum superlattice are. For $L=1c_1+9c_2$ (curve *1* in Fig. 4) μ_{nm} in the electron ground state decreases from $\mu_1=0.2\mu_0$ (at $\rho_0=1c_2$) to $\mu_{nm}=0.1\ \mu_0>\mu_2$ (at $\rho_0=30c_2$) and remains practically unchanged as ρ_0 increases further. At $\rho_0\approx 30c_2$ up to $\rho_0\to\infty$ (the limiting transition to a flat superlattice), the electron dispersion law $E_{nm}(q)$ remains practically unchanged and is identical to E_{nm} of a flat superlattice (with the same values of the parameters L, U_0, μ_1, and μ_2). As the investigations in the limit $\rho_0\to\infty$ (flat superlattice) show, when the width of the barrier is $a=0$ (the width of the well is finite $b=L$), there is no band gap in the energy range $0\leqslant E_{nm}\leqslant U_0$ and the curves $E(q)$ at the center of the Brillouin zone start from either the bottom or top and merge at the boundary of the Brillouin zone, and for this reason all energies are allowed.

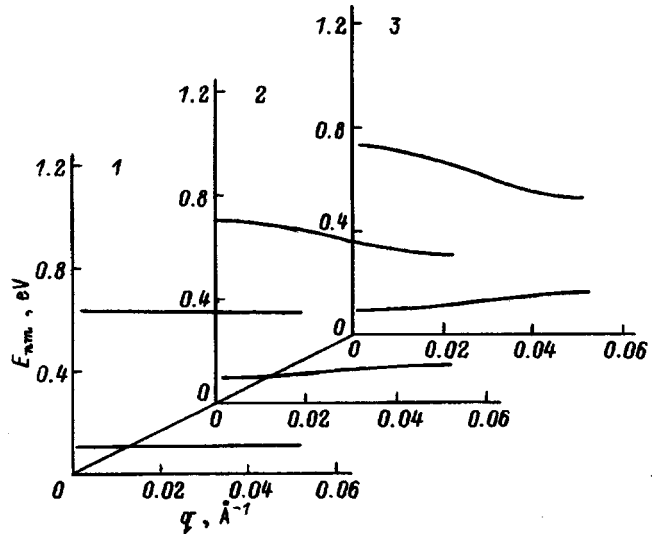

FIG. 3. Dispersion law of an electron with $m=0$ and $L=1c_1+9c_2$ for different values of the radius ρ_0 of the inner crystal. $\rho_0=0$ (*1*), $20c_2$ (*2*), and $100c_2$ (*3*).

An entirely different situation is observed for finite values of ρ_0. The radial symmetry of the cylindrical quantum superlattice (in other words, the curvature of the boundaries of the cylindrical surfaces) is so important that the character of the electron spectrum changes from that in the case of a flat superlattice. For finite values of ρ_0 and $b=L$ ($a=0$) (Fig. 2) there exists a band gap, whose width is determined by the parameters of the system.

We note that the electron effective mass is a tensor. The numerical calculations performed according to Eq. (12) for the longitudinal component $\mu_\parallel$ of the coherent electron effective mass in a quantum superlattice show that this quantity is close in value to the electron effective mass in the semiconductor HgS, characterizing the quantum well of the superlattice. The radial component of the electron effective mass μ_{nm} in the quantum superlattice (coherence state) depends strongly on the radius of the core of the heterostructure, the period and magnitude of the potential, and the thicknesses of the coaxial semiconductor layers.

Figure 5 shows the dispersion law $E_{nm}(q)$ for fixed

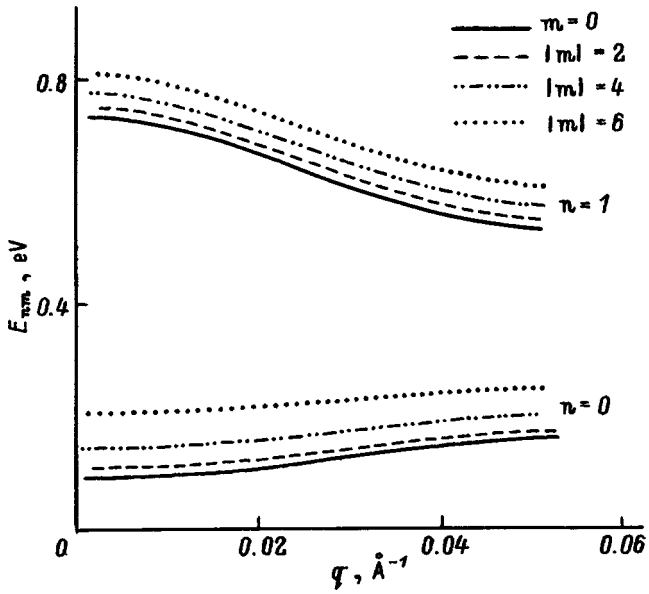

FIG. 5. Dispersion law of an electron with $\rho_0=20_2$ and $L=1c_1+9c_2$ for different values of the magnetic quantum number.

$\rho_0=20c_2$ and $L=1c_1+9c_2$ for different values of the magnetic quantum number. The larger the value of m, the higher the energy E_{nm} of the excited states of an electron in the superlattice is and in addition the positions of the allowed bands with $|m|\geqslant 1$ are shifted monotonically upwards relative to the positions of the bands with $m=0$. The picture of the energy spectrum is as follows: ground state—$n=0$, $m=0$; first excited state—$n=0$, $m=1$; second excited state—$n=0$, $m=2$, and so on. The curvature of $E_{nm}(q)$ is such that $\mu_{nm}>0$ for $n=0,2,4,\ldots$ and $\mu_{nm}<0$ for $n=1,3,5,\ldots$.

The main result of this work is that complicated coherent electron states with anisotropic effective masses, which depend on the parameters of the heterosystem, arise in a quantum superlattice with cylindrical symmetry. The anisotropy of the effective masses should be manifested in the corresponding optical (absorption coefficient, permittivity) and dynamic (conductivity) characteristics of the experimental systems.

[1] S. L. Goff and B. Stebe, Phys. Rev. B **47**, 1383 (1993).
[2] C. Greus, R. Spiegel, P. A. Knipp, and T. L. Reinecke, Phys. Rev. B **49**, 5753 (1994).
[3] G. Q. Hai, F. M. Peeters, J. T. Devreese, and L. Wendler, Phys. Rev. B **48**, 12016 (1993).
[4] C. Greus, L. Butov, and P. A. Knipp, Phys. Rev. B **47**, 7626 (1993).
[5] N. V. Tkach, V. I. Boĭchuk, V. A. Golovatskiĭ, and O. N. Voĭtsekhivskaya, Fiz. Tverd. Tela (St. Petersburg) **38**, 3161 (1996) [Phys. Solid State **38**, 1727 (1996)].
[6] D. Schooss, A. Mews, A. Eychmuller, and H. Weller, Phys. Rev. B **49**, 17 072 (1994).
[7] M. F. Lin, W. Kenneth, and K. Shung, Phys. Rev. B **47**, 6617 (1993).
[8] S. Flügge, *Practical Quantum Mechanics* [Springer-Verlag, Berlin, 1971; Mir, Moscow, 1974], Vol. 1.

Translated by M. E. Alferieff

Properties of the interaction of europium with Si(111) surface

A. Yu. Grigor'ev, A. M. Shikin, G. V. Prudnikova, S. A. Gorovikov, and V. K. Adamchuk

Institute of Physics, St. Petersburg State University, 198904 Petrodvorets, Russia
(Submitted August 4, 1997)
Fiz. Tverd. Tela (St. Petersburg) **40**, 562–567 (March 1998)

Formation of the Eu/Si(111) system as the metal layer thickness gradually increases from 0.5 to 60 monolayers (ML) deposited on the silicon surface at room temperature, and after heating at up to 900 °C, has been studied by Auger electron spectroscopy, electron-energy-loss spectroscopy, and low-energy-electron diffraction. It is shown that room-temperature film growth passes through three stages, depending on the Eu layer thickness: metal chemisorption, interdiffusion of the metal and substrate atoms, and buildup of the metal on the surface of the system. Heating of ultrathin (about one ML) Eu films deposited at room temperature results in ordering of metal atoms on the silicon surface with only weak interaction. Heating thick (above 15 ML) Eu layers on the silicon surface produces silicides whose structure depends on the heating temperature. © *1998 American Institute of Physics.* [S1063-7834(98)03703-4]

Rare-earth metals (REM) interacting with a silicon surface produce silicides, which possess a number of unique physicochemical properties, among them an extremely low Schottky barrier (0.3–0.4 eV) at the interface between the REM silicide and *n*-Si surface, fairly high electrical and heat conductivity, and comparatively low formation temperature.[1–3]

The present work studies the interaction of Eu with the silicon surface. Eu is normally in the divalent state and retains it in interaction with silicon, whereas when bound in a chemical compound its behavior resembles that of *s* metals. In this it differs from most REMs. The present study focuses primarily on the electronic and crystalline structures of systems consisting of a thin Eu layer on the Si(111)7×7 surface in their dependence on the annealing temperature and metal-layer thickness. The electronic structure of these systems was investigated by Auger electron spectroscopy (AES) and electron-energy-loss spectroscopy (EELS), and the surface crystalline structure, by low-energy electron diffraction (LEED).

1. EXPERIMENTAL TECHNIQUES

The studies presented in this work were carried out *in situ* in an ultrahigh vacuum at $(1-2)\times10^{-10}$ Torr. The sample was a $7\times5\times0.2$-mm plate of As-doped *n* silicon with a resistivity of $0.002\ \Omega\cdot$cm, with a polished (111) face. Eu was deposited by evaporation from a quartz crucible. The flux deposited onto the Si surface was monitored by means of a quartz piezomicrobalance. The sample was directly heated by passing dc current through the silicon plate. The heating temperature was determined by the magnitude of the current through the sample. The correspondence between the current and the heating temperature was verified in preliminary calibration experiments by means of an optical pyrometer. The silicon surface was cleaned by a brief high-temperature annealing at about 1100 °C. The cleanliness and crystalline perfection of the Si(111)7×7 surface in the course of experiments were monitored by AES and LEED.

The Auger and EEL spectra were obtained with a four-grid hemispherical retarding-field electron analyzer with an energy resolution of 0.25% and an electron beam normally incidence onto the sample. The analyzer design permitted observation of the LEED patterns as well. The analyzer and setup design are described in detail elsewhere.[4] The Auger spectra presented in this work were taken in the dN/dE mode at 1-keV primary-electron energy. The EEL data were measured in the dN/dE mode at the primary electron energy of 200 eV and subsequently processed to yield d^2N/dE^2 spectra.

2. EXPERIMENTAL RESULTS

Figure 1a shows some Auger spectra of the Eu/Si(111) system for different Eu-layer thicknesses (1, 7, 15, and 60 ML, with 1 ML$\approx$3.8 Å) deposited on the Si surface at room temperature, and an Auger spectrum of a clean Si(111) 7×7 surface, obtained in the kinetic energy interval of 60 to 150 eV. This energy interval permits one to observe simultaneously in the spectra the Si $L_{23}VV$ peak at about 92 eV and Auger peaks of europium at 82 eV (due to the $N_1N_{45}N_{45}$ and $N_{45}O_{23}O_{23}$ transitions), at about 103 eV (originating from the $N_{45}O_{23}N_{67}$ and $N_{45}O_{23}V$ Auger transitions), to be called in what follows the NON peak, the $N_{45}N_{67}N_{67}$ Auger peak at 122 eV, and peaks at 129 and 135 eV caused by hole recombination between the $4d$ and $4f$ levels. In describing the processes occurring in the Eu/Si(111) system, we shall subsequently focus attention primarily on the NON peak of Eu, because it is the strongest of all Eu Auger peaks and provides information on the valence band. A comparison of the spectra in Fig. 1a shows that the amplitude of the Eu $N_{45}O_{23}N_{67}$ peak grows, and that of the silicon $L_{23}VV$ peak, gradually decrease with increasing Eu layer thickness. The silicon peak at 91.5 eV shifts by about 0.6 eV toward lower kinetic energies even at coverages of one monolayer, and

 © 1998 American Institute of Physics

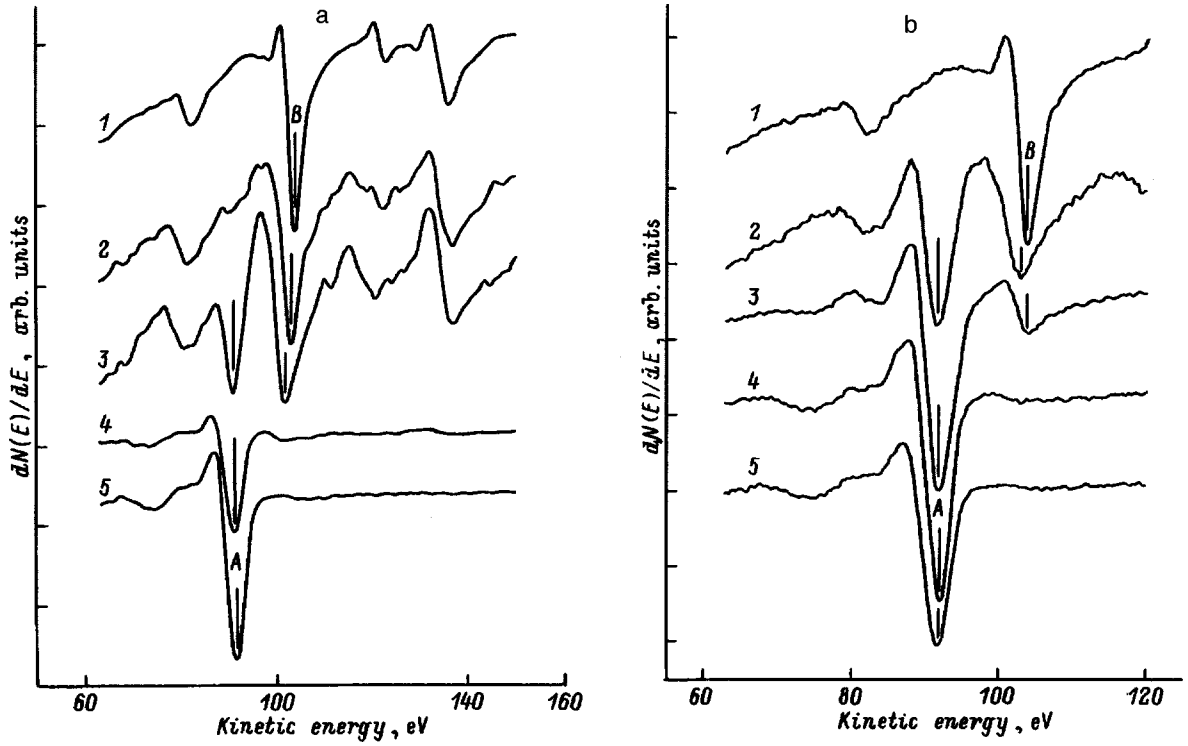

FIG. 1. Auger spectra of the Eu/Si(111) system. (a) Spectra obtained from Eu layers with different thicknesses deposited with $E_p=1$ keV at room temperature (ML): *1*—60, *2*—15, *3*—7, *4*—1, *5*—clean Si(111)7×7 surface; *A*-Si $L_{23}VV$ peak ($E=91.8$ eV), *B*-Eu $N_{45}O_{23}N_{67}$ peak ($E=103$ eV). (b) Spectra obtained after the heating of Eu layers with different thicknesses deposited at room temperature ($E_p=1$ keV): *1*—60 ML without heating, *2*—15 ML, heating at 400 °C; *3*—15 ML, heating at 700 °C (2×2 structure); *4*—1 ML, heating at 500 °C (3×1 structure); *5*—clean Si(111)7×7 surface; *A*-Si $L_{23}VV$ peak ($E=91.8$ eV), *B*-Eu $N_{45}O_{23}N_{67}$ peak ($E=103$ eV).

does not change position with further deposition of europium. The Eu peak at ≈103 eV shifts gradually toward higher kinetic energies with increasing thickness of the deposited layer. The relative change in amplitude of the Si $L_{23}VV$ peak (Fig. 2a) and of the Eu $N_{45}O_{23}N_{67}$ peak (Fig. 2b) with increasing metal-layer thickness permits one to follow the change in intensity of individual Auger peaks in more detail. The Auger peak amplitude was determined from the intensity change between the low- and high-energy extrema of the corresponding Auger dN/dE peaks. In Fig. 2a, the 100%-level is the amplitude corresponding to the LVV peak from clean silicon surface, and in Fig. 2b, that of the NON Eu peak for the 15-ML thick metal layer on Si surface. We see that the amplitudes of the Auger peaks under study vary nonuniformly with Eu layer thickness. The sharpest changes occur at metal layer thicknesses below 2 ML.

Figure 3a presents EEL spectra in the form $d^2N(E)/dE^2$ for the Eu/Si(111) system for metal layers four and 30 monolayers thick deposited at room temperature, and for a clean Si surface. The characteristic features of these spectra are the plasma loss peaks in silicon and europium (about 17.7 and 9 eV, respectively) and the Eu 5*p* EEL feature (at ≈25 eV). We readily see that the Eu EEL spectrum undergoes substantial changes even at $\theta=4$ ML. The silicon plasma-loss peak (17.7 eV) practically disappears against the background of the features associated with losses in the metal (core-level Eu 5*p* and plasma losses in europium at 8 eV) and a new peak at 12.5 eV. The EEL spectrum obtained from 30 monolayers of Eu exhibits a substantial increase in the Eu plasma loss

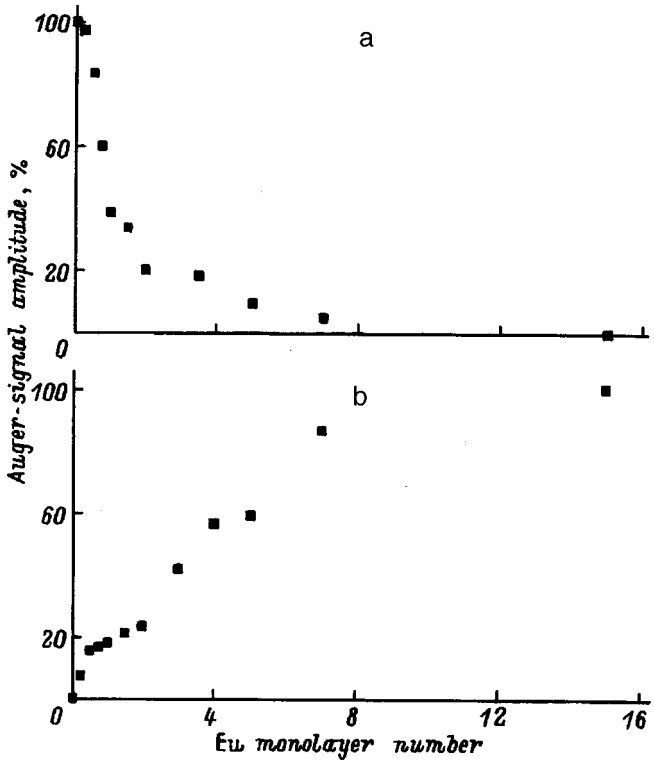

FIG. 2. Relative variation of the amplitude of (a) Si $L_{23}VV$ peak and (b) Eu $N_{45}O_{23}N_{67}$ peak with increasing thickness of Eu layer deposited at room temperature.

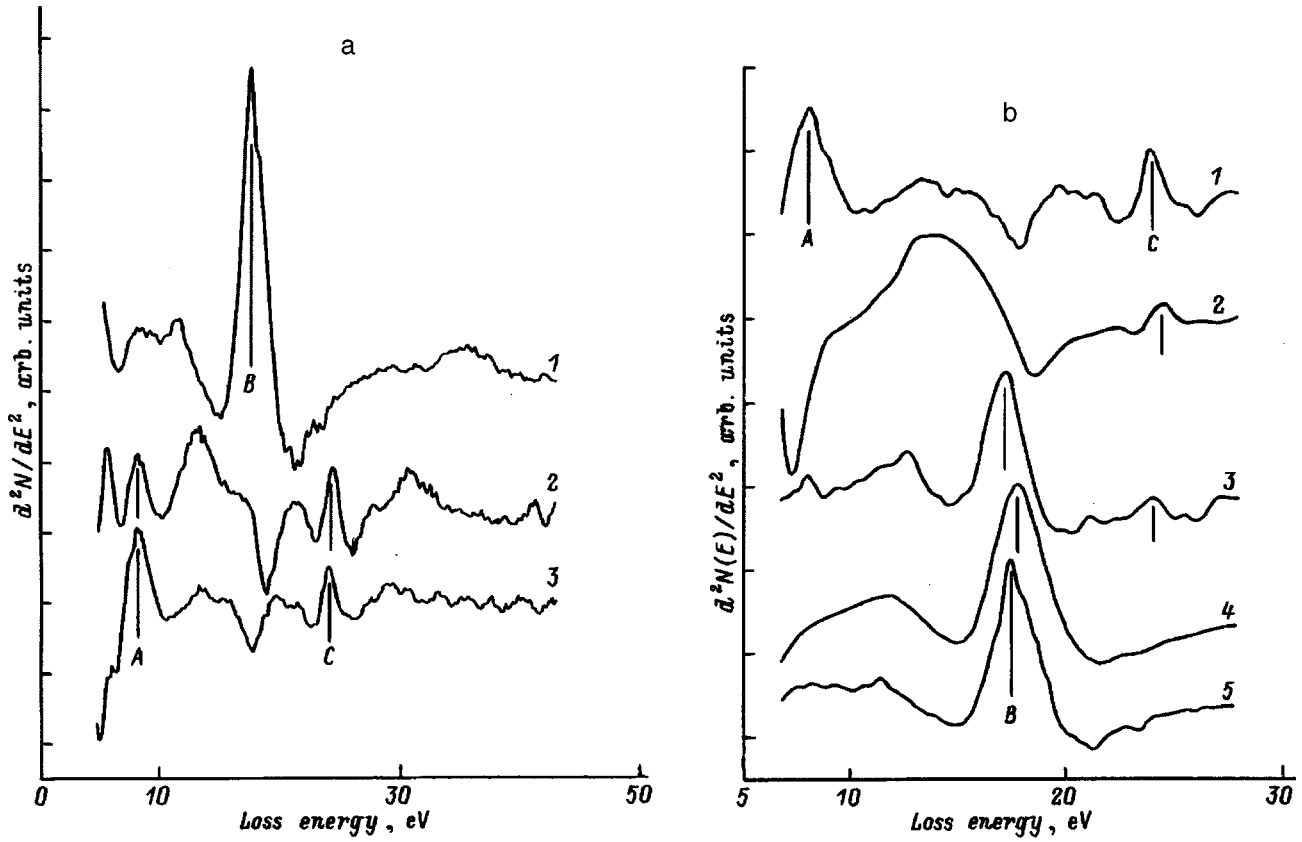

FIG. 3. EEL spectra of Eu/Si(111) system. (a) Spectra obtained from different thicknesses of Eu layer deposited with $E_p = 200$ eV at room temperature. *1*—clean Si(111)7×7 surface, *2*—four Eu ML, *3*—30 Eu ML, *A*-Eu plasma loss peak ($\hbar\omega = 8.1$ eV), *B*-Si bulk plasma loss peak ($\hbar\omega = 17.6$ eV), *C*-Eu 5*p* loss peak ($E = 24.5$ eV); (b) Spectra obtained after the heating of Eu layers with different thicknesses deposited at room temperature ($E_p = 200$ eV): *1*—30 ML without heating, *2*—15 ML, heating at 400 °C; *3*—15 ML, heating at 700 °C (2×2 structure); *4*—1 ML, heating at 500 °C (3×1 structure); *5*—clean Si(111)7×7 surface; *A*-Eu plasma loss peak ($\hbar\omega = 8.1$ eV), *B*-Si bulk plasma loss peak ($\hbar\omega = 17.6$ eV), *C*-Eu 5*p* loss peak ($E = 24.5$ eV).

peak and Eu 5*p* excitation loss feature, with the latter shifting by approximately 0.5 eV toward lower binding energies compared to a thin Eu layer on Si.

The Eu/Si(111) system produced by heating at different temperatures was studied with thin (1—2 ML) and thick (15 and 60 ML) Eu layers deposited at room temperature. It was established that the geometric and electronic structures of the systems forming after the heating of thick metal layers differ negligibly. The structure of these systems depends on the heating temperature. Figure 1b displays the most characteristic Auger spectra obtained after heating at different temperatures of a system consisting of 15 monolayers of Eu on a Si(111)7×7 surface. Also shown is an Auger spectrum of the system produced by heating one monolayer of the metal at a temperature of about 400 °C.

As follows from LEED patterns, structures with an ordered crystalline surface form only at sufficiently high heating temperatures (above 600 °C). It was established that systems prepared at heating temperatures of 700 and 800 °C are characterized by 2×2 and 3×3 ordered structures relative to silicon, respectively. In the case of the 2×2 structure the stoichiometry of the compound was tentatively estimated as $EuSi_{2.2}$. The estimate was made by comparing the silicon and europium Auger peak amplitudes in the spectra obtained.

Figure 3b shows EEL spectra of the same phases as in Fig. 1b. These spectra are dominated by a silicon plasma-loss peak shifted slightly toward lower binding energies. One also sees clearly in the spectrum of the 2×2 structure a feature at 13 eV.

An analysis of the compounds formed after the heating of the Eu/Si(111) system revealed that those that appear at relatively low temperatures are metastable; indeed, the composition and electronic structure of the surface change with time. For instance, while immediately after heating at $T \approx 400$ °C silicon is detected in considerable amounts on the surface (see Fig. 1b), after 12 hours of keeping the system at room temperature the Si $L_{23}VV$ Auger peak practically disappeared. Repeated heating, both at the same and at higher temperatures, up to 500 °C, does not affect the spectrum, which implies that the system thus formed is stable.

Studies of systems produced by heating one monolayer of europium on silicon surface showed that a number of ordered structures form there. When heated at $T \approx 400$ °C, the structure forming on the surface is 5×1, at higher temperatures (about 500 °C) it is 3×1, and for $T > 700$ °C, it is the 1×1 structure, which transforms gradually with increasing heating temperature to the 7×7 superstructure characteristic of clean Si surface. No such structures were observed when heating thick metal layers. The Auger spectrum of the 3×1 phase is shown in Fig. 1b, and the EEL spectrum is shown in Fig. 3b together with spectra of the systems produced by heating a thick Eu layer on the Si surface.

3. DISCUSSION OF RESULTS

The mechanisms of Eu film growth on Si surface can be analyzed by considering the dependences of the amplitudes of the most characteristic Eu and Si Auger peaks on the metal layer thickness displayed in Fig. 2a,b. We readily see that these graphs are nonmonotonic, with the slopes changing at a thickness of about two monolayers. This behavior implies that Eu films of different thickness grow by different mechanisms. For small thicknesses, the curves, on the whole, correspond to monotonic growth of Eu films on Si(111). Eu atoms start to interact with the substrate even at submonolayer coverages, which is implied by the shift of the Si $L_{23}VV$ peak at these thicknesses toward lower kinetic energies (Fig. 1a), and this shift is most likely connected with a charge transfer from Eu to Si atoms. This observation is in accord with the conclusions of Ref. 5.

As seen from Fig. 2, as the Eu film thickness increases above two monolayers, the rates of decrease of the silicon Auger peak amplitude and of the increase of the europium Auger peak amplitude slow down noticeably, which suggests a change in the pattern of interaction with the substrate. This behavior for Eu coverages with $\theta > 2$ can be identified with one of the two growth mechanisms, namely, the Stransky–Krastanov mechanism, involving formation of three-dimensional clusters on a uniform adsorbate layer, or the interdiffusion mechanism, where, starting with a certain adsorbate layer thickness, atoms of the substrate mix with those of the adsorbate, a process accompanied by breaking of atomic bonds in the upper layers of the substrate. In our case, the Si $L_{23}VV$ peak in the Auger spectrum was clearly seen even with Eu thicknesses above ten monolayers, whereas the silicon plasma loss peak disappeared from the EEL spectrum at a Eu film thickness of just four monolayers (Fig. 3a), which implies destruction of the energy bands formed by silicon atoms as a result of the rupture of Si–Si chemical bonds. This argues for the second, interdiffusion mechanism.

As evident from Fig. 2a, for Eu layers more than 7–10 ML thick, the $L_{23}VV$ peak of silicon practically disappears from the spectra. Starting from these thicknesses, further deposition leads to a buildup of Eu, and the surface structure acquires the features of a metallic Eu phase, which is indicated by the fact that the Auger spectrum of the system formed after deposition on the Si surface of a thick Eu layer (Fig. 1a) coincides with that of the metallic Eu phase.[6]

The above analysis implies that room-temperature formation of the Eu/Si(111) system passes through the following three stages: (1) For coverages less than two monolayers, Eu spreads uniformly over the silicon surface, and interaction of Eu atoms with the substrate becomes manifest already in this stage; (2) For Eu thicknesses above two monolayers, the bonds coupling silicon atoms in the near-surface layers of the substrate break, thus making possible interdiffusion of europium and silicon atoms; (3) For coverages exceeding 7–10 ML, europium starts to build up on the silicon surface.

Heating a thick layer of Eu on the surface of Si at high enough temperatures causes compounds with an ordered structure to form on the surface. An analysis of LEED patterns shows the formation on the surface at $T \approx 700$ °C of a 2×2 structure, and at $T \approx 800$ °C, of a 3×3 structure. As seen from Fig. 3b, the spectrum of the 2×2 EEL phase exhibits a noticeable shift of the silicon plasma loss peak and a feature in the region of 13 eV. This shows that Eu atoms interact with atoms of the substrate and become chemical bound. The Auger spectrum of this phase (Fig. 1a) permits certain conclusions on the character of this bonding. We see that the Si Auger peak does not change its position relative to the spectrum of the clean substrate, which suggests that this peak returned to its original position (as mentioned earlier, its energy changed in the course of room-temperature growth). One may thus conclude that there is no noticeable charge transfer between Si and Eu atoms in the systems formed after the heating. It follows that the bonding between atoms in this system is probably mostly covalent. This evidence gives credence to the assumption that the 2×2 and 3×3 structures relate to epitaxial silicides. For the 2×2 structure, the composition of this compound can be described by an approximate formula $EuSi_{2.2}$, which is in agreement with the reported silicide.[5,7]

Heating at $T \approx 400$ °C of a thick Eu layer deposited at room temperature on Si(111) produces a system with a high Si concentration on the surface (Fig. 1b) which does not generate any LEED pattern. When stored at room temperature, this system exhibits a decrease in the Si concentration on the surface, until it disappears completely in 12 h, as evidenced by the absence of the Si Auger signal in the spectra. Subsequent heating of the system up to $T \approx 500$ °C did not change the spectra noticeably.

It can be suggested that when a thick Eu layer on Si(111) is heated at $T \approx 400$ °C, Si atoms diffuse through the Eu layer toward the surface. The conditions on the surface are, however, not conducive to formation of strong chemical bonds between Si and Eu atoms, and therefore the excess of Si drifts away in time to become bonded at the interface separating europium and silicon, where a layer forms which precludes further Si diffusion to the surface in subsequent heatings.

Heating an ultrathin (one monolayer-thick) Eu film does not introduce any serious distortions into the silicon surface structure also, but gives rise to the formation of compounds with an ordered surface structure. As the temperature increases, 3×1 and 5×1 patterns appear. The 3×1 phase formed at a temperature of about 400 °C. The Auger and EEL spectra of this surface are shown in Figs. 1b and 3b, respectively. This system differs most significantly from those corresponding to bulk epitaxial silicides in the crystalline structure of the surface and a lower temperature of formation of the ordered surface structure. As seen from the Auger spectrum, formation of this system does not result in a shift of the Si $L_{23}VV$ peak toward lower kinetic energies, which was observed before the heating. Moreover, a more careful analysis of the spectrum revealed a reverse shift of the peak by about 0.4 eV, which indicates interaction between Eu and Si atoms different in character from that characteristic of bulk silicides. The EEL spectrum of the 3×1 surface is very close in shape to that of clean silicon surface. This suggests that the surface did not experience any destruc-

tive action from the side of the adsorbate. It may be conjectured that formation of ordered structures after heating of thin Eu layers on Si(111) does not involve destruction of Si–Si bonds in near-surface layers. In contrast to systems produced in the heating of thick Eu layers, europium atoms become distributed uniformly over silicon surface after the film heating and occupy preferred positions, in which they form strong, predominantly covalent chemical bonding with silicon atoms involving weak electron density transfer between the two species.

The results obtained in this work can be summed up as follows.

1. Eu atoms deposited on the Si(111) surface at room temperature interact with the substrate in three stages, depending on the actual metal layer thickness:

a) for Eu coverages below two monolayers, monotonic film growth on silicon surface, with no bonds between Si atoms in the upper layers being broken;

b) for Eu coverages from two to seven monolayers, mixing (interdiffusion) of Eu atoms with atoms in the topmost layers of the silicon substrate, which is accompanied by breaking of silicon bonds;

c) for thicknesses above 7–10 monolayers, metal buildup on the surface and formation of a solid metal layer as Eu deposition is continued.

2. Heating thick (above 15 ML) Eu layers at temperatures from 600 to 800 °C produces epitaxial europium silicides on the surface, with the structure and composition depending on the heating temperature. In particular, phases with 2×2 and 3×3 surface patterns were observed. Chemical interaction between Eu and Si atoms in these structures has a primarily covalent character.

3. Heating a thick Eu layer at temperatures of about 400 °C forms a metastable system, whose surface immediately after the heating is enriched in Si atoms. When maintained at room temperature, silicon atoms diffuse into the bulk and stabilize the interface. Repeated heating of the system after a considerable time (above 12 h) does not reproduce the effect, in other words, with time the system reaches a stable state.

4. Heating ultrathin (about one monolayer) Eu layers produces ordered structures on the surface different from those of epitaxial silicides. The differences consist in a lower formation temperature of the ordered structures (about 400 °C) and in the crystalline structure of the surface (one observed 3×1 and 5×1 surface structures). These structures form in the reconstruction of the Si(111) surface under a uniform flux of adsorbing Eu atoms.

Support of the Natural Sciences Application Center at the St. Petersburg State University, Russian Fund for Fundamental Research (Grant 96-03-34107a) and RFRF-DFG (Grant 96-02-00045G) is gratefully acknowledged.

[1] K. N. Tu, R. D. Thompson, and B. Y. Tsaur, Appl. Phys. Lett. **38**, 626 (1981).
[2] H. Norde, J. de Sousa Pires, F. d'Heurle, F. Pesavento, C. S. Petersson, and P. A. Tove, Appl. Phys. Lett. **38**, 865 (1981).
[3] R. D. Thompson, B. Y. Tsaur, and K. N. Tu, Appl. Phys. Lett. **38**, 535 (1981).
[4] A. M. Shikin, *Author's Abstract of Candidate Thesis* (LGU, Leningrad, 1985).
[5] W. A. Henle, M. G. Ramsey, F. P. Netzer, and K. Horn, Appl. Phys. Lett. **58**, 1605 (1991).
[6] V. Sh. Ivanov, I. A. Brytov, V. V. Korablev, N. A. Kozyreva, T. V. Kuznetsova, E. A. Tsukerman, and I. A. Kiseleva, *Album of Auger Spectra of Chemical Elements and Their Compounds* [in Russian] (VINITI, Moscow, 1986).
[7] G. Rossi, Surf. Sci. Rep. **7**, 1 (1987).

Translated by G. Skrebtsov

FULLERENES AND ATOMIC CLUSTERS

Copper nanoclusters in amorphous hydrogenated carbon

V. I. Ivanov-Omskiĭ, V. I. Siklitskiĭ, and S. G. Yastrebov

A. F. Ioffe Physicotechnical Institute, Russian Academy of Sciences, 194021 St. Petersburg, Russia
(Submitted September 1, 1997)
Fiz. Tverd. Tela (St. Petersburg) **40**, 568–572 (March 1998)

A study of the geometric characteristics of copper nanoclusters incorporated in an amorphous hydrogenated carbon matrix is reported. It makes use of small-angle x-ray scattering and transmission electron microscopy (100 keV). The fractal dimension and nanocluster diameter have been determined from the x-ray scattering indicatrix for different copper concentrations. TEM images of copper nanoclusters have been analyzed, and a cluster distribution function in size constructed. The shape of the distribution function is discussed in terms of the theory of nucleation of a new phase. © *1998 American Institute of Physics.* [S1063-7834(98)03803-9]

The interest in the physics of conducting clusters is partially stimulated by their application potential in micro- and nanoelectronics.[1] Modification of the properties of amorphous hydrogenated carbon (a-C:H) by incorporation of metallic nanoclusters is also of interest, because it may provide valuable information on the structure of a-C:H.[2] Copper, which does not form carbides, can be used to create various types of conducting clusters in the a-C:H dielectric matrix.[3] The main objective of this work was to obtain information on the shape, size, and size distribution function for copper-generated clusters incorporated in a-C:H. This was done by analyzing the images obtained by transmission electron microscopy (TEM) and the angular dependence of small-angle x-ray scattering intensity. The dependence of cluster-surface fractal dimension and of cluster size on copper concentration in the material under study has been established. The angular dependence of the x-ray scattering intensity is discussed in terms of the fractal approach to scatterer geometry.

1. EXPERIMENTAL

a-C:H layers were deposited by dc planar magnetron sputtering in an argon-hydrogen plasma (80 %Ar+20 %H_2) from a graphite target. Single-crystal silicon and KBr were used as substrates. Planetary motion of the sample holder ensured uniform composition over the growing film area. Copper was incorporated by sputtering a copper–graphite target representing an annular graphite cathode with copper plates arranged uniformly over its surface. As follows from calibration by secondary-ion mass spectroscopy, the percentage content of copper incorporated in a-C:H films agrees to within 2% with the area ratio of the graphite to copper target components. The substrate temperature at the beginning of sputtering was close to 200 °C. The average magnetron power was varied within 0.35–0.45 kW. The working-mixture pressure in the reactor could be varied in the 1–10 mTorr interval. The films were 0.1–1.5 μm thick. A Philips 400 TEM transmission electron microscope operating at 100 kV was used to observe the microstructure of a-C:H(Cu) directly and to identify it by selective electron diffraction. The ~100-nm thick a-C:H(Cu) films intended for this purpose were grown on a KBr substrate, after which the latter was removed by dissolving it in water. Small-angle x-ray scattering was measured with a RIGAKU diffractometer at 1.541 Å (Cu K_α radiation) with an angular resolution $<10'$. The measurements were performed in reflection geometry at 50 keV. The diffraction pattern was obtained within the 1.0–7.0° scattering angle range.

2. EXPERIMENTAL RESULTS

A. Small-angle x-ray scattering

Figure 1 presents the typical angular dependence of the x-ray intensity scattered from an a-C:H(Cu) film containing 6 at. % Cu for two spectral slit widths. One readily sees a maximum at small angles. Narrowing the spectral slit improves the resolution of the intensity peak while leaving the slope of the curve to the right of it practically unchanged.

Direct comparison of the intensities scattered by copper-free a-C:H and copper-doped a-C:H(Cu) films showed that the a-C:H matrix contributed little, which implies that it is the copper scatterers incorporated in the a-C:H matrix that produce the x-ray intensity scattered through small angles.

Classical theory of small-angle scattering of x-rays with a wavelength l from an ensemble of regular spheres[4] predicts that the scattered intensity passes through a maximum at an angle $\theta = l/2d$, where d is the sphere diameter. The shape and position of the peak in Fig. 1 show that the average size (diameter d) of copper scatterers in the ensemble is well defined and equal to 30 Å. The latter value, in its turn, agrees fairly well with estimates of the size of copper clusters incorporated in a-C:H by cosputtering of graphite and copper targets, which were derived from optical measurements.[3] By traditional theory,[4] which assumes the scatterer to be bounded by a smooth surface, the angular dependence of the

 © 1998 American Institute of Physics

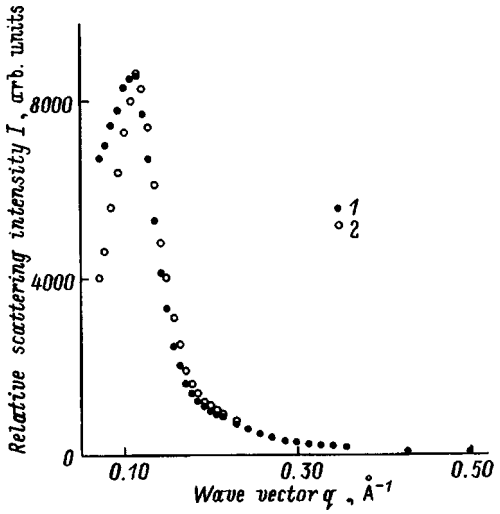

FIG. 1. Small-angle x-ray scattering intensity for copper-doped *a*-C:H samples. Spectral slit (mm): *1*—0.32, *2*—0.55.

scattered intensity $I(q)$ should follow a power law-dependence on momentum transfer q with a negative integer exponent α (Ref. 5):

$$I(q)\sim q^{-\alpha}, \quad \text{where } q=(4\pi/\lambda)\sin(\theta/2). \tag{1}$$

Here λ is the scattered wavelength. For spherical scatterers bounded by a smooth surface the exponent is $\alpha=4$.[4] This means that $\log I(q)$ is a linear function of log wave vector, $\log q$, and therefore a log–log scale is the most convenient way to present the experimental data (Fig. 2). As seen from Fig. 2, for all studied samples the scattered amplitude is indeed a power-law function of photon momentum for moderate scattering angles. Table I shows that the exponent turns out to be noninteger. To estimate the accuracy with which the exponent in Eq. (1) was determined, three samples with the same copper content (6 at. %) were subjected to a reproducibility test (see Fig. 3). The difference in the scattered

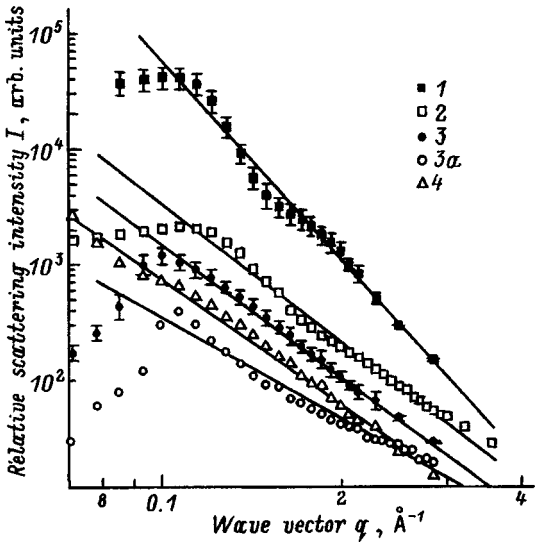

FIG. 2. Small-angle x-ray scattering intensity for samples with different copper concentrations C_{Cu} (at. %): *1*—4, *2*—6, *3*—14, *3*a—14 (the sample was annealed in vacuum at $T=240$ °C for 2 h), *4*—24.

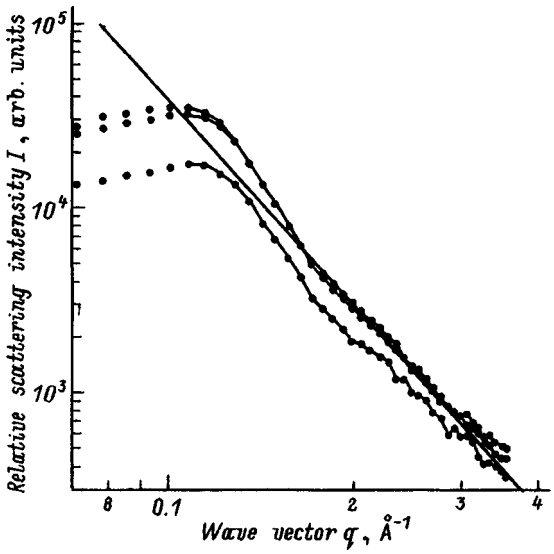

FIG. 3. Reproducibility of small-angle scattering data for three copper-doped *a*-C:H samples (6 at. % Cu).

amplitude can be attributed to differences in the geometric size of the samples, whereas the average slope of the curves is reproduced quite well, as can be judged from the spread in the exponent $\alpha=3.8\pm0.1$. Based on these data, we estimate the error in exponent determination to be ±0.1.

Although using the log–log scale makes the peaks smoother (compare Figs. 2 and 3), the position of the maximum in scattered intensity is seen to remain practically unchanged, with the exception of sample 4. This means that the average scatterer size practically does not depend on copper concentration, provided it is <24 at. % (see Table I). A certain deviation, from the monotonic course of experimental points to the right of the peak in Fig. 2 is the result of neglecting higher diffraction orders in Eq. (1), which appear, in particular, because the scattering clusters is nonspherical.

As seen from the data of Table I and Fig. 2 for samples 3 and 3a, annealing sample 3 in vacuum at $T=240$ °C for 2 h did not affect noticeably the peak position. This sample was chosen because its peak position was reliably known before the anneal. Thermal treatment did not produce any effect on the average copper-cluster size, while improving the peak resolution and changing significantly the slope of the curve (Fig. 2).

B. Transmission electron microscopy

Figure 4 presents a dark-field TEM image of copper-containing clusters in an *a*-C:H(Cu) sample with 9 at. % Cu. The data of Fig. 4 were used to construct a distribution function in cluster size (Fig. 5). The squares are experimental points, and the solid line approximates the points with a Gaussian

$$P(d)\sim\exp\left[-\frac{(d-d_{av})^2}{2b^2d_{av}^2}\right]. \tag{2}$$

Here d_{av} is the average cluster size. The best fit is obtained with $b=0.63$ and $d_{av}=2.8$ nm. Thus, the average diameter of the clusters in *a*-C:H which, as follows from the selective

TABLE I. Parameters of scattering clusters.

Sample No.	Copper concentration mean, at. %	Parameters of α Eq. (1)	Fractal dimension D	Scatterer diameter, Å	Comments
1	4	5.4	2.0**	32	Many spheres of different radii and with a smooth surface
2	6	3.9	2.1	30	Fractal scatterer
3	14	3.7	2.3	32	Same
3*a**	14	2.9	2.9***	30	Volume (mass) fractal
4	24	3.6	2.4	>48	Fractal scatterer

*Fractal dimension of spherical surface $D=2$.
**Sample 3 after annealing in vacuum.
***Fractal dimension of volume (mass) fractal $D=-a$.

electron diffraction measurements, may be regarded as copper particles,[6] is about 3 nm. The agreement of this estimate with the size of the x-ray scatterers derived at small scattering angles (see Table I) suggests that it is these scatterers that are seen in Fig. 4.

3. DISCUSSION OF RESULTS

The values of the exponent in Eq. (1) found in our experiment (Table I) for the sample with the smallest copper content can be related within the model of spherical scatterers to their size distribution. It was shown that the exponent α can be related to the power-law exponent $\gamma=7-\alpha$ describing the distribution of spherical scatterers in size d bounded by smooth surfaces, which can be written[7] as $P(d)\sim d^{-\gamma}$. For this reason the clusters in the sample with the lowest copper concentration were assigned the fractal dimension $D=2$ (see Table I).

In the case of the lowest copper concentration, γ turns out to be approximately 1.6. Extending this model to higher copper concentrations would, however, produce a unrealistically sharpened distribution. Therefore we propose to take into account, besides the contribution of the scatterer distribution function in size to the angular dependence of scattering intensity, the topology of the surface bounding the scatterer as well. Moreover, the contribution of these factors is assumed to be dependent on the scatterer concentration. For higher copper concentrations, we shall follow the approach[5] by which the values of the exponent in Eq. (1) lie within $3<\alpha<4$ and are related to the fractal dimension D of the scatterer surface through $D=6-\alpha$. The above considerations and the data in Table I suggest that the small-angle x-ray scattering in samples with concentrations above 4 at. % is due to scatterers with a complex surface topology, which can be described in terms of fractal concepts by a noninteger fractal dimension $D<3$. It was found that the dimension D increases with increasing copper concentration. This implies a change in scatterer surface shape from a smooth one at low copper concentration, to a rough one at higher concentrations. The data in Table I show also that the average scatterer diameter remains practically constant, except for the case with the highest copper concentration, and that the size of the scatterers, which most likely are copper clusters,[6] is determined by the mechanical properties of the a-C:H matrix and the parameters of its interaction with cluster material. For low copper concentrations, the distances between clusters are large and clusters are capable of retaining their shape and size, which are totally determined by these parameters. Under these conditions a spherical shape with a smooth surface appears to be natural because of the weak cluster interaction, on the one hand, and of the absence of the Cu–C interaction, on the other. This means that at low copper concentrations and with no cluster interaction the average size of the clusters should be determined only by the relative magnitude of their surface and volume free energies,[8] i.e., by the properties of the cluster and matrix materials, and should not depend on copper concentration. As seen from Table I, for copper concentrations below 24 at. % the average cluster size of 30 Å may be regarded as characteristic of copper clusters in the given medium. As the copper content increases above 24 at. %, the internal (volume) energy of copper clusters becomes large enough to overcome the resistance of the me-

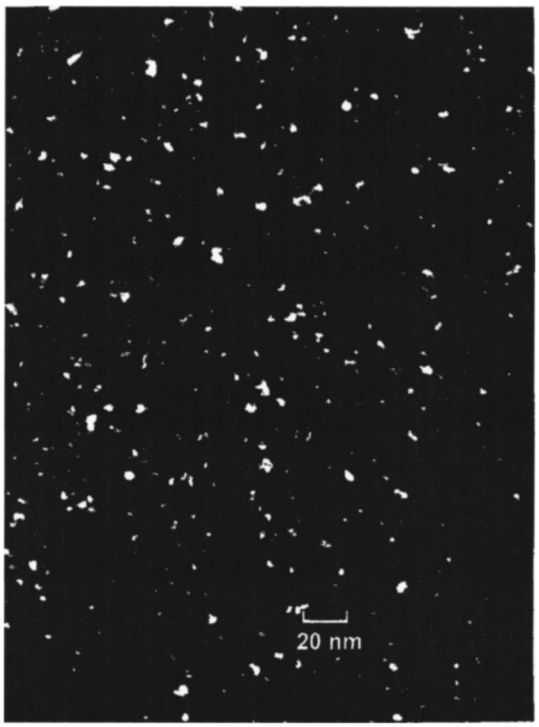

FIG. 4. Dark-field TEM image of copper-containing clusters in an a-C:H(Cu) sample with 9 at. % Cu.

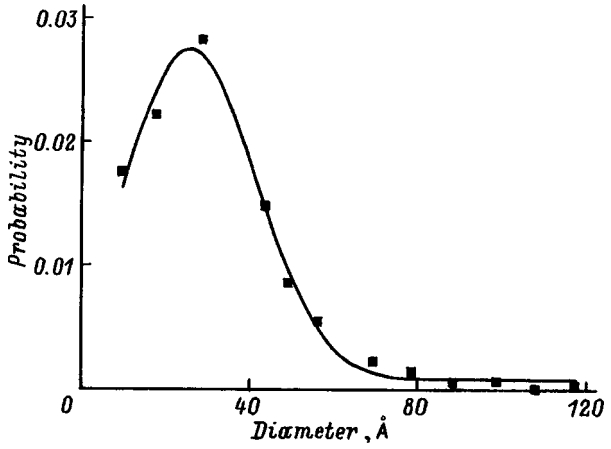

FIG. 5. Distribution function obtained from the TEM image of copper clusters (Fig. 4).

dium to increasing scatterer size. Note also that the vacuum-annealed sample with 14 at. % Cu rearranges its structure (see Table I). Viewed in the light of fractal concepts,[4] the cluster structure thus formed may be characterized as a result of coagulation of the scatterer surface roughness into a smoother structure. This follows from the fractal dimension $D=2.9$. This means, in its turn, that the scattering object resembles a snowball in structure.

The good fit of a Gaussian to the distribution function derived from the TEM images of clusters can be attributed to the fact that the image in Fig. 5 corresponds to the initial phase of formation of copper clusters in the stage of their nucleation. The simultaneous formation of the surrounding matrix interferes with their further growth. In this case the average size of the cluster d_{av} is a function of the ratio of the free energy per unit of its surface to the free energy stored in its volume.[8] The magnitude of the surface energy is determined by the cluster-matrix interaction.

The authors are grateful to A. A. Sitnikova and A. A. Suvorova for the electron microscope studies, to M. V. Baĭdakova for small-angle x-ray scattering measurements, and to A. M. Sedykh and T. K. Zvonareva for sample preparation.

Support of the Russian Fund for Fundamental Research (Grants 97-02-18110 and 97-03-32273), partial support of the Russian Program ''Physics of Solid State Nanostructures,'' of the Arizona University, and of the Russian Program ''Fullerenes and Atomic Clusters'' (Grant 94007) is gratefully acknowledged. One of the authors (V.I.S.) received support from the Government of St. Petersburg and the Ministry of General and Professional Education of the Russian Federation.

[1] J. Li, T. I. Seidel, and J. W. Mayer, MRS Bulletin XIX(8), 18 (1994).
[2] V. I. Ivanov-Omskiĭ and G. S. Frolova, Zh. Tekh. Fiz. **65**, No. 8, 186 (1995) [Tech. Phys. **40**, 851 (1995)].
[3] V. I. Ivanov-Omskii, A. V. Tolmachev, and S. G. Yastrebov, Philos. Mag. B **73**, 715 (1996).
[4] A. Guinier and G. Fournet, *Small-Angle Scattering of X-Rays* (Wiley, New York, 1955).
[5] H. D. Bale and P. W. Schmidt, Phys. Rev. Lett. **53**, 596 (1984).
[6] V. I. Ivanov-Omskii, S. G. Yastrebov, A. A. Suvorova, A. A. Sitnikova, and A. V. Tolmachev, J. Chem. Vapor Depos. **5**, 188 (1997).
[7] O. Glatter, J. Appl. Crystallogr. **12**, 166 (1979).
[8] E. M. Lifshitz and L. P. Pitaevskiĭ, *Physical Kinetics* [Pergamon Press, Oxford, 1981; Nauka, Moscow, 1979].

Translated by G. Skrebtsov

Heat conductivity of three-dimensional regular structures of crystalline and amorphous selenium incorporated in voids of synthetic opal

V. N. Bogomolov, N. F. Kartenko, L. S. Parfen'eva, A. V. Prokof'ev, and I. A. Smirnov

A. F. Ioffe Physicotechnical Institute, Russian Academy of Sciences, 194021 St. Petersburg, Russia

H. Misiorek, J. Mucha, and A. Jezowski

Institute for Low-Temperature and Structural Research, Polish Academy of Sciences, 50-950 Wrocław, Poland

(Submitted September 2, 1997)
Fiz. Tverd. Tela (St. Petersburg) **40**, 573–576 (March 1998)

Opal-based nanocomposites with selenium pressure-injected from the melt into first-order opal voids have been prepared. Two types of nanocomposites, with crystalline and amorphous selenium incorporated in opal voids, were studied. Their thermal conductivities were measured in the temperature range 4.2–200 K. An analysis of these data suggests that a new type of physical media has been developed, namely, quasicrystals with a large lattice constant and heavy ''atomic'' masses, formed from first-order opal voids interconnected by channels and filled by crystalline or amorphous selenium. © *1998 American Institute of Physics.* [S1063-7834(98)03903-3]

This work is a continuation of studies[1–3] of the thermal properties of nanocomposites with a regular crystalline structure. It reports an investigation of the heat conductivity of three-dimensional regular structures made up of crystalline and amorphous selenium incorporated in voids of synthetic opal.

The fractal structure of opals was described in detail in our earlier work.[1–5] Recall the main features of opals, which are needed for the understanding and discussion of the experimental results obtained in this work.

Opals consist of closely packed spheres of amorphous SiO_2 2000–2500 Å in diameter, which are usually called first-order spheres. These spheres contain an array of closely stacked spheres of a smaller size, ~300–400 Å (second-order spheres), which in turn are made up of densely packed particles on the order of 100 Å in size (third-order spheres).

The lattices of the closely-packed spheres in the opal contain octahedral and tetrahedral voids (termed appropriately first-, second-, and third-order). To make consideration simpler (and more revealing), these voids are approximated by spheres interconnected in each order by cylindrical ''channels.'' The diameters of the octahedral and tetrahedral voids and of the first-order channels are, respectively, 800, 400, and 300–400 Å.[1–3]

The first-order voids and SiO_2 spheres form a regular cubic lattice with a period $a \sim 3000–4000$ Å.[2–4]

The total theoretical porosity of the opal is 59% (the first-, second-, and third-order voids make up, respectively, 26, 19, and 14%). The real total porosity of the synthetic opals grown by us was shown[2,3] to be ~46–50%, with the porosity of the first-order sphere structure remaining equal to the theoretical value of 26%.

The thermal conductivity of synthetic opals is similar in magnitude and temperature behavior to that of standard amorphous materials.[1,2]

A thermal-conductivity study[3] of the nanocomposite

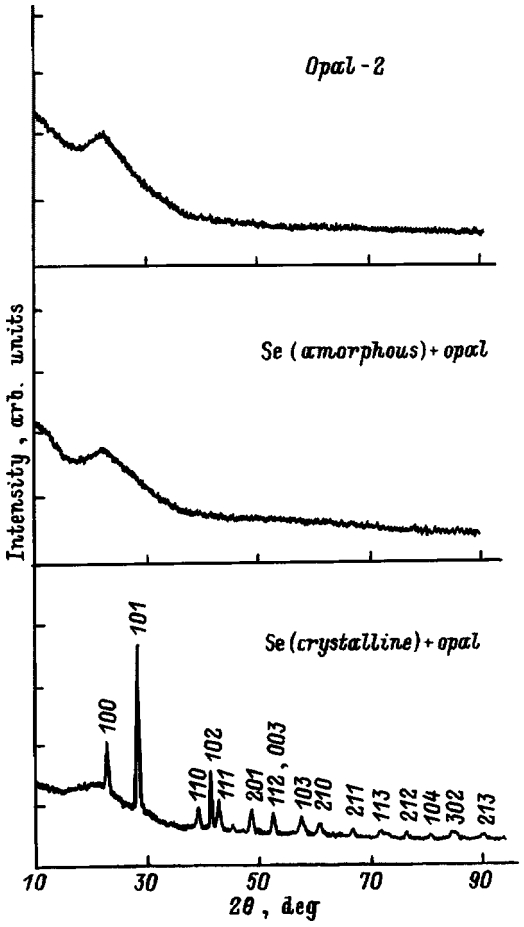

FIG. 1. Diffraction intensity curves for opal-2 and crystalline-Se–opal and amorphous-Se–opal nanocomposites. Selenium is incorporated in first-order voids of opal-2.

 © 1998 American Institute of Physics

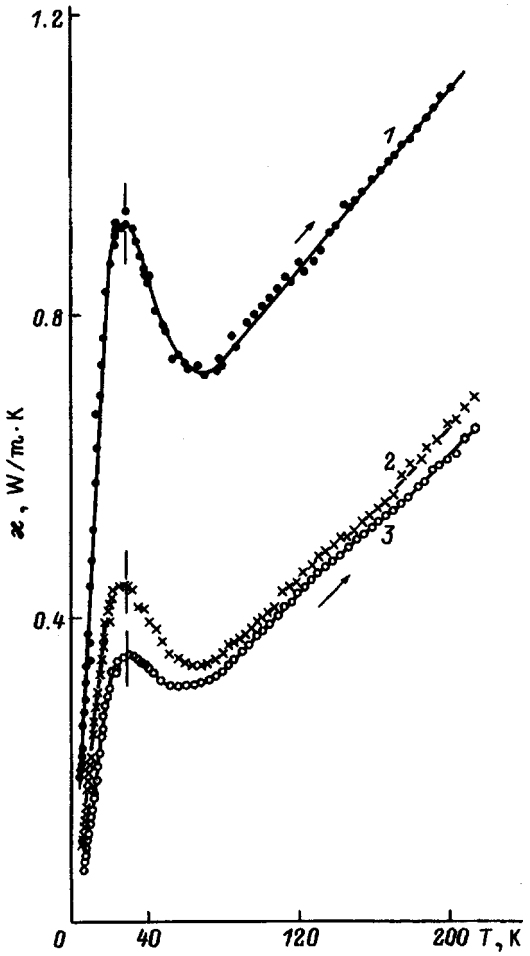

FIG. 2. Temperature dependence of the heat conductivity of (*1*) crystalline-Se–opal-2 nanocomposite and (*2*,*3*) two amorphous-Se–opal-2 nanocomposite samples. The measurements were performed from low (4.2 K) to high (200 K) temperatures. The figures next to the curves identify the sample.

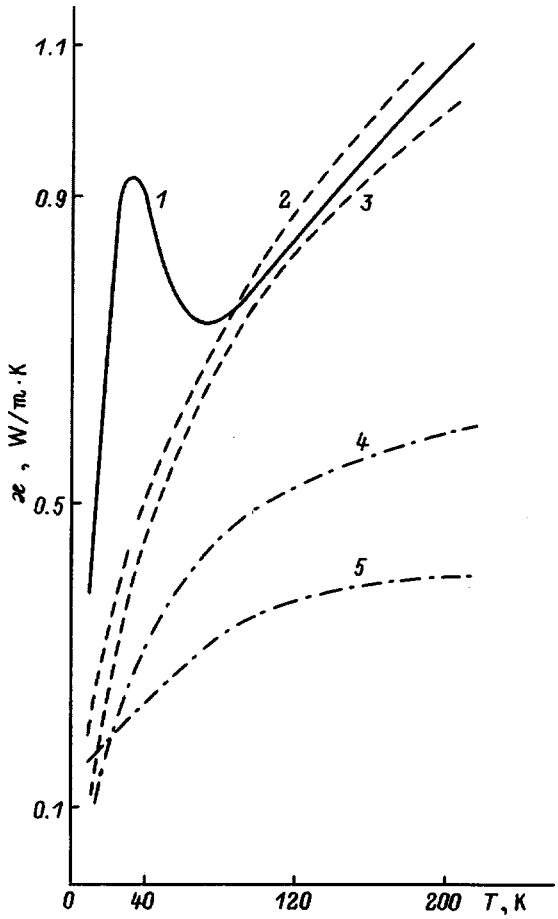

FIG. 3. (*1*) Thermal conductivity $\varkappa(T)$ of the crystalline-Se–opal-2 nanocomposite (sample 1); (*2*,*3*) calculation of $\varkappa$ using Eq. (1) and, respectively, the maximum and minimum values of $\varkappa_f(T)$ from Ref. 11; (4,5) data from Ref. 7; (4) $\varkappa$ of the composite 21.3% corundum (particle diameter 1.8 μm) in epoxy resin; (5) $\varkappa$ of the composite 21.4% quartz (particle diameter 11 μm) in epoxy resin.

made up of crystalline PbSe incorporated in first-order opal voids showed that lead selenide in the opal forms a regular crystalline quasilattice of microcrystals interconnected through the opal matrix, which gives rise to coherent effects and, as a consequence, confers on it properties characteristic of a bulk crystal.

The objectives of this work were (1) to extend the range of nanocomposites consisting of a crystalline substance incorporated in the opal matrix voids, and (2) to see whether introduction of an amorphous rather than crystalline substance into first-order opal voids produces a quasilattice in the nanocomposite.

With this purpose in mind, selenium was pressure-injected from the melt into the first-order opal voids. Density measurements of the samples thus obtained led to the conclusion that selenium completely filled the first-order voids (26%). Two types of nanocomposites were obtained by proper heat treatment of the samples (Fig. 1): (1) hexagonal crystalline selenium ($a=4.366$ Å, $c=4.954$ Å) in opal voids (sample 1); (2) amorphous selenium in opal voids (samples 2 and 3).

Opal-2[1)] was used for the preparation of the nanocomposites. The samples measured $1\times2\times8$ mm.

Phase analysis of the nanocomposites and unit-cell parameter determination of the crystalline selenium in opal-2 employed diffraction patterns obtained on a DRON-2 diffractometer (CuK_α radiation, Ni filter). The pattern presented in Fig. 1 shows well formed crystalline and amorphous selenium in the opal.

As pointed out in Ref. 2, x-ray diffraction studies provide information only on the structure of the material incorporated in opal voids on atomic or molecular scales, and not on the parameters of a cubic lattice with $a\sim3000-4000$ Å, which is formed of first-order voids interconnected by channels. This lattice can be characterized only by means of radiation with a substantially longer wavelength (for instance, by visible light).

The thermal conductivity ($\varkappa$) measurements of the nanocomposites were performed in a vacuum of 10^{-5} Torr on a setup similar to the one described in Ref. 6.

The experimental data on $\varkappa$ of the nanocomposites studied here are presented in Fig. 2. The thermal conductivity was measured in going from low (4.2 K) to high (200 K) temperatures.[2)]

A characteristic feature in the behavior of $\varkappa(T)$ is the presence of maxima around 30 K in both types of nanocom-

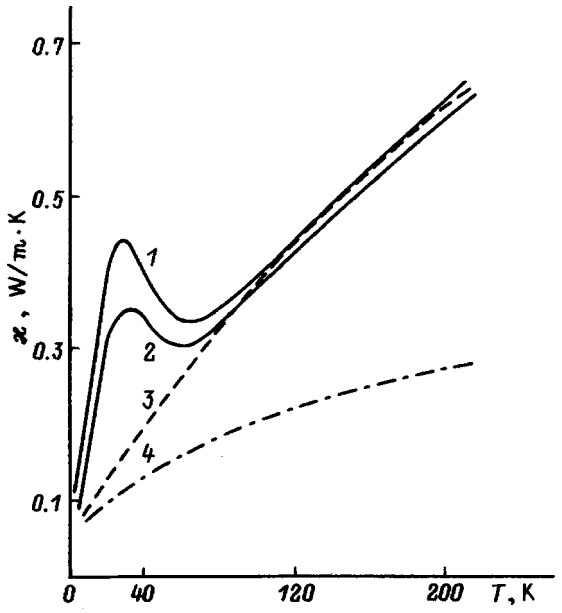

FIG. 4. (1,2) Thermal conductivity $\varkappa(T)$ of the amorphous-Se–opal-2 nanocomposite, sample 2 (*1*) and 3 (*2*); (*3*) calculation of $\varkappa$ using Eq. (1); (*4*) $\varkappa$ of the composite glass spheres (diameter 132 μm) in epoxy resin.

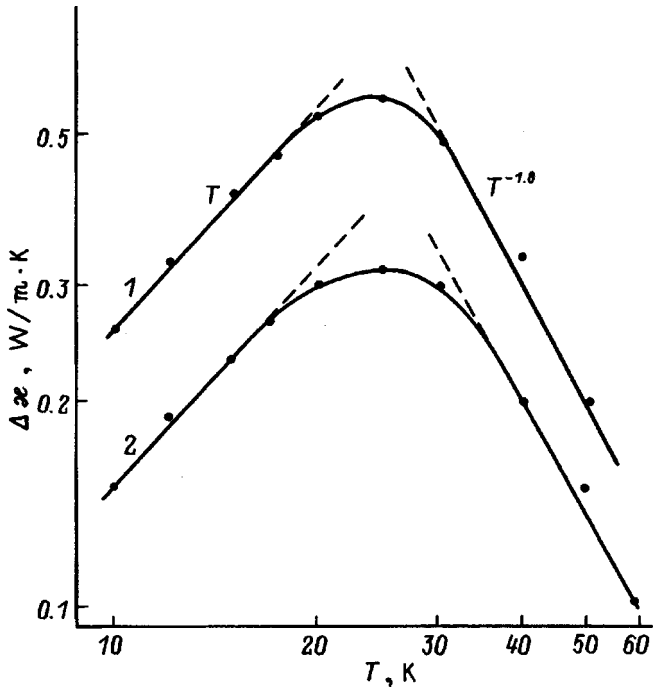

FIG. 5. Temperature dependence of $\Delta\varkappa=\varkappa-\varkappa_{\rm calc}$ for the crystalline-Se–opal-2 and amorphous-Se–opal-2 nanocomposites. The figures at the curves identify the samples.

posites, namely, in crystalline-Se–opal and amorphous-Se–opal, which is inherent only in crystalline materials.

In our discussion of the experimental data on $\varkappa(T)$ of the nanocomposites we shall take an approach different from the one used in Ref. 3.

There is a variety of expressions describing the magnitude and temperature dependence of the $\varkappa$ of composites, and they provide a good fit to experimental data. The relations used with our data were taken from Ref. 7, which studied the thermal conductivity over the range of powders or spheres of various materials (glass, crystalline quartz, corundum, diamond) incorporated in epoxy resin serving as an amorphous matrix. These relations were found[7] to provide good agreement between theory and experiment.

The $\varkappa(T)$ relation[7] for a composite can be written[3)]

$$\varkappa=\varkappa_m(A-2V_f+0.409BV_f^{7/3}-2.133CV_f^{10/3})/$$
$$(A+V_f+0.409BV_f^{7/3}-0.906CV_f^{10/3})\ldots, \qquad (1)$$

where $\varkappa$ is the thermal conductivity of the composite, V_f is the filler volume fraction, $A=(2+\varkappa_d)/(1-\varkappa_d)$, $C=(3-3\varkappa_d)/(4+3\varkappa_d)$, $B=(6+3\varkappa_d)/(4+3\varkappa_d)$, $\varkappa_d=\varkappa_f/\varkappa_m$, and $\varkappa_m$ and $\varkappa_f$ are, respectively, the thermal conductivities of the matrix and of the filler. We determined $\varkappa_m$ using the relations from Ref. 9 and the procedure recommended in Ref. 3. The values of $\varkappa_f$ for amorphous and crystalline selenium were taken, respectively, from a handbook[10] and Ref. 11.

The calculations of $\varkappa$ for the crystalline-Se–opal and amorphous-Se–opal nanocomposites are displayed graphically in Figs. 3 and 4. Also shown for comparison are data for some composites taken from Ref. 7.

As seen from Figs. 3 and 4, $\varkappa$ of the composite grows smoothly with temperature. Our nanocomposite differs from those studied earlier, including the materials investigated in Ref. 7, in that the filler particles, rather than being distributed randomly are arranged in a regular lattice in the opal matrix. This accounts for the crystal-like behavior of $\varkappa(T)$ reflected in the presence of a maximum around 30 K.[4)]

Figure 5 presents $\Delta\varkappa=\varkappa-\varkappa_{\rm calc}$ [where the second term is calculated from Eq. (1)] for both types of the nanocomposites studied here. It is found that for $T<T_{\max}$ we have $\Delta\varkappa\propto T$, and for $T>T_{\max}$ we have $\Delta\varkappa\propto T^{-1.8}$. The observed temperature dependence of $\Delta\varkappa$ requires further investigation.

Thus our experimental data on the thermal conductivity of the crystalline-Se–opal and amorphous-Se–opal nanocomposites imply that in opal selenium forms a regular quasilattice of microparticles. It may be added that the crystalline behavior of the thermal conductivity does not depend on the filler state, in other words, it is unimportant what microparticles the filler consists of, amorphous or crystalline.

We have apparently succeeded in developing by quasichemical engineering a new type of quasicrystals with heavy ''atomic'' masses and a large lattice constant.

Financial support of the Russian Fund for Fundamental Research (Grant 96-03-32458a) is gratefully acknowledged.

[1)]We retain here the terminology accepted in Refs. 1, 2.

[2)]Measurements made from high to low temperatures and in the opposite direction revealed a hysteresis in $\varkappa(T)$ of the nanocomposites similar to the one observed by us earlier[1,2] in opal-2. It was shown[2] that this temperature hysteresis is accounted for by the supercooled water, which is present in closed second- (or third-) order voids of opal-2 and does not contribute to $\varkappa$ when the thermal conductivity is measured from low to high temperatures.

[3)]Eq. (1) used in Ref. 7 was taken from Ref. 8.

[4)]Interestingly, the composite made up of two amorphous components (amorphous Se and amorphous opal) behaves as a crystalline substance.

[1] V. N. Bogomolov, L. S. Parfen'eva, A. V. Prokof'ev, I. A. Smirnov, S. M. Samoĭlovich, A. Jezowski, J. Mucha, and H. Misiorek, Fiz. Tverd. Tela (St. Petersburg) **37**, 3411 (1995) [Phys. Solid State **37**, 1874 (1995)].
[2] V. N. Bogomolov, D. A. Kurdyukov, L. S. Parfen'eva, A. V. Prokof'ev, S. M. Samoĭlovich, I. A. Smirnov, A. Jezowski, J. Mucha, and H. Misiorek, Fiz. Tverd. Tela (St. Petersburg) **39**, 392 (1997) [Phys. Solid State **39**, 341 (1997)].
[3] L. I. Arutyunyan, V. N. Bogomolov, N. F. Kartenko, D. A. Kurdyukov, V. V. Popov, A. V. Prokof'ev, I. A. Smirnov, and N. V. Sharenkova, Fiz. Tverd. Tela (St. Petersburg) **39**, 586 (1997) [Phys. Solid State **39**, 510 (1997)].
[4] V. N. Bogomolov and T. M. Pavlova, Fiz. Tekh. Poluprovodn. **29**, 826 (1995) [Semiconductors **29**, 428 (1995)].
[5] V. N. Bogomolov, Y. A. Kumzerov, S. G. Romanov, and V. V. Zhuravlev, Physica C **208**, 371 (1993).
[6] A. Jezowski, J. Mucha, and G. Pome, J. Phys. D **20**, 739 (1987).
[7] K. W. Garrett and H. M. Rosenberg, J. Phys. D **7**, 1247 (1974).
[8] R. E. Meredith and C. W. Tobias, J. Appl. Phys. **31**, 1270 (1960).
[9] E. Ya. Litovskiĭ, Izv. Akad. Nauk SSSR, Neorg. Mater. **16**, 559 (1980).
[10] *Thermal Conductivity of Solids: a Handbook* [in Russian], edited by A. S. Okhotin (Énergoatomizdat, Moscow, 1984).
[11] G. K. White, S. B. Woods, and M. T. Elford, Phys. Rev. **112**, 111 (1958).

Translated by G. Skrebtsov

Anomalies in the microwave conductivity of a polycrystalline C_{60} membrane

V. F. Masterov and A. V. Prikhod'ko

St. Petersburg State Technical University, 195251 St. Petersburg, Russia

O. I. Kon'kov and V. Yu. Davydov

A. F. Ioffe Physicotechnical Institute, Russian Academy of Sciences, 194021 St. Petersburg, Russia
(Submitted April 25, 1997; resubmitted September 22, 1997)
Fiz. Tverd. Tela (St. Petersburg) **40**, 577–579 (March 1998)

A study is reported of an anomaly in the microwave conductivity of a polycrystalline C_{60} membrane at $T_c = 260$ K (the transition width is 30 K). Raman scattering measurements indicate that the sample is the C_{60} fullerite without any signs of graphitization, amorphous phase, or the presence of C_{70}, and that the detected microwave conductivity jump can be unambiguously identified as due to the C_{60} phase. © *1998 American Institute of Physics.* [S1063-7834(98)04003-9]

Allotropic forms of carbon in different physical states (powder and crystalline graphite, powder fullerite, finely dispersed diamond) are known to reveal similar and interesting features in the behavior of the conductivity at frequencies of the order of 1 GHz (microwave conductivity) and/or at corresponding voltage pulse times of order 10^{-9} s, which are associated with desorption of intercalated oxygen.[1,2]

At the same time one observes in various allotropic forms of carbon and in the corresponding compounds, besides the oxygen-induced temperature anomalies in conductivity, temperature-driven phase transitions. For instance, graphite intercalation compounds[3] are capable of forming a large number of ordered structures, between which various phase transitions, including structural, can take place, that may be connected, for instance, with a change in the order in the layers, e.g., the order–disorder transition in the HNO_3 intercalant for $T < 252$ K). Stable and metastable phase transitions were found to exist in fullerenes as well. For instance, C_{60} exhibits a transition from the primitive cubic to fcc cubic structure at $T = 249$ K,[4–6] with a large degree of rotational disorder in central regions of the planes at high temperatures, and a preferred orientation for the rotating molecules in the low-temperature domain.

We are not aware of any publications on the investigation of structural phase transitions in allotropic carbon modifications, including the fullerenes, by microwave techniques (1-GHz frequency range). Such studies can provide information on what happens with the electromagnetic energy absorbed by a sample in a certain frequency interval.

It should be pointed out that the conductivity changes associated with structural phase transitions in C_{60} are extremely small (the change in conductivity at a phase transition crossed from the high-temperature side varies from about 10^{-9} to 3×10^{-8} Ω^{-1} cm^{-1}, Ref. 7). Therefore in microwave conductivity measurements one should, first, use a method capable of high enough resolution, and, second, it is desirable to take oriented polycrystalline samples with an as small as possible ratio of grain surface to volume in order to attain the maximum effect.

This work studies microwave conductivity anomalies in a polycrystalline C_{60} membrane.

In the microwave measurements we used a method developed by us,[2] which permits detection of very small conductivity changes. The samples were polycrystalline, grain-oriented membranes.

1. EXPERIMENTAL

A. Samples

The samples were membranes prepared of oriented polycrystalline C_{60} in a growth chamber by a technique similar to the one[8] used to produce crystalline fullerenes. The process is as follows. A 100-mg sample of 99%-pure C_{60} powder was placed in a cylindrical chamber mounted on the surface of a heater. The setup was placed into a vacuum chamber pumped out down to 10^{-6} Torr. After this, the crystallization zone was heated to 335 °C, with subsequent heating done at a rate of 0.1 K/s. After the temperature in the evaporation zone has reached 330 °C, the C_{60} powder starts to sublime, and samples form in the crystallization zone. The process continues up to 750 °C. The samples obtained in this way were 3 mm in diameter and 2 mm high at the center.

B. Spectrometric studies

The samples were characterized by Raman scattering spectroscopy. The studies were performed at room temperature with a DFS-24 double-grating monochromator, with its output fed into a computer. The spectra were excited with an argon laser (488 nm). The laser beam was focused to a 200-μm spot. The laser power on the sample was 1 mW. To exclude possible laser-induced modification of the fullerene sample, a control measurement was carried out which showed that a threefold increase of laser power did not produce noticeable changes in the spectra.

 © 1998 American Institute of Physics

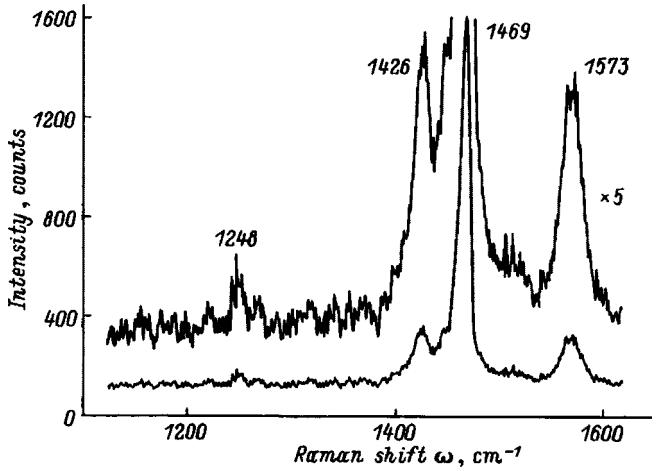

FIG. 1. Raman scattering spectrum of a polycrystalline C_{60} membrane.

Figure 1 presents a Raman spectrum obtained from a membrane. The spectrum of the sample under study is seen to contain sharp peaks characteristic of C_{60} (at 1248, 1426, 1469, and 1573 cm^{-1}, Ref. 9). No other features were observed in the spectrum around 1380 cm^{-1} (graphite) or 1360 cm^{-1} (glassy carbon). Neither were any features seen which could be assigned to C_{70}.

To determine the uniformity of the sample under study, measurements were performed on ten points over the membrane area. Their spectra were found to be identical with that of Fig. 1, which attests to a high uniformity of the sample in phase composition.

Thus experimental measurements indicate that the samples obtained consist only of C_{60}.

C. Microwave studies

Microwave conductivity measurements were carried out with a coaxial $\lambda/4$ resonator consisting of a symmetric two-wire line placed into a circular screen.[2] The coaxial resonator acted as a probe and could be moved over the sample surface. The frequency response of the signal P, with the sample (the distance of the probe to the sample surface was <0.1 mm) and without it, is displayed in Fig. 2a. Figure 2b presents the dependence of the maximum signal amplitude P_{max} (see Fig. 2a) on coordinate x, with the inset showing the resonator probe and the sample (the probe separation $L=0.5$ mm, the screen diameter $D=1$ mm, and the probe diameter $d=0.16$ mm). As seen from microwave loss measurements, the sample resistance practically does not change over all of the sample surface, and remains constant within the temperature interval 300–400 K, in contrast to the results obtained on fullerite powder.[1] Further increase of temperature confers to the temperature behavior of resistance a weakly semiconducting character.

Of most interest are studies of $P_{max}(T)$ at low temperatures. As the temperature is lowered, the sample resistance remains constant to 260 K, after which it increases within a certain temperature interval (a jump in resistance), which washes out in repeated cooling and heating cycles (curves *1* and *2* in Fig. 3). This washout can result from penetration into the sample of water vapor and oxygen, since the measurements were performed in an open system. The width of the transition varies under thermal cycling over the range 30–40 K.

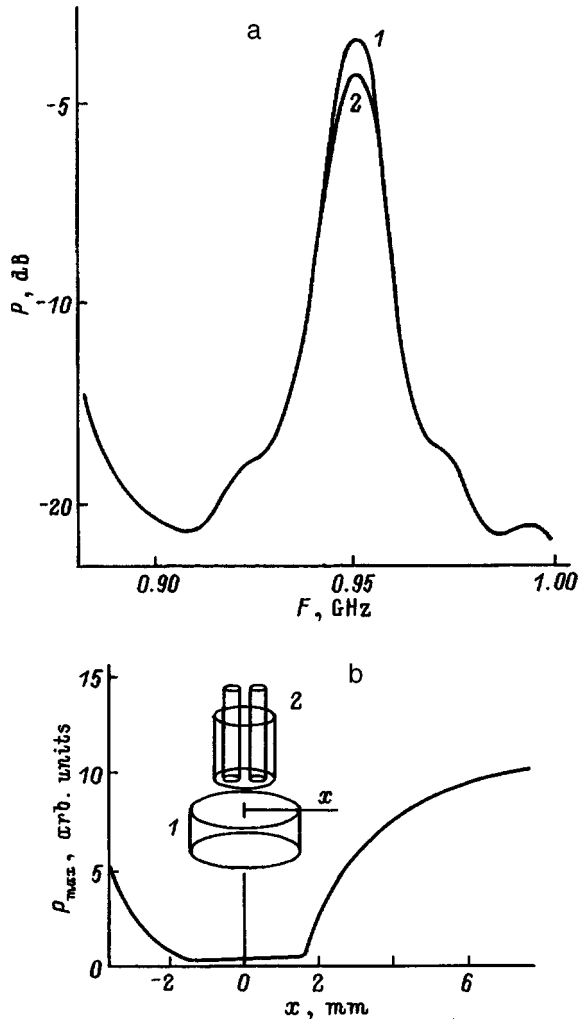

FIG. 2. (a) $P(F)$ relation without sample (*1*) and with a polycrystalline C_{60} membrane (*2*); (b) $P_{max}(x)$ relation for polycrystalline C_{60} membrane. Inset: *1*—sample, *2*—probe-resonator.

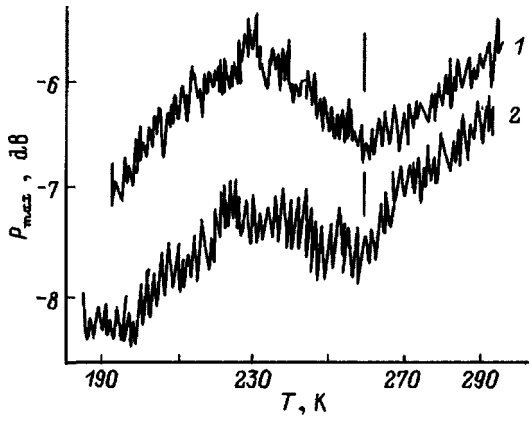

FIG. 3. $P_{max}(T)$ relation for polycrystalline C_{60} membrane. *1–2*—thermal cycling within 180–280 K. The arrow identifies the position of T_c.

2. DISCUSSION OF RESULTS

Based on the spectrometric studies which show that the sample under investigation was the C_{60} fullerite without any indications of graphitization and the presence of an amorphous phase or C_{70}, the above data on the temperature behavior of the resistance can be unambiguously identified with the C_{60} phase.

The absence of any anomaly in the $R(T)$ dependence in the temperature range 300–400 K suggests that oxygen only weakly affects the electrophysical properties of polycrystalline fullerite C_{60}. This is also argued for by the high sample resistance at room temperature and the semiconducting pattern of the $R(T)$ relation in the high-temperature domain. Note also that the sample conductivity practically does not change when the sample is stored under normal conditions for a prolonged time (up to three months).

The jump in resistance at $T=260$ K is evidently related to the structural phase transition observed to occur in single-crystal C_{60} samples.[5] The transition width in this case is 30 K, which is noticeably different from 0.4 K, the value observed in single crystals.[5] Since this difference cannot be associated in our case with the presence of other phases, as was assumed in Ref. 6, we can presume that it is related to defects in the samples.

Raman spectroscopy is known to be sensitive to phase transitions in C_{60}, as well as to the presence of oxygen in C_{60}.[10,11] Therefore studying the Raman scattering intensity as a function of temperature could provide a way of establishing the nature of the observed phenomenon, which is possibly connected with cooperative scattering from coherently vibrating C_{60} molecules with incorporated molecular oxygen. Note that we detected no effects related to intergranular desorption of molecular oxygen. Problems associated with grain orientation in the course of membrane growth also remain unclear. One should most likely expect the microwave conductivity in the growth direction and perpendicular to it to differ strongly.

Our studies show, however, that the electrophysical properties of polycrystalline C_{60} membranes in the microwave range depend only weakly on the environment. A phase transition associated with rotational disorder at high temperatures has been detected for the first time. Raman measurements show polycrystalline C_{60} membranes to be close to C_{60} single crystals.

Support of the ''Fullerenes and Atomic Clusters'' Scientific Council (Project ''Zone'' 94017) and of the Russian Fund for Fundamental Research (Grant 96-02-16886a) is gratefully acknowledged.

[1] V. F. Masterov, A. V. Prikhod'ko, N. I. Nemchuk, A. A. Shaklanov, and O. I. Kon'kov, Fiz. Tverd. Tela (St. Petersburg) **39**, 1703 (1997) [Phys. Solid State **39**, 1522 (1997)].
[2] V. F. Masterov, A. V. Prikhod'ko, O. I. Kon'kov, and A. A. Shaklanov, Fiz. Tverd. Tela (St. Petersburg) **39**, 97 (1997) [Phys. Solid State **39**, 84 (1997)].
[3] N. B. Brandt, S. M. Chudinov, and Ya. G. Ponomarev, ''Semimetals. I. Graphite and Its Compounds,'' *Modern Problems in Condensed Matter Sciences*, Vol. 20, edited by V. M. Agranovich and A. A. Maradudin (North-Holland, Amsterdam, 1988), p. 216.
[4] W. I. F. David, R. M. Ibberson, J. C. Matthewman, K. Prassides, T. J. S. Dennis, J. P. Hare, H. W. Kroto, R. Taylor, and D. R. M. Walton, Nature (London) **353**, 147 (1991).
[5] C. Wen, J. Li, K. Kitazawa, T. Aida, I. Honma, H. Komiyama, and K. Yamada, Appl. Phys. Lett. **61**, 2162 (1992).
[6] J. Mort, R. Ziolo, M. Machonkin, D. R. Huffman, and M. I. Ferguson, Chin. Phys. Lasers **186**, 284 (1991).
[7] H. Peimo, X. Yabo, Z. Xuejia, Z. Xinbin, and L. Wenzhou, J. Phys.: Condens. Matter **5**, 7013 (1993).
[8] K. Kitazawa and T. Araki, Japan Patent N 05-254989 (1993).
[9] R. Meilunas, R. P. H. Chang, S. Liu, M. Jensen, and M. M. Kappes, J. Appl. Phys. **70**, 5128 (1991).
[10] K. Akers, K. Fu, P. Zhang, and M. Moskovits, Science **259**, 1152 (1993).
[11] S. J. Duclos, R. C. Haddon, S. H. Glarum, A. F. Hebard, and K. B. Lyons, Solid State Commun. **80**, 481 (1991).

Translated by G. Skrebtsov

Crystalline structure of a C_{60}/C_{70} membrane

V. F. Masterov, A. V. Prikhod'ko, and T. R. Stepanova

St. Petersburg State Technical University, 195251 St. Petersburg, Russia

V. Yu. Davydov and O. I. Kon'kov

A. F. Ioffe Physicotechnical Institute, Russian Academy of Sciences, 194021 St. Petersburg, Russia
(Submitted July 17, 1997; resubmitted September 22, 1997)
Fiz. Tverd. Tela (St. Petersburg) **40**, 580–583 (March 1998)

The crystalline structure of a C_{60}/C_{70} membrane prepared by an original technique has been studied by x-ray diffraction and Raman spectroscopy. The effects of purification of the starting C_{60}/C_{70} mixture to C_{70} composition and of spatial separation of the C_{60} and C_{70} phases in the membrane have been revealed. The samples studied were established to have a composition gradient from C_{60} to C_{70}. The main structure of the membrane is shown to be an fcc lattice with $a=14.308$ Å. © *1998 American Institute of Physics.* [S1063-7834(98)04103-3]

Studies of the crystalline structure of fullerenes in the form of powder and thin films showed that at room temperature crystalline C_{60} can exist in two phases, fcc with parameter $a=14.2$ Å and hcp with $a=10.0$ Å and $c=16.0$ Å.[1–4] As a rule, the fcc lattice is characteristic of primary crystallization, and thermal treatment (heating to 800 °C, Ref. 3) results in formation of an hcp phase. Crystalline C_{70} also exists in two modifications, namely, fcc with $a=14.89$ Å and hcp with $a=10.53$ Å and $c=17.24$ Å.[4] Different lattice parameter measurements vary within 0.5 Å.[1–5] These discrepancies may be accounted for by the fact that van der Waals forces binding molecules in the crystal are weak, and therefore growth-induced stresses may strongly affect the lattice parameters. Therefore when comparing different measurement data one should take into account the technique by which the crystalline fullerene of interest was prepared.

This work deals with a structural study of a sample of bulk fullerene prepared from a C_{60}/C_{70} mixture.

1. SAMPLES

The samples were polycrystalline membranes fabricated by a modified technique involving sublimation of the original fullerene powder in a growth chamber.[6] Mass spectrometric analysis of the starting GG-4 powder yielded the following composition data: 67% C_{60}, 28% C_{70}, and 2% of the mixture $C_{76,78,84}$ (the powder was prepared and characterized within the State Program ''Fullerenes and Atomic Clusters''). The samples were hemispherical, 3 mm in diameter and 2 mm high in the center. Figure 1 displays schematically the sample and presents a photograph of its section. The side on which sample growth originated is plane I, and the final side is hemisphere II.

2. RAMAN SCATTERING

Our Raman study was carried out at room temperature with a double-grating DFS-24 monochromator. The spectra were excited with an argon laser ($\lambda=488$ nm). The laser power density did not exceed 10 W/cm^2. Control measurements carried out with the excitation density increased three times did not reveal any significant changes in the spectra.

The Raman spectrum of the original powder, shown in Fig. 2a (curve *1*), has lines corresponding to a C_{60}/C_{70} mixture (Table I). Figure 2b presents Raman spectra obtained from sides I and II of the membrane (curves *1* and *2*, respectively). The frequencies of the spectral lines seen in these spectra are also given in Table I. As seen from Fig. 2 and Table I, the Raman spectrum obtained from side I contains sharp peaks characteristic of C_{60}, and that of side II, peaks of C_{70} (see Ref. 7). No other features were detected in the spectrum around 1380 cm^{-1} (graphite) or 1560 cm^{-1} (glassy carbon).

Figure 2a (curve *2*) is the spectrum of the powder left after the membrane preparation. It is seen to differ strongly from the original one and to be close to that of C_{70} fullerene.

3. X-RAY DIFFRACTION ANALYSIS

X-ray structural characterization of the samples was performed with a Geigerflex system (Cu K_α radiation). X-ray diffractograms were also obtained from two sides, I and II. The X-ray spectra are presented in Fig. 3, with the positions of some diffraction maxima being specified in Table II. The data suggest that the structure of side I is dominated by an fcc lattice with parameter $a=14.308$ Å. One also detects a second phase in amounts of about 1%, which has a primitive tetragonal lattice with parameters $a=15.67$ Å and $c=17.72$ Å. The main phase on side II (Fig. 3b) also has an fcc lattice with $a=14.511$ Å. One observes a tetragonal phase amounting to about 4% of total sample volume (see Table II). Thus the main structural component of the sample is an fcc lattice whose parameter varies from 14.308 to 14.511 Å. The lattice parameters of the second phase do not change, and only its amount varies.

Note that the x-ray diffraction pattern of side I is characteristic of a polycrystal with randomly oriented crystallites.[3] At the same time the diffraction data for side II

 © 1998 American Institute of Physics

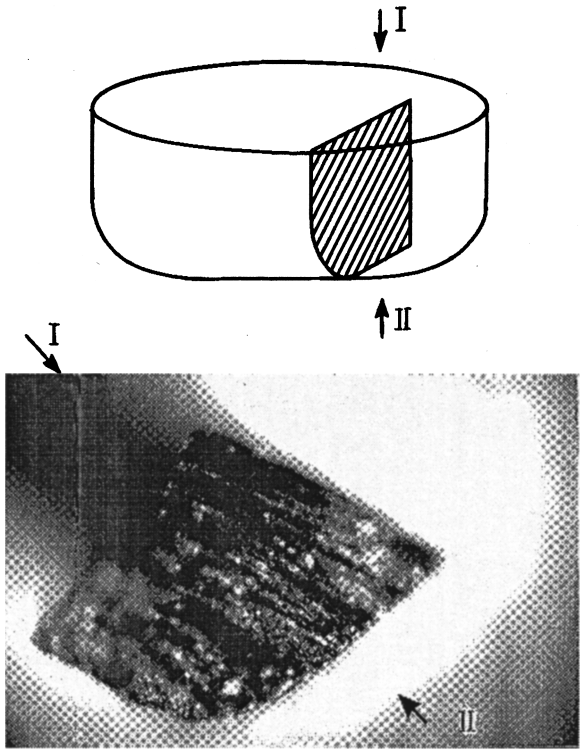

FIG. 1. General view (top) and photograph of a section of polycrystalline C_{60}/C_{70} membrane (bottom).

reveal a preferred orientation in crystallite growth, which is indicated by an increase in the intensity of [220] reflection, and a decrease of [111] reflection.

The x-ray analysis did not also reveal noticeable indications of an amorphous phase or of graphitization, despite the increase of the sublimation temperature during the preparation of the sample up to 750 °C. Note that heating pressed C_{60} powder at temperatures 600–800° converts it to amorphous carbon.[3]

TABLE I. Raman shift (in cm^{-1}) for the memebrane and C_{60}/C_{70} membrane (bottom).

Side I	Side II	Starting powder	Final powder	Composition
	221	221	221	C_{70}
	225	225	225	C_{70}
	250	250	250	C_{70}
	257	257	257	C_{70}
270		270		C_{60}
	409	409	409	C_{70}
438		430		C_{60}
	454	454	454	C_{70}
494		494		C_{60}
	505	505	505	C_{70}
	1185	1185	1185	C_{70}
	1225	1225	1225	C_{70}
	1367	1367	1367	C_{70}
1425		1425		C_{60}
	1443	1443	1443	C_{70}
	1467	1467	1467	C_{70}
1468		1468		C_{60}
	1512	1512	1512	C_{70}
	1562	1562	1562	C_{70}
1569		1569		C_{60}

4. DISCUSSION OF RESULTS

A comparison of Raman data with x-ray diffraction analysis suggests that the sample under study is a fullerite with a composition varying from C_{60} to C_{70}. Indeed, as follows from Raman measurements, side I is the C_{60} fullerene and side II is C_{70}. Note that the sample is analyzed in this case only to a depth of a few μm, whereas x-ray characterization probes the sample to a depth two orders of magnitude larger [the half-attenuation depth for Cu K_α radiation in graphite is 0.36 mm (Ref. 8)]. For fcc C_{60}, $a=14.17$ Å, and for C_{70} it is $a=14.89$ Å. In our case, on side I $a=14.308$ Å, and on side II $a=14.511$ Å. Thus the detected increase of the lattice parameter with crystal growth is

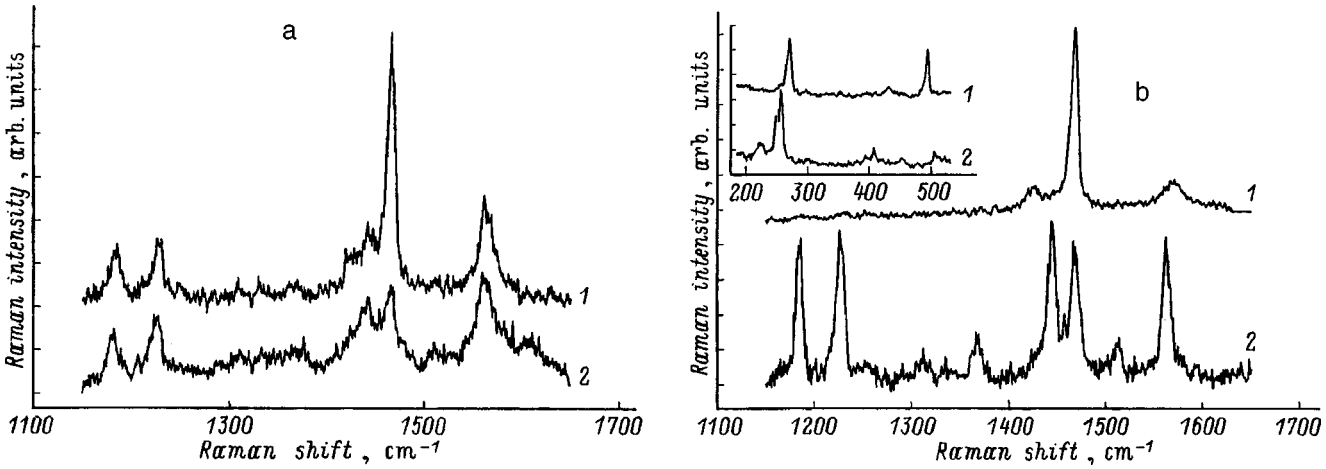

FIG. 2. Raman scattering spectra (a) of the starting C_{60}/C_{70} mixture in the beginning (*1*) and at the end (*2*) of sublimation, and (b and inset) of a polycrystalline C_{60}/C_{70} membrane for (*1*) side I and (*2*) side II.

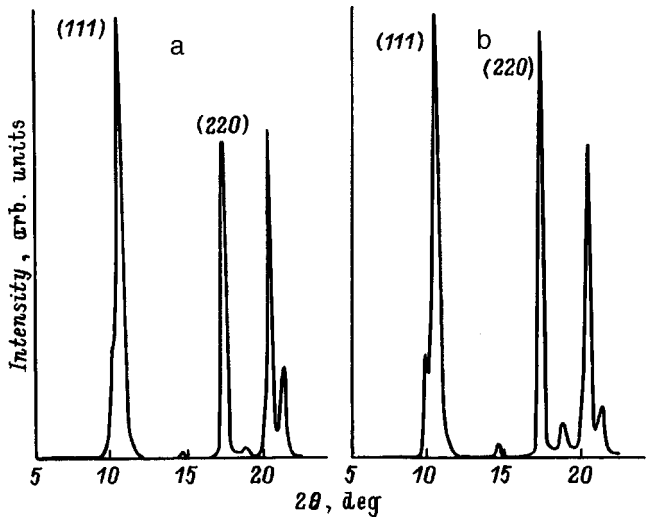

FIG. 3. X-ray diffraction spectrum of a polycrystalline C_{60}/C_{70} membrane for (a) side I and (b) side II.

in accord with the assumption that C_{60} molecules are replaced in the course of growth by C_{70} to form a variable-composition C_{60}/C_{70} solid solution.

It was suggested earlier that the stresses building up in the sample in the course of growth can strongly affect the lattice parameters. In an experiment involving development of the technique the temperature field where the sample was located was varied. It was established that in order to obtain polycrystalline samples (membranes) with a variable composition, the temperature field should have spatial and temporal gradients (temperature range 350–800 °C). The conditions in the growth chamber are apparently similar to those characteristic of temperature-gradient crystallization chambers with slow heating or cooling of the batch. One of the phenomena capable of stimulating the growth of large crystallites (0.2 mm or more in diameter) could be the thermocapillary effect by which pores evaporate during crystallization in the presence of a temperature gradient.[9] This effect could also be responsible for the absence of disordered (amorphous) regions in the sample, which is indicated by x-ray and Raman measurements.

The initial stage in membrane formation could be similar to the growth of thin (10 μm) C_{60} films on mica substrates.[10] The fcc (111) structure begins to form on disordered three-dimensional islands; the island atoms are bound more strongly to one another than to the substrate, and this accounts for the mosaic structure of the crystallites (Fig. 1), which in our case persists up to the mm scale.

An interesting experimental observation relating to modification of the starting fullerene mixture in the course of sublimation might be worth mentioning. As already pointed out, the spectrum of this mixture practically coincides with that characteristic of C_{70} (see Fig. 2 and Table I). Directed purification of the mixture could be an efficient method of producing very high-purity C_{70} or C_{60} membranes.

Such membranes could most likely be used in developing materials with unique electrical properties, ranging from semi- to superconducting. For example, by growing a membrane on $n(p)$-Si, one could produce comparatively easily a $C_{70}/n(p)$-Si heterostructure,[11] while the starting mixture with an addition of metallic impurities could be used to prepare conducting (or superconducting) systems.

Thus a study of C_{60}/C_{70} membranes has revealed spatial separation of the phase composition and modification of the starting mixture, and established the following structural features:

1) The crystalline structure can be identified with a fullerene with composition varying from C_{60} in the beginning of the growth to C_{70} at the end of sample formation;

2) The main structure is an fcc lattice whose parameter a varies from 14.308 to 14.511 Å with increasing C_{70} content;

3) The presence of a second, tetragonal phase with $a=16.57$ Å and $c=17.71$ Å has been established.

Support of the ''Fullerenes and Atomic Clusters'' Scientific Council (Project 94017 ''Zone'') and of the Russian Fund for Fundamental Research (Grant 96-02-16886a) is gratefully acknowledged.

TABLE II. X-ray diffraction characterization (Cu K_α radiation) of a membrane with fcc lattice parameter $a=14.308$ Å (side I) and $a=14.511$ Å (side II) and tetragonal lattice parameters $a=16.57$ Å and $c=17.72$ Å (sides I and II).

	Side I			Side II				
No. n/n	d, Å	2θ, deg.	I, arb. units	d, Å	2θ, deg.	I, arb. units	hkl	Composition
1	8.742	10.06	18	8.864	9.97	22	200	tetr
2	8.261	10.70	100	8.378	10.55	100	111	fcc
3	7.824	11.30	3	7.817	11.30	4	201	tetr
4	6.097	14.66	1	6.062	14.60	3	220	tetr
5	5.057	17.52	53	5.095	17.39	97	220	fcc
6	4.691	18.90	2	4.696	18.88	8	312	tetr
7	4.310	20.59	54	4.341	20.44	69	311	fcc
8	4.143	21.43	15	4.164	21.32	13	222	fcc
9	3.279	27.17	5	3.305	26.95	5	331	fcc
10	3.209	27.77	4	3.216	27.71	8	420	fcc
11	2.915	30.64	9	2.933	30.45	8	422	fcc
12	2.751	32.51	8	2.767	32.32	7	513.333	fcc

[1] W. Krätschmer, L. D. Lamb, K. Fostiropoulos, and D. R. Huffman, Nature (London) **347**, 354 (1990).
[2] A. F. Hebard, R. C. Haddon, R. M. Fleming, and A. R. Kortan, Appl. Phys. Lett. **59**, 2109 (1991).
[3] C. S. Sundar, A. Bharathi, Y. Hariharan, J. Janaki, V. Sankara Sastry, and T. S. Radhakrishnan, Solid State Commun. **84**, 823 (1992).
[4] M. C. Valsakumar, N. Subramanian, M. Yousuf, P. Ch. Sahu, Y. Hariharan, A. Bharathi, V. Sankara Sastry, J. Janaki, G. V. N. Rao, T. S. Radhakrishnan, and C. S. Sundar, Phys. Rev. B **48**, 9080 (1993).
[5] L. Akselrod, H. J. Byrne, T. E. Sutto, and S. Roth, Chin. Phys. Lasers **233**, 436 (1995).
[6] V. F. Masterov, A. V. Prikhod'ko, O. I. Kon'kov, and V. Yu. Davydov, Fiz. Tverd. Tela (St. Petersburg) **40**, 577 (1998) [Phys. Solid State **40**, 532 (1998)].
[7] R. Meilunas, R. P. H. Chang, S. Liu, M. Jensen, and M. M. Kappes, J. Appl. Phys. **70**, 5128 (1991).
[8] L. I. Mirlin, *Handbook on X-ray Diffraction Characterization of Polycrystals* [In Russian] (GIFML, Moscow, 1961).
[9] S. A. Churin, Pis'ma Zh. Tekh. Fiz. **23**, No. 8, 85 (1997) [Tech. Phys. Lett. **23**, 329 (1997)].
[10] A. Fartash, Appl. Phys. Lett. **64**, 1877 (1994).
[11] K. M. Chen, K. Wu, Y. Chen, Y. Q. Jia, S. X. Lin, C. Y. Li, Z. N. Gu, and X. H. Zhou, Appl. Phys. Lett. **67**, 1683 (1995).

Translated by G. Skrebtsov

Structure, internal friction, and Young's modulus of fractal carbon deposits

I. V. Zolotukhin, Yu. V. Sokolov, and V. P. Ievlev

Voronezh State Technical University, 394026 Voronezh, Russia
(Submitted June 25, 1997; resubmitted October 27, 1997)
Fiz. Tverd. Tela (St. Petersburg) **40**, 584–586 (March 1998)

We have observed that carbon deposits obtained by atomizing graphite in an electric arc in an atmosphere of argon and helium exhibit porosity and possess fractal structure. The results of measurements of the internal friction Q^{-1} and the effective Young's modulus E as a function of temperature are presented. Data on the resistivity, density, and microhardness of the carbon deposits are presented. A possible mechanism for formation of fractal structures in carbon deposits is discussed. © *1998 American Institute of Physics.* [S1063-7834(98)04203-8]

Interest in condensed media possessing a fractal structure has intensified in recent years. Obvious examples of such media are carbon deposits obtained by the deposition of carbon on a cathode as a result of the atomization of graphite in an electric arc.[1] Studies of the properties have established that carbon deposits have higher values of microhardness, which are associated with the presence of local microdistortions and finely dispersed regions, than graphite.[2] The structure and mechanisms leading to the formation of a carbon deposit are not entirely clear from the works mentioned above. Moreover, other physical properties of carbon deposits have not been determined at all. In the present work we studied the structure and some physical properties of carbon deposits obtained by atomizing graphite in an electric arc in an atmosphere of argon and helium.

We obtained a carbon deposit by atomizing an OSCh-7-3 graphite rod in an arc discharge with the following parameters: current—180 A and voltage—15–20 V. The atomized graphite was deposited on a flat polished surface of a graphite cathode under argon or helium pressure in the range 10–600 torr. The deposition time was 30 s. The carbon deposit was 500 μm thick. The resulting flat layer of carbon deposit was separated from the polished surface of the graphite cathode. A portion of the deposit was used for studying the surface structure with a REM-300 scanning electron microscope and a portion was cut into plates, whose surface was worked and polished. Samples of single-crystal graphite were subjected to the same treatment. After being mechanically processed the graphite and carbon deposit samples had the following dimensions: length—5–10 mm, width—1.5–2.5 mm, and thickness—0.1–1.3 mm. The stresses obtained as a result of mechanical treatment were removed by annealing at 873 K. The density of the carbon deposits was determined with an error of 3–5% by means of hydrostatic weighing in M20 balances. The resistivity was measured at room temperature by a four-probe method with a relative error of 10%. The microhardness was measured with a relative error of 15% on a PMT-3 apparatus.

The internal friction of cantilevered samples was measured by the method of Ref. 3 in the frequency interval 10^2-10^4 Hz with relative deformation no greater than 10^{-5}. The relative error in measuring Q^{-1} was at most 1–3%. The effective Young's modulus was measured by exciting flexural resonant oscillations in the sample and calculated using the expression[4,5]

$$E=48\pi^2 l^4 \rho f^2/m^4 h^2, \tag{1}$$

where $m=1.8751$, l is the length, ρ is the density, h is the thickness of the sample, and f is the resonant frequency of the oscillations. The main error in determining E is associated with the nonuniformity of the sample thickness and is less than 5%.

Figure 1 shows the results of measurements of the internal friction Q^{-1} (a) and Young's modulus E (b) as a function of temperature. The highest level of internal friction ($\sim 1\times 10^{-2}$) is observed in the case of a carbon deposit obtained in an argon atmosphere (curve *1*) and the lowest level is obtained for a carbon deposit obtained in helium ($\sim 5\times 10^{-3}$) (curve *2*). Heating up to 900 K does not reveal any features in the Q^{-1} curves and characterizes the structural stability of the materials obtained.

One feature of $E(T)$ in both the graphite and carbon deposits is a weak temperature dependence in the range 293–900 K, attesting to the weak effect of temperature on the bond strength of the particles forming the deposit.

The values of Young's modulus, internal friction, microhardness, resistivity, and density for deposits and single-crystal graphite at 300 K are presented in Table I. One can see that the microhardness H_V of the carbon deposits obtained in argon and helium equals 5.95 and 6.87 GPa, respectively, while H_V of single-crystal graphite equals 0.05 GPa. The data show that covalent bonds are realized between carbon atoms in the deposit.

The surface structure of the carbon deposits is presented in Fig. 2a. It is reminiscent of the structure of dust particles grown in a helium plasma with graphite electrodes with a microwave discharge with frequency 15 MHz and pressure 1 Torr.[6] Quite large (~ 1 μm) cloud-shaped formations are visible with higher magnification (Fig. 2b); these formations in turn consist of smaller, rounded clusters 0.2–0.3 μm in size. In the case of the carbon deposit obtained in a helium atmosphere the surface of such clusters (Fig. 2c) seems to be coated with a ''lint'' consisting of carbon filaments of the

 © 1998 American Institute of Physics

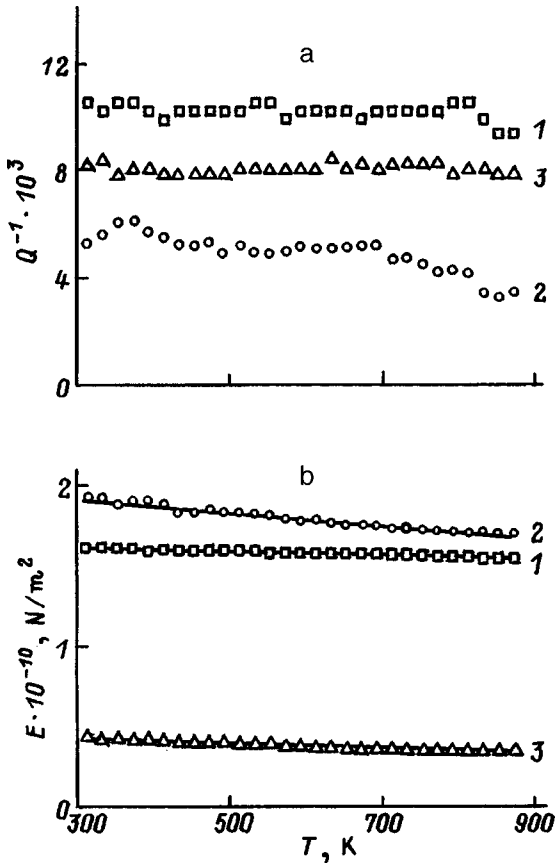

FIG. 1. Internal friction (a) and Young's modulus (b) versus temperature for carbon deposits obtained in argon (*1*) and helium (*2*). 3—For single-crystal graphite.

order of 3–4 μm long and about 0.065–0.15 μm in diameter. Such lint is not observed in the case when the deposit is obtained in an argon atmosphere.

An STM study of the initial stages of nucleation of carbon deposits showed that the structure consists of 6–8 nm spherical carbon clusters and solid capsules up to 5–10 diameters long. According to our models, some spherical clusters have an amorphous carbon structure. The other clusters are multilayered spherical or polyhedral formations of carbon (structurally similar to fullerenes) whose surface consists of pentagons and hexagons. The ideas presented above agree with Ref. 7, according to which amorphous and block-structured particles are formed on the cathode as a result of cooling of the fused carbon nanocrystals. The solid capsules are most likely multishell nanotubes with closed ends. The spherical clusters and solid capsules serve as the main material for the formation of 0.15–0.45 μm aggregates. In the process of formation of a carbon deposit, aggregates form macroscopic cloud-shaped formations $\sim$1 μm in size, which

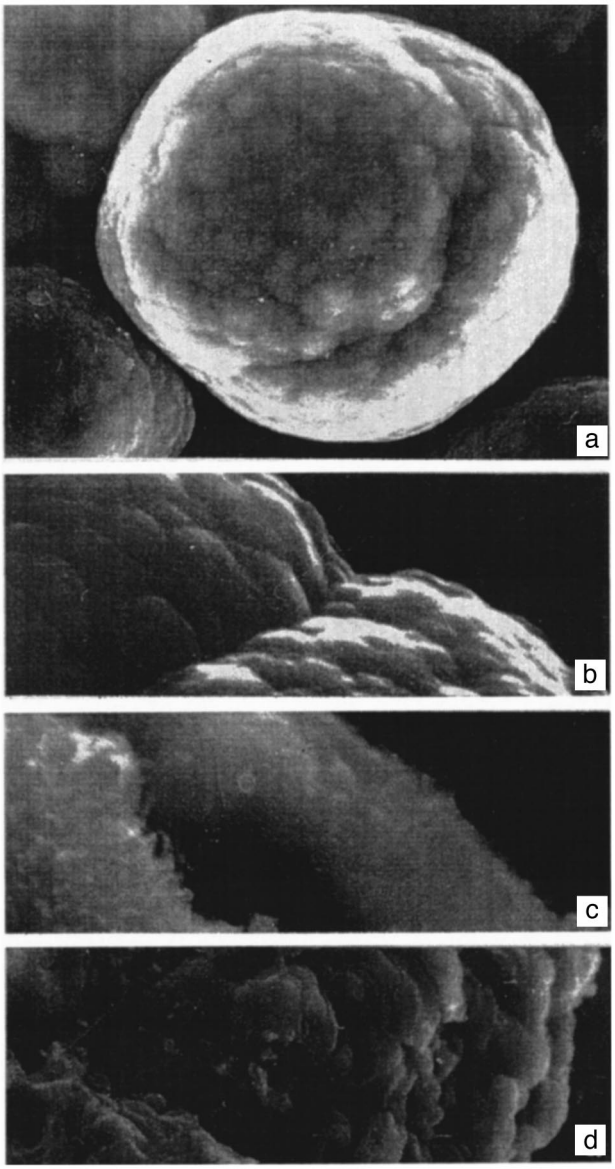

FIG. 2. Surface structure of carbon deposits obtained in a helium atmosphere. a—$\times$1700, b—$\times$10800, c—$\times$7800, d—$\times$1420.

in turn form a $\sim$40 μm structure reminiscent of a head of cauliflower. The process leading to the formation of the structure of the carbon deposit can be represented qualitatively as follows. Small fractal aggregates form from the carbon clusters produced in the electric plasma. These fractal aggregates then stick together by the mechanism of dust-particle formation,[8] just as in a self-organizing system with a high rate of dissipation of energy.

The density of the carbon deposits equals 59–61% of the density of the single-crystal graphite, while the microhard-

TABLE I. Some physical properties of carbon deposits obtained in an atmosphere of argon and helium and of single-crystal graphite at 300 K.

Material	$E\times10^{-10}$, N/m^2	$Q^{-1}\times10^3$	H_v, GPa	ρ_r, $\Omega\cdot$m	ρ, g/cm^3
Carbon deposit (argon)	1.625	10.88	5.95	$(1.74-4.17)\times10^{-4}$	1.32
Carbon deposit (helium)	1.924	5.44	6.87	$(1.36-2.00)\times10^{-4}$	1.36
Single-crystal graphite	0.43	8.09	0.05	2.63×10^{-5}	2.23

ness is 120–130 times higher than that of single-crystal graphite. These data show that the structure of a carbon deposit consists of a quite rigid framework with a substantial volume of porosity. This is demonstrated by the extended surface of a chip of the carbon deposit (Fig. 2d).

To calculate the fractal dimension of the carbon deposits we shall use a model of fractal aggregates consisting of clusters with radius r_0 and the graphite density ρ_0.[9] The number of clusters in a fractal aggregate whose radius satisfies $R \gg r_0$ is determined as

$$N(r)=(R/r_0)^D, \quad 1<D<3, \tag{2}$$

where D is the fractal dimension. From Eq. (2) follows an expression for the density of the substance in a sphere of radius R

$$\rho=\rho_0(r_0/R)^{3-D}, \tag{3}$$

where ρ is the density of the carbon deposit. For carbon deposits obtained in argon and helium the density equals, respectively, 1.32 and 1.36 g/cm^3, R equals 4.5×10^{-5} and 1.5×10^{-5} cm, $\rho_0=2.23$ g/cm^3, and $r_0=4\times10^{-7}$ cm. We obtain $D=2.89$ and 2.86, respectively.

In summary, the properties of carbon deposits are similar to those of SiO_2 aerogels, whose fractal nature is well known.[9] As a result of their high porosity carbon deposits can be recommended for use as adsorbents and thermal insulators.

[1] V. P. Bubnov, I. S. Krainskiĭ, E. É. Laukhina, and É. B. Yagubskiĭ, Izv. Akad. Nauk. SSR, Ser. Khi. **5**, 805 (1994).
[2] Yu. S. Grushko, V. M. Egorov, I. N. Zimkin, T. S. Orlova, and B. I. Smirnov, Fiz. Tverd. Tela (St. Petersburg) **37**, 1838 (1995) [Phys. Solid State **37**, 1001 (1995)].
[3] V. K. Belonogov, I. V. Solotukhin, V. M. Ievlev, and V. S. Postnikov, Fiz. Khim. Obrab. Mater. **5**, 164 (1968).
[4] T. J. Koneko, J. Non-Cryst. Solids **21**, 435 (1976).
[5] K. Ouzimi, H. Honda, H. Yokota, and H. Ebisu, Thin Solid Films **34**, 221 (1976).
[6] A. Garscadden, Plasma Sources Sci. Technol. **3**, 239 (1994).
[7] Yu. E. Lozovik and A. M. Popov, Usp. Fiz. Nauk **167**, 751 (1997).
[8] V. N. Tsytovich, Usp. Fiz. Nauk **167**, 57 (1997).
[9] B. M. Smirnov, Usp. Fiz. Nauk **152**, 133 (1987) [Sov. Phys. Usp. **30**, 420 (1987)].

Translated by M. E. Alferieff